

DOC FILE COPY



**DYNAMICS
RESEARCH
CORPORATION**



ADA 079924

Report No. NADC-76097-30-Vol-3

14 DR-287U-1273-Vol-3



6
APPLICATION OF THE ESTIMATION-BEFORE-MODELING
(EBM) SYSTEM IDENTIFICATION METHOD TO THE
HIGH ANGLE OF ATTACK/SIDESLIP
FLIGHT OF THE T-2C JET TRAINER AIRCRAFT.

Volume III • Identification of T-2C
Aerodynamics, Stability and Control
Characteristics from Actual Flight Test Data

9 Final Rept.

11 April 1979

12256

DDC

REPORTING JAN 29 1980
RECEIVED A

10 Harold L. Stalsford
Prepared for
Naval Air Development Center
Warminster, Pennsylvania 18974

15
Contract No. N62269-76-C-0342

Prepared by:

DYNAMICS RESEARCH CORPORATION

Systems Division

60 Concord Street

Wilmington, Massachusetts 01887

408218

APPROVED FOR PUBLIC RELEASE: DISTRIBUTION UNLIMITED

Unclassified

SECURITY CLASSIFICATION OF THIS PAGE (When Data Entered)

DD FORM 1 JAN 73 1473 EDITION OF 1 NOV 68 IS OBSOLETE

Unclassified

SECURITY CLASSIFICATION OF THIS PAGE (Initial Date Entered)

Unclassified

SECURITY CLASSIFICATION OF THIS PAGE (If Different From Document)

In the second step of the EBM method, the step-wise multiple linear regression technique and subspace modeling are used to identify detailed models of $C_{\alpha y}$, $C_{\alpha \beta}$, $C_{\alpha n}$ and $C_{\alpha m}$. Partial results are given for $C_{\alpha y}$ and $C_{\alpha n}$. The state and control derivatives of the identified model agree well with the wind tunnel model. Most of the identified dynamic derivatives compare well with the theoretically predicted value at low alpha and some compare well at high alpha. One identified dynamic derivative which doesn't compare well at high alpha is $C_{n \alpha}$. At high alpha, $C_{n \alpha}$ is predicted to have values above .10; the identified model gives values around -.075. The simulation study of Ref. [1] not only found the theoretical prediction model of $C_{n \alpha}$ to be inaccurate at high alpha but found that synthetic responses generated by using a constant value of -.06 mimics the real data fairly well. The derivatives $C_{y \alpha}$, $C_{\beta \alpha}$, $C_{n \alpha}$ and $C_{m \alpha}$ are identified as nonlinear functions of α and β . The derivative $C_{m \beta}$ is identified as a nonlinear function of α and δ_e .

Unclassified

SECURITY CLASSIFICATION OF THIS PAGE (If Different From Document)

FOREWORD

The work described in this report was sponsored by the Flight Dynamics Branch of the Air Vehicle Technology Department of the Naval Air Development Center. Mr. Robert L. Fortenbaugh, Mr. A. Piranian, Mr. Ronald L. Nave and Mr. John Clark served as the Navy Technical Monitors for the Naval Air Development Center. Mr. Carmen J. Mazza was NADC program manager.

The project was managed by Dr. Harold Stalford. The author extends his thanks to Mr. Joseph D. Mason who provided computational support.

Perception For	1
PPPE	2
PPPE	3
PPPE	4
PPPE	5
PPPE	6
PPPE	7
PPPE	8
PPPE	9
PPPE	10
PPPE	11
PPPE	12
PPPE	13
PPPE	14
PPPE	15
PPPE	16
PPPE	17
PPPE	18
PPPE	19
PPPE	20
PPPE	21
PPPE	22
PPPE	23
PPPE	24
PPPE	25
PPPE	26
PPPE	27
PPPE	28
PPPE	29
PPPE	30
PPPE	31
PPPE	32
PPPE	33
PPPE	34
PPPE	35
PPPE	36
PPPE	37
PPPE	38
PPPE	39
PPPE	40
PPPE	41
PPPE	42
PPPE	43
PPPE	44
PPPE	45
PPPE	46
PPPE	47
PPPE	48
PPPE	49
PPPE	50
PPPE	51
PPPE	52
PPPE	53
PPPE	54
PPPE	55
PPPE	56
PPPE	57
PPPE	58
PPPE	59
PPPE	60
PPPE	61
PPPE	62
PPPE	63
PPPE	64
PPPE	65
PPPE	66
PPPE	67
PPPE	68
PPPE	69
PPPE	70
PPPE	71
PPPE	72
PPPE	73
PPPE	74
PPPE	75
PPPE	76
PPPE	77
PPPE	78
PPPE	79
PPPE	80
PPPE	81
PPPE	82
PPPE	83
PPPE	84
PPPE	85
PPPE	86
PPPE	87
PPPE	88
PPPE	89
PPPE	90
PPPE	91
PPPE	92
PPPE	93
PPPE	94
PPPE	95
PPPE	96
PPPE	97
PPPE	98
PPPE	99
PPPE	100
PPPE	101
PPPE	102
PPPE	103
PPPE	104
PPPE	105
PPPE	106
PPPE	107
PPPE	108
PPPE	109
PPPE	110
PPPE	111
PPPE	112
PPPE	113
PPPE	114
PPPE	115
PPPE	116
PPPE	117
PPPE	118
PPPE	119
PPPE	120
PPPE	121
PPPE	122
PPPE	123
PPPE	124
PPPE	125
PPPE	126
PPPE	127
PPPE	128
PPPE	129
PPPE	130
PPPE	131
PPPE	132
PPPE	133
PPPE	134
PPPE	135
PPPE	136
PPPE	137
PPPE	138
PPPE	139
PPPE	140
PPPE	141
PPPE	142
PPPE	143
PPPE	144
PPPE	145
PPPE	146
PPPE	147
PPPE	148
PPPE	149
PPPE	150
PPPE	151
PPPE	152
PPPE	153
PPPE	154
PPPE	155
PPPE	156
PPPE	157
PPPE	158
PPPE	159
PPPE	160
PPPE	161
PPPE	162
PPPE	163
PPPE	164
PPPE	165
PPPE	166
PPPE	167
PPPE	168
PPPE	169
PPPE	170
PPPE	171
PPPE	172
PPPE	173
PPPE	174
PPPE	175
PPPE	176
PPPE	177
PPPE	178
PPPE	179
PPPE	180
PPPE	181
PPPE	182
PPPE	183
PPPE	184
PPPE	185
PPPE	186
PPPE	187
PPPE	188
PPPE	189
PPPE	190
PPPE	191
PPPE	192
PPPE	193
PPPE	194
PPPE	195
PPPE	196
PPPE	197
PPPE	198
PPPE	199
PPPE	200
PPPE	201
PPPE	202
PPPE	203
PPPE	204
PPPE	205
PPPE	206
PPPE	207
PPPE	208
PPPE	209
PPPE	210
PPPE	211
PPPE	212
PPPE	213
PPPE	214
PPPE	215
PPPE	216
PPPE	217
PPPE	218
PPPE	219
PPPE	220
PPPE	221
PPPE	222
PPPE	223
PPPE	224
PPPE	225
PPPE	226
PPPE	227
PPPE	228
PPPE	229
PPPE	230
PPPE	231
PPPE	232
PPPE	233
PPPE	234
PPPE	235
PPPE	236
PPPE	237
PPPE	238
PPPE	239
PPPE	240
PPPE	241
PPPE	242
PPPE	243
PPPE	244
PPPE	245
PPPE	246
PPPE	247
PPPE	248
PPPE	249
PPPE	250
PPPE	251
PPPE	252
PPPE	253
PPPE	254
PPPE	255
PPPE	256
PPPE	257
PPPE	258
PPPE	259
PPPE	260
PPPE	261
PPPE	262
PPPE	263
PPPE	264
PPPE	265
PPPE	266
PPPE	267
PPPE	268
PPPE	269
PPPE	270
PPPE	271
PPPE	272
PPPE	273
PPPE	274
PPPE	275
PPPE	276
PPPE	277
PPPE	278
PPPE	279
PPPE	280
PPPE	281
PPPE	282
PPPE	283
PPPE	284
PPPE	285
PPPE	286
PPPE	287
PPPE	288
PPPE	289
PPPE	290
PPPE	291
PPPE	292
PPPE	293
PPPE	294
PPPE	295
PPPE	296
PPPE	297
PPPE	298
PPPE	299
PPPE	300
PPPE	301
PPPE	302
PPPE	303
PPPE	304
PPPE	305
PPPE	306
PPPE	307
PPPE	308
PPPE	309
PPPE	310
PPPE	311
PPPE	312
PPPE	313
PPPE	314
PPPE	315
PPPE	316
PPPE	317
PPPE	318
PPPE	319
PPPE	320
PPPE	321
PPPE	322
PPPE	323
PPPE	324
PPPE	325
PPPE	326
PPPE	327
PPPE	328
PPPE	329
PPPE	330
PPPE	331
PPPE	332
PPPE	333
PPPE	334
PPPE	335
PPPE	336
PPPE	337
PPPE	338
PPPE	339
PPPE	340
PPPE	341
PPPE	342
PPPE	343
PPPE	344
PPPE	345
PPPE	346
PPPE	347
PPPE	348
PPPE	349
PPPE	350
PPPE	351
PPPE	352
PPPE	353
PPPE	354
PPPE	355
PPPE	356
PPPE	357
PPPE	358
PPPE	359
PPPE	360
PPPE	361
PPPE	362
PPPE	363
PPPE	364
PPPE	365
PPPE	366
PPPE	367
PPPE	368
PPPE	369
PPPE	370
PPPE	371
PPPE	372
PPPE	373
PPPE	374
PPPE	375
PPPE	376
PPPE	377
PPPE	378
PPPE	379
PPPE	380
PPPE	381
PPPE	382
PPPE	383
PPPE	384
PPPE	385
PPPE	386
PPPE	387
PPPE	388
PPPE	389
PPPE	390
PPPE	391
PPPE	392
PPPE	393
PPPE	394
PPPE	395
PPPE	396
PPPE	397
PPPE	398
PPPE	399
PPPE	400
PPPE	401
PPPE	402
PPPE	403
PPPE	404
PPPE	405
PPPE	406
PPPE	407
PPPE	408
PPPE	409
PPPE	410
PPPE	411
PPPE	412
PPPE	413
PPPE	414
PPPE	415
PPPE	416
PPPE	417
PPPE	418
PPPE	419
PPPE	420
PPPE	421
PPPE	422
PPPE	423
PPPE	424
PPPE	425
PPPE	426
PPPE	427
PPPE	428
PPPE	429
PPPE	430
PPPE	431
PPPE	432
PPPE	433
PPPE	434
PPPE	435
PPPE	436
PPPE	437
PPPE	438
PPPE	439
PPPE	440
PPPE	441
PPPE	442
PPPE	443
PPPE	444
PPPE	445
PPPE	446
PPPE	447
PPPE	448
PPPE	449
PPPE	450
PPPE	451
PPPE	452
PPPE	453
PPPE	454
PPPE	455
PPPE	456
PPPE	457
PPPE	458
PPPE	459
PPPE	460
PPPE	461
PPPE	462
PPPE	463
PPPE	464
PPPE	465
PPPE	466
PPPE	467
PPPE	468
PPPE	469
PPPE	470
PPPE	471
PPPE	472
PPPE	473
PPPE	474
PPPE	475
PPPE	476
PPPE	477
PPPE	478
PPPE	479
PPPE	480
PPPE	481
PPPE	482
PPPE	483
PPPE	484
PPPE	485
PPPE	486
PPPE	487
PPPE	488
PPPE	489
PPPE	490
PPPE	491
PPPE	492
PPPE	493
PPPE	494
PPPE	495
PPPE	496
PPPE	497
PPPE	498
PPPE	499
PPPE	500
PPPE	501
PPPE	502
PPPE	503
PPPE	504
PPPE	505
PPPE	506
PPPE	507
PPPE	508
PPPE	509
PPPE	510
PPPE	511
PPPE	512
PPPE	513
PPPE	514
PPPE	515
PPPE	516
PPPE	517
PPPE	518
PPPE	519
PPPE	520
PPPE	521
PPPE	522
PPPE	523
PPPE	524
PPPE	525
PPPE	526
PPPE	527
PPPE	528
PPPE	529
PPPE	530
PPPE	531
PPPE	532
PPPE	533
PPPE	534
PPPE	535
PPPE	536
PPPE	537
PPPE	538
PPPE	539
PPPE	540
PPPE	541
PPPE	542
PPPE	543
PPPE	544
PPPE	545
PPPE	546
PPPE	547
PPPE	548
PPPE	549
PPPE	550
PPPE	551
PPPE	552
PPPE	553
PPPE	554
PPPE	555
PPPE	556
PPPE	557
PPPE	558
PPPE	559
PPPE	560
PPPE	561
PPPE	562
PPPE	563
PPPE	564
PPPE	565
PPPE	566
PPPE	567
PPPE	568
PPPE	569
PPPE	570
PPPE	571
PPPE	572
PPPE	573
PPPE	574
PPPE	575
PPPE	576
PPPE	577
PPPE	578
PPPE	579
PPPE	580
PPPE	581
PPPE	582
PPPE	583
PPPE	584
PPPE	585
PPPE	586
PPPE	587
PPPE	588
PPPE	

TABLE OF CONTENTS

	<u>Page No.</u>
1. INTRODUCTION	1-1
1.1 Background	1-1
1.2 Scope of Flight Data Analysis Study	1-1
1.3 Estimation Before Modeling (EBM) Method	1-2
2. SCENARIO OF THE T-2C SYSTEM IDENTIFICATION PROBLEM	2-1
2.1 Flight Test Conditions and Description of Maneuvers	2-1
2.2 T-2C Instrumentation-Measurement Equation	2-3
2.3 The T-2C Aircraft Constants	2-7
2.4 Equations of Motion	2-10
2.5 Transformation to Non-dimensional Aerodynamic Coefficients	2-12
3. ESTIMATION RESULTS	3-1
3.1 Comparison of Estimated Values with Measured Values	3-1
3.2 Estimates of Biases and Scale Factors	3-2
3.3 Some Observations on the T-2C Data	3-4
4. IDENTIFICATION OF THE T-2C LATERAL AERODYNAMICS CHARACTERISTICS	4-1
4.1 Construction of Subspaces for Lateral Modeling	4-1
4.2 Identification of C_y	4-4
4.3 Identification of C_s	4-13
4.4 Identification of C_n	4-24
5. IDENTIFICATION OF THE T-2C LONGITUDINAL AERODYNAMICS CHARACTERISTICS	5-1
5.1 Construction of Subspaces for Longitudinal Modeling	5-1
5.2 Identification of C_m	5-3
5.3 Results on the C_z Model	5-24
5.4 Results on the C_x Model	5-25
6. SUMMARY OF RESULTS AND CONCLUSIONS	6-1
7. RECOMMENDATIONS	7-1
REFERENCES	R-1

APPENDICES

		<u>Page No.</u>
Appendix A	Comparison of Airspeed Measurements	A-1
B	Estimation Results of the T-2C Flight Test Data	B-1
C	Modeling Results: C_y Model in Equation Form	C-1
D	Modeling Results: C_s Model in Equation Form	D-1
E	Modeling Results: C_n Model in Equation Form	E-1
F	Modeling Results: C_m Curves	F-1
G	Modeling Results: C_z Curves	G-1
H	Modeling Results: C_x Curves	H-1
I	Modeling Results: C_m Model in Equation Form	I-1

LIST OF FIGURES

<u>Fig. No.</u>		<u>Page No.</u>
4.2-1	Comparison between the $C_{y_{\delta_r}}$ identified model and the wind tunnel model.	4-6
4.2-2	Comparison between the C_y and the $C_{y_{\beta}}$ identified models and the wind tunnel model for $\beta = 0^\circ, 1^\circ, 2^\circ, 3^\circ$.	4-8
4.2-3	Comparison between the C_y and the $C_{y_{\beta}}$ identified models and the wind tunnel model for $\beta = 4^\circ, 5^\circ, 6^\circ, 7^\circ$.	4-9
4.2-4	Comparison between the C_y and the $C_{y_{\beta}}$ identified models and the wind tunnel model for $\beta = 8^\circ, 9^\circ, 10^\circ$.	4-10
4.2-5	Comparison between the $C_{y_{\beta}}$ identified model and the wind tunnel model for $\alpha = 10.5^\circ, 11.5^\circ, 12.5^\circ, 13.5^\circ, 14.5^\circ, 15.5^\circ, 16.5^\circ, 17.5^\circ$.	4-11
4.2-6	Comparison between the $C_{y_{\beta}}$ identified model and the wind tunnel model for $\alpha = 18.5^\circ, 19.5^\circ, 20.5^\circ, 21.5^\circ, 22.5^\circ, 23.5^\circ, 24.5^\circ, 27.5^\circ$.	4-12
4.3-1	Comparison between the C_{δ} identified model and the theoretical prediction model of Bihrlle Applied Research.	4-15
4.3-2	Comparison between the C_{δ} identified model and the theoretical prediction model of Bihrlle Applied Research.	4-16
4.3-3	Comparison between the C_{δ_a} identified model and the wind tunnel model.	4-17
4.3-4	Comparison between the C_{δ_r} identified model and the wind tunnel model.	4-18
4.3-5	Comparison between the C_{δ} and the $C_{\delta_{\beta}}$ identified models and the wind tunnel model for $\beta = 0^\circ, 1^\circ, 2^\circ, 3^\circ$.	4-19
4.3-6	Comparison between the C_{δ} and the $C_{\delta_{\beta}}$ identified models and the wind tunnel model for $\beta = 4^\circ, 5^\circ, 6^\circ, 7^\circ$.	4-20

<u>Fig. No.</u>		<u>Page No.</u>
4.3-7	Comparison between the C_L and the C_L identified models and the wind tunnel model for $\beta = 8^\circ, 9^\circ, 10^\circ$.	4-21
4.3-8	Comparison between the C_L identified model and the wind tunnel model for $\alpha = 10.5^\circ, 11.5^\circ, 12.5^\circ, 13.5^\circ, 14.5^\circ, 15.5^\circ, 16.5^\circ, 17.5^\circ$.	4-22
4.3-9	Comparison between the C_L identified model and the wind tunnel model for $\alpha = 18.5^\circ, 19.5^\circ, 20.5^\circ, 21.5^\circ, 22.5^\circ, 23.5^\circ, 24.5^\circ, 27.5^\circ$.	4-23
4.4-1	Comparison between the C_n identified model and the theoretical prediction model of Bihrlle Applied Research.	4-26
4.4-2	Comparison between the C_n identified model and the theoretical prediction model of Bihrlle Applied Research.	4-27
4.4-3	Comparison between the $C_{n\delta_r}$ identified model and the wind tunnel model.	4-28
4.4-4	Comparison between the C_n and the C_n identified models and the wind tunnel model for $\beta = 0^\circ, 1^\circ, 2^\circ, 3^\circ$.	4-30
4.4-5	Comparison between the C_n and the C_n identified models and the wind tunnel model for $\beta = 4^\circ, 5^\circ, 6^\circ, 7^\circ$.	4-31
4.4-6	Comparison between the C_n and the C_n identified models and the wind tunnel model for $\beta = 8^\circ, 9^\circ, 10^\circ$.	4-32
4.4-7	Comparison between the C_n identified model and the wind tunnel model for $\alpha = 10.5^\circ, 11.5^\circ, 12.5^\circ, 13.5^\circ, 14.5^\circ, 15.5^\circ, 16.5^\circ, 17.5^\circ$.	4-33
4.4-8	Comparison between the C_n identified model and the wind tunnel model for $\alpha = 18.5^\circ, 19.5^\circ, 20.5^\circ, 21.5^\circ, 22.5^\circ, 23.5^\circ, 24.5^\circ, 27.5^\circ$.	4-34
5.2-1	Comparison between the C_m identified model and the theoretical prediction of Bihrlle Applied Research.	5-8

<u>Fig. No.</u>	<u>Page No.</u>
5.2-2 Comparison between the C_m identified model and the theoretical prediction of Bihrlé Applied Research.	5-9
5.2-3 Comparison between the C_m identified model and the wind tunnel model for $\delta_e = -7.5^\circ, -6.5^\circ, -5.5^\circ, -4.5^\circ, -3.5^\circ, -2.5^\circ, -1.5^\circ, -0.5^\circ$.	5-11
5.2-4 Comparison between the C_m identified model and the wind tunnel model for $\delta_e = -15.5^\circ, -14.5^\circ, -13.5^\circ, -12.5^\circ, -11.5^\circ, -10.5^\circ, -9.5^\circ, -8.5^\circ$.	5-12
5.2-5 Comparison between the C_m identified model and the wind tunnel model for $\delta_e = -23.5^\circ, -22.5^\circ, -21.5^\circ, -20.5^\circ, -19.5^\circ, -18.5^\circ, -17.5^\circ, -16.5^\circ$.	5-13
5.2-6 Comparison between the C_m , C_m identified models and the wind tunnel model for $\delta_e = -27.5^\circ, -26.5^\circ, -25.5^\circ, -24.5^\circ$.	5-14
5.2-7 Comparison between the C_m identified model and the wind tunnel model for $\delta_e = -7.5^\circ, -6.5^\circ, -5.5^\circ, -4.5^\circ, -3.5^\circ, -2.5^\circ, -1.5^\circ, -0.5^\circ$.	5-15
5.2-8 Comparison between the C_m identified model and the wind tunnel model for $\delta_e = -15.5^\circ, -14.5^\circ, -13.5^\circ, -12.5^\circ, -11.5^\circ, -10.5^\circ, -9.5^\circ, -8.5^\circ$.	5-16
5.2-9 Comparison between the C_m identified model and the wind tunnel model for $\delta_e = -23.5^\circ, -22.5^\circ, -21.5^\circ, -20.5^\circ, -19.5^\circ, -18.5^\circ, -17.5^\circ, -16.5^\circ$.	5-17
5.2-10 Comparison between the C_m identified model and the wind tunnel model for $\alpha = 1.5^\circ, 2.5^\circ, 3.5^\circ, 4.5^\circ, 5.5^\circ, 6.5^\circ, 7.5^\circ, 8.5^\circ$.	5-18
5.2-11 Comparison between the C_m identified model and the wind tunnel model for $\alpha = 1.5^\circ, 2.5^\circ, 3.5^\circ, 4.5^\circ, 5.5^\circ, 6.5^\circ, 7.5^\circ, 8.5^\circ$.	5-19
5.2-12 Comparison between the C_m identified model and the wind tunnel model for $\alpha = 17.5^\circ, 18.5^\circ, 19.5^\circ, 20.5^\circ, 21.5^\circ, 22.5^\circ, 23.5^\circ, 24.5^\circ$.	5-20
5.2-13 Comparison between the C_m identified model and the wind tunnel model for $\alpha = 1.5^\circ, 2.5^\circ, 3.5^\circ, 4.5^\circ, 5.5^\circ, 6.5^\circ, 7.5^\circ, 8.5^\circ$.	5-21

<u>Fig. No.</u>		<u>Page No.</u>
5.2-14	Comparison between the C_{m_δ} identified model and the wind tunnel model for $\alpha = 9.5^\circ, 10.5^\circ, 11.5^\circ, 12.5^\circ, 13.5^\circ, 14.5^\circ, 15.5^\circ, 16.5^\circ$.	5-22
5.2-15	Comparison between the C_{m_δ} identified model and the wind tunnel tunnel model for $\alpha = 17.5^\circ, 18.5^\circ, 19.5^\circ, 20.5^\circ, 21.5^\circ, 22.5^\circ, 23.5^\circ, 24.5^\circ$.	5-23
A-1	A comparison between the time histories of the coarse and the fine values of the total airspeed measurement for maneuvers F1M1 through F4M1.	A-2
A-2	A comparison between the time histories of the coarse and the fine values of the total airspeed measurement for maneuvers F4M2 through F4M9.	A-3
A-3	A comparison between the time histories of the coarse and fine values of the total airspeed measurement for maneuvers F4M10 and F6M1.	A-4
B-1	Comparison between the measured and the estimated values of maneuver 1 of flight 1.	B-2
B-2	Comparison between the measured and the estimated values of maneuver 1 of flight 2.	B-6
B-3	Comparison between the measured and the estimated values of maneuver 2 of flight 2.	B-10
B-4	Comparison between the measured and the estimated values of maneuver 3 of flight 2.	B-14
B-5	Comparison between the measured and the estimated values of maneuver 1 of flight 3.	B-18
B-6	Comparison between the measured and the estimated values of maneuver 2 of flight 3.	B-22
B-7	Comparison between the measured and the estimated values of maneuver 3 of flight 3.	B-26
B-8	Comparison between the measured and the estimated values of maneuver 1 of flight 4.	B-30

<u>Fig. No.</u>	<u>Page No.</u>
B-9 Comparison between the measured and the estimated values of maneuver 2 of flight 4.	B-34
B-10 Comparison between the measured and the estimated values of maneuver 3 of flight 4.	B-38
B-11 Comparison between the measured and the estimated values of maneuver 4 of flight 4.	B-42
B-12 Comparison between the measured and the estimated values of maneuver 5 of flight 4.	B-46
B-13a Comparison between the measured and the estimated values of maneuver 6a of flight 4.	B-50
B-13b Comparison between the measured and the estimated values of maneuver 6b of flight 4.	B-54
B-14 Comparison between the measured and the estimated values of maneuver 7 of flight 4.	B-58
B-15 Comparison between the measured and the estimated values of maneuver 8 of flight 4.	B-62
B-16 Comparison between the measured and the estimated values of maneuver 9 of flight 4.	B-66
B-17a Comparison between the measured and the estimated values of maneuver 10a of flight 4.	B-70
B-17b Comparison between the measured and the estimated values of maneuver 10b of flight 4.	B-74
B-18 Comparison between the measured and the estimated values of maneuver 1 of flight 6.	B-78

<u>Figure No.</u>		<u>Page No.</u>
F-1	Comparison between the wind tunnel model of C_m and the real data values for δ_e between -2° and 0° .	F-2
F-2	Comparison between the wind tunnel model of C_m and the real data values for δ_e between -4° and -2° .	F-3
F-3	Comparison between the wind tunnel model of C_m and the real data values for δ_e between -6° and -4° .	F-4
F-4	Comparison between the wind tunnel model of C_m and the real data values for δ_e between -8° and -6° .	F-5
F-5	Comparison between the wind tunnel model of C_m and the real data values for δ_e between -10° and -8° .	F-6
F-6	Comparison between the wind tunnel model of C_m and the real data values for δ_e between -12° and -10° .	F-7
F-7	Comparison between the wind tunnel model of C_m and the real data values for δ_e between -14° and -12° .	F-8
F-8	Comparison between the wind tunnel model of C_m and the real data values for δ_e between -16° and -14° .	F-9
F-9	Comparison between the wind tunnel model of C_m and the real data values for δ_e between -18° and -16° .	F-10
F-10	Comparison between the wind tunnel model of C_m and the real data values for δ_e between -20° and -18° .	F-11
F-11	Comparison between the wind tunnel model of C_m and the real data values for δ_e between -22° and -20° .	F-12
F-12	Comparison between the wind tunnel model of C_m and the real data values for δ_e between -24° and -22° .	F-13
F-13	Comparison between the wind tunnel model of C_m and the real data values for δ_e between -26° and -24° .	F-14
F-14	Comparison between the wind tunnel model of C_m and the real data values for δ_e between -28° and -26° .	F-15

<u>Figure No.</u>		<u>Page No.</u>
G-1	Comparison between the wind tunnel model of C_z and the real data values for δ_e between -2° and 0° .	G-2
G-3	Comparison between the wind tunnel model of C_z and the real data values for δ_e between -4° and -2° .	G-3
G-3	Comparison between the wind tunnel model of C_z and the real data values for δ_e between -6° and -4° .	G-4
G-4	Comparison between the wind tunnel model of C_z and the real data values for δ_e between -8° and -6° .	G-5
G-5	Comparison between the wind tunnel model of C_z and the real data values for δ_e between -10° and -8° .	G-6
G-6	Comparison between the wind tunnel model of C_z and the real data values for δ_e between -12° and -10° .	G-7
G-7	Comparison between the wind tunnel model of C_z and the real data values for δ_e between -14° and -12° .	G-8
G-8	Comparison between the wind tunnel model of C_z and the real data values for δ_e between -16° and -14° .	G-9
G-9	Comparison between the wind tunnel model of C_z and the real data values for δ_e between -18° and -16° .	G-10
G-10	Comparison between the wind tunnel model of C_z and the real data values for δ_e between -20° and -18° .	G-11
G-11	Comparison between the wind tunnel model of C_z and the real data values for δ_e between -22° and -20° .	G-12
G-12	Comparison between the wind tunnel model of C_z and the real data values for δ_e between -24° and -22° .	G-13
G-13	Comparison between the wind tunnel model of C_z and the real data values for δ_e between -26° and -24° .	G-14
G-14	Comparison between the wind tunnel model of C_z and the real data values for δ_e between -28° and -26° .	G-15

<u>Figure No.</u>		<u>Page No.</u>
H-1	Comparison between the wind tunnel model of C_x and the real data values for δ_e between -2° and 0° .	H-2
H-2	Comparison between the wind tunnel model of C_x and the real data values for δ_e between -4° and -2° .	H-3
H-3	Comparison between the wind tunnel model of C_x and the real data values for δ_e between -6° and -4° .	H-4
H-4	Comparison between the wind tunnel model of C_x and the real data values for δ_e between -8° and -6° .	H-5
H-5	Comparison between the wind tunnel model of C_x and the real data values for δ_e between -10° and -8° .	H-6
H-6	Comparison between the wind tunnel model of C_x and the real data values for δ_e between -12° and -10° .	H-7
H-7	Comparison between the wind tunnel model of C_x and the real data values for δ_e between -14° and -12° .	H-8
H-8	Comparison between the wind tunnel model of C_x and the real data values for δ_e between -16° and -14° .	H-9
H-9	Comparison between the wind tunnel model of C_x and the real data values for δ_e between -18° and -16° .	H-10
H-10	Comparison between the wind tunnel model of C_x and the real data values for δ_e between -20° and -18° .	H-11
H-11	Comparison between the wind tunnel model of C_x and the real data values for δ_e between -22° and -20° .	H-12
H-12	Comparison between the wind tunnel model of C_x and the real data values for δ_e between -24° and -22° .	H-13
H-13	Comparison between the wind tunnel model of C_x and the real data values for δ_e between -26° and -24° .	H-14
H-14	Comparison between the wind tunnel model of C_x and the real data values for δ_e between -28° and -26° .	H-15

LIST OF TABLES

<u>Table No.</u>		<u>Page No.</u>
2.1-1	Description of the Actual T-2C Data Processed with the EBM System Identification Method	2-1
2.2-1	Location Values of Instruments in the T-2C Instrumentation Package	2-5
2.3-1	Values of the T-2C Aircraft Constants that vary from Maneuver to Maneuver	2-9
C-1	Identified Parameter of C_y	C-3
D-1	Identified Parameters of C_s	D-4
E-1	Identified Parameters of C_n	E-3
I-1	Identified α -parameters of C_m Model	I-3
I-2	Identified β -parameters of C_m Model	I-5
I-3	Identified Dynamic Derivatives of C_m Model	I-6

LIST OF SYMBOLS

Variable	Description	Units
a_{xm_i}	Longitudinal acceleration measured along aircraft x-body axis at i, i = nose	(m/sec ²)
a_{ym_i}	Lateral acceleration measured along aircraft y-body axis at i, i = cg, nose, tail	(m/sec ²)
a_{zm_i}	Vertical acceleration measured along aircraft z-body axis at i, i = cg, nose, tail, R, L	(m/sec ²)
b	Reference wingspan	(m)
C_l	Roll moment coefficient about x-body axis	
C_m	Pitch moment coefficient about y-body axis	
C_n	Yaw moment coefficient about z-body axis	
C_x	Axial force coefficient along x-body axis	
C_y	Side force coefficient along y-body axis	
C_z	Normal force coefficient along z-body axis	
$\delta C_y / \delta \beta$	$\delta C_y / \delta \beta$; Other combinations occur where y is changed to x, z, l, m, n and β is changed to another state, to a control, or to α or $\dot{\beta}$.	
C_z	Normal force coefficient along z-body axis	
\bar{c}	Mean aerodynamic chord	(m)
g	Acceleration due to gravity = 9.806 m/sec ²	(m/sec ²)
h_{ex}	Angular momentum at both T-2C engines (Newton-m-sec)	
I_x	Moment of inertia about x body axis	(kg m ²)
I_y	Moment of inertia about y body axis	(kg m ²)
I_z	Moment of inertia about z body axis	(kg m ²)
I_{xz}	Cross product of inertial about x, z body axes	(kg m ²)

Variable	Description	Units
ι_x	Distance along x-axis between aerodynamic center and center of gravity (positive for a. c. forward of c. g.)	(m)
ι_z	Distance along z-axis between aerodynamic center and center of gravity (positive for a. c. below c. g.)	(m)
ι_{z_e}	Distance along z-axis between thrust axis and center of gravity (positive for thrust axis below c. g.)	(m)
m	Aircraft mass	(kg)
p	Aircraft x-body axis roll rate	(rad/sec)
q	Aircraft y-body axis pitch rate	(rad/sec)
r	Aircraft z-body axis yaw rate	(rad/sec)
S	Reference wing area	(m ²)
T_x	Thrust component along x-body axis direction	(Newtons)
T_z	Thrust component along z-body axis direction	(Newtons)
u	Speed along aircraft x-body axis with respect to a nonmoving free stream air mass	(m/sec)
v	Aircraft total airspeed	(m/sec)
w	Speed along aircraft y-body axis with respect to a nonmoving free stream air mass	(m/sec)
	Speed along aircraft z-body axis with respect to a nonmoving free stream air mass	(m/sec)

Variable	Description	Units
x	Aircraft c.g. position along the longitudinal axis of earth fixed axes oriented with respect to aircraft body axes by Euler angles. Positive when c.g. is forward of axis system origin.	(m)
\bar{x}_i	Distance between c.g. and sensor i measured along x -body axis, $i = \alpha, \beta, V$. Positive for sensor forward of c.g.	(m)
\bar{x}_{x_i}	Distance between c.g. and longitudinal accelerometer at i measured along x -body axis, $i = \text{NOSE}$. Positive for accelerometer forward of c.g.	(m)
\bar{x}_{y_i}	Distance between c.g. and lateral accelerometer at i measured along x -body axis, $i = \text{c.g., nose, tail}$. Positive for accelerometer forward of c.g.	(m)
\bar{x}_{z_i}	Distance between c.g. and vertical accelerometer at i measured along x -body axis, $i = \text{c.g., nose, tail}$. Positive for accelerometer forward of c.g.	(m)
y	Aircraft c.g. position along the lateral axis of earth fixed axes oriented with respect to aircraft body axes oriented with respect to aircraft body axes by Euler angles. Positive when c.g. is right of axis system origin.	(m)
\bar{y}_i	Distance between c.g. and sensor i . Positive for sensor right of c.g.	(m)
\bar{y}_{x_i}	Distance between c.g. and longitudinal accelerometer at i measured along y -body axis, $i = \text{NOSE}$. Positive for accelerometer right of c.g.	(m)

Variable	Description	Units
\bar{y}_i	Distance between c.g. and lateral accelerometer at i measured along y -body axis, i = c.g., NOSE, TAIL. Positive for accelerometer right of c.g.	(m)
\bar{y}_{z_i}	Distance between c.g. and vertical accelerometer at i measured along y -body axis, i = CG, NOSE, TAIL, R.L. Positive for accelerometer right of c.g.	(m)
z	Aircraft c.g. position along the vertical axis of earth fixed axes oriented with respect to aircraft body axes by Euler angles. Positive when c.g. is below axis system origin.	(m)
\bar{z}_i	Distance between c.g. and sensor i measured along z -body axis, $i = \alpha, \beta, V$. Positive for sensor below c.g.	(m)
\bar{z}_{x_i}	Distance between c.g. and longitudinal accelerometer at i measured along z -body axis, i = NOSE. Positive for accelerometer below c.g.	(m)
\bar{z}_{y_i}	Distance between c.g. and lateral accelerometer at i measured along z -body axis, i = CG, NOSE, TAIL. Positive for accelerometer below c.g.	(m)
\bar{z}_{z_i}	Distance between c.g. and vertical accelerometer at i measured along z -body axis, i = c.g., NOSE, TAIL, R.L. Positive for accelerometer below c.g.	(m)

Variable	Description	Units
α	Angle of attack	(rad)
$\dot{\alpha}$	Time derivative of α	(rad/sec)
β	Sideslip angle	(rad)
$\dot{\beta}$	Time derivative of β	(rad/sec)
δ_a	Aileron deflection (+ δ_a \rightarrow left wing down roll)	(rad)
δ_e	Elevator deflection (+ δ_e \rightarrow nose down pitch)	(rad)
δ_r	Rudder deflection (+ δ_r \rightarrow nose left yaw)	(rad)
θ	Euler pitch angle	(rad)
ρ	Air density	(kg/m ³)
ϕ	Euler bank angle	(rad)

LIST OF SUBSCRIPTS

o	Denotes reference value
c.g.	Center of gravity
L	Left wingtip
m	Designates a measured quantity when used as a subscript
R	Right wingtip
s	Stability axes
NOSE	Nose
TAIL	Tail

1. INTRODUCTION

1.1 BACKGROUND

Our previous effort which is documented as Volume II (Ref. [1]) has demonstrated that the Estimation-Before-Modeling (EBM) system identification method extracts with precision the nonlinear aerodynamics of the high angle of attack/sideslip domain for aircraft. This demonstration was carried out using synthetically generated data from a T-2C wind tunnel model and a set of theoretically predicted dynamic derivatives, provided by the Naval Air Development Center (NADC). The data of that simulation study were generated by exciting the synthetic model with the controls and the initial states contained in actual T-2C flight data provided by NADC. The T-2C light jet trainer aircraft was instrumented and operated by NADC for the express purpose of providing high angle of attack/sideslip flight data for system identification studies. The measurement equations and the noise levels of the collected data were used in generating the synthetic measurements for the simulation study. As a result, the EBM methodology was tested under controlled but realistic simulated conditions. The identified model closely follows the nonlinearities of the dynamic derivatives and is an excellent match to the control and state derivatives of the wind tunnel model. The predicted responses of the identified model are good matches to the corresponding responses of the wind tunnel model. The work documented in Volume II validates, therefore, the excellent performance capability of the EBM system identification method. This present volume contains the application of this method to real data.

1.2 SCOPE OF FLIGHT DATA ANALYSIS STUDY

The EBM system identification method is used to process eighteen T-2C flight maneuvers containing over 600 seconds of data sampled at

20 Hertz. The instrumentation of the T-2C provided 24 measured quantities including three controls. The first step of the EBM method provides optimal estimates of the aircraft states, of the aerodynamic forces and moments and of the biases and scale factors in the measurements. The second step of the EBM method identifies detailed models of the lateral aerodynamic coefficients C_y , C_l and C_n and of the longitudinal aerodynamic coefficient C_m . Time did not permit the identification of a detail model of C_x and C_z ; but partial models are presented. The identified models are compared to the T-2C wind tunnel model and to the theoretical predictions of Ref. [2].

1.3 ESTIMATION BEFORE MODELING (EBM) METHOD

The Estimation Before Modeling (EBM) system identification method is a two-step approach to the modeling of aircraft aerodynamics. The first step uses Gauss-Markov processes to model the accelerations due to aerodynamic forces and moments and it employs an extended Kalman-Bucy filter/Bryson-Frazier smoother to generate estimates of states, aerodynamic forces and moments time histories, and measurement biases and scale factors. A description of the filter/smooth is presented in Appendix B of Volume II (Ref. [1]).

In the second step, Stepwise Multiple Linear Regression (SMLR) is used together with subspace modeling to identify the dependency of an aerodynamic coefficient on aircraft states and controls. A detailed account of step two is presented in Section 1.3 and Appendix C of Volume II (Ref. [1]).

2. SCENARIO OF THE T-2C SYSTEM IDENTIFICATION PROBLEM

2.1 FLIGHT TEST CONDITIONS AND DESCRIPTIONS OF MANEUVERS

The T-2C flight test data were gathered with gear up and speed brake retracted under the following conditions:

True Airspeed	-	75 to 150 meters/sec
Mach No.	-	0.25 to 0.4
Altitude	-	6000 to 7600 meters

The throttles were fixed during maneuvers. The Naval Air Development Center provided four sets of flight data consisting of eighteen maneuvers, amounting to over 600 seconds of 20 Hertz data. The type of input used to generate each maneuver is described in the last column of Table 2.1-1. The first column gives the date of the flight set and the second column denotes the flight number and the maneuver number that goes with the input used.

The time histories of the inputs are presented in Appendix B for all of the maneuvers. The maneuvers F1M1, F4M9 and F6M1 have 360° rolls and the maneuver F4M10 has two 360° rolls. The angle of attack, α , ranges from -4° to 40° and the sideslip angle, β , covers the range from -14° to 26°. Most of the maneuvers have a trim α between 10.5° and 11.5° and a trim V (i.e., true airspeed) between 90.0 and 95.0 meters/sec. The maneuvers F4M7 and F4M8 have a trim α between 5.5° and 6.5° and a trim V between 115 and 120 meters/sec.

TABLE 2.1-1 Description of the Actual T-2C Data Processed
with the EBM System Identification Method

Date of Flight	Flight No. and Maneuver No.	Approximate Duration of Maneuver (sec.)	Type of Input
Nov. 5, 1975	F1M1	16	Aft Stick, full rudder pedal (360° roll)
Dec. 10, 1975	F2M1 F2M2 F2M3	34 35 40	Random fore & aft stick Random side to side lateral stick Sequential doublets - δ_e , δ_a , δ_r
Dec. 29, 1975	F3M1 F3M2 F3M3	34 25 39	Longitudinal Doublet Random Side to Side Rudder Input Sequential Random - δ_e , δ_a , δ_r ($\beta_o = 0^\circ$)
Aug. 26, 1976	F4M1 F4M2 F4M3 F4M4 F4M5 F4M6 F4M7 F4M8 F4M9 F4M10 F6M1	21 75 46 30 60 38 40 29 29 28 17	Longitudinal Stick ramp plus sine wave Sequential Random - δ_e , δ_a , δ_r ($\beta_o = -5^\circ$) Sequential Random - δ_e , δ_a , δ_r ($\beta_o = 5^\circ$) Full aft Stick plus pulses (spin) Longitudinal Limit Cycle Shallow Bank to Stall Steep Bank to Stall (360° roll) Pull-up from Dive (360° roll) Coordinated Control Spin Entry (360° roll) Coordinated Control Spin Entry (2-360° rolls) Aft Stick, full Lateral Stick

2.2 T-2C INSTRUMENTATION - MEASUREMENT EQUATIONS

Table 2.2-1 lists the twenty-four variables that are sensed by the T-2C instrumentation package and provides measurement range and location with respect to the normal flight test center of gravity for each sensor. This package as well as the data acquisition techniques are essentially the same as those described in detail in Ref. [3] for the NADC YT-2B airplane and will not be discussed here. Three of the twenty-four variables are control variables and three others are the angular acceleration variables \dot{p} , \dot{q} and \dot{r} . The angular acceleration measurements were not of good quality and, therefore, were not used in our study.

The measurement equations relating the sensed angle of attack, sideslip angle and total airspeed variables to aircraft body-axes states are:

$$\alpha_m = \tan^{-1} \left(\frac{w - q \bar{x}_\alpha + p \bar{y}_\alpha}{u + q \bar{z}_\alpha - r \bar{y}_\alpha} \right)$$

$$\beta_m = \tan^{-1} \left(\frac{v - p \bar{z}_\beta + r \bar{x}_\beta}{u + q \bar{z}_\beta - r \bar{y}_\beta} \right)$$

$$V_m = [(u + q \bar{z}_V - r \bar{y}_V)^2 + (v + r \bar{x}_V - p \bar{z}_V)^2 + (w + p \bar{y}_V - q \bar{x}_V)^2]^{1/2}$$

The measurement equations relating the sensed roll, pitch and yaw rates, attitude, altitude, angular accelerations and control variables to aircraft states are as follows:

$$p_m = p$$

$$\dot{p}_m = \dot{p}$$

$$q_m = q$$

$$\dot{q}_m = \dot{q}$$

$$r_m = r$$

$$\dot{r}_m = \dot{r}$$

$$\theta_m = \theta$$

$$\delta_a = \delta_a$$

$$\phi_m = \phi$$

$$\delta_e = \delta_e$$

$$h_m = -z$$

$$\delta_r = \delta_r$$

The nine measurement equations relating the sensed linear acceleration variables to aircraft body-axes states are as follows:

$$\left(a_{x_m} \right)_i = B_1 - (r^2 + q^2) \bar{x}_{x_i} + (p q - \dot{r}) \bar{y}_{x_i} + (p r + \dot{q}) \bar{z}_{x_i}$$

$$\left(a_{y_m} \right)_j = B_2 + (p q + \dot{r}) \bar{x}_{y_j} - (p^2 + r^2) \bar{y}_{y_j} + (q r - \dot{p}) \bar{z}_{y_j}$$

$$\left(a_{z_m} \right)_k = B_3 + (p r - \dot{q}) \bar{x}_{z_k} + (q r + \dot{p}) \bar{y}_{z_k} - (p^2 + q^2) \bar{z}_{z_k}$$

where $i = \text{nose}$, $j = \text{c.g.}$, NOSE and TAIL , and $k = \text{c.g.}$, NOSE , TAIL , R and L . The values of the \bar{x} 's, \bar{y} 's and \bar{z} 's are given in Table 2.2-1. For example, $\bar{x}_{x_{\text{NOSE}}} = 4.62$ meters, $\bar{y}_{x_{\text{NOSE}}} = -.13$ meters and $\bar{z}_{x_{\text{NOSE}}} = 0.18$ meters. The states B_1 , B_2 and B_3 are the fore-aft, the lateral, and the normal accelerations at c.g., respectively.

Table 2.2-1 Location Values of Instruments

in the T-2C Instrumentation Package;

Positive \bar{x} means Instrument is Foward ofc.g., Positive \bar{y} - right of c.g., Positive \bar{z} - below c.g.

No.	Measured Quantity	Location in Meters			Measurement Range
		\bar{x}	\bar{y}	\bar{z}	
1.	Angle of Attack (α_m)	7.04	0	0	-15° to 45°
2.	Sideslip Angle (β_m)	7.13	0	0	$\pm 30^\circ$
3.	Airspeed (V_m)	4.62	0.13	0.18	0-500 kt; ± 50 kt
4.	Roll Rate (p_m)	4.04	0.13	0.05	± 150 deg/sec
5.	Pitch Rate (q_m)	0.12	0	0.58	± 45 deg/sec
6.	Yaw Rate (r_m)	4.04	-0.13	0.05	± 150 deg/sec.
7.	Pitch Angle (θ_m)	4.04	0.13	0.05	± 90 deg.
8.	Roll Angle (ϕ_m)	4.04	0.13	0.05	± 180 deg.
9.	Altitude (h_m)	4.04	0.13	0.05	0 - 10670 m
10.	Roll acceleration (\ddot{p}_m)	0.12	0	0.58	± 275 deg/sec. ²
11.	Pitch acceleration (\ddot{q}_m)	0.12	0	0.58	± 450 deg/sec. ²
12.	Yaw acceleration (\ddot{r}_m)	4.62	0	0	± 275 deg/sec. ²
13.	Fore-Aft Acceleration (a_x) m NOSE	4.62	-0.13	0.18	± 1.0 g
14.	Lateral Acceleration at c.g. (a_y) m c.g.	0.12	-0.02	0.58	± 1.0 g
15.	Lateral Acceleration at NOSE (a_y) m NOSE	4.62	-0.13	0.18	± 1.0 g
16.	Lateral Acceleration at Tail (a_y) m TAIL	-3.89	0.71	-0.08	± 1.0 g
17.	Normal Acceleration at c.g. (a_z) m c.g.	0.12	0.02	0.58	± 3.5 g
18.	Normal Acceleration at Nose (a_z) m NOSE	4.04	-0.13	0.05	± 5.0 g
19.	Normal Acceleration at TAIL (a_z) m TAIL	-3.89	0.71	-0.08	± 3.5 g
20.	Normal Acceleration at Right Wing Tip (a_z) m R	-0.89	5.08	0.05	± 3.5 g

Table 2.2-1 (Continued)

No.	Measured Quantity	Location in Meters			Measurement Range
		\bar{x}	\bar{y}	\bar{z}	
21	Normal Acceleration at Left Wing Tip (a_z) m L	-0.89	-5.08	0.05	± 3.5 g
22	Aileron (δ_a) m	-0.97	4.06	0.05	± 13 deg
23	Elevator (δ_e) m	-5.01	0.05	-1.19	-27.5 to 15 deg.
24	Rudder (δ_r) m	-5.01	0.05	-0.72	± 24 deg.

2.3 THE T-2C AIRCRAFT CONSTANTS

The aircraft constants required in the kinematical and force and moment equations of the T-2C are given in this section.

The reference wing area, the mean aerodynamic chord and the reference wingspan are

$$S = 23.7 \text{ m}^2$$

$$\bar{c} = 2.26 \text{ m}$$

$$b = 11.62 \text{ m}$$

The distance along the z-axis between the aerodynamic center and the center of gravity and the distance along the z-axis between the thrust axis and the center of gravity are

$$l_z = 0 \text{ m}$$

$$l_{z_e} = .49 \text{ m}$$

The moments of inertia about the body axes are

$$I_x = 12212 \text{ kg m}^2$$

$$I_y = 19811 \text{ kg m}^2$$

$$I_z = 25781 \text{ kg m}^2$$

$$I_{xz} = 0 \text{ kg m}^2$$

The total angular momentum of both engines is

$$h_{e_x} = 2448 \text{ Newtons-m-sec}$$

The engines do not counter rotate. They rotate clockwise from the rear of the aircraft.

The values for the mass m , the thrust T_x along the x body-axis and the moment arm ℓ_x (i.e., the distance along the x -axis between the aerodynamic center and the center of gravity) are given in Table 2.3-1. The thrust T_z along the z body axis is zero.

Table 2.3-1 Values of the T-2C Aircraft Constants that Vary from
Maneuver to Maneuver

Maneuver Number	m Mass (kg)	T_x Thrust (Newtons)	l_x Moment Arm (Meters)
F1M1	5275	4130	.042
F2M1	5330	4092	.065
F2M2	5198	3968	.072
F2M3	5039	3884	.054
F3M1	5384	4119	.055
F3M2	5039	3823	.046
F3M3	4944	3835	.068
F4M1	5420	4107	.041
F4M2	5371	4154	.044
F4M3	5325	4012	.021
F4M4	5266	3990	.021
F4M5	5216	3991	.050
F4M6	5171	3928	.048
F4M7	5126	3229	.203
F4M8	5080	3226	.177
F4M9	5035	3823	.017
F4M10	4990	3828	.030
F6M1	5207	4486	.006

2.4 EQUATIONS OF MOTION

The following kinematical relations for a rigid aircraft are given with reference to body axes at the center of gravity:

$$\begin{aligned}
 \dot{u} &= r v - q w - g \sin \theta + B_1 \\
 \dot{v} &= p w - r u + g \cos \theta \sin \phi + B_2 \\
 \dot{w} &= q u - p v + g \cos \theta \cos \phi + B_3 \\
 \dot{p} &= p q C_{41} + q r C_{42} + q C_{43} + B_4 + C_{44} B_6 \\
 \dot{q} &= p r C_{51} + (r^2 - p^2) C_{52} - r C_{53} + B_5 \\
 \dot{r} &= p q C_{61} + q r C_{62} + q C_{63} + B_6 + C_{64} B_4 \\
 \dot{\theta} &= q \cos \phi - r \sin \phi \\
 \dot{\phi} &= p + q \tan \theta \sin \phi + r \tan \theta \cos \phi \\
 \dot{z} &= -u \sin \theta + v \cos \theta \sin \phi + w \cos \theta \cos \phi
 \end{aligned}$$

where B_1, B_2, \dots, B_6 are the accelerations at the center of gravity due to aerodynamic and thrust forces and moments acting on the body of the aircraft.

The constant coefficients C_{41} through C_{64} are given by:

$$C_{41} = \frac{I_{xz}(I_z + I_x - I_y)}{I_x I_z - I_{xz}^2} \quad C_{51} = \frac{I_z - I_x}{I_y}$$

$$C_{42} = \frac{I_z(I_y - I_z) - I_{xz}^2}{I_x I_z - I_{xz}^2} \quad C_{52} = \frac{I_{xz}}{I_y}$$

$$C_{43} = \frac{I_{xz} h e_x}{I_x I_z - I_{xz}^2} \quad C_{53} = \frac{h e_x}{I_y} \quad C_{44} = \frac{I_{xz}}{I_x}$$

$$C_{61} = \frac{I_x (I_x - I_y) + I_{xz}^2}{I_x I_z - I_{xz}^2} \quad C_{62} = \frac{I_{xz} (I_y - I_z - I_x)}{I_x I_z - I_{xz}^2}$$

$$C_{63} = \frac{I_x h e_x}{I_x I_z - I_{xz}^2} \quad C_{64} = \frac{I_{xz}}{I_x}$$

2.5 TRANSFORMATION TO NON-DIMENSIONAL AERODYNAMIC COEFFICIENTS

The first step of the EBM method provides estimates of the time histories of the acceleration terms $B_1(t)$, $B_2(t)$, ..., $B_6(t)$ for each maneuver. The time histories of the non-dimensional aerodynamic coefficients, $C_x(t)$, $C_y(t)$, $C_z(t)$, $C_\ell(t)$, $C_m(t)$ and $C_n(t)$, are calculated using the following transformations:

$$B_1 = \frac{T_x}{m} + \frac{\rho V^2}{2m} S C_x$$

$$B_2 = \frac{\rho V^2}{2m} S C_y$$

$$B_3 = \frac{\rho V^2}{2m} S C_z + \frac{T_z}{m}$$

$$B_4 = \frac{\rho V^2}{2} \frac{S_b}{I_x} C_\ell - \frac{I_x I_z}{I_x I_z - I_{xz}^2}$$

$$B_5 = \frac{\rho V^2}{2} \frac{S_c}{I_y} C_m + \frac{1}{I_y} \{ \iota_z T_x - \iota_x m(B_3 - \frac{T_z}{m}) +$$

$$\iota_z m(B_1 - \frac{T_x}{m}) \}$$

$$B_6 = \frac{\rho V^2}{2} \frac{S_b}{I_z} C_n \left(\frac{I_x I_z}{I_x I_z - I_{xz}^2} \right)$$

The time histories of the non-dimensional aerodynamic coefficients together with the time histories of the states and the controls are used in the second step of the EBM method to identify models of C_x , C_y , C_z , C_ℓ , C_m and C_n .

3. ESTIMATION RESULTS

The extended Kalman-Bucy filter/Bryson-Frazier smoother as discussed in Ref. [1] was used to process the eighteen maneuvers F1M1, F2M1, ..., F6M1 to obtain the estimation results of this study. Bias states and scale factor states were added to the filter/smooth to handle the instrumentation biases and scale factors that are inherent in real data.

In addition to using the filter/smooth, a simple technique was used in determining the scale factors of α and β . Let I be the number of times that the time history of the measured α crosses its trim value and the J be the number of such times for β . All measured quantities are corrected to c.g. location. The v and w equations

$$\dot{v}_a = p w_a - r u + g \cos \theta \sin \phi + a_{y_{c.g.}} + b_j$$

$$\dot{w}_a = q u - p v_a + g \cos \theta \cos \phi + a_{z_{c.g.}} + b_i$$

with $u = \sqrt{V^2 - (v_a^2 + w_a^2)}$ are integrated using pre-smoothed values of $V, p, q, r, \theta, \phi, a_{y_{c.g.}}$ and $a_{z_{c.g.}}$; the acceleration biases b_i and b_j are computed over the intervals $[t_{i-1}, t_i]$ and $[t_{j-1}, t_j]$, respectively, so as to satisfy the state constraints $\alpha_a(t_i) = \alpha(t_i)$, $i = 1, 2, \dots, I$ and $\beta_a(t_j) = \beta(t_j)$ $j = 1, 2, \dots, J$ where α_a and β_a are the integrated values. The angle of attack scale factor is the correlation coefficient of the two time histories $\alpha_a(t)$ and $\alpha(t)$. The sideslip angle scale factor is similarly given.

3.1 COMPARISON OF ESTIMATED VALUES WITH MEASURED VALUES

The filter/smooth which uses the equations of motion of Section 2.4 provided estimates of the states u , v , w , p , q , r , θ , ϕ , altitude, the accelerations B_1 , B_2 , ..., B_6 and the biases and scale factors. These estimated values were used in the measurement equations of Section 2.2 to obtain the curves labeled "Estimated Values" that are plotted in Appendix B. Figures B-1 through B-18 contain the results for each of the eighteen maneuvers. There are four pages for each maneuver. The first page shows the plots of α and β . The second presents the measured values of the controls δ_e , δ_a , δ_r ; the smoothed values of the controls are not compared in these figures with the measured values. The third page consists of the variables V , p , q , r , θ , ϕ , altitude and $a_{z_{c.g.}}$. The fourth page covers the eight accelerations a_{z_R} , a_{z_L} , $a_{z_{NOSE}}$, $a_{z_{TAIL}}$, $a_{y_{NOSE}}$, $a_{y_{TAIL}}$, $a_{y_{c.g.}}$ and $a_{x_{NOSE}}$. The measured values of the sensed quantities with biases and scale factors removed are plotted using a solid line which appears as a noisy curve. The estimated values are plotted using a dashed line with x's on it, which appears in most cases as a solid line with x's on it.

3.2 ESTIMATES OF BIASES AND SCALE FACTORS

The angle of attack sensor has a measurement range from -15° to 45° and is centered on $\alpha = 15^\circ$ which is stall. The relationship between the true angle of attack α and the measured angle of attack α_m is

$$\alpha = 15^\circ + \lambda_\alpha (\alpha_m - 15^\circ) + b_\alpha + \text{noise}$$

where λ_α is the scale factor and b_α is the bias. The sideslip angle sensor has a measurement range from -30° to 30° and is centered on

$\beta = 0$. The relationship between the true sideslip angle β and the measured sideslip angle β_m is

$$\beta = 0^\circ + \lambda_\beta (\beta_m - 0^\circ) + b_\beta + \text{noise}$$

The scale factor λ_α for the angle of attack was estimated to be 0.78. The bias b_α was estimated to be 2° for maneuvers F1M1, F2M1, ..., F3M3, and F6M1 and 0° for the maneuvers F4M1, F4M2, ..., F4M10.

The scale factor λ_β for the sideslip angle was estimated to be 0.805. The bias b_β varied from one maneuver to the next. For maneuvers F1M1, F2M1, ..., F3M3 and F6M1 it varied between 0.1° and 1.7° . For the maneuvers in flight 4 it varied from 0.8° to 5.1° .

Two sensors were used to measure the total airspeed. One sensor has a measurement range of 500 knots; its value is called a "coarse" value. The other sensor has a range of 100 knots and its value is called a "fine" value. A comparison between these two values is presented for each maneuver in Figures A-1, A-2 and A-3 in Appendix A. The fine values are 3.9 m/sec larger than the coarse values for maneuvers F1M1, F2M1, ..., F3M3 and F6M1. The fine and coarse values coincide for the maneuvers in flight 4.

The maneuvers exhibiting the 3.9 m/sec difference were flown between Nov. 5 and Dec. 29, 1975. The maneuvers of flight 4 were flown on Aug. 26, 1976 which is seven months after flight 3. The fine airspeed measurement which has one-fifth the noise level of the coarse airspeed measurement was used as the measured variable in the filter/smoothen. It has a bias of -3.9 m/sec for the maneuvers of flights 1, 2, 3 and 6 and no bias for the maneuvers of flight 4.

Large biases were estimated for the roll and pitch rates. The roll rate bias b_p was estimated to be $-.1065$ rad/sec which is -6.1 deg/sec. The pitch rate bias b_q was estimated to be $-.0479$ rad/sec which is -2.7 deg/sec. The yaw rate bias b_r was estimated within $\pm .02$ rad/sec which is within its large noise level. An axis alignment bias of the rate gyro was estimated as 3° .

The trim values of δ_a and δ_r from the eighteen maneuvers were plotted against each other. The eighteen points (δ_a, δ_r) lie nearly on a straight line which crosses the δ_a -axis at $\delta_a = 1.8^\circ$. There is a cluster of twelve points at this crossing. The line should cross at $\delta_a = 0^\circ$ because with $\delta_r = 0$ trim conditions should follow from $\delta_a = 0$ and not from $\delta_a = 1.8^\circ$. This value of 1.8° was accepted as the bias on δ_a . The other controls δ_r and δ_e had no biases.

The bias of the Fore-Aft acceleration a_x was estimated _{NOSE} to be 0.6 m/sec² and the biases of the lateral accelerations a_y and _{c.g.} a_y are $-.13$ m/sec². The bias of the lateral acceleration a_y _{TAIL} is within its large noise level. The normal acceleration measurement at the center of gravity has a bias of -1.6 m/sec² and the off c.g. normal acceleration measurements have a bias of 1.0 m/sec².

3.3 SOME OBSERVATIONS ON THE T-2C DATA

A correlation analysis of the data revealed that the measured quantities belong to two distinct groups. The first group consisted of α , β , p , q , θ , ϕ , δ_e and δ_a . The second group consisted of the remaining measured quantities (i.e., all accelerations, r , δ_r , altitude and airspeed). During the trim portion of each maneuver the noise of any member of the first group is 80% to 95% correlated with the noise of any other member of the first group and is 0% to 10% correlated with the noise of any member in the second group. Similarly, the members of the second group exhibit the same noise correlation

characteristic with each other. The reason that there are two groups and not one is because single channels were used to measure the quantities of the first group whereas a commutator working off a single channel was used for the second group. The reason that there is any group having such a high correlation has not been explained. The commutator had the effect of adding 4 to 5 times the noise level of a single channel level. For example, p and r should normally exhibit the same noise level characteristic during trim since they have the range ± 150 deg/sec and since they are measured with the same type of instrument. From the plots of p and r in Figure B-1 we observe that the noise level on r is 4 to 5 times higher than it is on p . The variable p belongs to group one, and r belongs to the second group. Also, we note in Figure B-1 that the noise level on δ_r is considerably higher than it is on δ_e and δ_a . Single channels should be used for all quantities since this keeps the noise levels to a minimum. Also, common noise sources should be isolated and removed, if possible, from the instrumentation.

The data exhibits noise from a nose boom vibrating between 6 and 7 hertz with amplitudes as high as several degrees in α and β . The off c.g. acceleration measurements exhibit high vibrational noise.

There are occasional losses of total airspeed measurement over extended intervals. In some cases the airspeed would change abruptly by 20 m/sec.

4. IDENTIFICATION OF THE T-2C LATERAL AERODYNAMIC CHARACTERISTICS

4.1 CONSTRUCTION OF SUBSPACES FOR LATERAL MODELING

The lateral coefficients C_y , C_ℓ and C_n are functions of the following variables:

- α - angle of attack
- β - sideslip angle
- p - roll rate
- r - yaw rate
- δ_a - aileron deflection
- δ_r - rudder deflection
- $\dot{\beta}$ - rate of sideslip

The states α and β are used for defining the subspaces for modeling. The subspaces in α are created by partitioning α at -4° , -3° , -2° , ..., 23° , 24° , 25° , 30° , 35° and 40° . That is, one degree intervals are selected between -4° and 25° and five degrees intervals are chosen between 25° and 40° . The eighteen data files (i.e., one for each of the maneuvers F1M1, F2M1, ..., F4M10, and F6M1) created by the estimation phase of the EBM system identification method are transformed into thirty-two new data files by using the partitions on α and by collecting together the data from all eighteen maneuvers having an angle of attack within an α interval.

The subspaces in β are handled by using spline functions. Since the lateral coefficients are antisymmetric with respect to the sideslip angle, a cubic spline function having only odd powers of β is used. This ensures that the derivatives with respect to β are continuous and are symmetric in β . For example, using C_y to illustrate we have (assuming linear terms in δ_r , p , r and $\dot{\beta}$)

$$C_y(\alpha, \beta, \delta_r = 0, p = 0, r = 0, \dot{\beta} = 0) = C_{y_{\beta_0}}(\alpha) \cdot \beta + \sum_{i=1}^N C_{y_{\beta_i}}(\alpha) \cdot f(\beta, \beta_i, \beta_{i+1})$$

where β_i and β_{i+1} are spline knots on the $|\beta|$ axis satisfying $0 \leq \beta_1 < \beta_2 < \dots < \beta_{N+1}$ and where $f(\beta, \beta_i, \beta_{i+1})$ is defined as

$$f(\beta, \beta_i, \beta_{i+1}) = \begin{cases} 0 & 0 \leq \beta \leq \beta_i \\ \frac{1}{3} (\beta - \beta_i)^3 & \beta_i \leq \beta \leq \beta_{i+1} \\ (\beta_{i+1} - \beta_i)^2 (\beta - \frac{1}{3} \beta_i - \frac{2}{3} \beta_{i+1}) & \beta_{i+1} \leq \beta \end{cases}$$

$$f(-\beta, \beta_i, \beta_{i+1}) = -f(\beta, \beta_i, \beta_{i+1}) \quad \beta > 0.$$

The derivative of C_y with respect to β is given by

$$C_{y_{\beta}}(\alpha, \beta) = C_{y_{\beta_0}}(\alpha) + \sum_{i=1}^N C_{y_{\beta_i}}(\alpha) \cdot \frac{\partial f}{\partial \beta}(\beta, \beta_i, \beta_{i+1})$$

where

$$\frac{\partial f}{\partial \beta}(\beta, \beta_i, \beta_{i+1}) = \begin{cases} 0 & 0 \leq \beta \leq \beta_i \\ (\beta - \beta_i)^2 & \beta_i \leq \beta \leq \beta_{i+1} \\ (\beta_{i+1} - \beta_i)^2 & \beta_{i+1} \leq \beta \end{cases}$$

$$\frac{\partial f}{\partial \beta}(-\beta, \beta_i, \beta_{i+1}) = \frac{\partial f}{\partial \beta}(\beta, \beta_i, \beta_{i+1}) \quad \beta > 0.$$

We observe from these derivatives that $C_{y_{\beta}}(\alpha, \beta)$ is an even function with respect to β and is, therefore, symmetric in β .

Let $\beta_{\max}(\alpha)$ denote the maximum value of $|\beta|$ attained at a given angle of attack α by all eighteen maneuvers. At a given α the subspaces in β are created by choosing knots β_1, β_2, \dots in the β -space $[0, \beta_{\max}(\alpha)]$. The five following knot sets are used in the modeling of the lateral coefficients:

<u>Set</u>	<u>Knots on β axis</u>
I	$0^\circ, \beta_{\max}(\alpha)$
II	$0^\circ, 5^\circ, \beta_{\max}(\alpha)$
III	$0^\circ, 10^\circ, \beta_{\max}(\alpha)$
IV	$0^\circ, 2^\circ, 10^\circ, \beta_{\max}(\alpha)$
V	$0^\circ, 5^\circ, 10^\circ, \beta_{\max}(\alpha)$

4.2 IDENTIFICATION OF C_y

As discussed in Section 4.1 the modeling of C_y is conducted on subspaces of the α -space -4° to 40° . The subspaces are one degree intervals $[\alpha_i, \alpha_i + 1^\circ]$, $\alpha_i = -4^\circ, -3^\circ, \dots, 24^\circ$ and five degrees intervals $[\alpha_i, \alpha_i + 5^\circ]$, $\alpha_i = 25^\circ, 30^\circ, 35^\circ$.

Let α_1 be the left hand endpoint of an α -interval and let α_2 be the right hand endpoint. Let $\bar{\alpha}$ be the midpoint:

$$\bar{\alpha} = \frac{\alpha_1 + \alpha_2}{2}$$

The estimation results of all eighteen maneuvers having an angle of attack within the α -interval $[\alpha_1, \alpha_2]$ is processed using the stepwise multiple linear regression (SMLR) technique, the modeling phase of the EBM system identification method. The following model with α fixed at $\alpha = \bar{\alpha}$ is used in the SMLR technique to identify a model for the α -interval $[\alpha_1, \alpha_2]$:

$$C_y(\alpha = \bar{\alpha}, \beta, p, r, \delta_a, \delta_r, \dot{\beta}) = C_{y_{\delta_a}}(\bar{\alpha}) \cdot \delta_a + C_{y_{\delta_r}}(\bar{\alpha}) \cdot \frac{pb}{2v} + C_{y_r}(\bar{\alpha}) \cdot \frac{rb}{2v} + C_{y_{\dot{\beta}}}(\bar{\alpha}) \cdot \frac{\dot{\beta}b}{2v} + C_{y_{\beta_o}}(\bar{\alpha}) \cdot \beta + \sum_{i=1}^N C_{y_{\beta_i^3}}(\bar{\alpha}) \cdot f(\beta, \beta_i, \beta_{i+1}) + \text{other possible terms.}$$

The SMLR technique found the parameters $C_{y_{\delta_a}}(\alpha)$, $C_{y_p}(\alpha)$, $C_{y_r}(\alpha)$ and $C_{y_{\dot{\beta}}}(\alpha)$ to be statistically insignificant. The identification of the remaining parameters are given in Table C-1 of Appendix C. For example, at $\bar{\alpha} = 18.5^\circ$, the identified parameters are:

$$C_{y_{\delta_r}}(\bar{\alpha} = 18.5^\circ) = .076$$

$$C_{y_{\beta_0}}(\bar{\alpha} = 18.5^\circ) = -.67$$

$$C_{y_{\beta_1^3}}(\bar{\alpha} = 18.5^\circ) = -4.56$$

$$C_{y_{\beta_2^3}}(\bar{\alpha} = 18.5^\circ) = 14.76$$

where the knots are $\beta_1 = 0^\circ$, $\beta_2 = 5^\circ$, and $\beta_3 = 18^\circ$. Due to the sparsity of data at low angles of attack and at high angles of attack several α -intervals were combined in order to identify the parameters. For example, at the low end of the α -spectrum the following equation form was used in the SMLR program:

$$\begin{aligned}
 C_y = & C_{y_{\delta_r}} \cdot \delta_r \cdot \chi_{(-4^\circ, 7^\circ)}(\alpha) + C_{y_{\beta_1}}(\bar{\alpha}_1) \cdot \beta \cdot \chi_{(-4^\circ, 5^\circ)}(\alpha) \\
 & + C_{y_{\beta_0}}(\bar{\alpha}_2) \cdot \beta \cdot \chi_{(5^\circ, 6^\circ)}(\alpha) + C_{y_{\beta_0}}(\bar{\alpha}_3) \cdot \beta \cdot \chi_{(6^\circ, 7^\circ)}(\alpha) \\
 & + C_{y_{\beta_1^3}}(\bar{\alpha}_1) \cdot f(\beta, 0^\circ, 10^\circ) \cdot \chi_{(-4^\circ, 5^\circ)}(\alpha) \\
 & + C_{y_{\beta_1^3}}(\bar{\alpha}_2) \cdot f(\beta, 0^\circ, 10^\circ) \cdot \chi_{(5^\circ, 6^\circ)}(\alpha) \\
 & + C_{y_{\beta_1^3}}(\bar{\alpha}_3) \cdot f(\beta, 0^\circ, 12^\circ) \cdot \chi_{(6^\circ, 7^\circ)}(\alpha)
 \end{aligned}$$

where $\chi_{(a, b)}(\alpha)$ is the characteristic function of the set $[a, b]$ defined as

$$\chi_{(a, b)}(\alpha) = \begin{cases} 1 & \text{if } a \leq \alpha \leq b \\ 0 & \text{if } \alpha < a \text{ or } b < \alpha \end{cases}$$

and where $\alpha_1 = 0.5^\circ$, $\alpha_2 = 5.5^\circ$ and $\alpha_3 = 6.5^\circ$. The estimate of a parameter holds over the range of the characteristic function that multiplies it. The value of C_{y_δ} was identified as .118. Since the range of the characteristic function that multiplies C_{y_δ} is from -4° to 7° , the estimate of $C_{y_\delta} = .118$ is tabulated for each of the intervals $[-4^\circ, 5^\circ]$, $[5^\circ, 6^\circ]$ and $[6^\circ, 7^\circ]$ listed in the first column of Table C-1. The other six parameters are tabulated in Table C-1 under the column headings of $C_{y_\beta_0}$ and $C_{y_\beta_3}$. Characteristic functions were used also at the high angles of attack to obtain the identified parameters of Table C-1 over the α -range between 24° and 40° .

The aerodynamic derivative $C_{y_\delta}(\alpha)$ which is given in Table C-1 is plotted in Figure 4.2-1 where it is compared with the wind tunnel model.

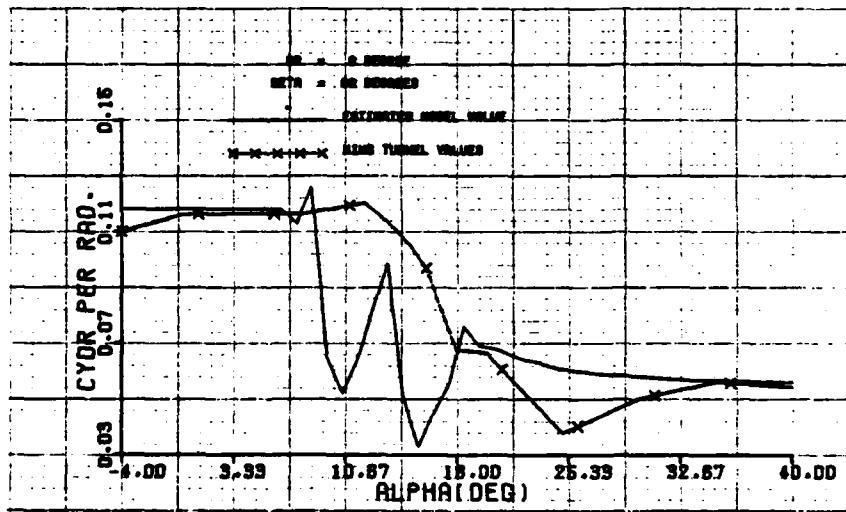


Fig. 4.2-1 Comparison between the C_{y_δ} identified model and the wind tunnel model

The parameters given in Table C-1 were used to plot Figures 4.2-2 through 4.2-6. These figures compare the identified models of $C_y(\alpha)$ and of $C_{y\beta}(\alpha)$ with the wind tunnel model for $\delta_r = 0$ and for $\beta = 0^\circ, 1^\circ, \dots, 10^\circ$. The derivative $C_{y\beta}(\beta)$ for $\alpha = 10.5^\circ, 11.5^\circ, \dots, 23.5^\circ, 24.5^\circ, 27.5^\circ$ is presented in Figures 4.2-5 and 4.2-6. Observe in Figure 4.2-6 the match between the identified $C_{y\beta}(\beta)$ and the wind tunnel for $\alpha = 20.5^\circ, 21.5^\circ$ and 22.5° as well as for $\alpha = 27.5^\circ$.

The SMLR technique estimates in addition to the parameters of Table C-1 a value for $C_{y0}(\bar{\alpha})$ at each of the α - intervals. The parameter $C_{y0}(\bar{\alpha})$ is the value of the side force coefficient C_y whenever all states and all controls are zero except $\alpha, \alpha = \bar{\alpha}$. The estimated values of $C_{y0}(\bar{\alpha})$ were of the order 10^{-4} which being negligible were taken as zero.

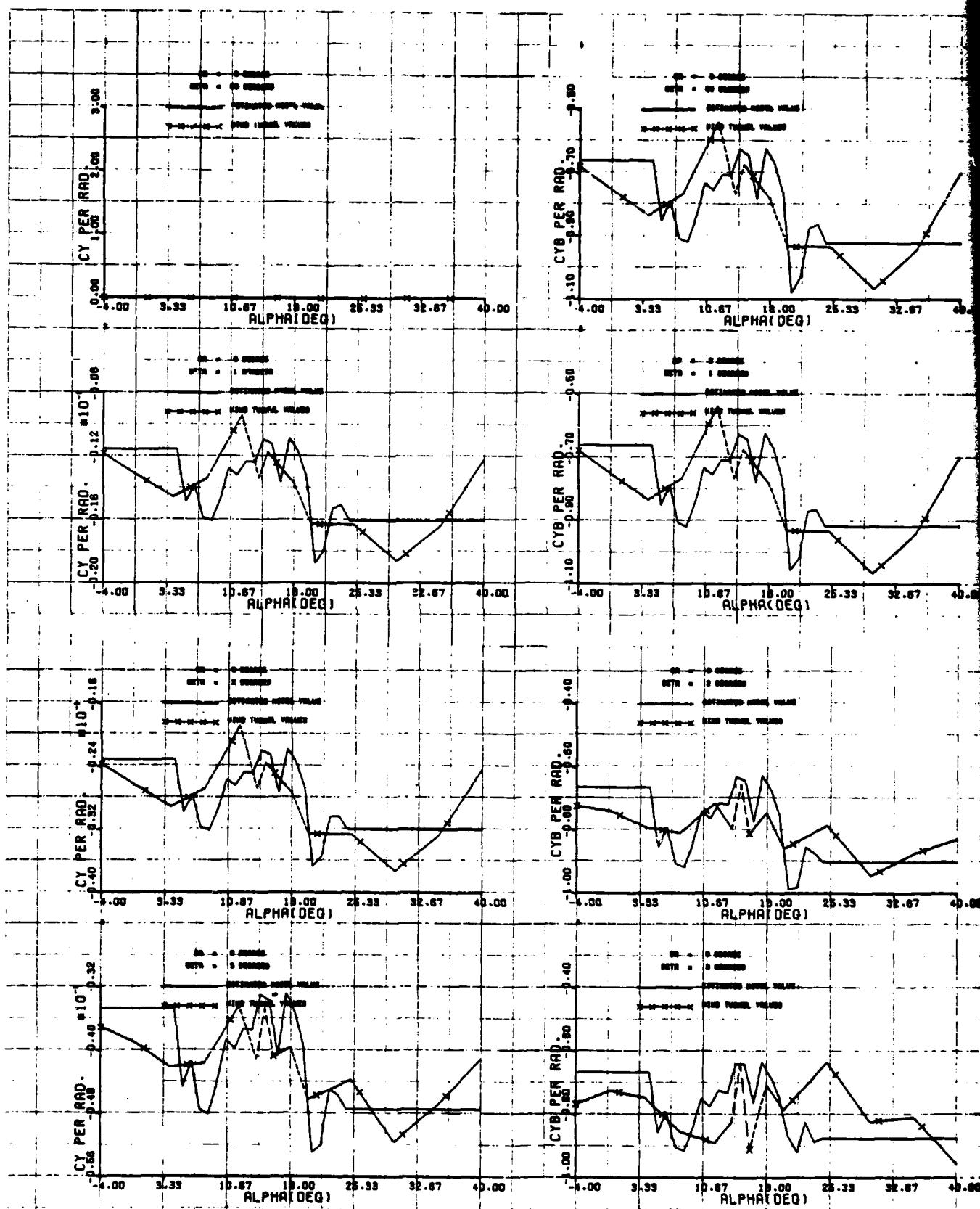


Fig. 4.2-2 Comparison between the C_y and the C_y^β identified models and the wind tunnel model for $\beta = 0^\circ, 1^\circ, 2^\circ, 3^\circ$.

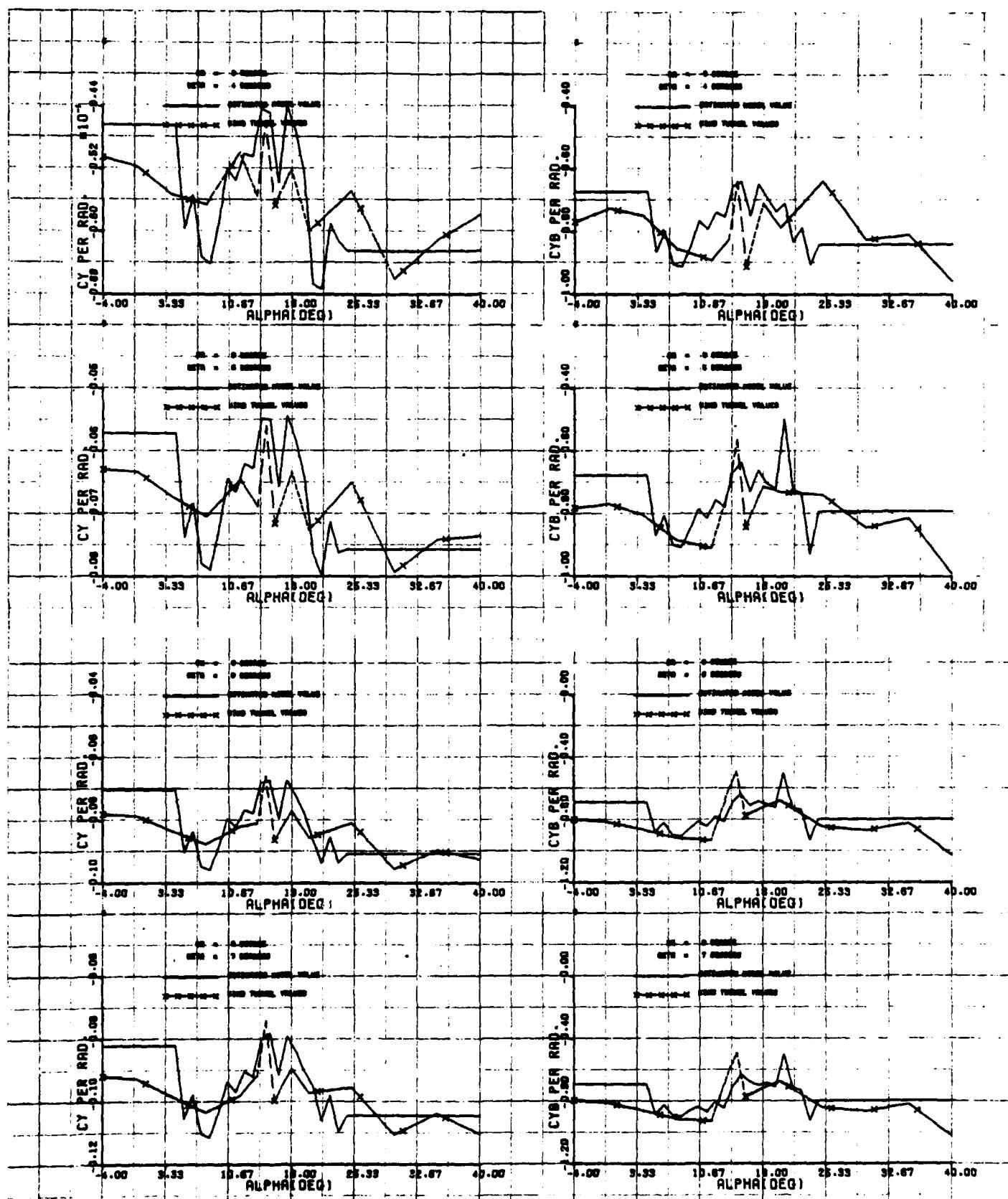


Fig. 4.2-3 Comparison between the C_y and the $C_{y\beta}$ identified models and the wind tunnel model for $\beta = 4^\circ, 5^\circ, 6^\circ, 7^\circ$.

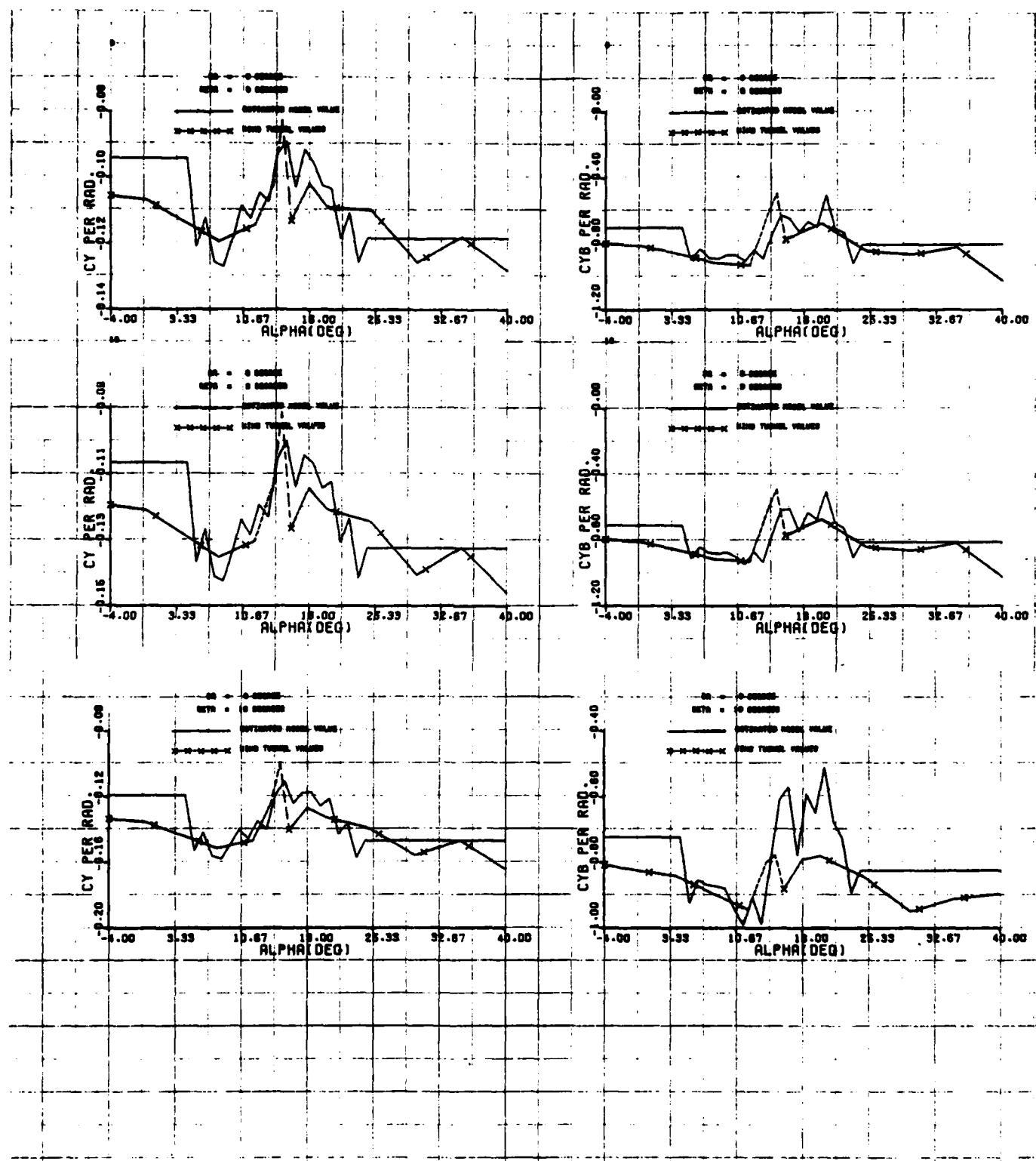


Fig. 4.2-4 Comparison between the C_y and the $C_{y\beta}$ identified models and the wind tunnel model for $\beta = 8^\circ, 9^\circ, 10^\circ$

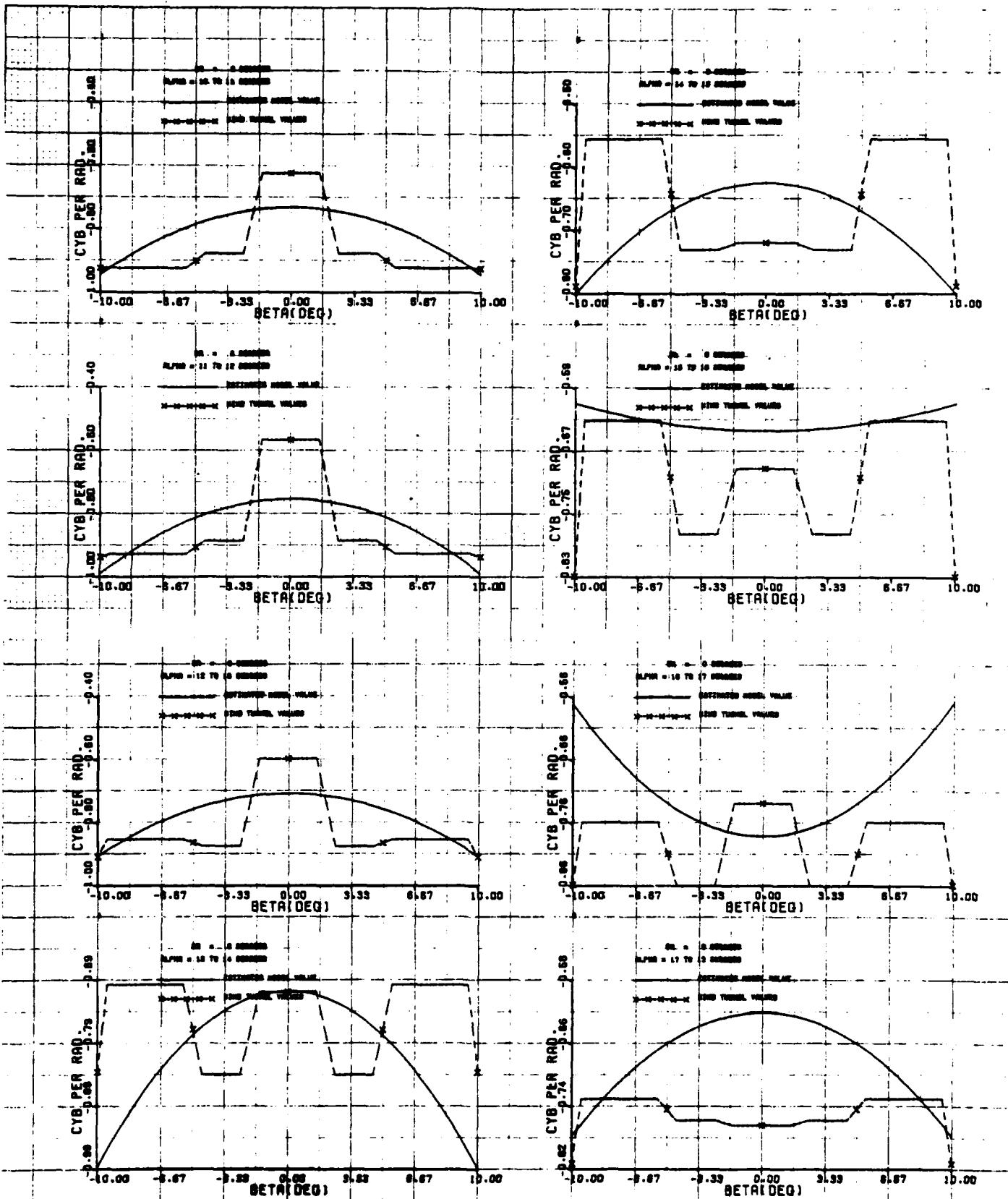


Fig. 4.2-5 Comparison between the C_y identified model and the wind tunnel model for $\alpha = 10.5^\circ, 11.5^\circ, 12.5^\circ, 13.5^\circ, 14.5^\circ, 15.5^\circ, 16.5^\circ, 17.5^\circ$

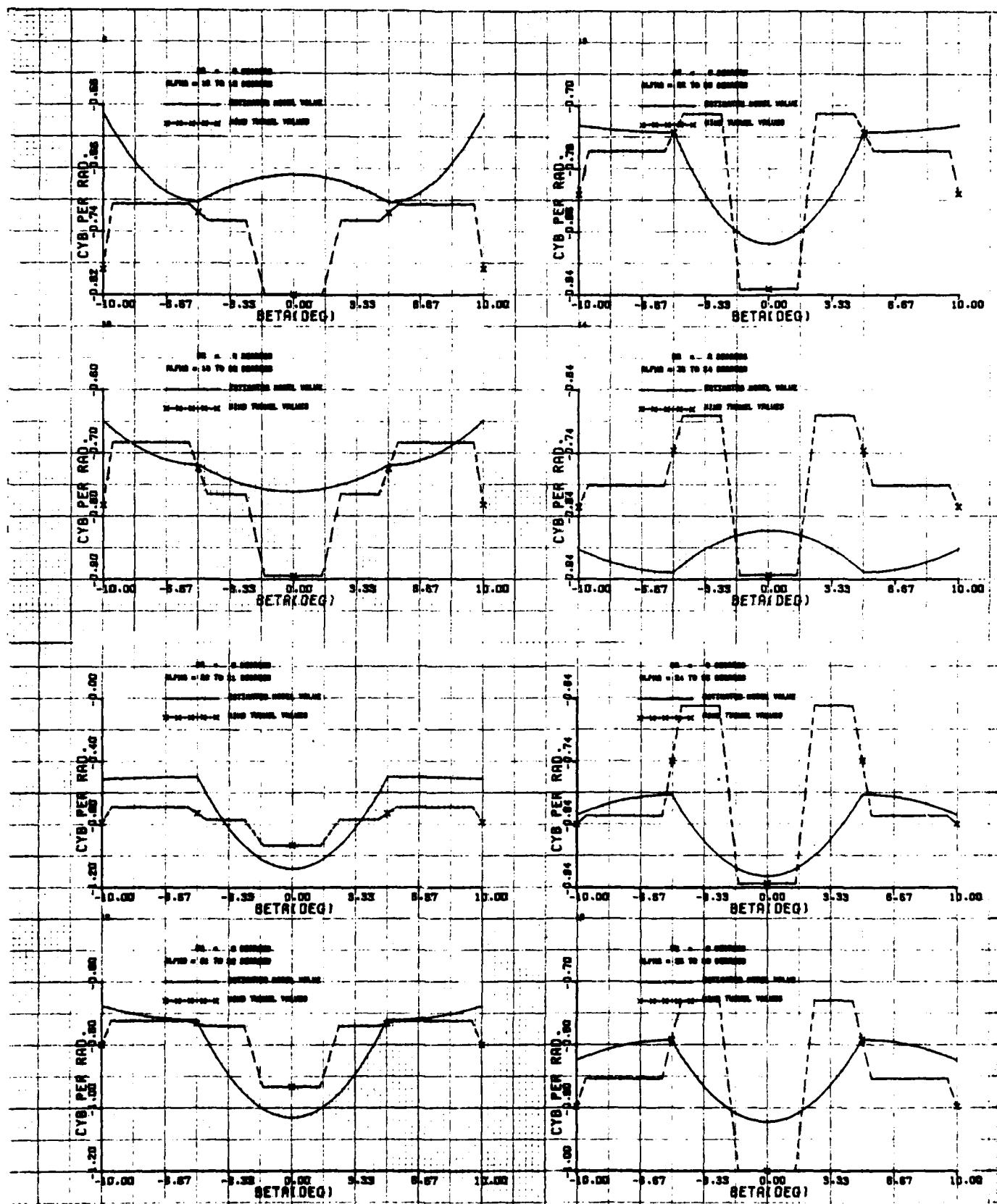


Fig. 4.2-6 Comparison between the C_{yB} identified model and the wind tunnel model for
 $\alpha = 18.5^\circ, 19.5^\circ, 20.5^\circ, 21.5^\circ, 22.5^\circ, 23.5^\circ, 24.5^\circ, 27.5^\circ$

4.3 IDENTIFICATION OF C_{ℓ}

The modeling of C_{ℓ} is conducted on subspaces of the α -space -4° to 40° . The subspaces are one degree intervals $[\alpha_i, \alpha_i + 1^{\circ}]$, $\alpha_i = -4^{\circ}, -3^{\circ}, \dots, 24^{\circ}$ and five degrees intervals $[\alpha_i, \alpha_i + 5^{\circ}]$, $\alpha_i = 25^{\circ}, 30^{\circ}, 35^{\circ}$. Let $\bar{\alpha}$ denote the midpoint of an α -interval. The following model with α fixed at $\alpha = \bar{\alpha}$ is used in the SMLR program to identify the aerodynamic coefficient C_{ℓ} for the α -interval being modeled:

$$\begin{aligned}
 C_{\ell}(\bar{\alpha}, \beta, p, r, \delta_a, \delta_r, \dot{\beta}) &= C_{\ell} \delta_a(\bar{\alpha}) \cdot \delta_a + C_{\ell} \delta_r(\bar{\alpha}) \cdot \delta_r \\
 &+ C_{\ell} p(\bar{\alpha}) \cdot \frac{pb}{2V} + C_{\ell} r(\bar{\alpha}) \cdot \frac{rb}{2V} + C_{\ell} \dot{\beta}(\bar{\alpha}) \cdot \frac{\dot{\beta}b}{2V} \\
 &+ C_{\ell} \beta_o(\bar{\alpha}) \cdot \beta + \sum_{i=1}^N C_{\ell} \beta_i^3(\bar{\alpha}) \cdot f(\beta, \beta_i, \beta_{i+1}) + \text{other possible terms.}
 \end{aligned}$$

The parameter $C_{\ell} \beta(\bar{\alpha})$ was determined by the SMLR technique to be statistically insignificant. The identified values of the other parameters are presented in Tables D-1 and D-2 of Appendix D. For example, at $\bar{\alpha} = 14.5^{\circ}$, the identified parameters are:

$$\begin{aligned}
 C_{\ell} \delta_a(\bar{\alpha} = 14.5^{\circ}) &= -.148 \text{ per rad} \\
 C_{\ell} \delta_r(\bar{\alpha} = 14.5^{\circ}) &= .0127 \text{ per rad} \\
 C_{\ell} p(\bar{\alpha} = 14.5^{\circ}) &= -.225 \text{ per rad} \\
 C_{\ell} r(\bar{\alpha} = 14.5^{\circ}) &= .310 \text{ per rad} \\
 C_{\ell} \beta_o(\bar{\alpha} = 14.5^{\circ}) &= -.037 \text{ per rad}
 \end{aligned}$$

$$C_{\ell} \beta_1^3 (\bar{\alpha} = 14.5^\circ) = 14.23 \text{ per rad}^3$$

$$C_{\ell} \beta_2^3 (\bar{\alpha} = 14.5^\circ) = -11.21 \text{ per rad}^3$$

$$C_{\ell} \beta_3^3 (\bar{\alpha} = 14.5^\circ) = 102.2 \text{ per rad}^3$$

β_3

where the knots are $\beta_1 = 0^\circ$, $\beta_2 = 2^\circ$, $\beta_3 = 10^\circ$ and $\beta_4 = 15^\circ$.

Due to the sparsity of data at low and high angles of attack, characteristic functions (as discussed in Section 4.2) were used to combine several α -intervals in the modeling of C_{ℓ} . For instance, the α -intervals below $\alpha = 6^\circ$ were combined using characteristic functions as well as those above $\alpha = 22^\circ$. In addition to using characteristic functions, the following procedure was used to identify the slopes of $C_{\ell}(\alpha)$ and $C_{\ell}(\alpha)$ at low and high angles of attack: we use $C_{\ell_p}(\alpha)$ to illustrate it. The value of $C_{\ell_p}(\bar{\alpha} = 21.5^\circ)$ has been identified by processing the data in the α -interval $[21^\circ, 22^\circ]$. It is desired to identify the slope of $C_{\ell_p}(\alpha)$ for α in the range 22° to 40° . This is accomplished by modifying the term $C_{\ell_p}(\bar{\alpha}) \cdot \frac{pb}{2V}$ as

$$[C_{\ell_p}(\alpha = 21.5^\circ) + A \cdot \frac{(\alpha - 21.5^\circ)}{57.29}] \cdot \frac{pb}{2V} \cdot x(\alpha) \quad (22^\circ, 40^\circ)$$

and identifying the slope A by processing the data in all α -intervals between 22° and 40° . The slope A is then used to evaluate $C_{\ell_p}(\alpha)$ for any α in the range 22° to 40° :

$$C_{\ell_p}(\alpha) = C_{\ell_p}(\alpha = 21.5^\circ) + A \cdot \frac{(\alpha - 21.5^\circ)}{57.29} \quad 22^\circ \leq \alpha \leq 40^\circ$$

This procedure was used in obtaining the tabulated values in Table D-2 for $\alpha = 22.5^\circ, 23.5^\circ, 24.5^\circ, 27.5^\circ, 32.5^\circ$ and 37.5° and in obtaining $C_{\ell_r}(\alpha)$ for α in the range -4° to 10° .

The identified dynamic derivative $C_{\ell_r}(\alpha)$ which is tabulated in Table D-2 is plotted in Figure 4.3-1 where it is compared with the theoretical prediction model of Bihrlle Applied Research, Ref. [2]. At low α the identified model of $C_{\ell_r}(\alpha)$ has slightly smaller values than $C_{\ell_p}(\alpha)$.

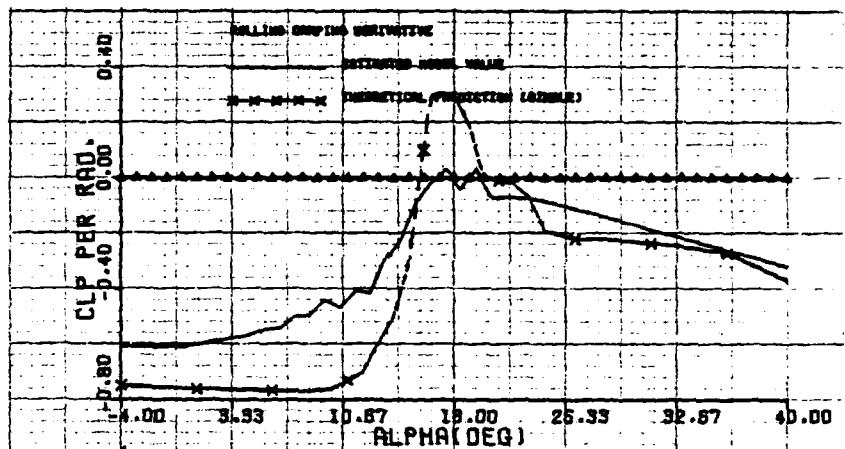


Fig. 4.3-1 Comparison between the C_{ℓ_r} identified model and the theoretical prediction model of Bihrlle Applied Research

the theoretical prediction model. The two curves cross at about 15.5° and the identified model hovers about the zero axis between 16° and 20° whereas the theoretical prediction goes positive and reaches a peak of 0.30 per rad. The two curves agree for α above 20° .

The tabulated values of $C_{l_r}(\alpha)$ in Table D-2 are plotted in Figure 4.3-2 where it is compared with the theoretical prediction model of Ref. [2]. The identified value of $C_{l_r}(\alpha)$ has a slightly

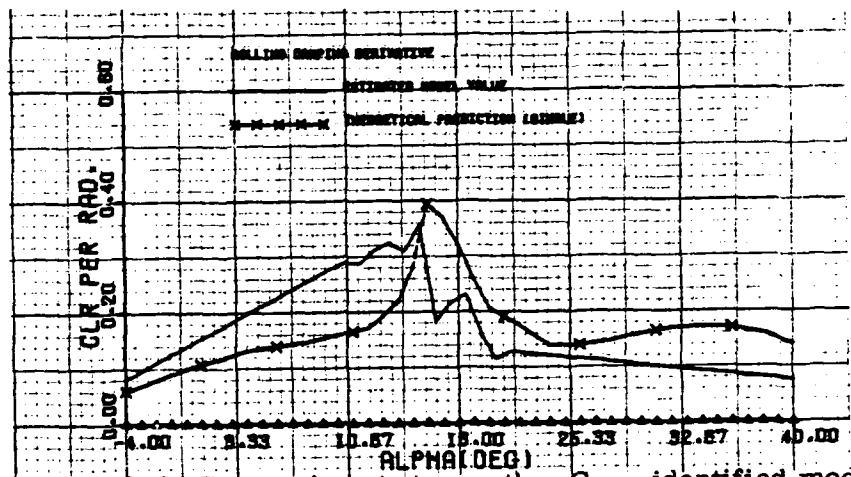


Fig. 4.3-2 Comparison between the C_{l_r} identified model and the theoretical prediction model of Bihrlle Applied Research

steeper slope at low angles of attack but drops off more sharply at stall than the theoretical prediction model. Above $\alpha = 18^\circ$ the identified model lies slightly under the theoretical prediction.

The tabulated values of $C_{l_r}(\alpha)$ in Table D-1 are plotted in

Figure 4.3-3, together with the wind tunnel model for $\beta = 0^\circ$. The identified model of $C_{l_r}(\alpha)$ compares well with the wind tunnel model at low α . Its drop in controllability above stall coincides with the wind tunnel model's drop. Between 18° and 26° angles of attack the identified

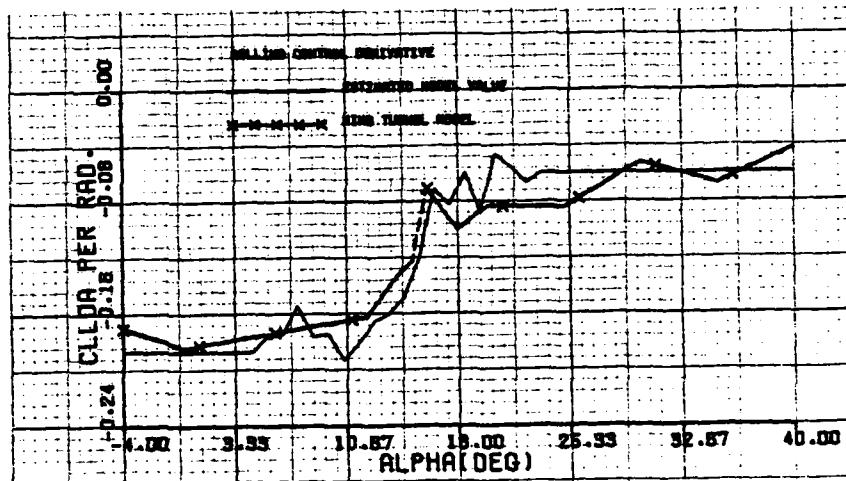


Fig. 4.3-3 Comparison between the $C_{l_{\delta}^a}$ identified model and the wind tunnel model

model has a slightly smaller magnitude than the wind tunnel, but they coincide above 30° .

The identified values of $C_{l_{\delta}^a}$ in Table D-1 are plotted in

Figure 4.3-4 where it is compared with the wind tunnel model for $\beta = 0^\circ$. They compare well except for α between stall and 20° where the wind tunnel model seesaws to double its magnitude and the identified model seesaws about zero.

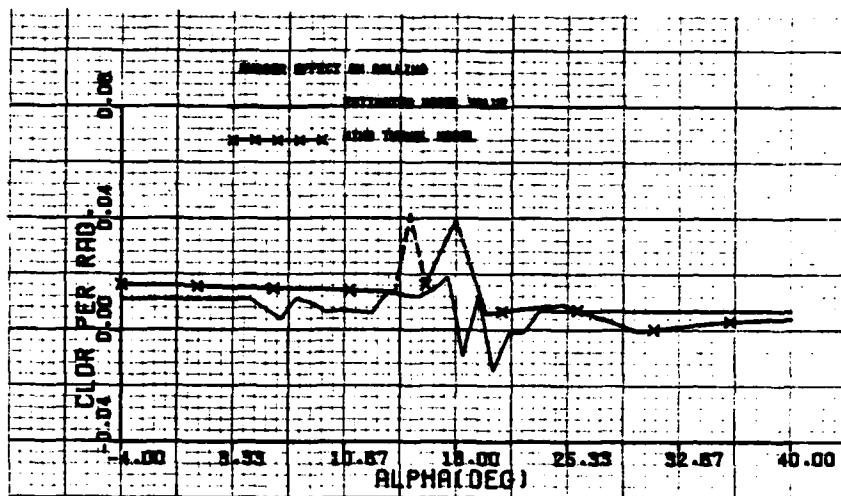


Fig. 4.3-4 Comparison between the $C_{l\alpha}$ identified model and the wind tunnel model

The other identified parameters of Table D-1 were used to plot Figures 4.3-5 through 4.3-9 where $C_{l\alpha}(\alpha)$ and $C_{l\beta}(\alpha)$, $-4^\circ \leq \alpha \leq 40^\circ$, are compared with the wind tunnel model for $\beta = 0^\circ, 1^\circ, \dots, 10^\circ$ and where $C_{l\beta}(\beta)$, $0 \leq \beta \leq 10^\circ$, is compared with the wind tunnel model for $\alpha = 10.5^\circ, 11.5^\circ, \dots, 23.5^\circ, 24.5^\circ, 27.5^\circ$.

The SMLR technique estimates in addition to the parameters of Tables D-1 and D-2 a value for $C_{l\alpha}(\bar{\alpha})$ at end of the α -intervals. The parameter $C_{l\alpha}(\bar{\alpha})$ is the value of the rolling moment coefficient $C_{l\alpha}$ whenever all states and all controls are zero except $\alpha - \alpha = \bar{\alpha}$. The estimated values of $C_{l\alpha}(\bar{\alpha})$ were of the order 10^{-4} to 10^{-5} which being negligible were taken as zero.

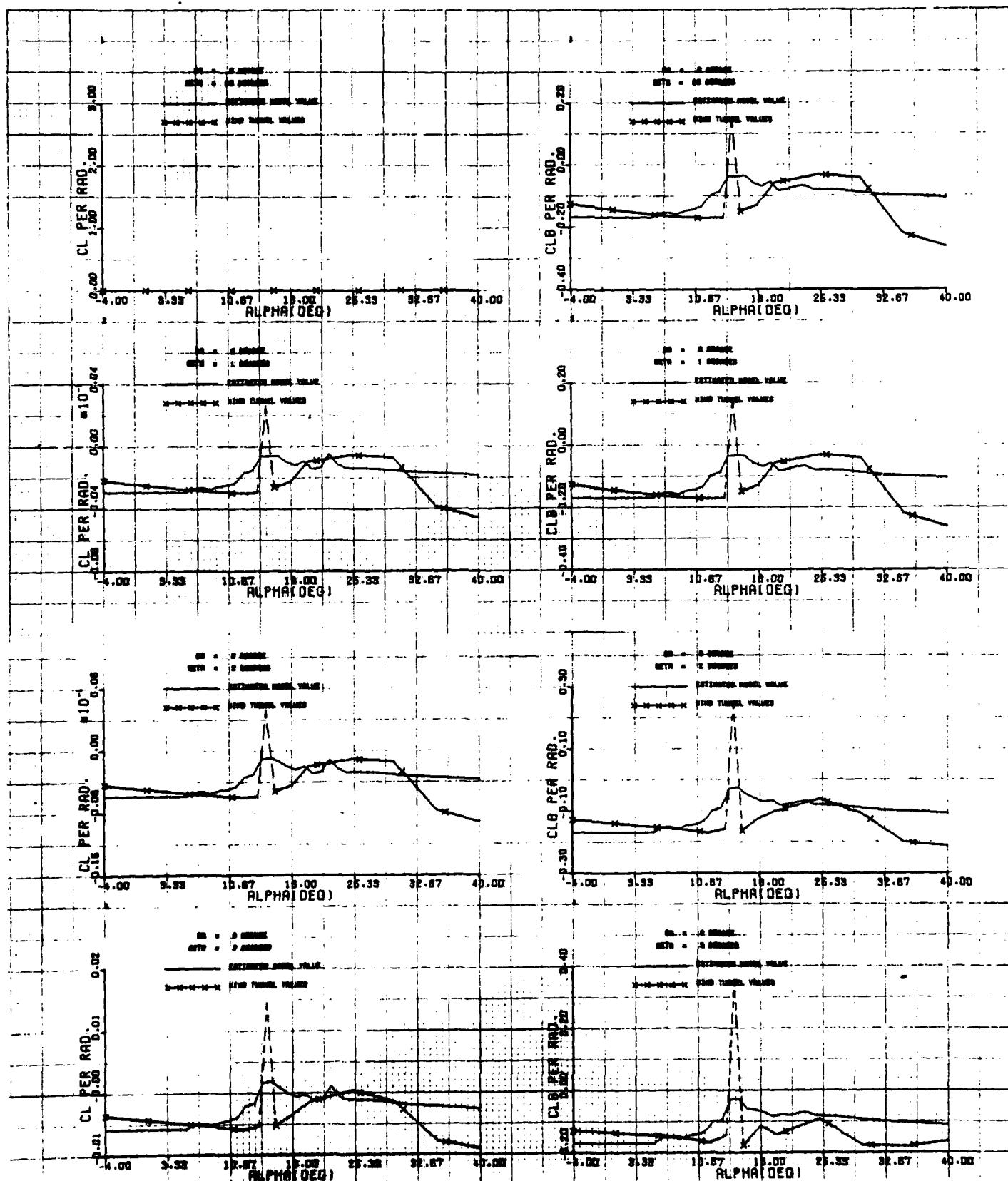


Fig. 4.3-5 Comparison between the C_{α} and the C_{β} identified models and the wind tunnel model for $\beta = 0^\circ, 1^\circ, 2^\circ, 3^\circ$.

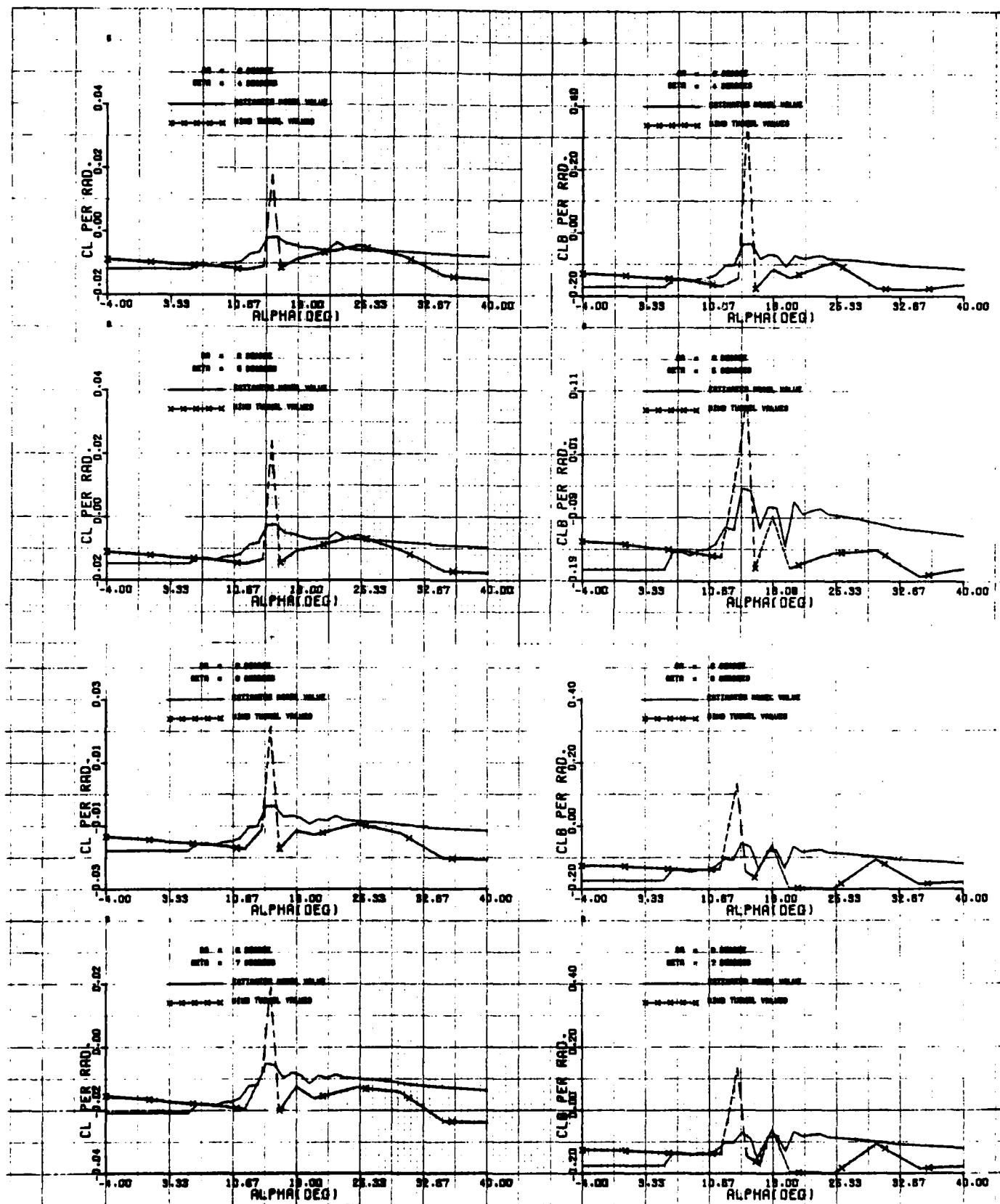


Fig. 4.3-6 Comparison between the C_l and the $C_{l\beta}$ identified models and the wind tunnel model for $\beta = 4^\circ, 5^\circ, 6^\circ, 7^\circ$

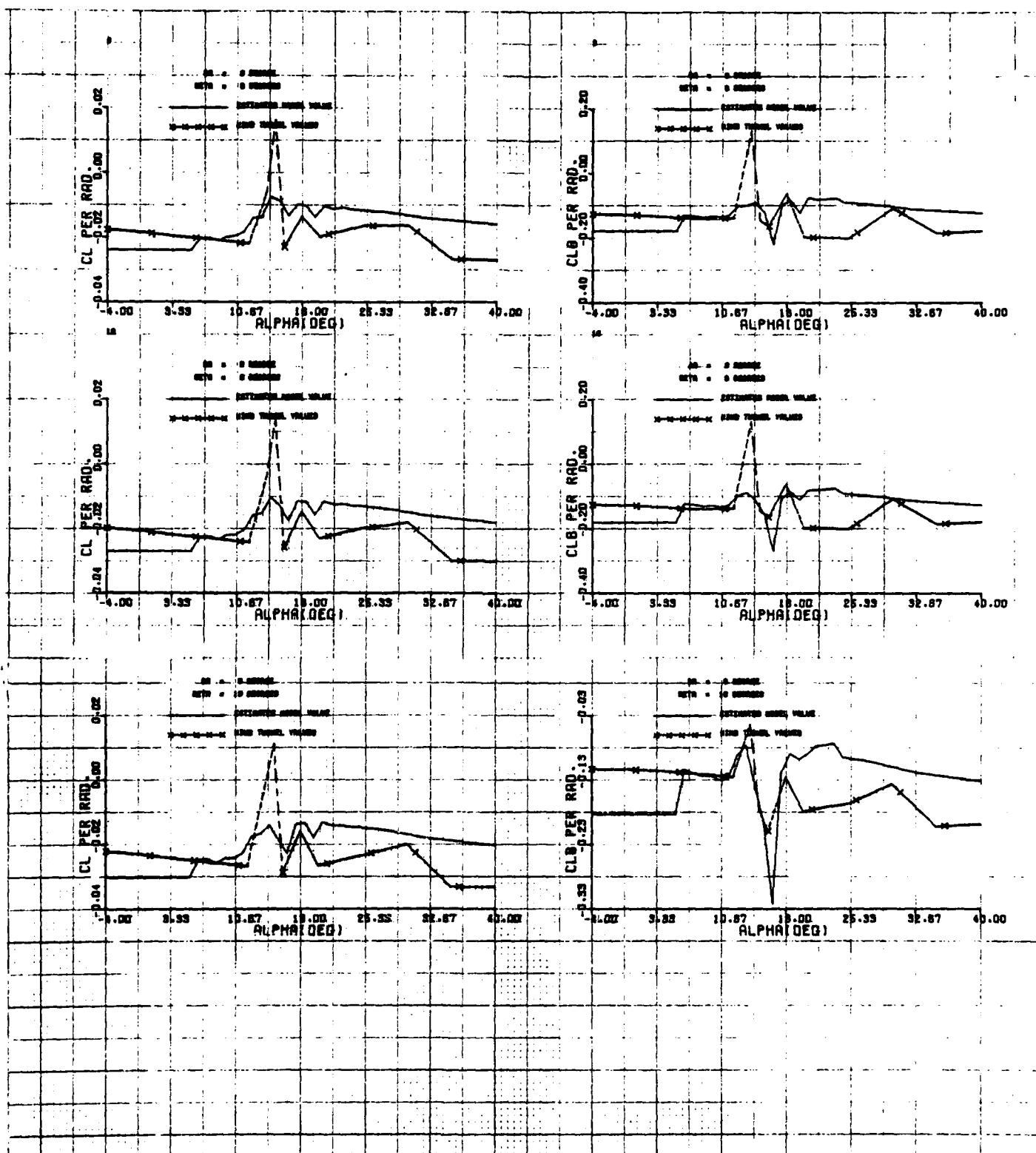


Fig. 4.3-7 Comparison between the C_L and the $C_{L\beta}$ identified models and the wind tunnel model for $\beta = 8^\circ, 9^\circ, 10^\circ$

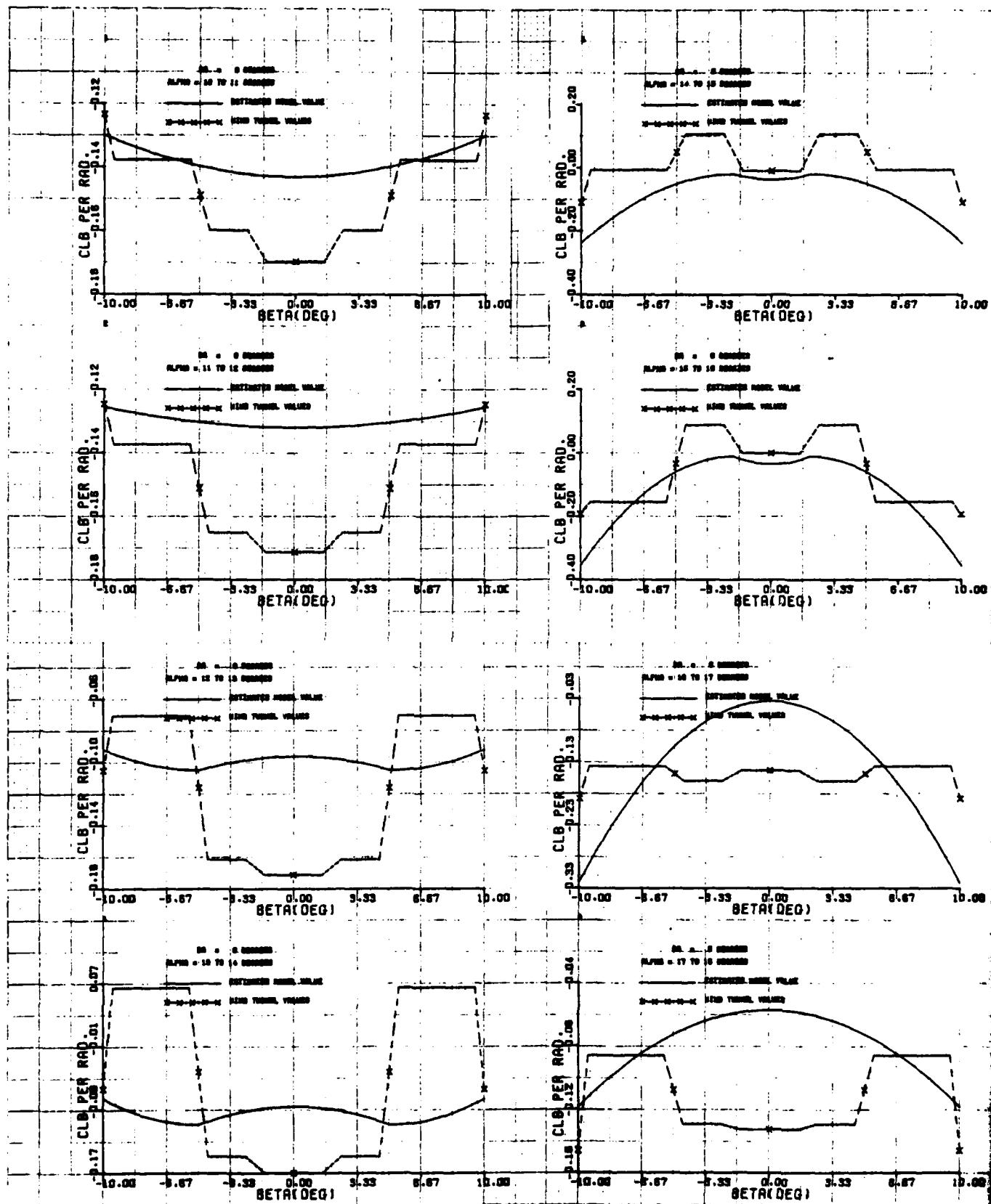


Fig. 4.3-8 Comparison between the C_L identified model and the wind tunnel model for $\alpha = 10.5^\circ, 11.5^\circ, 12.5^\circ, 13.5^\circ, 14.5^\circ, 15.5^\circ, 16.5^\circ, 17.5^\circ$

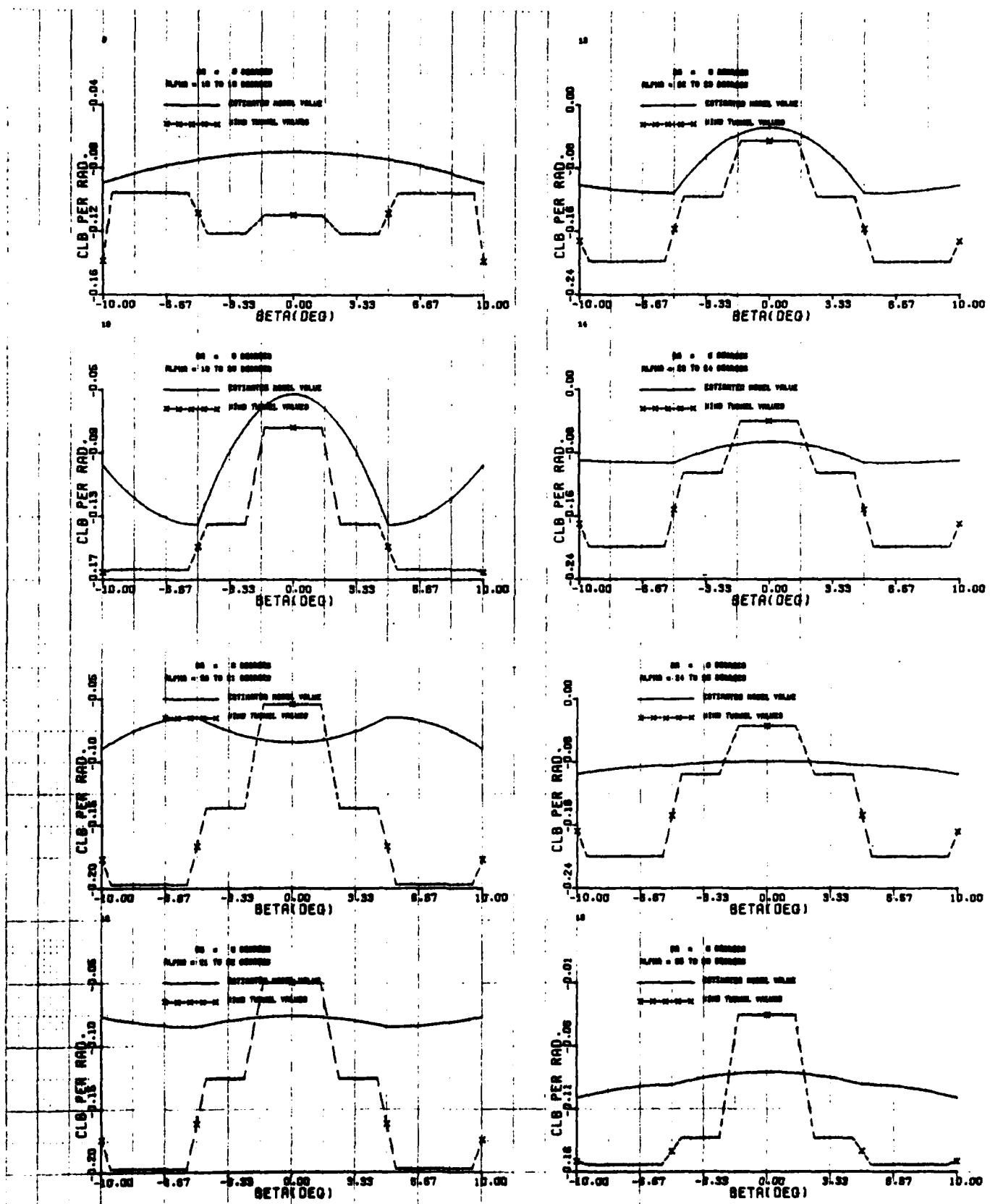


Fig. 4.3-9 Comparison between the C_lB identified model and the wind tunnel model for $\alpha = 18.4^\circ, 19.5^\circ, 20.5^\circ, 21.5^\circ, 22.5^\circ, 23.5^\circ, 24.5^\circ, 27.5^\circ$

4.4 IDENTIFICATION OF C_n

The modeling of C_n is conducted on subspaces of the α -space -4° to 40° . The subspaces are one degree intervals $[\alpha_i, \alpha_i + 1^\circ]$, $\alpha_i = -4^\circ, -3^\circ, \dots, 24^\circ$ and five degrees intervals $[\alpha_i, \alpha_i + \alpha_i + 5^\circ]$, $\alpha_i = 25^\circ, 30^\circ, 35^\circ$. Let $\bar{\alpha}$ denote the midpoint of an α -interval. The following model with α fixed at $\alpha = \bar{\alpha}$ is used in the SMLR program to identify the aerodynamic coefficient C_n over a given α -interval:

$$\begin{aligned}
 C_n(\bar{\alpha}, \beta, p, r, \delta_a, \delta_r, \beta) &= C_{n_{\delta_a}}(\bar{\alpha}) \cdot \delta_a + C_{n_{\delta_r}}(\bar{\alpha}) \cdot \delta_r \\
 &+ C_{n_p}(\bar{\alpha}) \cdot \frac{pb}{2V} + C_{n_r}(\bar{\alpha}) \cdot \frac{rb}{2V} + C_{n_{\beta}}(\bar{\alpha}) \cdot \frac{\beta b}{2V} \\
 &+ C_{n_{\beta_o}}(\bar{\alpha}) \cdot \beta + \sum_{i=1}^N C_{n_{\beta_i}}(\bar{\alpha}) \cdot f(\beta, \beta_i, \beta_{i+1}) + \text{other possible terms.}
 \end{aligned}$$

The parameter $C_{n_{\delta_a}}(\bar{\alpha})$ and $C_{n_{\delta_r}}(\bar{\alpha})$ were determined by the SMLR program to be statistically insignificant. The identified values of the other parameters are presented in Tables E-1 and E-2 of Appendix E. For example, at $\bar{\alpha} = 13.5^\circ$, the identified parameters are:

$$\begin{aligned}
 C_{n_{\delta_r}}(\bar{\alpha} = 13.5^\circ) &= -.032 \text{ per rad} \\
 C_{n_p}(\bar{\alpha} = 13.5^\circ) &= -.098 \text{ per rad} \\
 C_{n_r}(\bar{\alpha} = 13.5^\circ) &= -.1816 \text{ per rad} \\
 C_{n_{\beta_o}}(\bar{\alpha} = 13.5^\circ) &= .052 \text{ per rad} \\
 C_{n_{\beta_1}}(\bar{\alpha} = 13.5^\circ) &= 4.18 \text{ per rad}^3
 \end{aligned}$$

$$C_n (\alpha = 13.5^\circ) = -15.93 \text{ per rad}^3$$

β_2^3

$$C_n (\alpha = 13.5^\circ) = 32.19 \text{ per rad}^3$$

β_3^3

where the knots are $\beta_1 = 0^\circ$, $\beta_2 = 5^\circ$, $\beta_3 = 10^\circ$ and $\beta_4 = 16^\circ$.

Due to the sparsity of data at low and high angles of attack, characteristic functions (as discussed in Section 4.2) were used to combine several α -intervals in the modeling of C_n . In addition to using characteristic functions, the procedure for estimating slopes described in Section 4.3 was used to identify $C_{n_p}(\alpha)$, $C_{n_r}(\alpha)$ and $C_{n_{\delta_r}}(\alpha)$ for α above 25° . The procedure was used to identify $C_{n_p}(\alpha)$ and $C_{n_{\delta_r}}(\alpha)$ over the α range 25° to 40° and $C_{n_r}(\alpha)$ over the α range 30° to 40° .

The identified dynamic derivative $C_n(\alpha)$ which is tabulated in Table E-2 is plotted in Figure 4.4-1 where it is compared with the theoretical prediction model of Bihrlle Applied Research, Ref. [2]. The identified model agrees with the theoretical prediction at angles of attack below stall. The identified model reaches its highest positive value of .113 at $\alpha = 16.5^\circ$ whereas the theoretical prediction model continues to grow reaching its peak of 0.365 at $\alpha = 18^\circ$. After reaching a peak at $\alpha = 16.5^\circ$ the identified model drops off to a value of -.076 at $\alpha = 20.5^\circ$, rises to .048 at $\alpha = 22.5$; then drops to -.051 at $\alpha = 23.5$ before leveling off about -.075 over the α range $[25^\circ, 40^\circ]$. The theoretical prediction model, on the other hand, drops from its peak at $\alpha = 18^\circ$ to .12 at $\alpha = 20.5^\circ$, climbs to .14 at $\alpha = 22^\circ$, drops slightly to .13 at $\alpha = 24^\circ$, then rises to .195 at $\alpha = 30^\circ$ before dropping to .06 at $\alpha = 38^\circ$. A significant difference between these two models is that over the α range $[20^\circ, 35^\circ]$

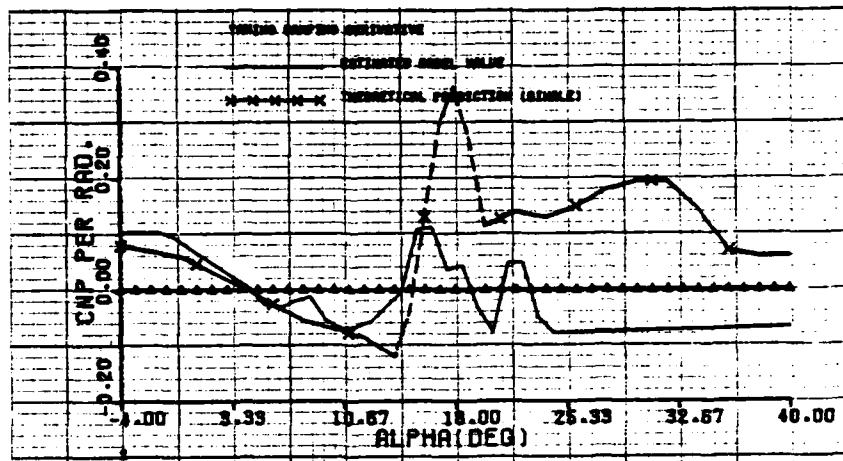


Fig. 4.4-1 Comparison between the C_n identified model and the theoretical prediction model of Bihrlle Applied Research

the theoretical prediction model has values greater than .10 while the identified model has values around -.075 except for the sharp rise and decline between $\alpha = 21^\circ$ and 23° where it peaks at .048. This difference is highly significant as has been demonstrated by the findings of the simulation study of [1]. Therein, the initial conditions and the recorded control time histories of the actual T-2C flight data were used to drive the synthetic T-2C model composed of the wind tunnel model and the theoretical prediction model of Bihrlle Applied Research. The synthetic responses were drastically different from the actual flight data until a change in the theoretical prediction model of C_n^p (i.e., the same as given in Figure 4.4-1) was made. For example, one synthetic maneuver reached 60° in α while the real data did not go beyond $\alpha = 25^\circ$. Other synthetic maneuvers exhibited large yaw and roll spin rates. An inspection of the states revealed a greater degree of instability for the theoretical

prediction model of C_{n_p} . By trial and error a constant value of $C_{n_p} = -.06$ was found to give stability to the simulated data and to provide data which agreed better with the actual flight data. Section 2 of Ref. [1] contains a more detailed discussion of the problem. Therein, note also the results in Figure 4.17. Therefore, the identified model of C_{n_p} obtained by processing the actual T-2C flight data agrees with the modification of C_{n_p} obtained by trial and error in Ref. [1].

The tabulated values of $C_{n_p}(\alpha)$ in Table E-2 are plotted in Figure 4.4-2 where it is compared with the theoretical prediction model of Ref. [2]. Amazingly, the theoretical prediction model agrees well with identified model. There appears, however, to be a difference between the curves of about 1° shift in α .

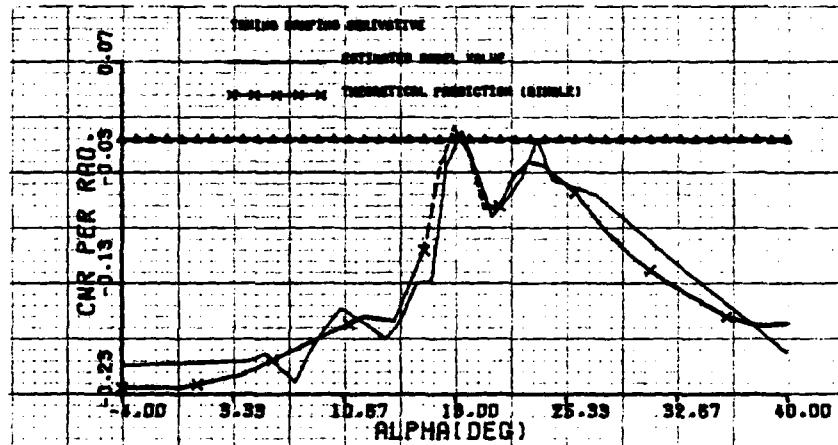


Fig. 4.4-2 Comparison between the C_{n_r} identified model and the theoretical prediction model of Bihrl Applied Research

The tabulated values of $C_{n_{\delta_r}}(\alpha)$ in Table E-1 are plotted in Figure 4.4-3 where it is compared with the wind tunnel model for $\beta = 0^\circ$. The identified model indicates a slightly smaller performance than that expected by the wind tunnel results.

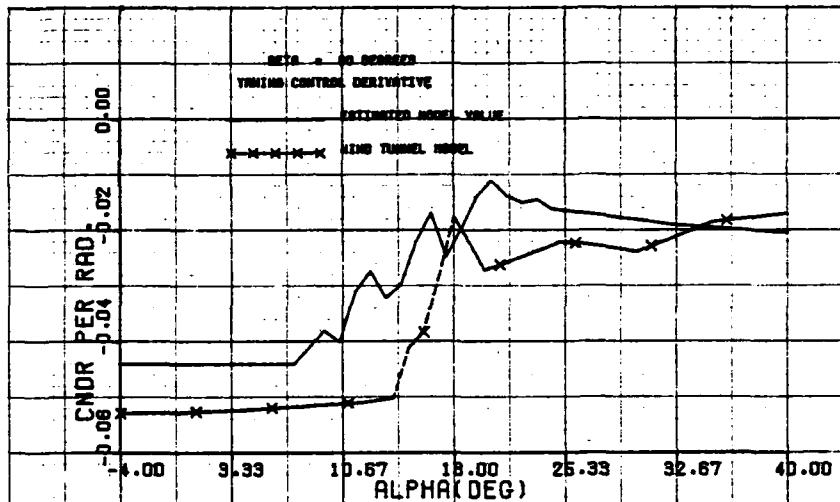


Fig. 4.4-3 Comparison between the $C_{n_{\delta_r}}$ identified model and the wind tunnel model

The other identified parameters of Table E-1 were used to plot Figures 4.4-4 through 4.4-8 where $C_n(\alpha)$ and $C_{n_{\beta}}(\alpha)$, $-4^\circ \leq \alpha \leq 40^\circ$, are compared with the wind tunnel model for $\beta = 0^\circ, 1^\circ, \dots, 10^\circ$ and where $C_{n_{\beta}}(\beta)$, $0 \leq \beta \leq 10^\circ$, is compared with the wind tunnel model for $\alpha = 10.5^\circ, 11.5^\circ, \dots, 23.5^\circ, 24.5^\circ, 27.5^\circ$. The rudder control equals zero in these figures.

The SMLR technique estimates in addition to the parameters of Tables E-1 and E-2 a value for $C_{n_0}(\bar{\alpha})$ at each of the α -intervals.

The parameter $C_{n_0}(\bar{\alpha})$ is the value of the yawing moment coefficient C_n whenever all states and controls are zero with the exception of $\alpha = \bar{\alpha}$. The estimated values of $C_{n_0}(\bar{\alpha})$ were of the order 10^{-4} to 10^{-5} which being negligible were taken as zero. A linear term involving \dot{p} was identified to have a nearly constant value of 1.1 for all α -intervals.

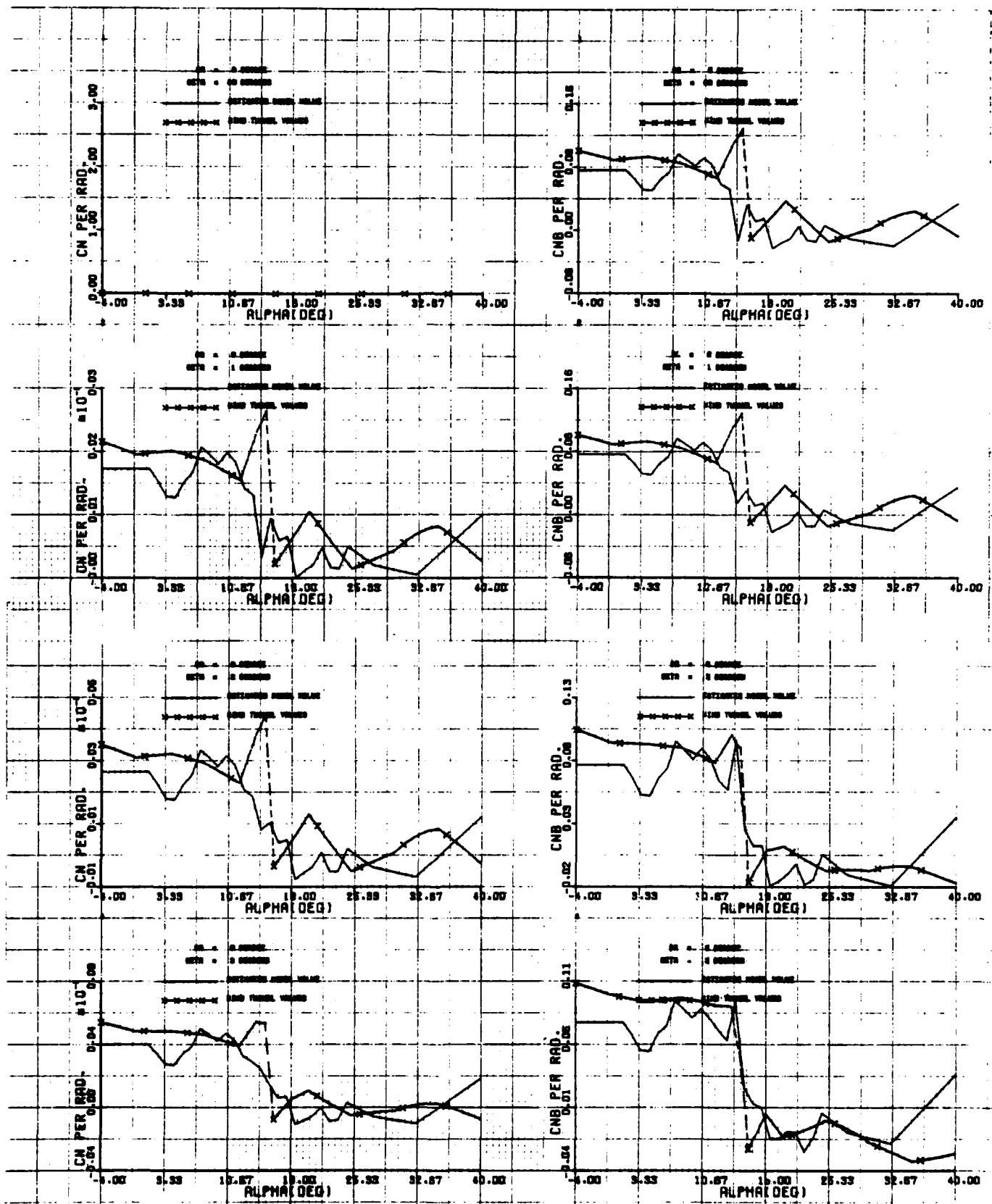


Fig. 4.4-4 Comparison between the C_n and the C_{nB} identified: models and the wind tunnel model for $\beta = 0^\circ, 1^\circ, 2^\circ, 3^\circ$

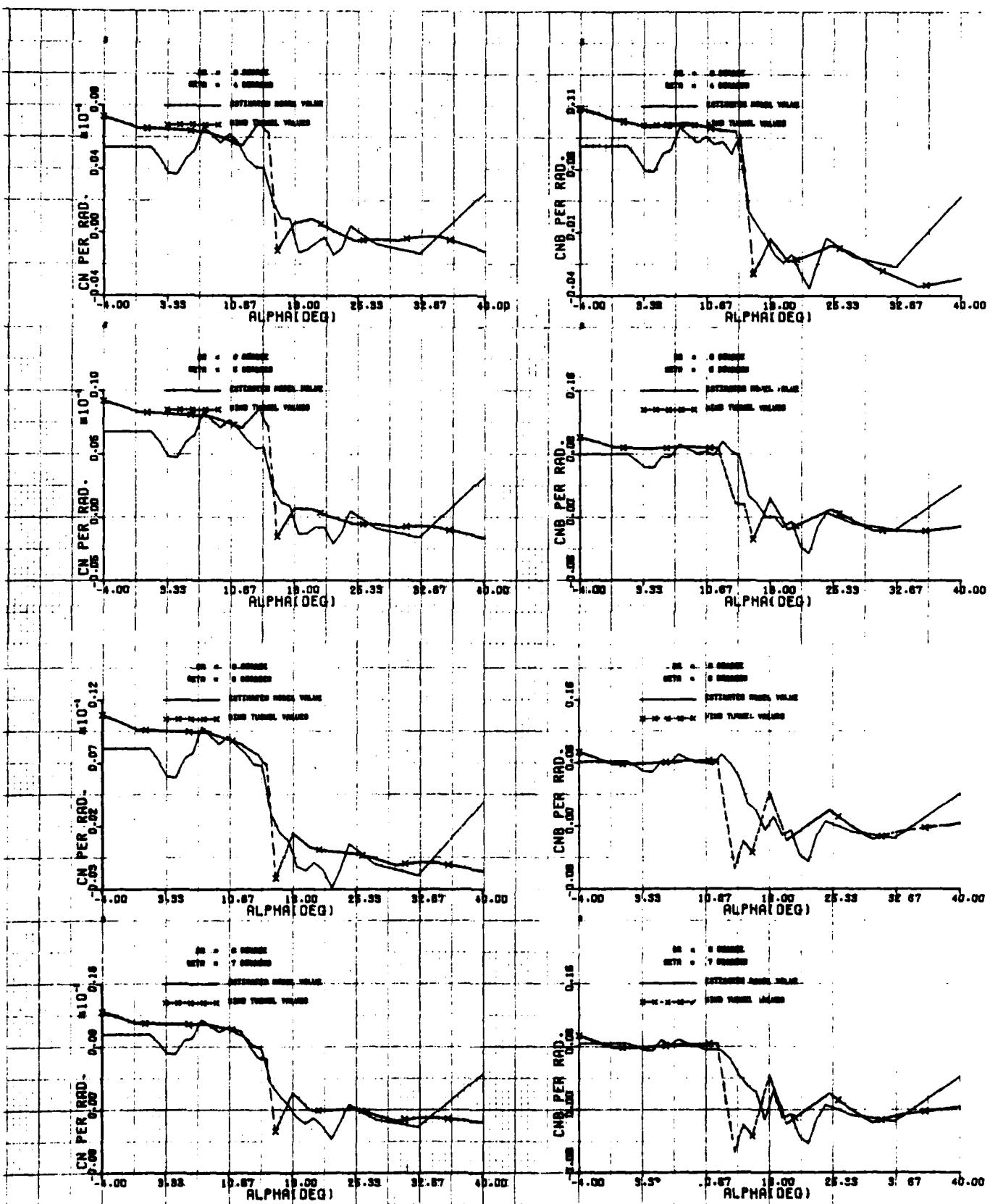


Fig. 4.4-5 Comparison between the C_n and the C_{nB} identified models and the wind tunnel model for $\beta = 4^\circ, 5^\circ, 6^\circ, 7^\circ$

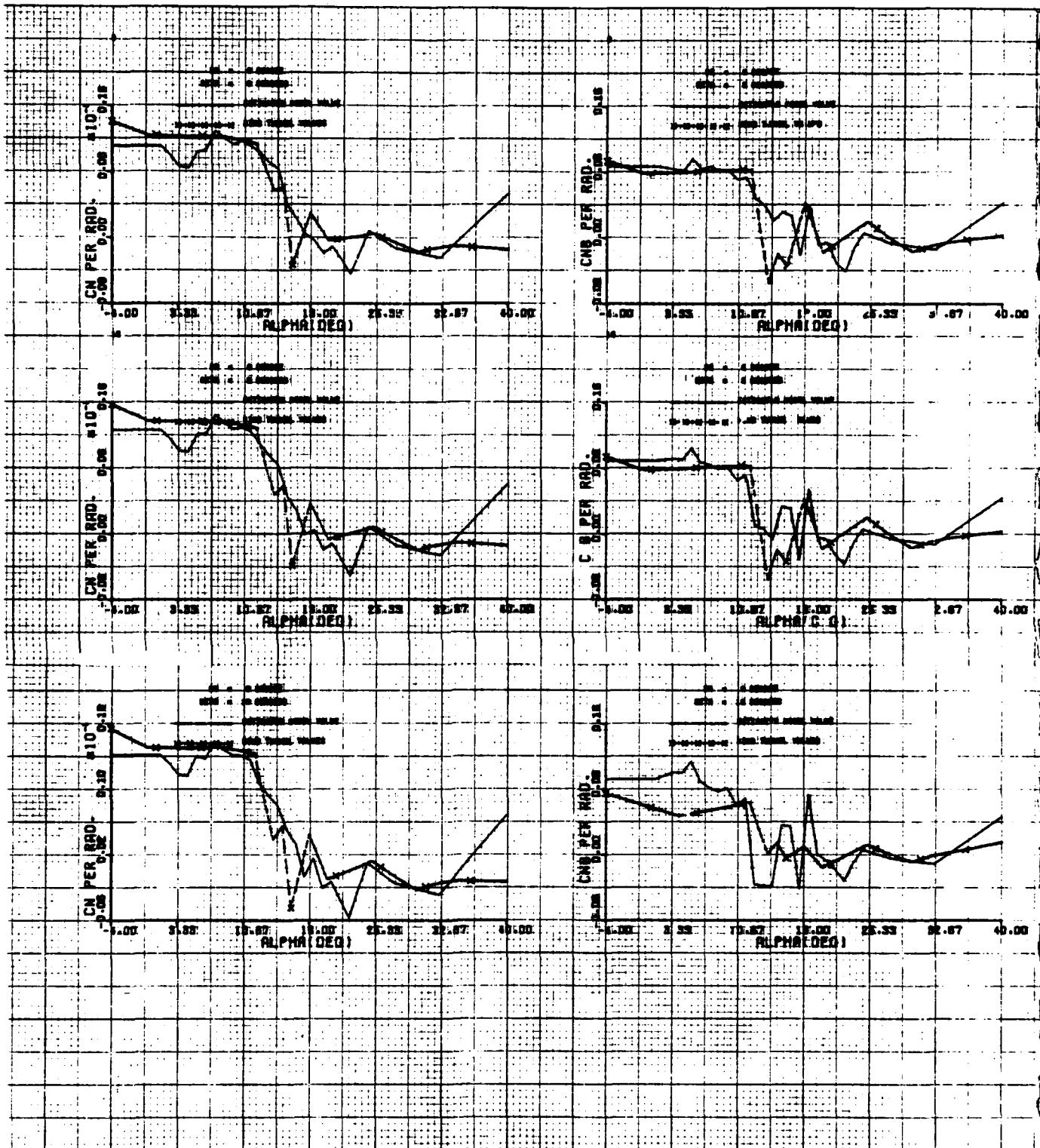


Fig. 4.4-6 Comparison between the C_n and the C_{n_β} identified models and the wind tunnel model for $\beta = 8^\circ, 9^\circ, 10^\circ$

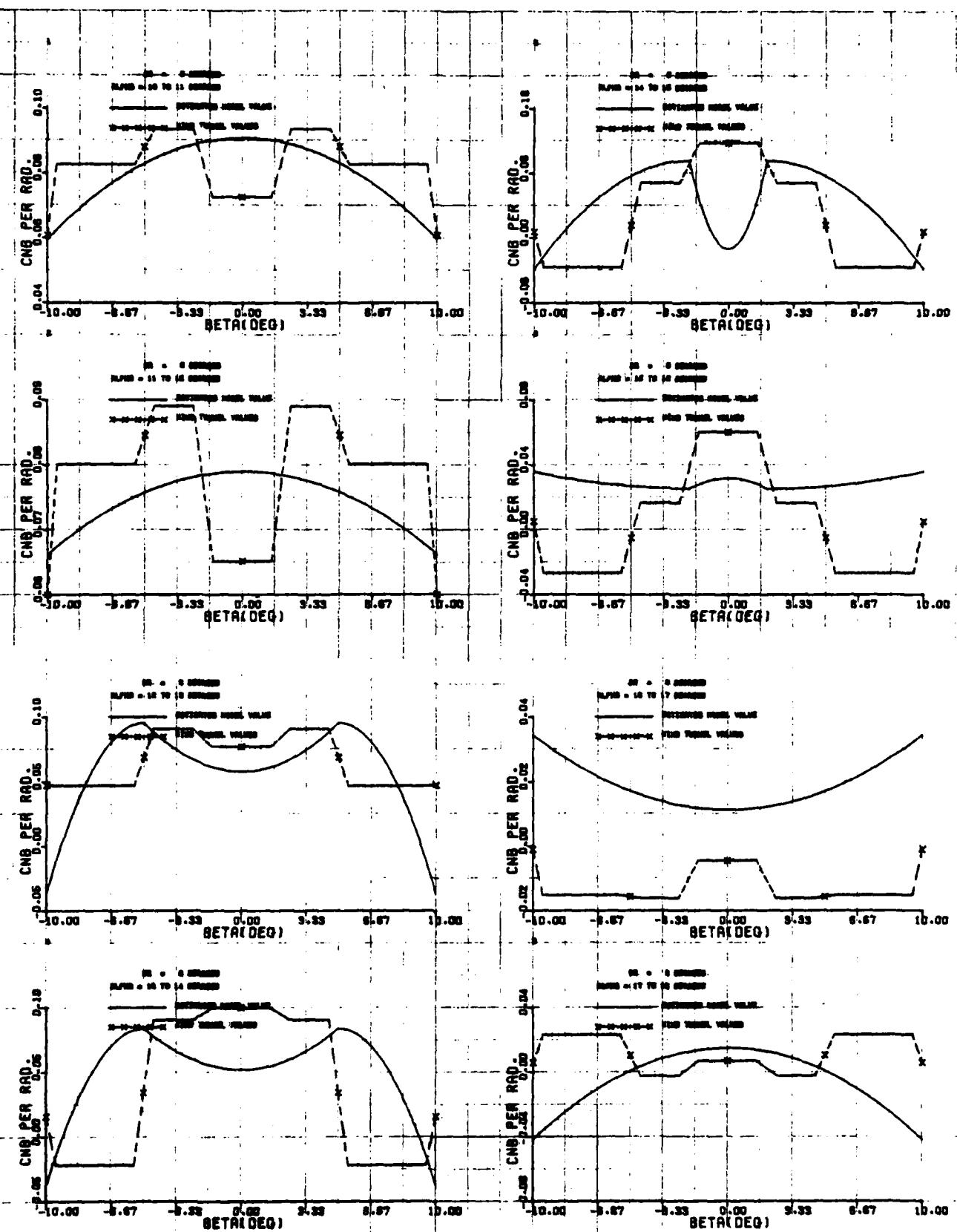


Fig. 4.4-7 Comparison between the C_{nB} identified model and the wind tunnel model for $\alpha = 10.5^\circ, 11.5^\circ, 12.5^\circ, 13.5^\circ, 14.5^\circ, 15.5^\circ, 16.5^\circ, 17.5^\circ$

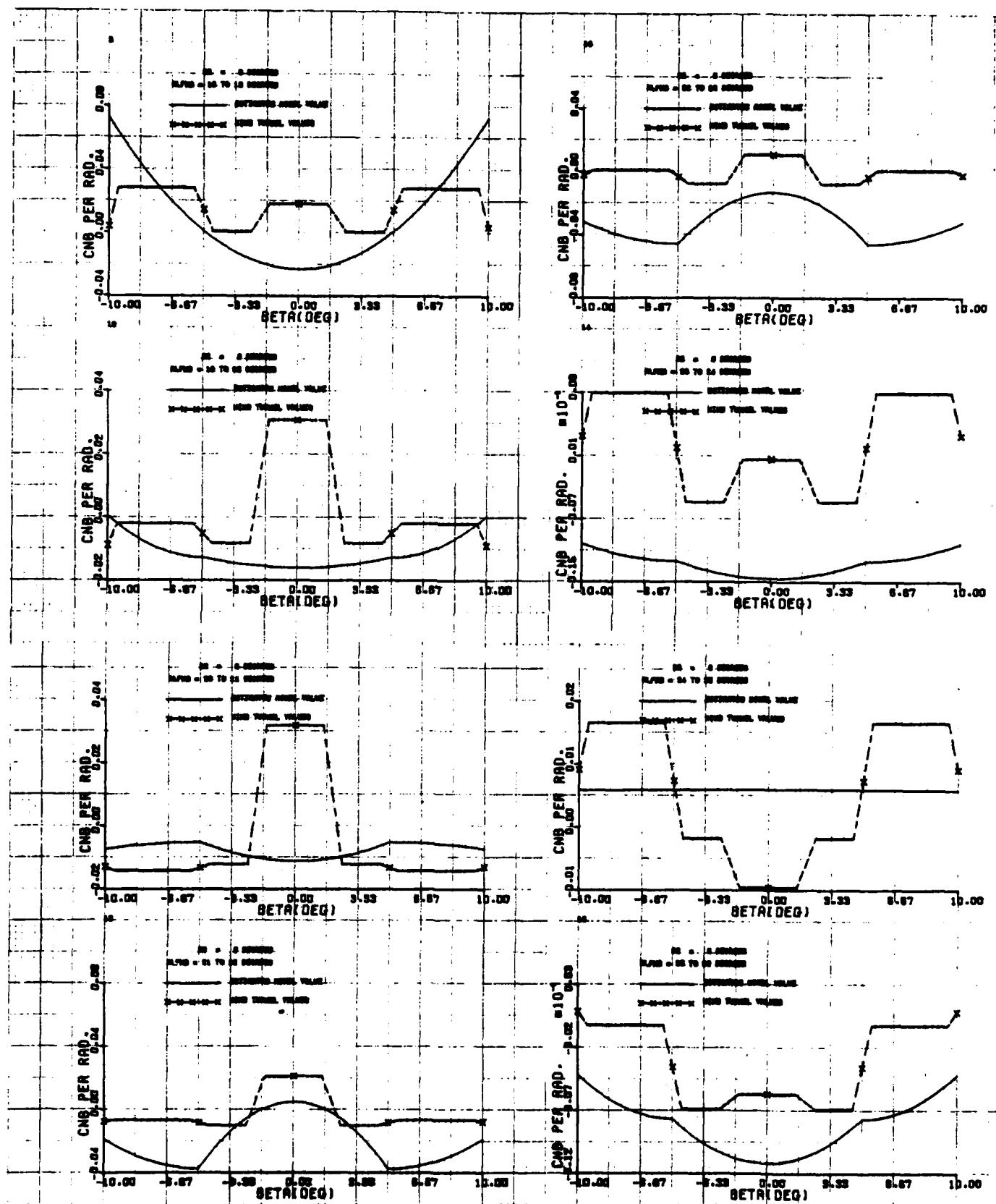


Fig. 4.4-8 Comparison between the C_{n_B} identified model and the wind tunnel model for

$\alpha = 18.5^\circ, 19.5^\circ, 20.5^\circ, 21.5^\circ, 22.5^\circ, 23.5^\circ, 24.5^\circ, 27.5^\circ$

5. IDENTIFICATION OF THE T-2C LONGITUDINAL AERODYNAMIC CHARACTERISTICS

5.1 CONSTRUCTION OF SUBSPACES FOR LONGITUDINAL MODELING

The longitudinal coefficients C_x , C_z , and C_m are functions of the following variables:

α	-	angle of attack
β	-	sideslip angle
q	-	pitch rate
δ_e	-	elevator deflection
$\dot{\alpha}$	-	α rate

The states α , β and δ_e are used for defining the subspaces for modeling. Subspace modeling is conducted in two steps for the modeling of C_m . The first uses a partitioning of the α space $[-4^\circ, 40^\circ]$ together with spline functions to handle the subspaces of the β and the δ_e space. The subspaces in α are generated by partitioning the α space into one degree intervals $[\alpha_i, \alpha_i + 1^\circ]$, $\alpha_i = -4^\circ, -3^\circ, \dots, 24^\circ$ and five degrees intervals $[\alpha_i, \alpha_i + 5^\circ]$, $\alpha_i = 25^\circ, 30^\circ, 35^\circ$. The eighteen estimation data files (i.e., one for each of the maneuvers F1M1, F2M1, ..., F4M10 and F6M1) generated by the estimation phase of the EBM system identification method are transformed into thirty-two new estimation data files for modeling by using the partitions on α and by collecting together the data from all eighteen maneuvers having an angle of attack within a given α -interval. In this first step the subspaces in β and δ_e are handled by using spline functions. Since a longitudinal coefficient is symmetric with respect to the sideslip angle, a quadratic spline function as a function of $|\beta|$ is used.

The second step uses a partitioning of the δ_e space $[-28^\circ, 2^\circ]$ together with spline functions to handle the subspaces of α . The space of δ_e is partitioned into one degree intervals $[\delta_{e_i}, \delta_{e_i} + 1^\circ]$, $\delta_{e_i} = -28^\circ, -27^\circ, \dots, 1^\circ$. The eighteen estimation data files generated by the estimation phase of the EBM method are transformed into thirty new estimation data files for modeling by using the partitions on δ_e and by collecting together the data from all eighteen maneuvers having an elevator control deflection within a given δ_e -interval. In this second step the subspaces in α are handled by using spline functions.

5.2 IDENTIFICATION OF C_m

The estimated values of $C_m(t)$ are compared with the wind tunnel values in Figures F-1 through F-14 of Appendix F. The elevator control δ_e was used to subdivide the $C_m(t)$ estimates of all eighteen maneuvers into data subsets. The first data subset consists of the $C_m(t)$ estimate for which $\delta_e(t)$ is a value between -1.0° and 0.0° . The second data subset is over the elevator control interval of -2.0° to -1.0° . The data subsets cover the entire range of the elevator control in one degree intervals with the last data subset covering the interval from -28.0° to -27.0° . Each data subset was ordered with respect to the angle of attack variable and then plotted as a figure in Appendix F. The wind tunnel values were generated by evaluating the wind tunnel model using the estimated states and controls. Note that the range of the angle of attack depends on the elevator control interval. For example, for the interval of $\delta_e = -1^\circ$ to 0° , the range on α is from -1.36° to 18.94° whereas for the interval of $\delta_e = -27^\circ$ to -26° the range of α is from 15.51° to 37.54° . This is to be expected since during maneuvers a small elevator control setting tends to produce low alpha and a large negative setting generates high alpha. The curves have dependency on all states by nature of the flight maneuvers. The fair agreement between the real data values and the wind tunnel values indicates a likeness between the actual aircraft and its wind tunnel model. There is, however, a noticeable difference. At angles of attack below stall, the real data values are above the wind tunnel values over the elevator control range -4° to 0° ; they coincide over $\delta_e = -6^\circ$ to -4° and they lie below the wind tunnel values over $\delta_e = -28^\circ$ to -27° . The models that we identify for C_m should exhibit this same phenomenon.

Our objective in modeling C_m is to identify a model of C_m for each of the δ_e -subspaces $[\delta_{e_i}, \delta_{e_i} + 1^\circ]$, $\delta_{e_i} = -28^\circ, -27^\circ, \dots, 1^\circ$.

That is, we model "the real data values" curves given in Appendix F.

Let $\bar{\delta}_e$ be the midpoint of a δ_e -interval. An equation for modeling C_m on this δ_e -interval, valid at $\delta_e = \bar{\delta}_e$ is:

$$C_m(\alpha, \beta, q, \dot{\alpha}, \delta_e = \bar{\delta}_e) = C_{m_0}(\bar{\delta}_e) + C_{m_q}(\alpha) \cdot q + C_{m_{\dot{\alpha}}}(\alpha) \cdot \frac{\dot{\alpha} - \dot{\alpha}_c}{2V} + C_{m_{\beta_0}}(\alpha) \cdot |\beta| + \sum_{j=1}^3 C_{m_{\beta_j}}(\alpha) \cdot h(\beta, \beta_j, \beta_{j+1}) + C_{m_{\alpha_0}}(\bar{\delta}_e) \cdot (\alpha - \alpha_1) + \sum_{i=1}^6 C_{m_{\alpha_i}}(\bar{\delta}_e) \cdot g(\alpha, \alpha_i, \alpha_{i+1})$$

where $\beta_1, \beta_2, \beta_3, \beta_4$ are the knots on the $|\beta|$ -axis satisfying $0 \leq \beta_1 < \beta_2 < \beta_3 < \beta_4$, where $h(\beta, \beta_j, \beta_{j+1})$ is a quadratic spline function defined as

$$h(\beta, \beta_j, \beta_{j+1}) = \begin{cases} 0 & |\beta| < \beta_j \\ \frac{1}{2} (|\beta| - \beta_j)^2 & \beta_j \leq |\beta| \leq \beta_{j+1} \\ (\beta_{j+1} - \beta_j) (|\beta| - \frac{1}{2} \beta_j - \frac{1}{2} \beta_{j+1}) & \beta_{j+1} < |\beta| \end{cases}$$

where $\alpha_1, \alpha_2, \dots, \alpha_7$ are the knots on the α -axis satisfying $-4 \leq \alpha_1 < \alpha_2 < \dots < \alpha_7$, where $g(\alpha, \alpha_i, \alpha_{i+1})$ is a quadratic spline function defined as

$$g(\alpha, \alpha_i, \alpha_{i+1}) = \begin{cases} 0 & \alpha < \alpha_i \\ \frac{1}{2} (\alpha - \alpha_i)^2 & \alpha_i \leq \alpha \leq \alpha_{i+1} \\ (\alpha_{i+1} - \alpha_i) (\alpha - \frac{1}{2} \alpha_i - \frac{1}{2} \alpha_{i+1}) & \alpha_{i+1} < \alpha \end{cases}$$

The parameters $C_{m_q}(\alpha)$, $C_{m_{\dot{\alpha}}}(\alpha)$, $C_{m_{\beta_0}}(\alpha)$, $C_{m_{\beta_j^2}}(\alpha)$ in the

preceding equation are functions of α and not δ_e . Thus, these parameters can be better estimated by processing the estimation data partitioned in α -intervals. Let $\bar{\alpha}$ be the midpoint of an α -interval. An equation for modeling C_m on this α -interval, valid at $\alpha = \bar{\alpha}$ is:

$$C_m(\alpha = \bar{\alpha}, \beta, q, \dot{\alpha}, \delta_e) = C_{m_0}(\bar{\alpha}) + C_{m_q}(\bar{\alpha}) \cdot q + C_{m_{\dot{\alpha}}}(\bar{\alpha}) \cdot \frac{\dot{\alpha} - \dot{\alpha}_c}{2V}$$

$$+ C_{m_{\beta_0}}(\bar{\alpha}) \cdot |\beta| + \sum_{j=1}^3 C_{m_{\beta_j^2}}(\bar{\alpha}) \cdot h(\beta, \beta_j, \beta_{j+1})$$

$$+ C_{m_{\delta_{e_0}}}(\bar{\alpha})(\delta_e - \delta_{e_1}) + \sum_{k=1}^3 C_{m_{\delta_{e_k}}}(\bar{\alpha}) \cdot F(\delta_e, \delta_{e_k}, \delta_{e_{k+1}})$$

where $\delta_{e_1}, \delta_{e_2}, \delta_{e_3}, \delta_{e_4}$ are the knots on the δ_e -axis satisfying

$-28^\circ \leq \delta_{e_1} < \delta_{e_2} < \delta_{e_3} < \delta_{e_4}$ and where $F(\delta_e, \delta_{e_k}, \delta_{e_{k+1}})$ is a quadratic spline function defined as

$$F(\delta_e, \delta_{e_k}, \delta_{e_{k+1}}) = \begin{cases} 0 & \delta_e < \delta_{e_k} \\ \frac{1}{2}(\delta_e - \delta_{e_k})^2 & \delta_{e_k} \leq \delta_e \leq \delta_{e_{k+1}} \\ (\delta_{e_{k+1}} - \delta_{e_k})(\delta_e - \frac{1}{2}\delta_{e_k} - \frac{1}{2}\delta_{e_{k+1}}) & \delta_{e_{k+1}} < \delta_e \end{cases}$$

The SMLR technique has been used to process the data in each α -interval.

The identification of the parameters

$C_{m_q}(\bar{\alpha}), C_{m_{\dot{\alpha}}}(\bar{\alpha}), C_{m_{\beta_0}}(\bar{\alpha}), C_{m_{\beta_j^2}}(\bar{\alpha}), j = 1, 2, 3$, are given in Tables I-2

and I-3. Characteristic functions which are discussed in Section 4.2 used

used in identifying these parameters. At $\bar{\alpha} = 14.5^\circ$ we note in these tables that

$$C_{m_q}(\bar{\alpha} = 14.5^\circ) = 3.97 \text{ per rad}$$

$$C_{m_{\dot{\alpha}}}(\bar{\alpha} = 14.5^\circ) = -.76 \text{ per rad}$$

$$C_{m_{\beta_0}}(\bar{\alpha} = 14.5^\circ) = .66 \text{ per rad}$$

$$C_{m_{\beta_1^2}}(\bar{\alpha} = 14.5^\circ) = -12.91 \text{ per rad}^2$$

$$C_{m_{\beta_2^2}}(\bar{\alpha} = 14.5^\circ) = 7.98 \text{ per rad}^2$$

$$C_{m_{\beta_3^2}}(\bar{\alpha} = 14.5^\circ) = -17.34 \text{ per rad}^2$$

where $\beta_1 = 0^\circ$, $\beta_2 = 5^\circ$, $\beta_3 = 10^\circ$ and $\beta_4 = 15^\circ$.

The parameters $C_{m_{\delta_{e_0}}}(\bar{\alpha})$ and $C_{m_{\delta_{e_k}}}(\bar{\alpha})$, $k = 1, 2, 3$ were used to plot

in Figures 5.2-14 and 5.2-15 the derivative $C_{m_{\delta_e}}(\bar{\delta}_e)$ for the midpoints $\bar{\alpha} = 9.5^\circ, 10.5^\circ, \dots, 24.5^\circ$

Using the SMLR technique and the estimates of the parameters given in Tables I-2 and I-3, the estimation data in each δ_e -interval are processed to estimate the derivatives $C_{m_{\delta_e}}(\bar{\delta}_e)$, $C_{m_{\alpha_0}}(\bar{\delta}_e)$, $C_{m_{\alpha_i^2}}(\bar{\delta}_e)$, $i = 1, 2, \dots, 6$. The results are given in Table I-1. For example, at

$$\bar{\delta}_e = -17.5^\circ,$$

$$C_{m_{\delta_e}}(\bar{\delta}_e = -17.5^\circ) = .204$$

$$C_{m_{\alpha_0}}(\bar{\delta}_e = -17.5^\circ) = -1.18 \text{ per rad}$$

$$C_{m_{\alpha_1}^2}(\bar{\delta}_e = -17.5^\circ) = 9.09 \text{ per rad}^2$$

$$C_{m_{\alpha_2}^2}(\bar{\delta}_e = -17.5^\circ) = 77.8 \text{ per rad}^2$$

$$C_{m_{\alpha_3}^2}(\bar{\delta}_e = -17.5^\circ) = -11.54 \text{ per rad}^2$$

$$C_{m_{\alpha_4}^2}(\bar{\delta}_e = -17.5^\circ) = 36.96 \text{ per rad}^2$$

$$C_{m_{\alpha_5}^2}(\bar{\delta}_e = -17.5^\circ) = -2.63 \text{ per rad}^2$$

$$C_{m_{\alpha_6}^2}(\bar{\delta}_e = -17.5^\circ) = 17.72 \text{ per rad}^2$$

The identified model of C_m is, therefore,

$$\begin{aligned} C_m(\alpha, \beta, q, \dot{\alpha}, \bar{\delta}_e) &= C_{m_0}(\bar{\delta}_e) + C_{m_q}(\alpha) \cdot q + C_{m_{\dot{\alpha}}}(\alpha) \cdot \frac{\dot{\alpha} c}{2 V} \\ &+ C_{m_{\beta_0}}(\alpha) \cdot |\beta| + \sum_{j=1}^3 C_{m_{\beta_j}^2}(\alpha) \cdot h(\beta, \beta_j, \beta_{j+1}) \\ &+ C_{m_{\alpha_0}^2}(\bar{\delta}_e) \cdot (\alpha - \alpha_1) + \sum_{i=1}^6 C_{m_{\alpha_i}^2}(\bar{\delta}_e) \cdot g(\alpha, \alpha_i, \alpha_{i+1}) \end{aligned}$$

where the parameters $C_{m_0}(\bar{\delta}_e)$, $C_{m_{\alpha_0}^2}(\bar{\delta}_e)$, $C_{m_{\alpha_i}^2}(\bar{\delta}_e)$, $i = 1, 2, \dots, 6$

are computed by making interpolations in Table I-1 and where the parameters $C_{m_q}(\alpha)$, $C_{m_{\dot{\alpha}}}(\alpha)$, $C_{m_{\beta_0}}(\alpha)$ and $C_{m_{\beta_j}^2}(\alpha)$ are calculated by making interpolations in Tables I-2 and I-3.

The dynamic derivative $C_{m_q}(\alpha)$ which is given in Table I-3 is plotted in Figure 5.2-1 where it is compared with the theoretical prediction model of Ref. [2]. The identified model of C_{m_q} varies between

-11.4 and -8.0 at α below 4.5° . It then climbs slowly to its peak of 5.61 at $\alpha = 13.5^\circ$ before falling to -7.7 at $\alpha = 18.5^\circ$ where it levels off to values between -7.7 and -6.3 for α beyond 18.5° . The theoretical model holds almost level with a value of -10.3 below $\alpha = 14^\circ$. It climbs sharply to a peak of 6.9 at $\alpha = 16^\circ$ before dropping slowly to -4.5 at $\alpha = 30^\circ$.

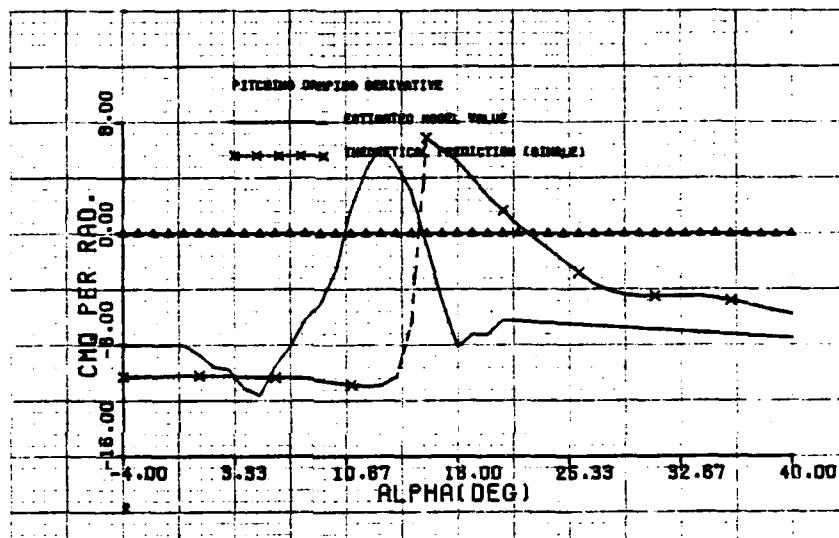


Fig. 5.2-1 Comparison between the $C_{m\alpha}$ identified model and the theoretical prediction of Bihrlle Applied Research.

The identified model has positive values between 11° and 16° alpha whereas the theoretical model has positive values between 15.5° and 22.5° alpha.

The dynamic derivative $C_{m\alpha}(\alpha)$ given in Table I-3 is plotted in Figure 5.2-2 where it is compared with the theoretical prediction model of Ref. [1]. The identified model of $C_{m\alpha}$ is a constant of -.23 below $\alpha = 13.5^\circ$ where it drops off to -2.58 at $\alpha = 17.5^\circ$. It then rises

with the same slope as the theoretical model until $\alpha = 20.5^\circ$ before tapering off to -1.8 at $\alpha = 40^\circ$. The theoretical model of C_{m_α} is nearly a constant of -3.3 below $\alpha = 16^\circ$, and it is zero above $\alpha = 24^\circ$.

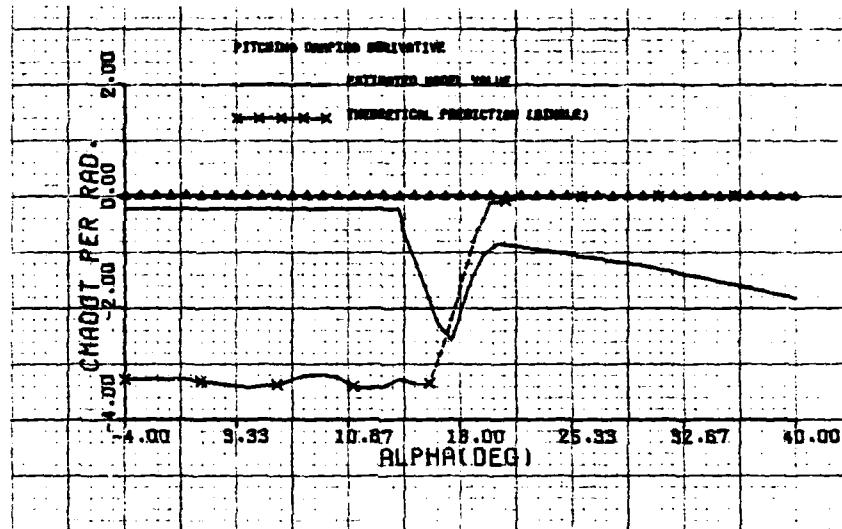


Fig. 5.2-2 Comparison between the C_{m_α} identified model and the theoretical prediction of Bihrlle Applied Research

The identified parameters of Table I-1 were used to plot Figures 5.2-3 through 5.2-9 where $C_m(\alpha)$ and $C_{m_\alpha}(\alpha)$ are compared with the wind tunnel model for δ_e between -27.5° and -0.5° . The identified parameters of Table I-2 were used to plot Figures 5.2-10 through 5.2-12 where $C_{m_\beta}(\beta)$ are compared with the wind tunnel model for α between 1.5° and 24.5° .

On the left hand side in Figure 5.2-3, δ_e varies top to bottom from $\delta_e = -7.5^\circ$ to -4.5° ; on the right hand side it varies top to bottom from $\delta_e = -3.5^\circ$ to -0.5° . Note as δ_e decreases from 0.5° to -6.5°

that the gap between the identified C_m and the wind tunnel model reduces to nearly zero. Also note that the identified model is above the wind tunnel model. Then in Figure 5.2-4 we note that as δ_e decreases further, the wind tunnel model is above the identified model and it opens up a gap for α below stall. In Figure 5.2-6 we see that the identified model of $C_m(\alpha)$ compares well with the wind tunnel model for α above stall and for δ_e between -27.5° and -24.5° .

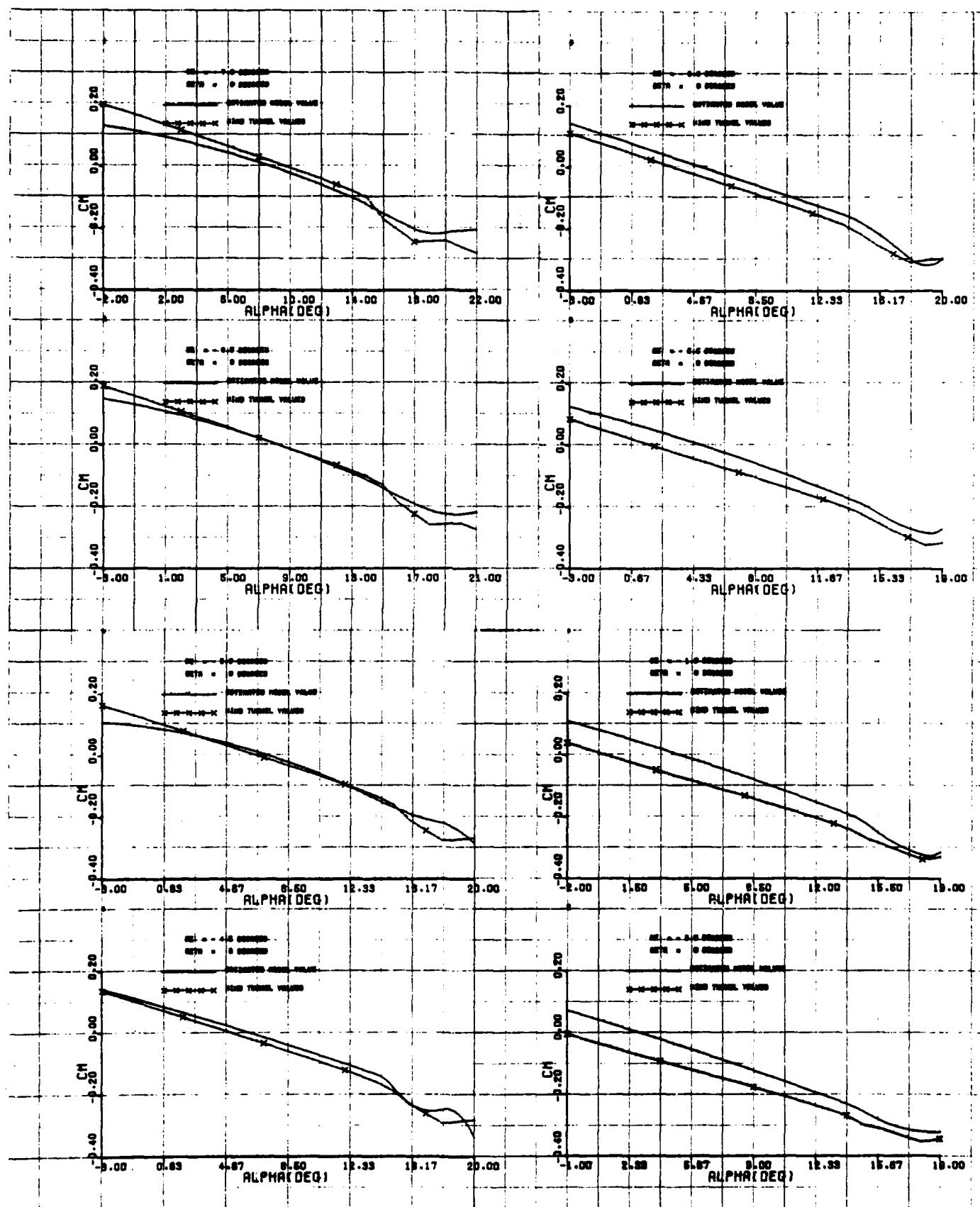


Fig. 5.2-3 Comparison between the C_m identified model and the wind tunnel model for $\delta_e = -7.5^\circ, -6.5^\circ, -5.5^\circ, -4.5^\circ, -3.5^\circ, -2.5^\circ, -1.5^\circ, -0.5^\circ$.

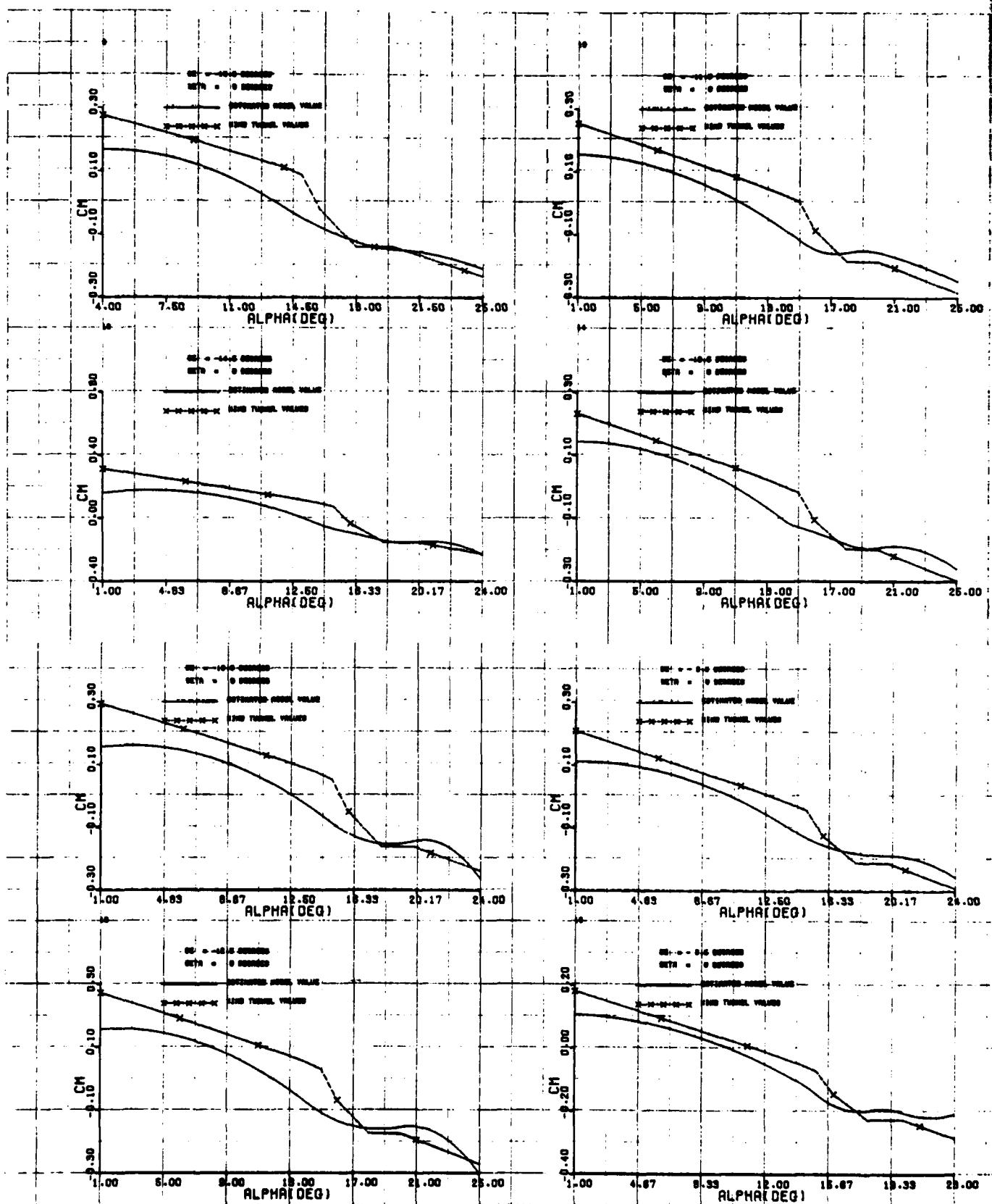


Fig. 5.2-4 Comparison between the C_m identified model and the wind tunnel model for $\delta_e = -15.5^\circ, -14.5^\circ, -13.5^\circ, -12.5^\circ, -11.5^\circ, -10.5^\circ, -9.5^\circ, -8.5^\circ$

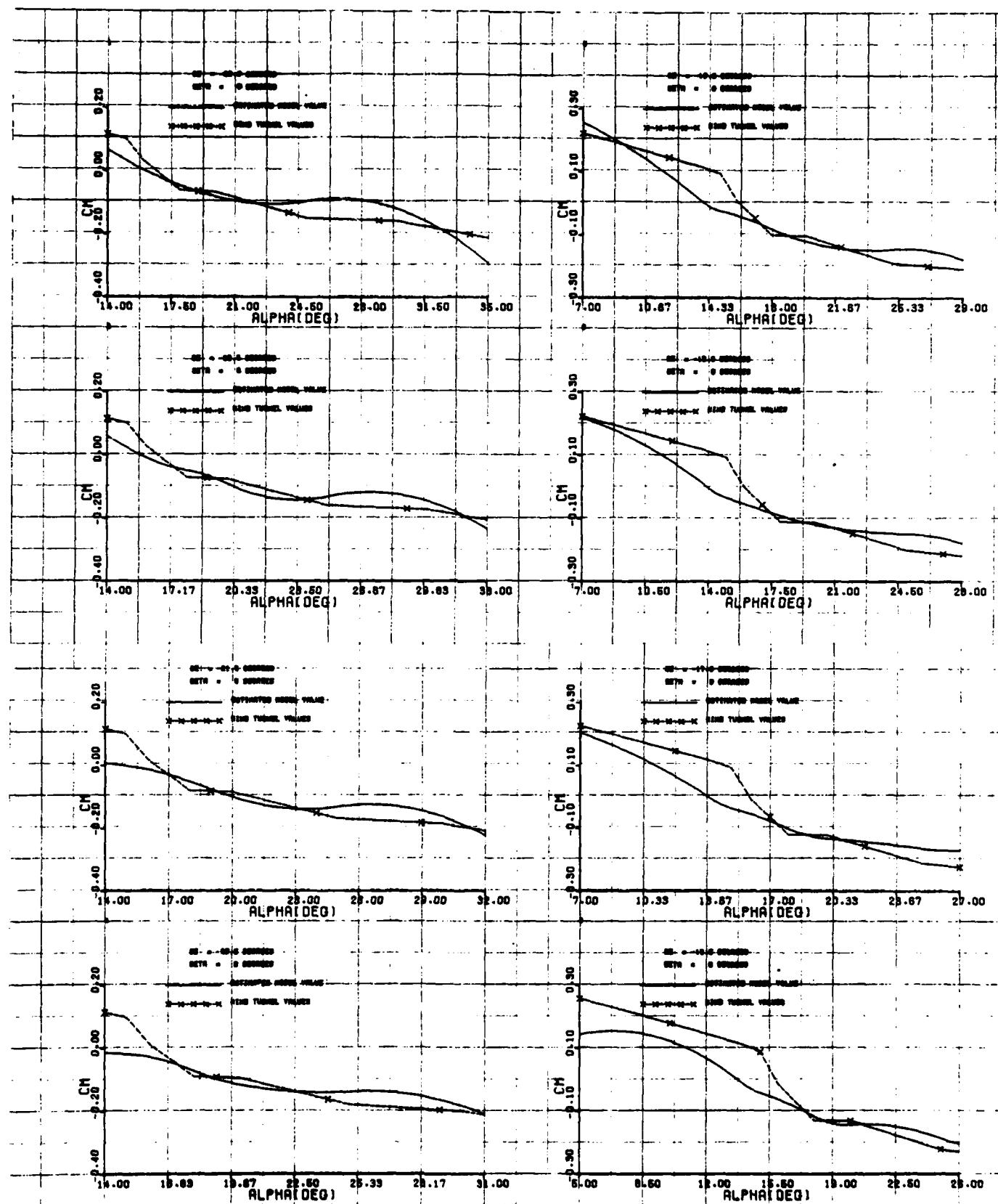


Fig. 5.2.5 Comparison between the C_m identified model and the wind tunnel model for $\delta_e = -23.5^\circ, -22.5^\circ, -21.5^\circ, -20.5^\circ, -19.5^\circ, -18.5^\circ, -17.5^\circ, -16.5^\circ$

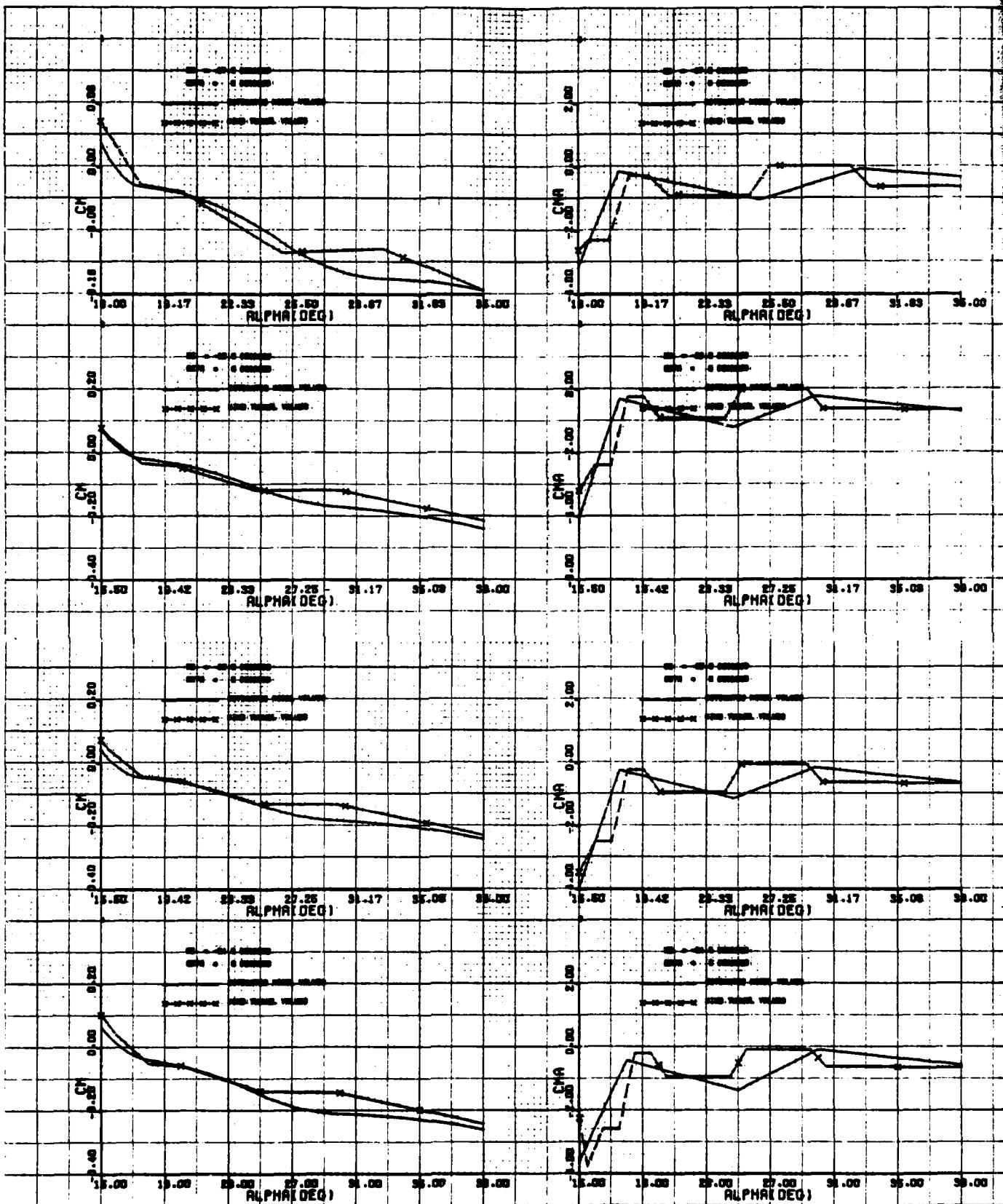


Fig. 5.2-6 Comparison between the C_m , C_m identified models and the wind tunnel model for $\delta_e = -27.5^\circ$, -26.5° , -25.5° , -24.5°

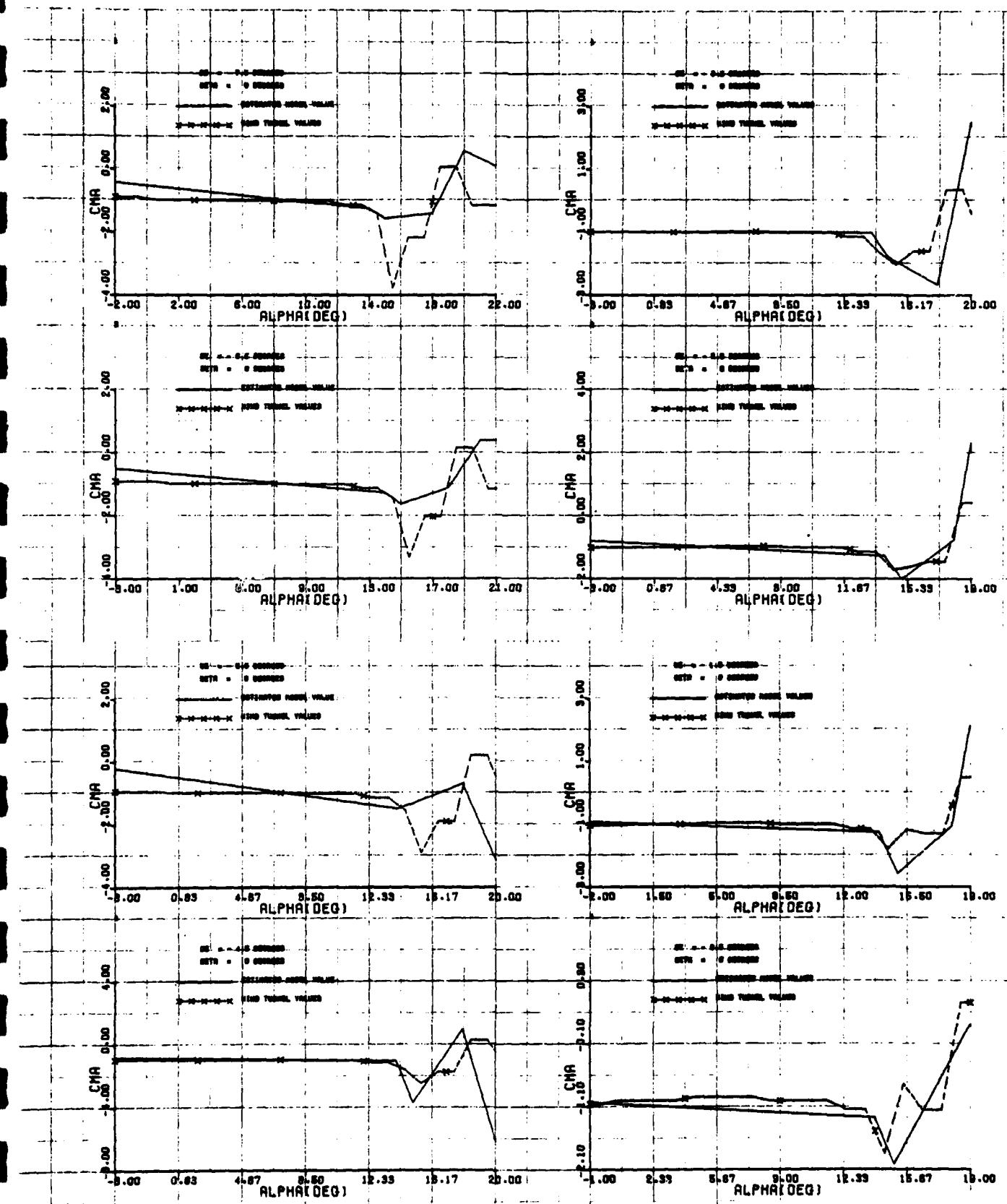


Fig. 5.2-7 Comparison between the C_{m_a} identified model and the wind tunnel model for $\delta_e = -7.5^\circ, -6.5^\circ, -5.5^\circ, -4.5^\circ, -3.5^\circ, -2.5^\circ, -1.5^\circ, -0.5^\circ$

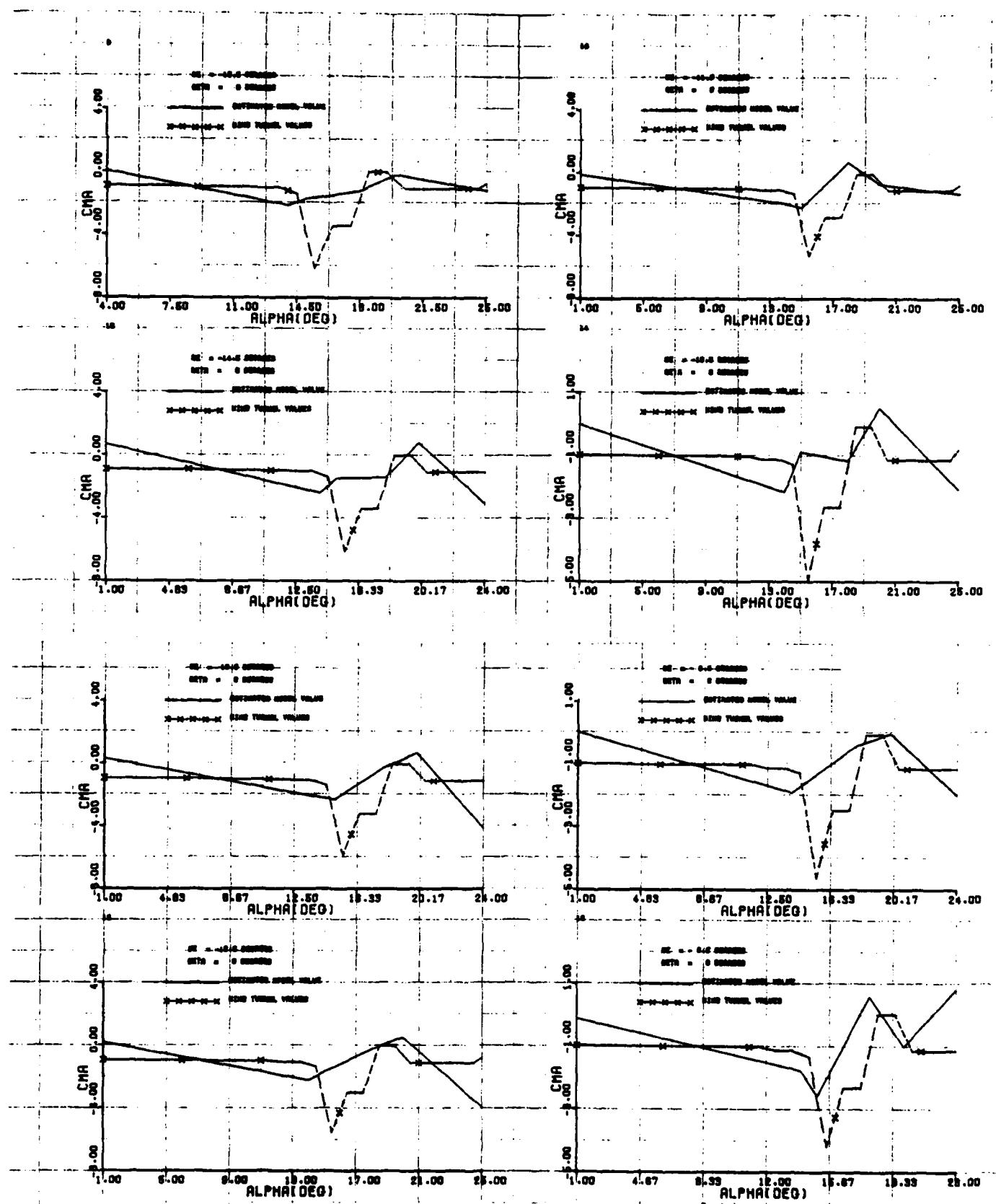


Fig. 5.2-8 Comparison between the C_m identified model and the wind tunnel model for $\delta_e = -15.5^\circ, -14.5^\circ, -13.5^\circ, -12.5^\circ, -11.5^\circ, -10.5^\circ, -9.5^\circ, -8.5^\circ$.

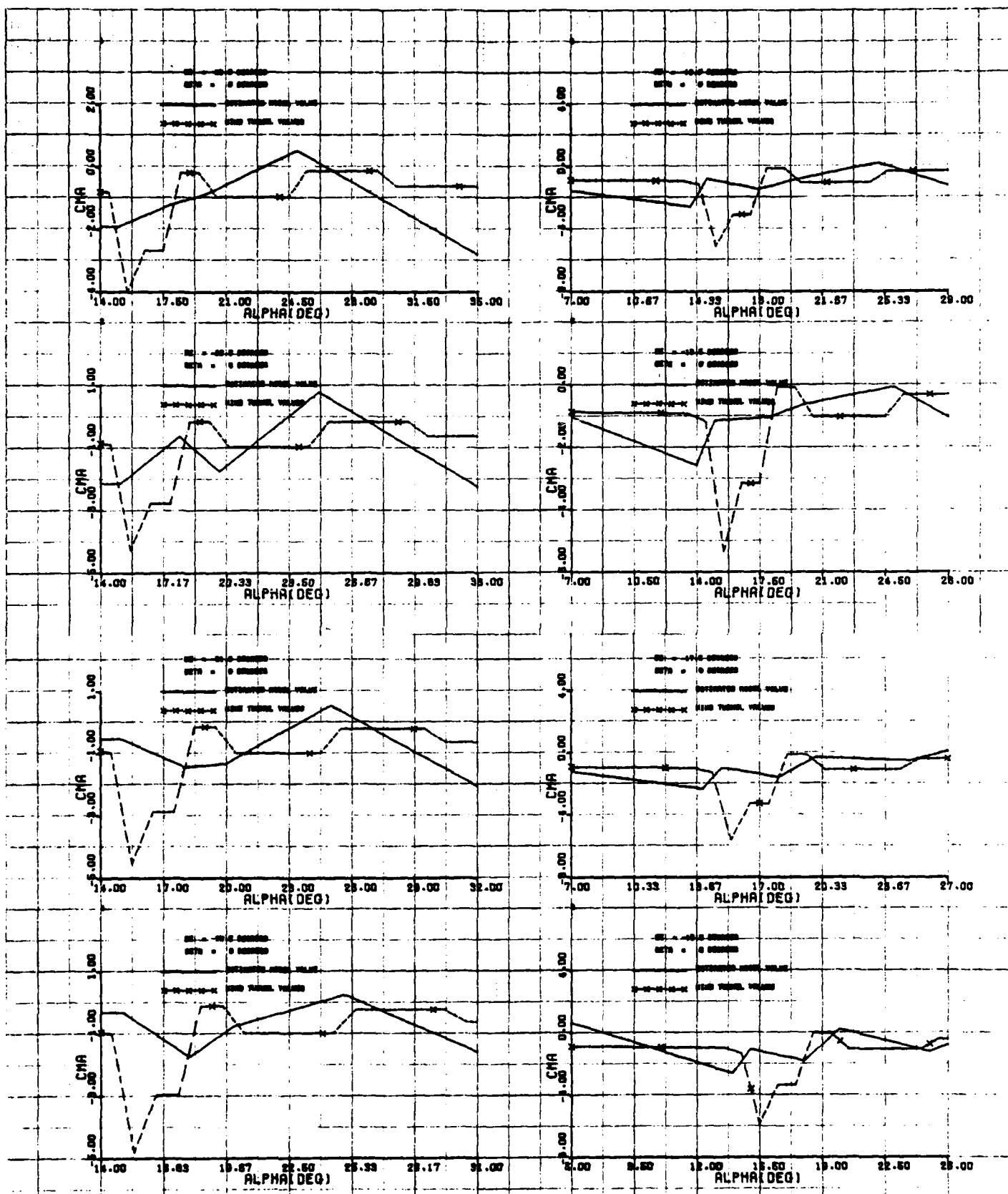


Fig. 5.2-9 Comparison between the C_{m_α} identified model and the wind tunnel model for $\alpha_e = -23.5^\circ, -22.5^\circ, -21.5^\circ, -20.5^\circ, -19.5^\circ, -18.5^\circ, -17.5^\circ, -16.5^\circ$

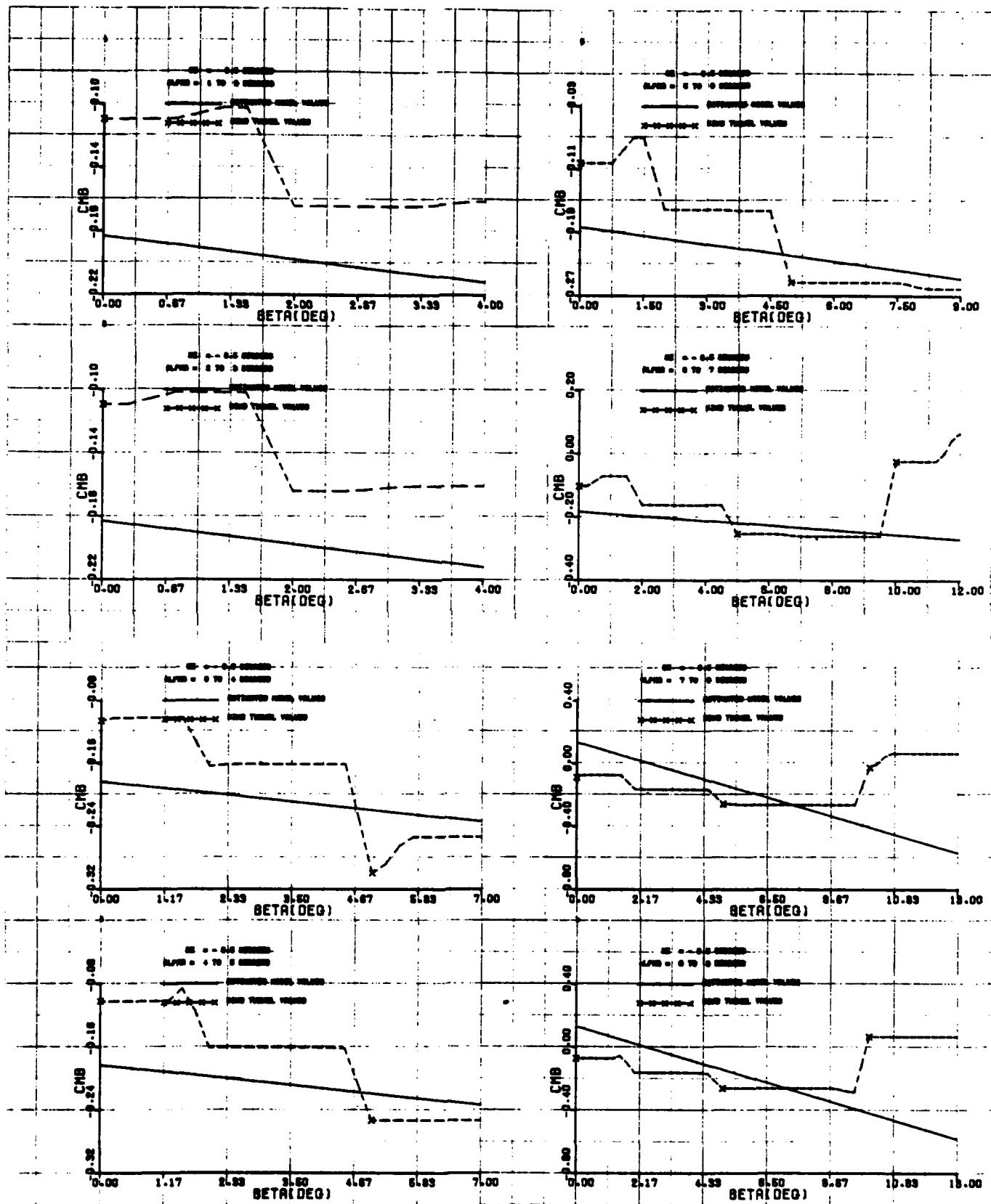


Fig. 5.2-10 Comparison between the C_m identified model and the wind tunnel model for $\alpha = 1.5^\circ, 2.5^\circ, 3.5^\circ, 4.5^\circ, 5.5^\circ, 6.5^\circ, 7.5^\circ, 8.5^\circ$

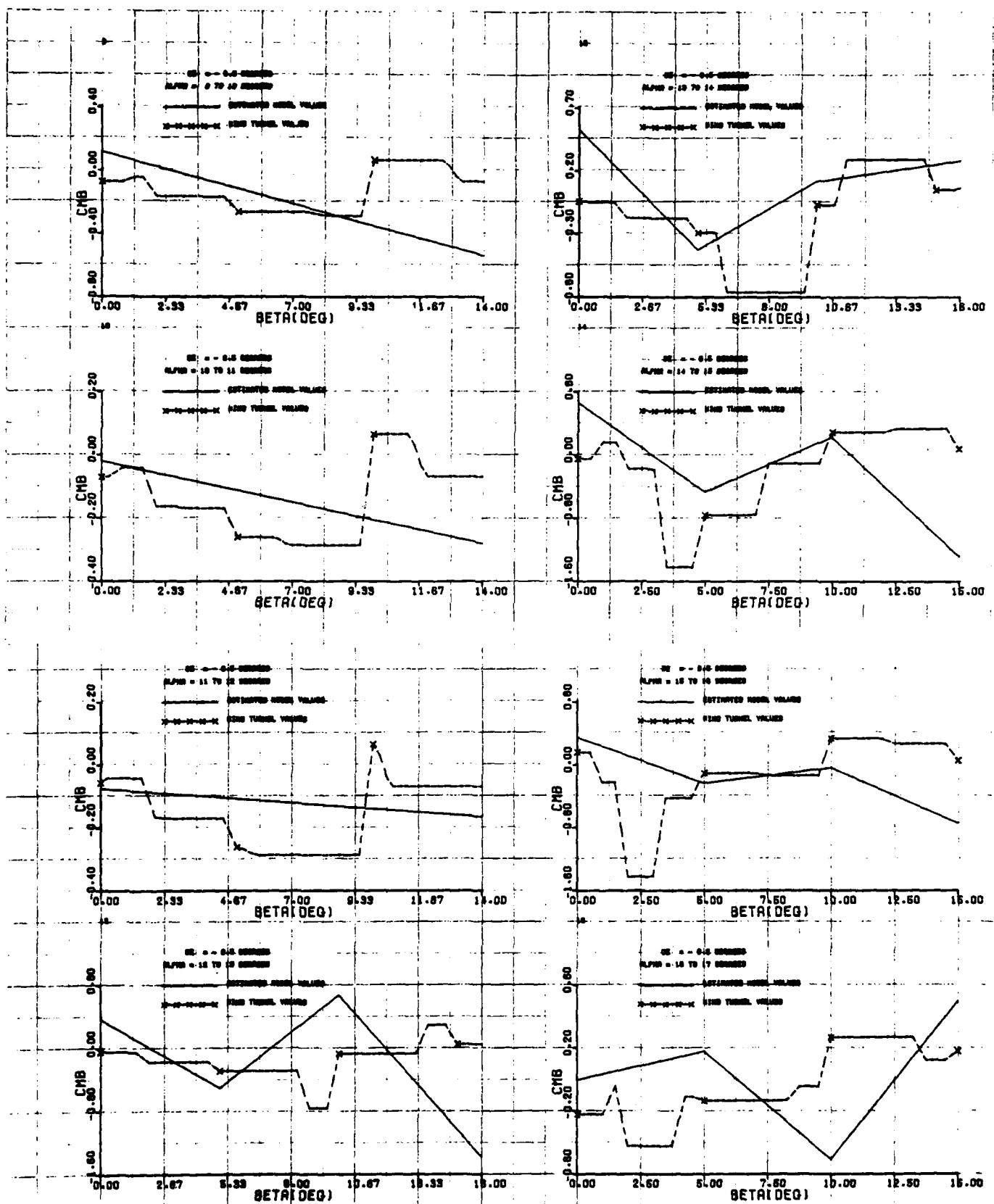


Fig. 5.2-11 Comparison between the C_m identified model and the wind tunnel model for $\beta = 9.5^\circ, 10.5^\circ, 11.5^\circ, 12.5^\circ, 13.5^\circ, 14.5^\circ, 15.5^\circ, 16.5^\circ$

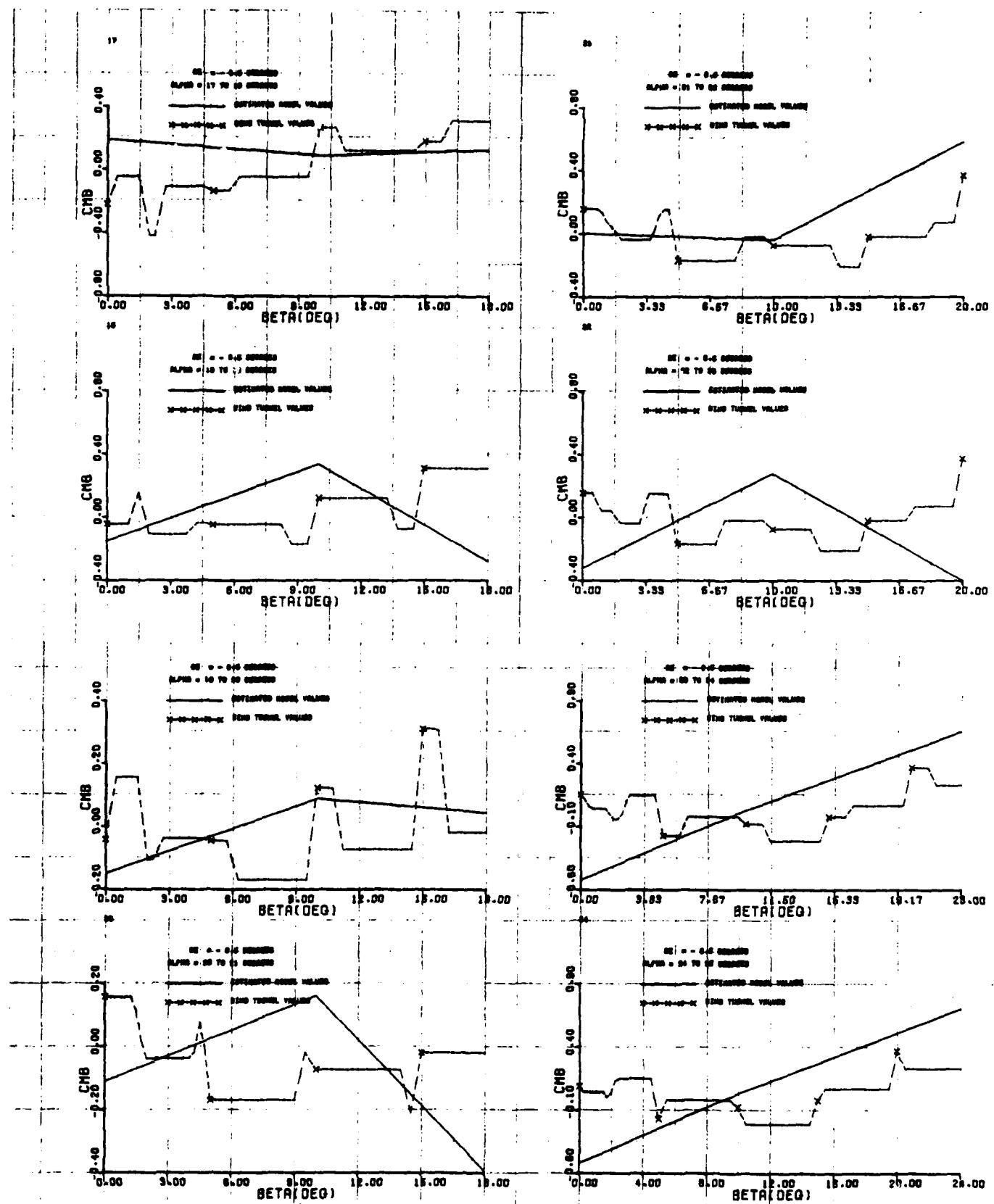


Fig. 5.2-12 Comparison between the C_m identified model and the wind tunnel model for $\alpha = 17.5^\circ, 18.5^\circ, 19.5^\circ, 20.5^\circ, 21.5^\circ, 22.5^\circ, 23.5^\circ, 24.5^\circ$

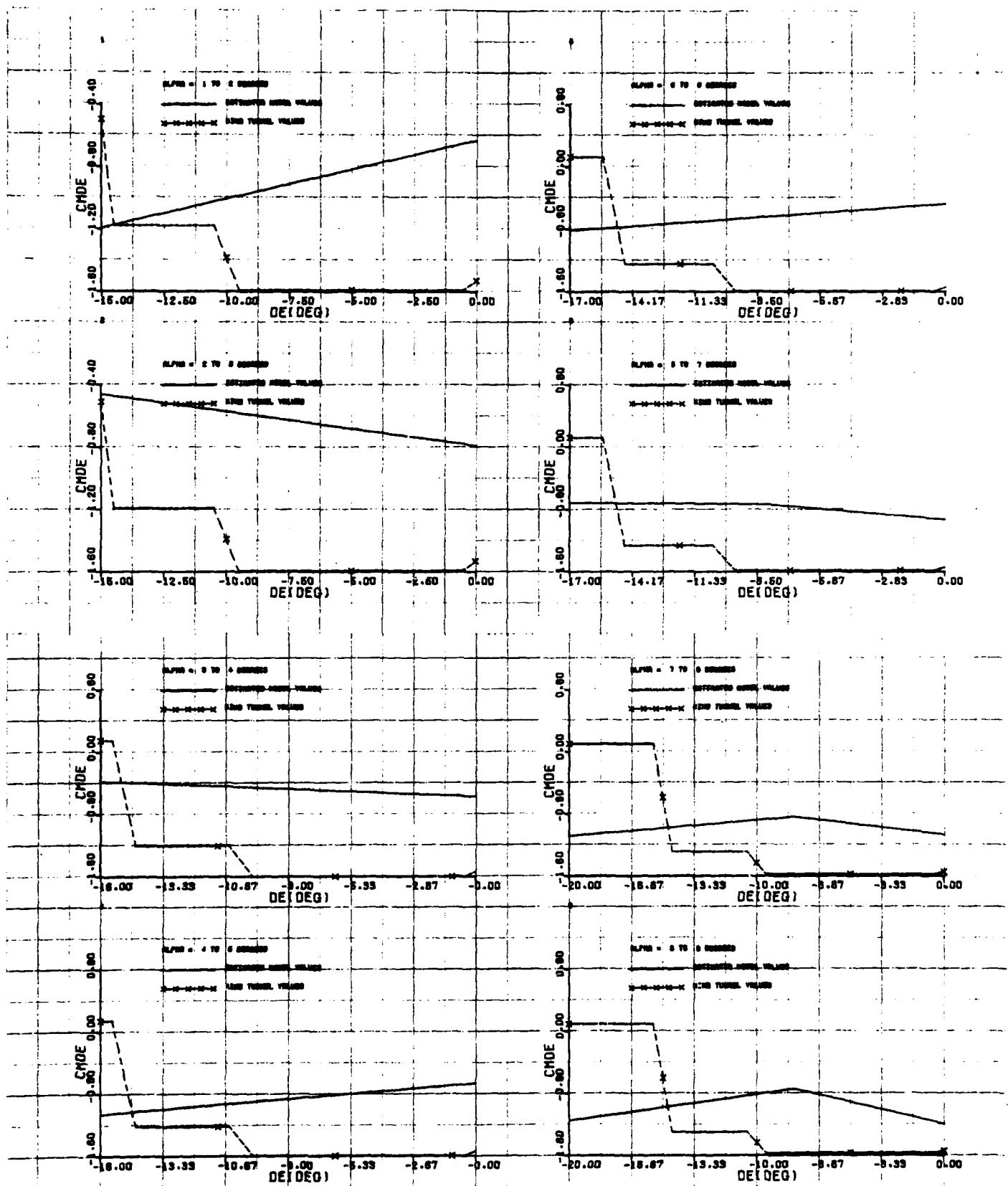


Fig. 5.2-13 Comparison between the C_{m_6} identified model and the wind tunnel model for
 $\alpha = 1.5^\circ, 2.5^\circ, 3.5^\circ, 4.5^\circ, 5.5^\circ, 6.5^\circ, 7.5^\circ, 8.5^\circ$

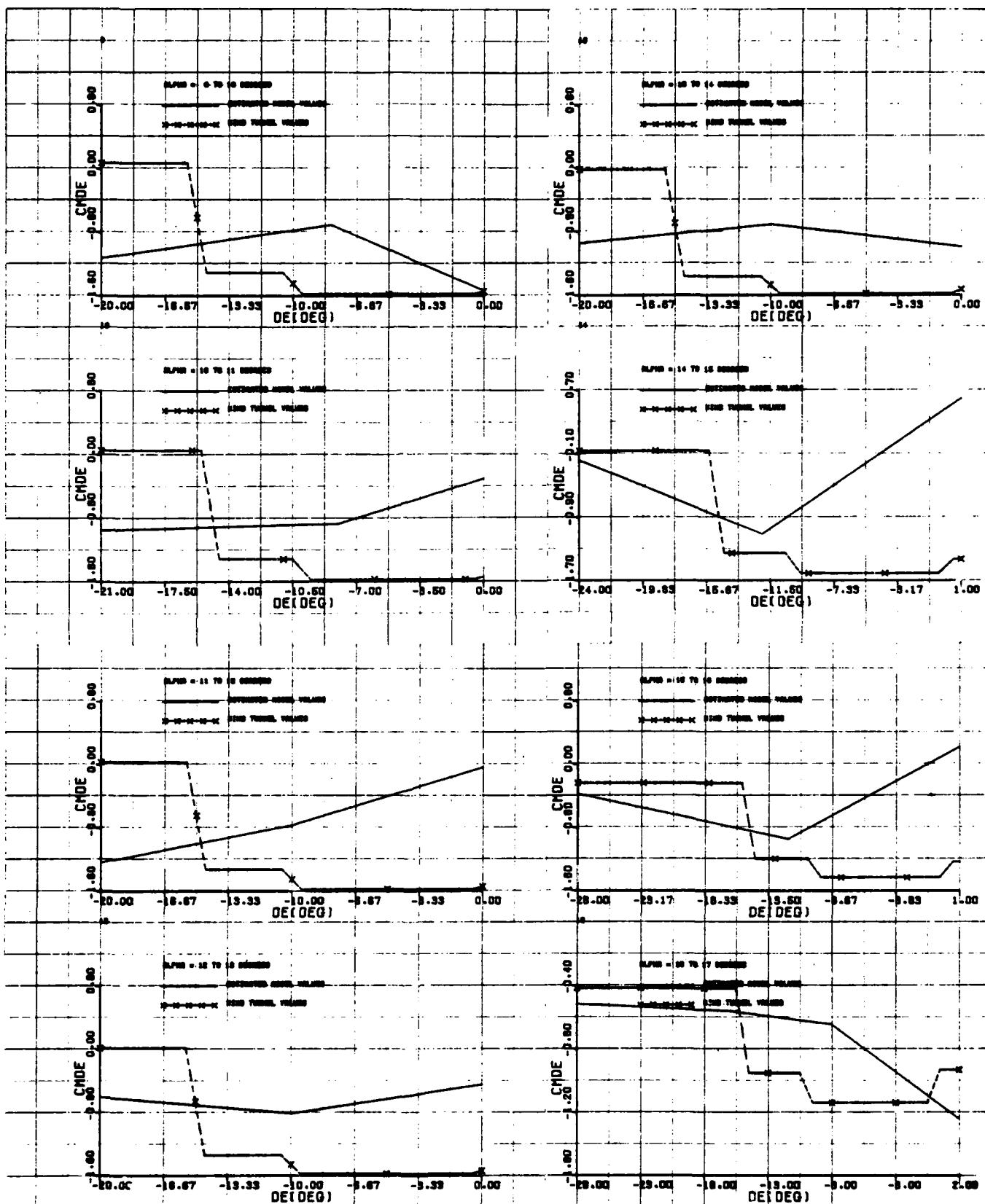


Fig. 5.2-14 Comparison between the C_m identified model and the wind tunnel model
 $\alpha = 9.5^\circ, 10.5^\circ, 11.5^\circ, 12.5^\circ, 13.5^\circ, 14.5^\circ, 15.5^\circ, 16.5^\circ$

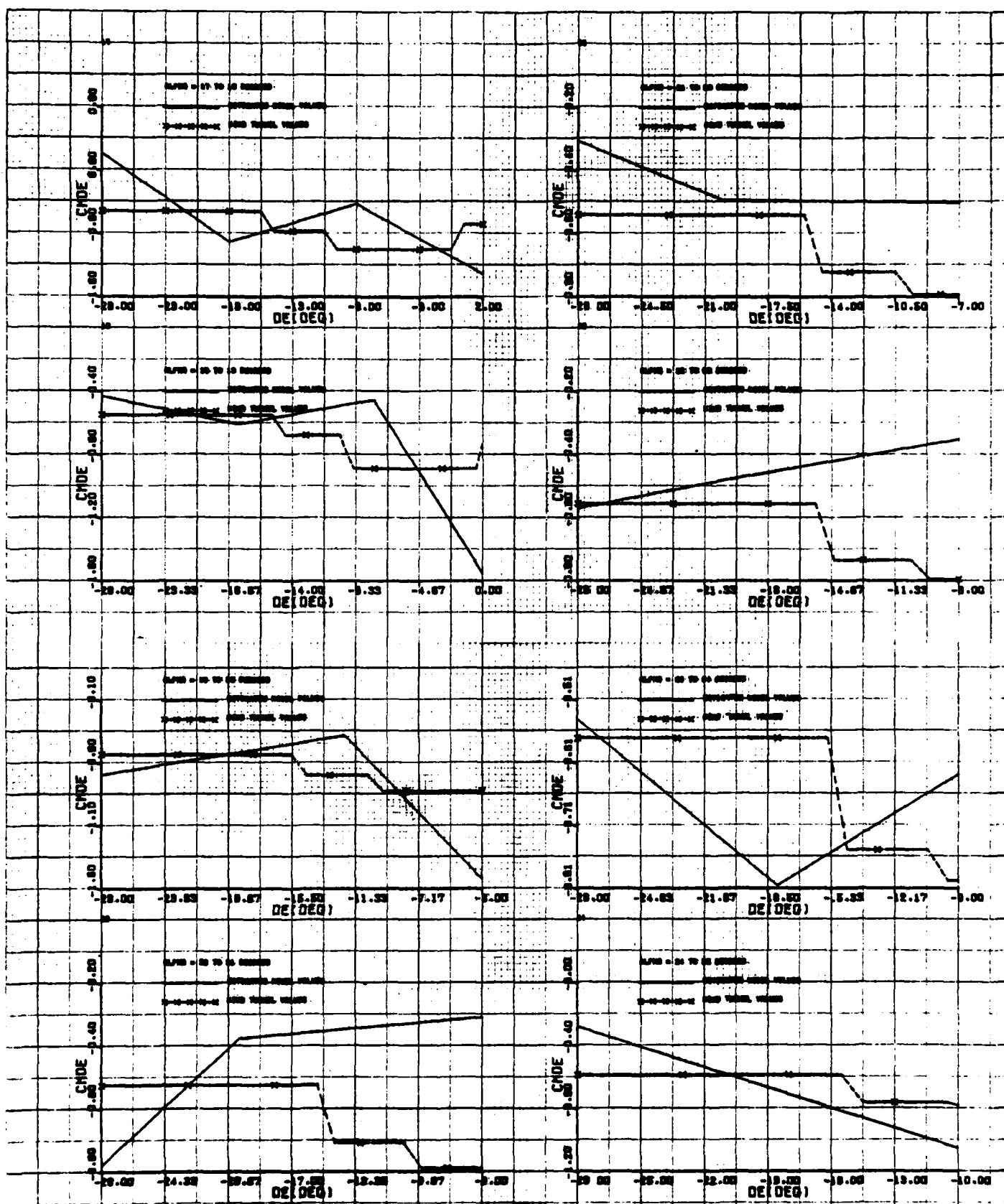


Fig. 5.2-15 Comparison between the $C_{m_{\alpha}}$ identified model and the wind tunnel model for $\alpha = 17.5^\circ, 18.5^\circ, 19.5^\circ, 20.5^\circ, 21.5^\circ, 22.5^\circ, 23.5^\circ, 24.5^\circ$

5.3 RESULTS ON THE C_z MODEL

The estimated values of $C_z(t)$ are compared with the wind tunnel values in Figures G-1 through G-14 in Appendix G. The elevator control δ_e was used to subdivide the $C_z(t)$ estimates obtained from the eighteen maneuvers into data subsets. These subsets were ordered with respect to alpha and then plotted in the figures of Appendix F, labeled as real data values. The figures show a comparison with the wind tunnel model. The data in these subsets were never processed to generate an equation model of C_z , but the figures show that the model of the actual aircraft is close to that given by the wind tunnel analysis. In these figures observe that, below stall, the real data values almost coincide with the wind tunnel values which implies that the actual $C_{z\alpha}$ is close to the wind tunnel model. Around stall there appears to be a hysteresis effect in the real data that is not accounted for by the wind tunnel model. For example, this can be observed in Figure G-8 for $\delta_e = -14.5^\circ$.

The curves given in Appendix G constitute the extent to which we compared the wind tunnel model with that which arises out of the real data for the coefficient C_z . Time permitting, we could have identified an equation model for C_z by using SMLR technique just as we did for C_m .

5.4 RESULTS ON THE C_x MODEL

The estimated values of $C_x(t)$ are compared with the wind tunnel values in Figures H-1 through H-14. In these figures the aerodynamic coefficient C_x is shown as a function of alpha for fixed one degree intervals of the elevator control. The range of the elevator control covers -28° to 0° . The figures were obtained as follows: A one-degree δ_e -interval was selected. All eighteen maneuvers were searched to find all $C_x(t)$ estimates having a corresponding δ_e within the selected δ_e -interval. The $C_x(t)$ estimates were then ordered according to alpha and plotted as a "real data values" curve in Appendix H. The estimated states were used to evaluate the wind tunnel model in order to get a comparison. These curves have a dependency on β , q and $\dot{\alpha}$ built into them by the nature of the maneuvers.

The curves in Appendix H exhibit some differences between the wind tunnel model and the actual aircraft. An hysteresis effect can be observed in the figures, especially Figure H-8. The real data values are above the wind tunnel values at low alpha and at high alpha. Near stall they are below the wind tunnel values.

The curves given in Appendix H constitute the extent to which we compared the wind tunnel model with that arising out of the real data for the coefficient C_x . Time permitting, the SMLR technique could have been used to generate an equation model for C_x , just as was done for C_m .

6. SUMMARY OF RESULTS AND CONCLUSIONS

The EBM methodology has been tested on actual flight test data. The first step of the EBM method processed the eighteen maneuvers of data which had been collected over a period of ten months and it estimated an angle of attack bias of 2° and a total airspeed bias of -3.9 m/sec for the first eight maneuvers and none for the ten maneuvers of flight four. Scale factors of angle of attack and sideslip angle were estimated as 0.78 and 0.805, respectively. Large biases were estimated for a number of the measured variables. The roll and pitch rates have the large biases of -6.1 deg/sec and -2.7 deg/sec , respectively. The bias of the fore-aft acceleration is 0.6 m/sec^2 and the normal acceleration (at c. g.) is -1.6 m/sec^2 while the normal accelerations off c. g. are 1.0 m/sec^2 . The bias of the axis alignment of the rate gyro is 3° . The noise levels on the yaw rate, the rudder deflection, the total airspeed and the acceleration measurements are unduly high due to the use of a commutator to handle many measured quantities rather than the use of a single channel for each quantity. There are losses of the airspeed measurement over extended intervals of flight. The roll angle measurement was not accurate near a roll angle of 180° . The vibrations in the nose boom caused large oscillatory deflections in the angle-of-attack and sideslip angle measurements. The estimation results presented in Appendix B demonstrate that the first step of the EBM method performed well on this test flight data.

The second step of the EBM method identified detailed nonlinear models of C_y , C_z , C_n and C_m with partial results for C_x and C_z . The derivatives $C_{y\beta}$, $C_{z\beta}$, $C_{n\beta}$ and $C_{m\beta}$ are identified as nonlinear functions of α and β and the derivative $C_{m\alpha}$ is identified as a nonlinear function of α and δ_e . The identified models and derivatives are compared with the wind tunnel model. Many of the identified derivatives

match well with the wind tunnel model. For example, Figure 4.2-6 shows some excellent matches for $C_{y\delta_a}$ with α between 18° and 30° and with $|\beta|$ between 0° and 10° . Figure 5.2-6 presents excellent matches for $C_{m\delta_a}$ with δ_e between -28° and -24° and with α between 15° and 39° .

The identified nonlinear models of the control derivatives C_{δ_a} and C_{δ_r} are excellent matches to the wind tunnel model. The identified derivatives $C_{y\delta_r}$ and $C_{n\delta_r}$ have a smaller magnitude than the wind tunnel model for some angles of attack.

The identified dynamic derivatives are compared with the theoretical prediction models of Ref. [2]. The identified C_{n_p} compares well for all alpha but C_{n_p} only matches at low alpha. At high alpha C_{n_p} is predicted to have values above .10 but the identified model shows that the values are around -.075. The simulation study of Ref. [1] found that the theoretical prediction of C_{n_p} is inaccurate at high α and that a constant value of -.06 provided a better model for generating synthetic responses that mimics more closely the real data. The identified model of C_{n_p} obtained by processing the actual T-2C flight data agrees with the modification of the theoretical model of C_{n_p} obtained by trial and error in Ref. [1].

The identified models of C_{δ_p} and C_{δ_r} agree fairly well with the theoretical prediction models with the exception that the identified model hovers about a zero value around stall but the theoretical model shows positive values. The identified model of C_{δ_r} drops off more sharply after stall than the theoretical does.

The modeling results of this study demonstrate that the EBM system identification method provides accurate nonlinear modeling of high α/β aerodynamics stability and control characteristics from actual flight test data.

7. RECOMMENDATIONS

We recommend the following for improving the flight test data for system identification studies:

I. Instrumentation Improvement

- A. Measure the Euler yaw angle ψ . This will permit better accuracy in estimating the bias on the yaw rate r .
- B. Use sensors that measure the absolute values of the Euler pitch and bank angles, θ and ϕ , rather than measurements that are relative to arbitrary initial settings. This will allow the use of all maneuvers to estimate the biases of θ and ϕ , and it will provide a check on the condition $\theta = \alpha$ at trim.
- C. Measure critical engine parameters for estimating thrust of engines. This will permit using the actual values of a varying thrust to identify a better drag model.
- D. Use bank angle sensors that measure accurately through rolls greater than 180° . This will permit better estimation results at these bank angles during high roll rates and it will provide continuity through $\phi = 180^\circ$.
- E. Measure reliably the angular acceleration rates p , q and r . This will provide a check on off-c.g. acceleration measurements and more accurate estimation of $C_f(t)$, $C_m(t)$ and $C_n(t)$.
- F. Use nose boom with less vibrational characteristics than is on the T-2C. This will provide better α and β -data for estimation and modeling.
- G. Use airspeed sensors which do not give a loss of measurements over extended intervals of flight. This permits better estimation and modeling results.

H. Use single channels for all measured variables. This provides the best signal-to-noise ratio for a measured quantity as compared to using a commutator.

I. Use pulse coded modulation (PCM) rather than pulse amplitude modulation (PAM). This will provide cleaner signals.

II. Rigorous Calibration and Consistency Checkout

A. Calibrate instrumentation using static data gathered in hangar (i.e., with aircraft in hangar, isolated from wind, turn instrumentation power on and record a 100 seconds of data). This will permit the isolation and removal of unnecessary biases in linear and angular accelerations, in p , q and r , and in θ and ϕ .

B. Calibrate instrumentation using dynamic data gathered on long runway (i.e., record data with aircraft jetting down runway in takeoff phase). This will permit the isolation and removal of unnecessary biases in α and β .

C. Calibrate instrumentation using dynamic data gathered in trim flight for various trim values of sideslip angle and total airspeed. This will permit the isolation and removal of biases in the controls for equilibrium flight.

D. Check out the consistency of the measured variables using several representative maneuvers of flight data. Use the equations of motion to test for consistency. This will provide a checkout on scale factors and axis alignment as well as the compatibility of the measured variables.

E. Fly calibration maneuvers before and after each flight set of maneuvers.

III. Improve Design of Maneuvers for System Identification

- A. Fly more maneuvers and vary the variables such as trim airspeed and sideslip angle.
- B. Design the maneuvers so that a good amount of data is provided at high and low α and at high β extremes rather than a few isolated data points.
- C. Start and end each maneuver with long trim times.

IV. Precise Calculation of Aircraft Constants

- A. Compute the aircraft mass for the beginning and the end of each maneuver.
- B. Compute the limits on the changes in the moments of inertia due to weight distribution changes such as fuel consumption during maneuvers.
- C. Provide calculations on the location of the center of gravity with respect to the aerodynamic center for each maneuver.

REFERENCES

- [1] H. Stalford and S. Ramachandran, "Application of the Estimation-Before-Modeling (EBM) System Identification Method to the High Angle of Attack/Sideslip Flight of the T-2C Jet Trainer Aircraft", Volume II, Simulation Study Using T-2C Wing Tunnel Model, 23 June 1978, Report R-254U, Dynamics Research Corporation.
- [2] Barnhart, Billy, "Estimated Dynamic Derivatives for T-2C Aircraft from -8 to +45 degrees Angle of Attack", Technical Memo Report No. BAR 2-76, Vol. II, Bihrlle Applied Research, Inc., Nov. 22, 1976.
- [3] Schuetz, A. J., "Low Angle of Attack Longitudinal Aerodynamic Parameters of Navy T-2 Trainer Aircraft Extracted from Flight Data: A Comparison of Identification Techniques, Volume I: Data Acquisition and Modified Newton-Raphson Analysis", NADC-74180-30, 23 June 1975.

APPENDIX A
COMPARISON OF AIRSPEED MEASUREMENTS

Two instruments were used to measure the total airspeed of the T-2C. One instrument had a measurement range of 500 knots. Its measurement value is called a "coarse" value. The other instrument had a measurement range of 100 knots and had the capability to be centered on any increment of 50 knots. Its measured value is called a "fine value".

The Figures A-1 through A-3 show a comparison between the time histories of the coarse and fine values. The coarse value is denoted by a solid line and the fine value is plotted by a dashed line with crosses on it. In most cases the dashes are so close together that the "fine value" curve may appear as a solid line with crosses on it. All eighteen maneuvers are covered in these figures. Note that there is an approximately four meter/sec difference between the coarse and fine values for all maneuvers except those in flight number four (i.e., F4M1, F4M2, . . . , F4M10).

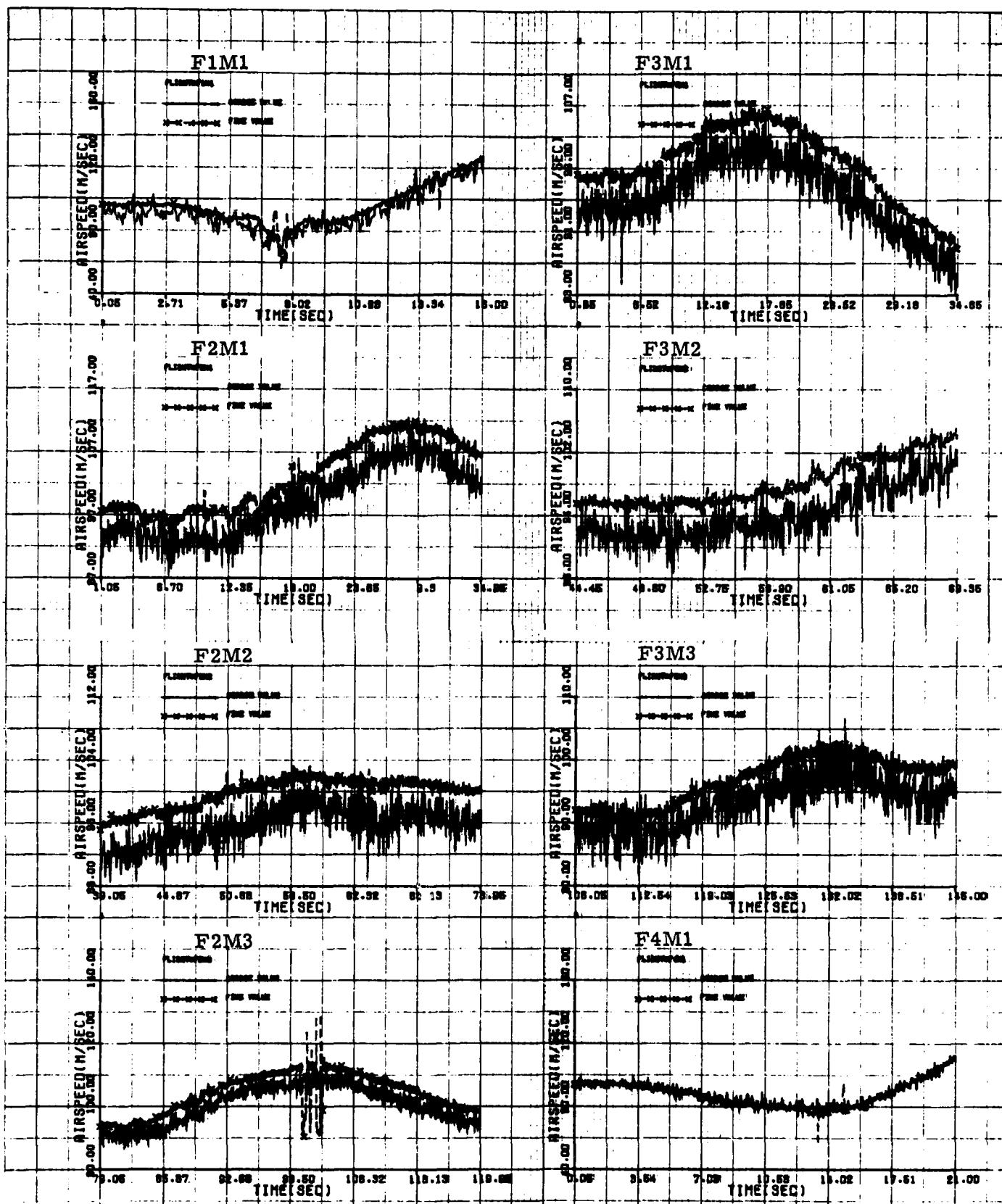


Fig. A-1 A comparison between the time histories of the coarse and the fine values of the total airspeed measurement for maneuvers F1M1 through F4M1

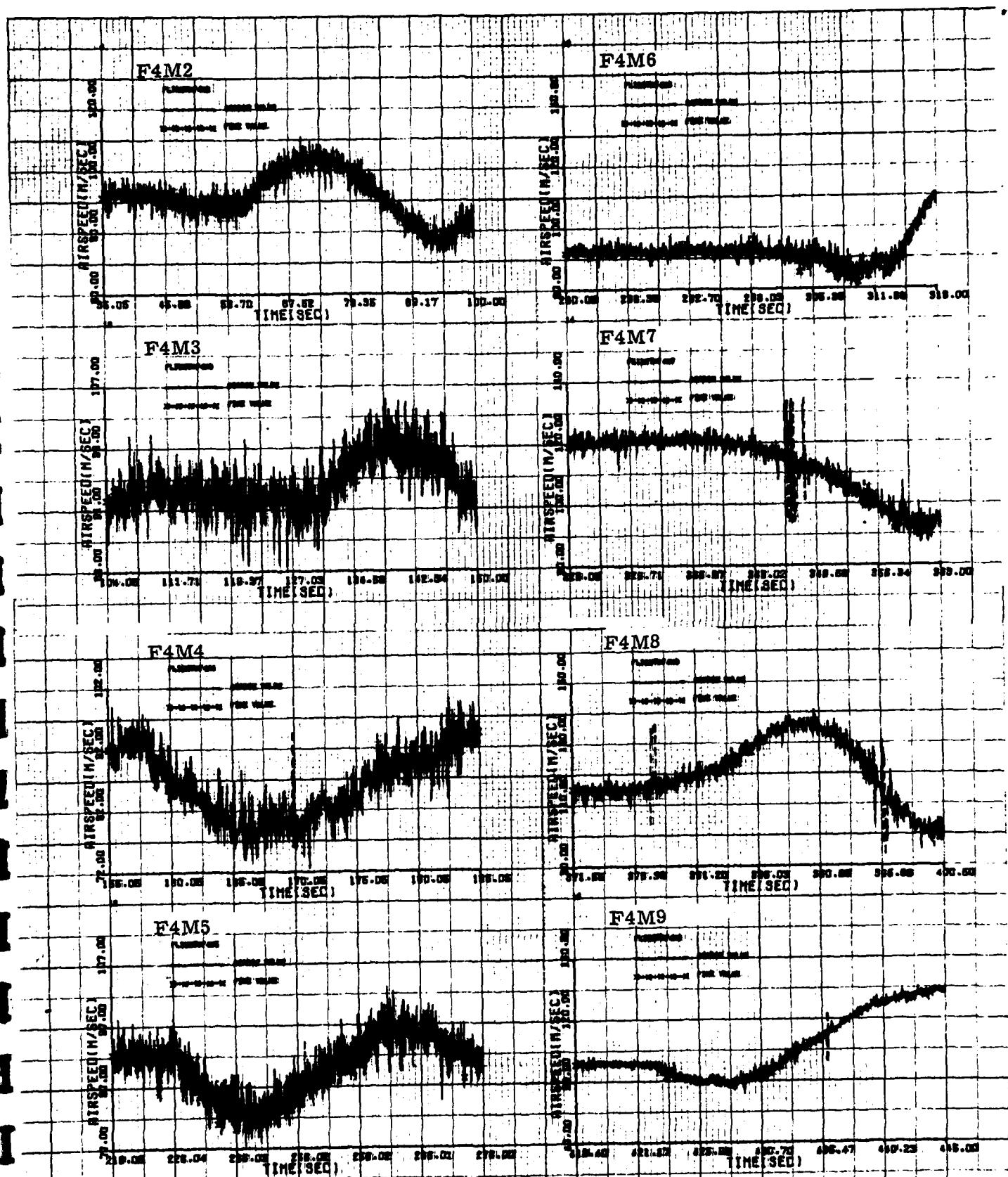


Fig. A-2 A comparison between the time histories of the coarse and the fine values of the total airspeed measurement for maneuvers F4M2 through F4M9

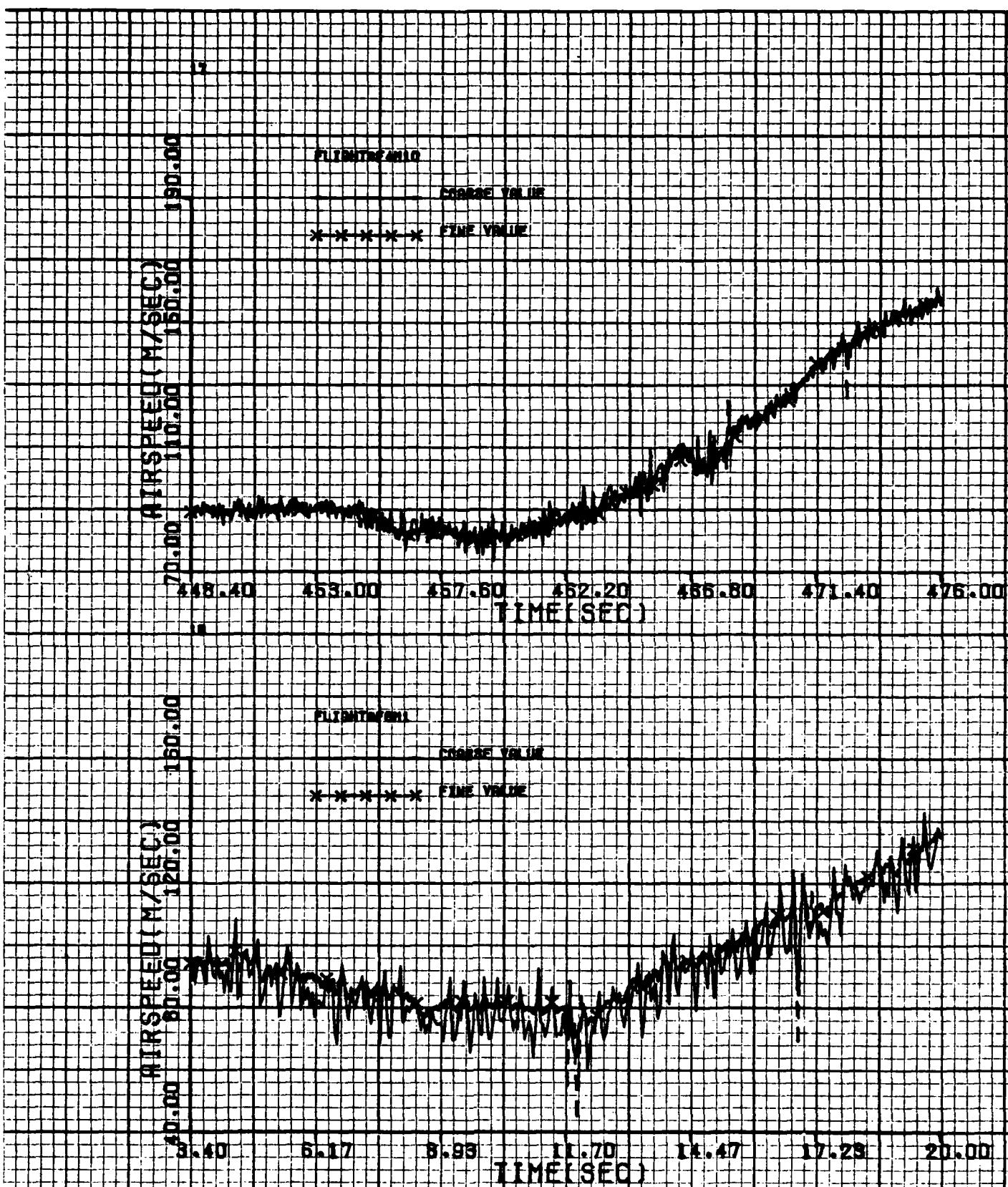


Figure A-3 A comparison between the time histories of the coarse and fine values of the total airspeed measurement for maneuvers F4M10 and F6M1

APPENDIX B

ESTIMATION RESULTS OF THE T-2C FLIGHT TEST DATA

The estimation results which are an output of the first step of the EBM method are presented for all maneuvers in Figures B-1 through B-18. The results cover four pages for each maneuver. The first page contains the angle-of-attack and sideslip results. The second page covers the time history of the three controls: elevator, aileron, and rudder. The third page contains airspeed, roll rate, pitch rate, yaw rate, pitch angle, roll angle, altitude, and normal acceleration at the center-of-gravity. The fourth page consists of the remaining eight accelerations: the normal acceleration at the right and left wing tips and at the nose and tail, the lateral acceleration at center-of-gravity, nose and tail, and the fore - aft acceleration at the nose.

These figures give a comparison between the estimation results of the first step of the EBM method and the measured values of the T-2C flight test data that were an input to the EBM method. The estimated values satisfy the differential equations contained in Equations (A-1) through (A-9) of Appendix A of Volume 2.

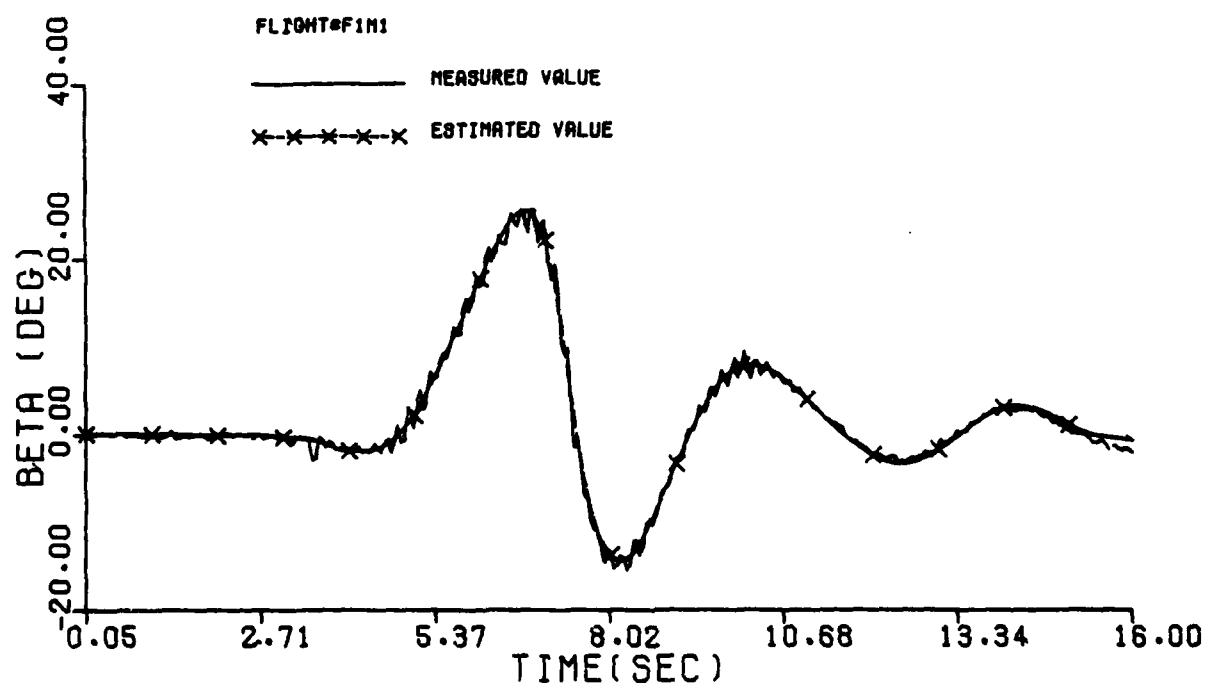
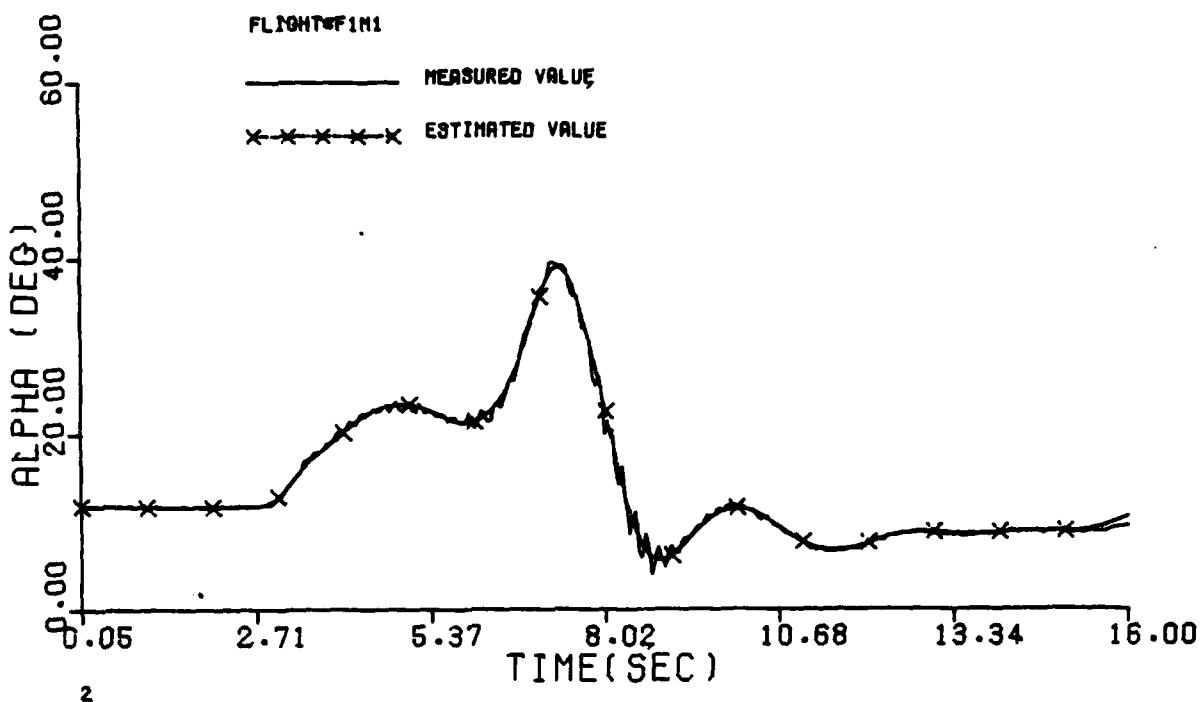


Figure B-1 Comparison Between the Measured and the Estimated Values of Maneuver 1 of Flight 1

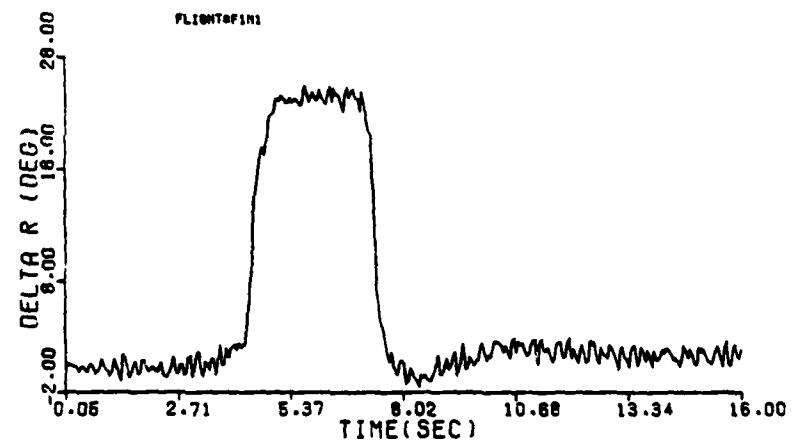
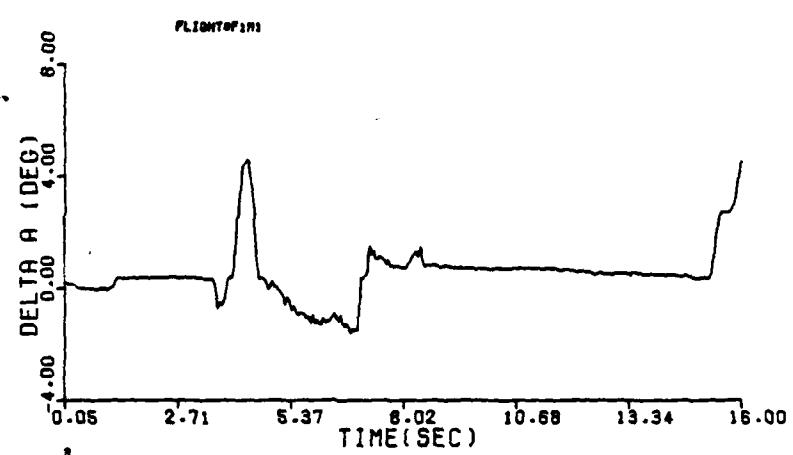
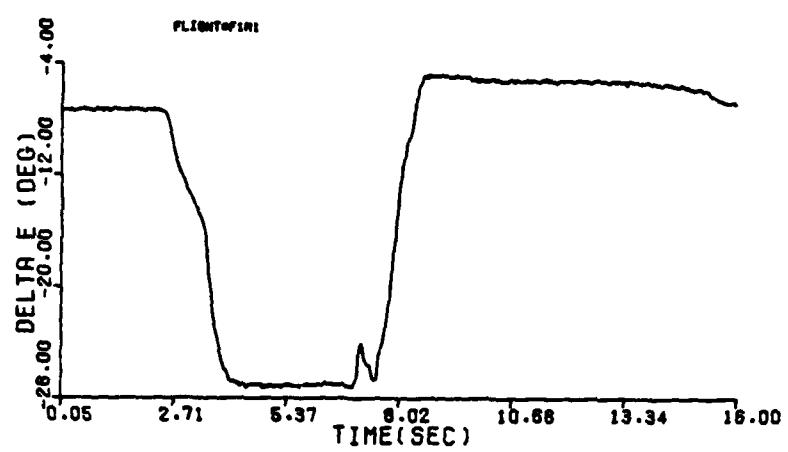


Figure B-1 (cont'd)

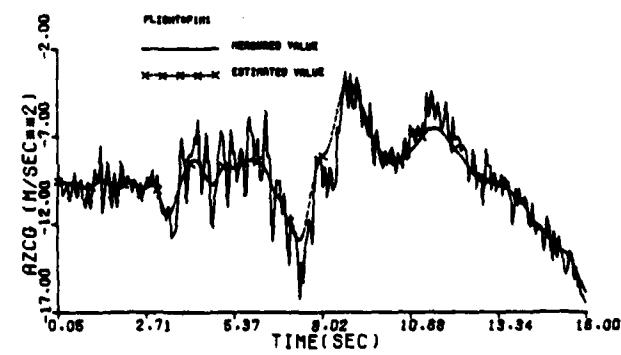
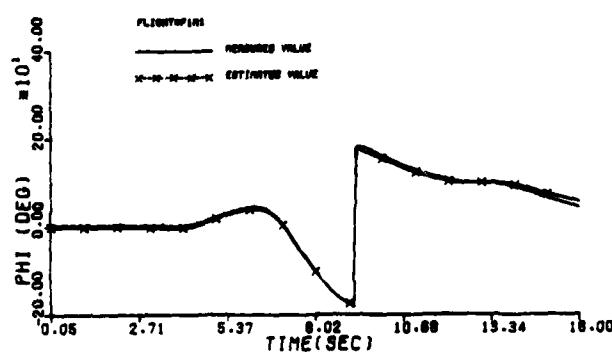
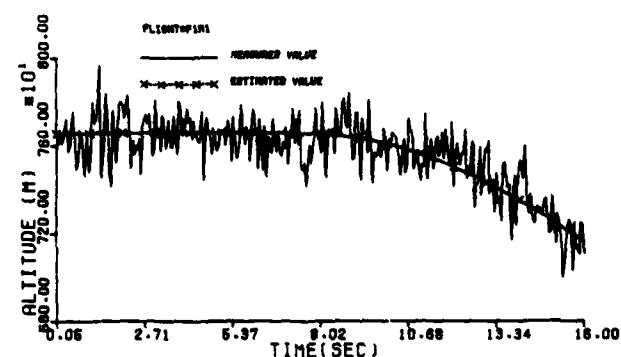
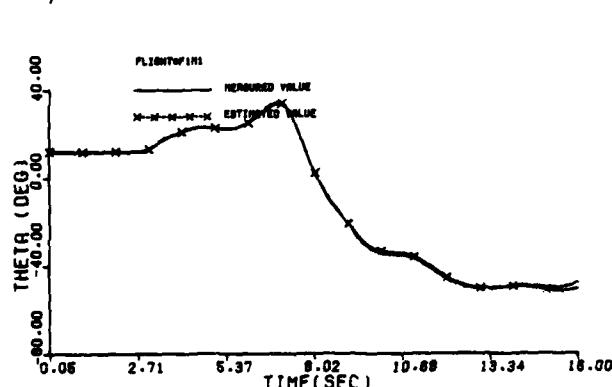
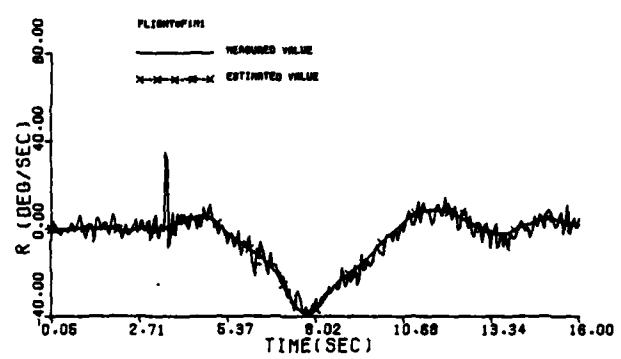
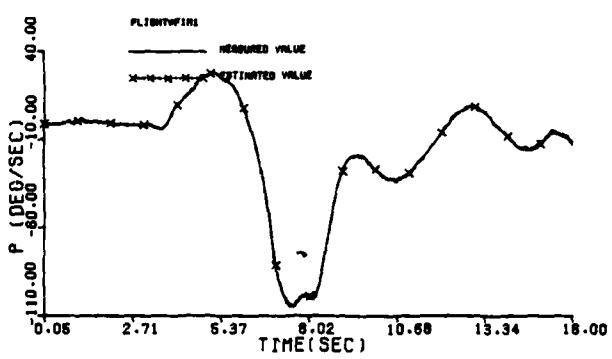
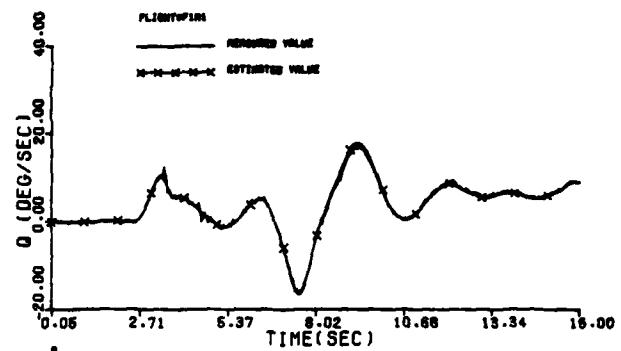
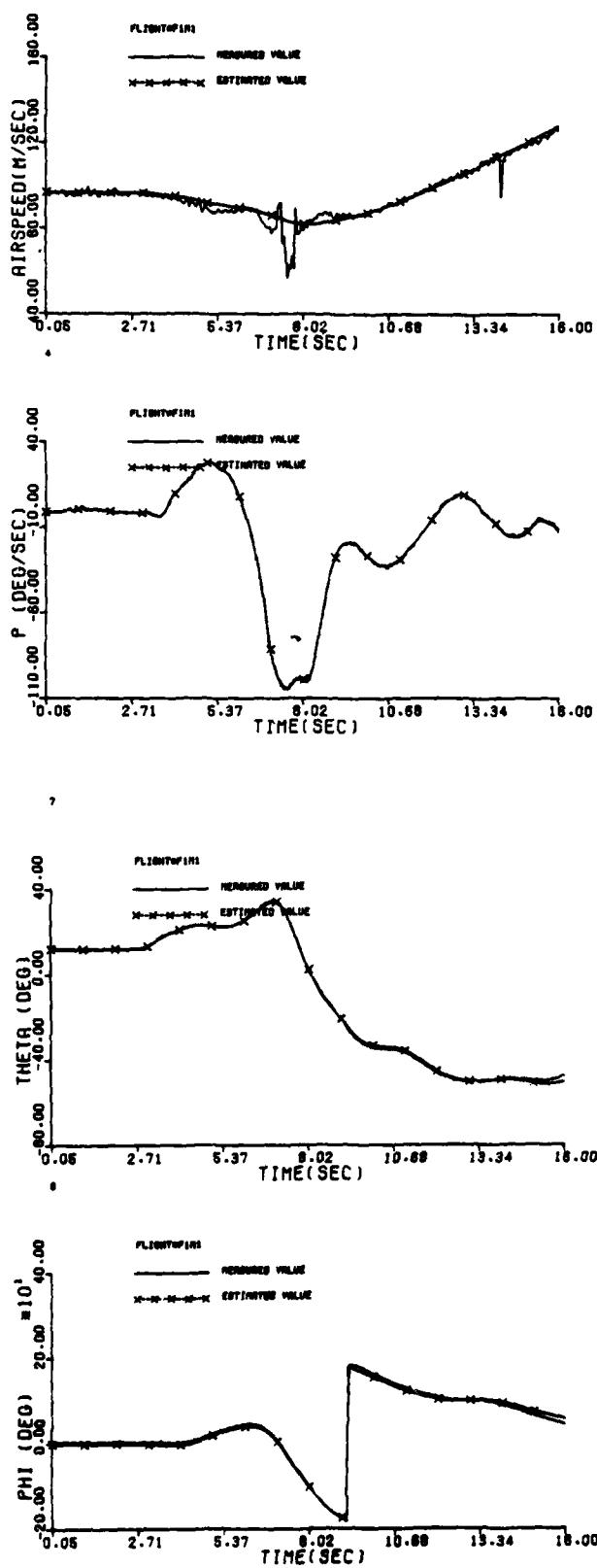


Figure B-1 (cont'd)

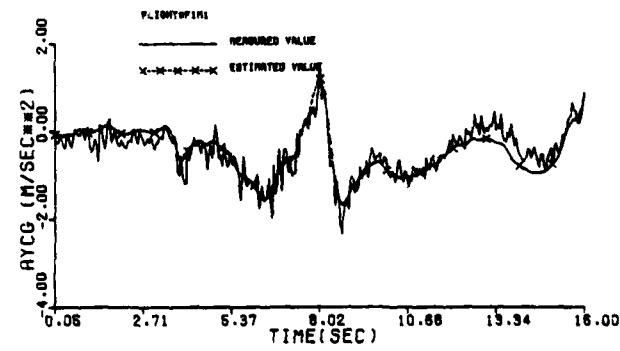
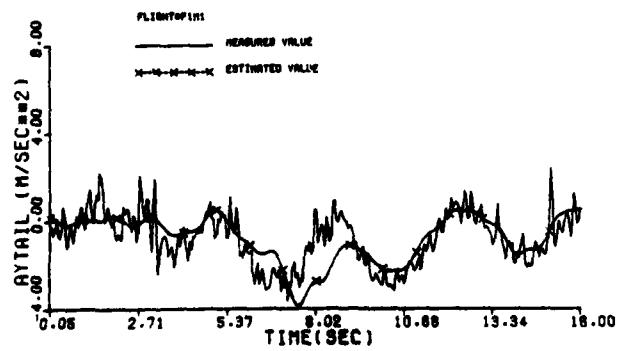
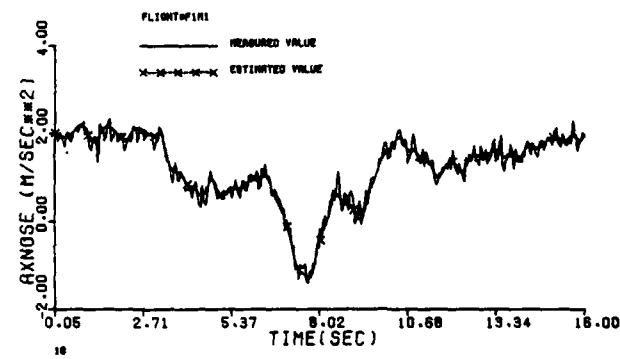
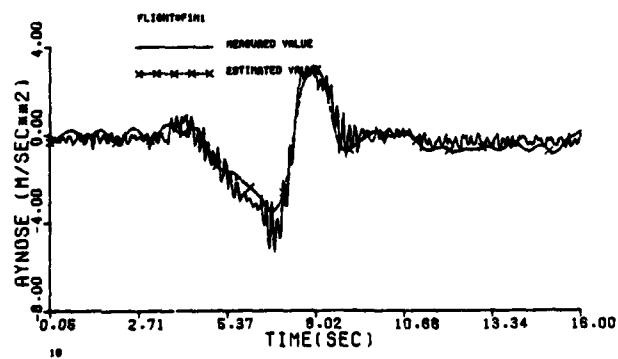
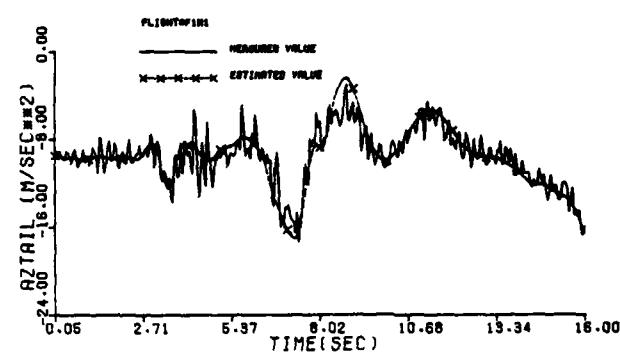
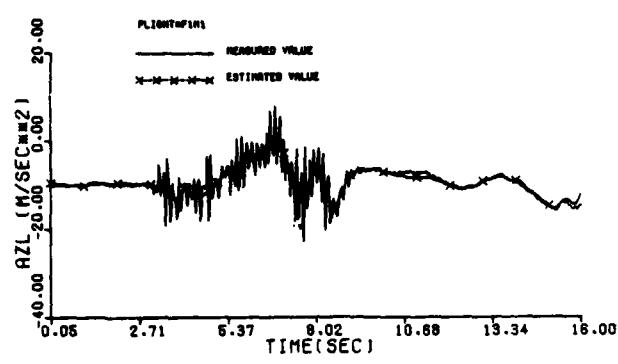
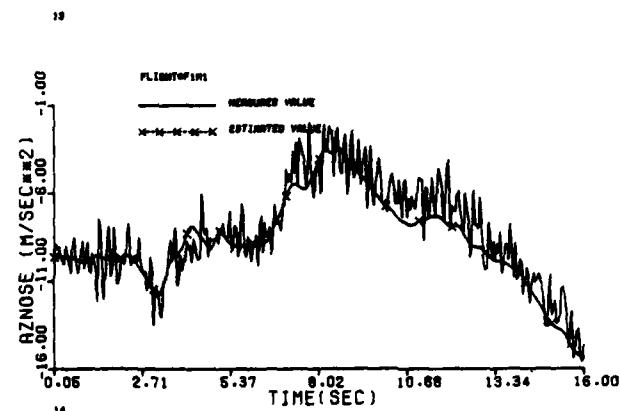
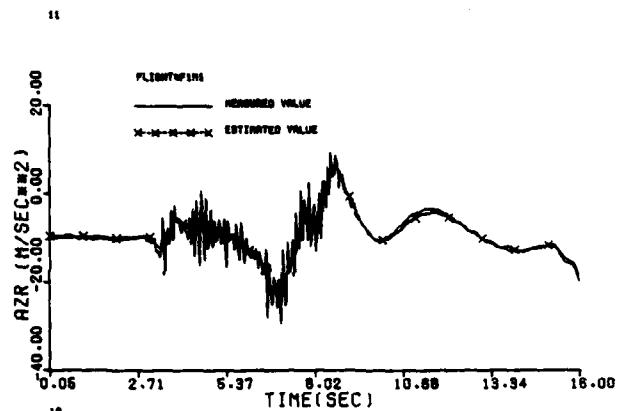


Figure B-1 (concluded)

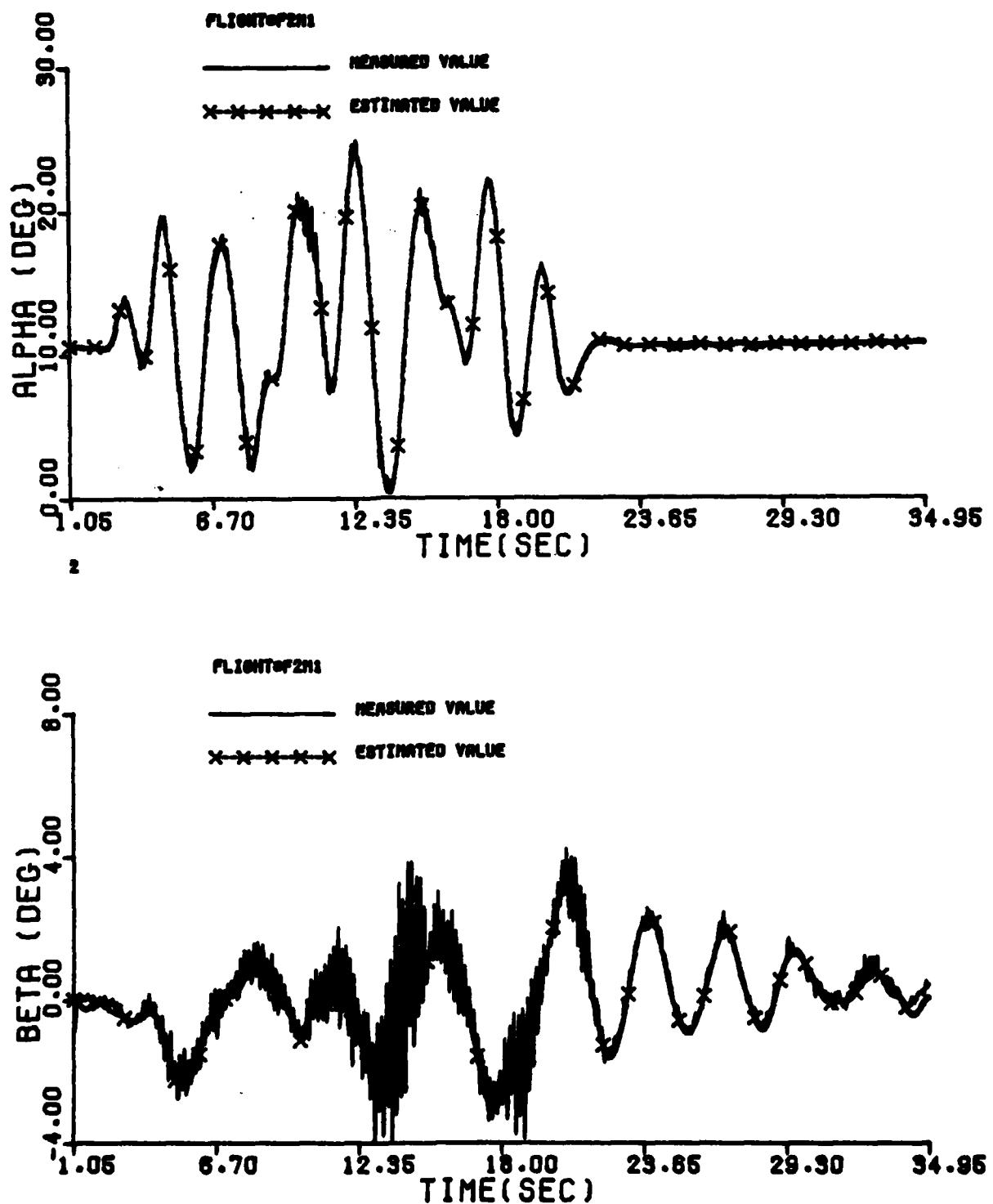


Figure B-2 Comparison Between the Measured and the Estimated Values of Maneuver 1 of Flight 2

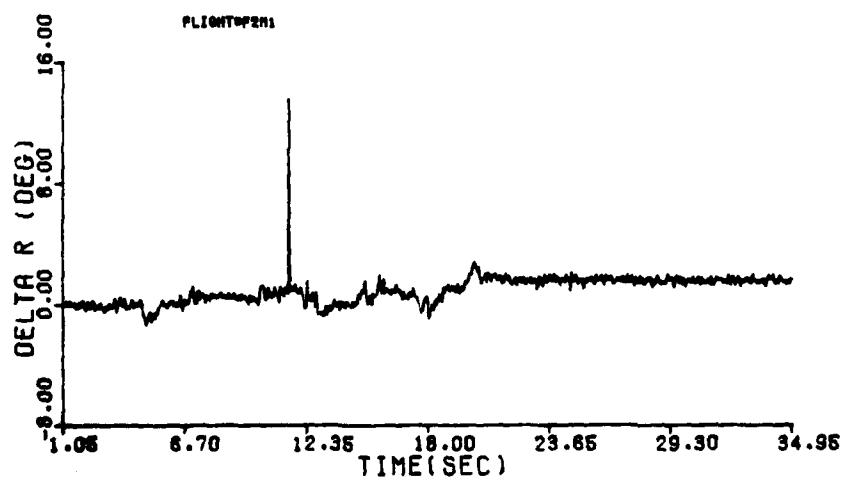
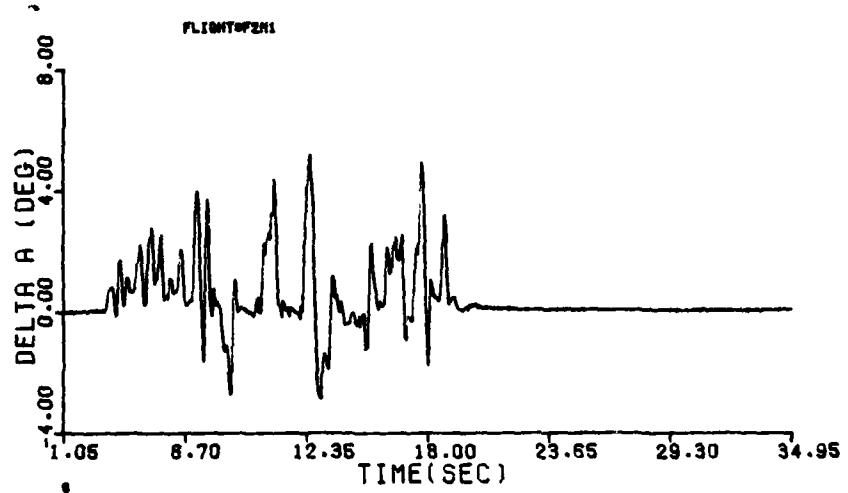
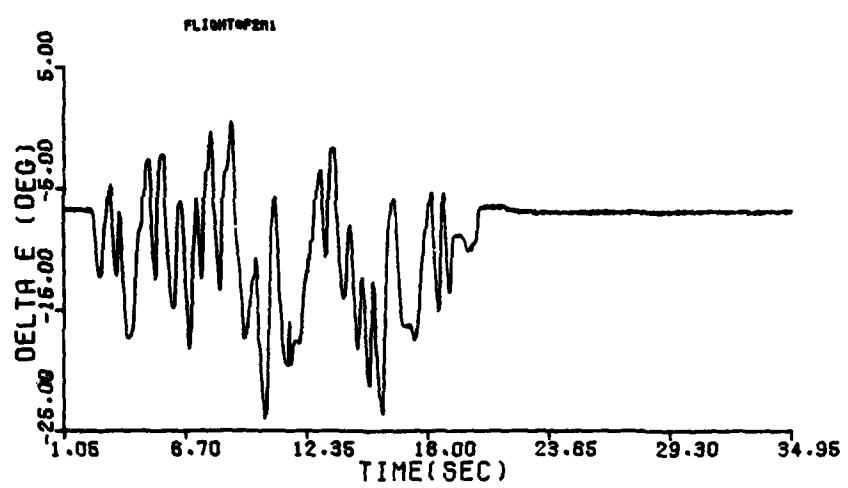


Figure B-2 (cont'd)

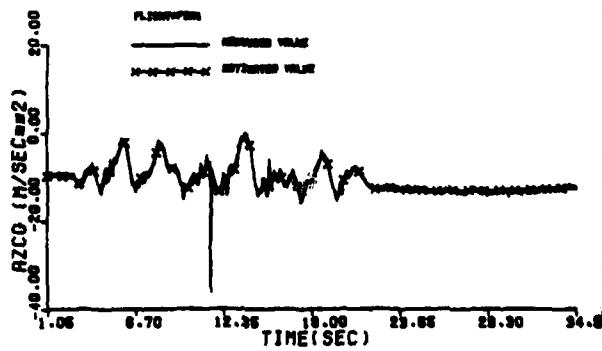
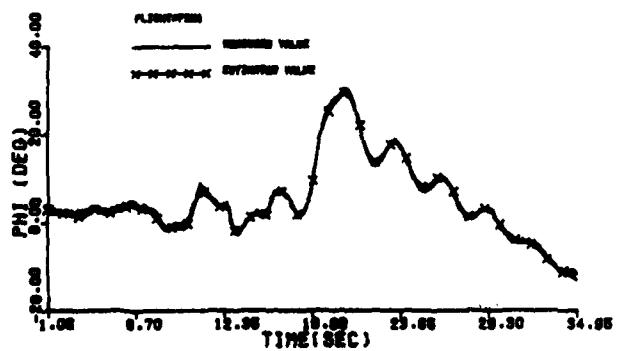
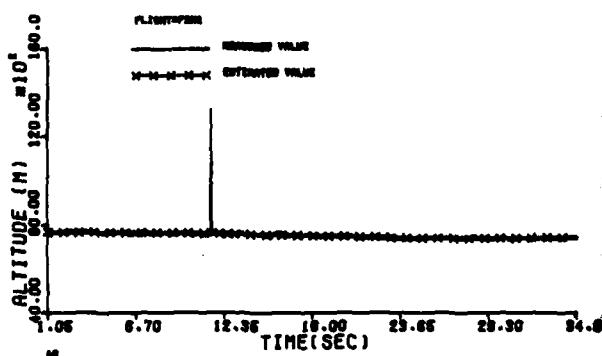
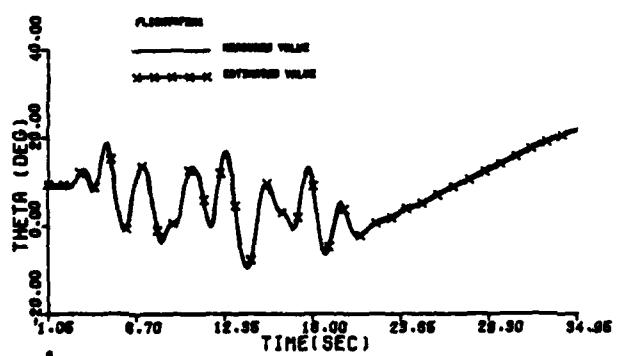
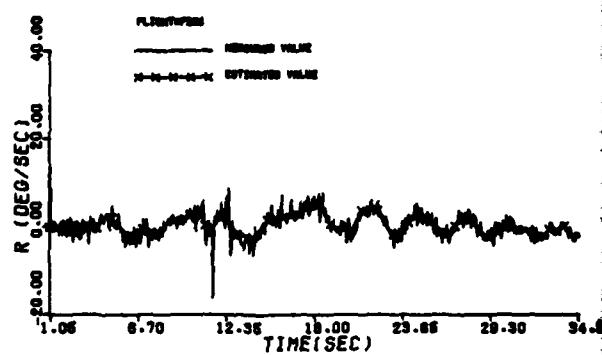
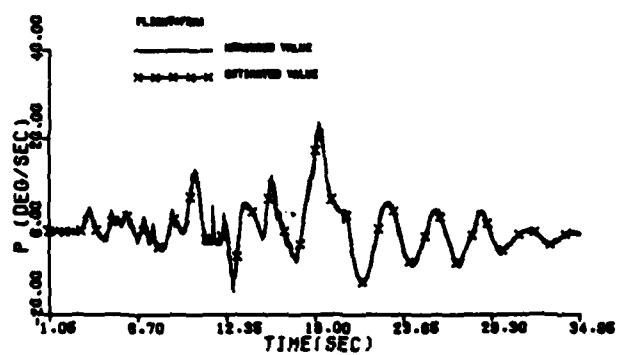
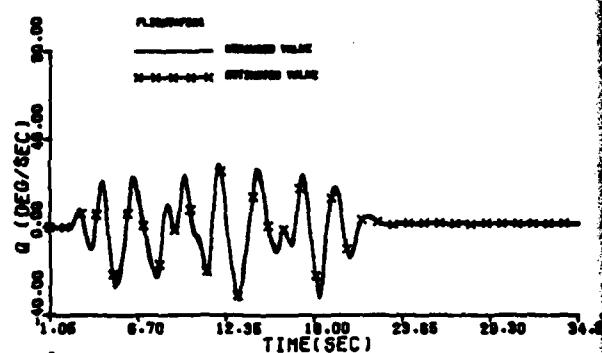
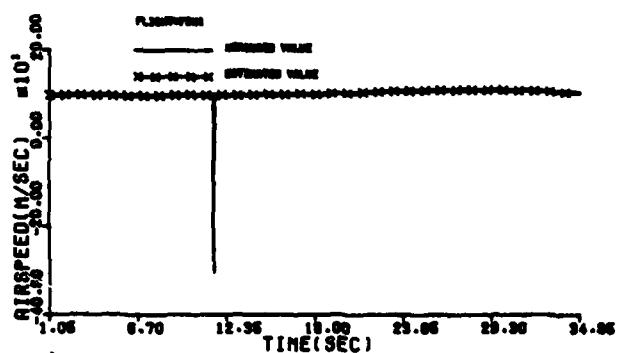


Figure B-2 (cont'd)

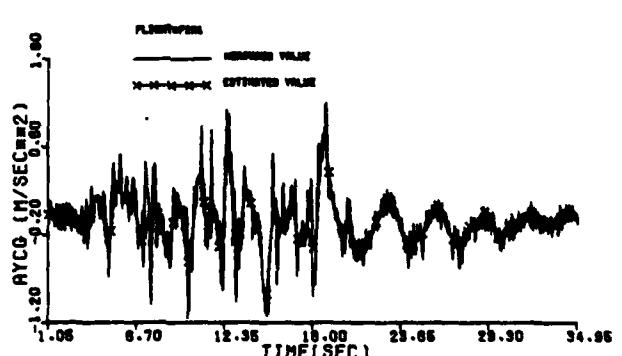
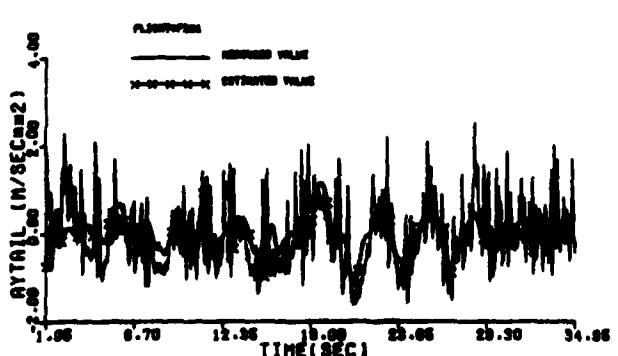
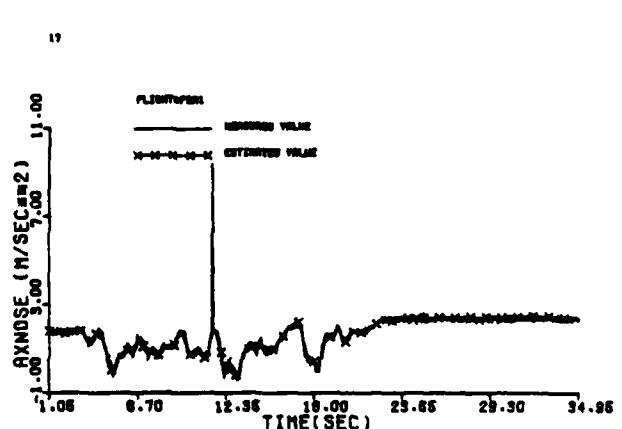
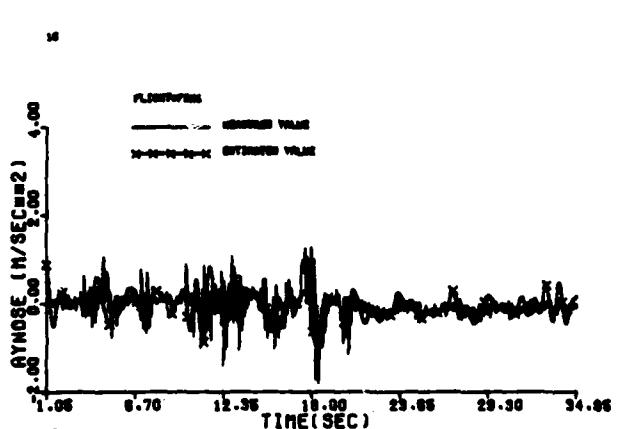
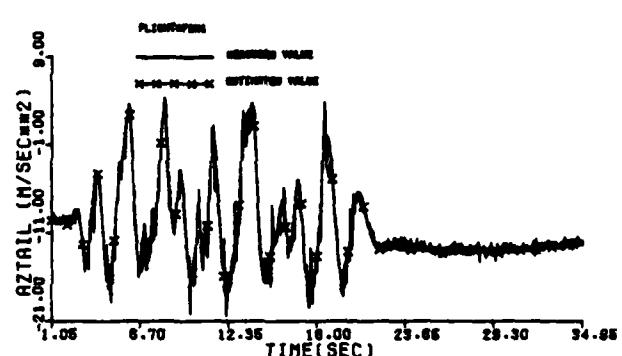
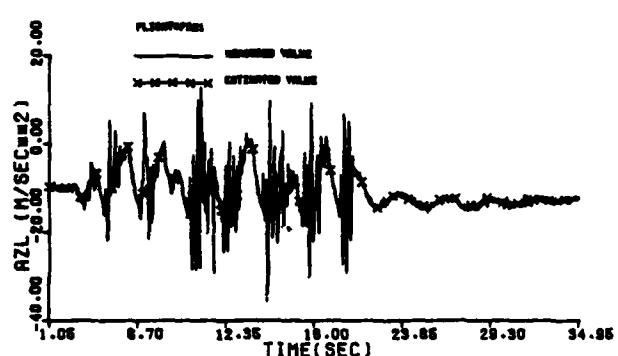
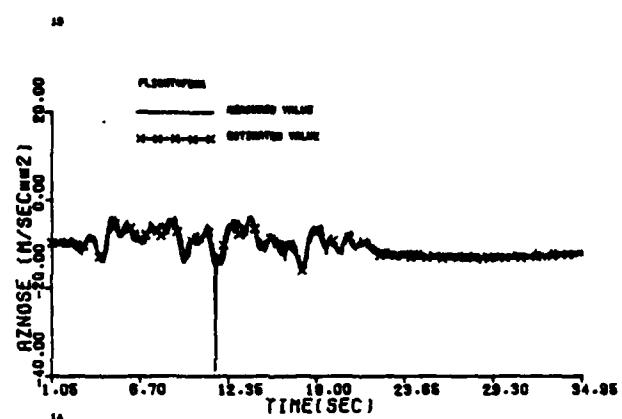
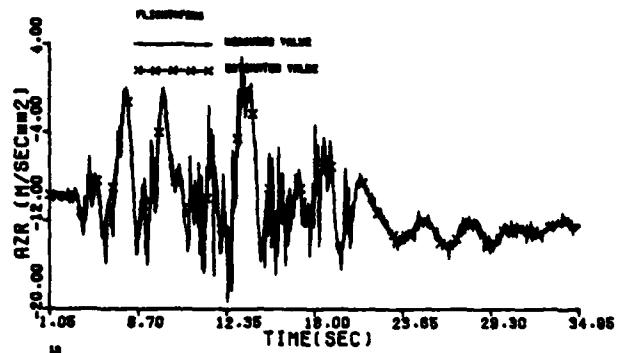


Figure B-2 (concluded)

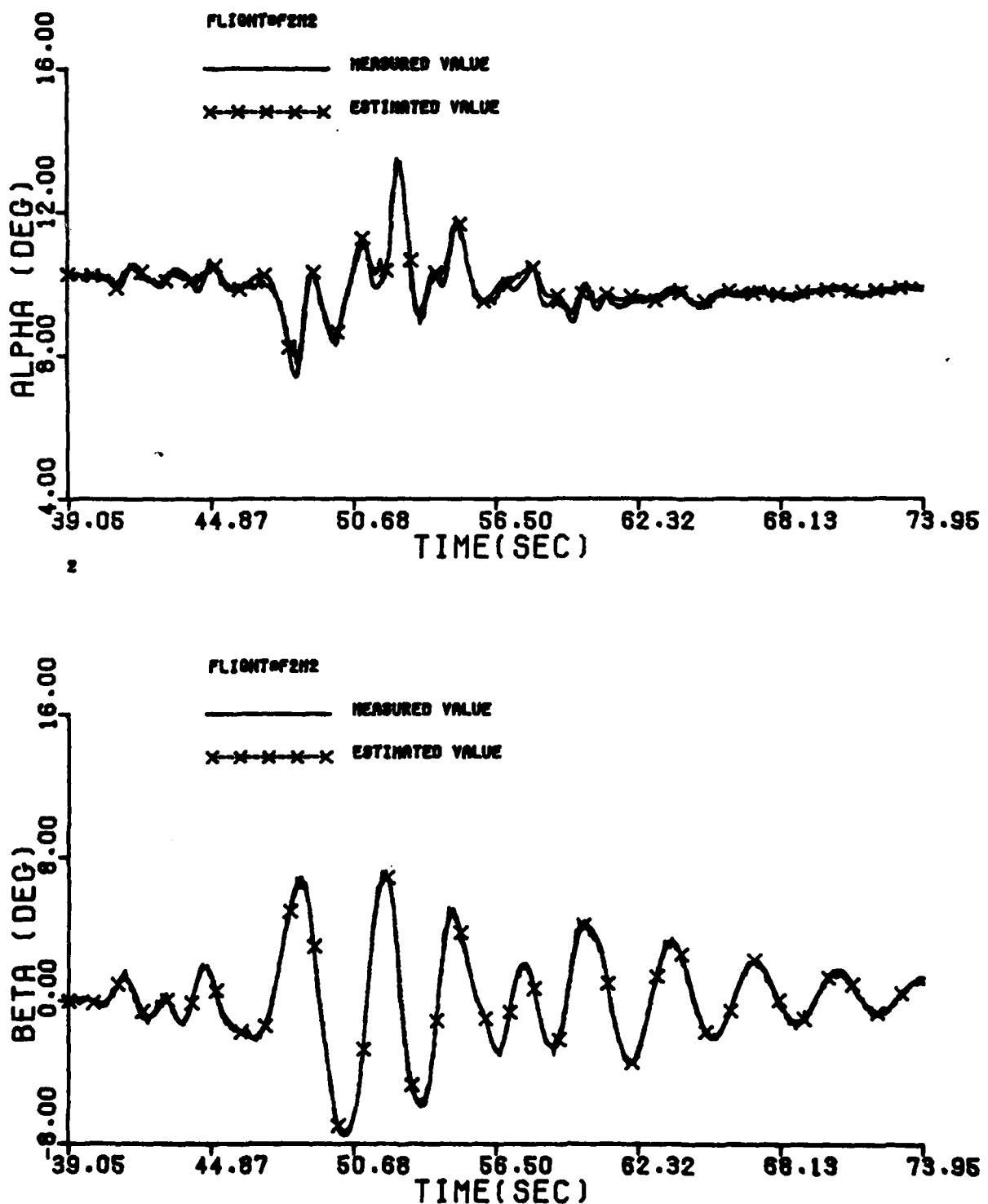


Figure B-3 Comparison Between the Measured and the Estimated Values of Maneuver 2 of Flight 2

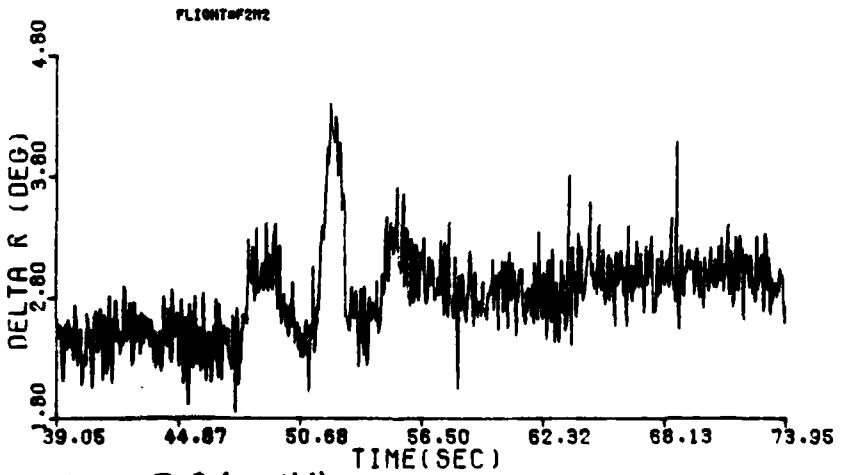
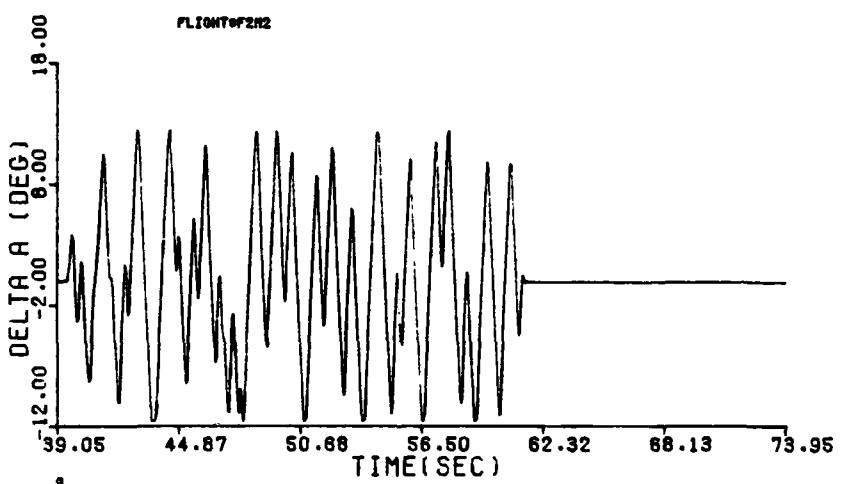
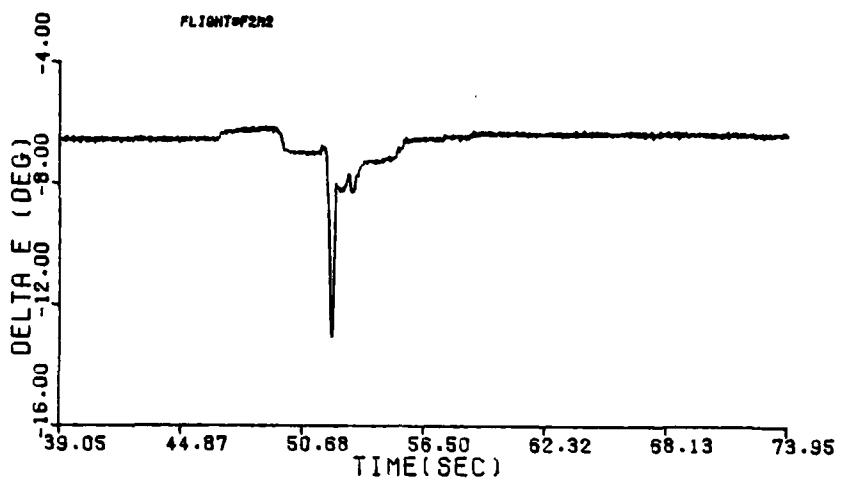


Figure B-3 (cont'd)

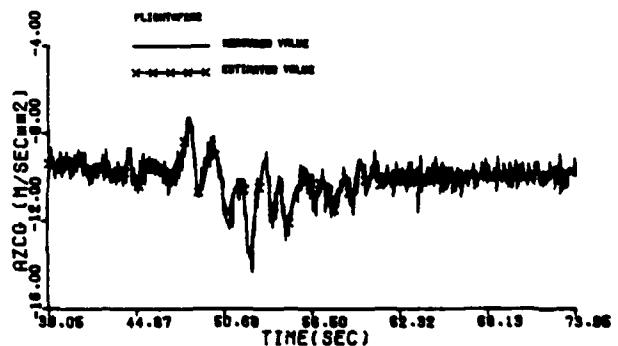
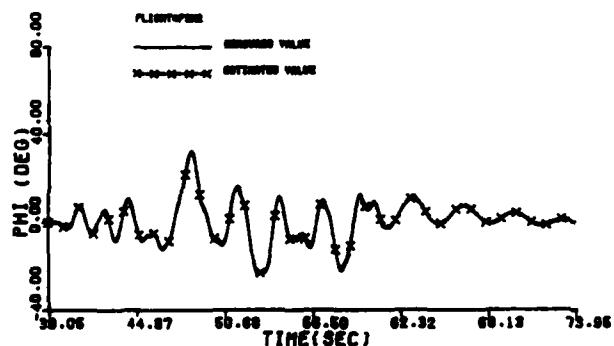
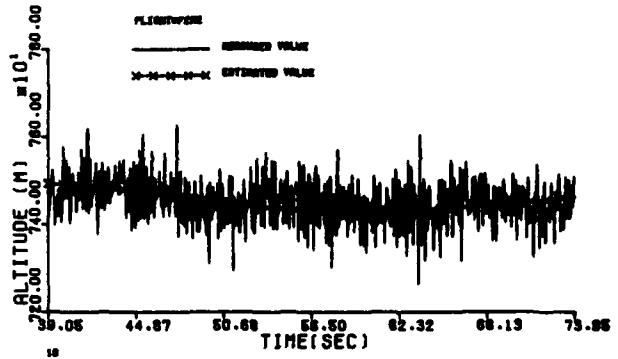
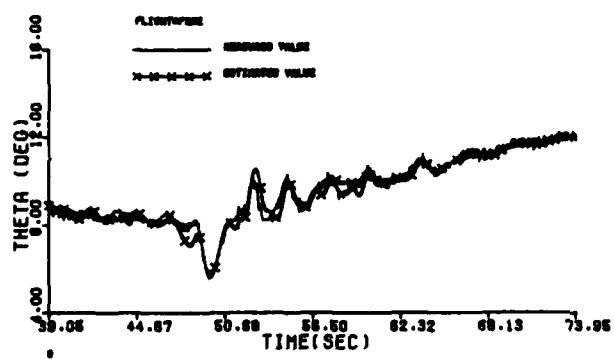
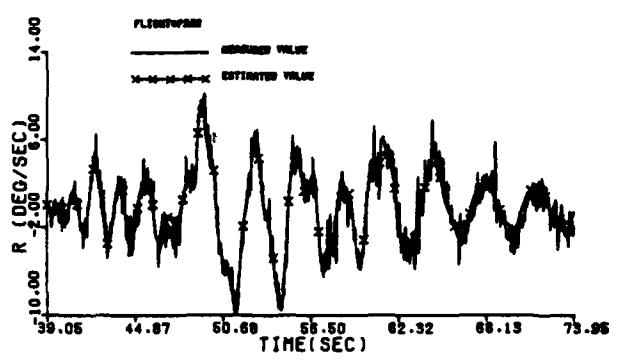
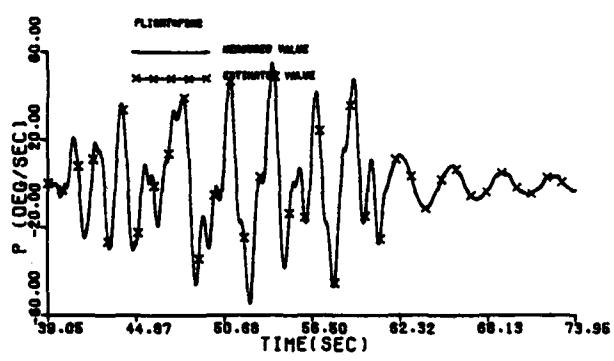
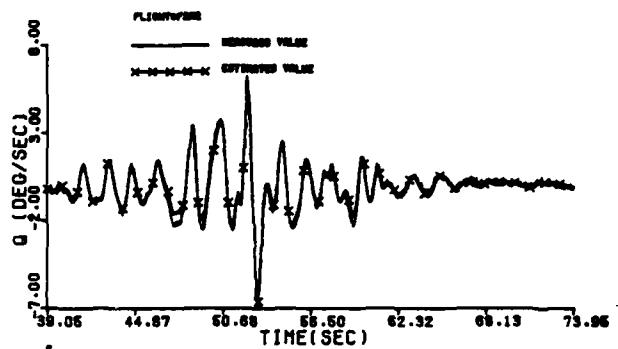
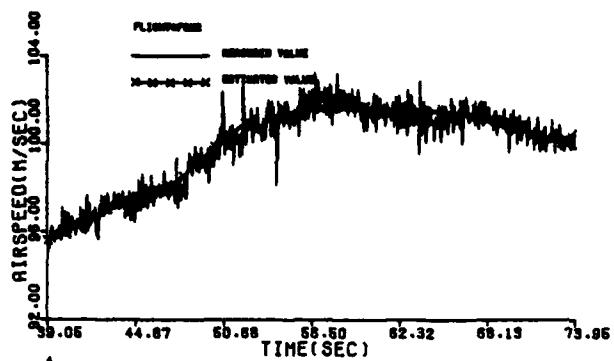


Figure B-3 (cont'd)

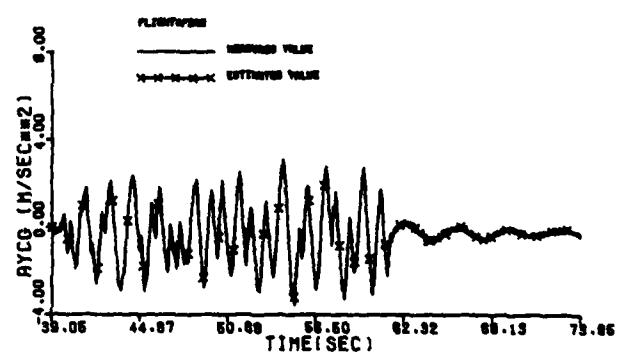
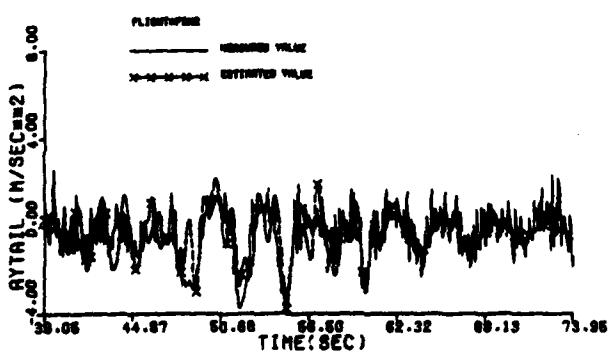
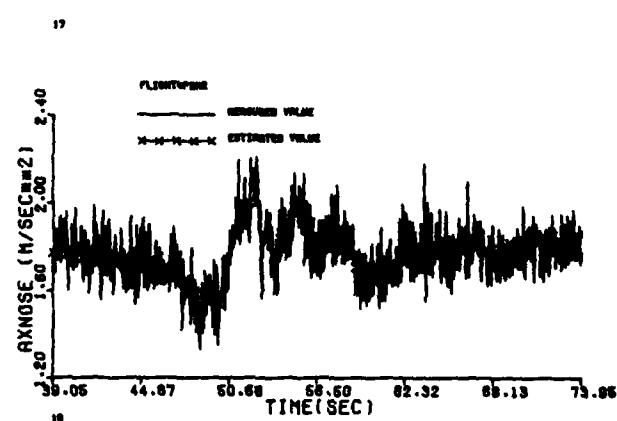
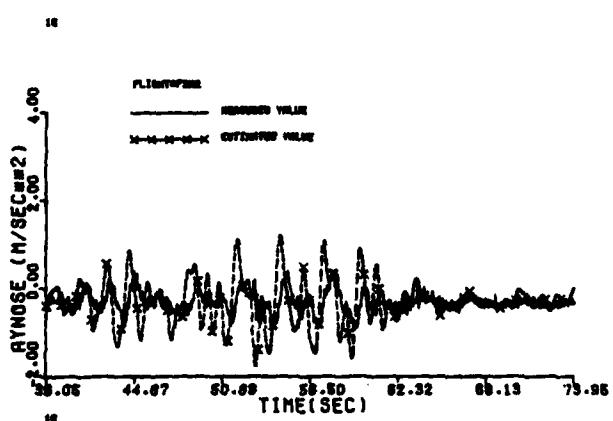
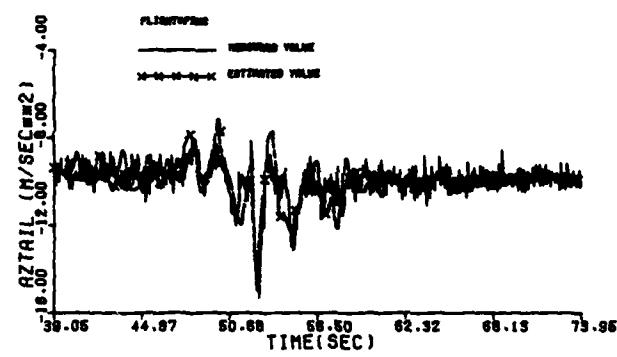
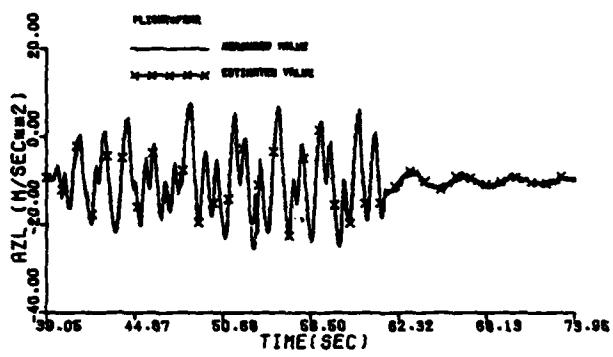
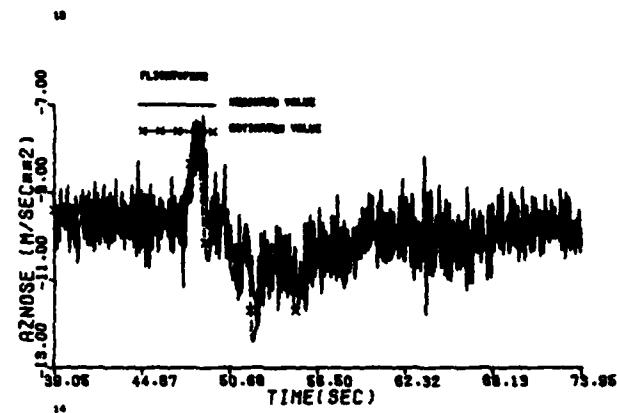
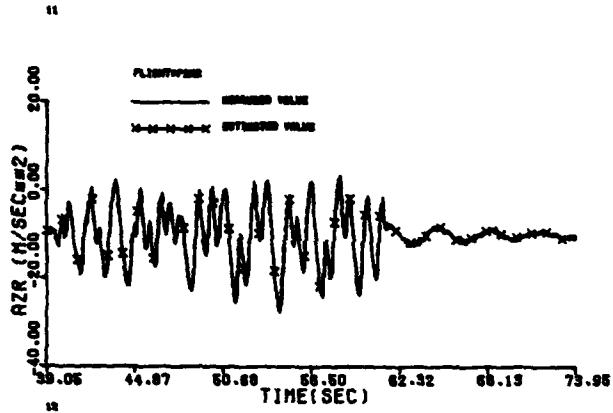


Figure B-3 (concluded)

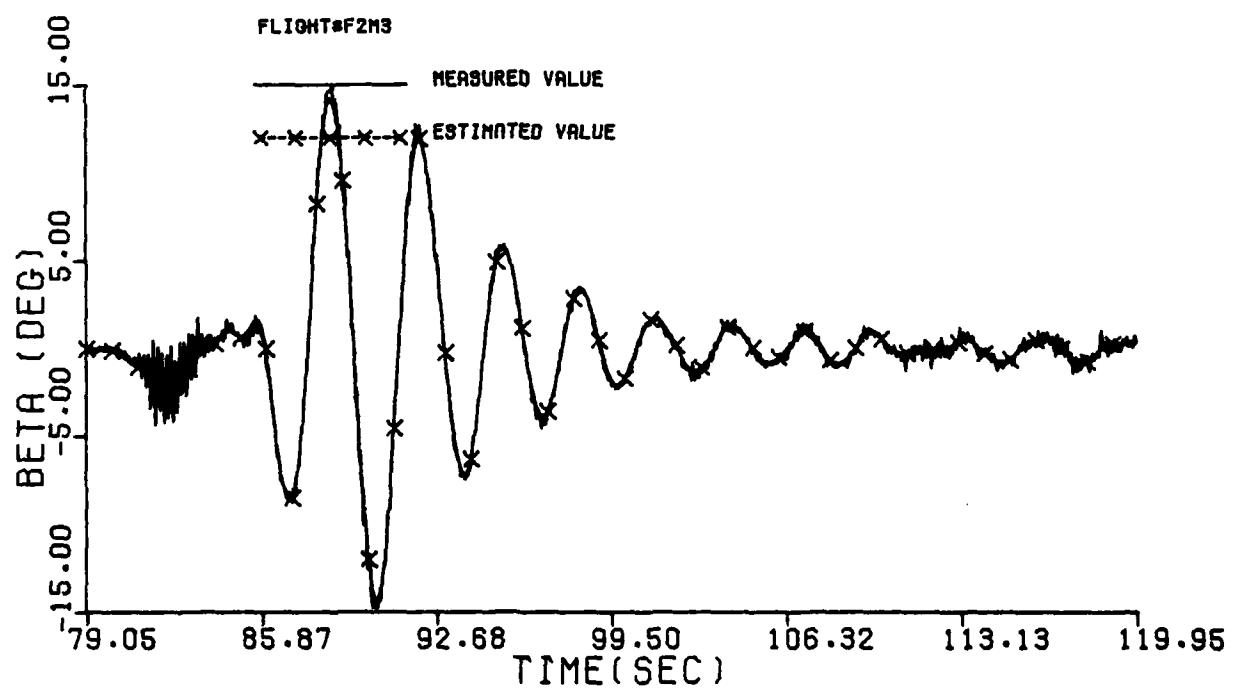
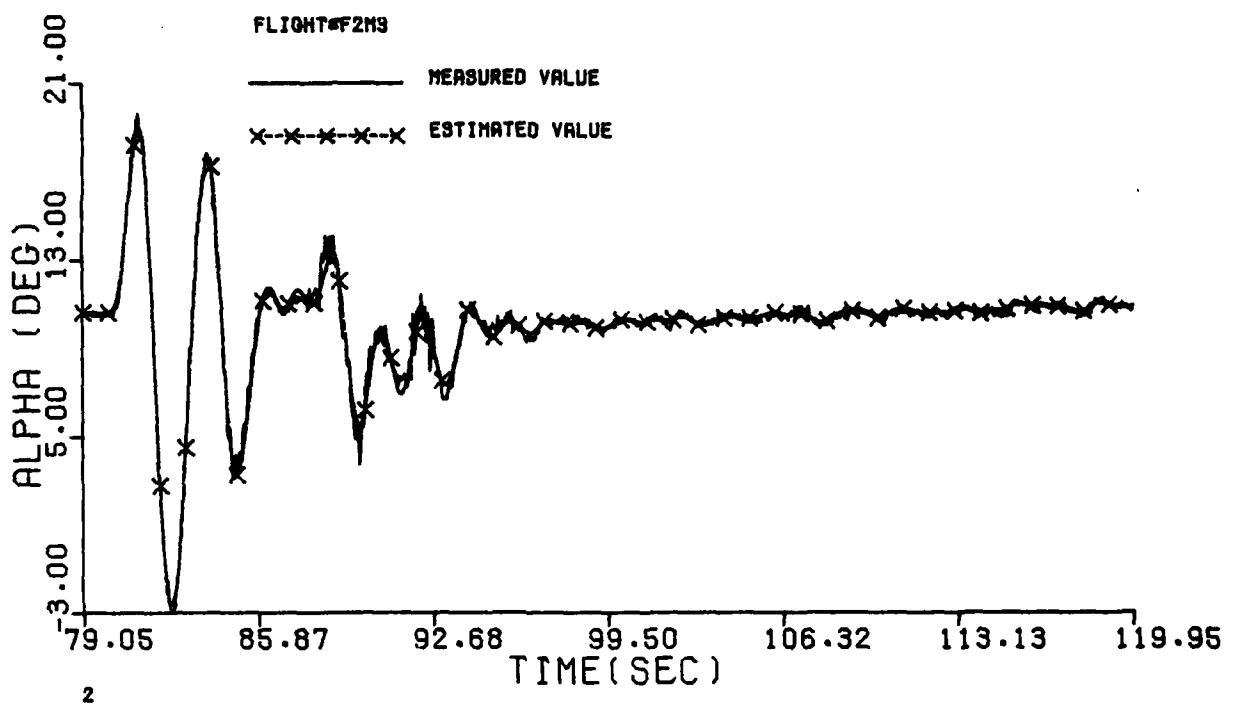


Figure B-4 Comparison Between the Measured and the Estimated Values of Maneuver 3 of Flight 2

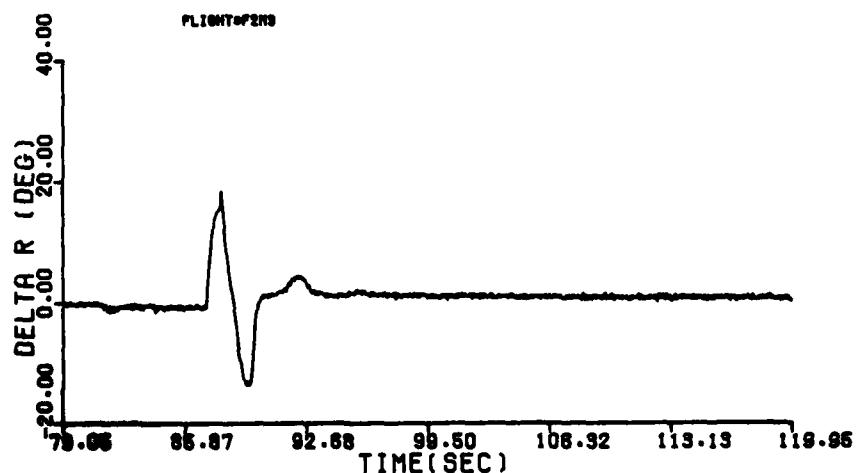
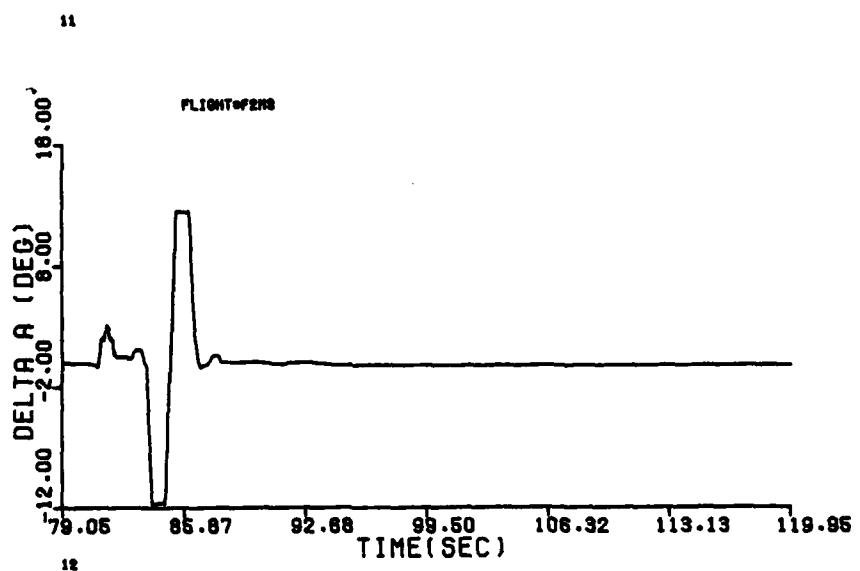
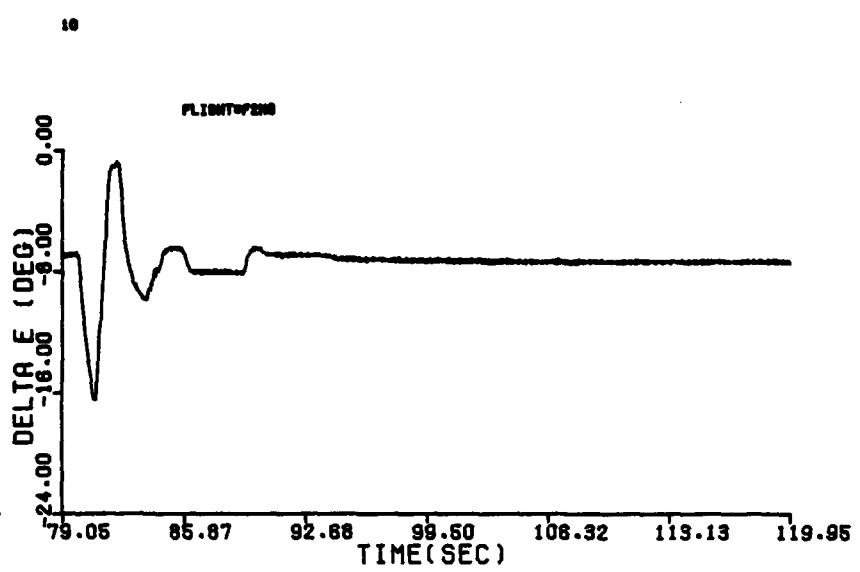


Figure B-4 (cont'd)

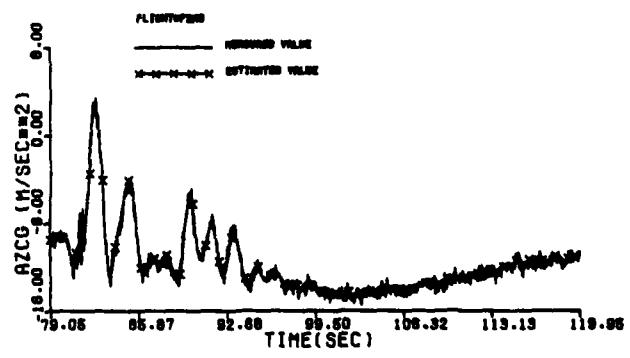
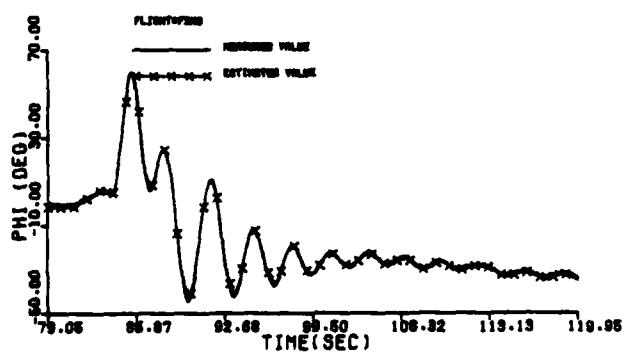
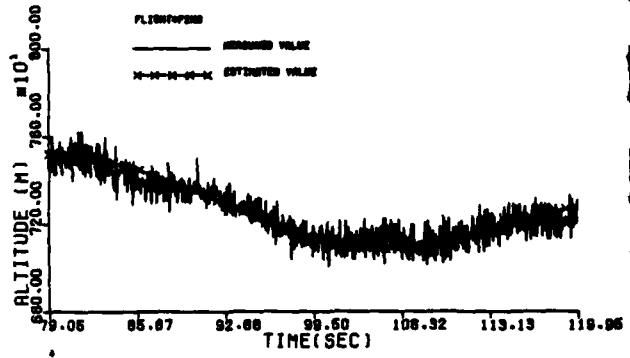
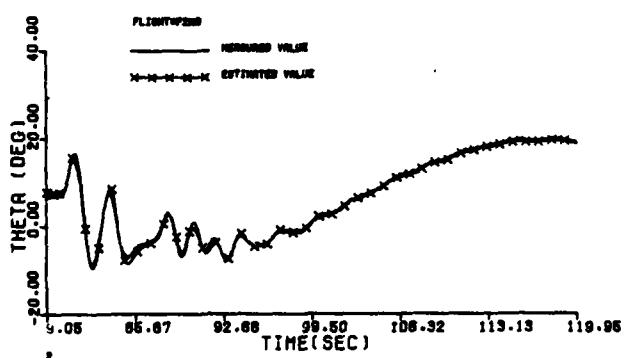
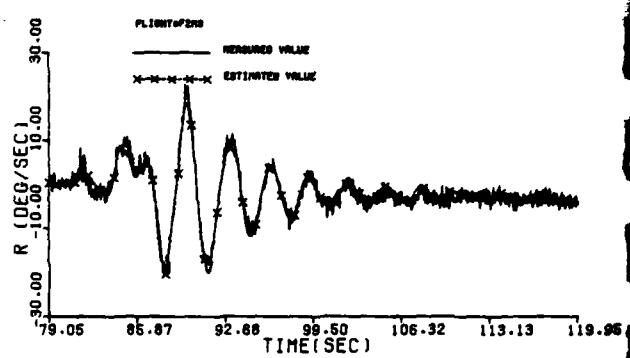
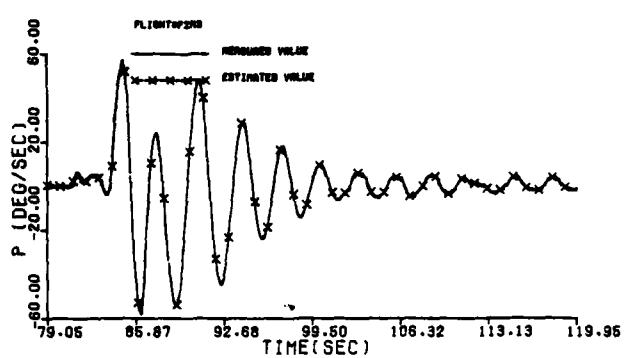
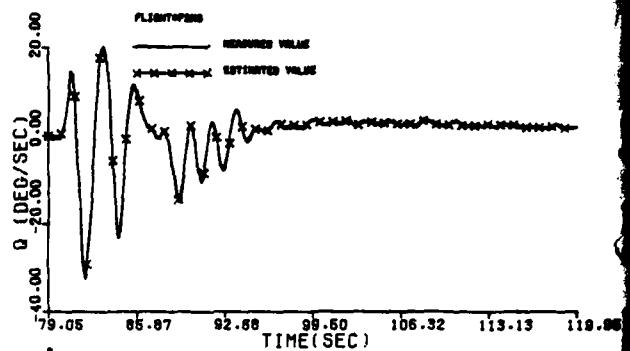
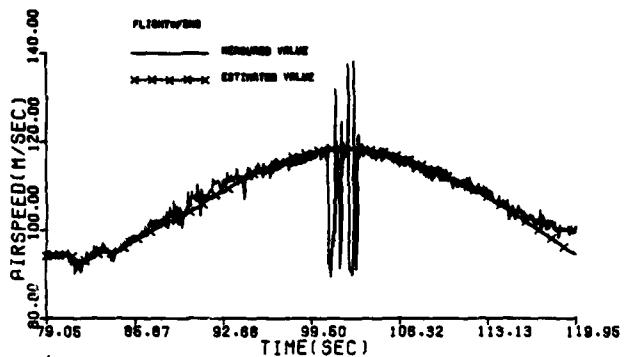


Figure B-4 (cont'd)

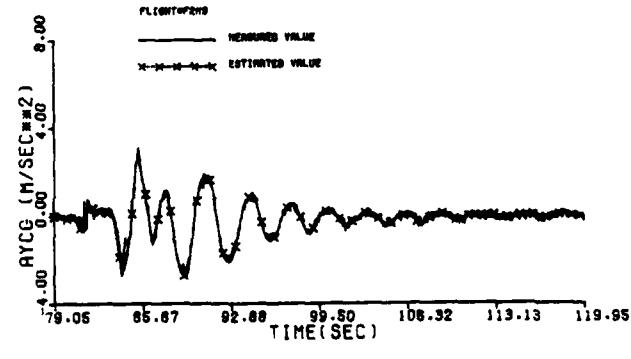
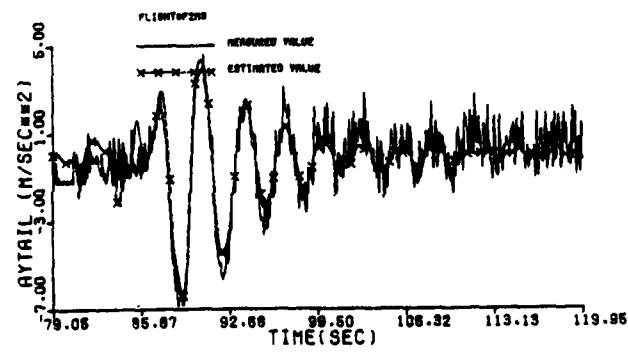
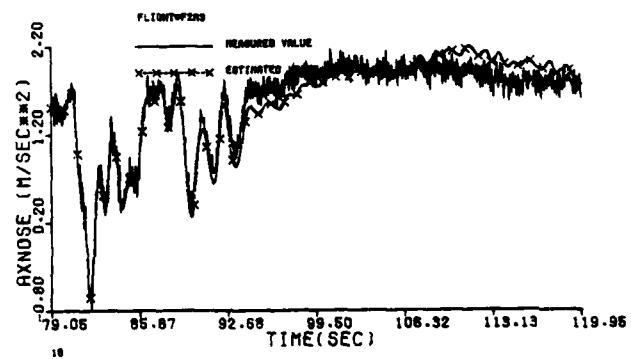
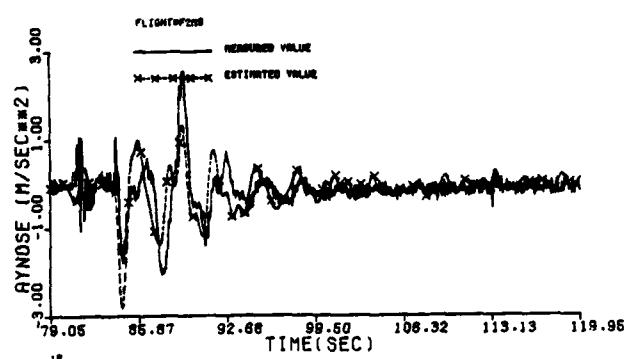
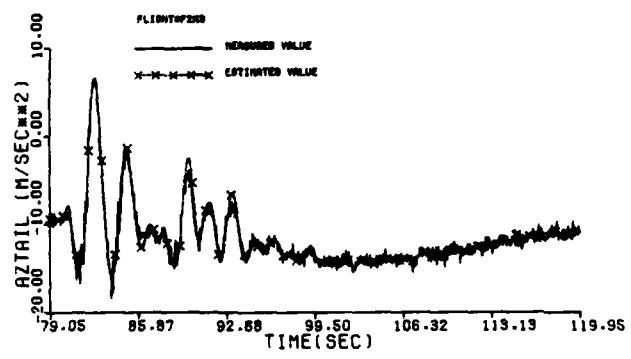
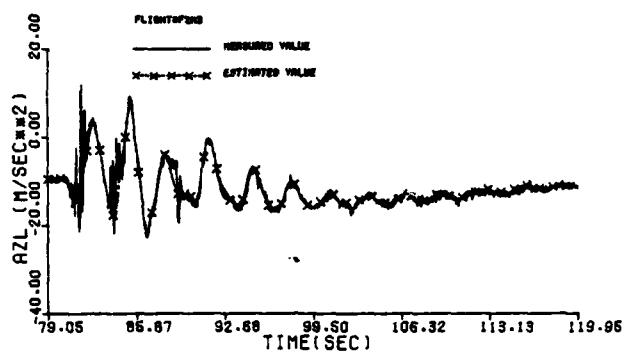
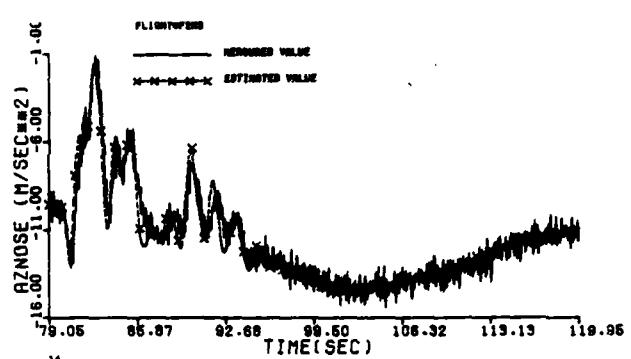
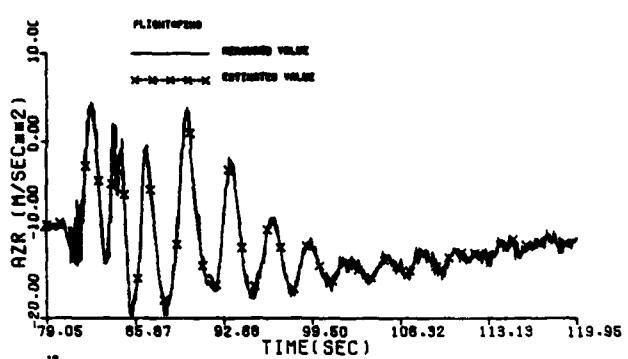


Figure B-4 (concluded)

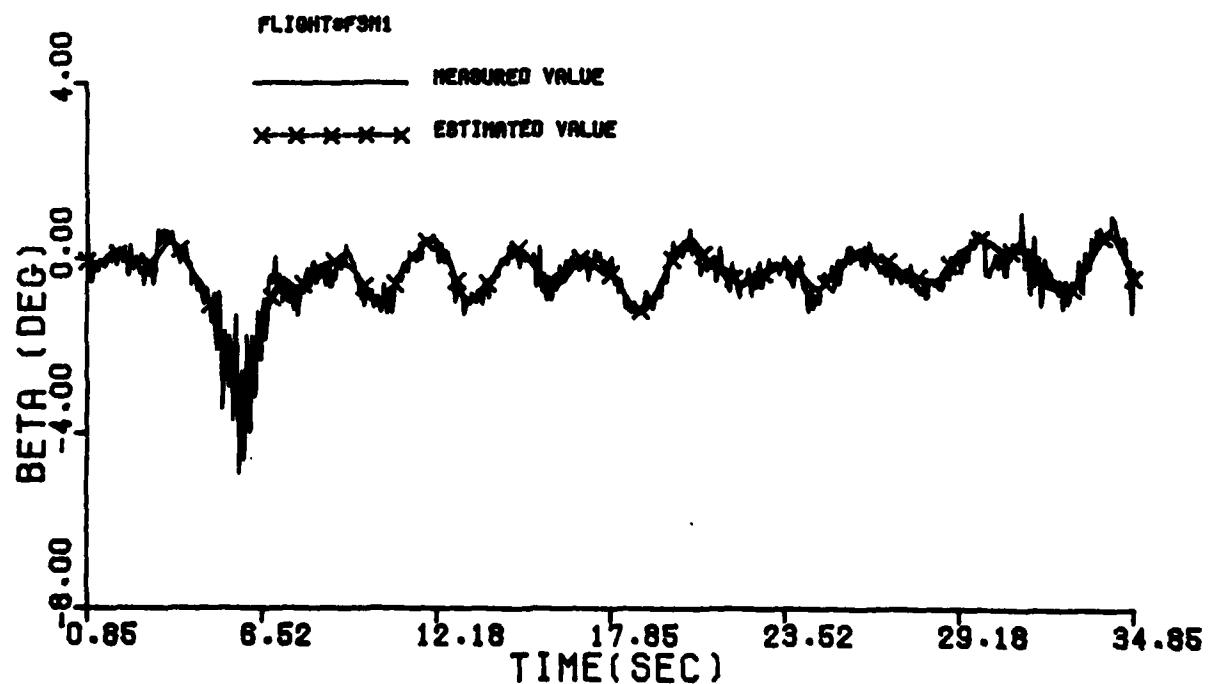
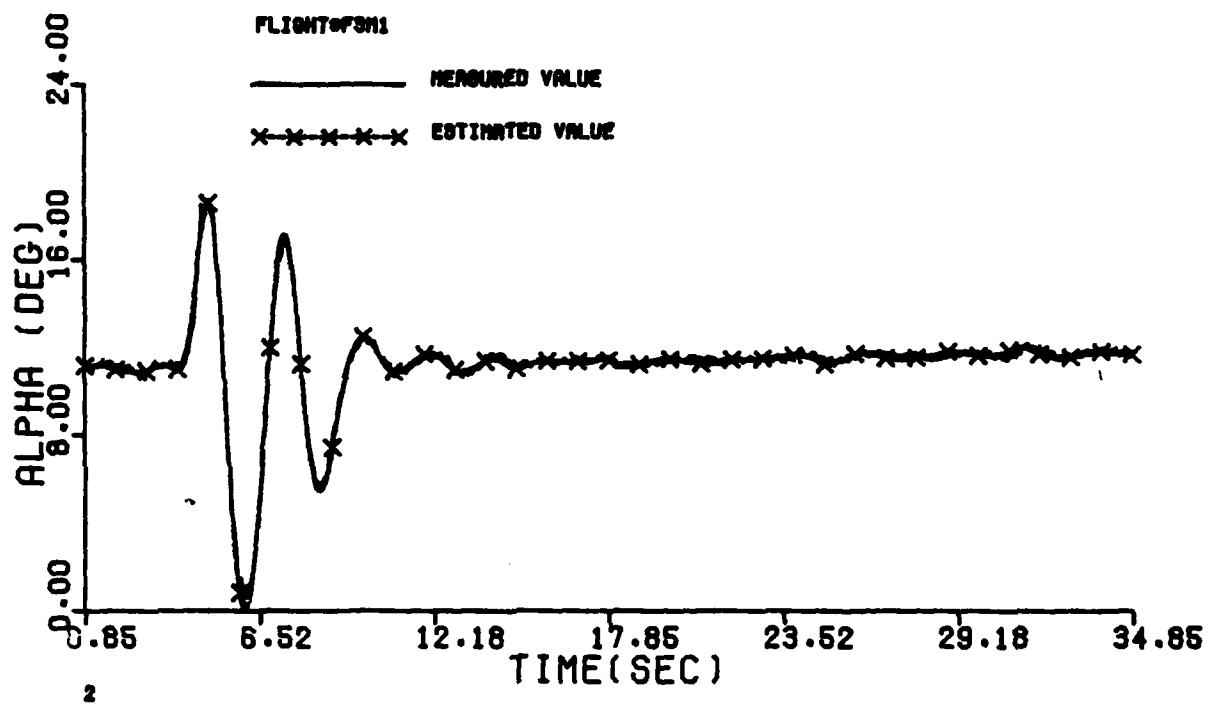


Figure B-5 Comparison Between the Measured and the Estimated Values of Maneuver 1 of Flight 3

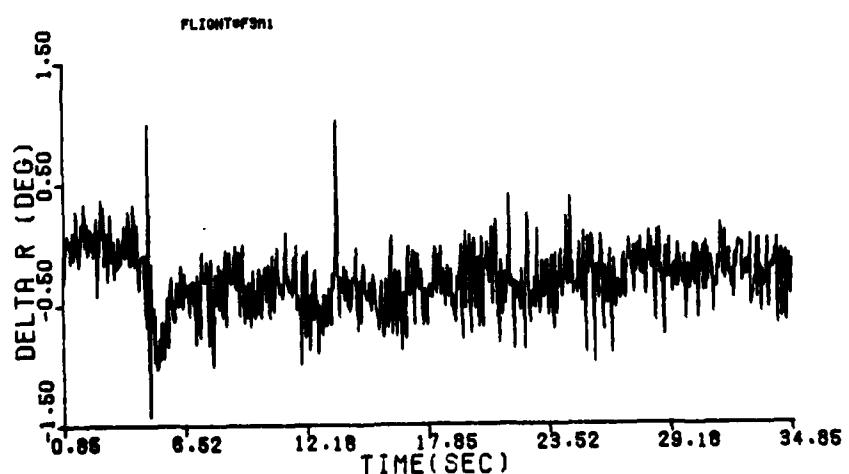
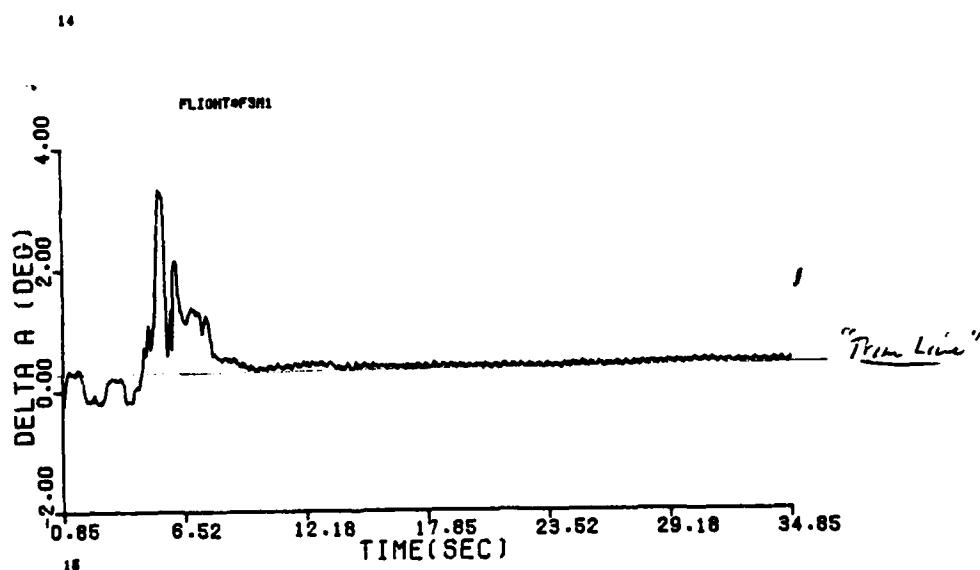
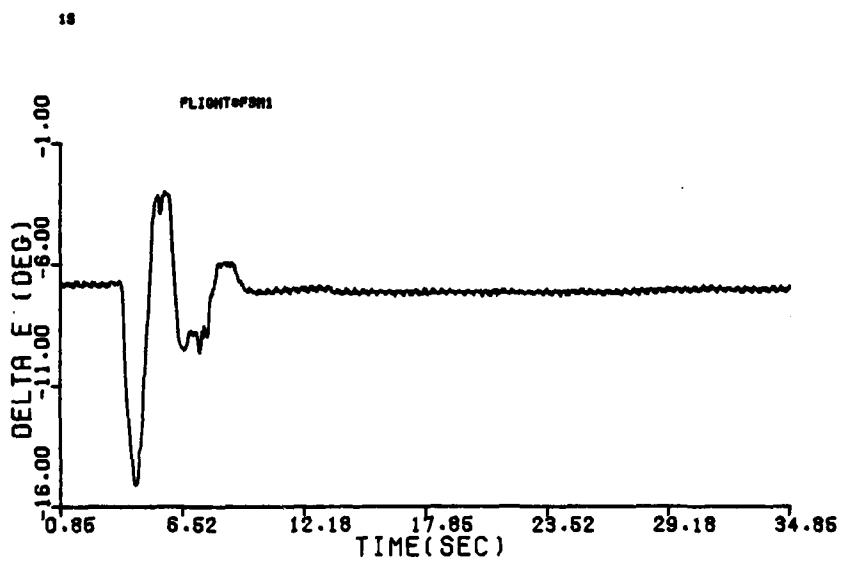


Figure B-5 (cont'd)

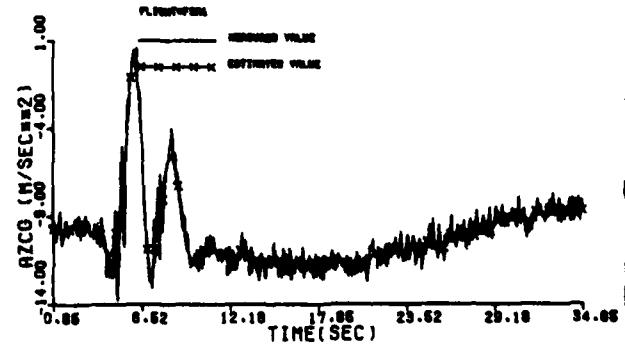
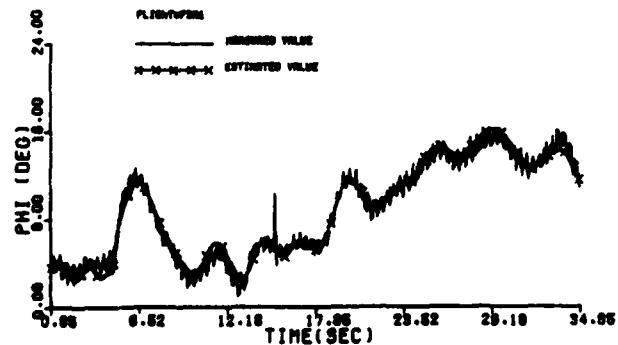
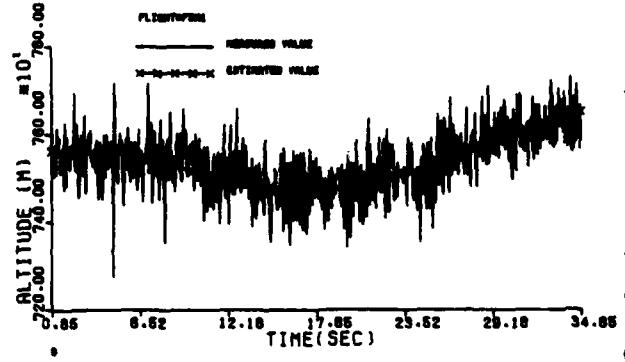
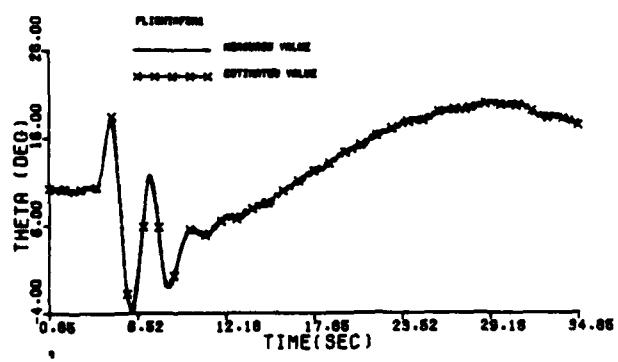
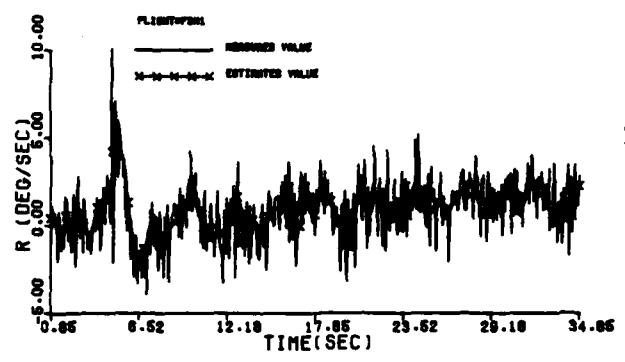
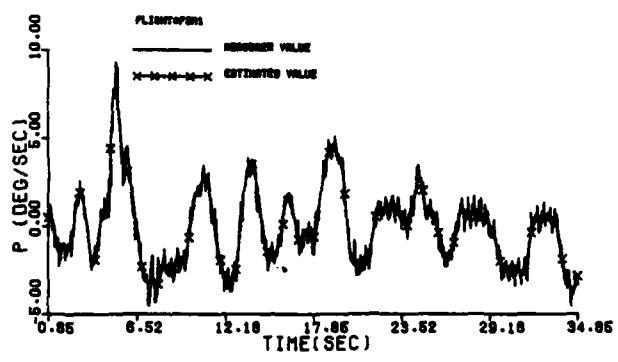
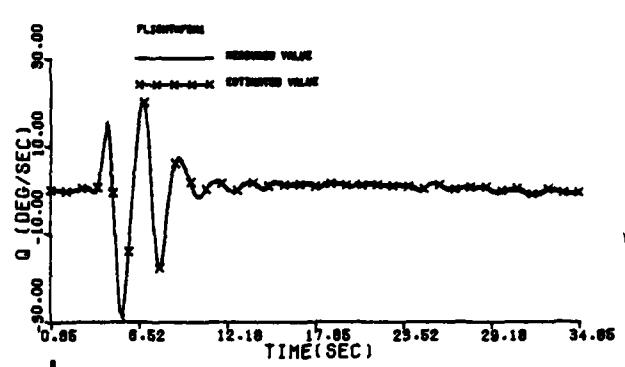
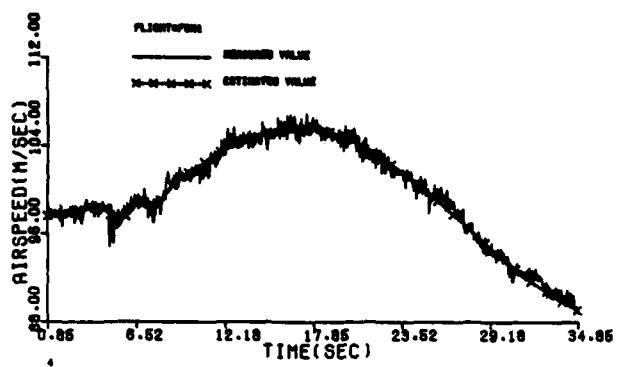


Figure B-5 (cont'd)

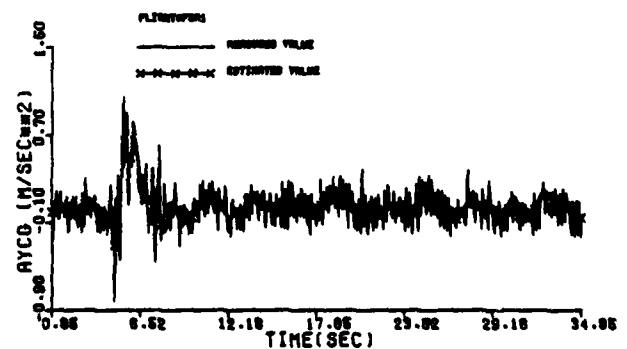
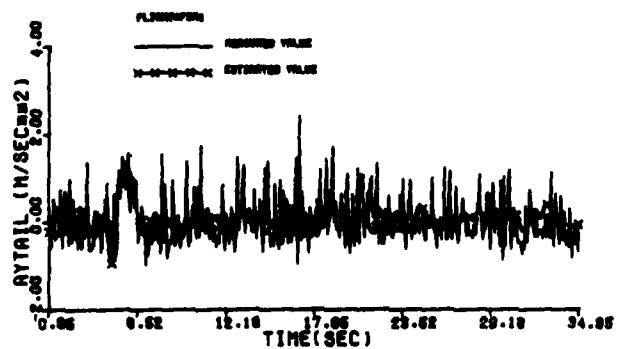
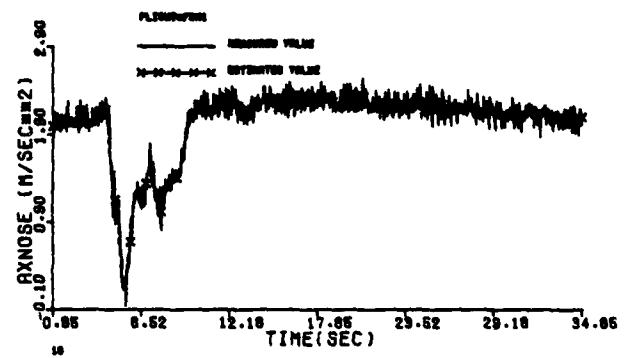
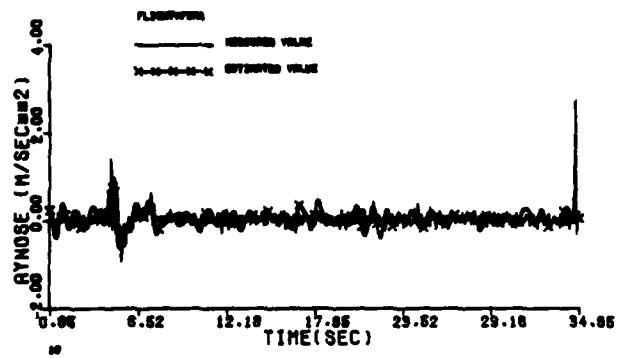
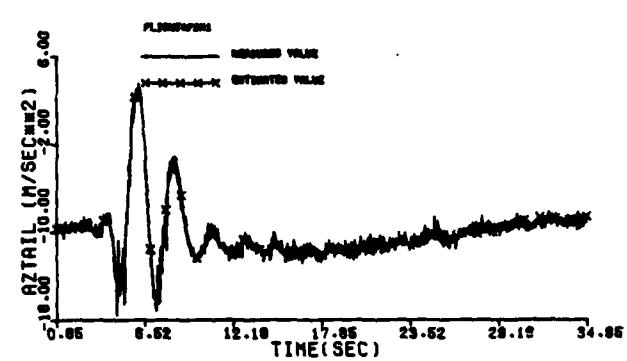
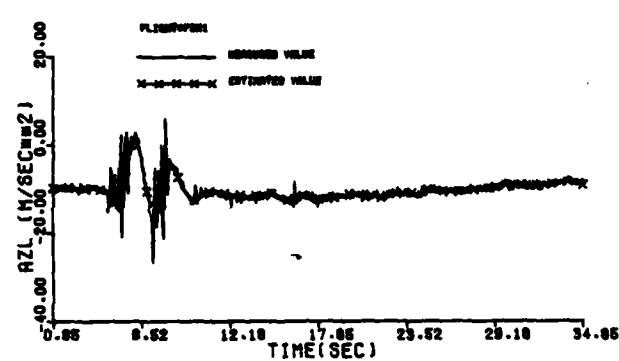
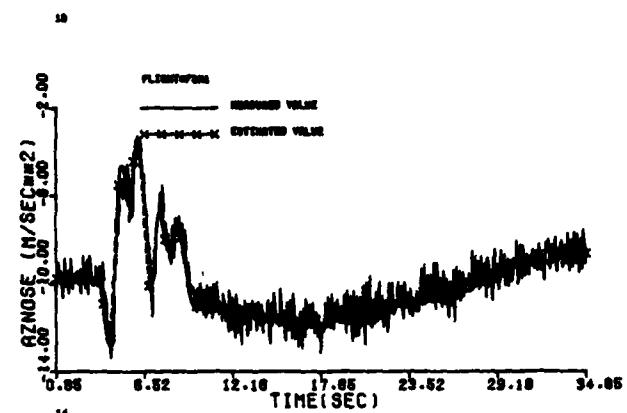
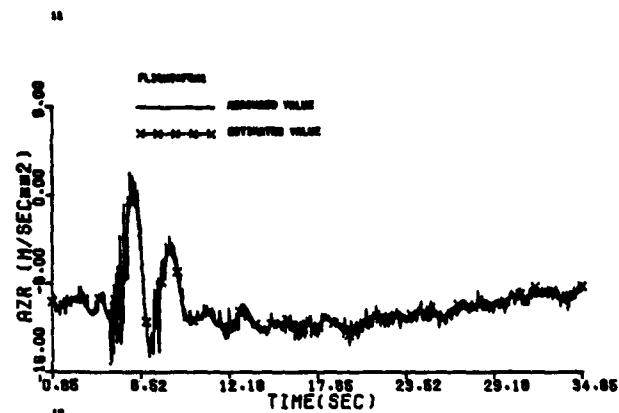


Figure B-5 (concluded)

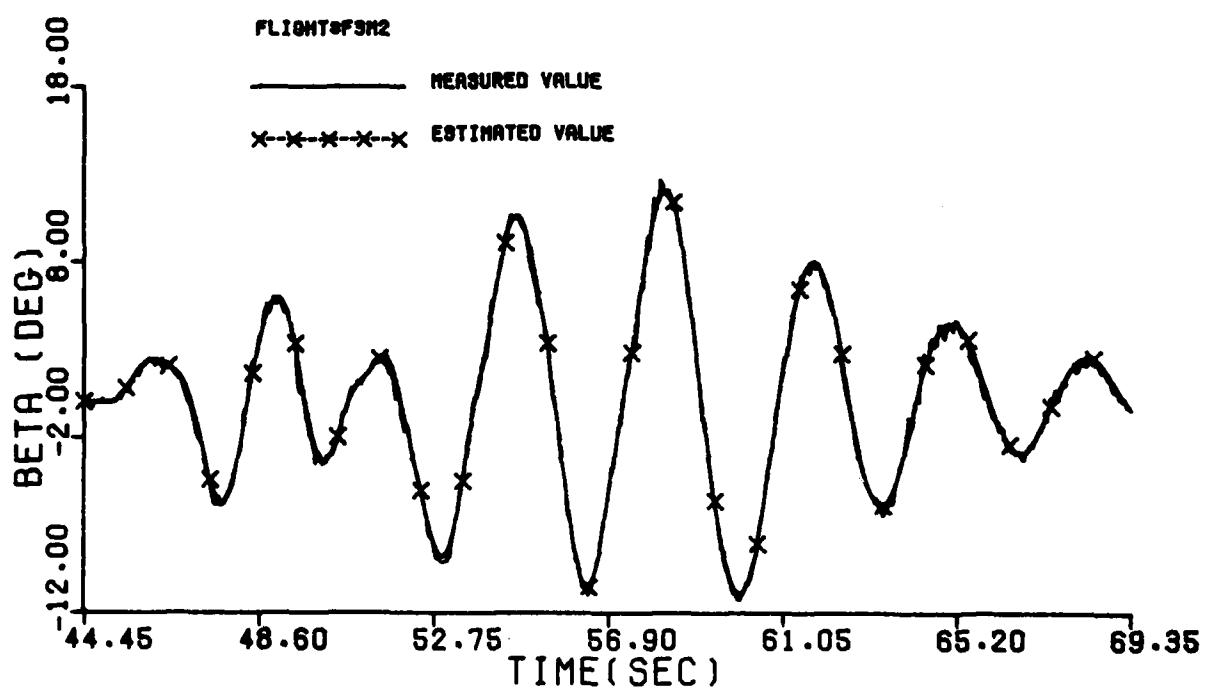
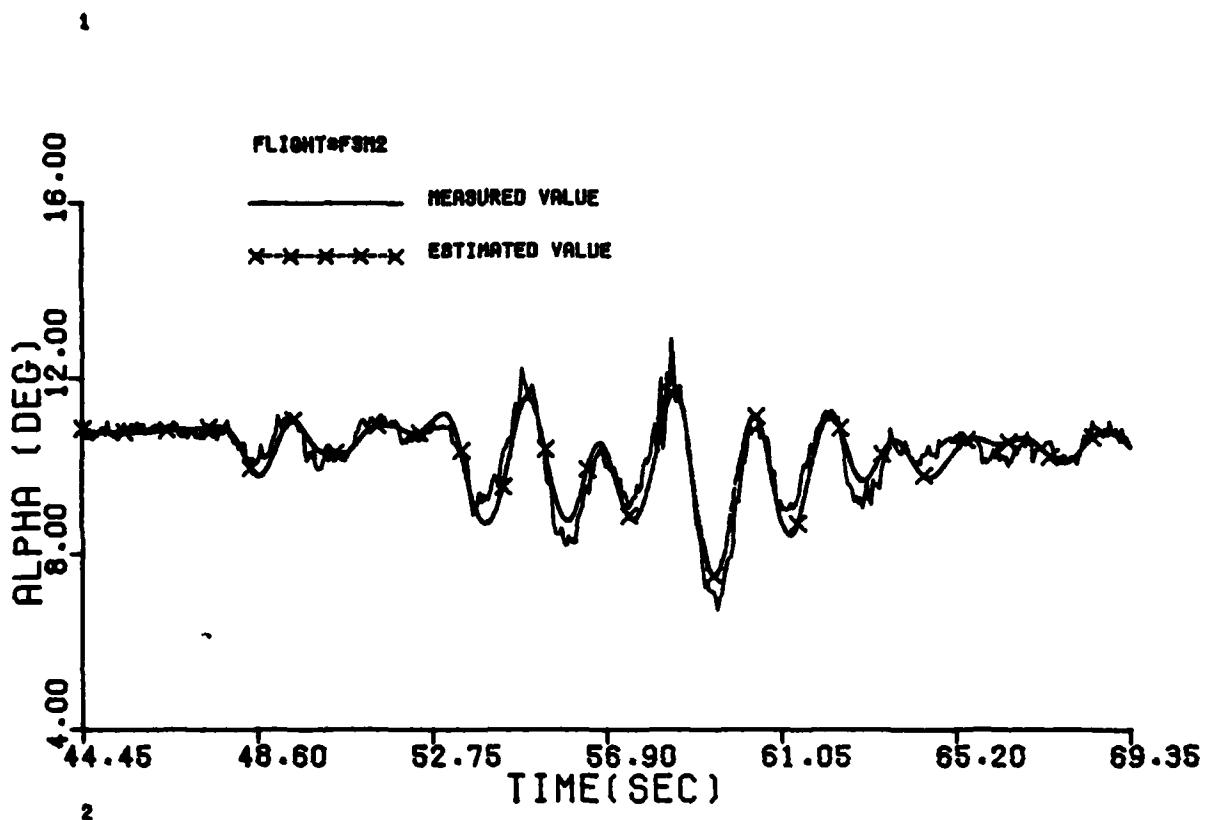


Figure B-6 Comparison Between the Measured and the Estimated Values of Maneuver 2 of Flight 3

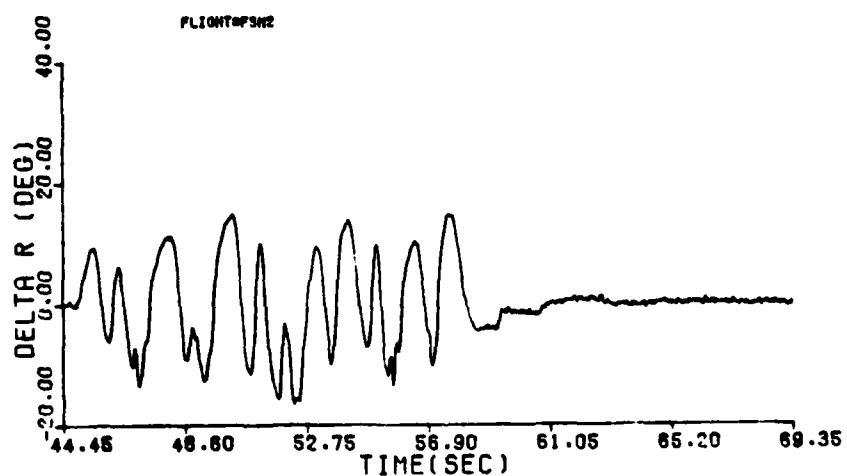
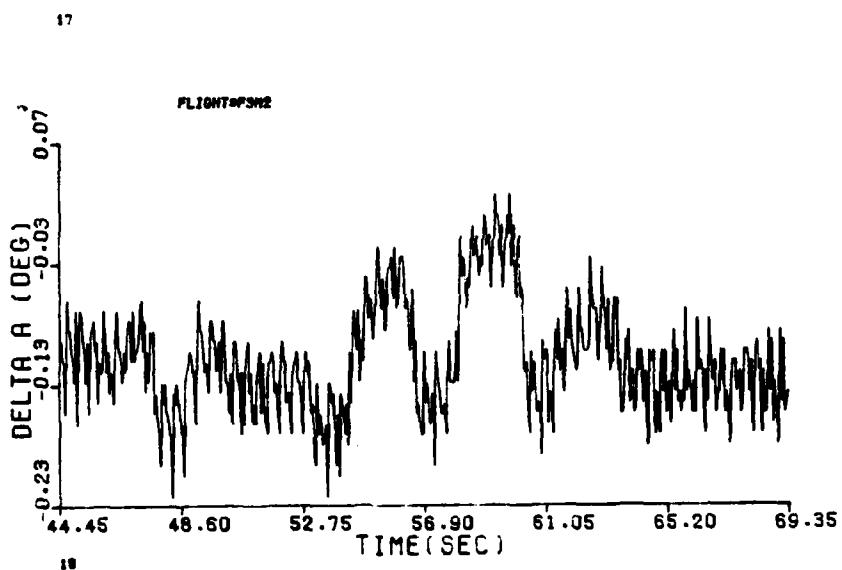
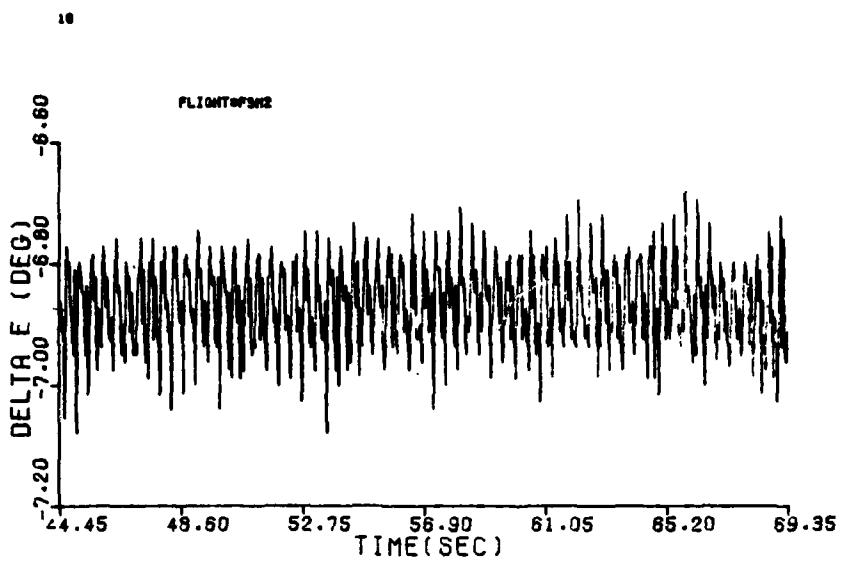


Figure B-6 (cont'd)

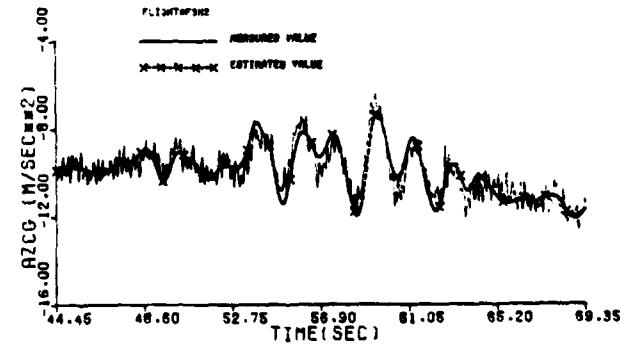
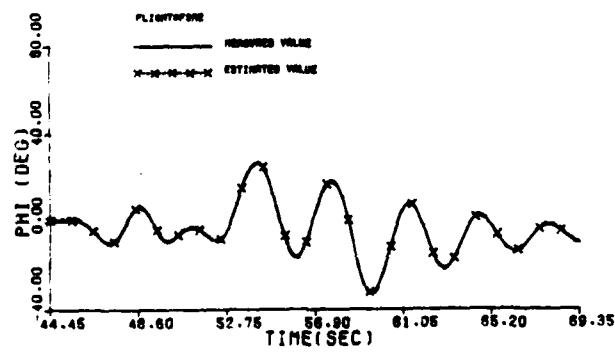
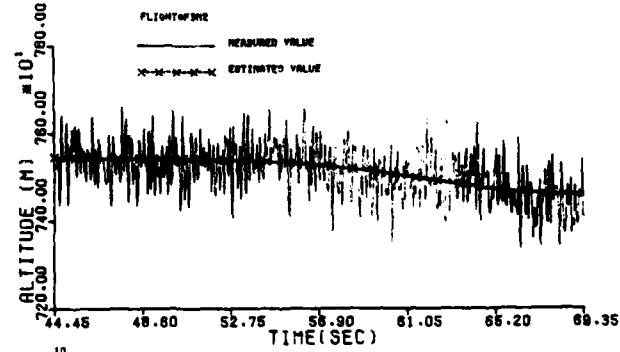
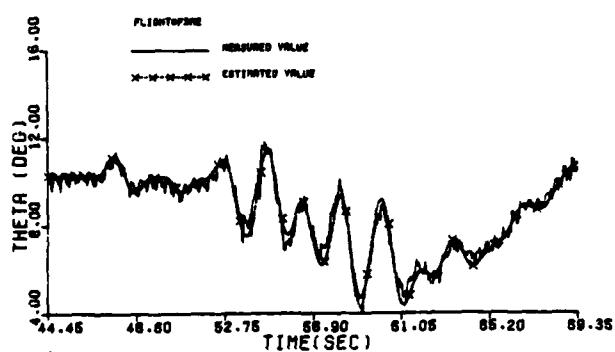
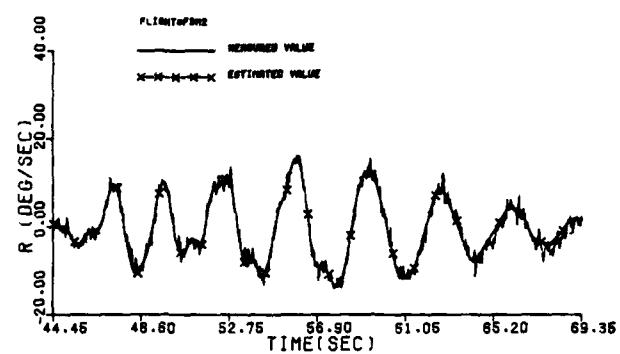
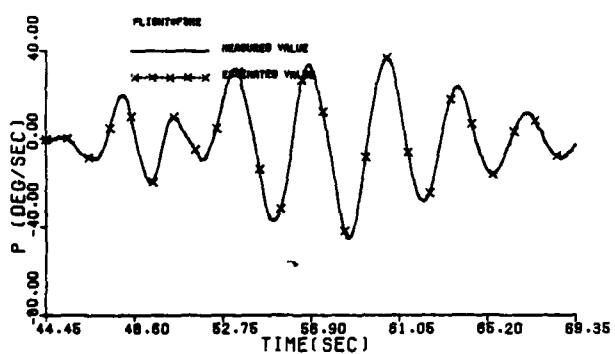
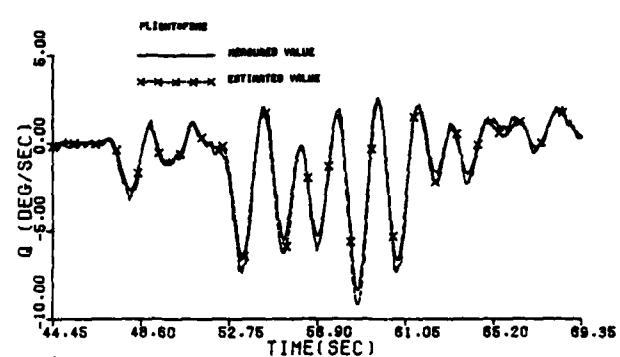
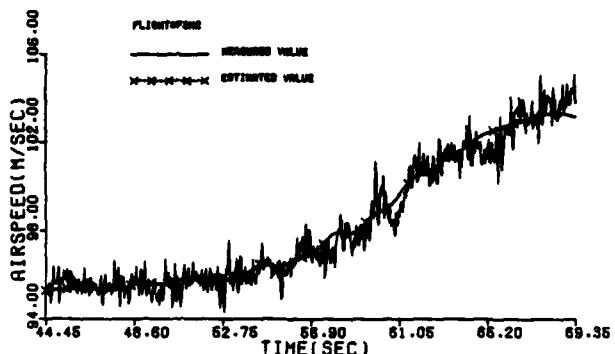


Figure B-6 (cont'd)

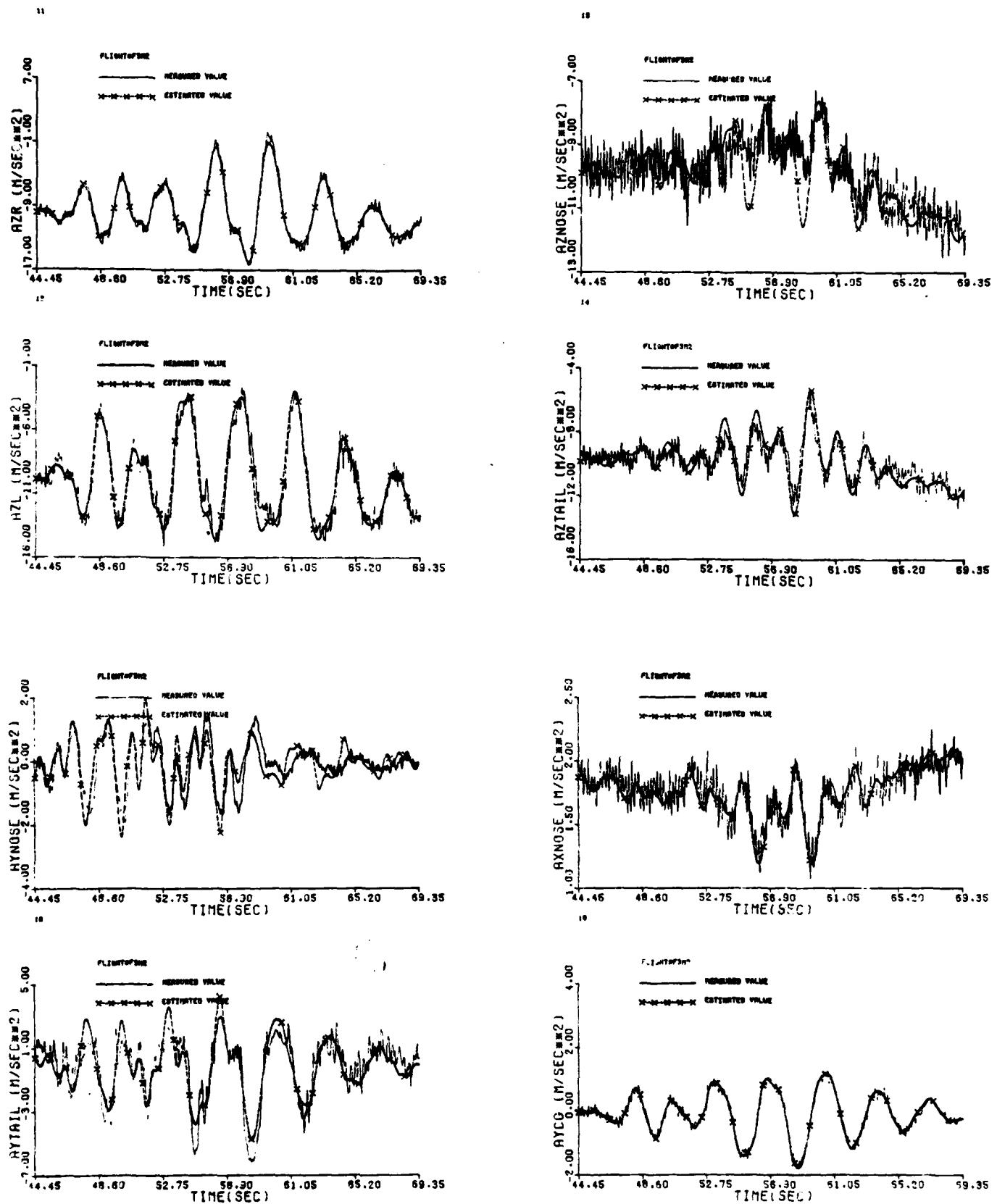


Figure B-6 (concluded)

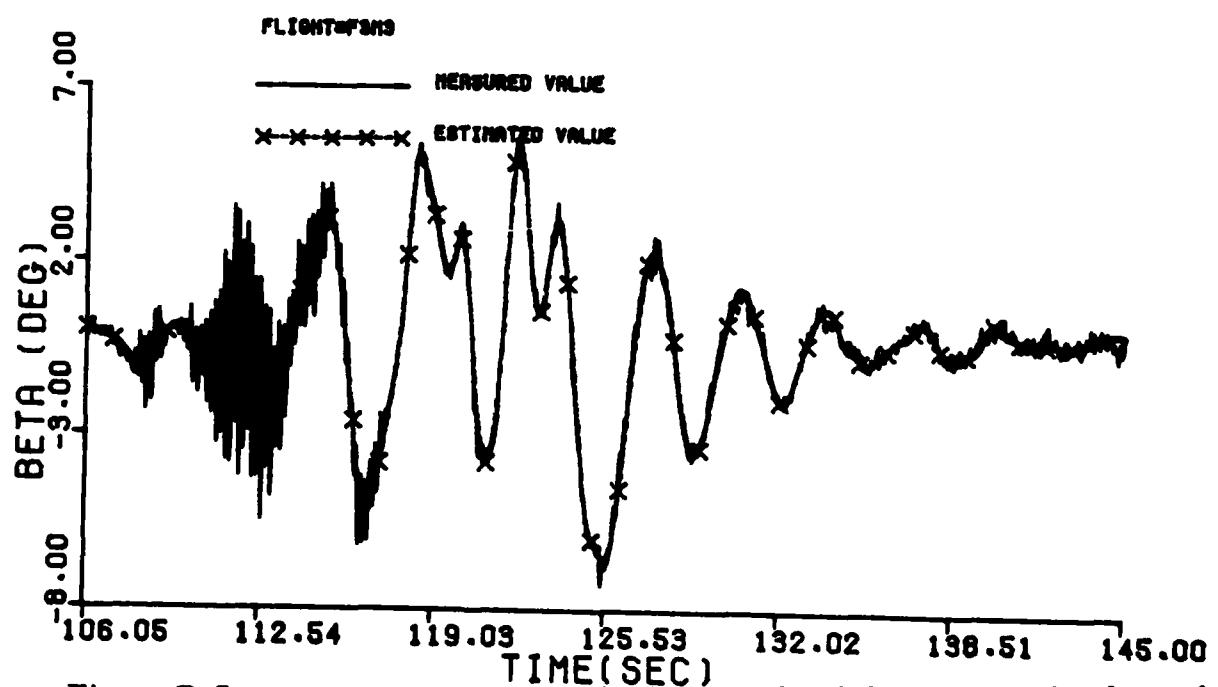
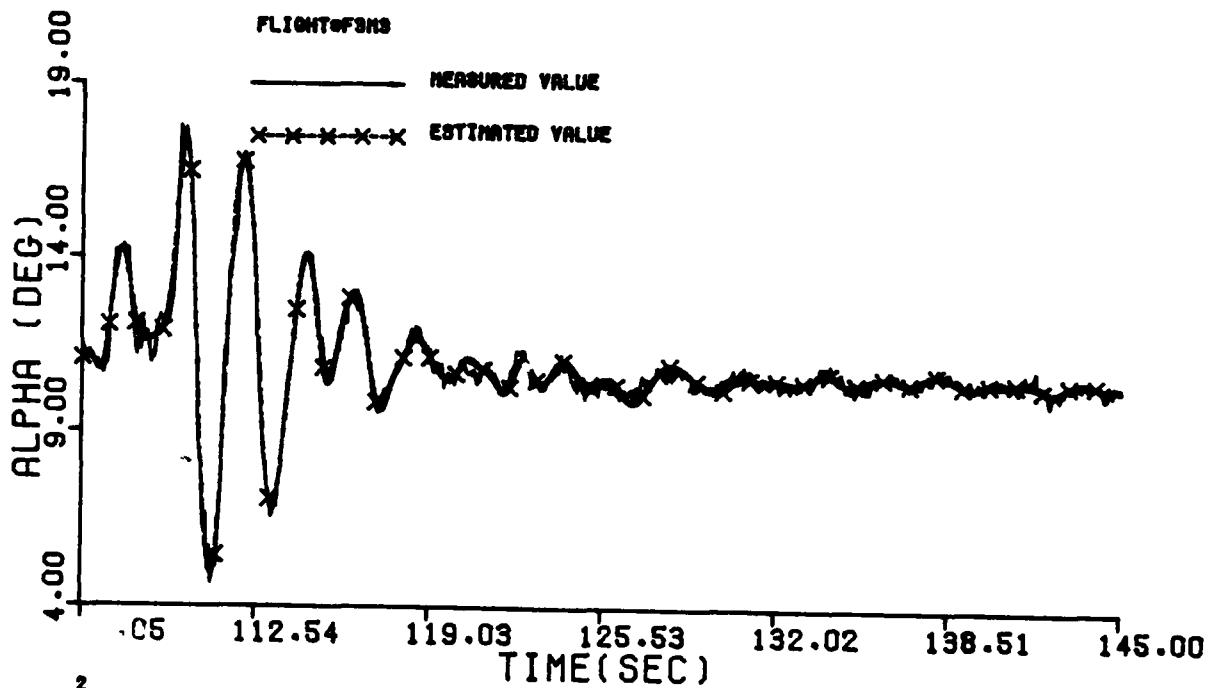


Figure B-7 Comparison Between the Measured and the Estimated Values of Maneuver 3 of Flight 3
B-26

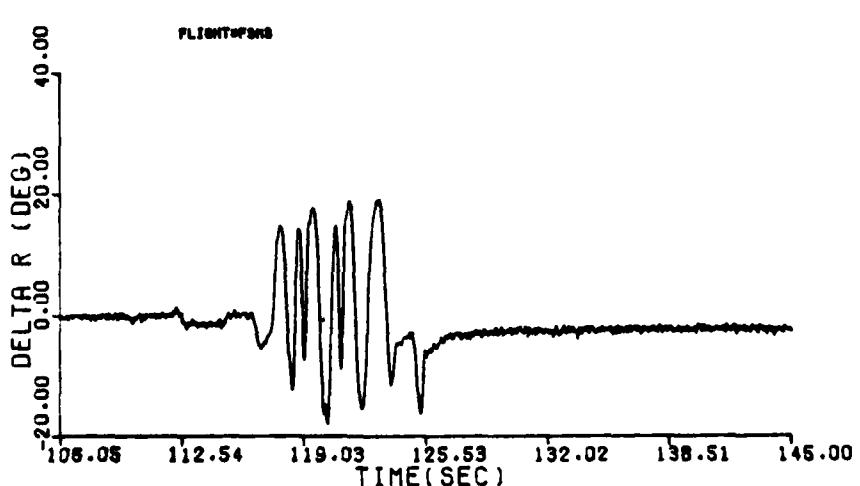
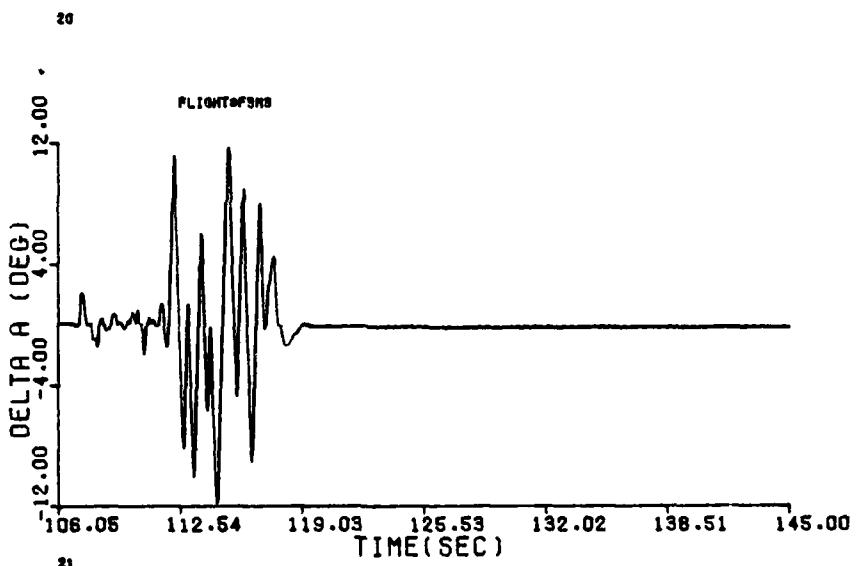
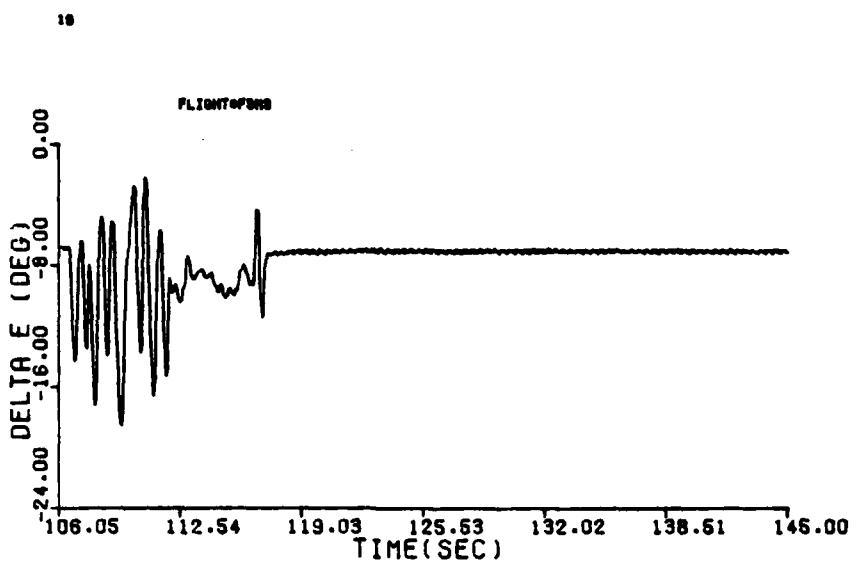


Figure B-7 (cont'd)

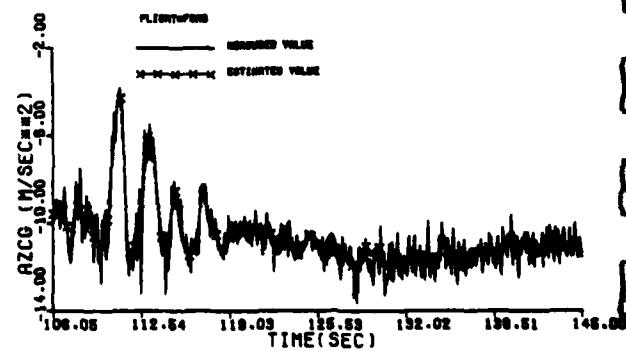
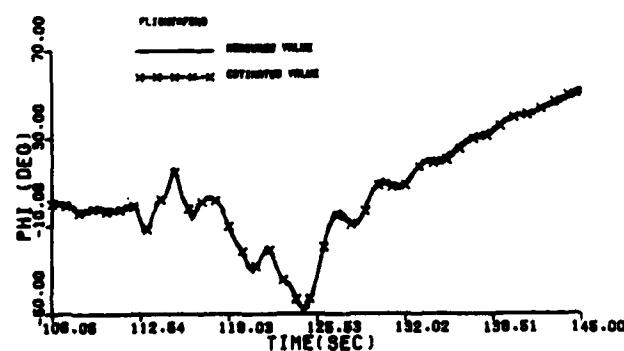
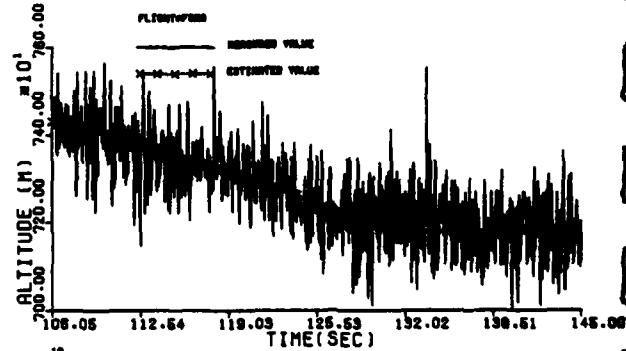
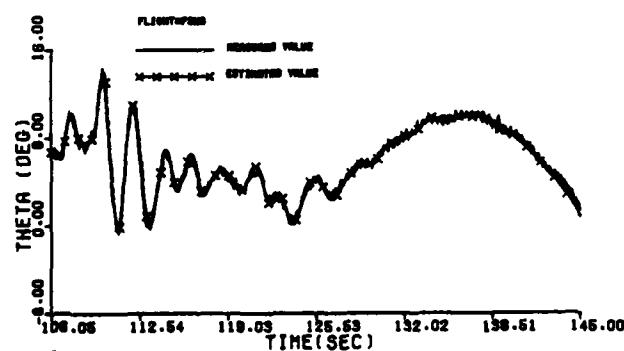
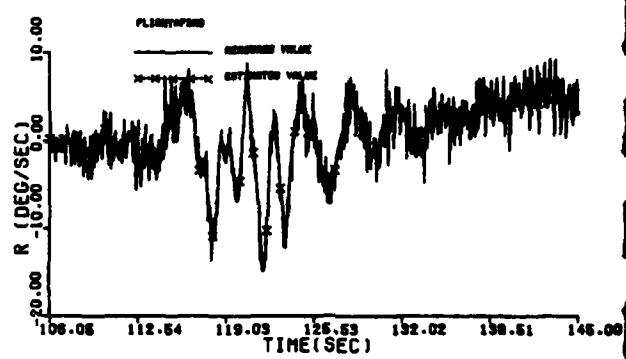
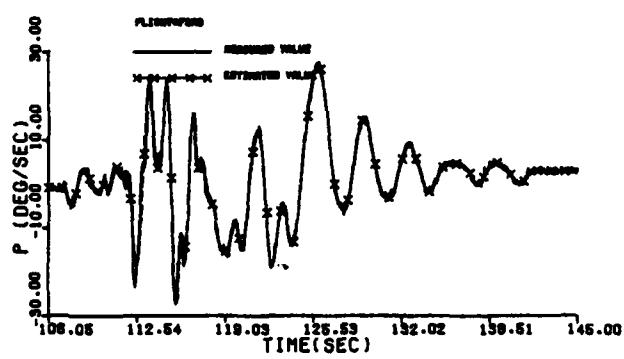
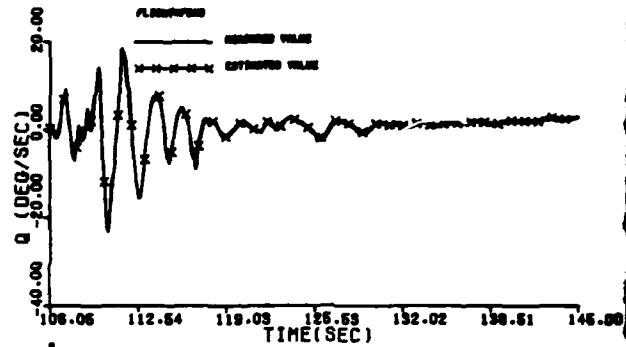
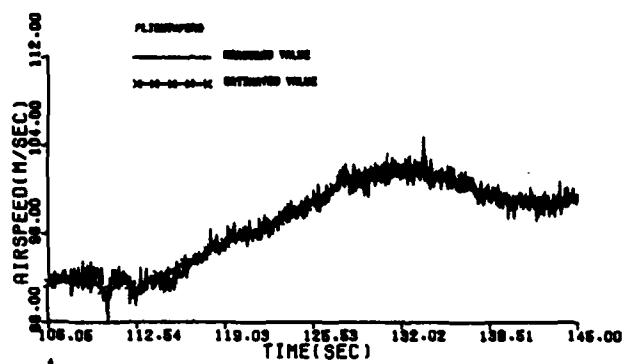


Figure B-7 (cont'd)

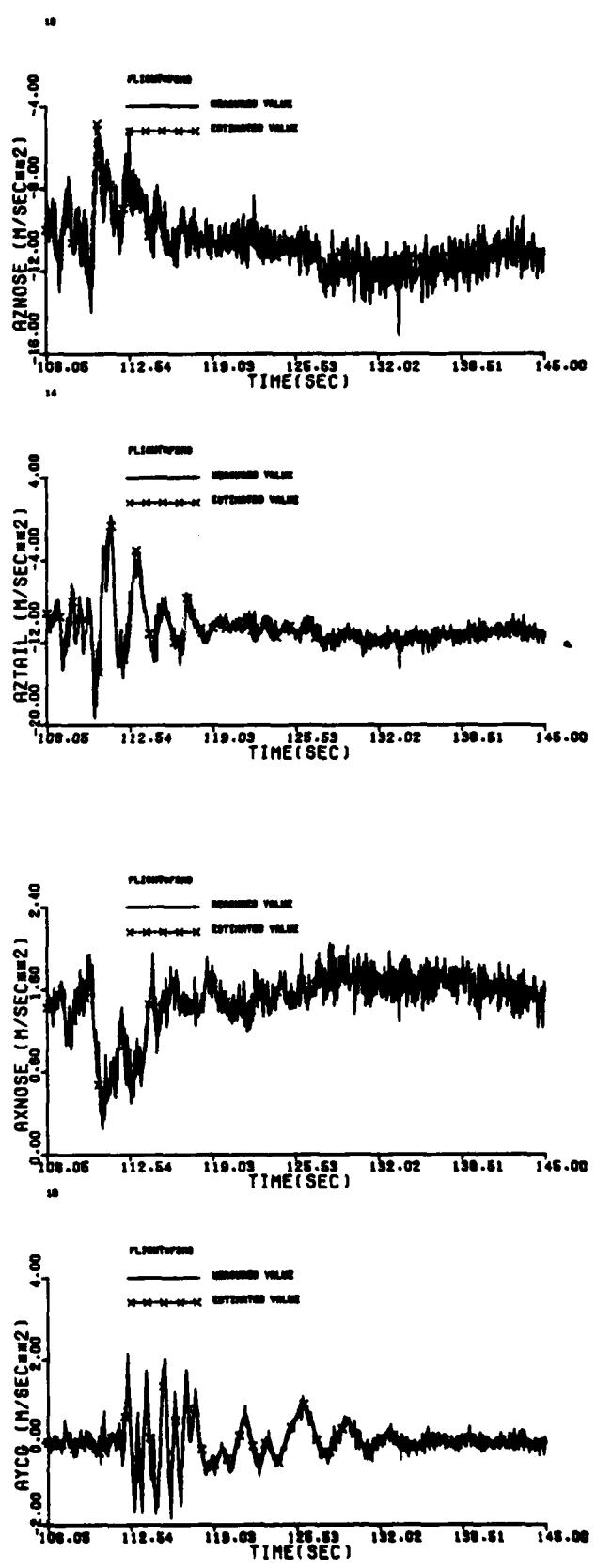
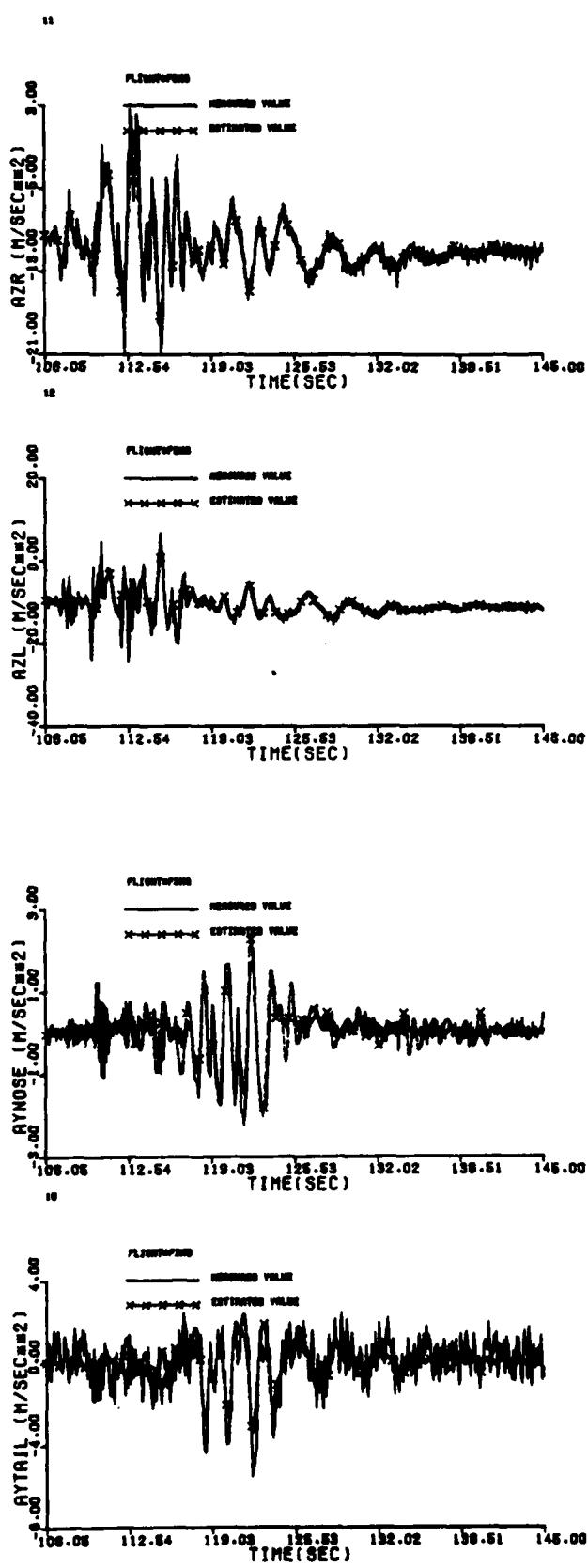


Figure B-7 (concluded)

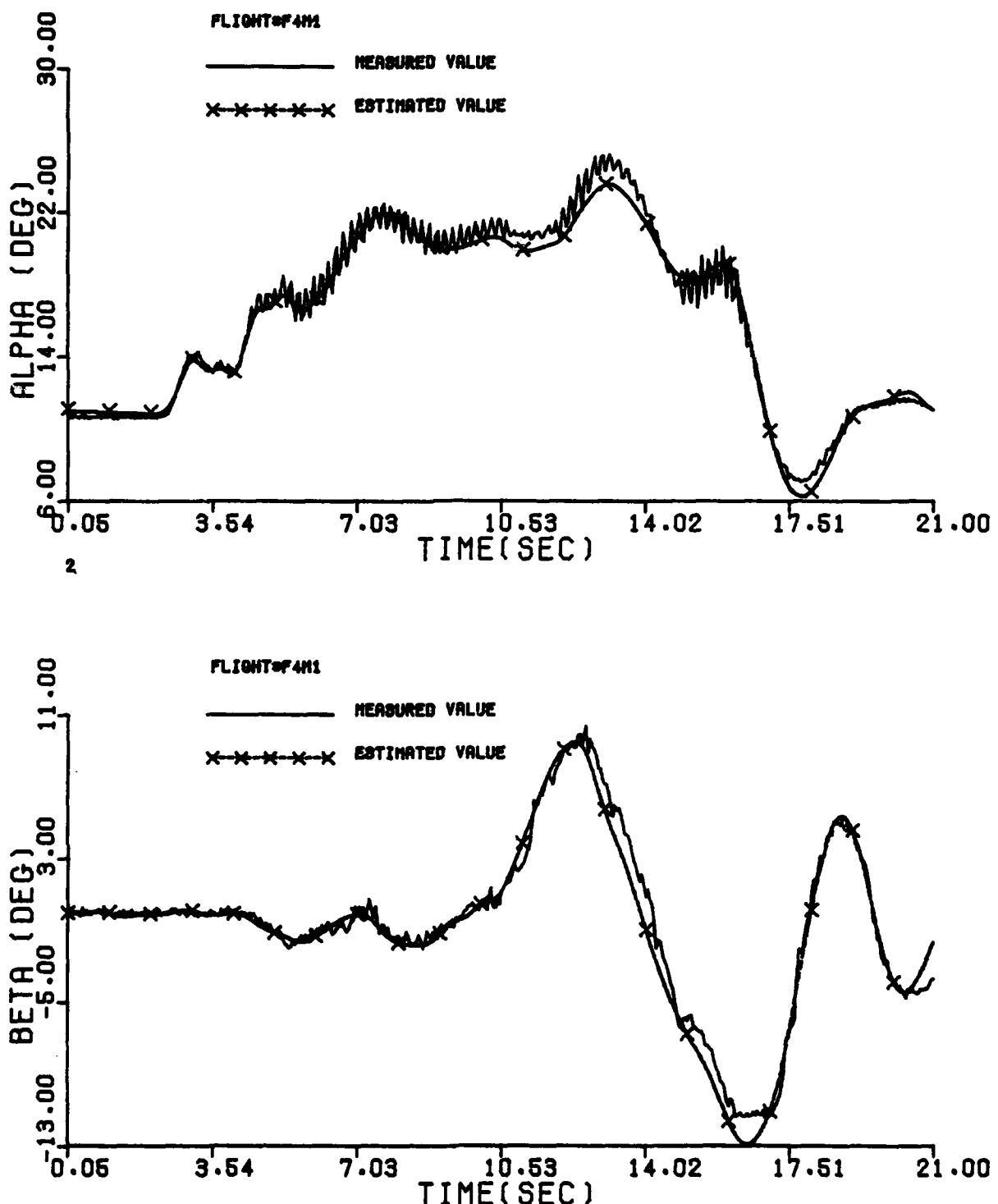


Figure B-8 Comparison Between the Measured and the Estimated Values of Maneuver 1 of Flight 4

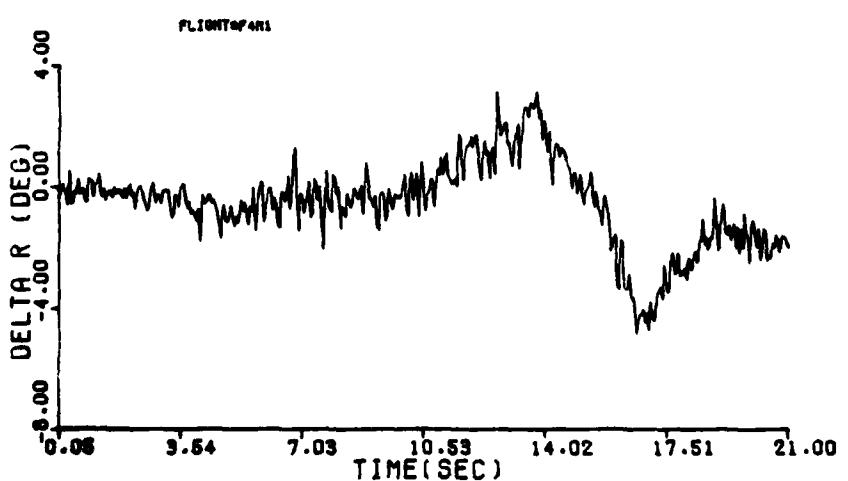
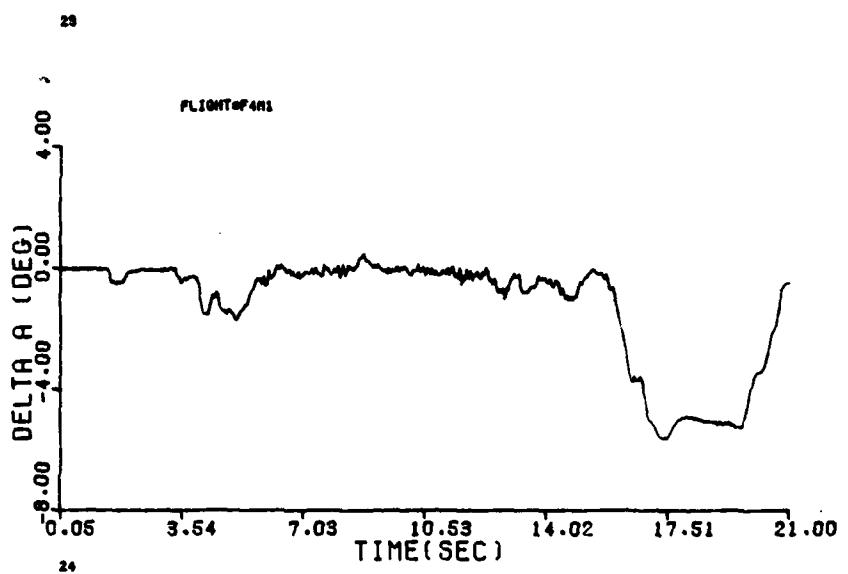
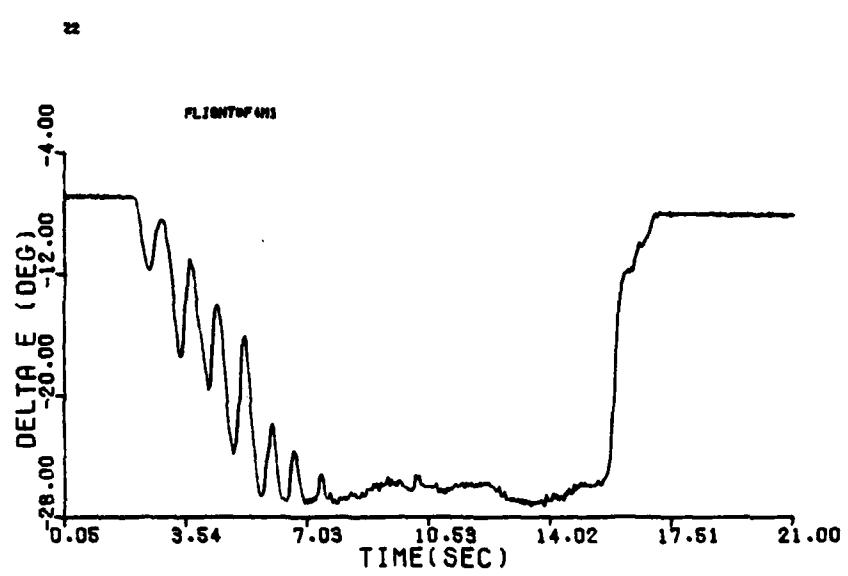


Figure B-8 (cont'd)

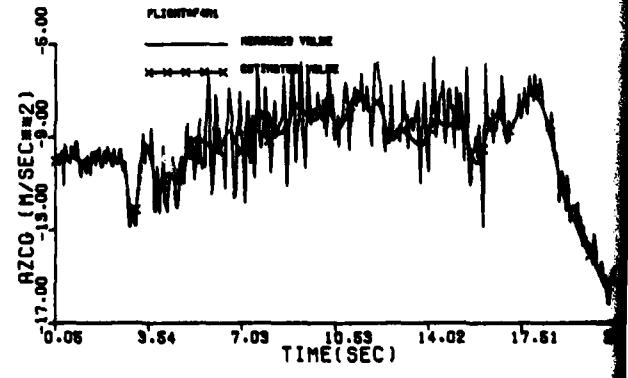
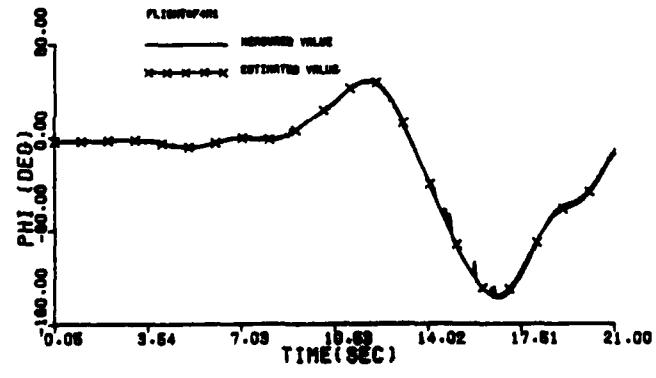
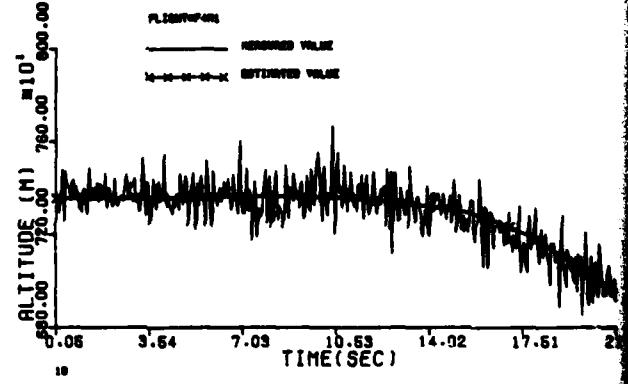
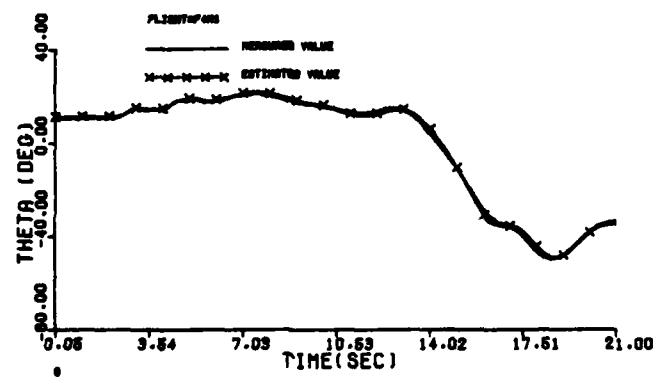
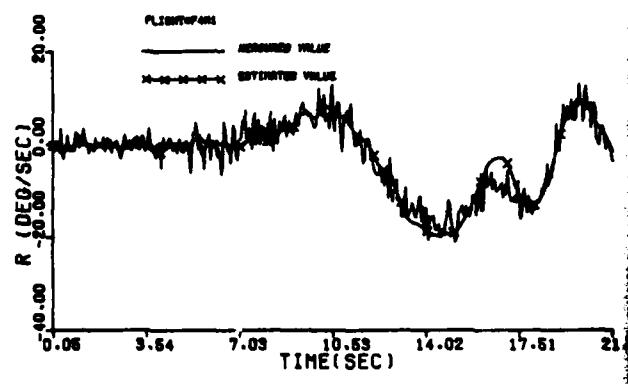
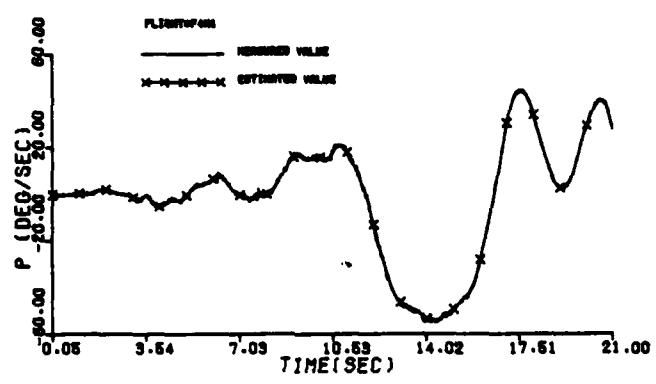
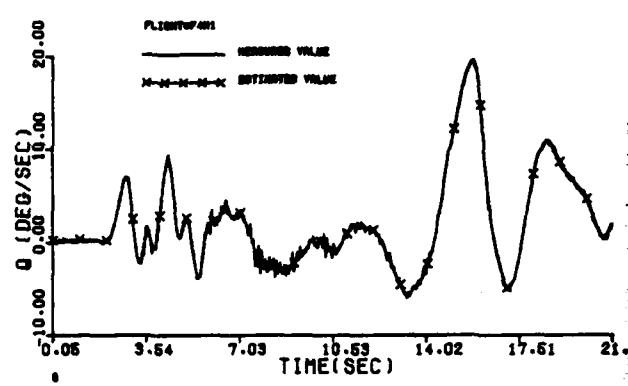
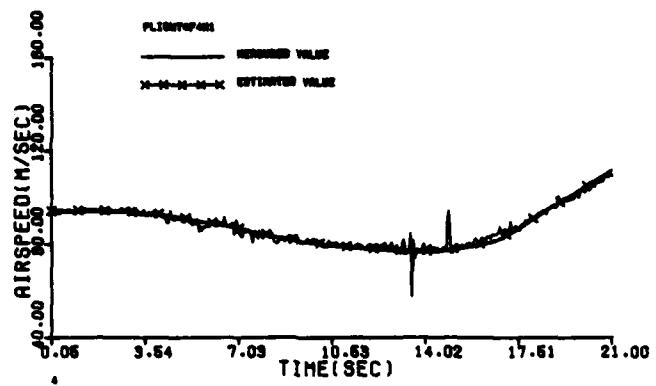


Figure B-8 (cont'd)

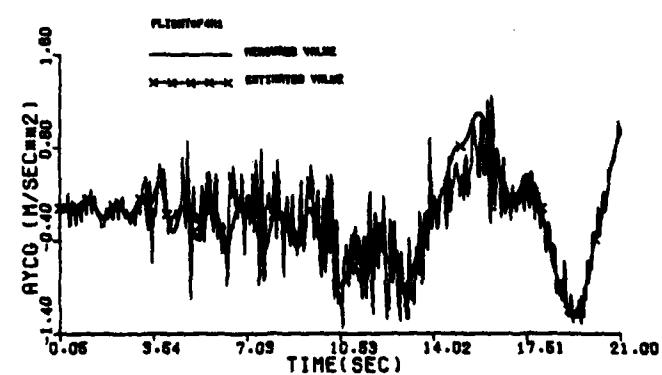
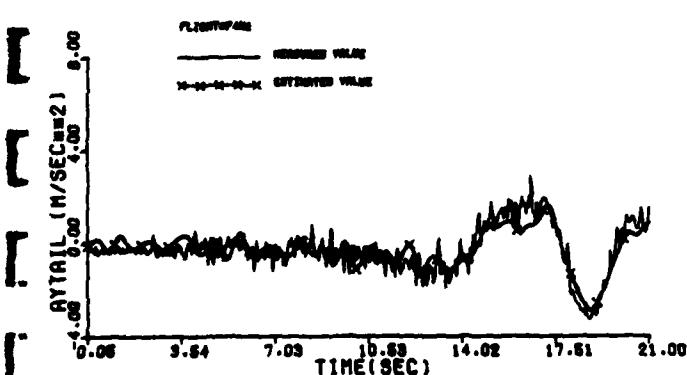
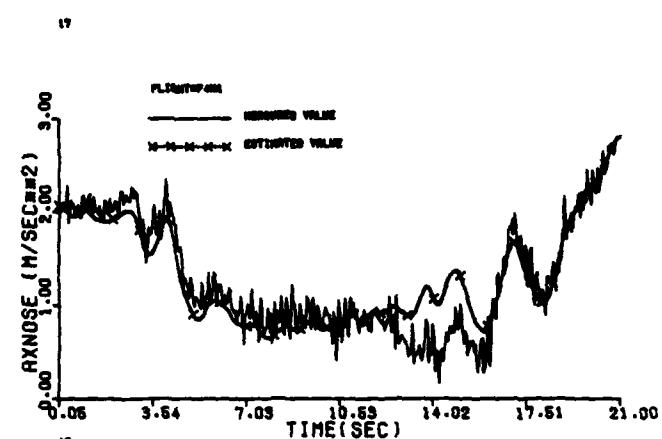
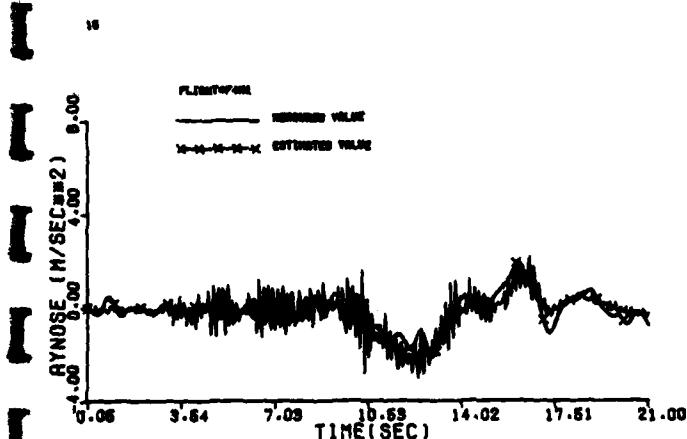
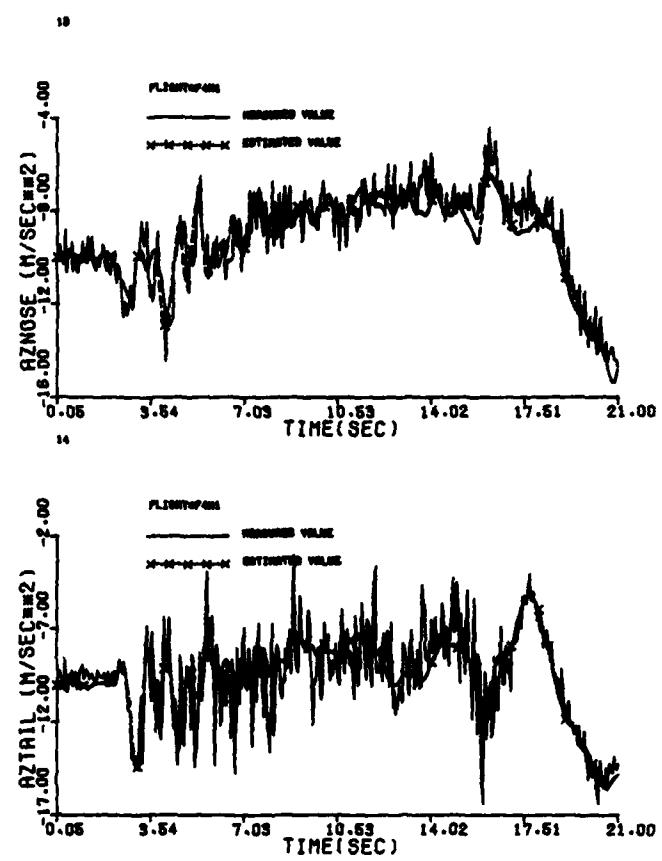
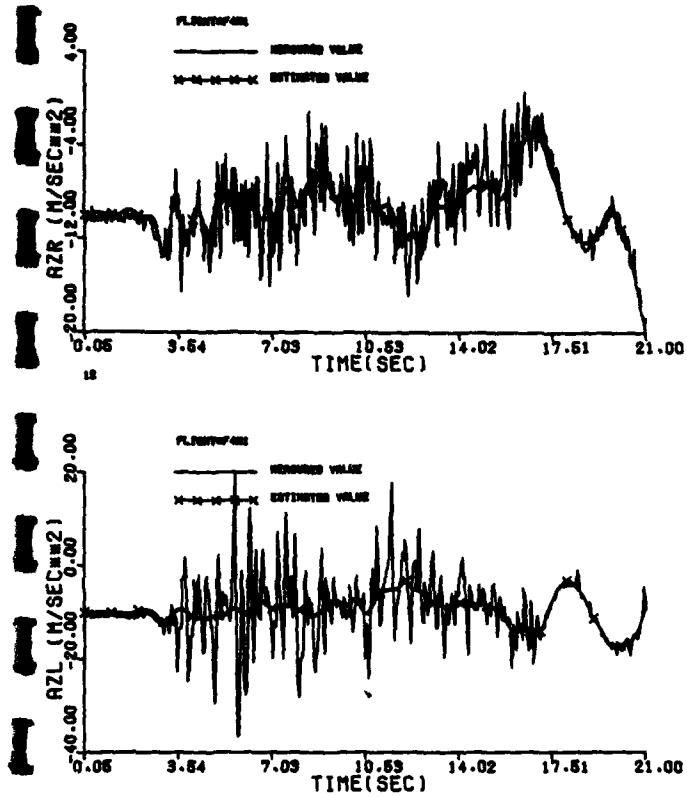


Figure B-8 (concluded)

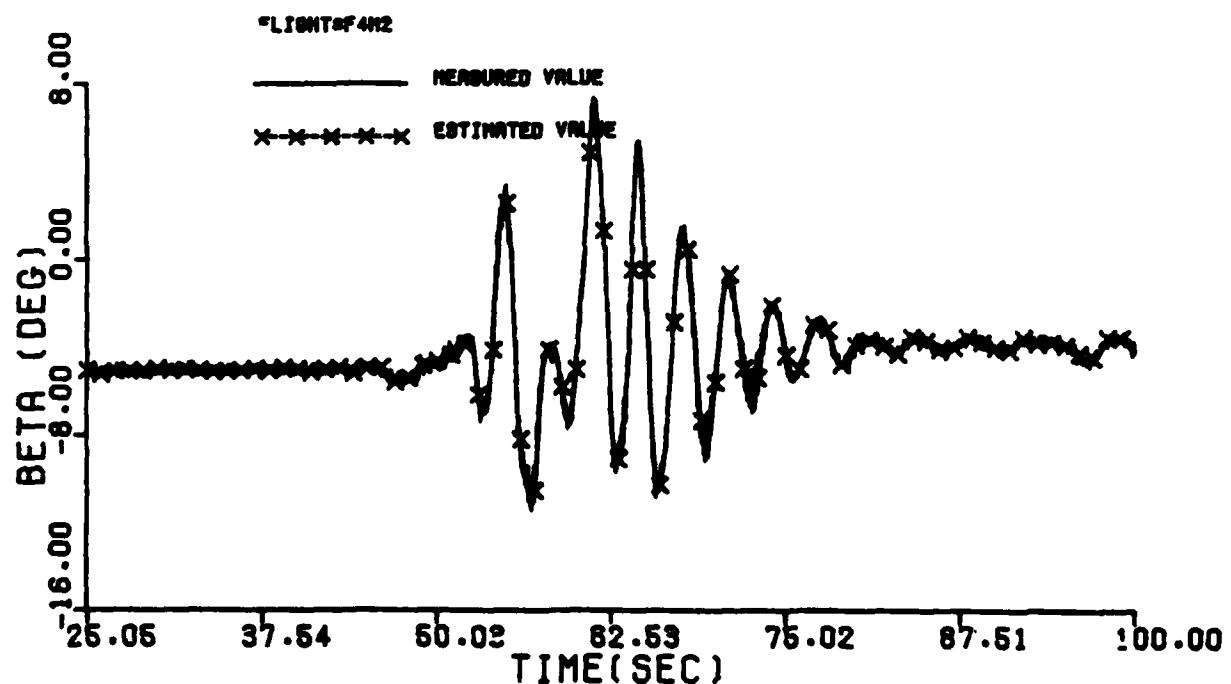
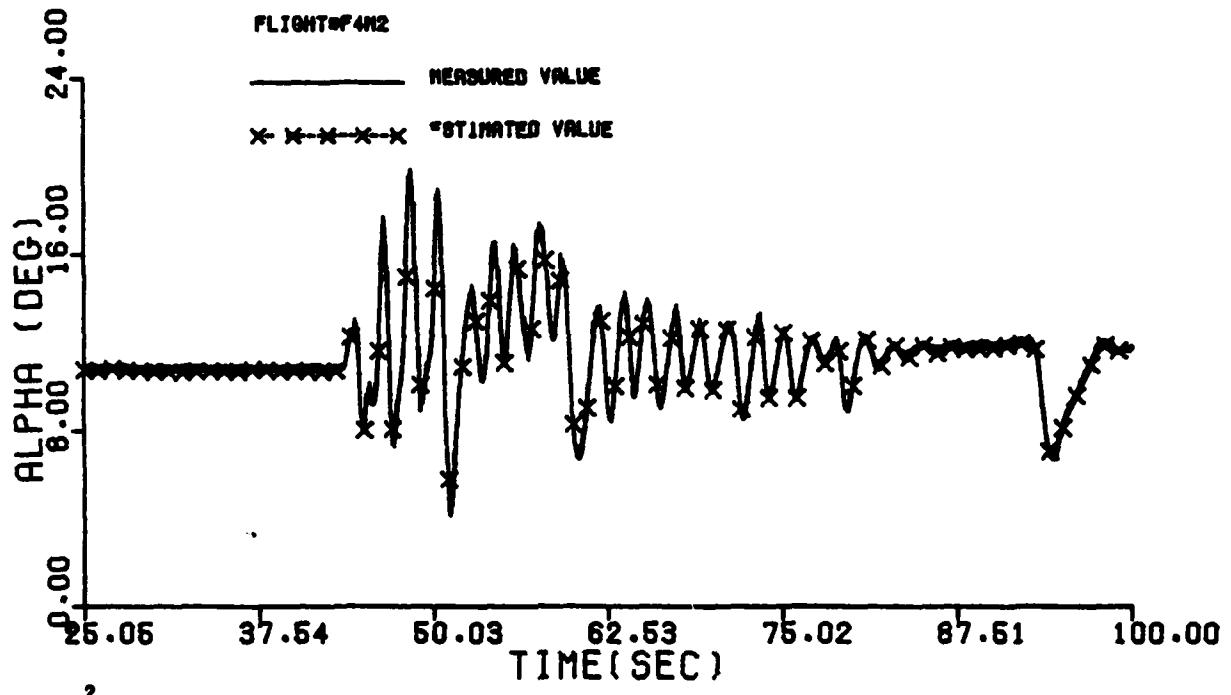


Figure B-9 Comparison Between the Measured and the Estimated Values of Maneuver 2 of Flight 4

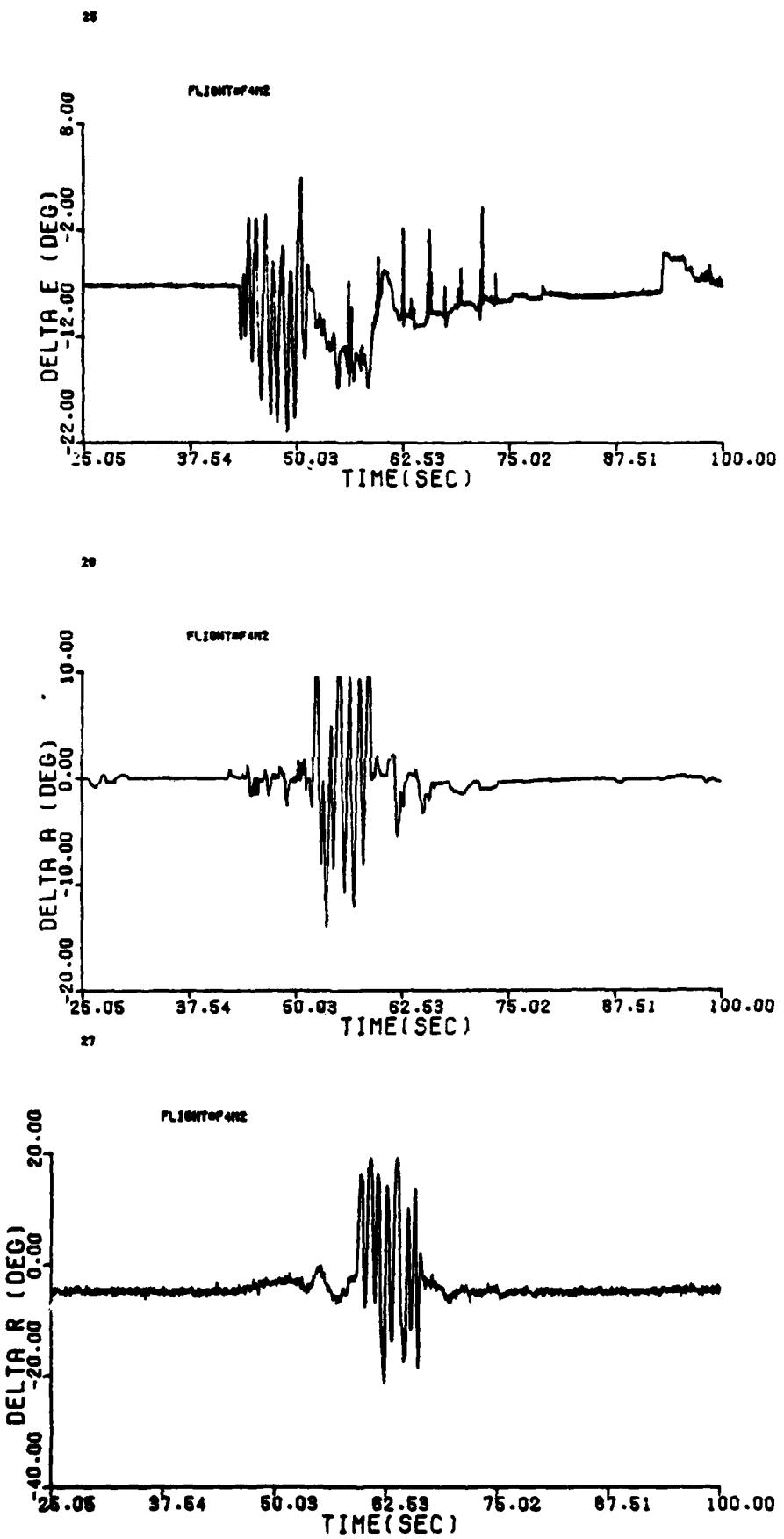


Figure B-9 (cont'd)

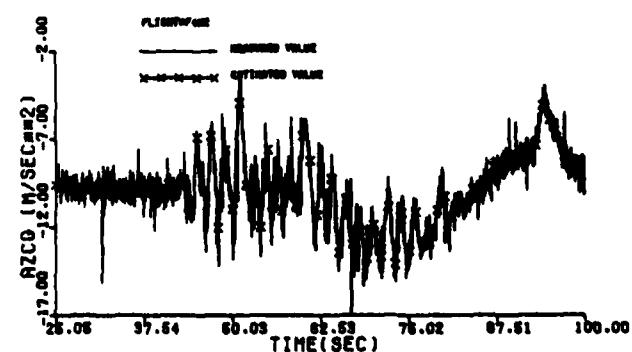
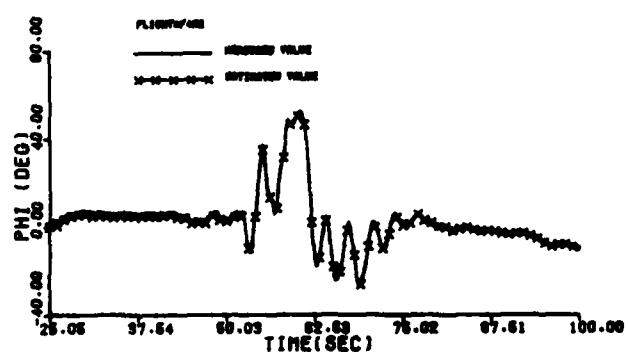
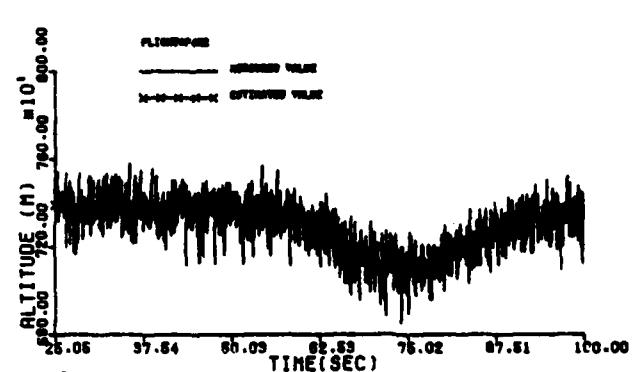
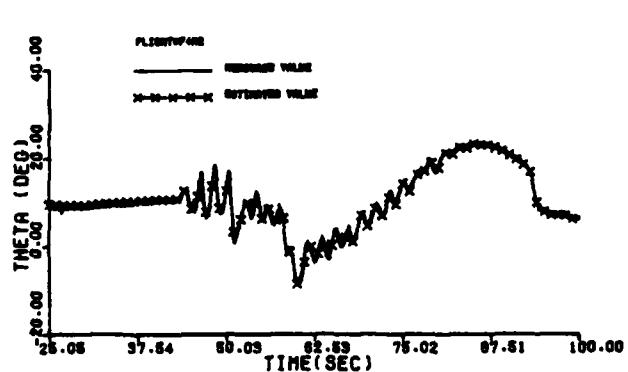
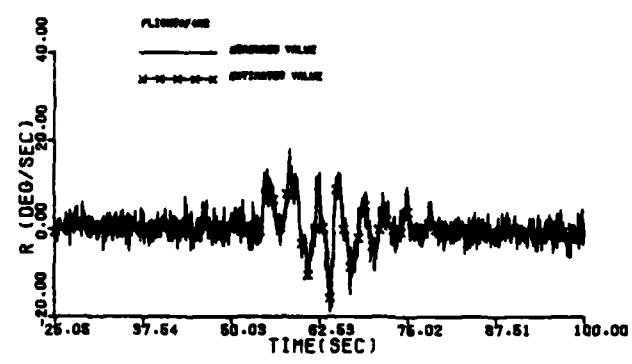
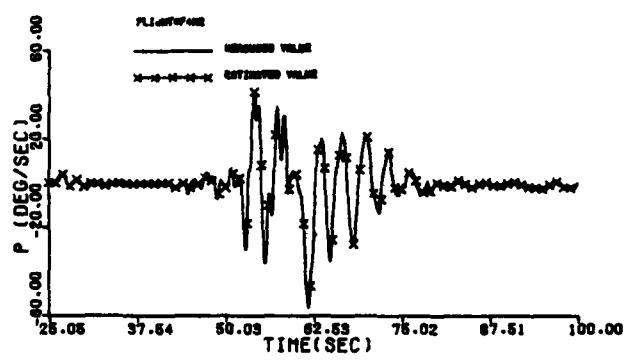
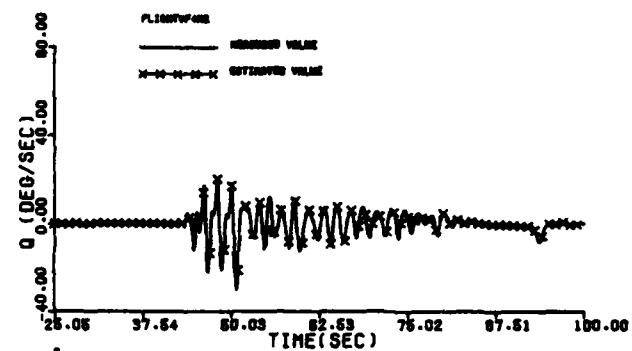
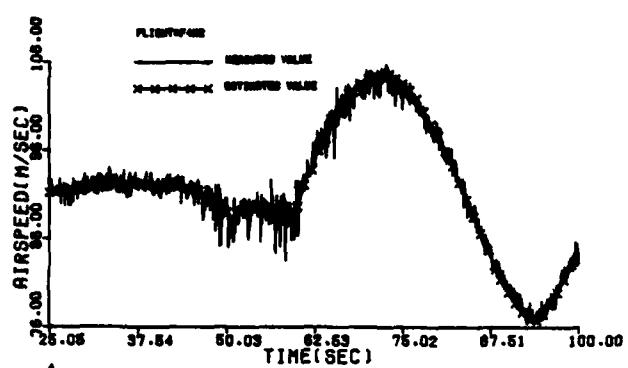


Figure B-9 (cont'd)

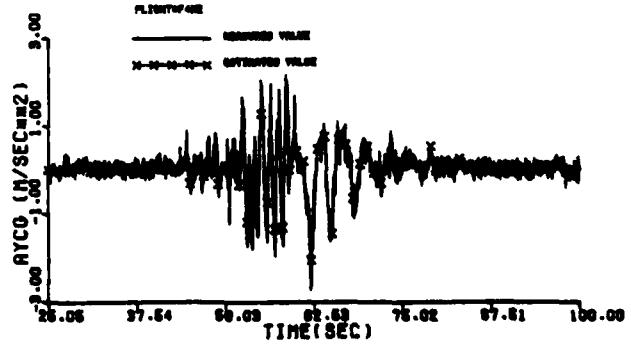
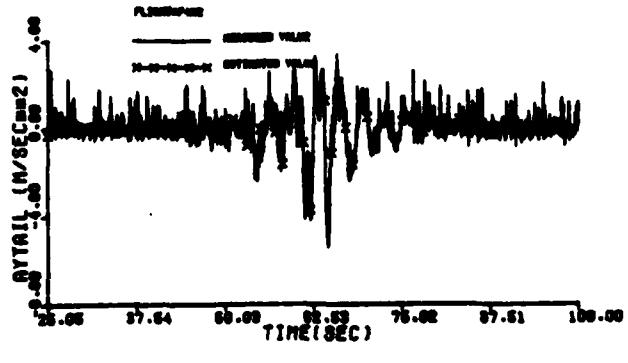
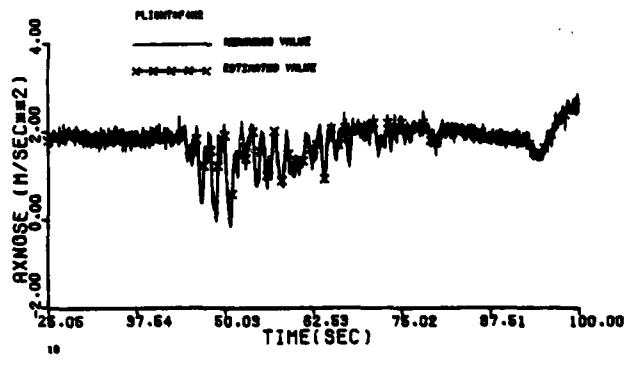
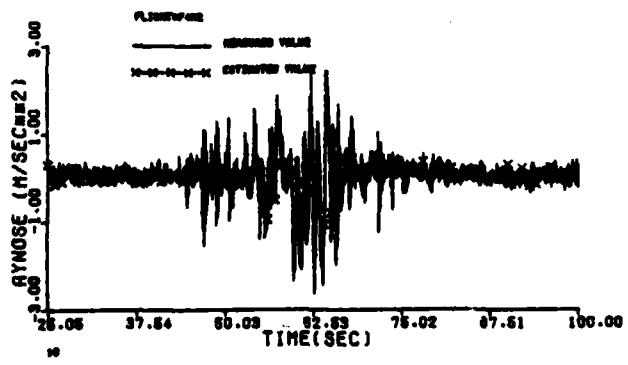
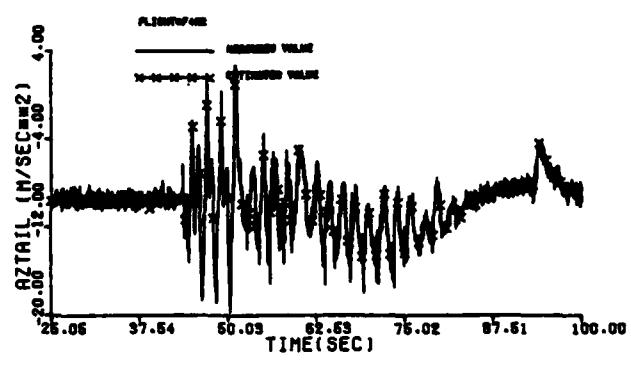
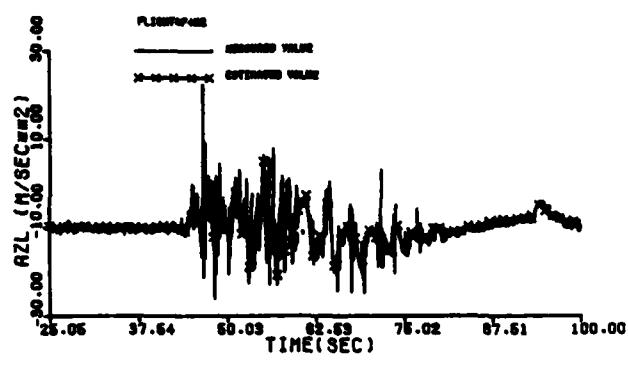
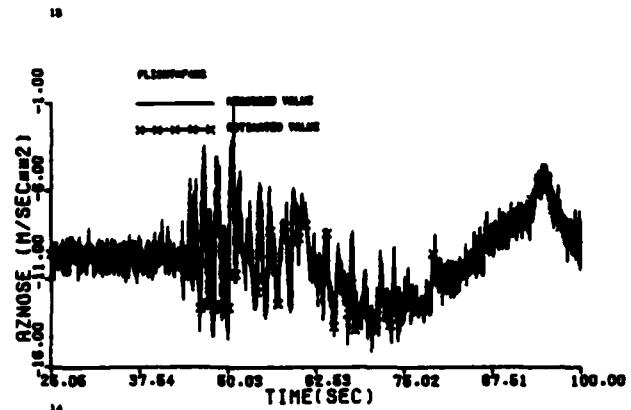
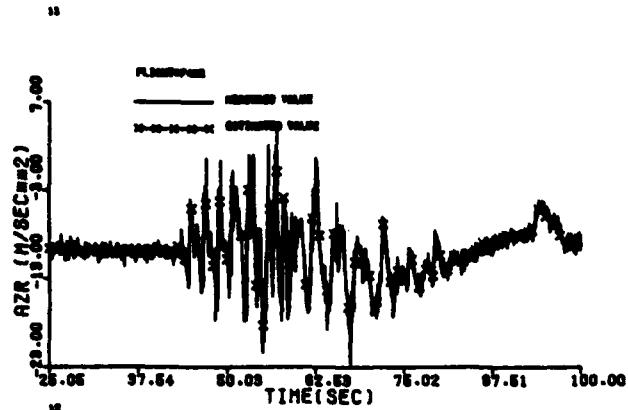


Figure B-9 (concluded)

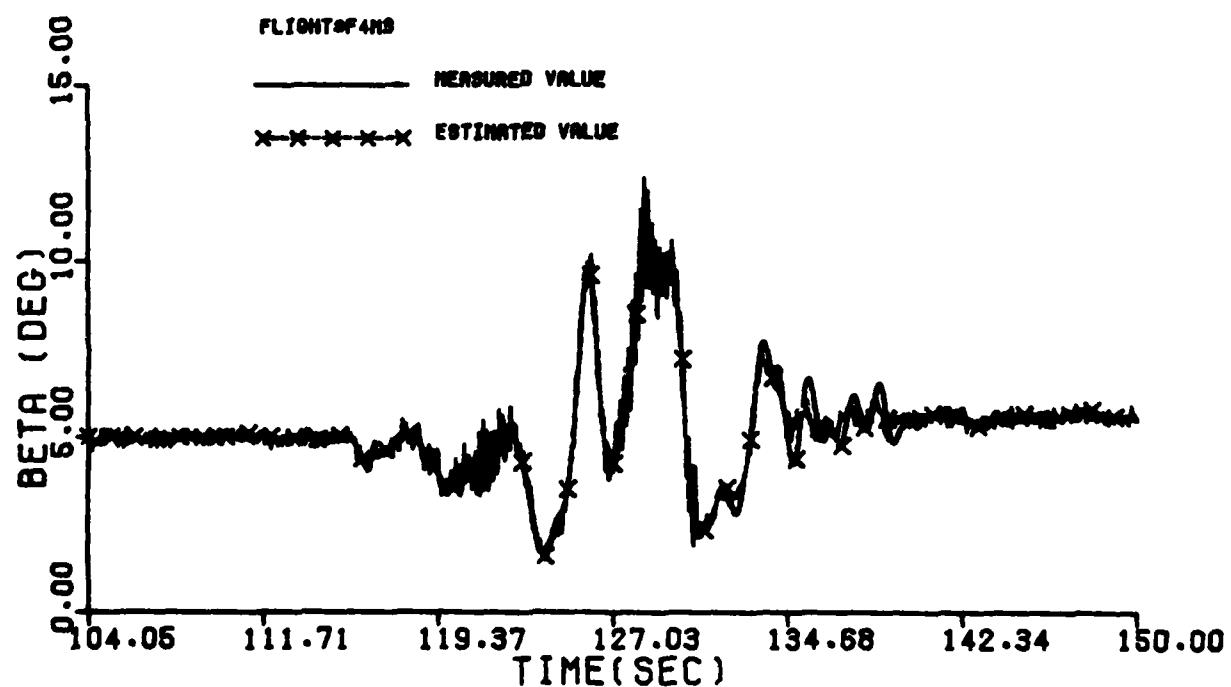
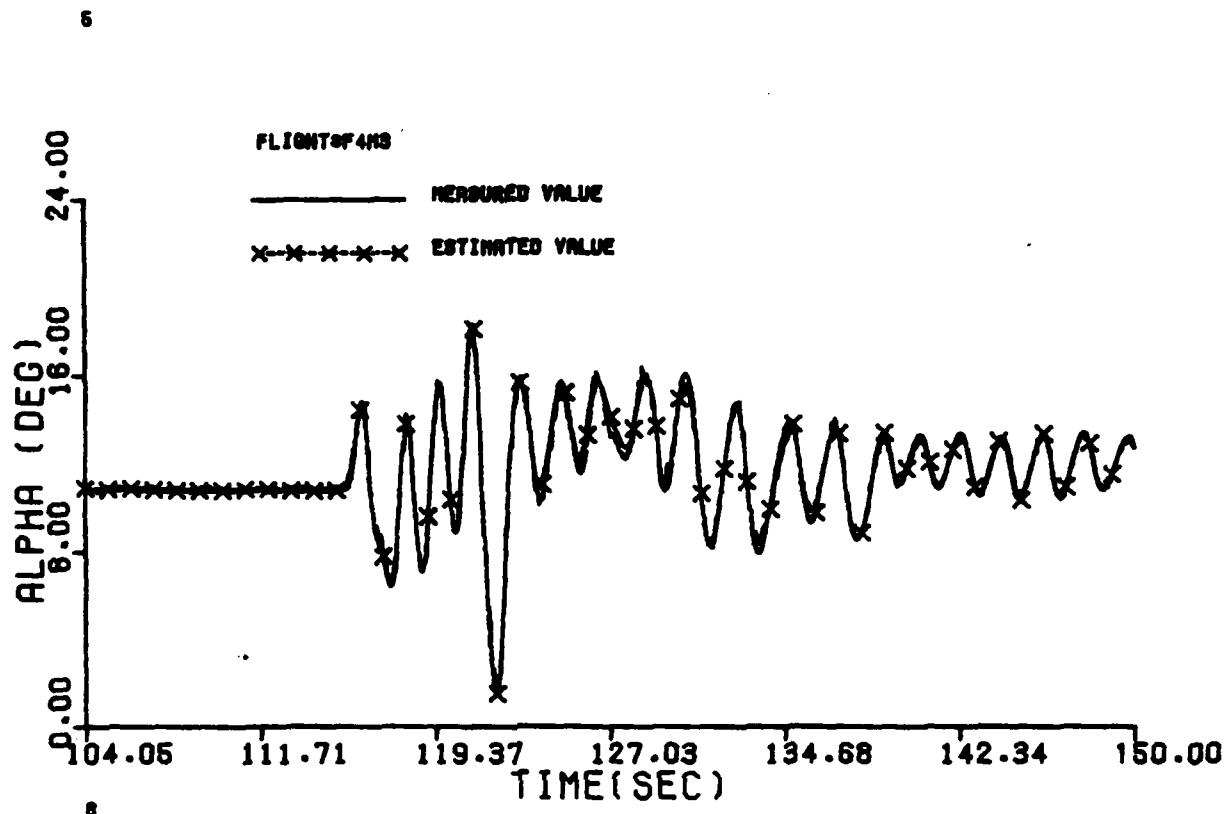


Figure B-10 Comparison Between the Measured and the Estimated Values of Maneuver 3 of Flight 4

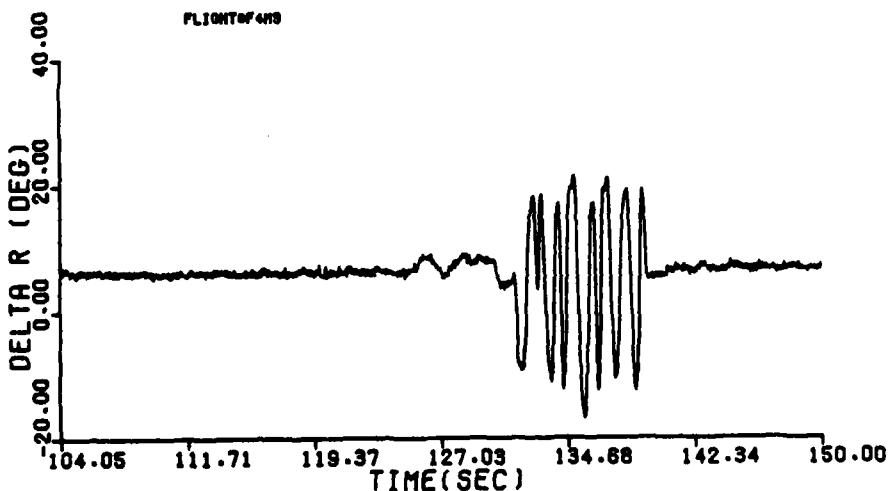
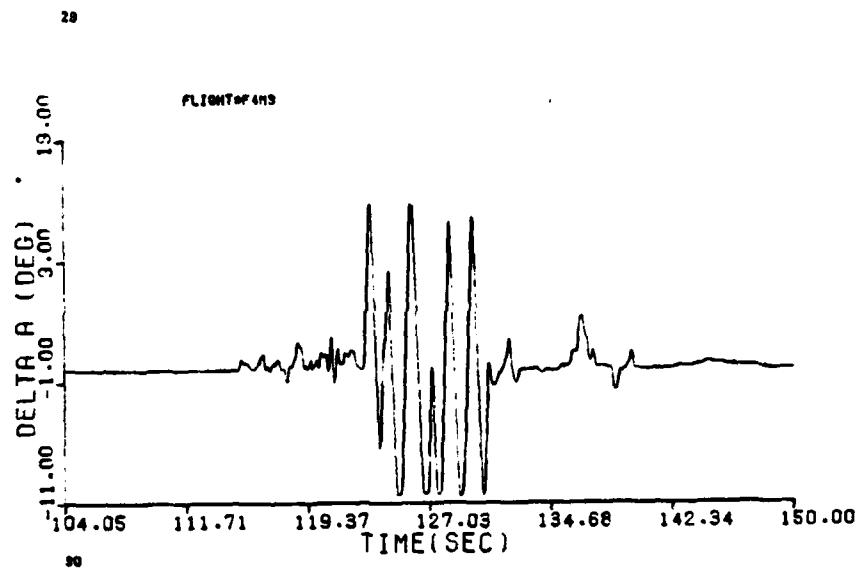
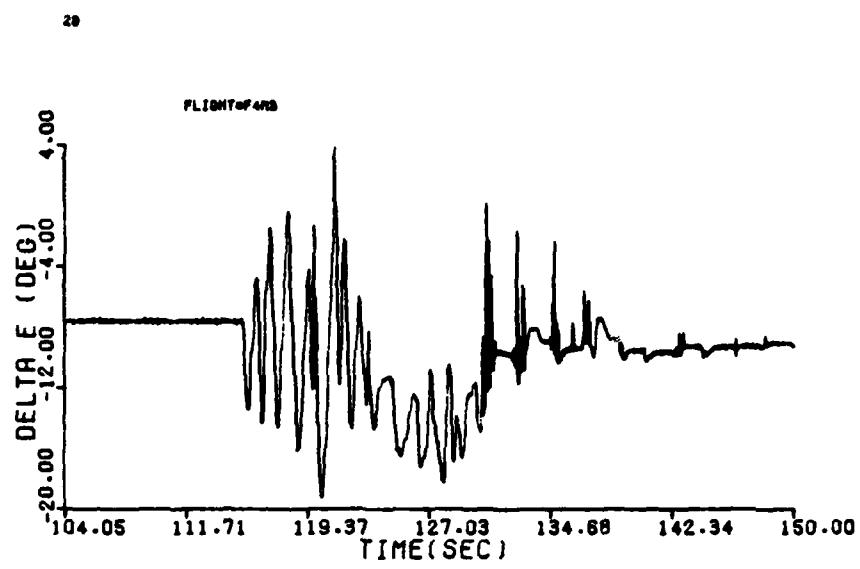


Figure B-10 (cont'd)

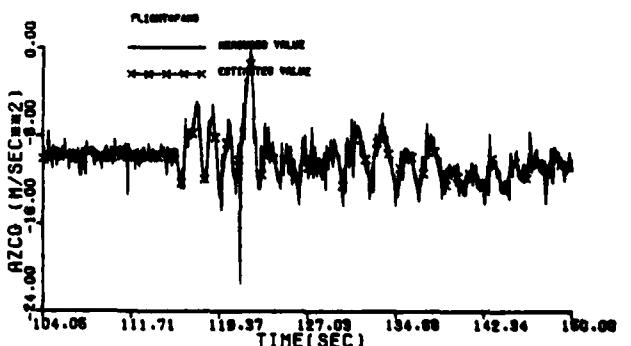
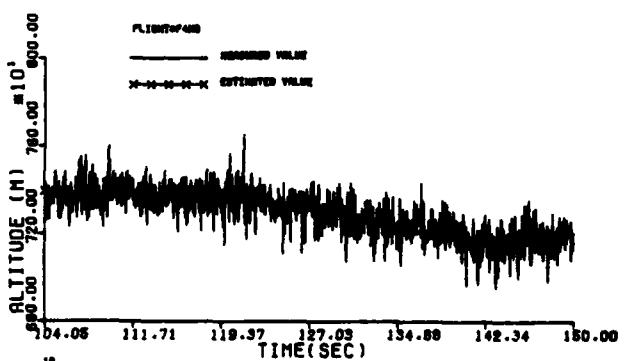
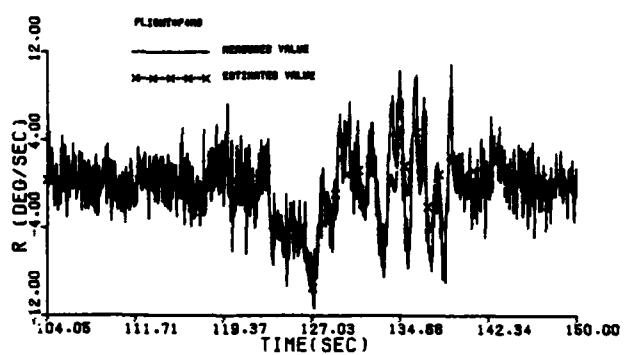
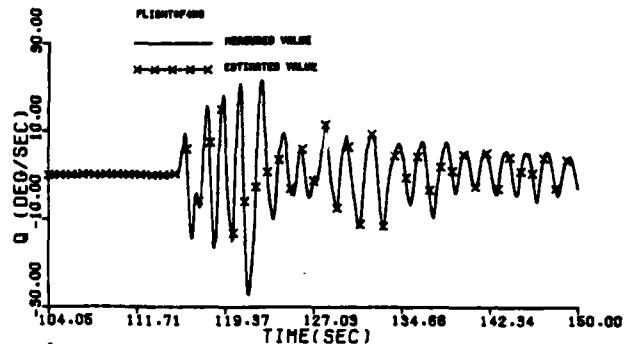
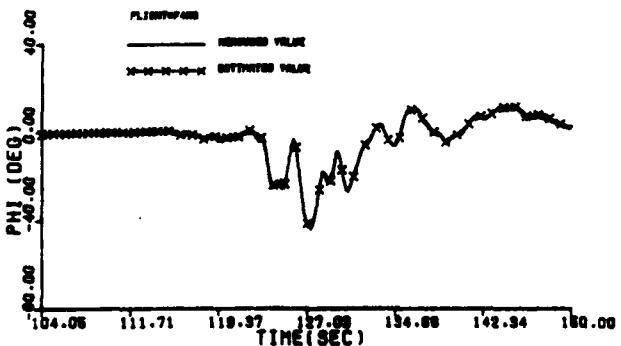
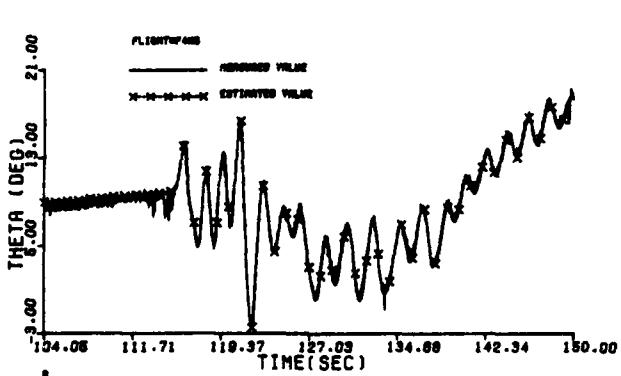
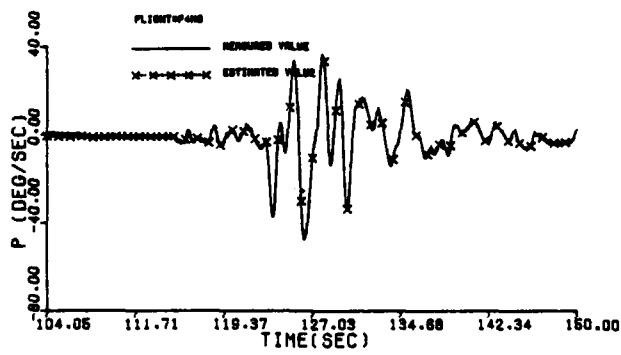
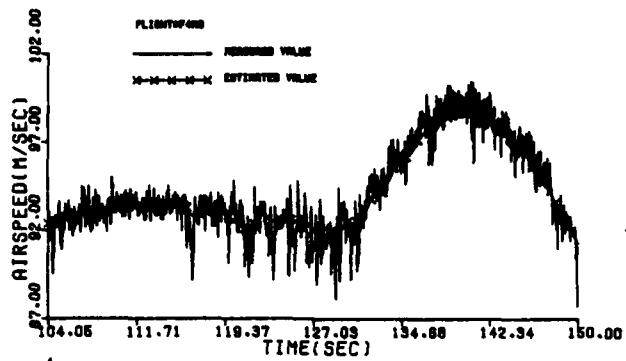


Figure B-10 (cont'd)

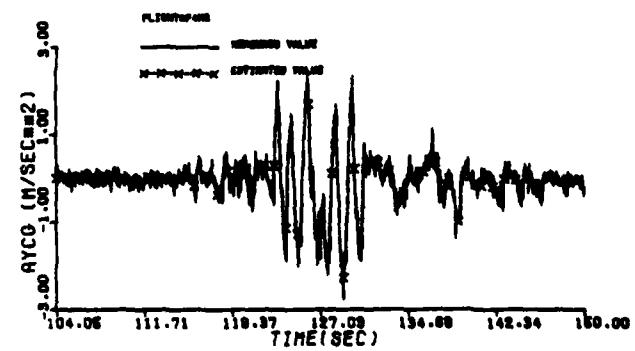
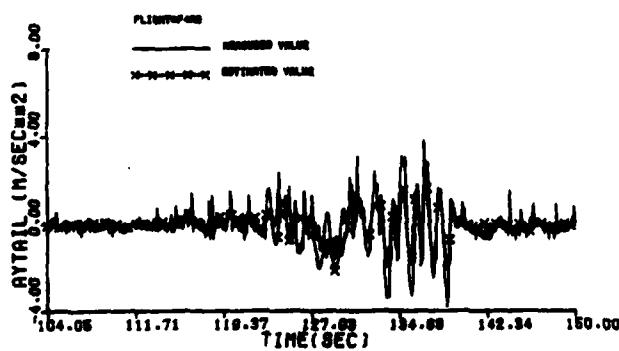
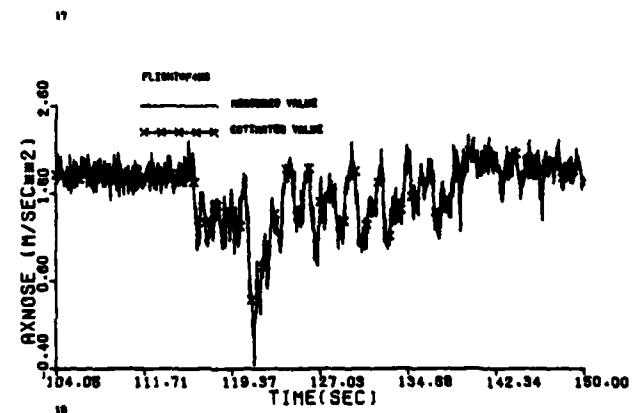
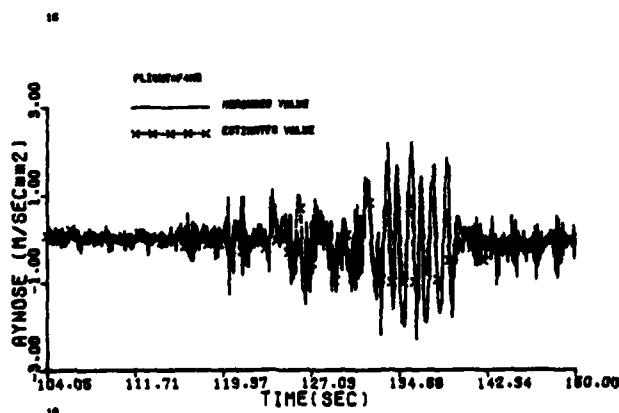
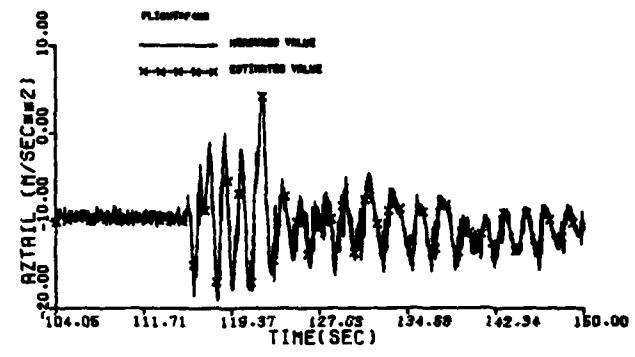
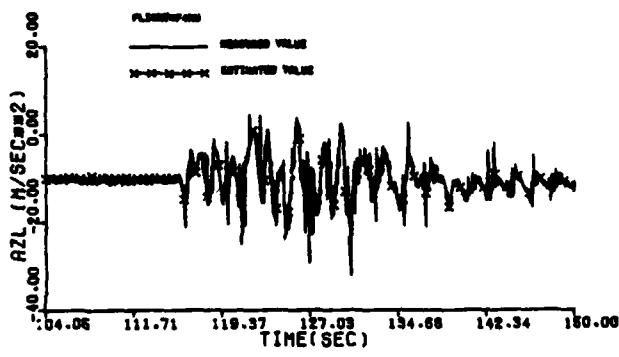
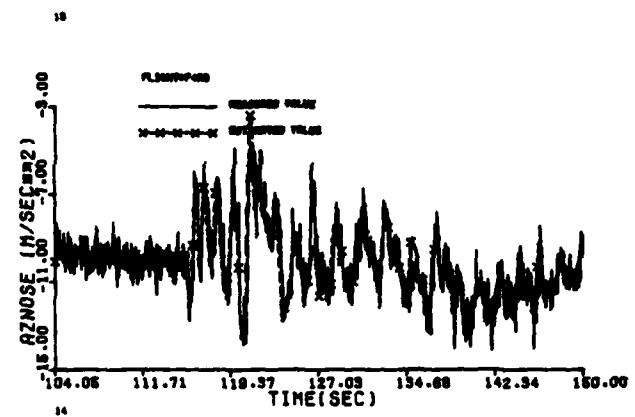
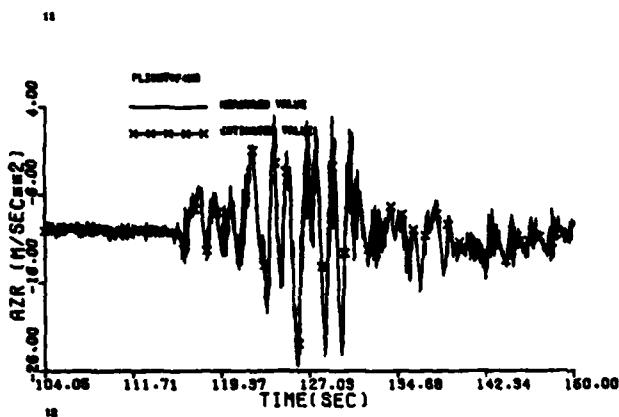


Figure B-10 (concluded)

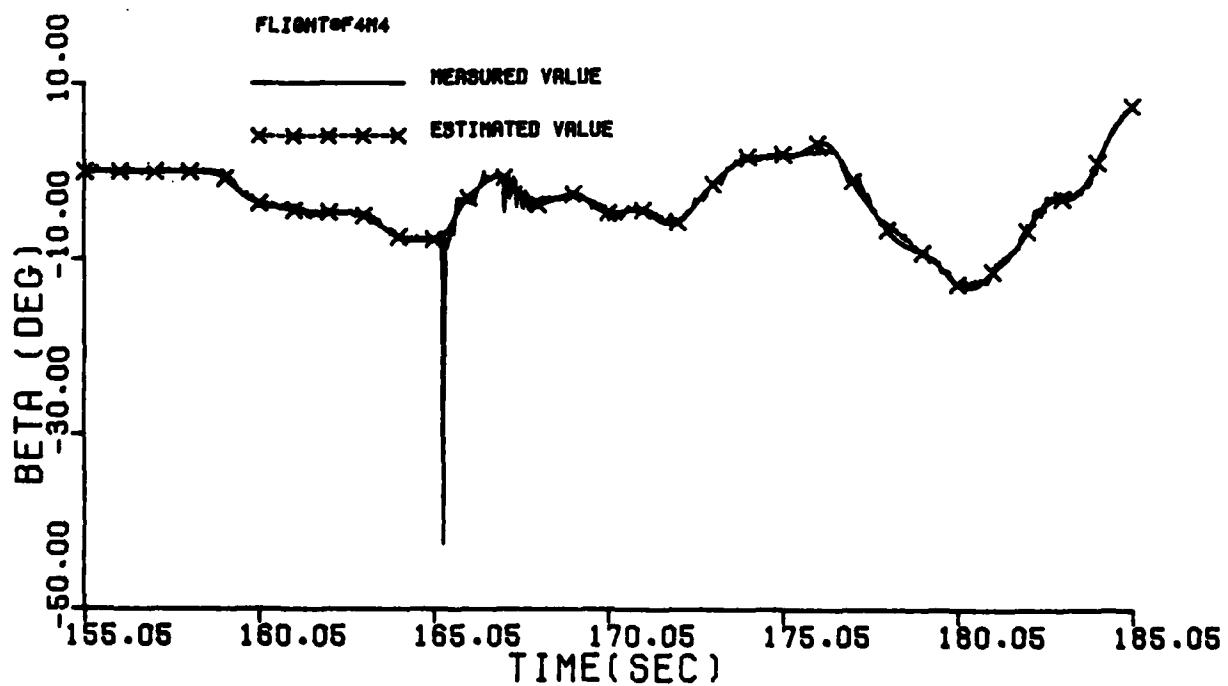
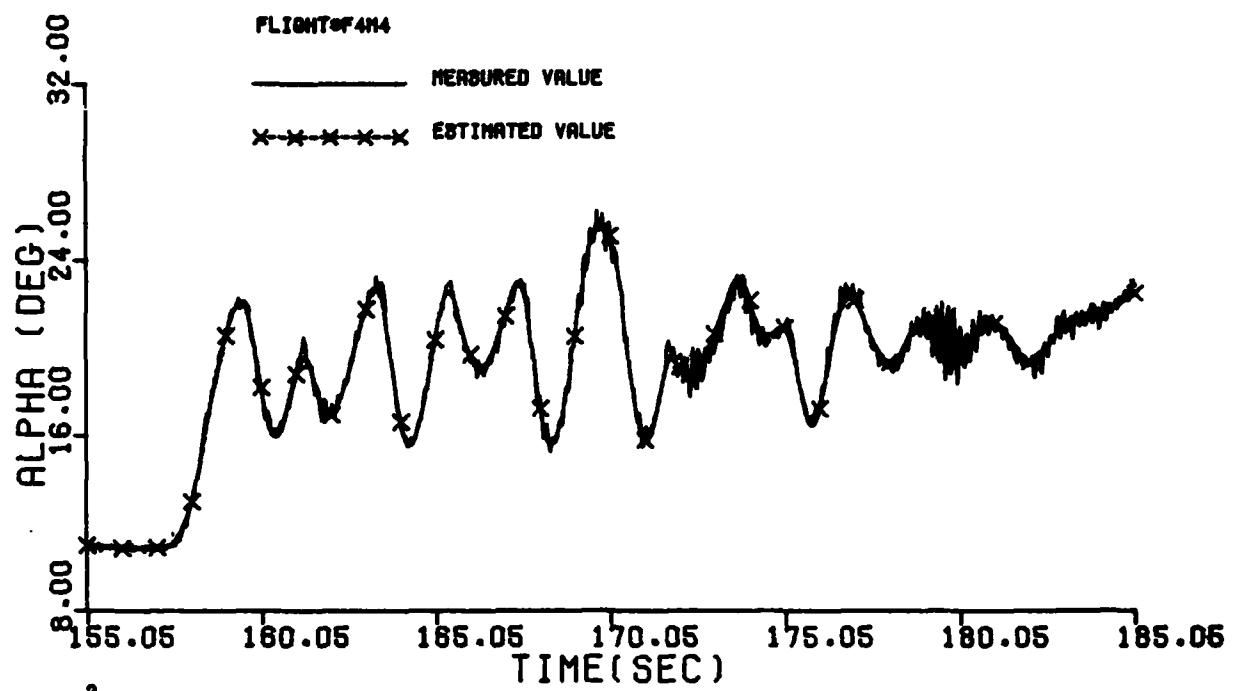


Figure B-11 Comparison Between the Measured and the Estimated Values of Maneuver 4 of Flight 4

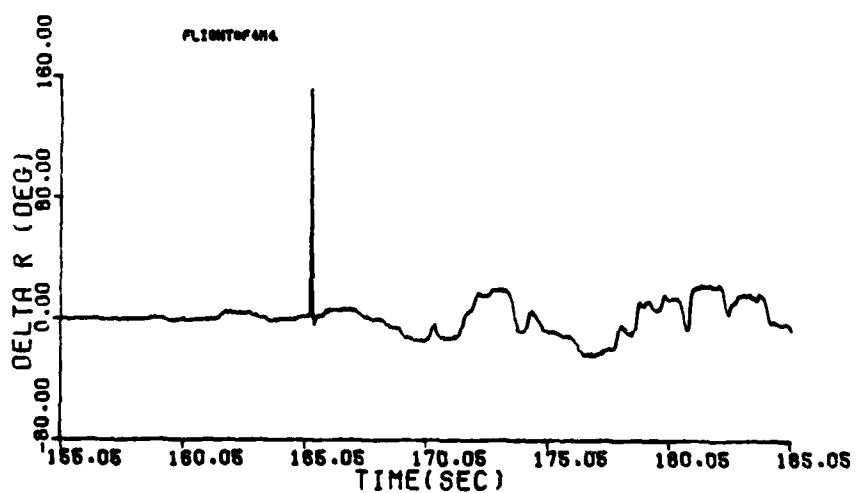
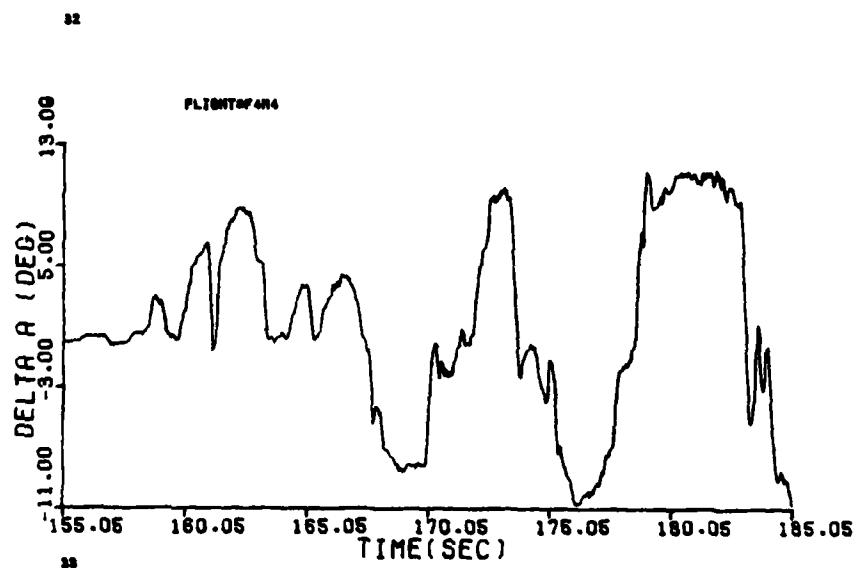
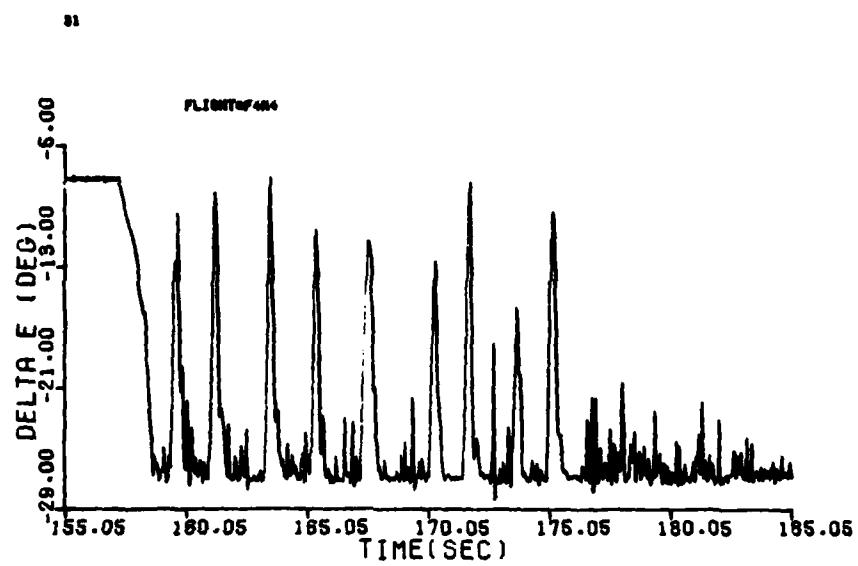


Figure B-11 (cont'd)

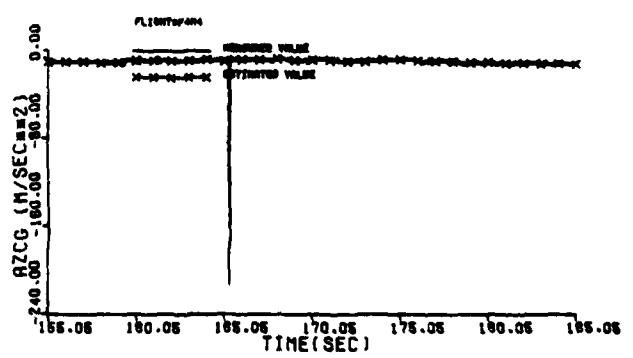
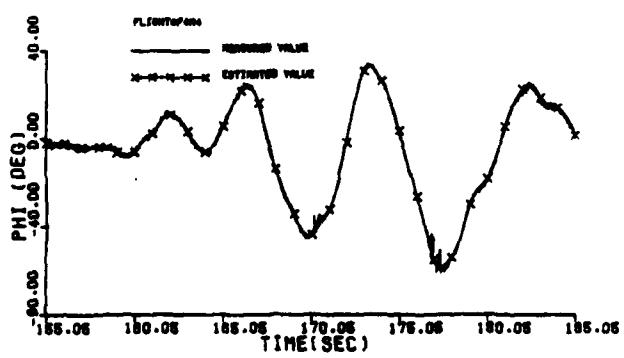
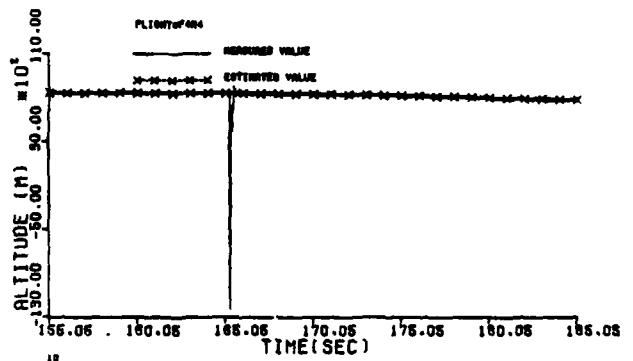
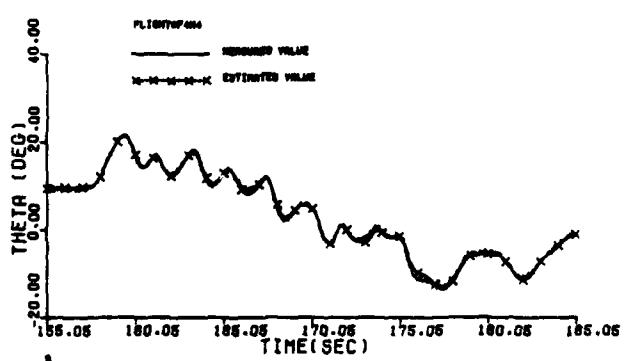
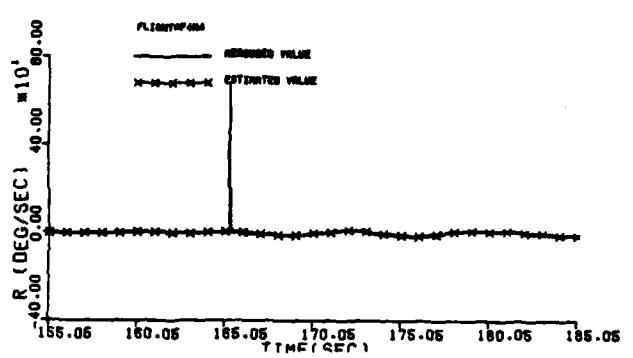
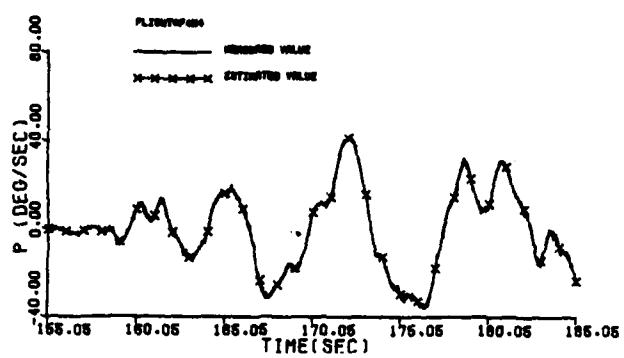
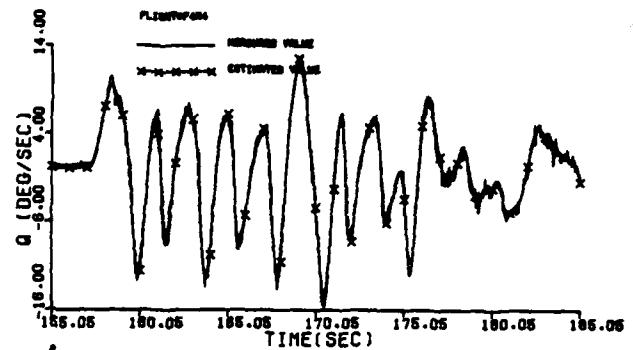
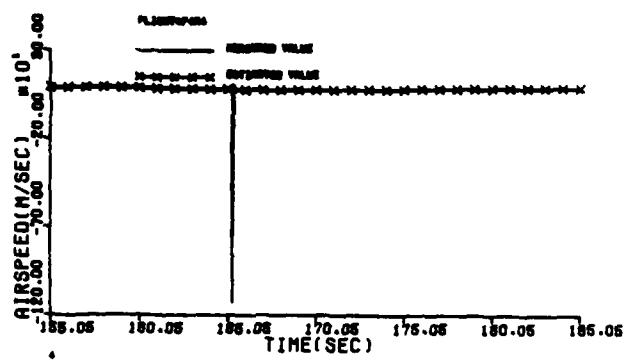


Figure B-11 (cont'd)

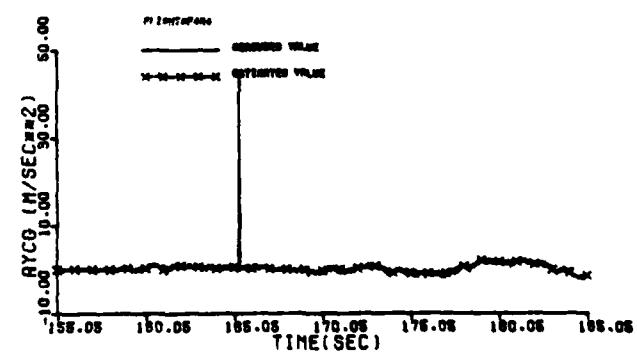
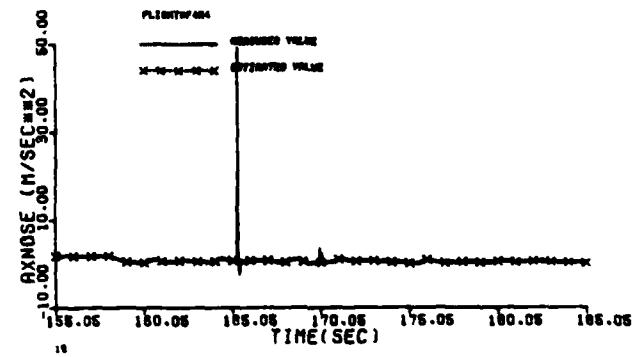
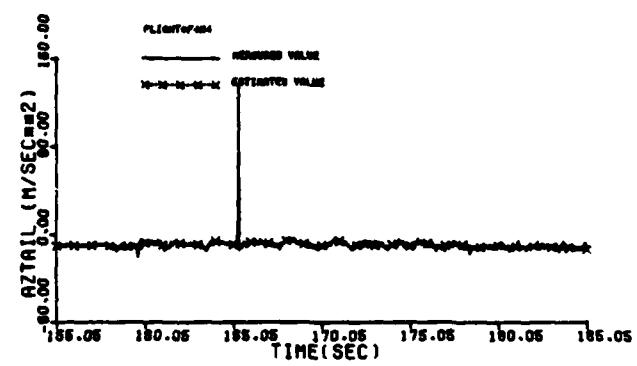
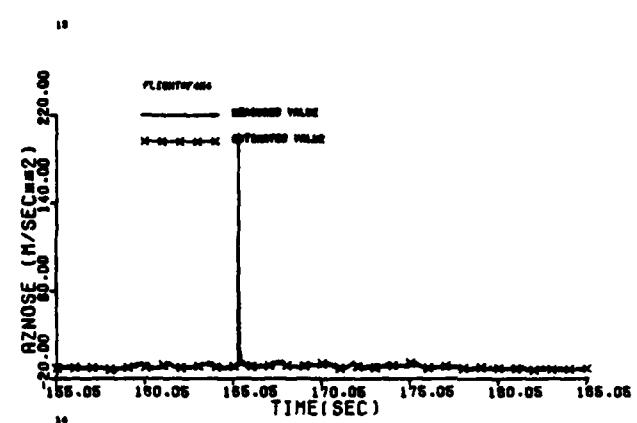
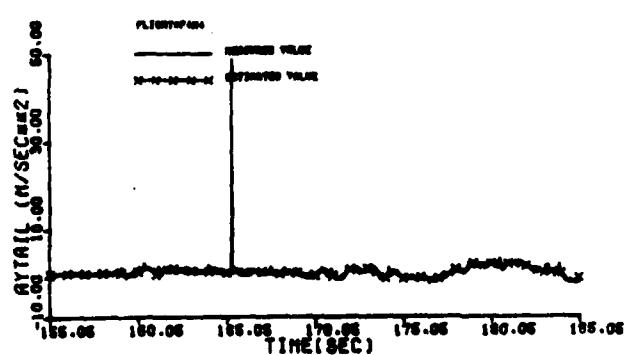
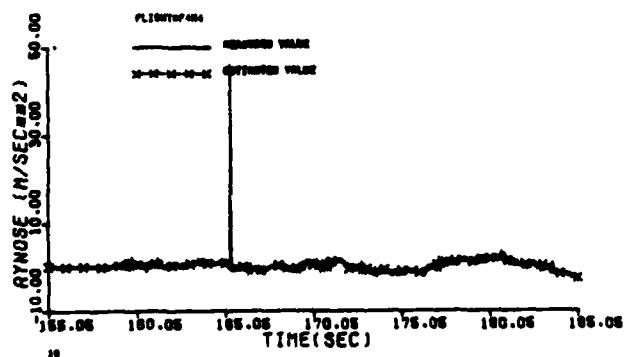
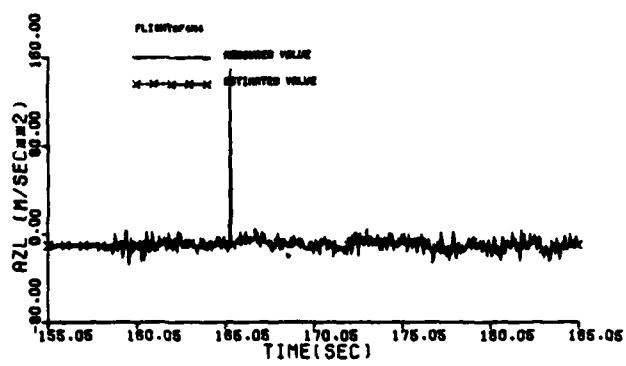
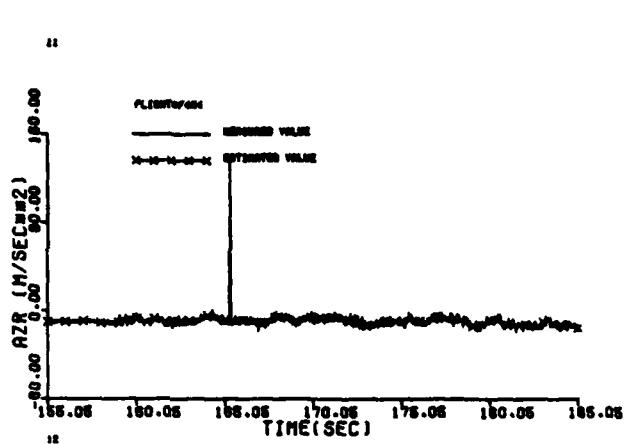


Figure B-11 (concluded)

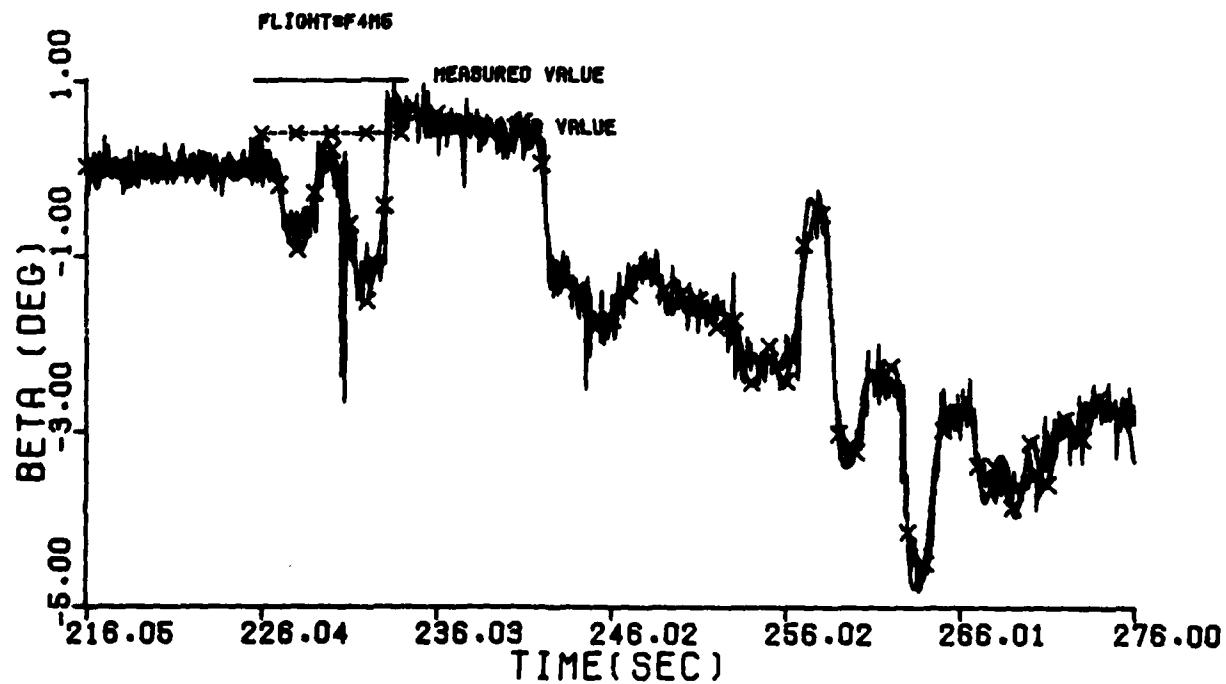
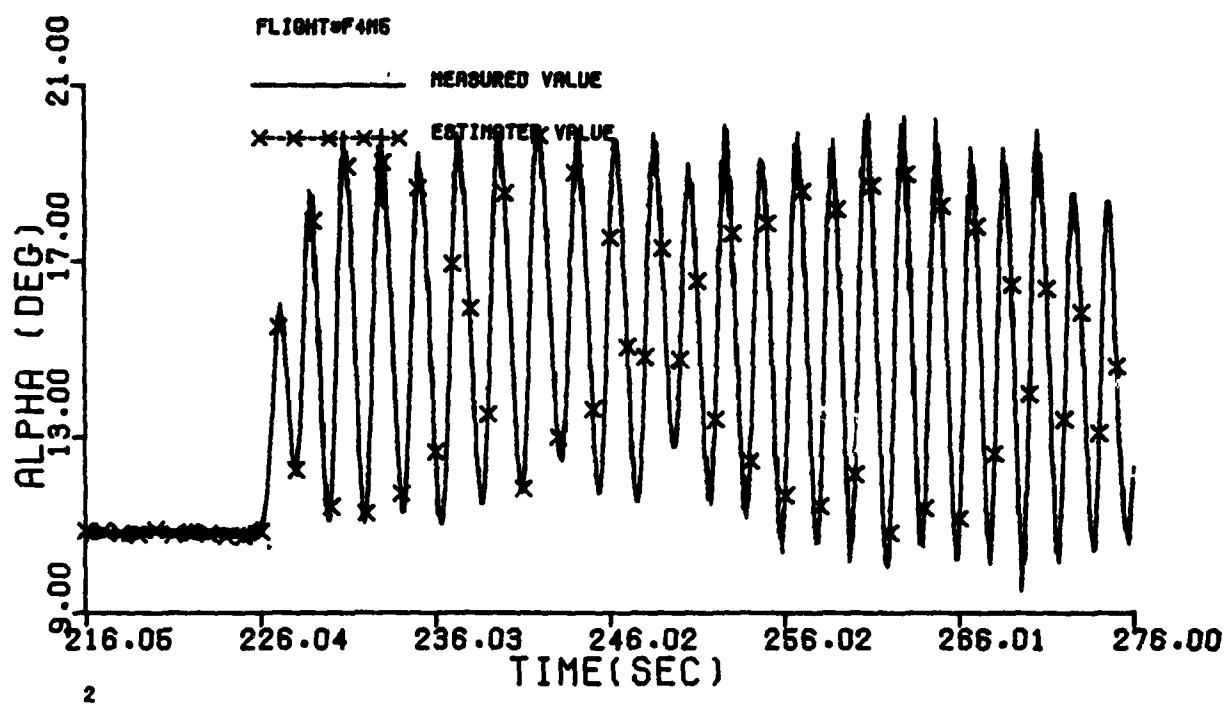


Figure B-12 Comparison Between the Measured and the Estimated Values of Maneuver 5 of Flight 4

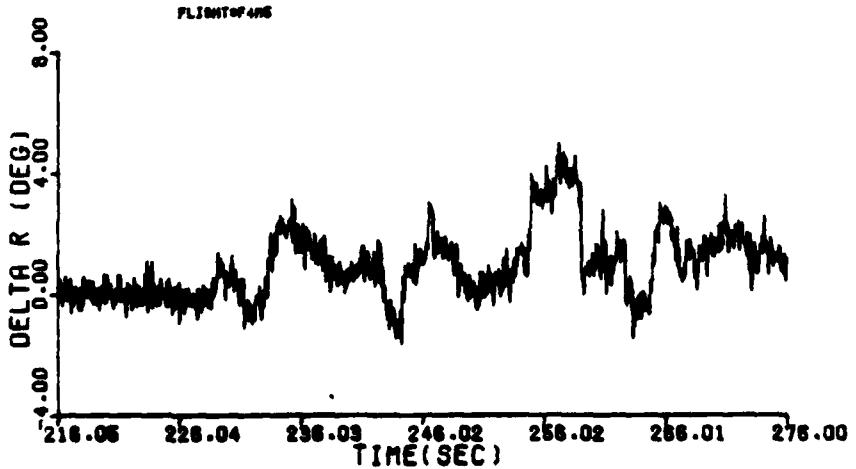
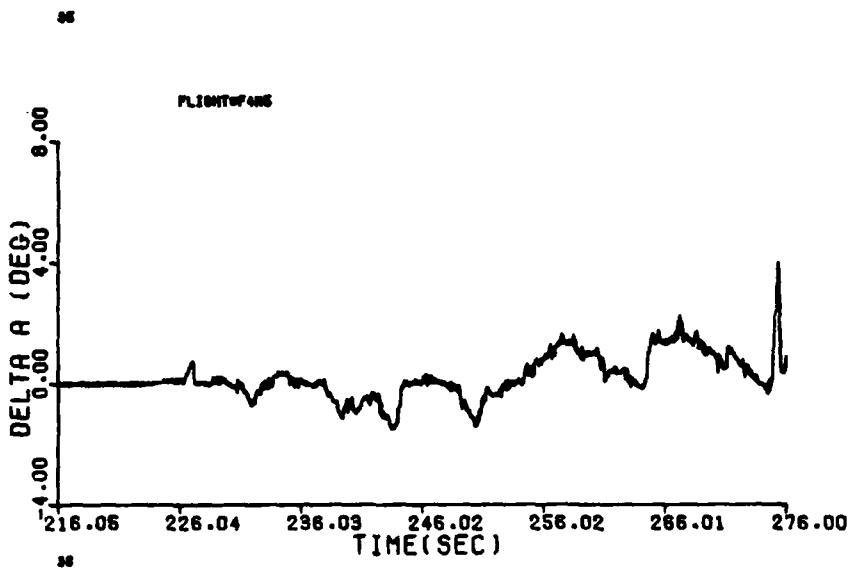
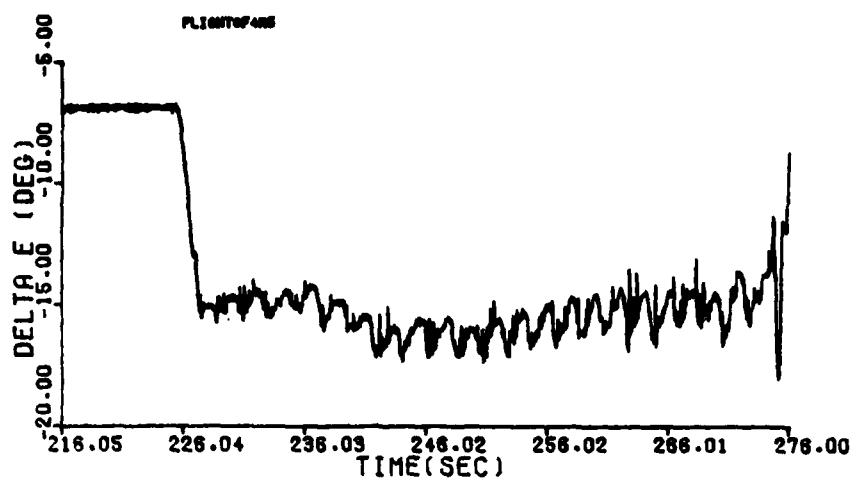


Figure B-12 (cont'd)

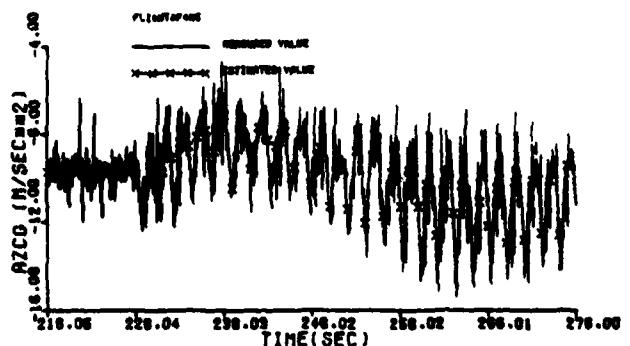
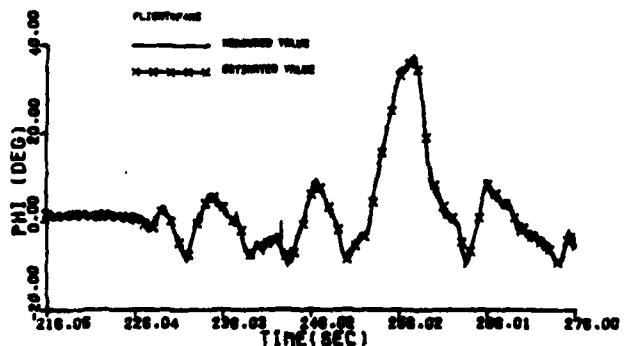
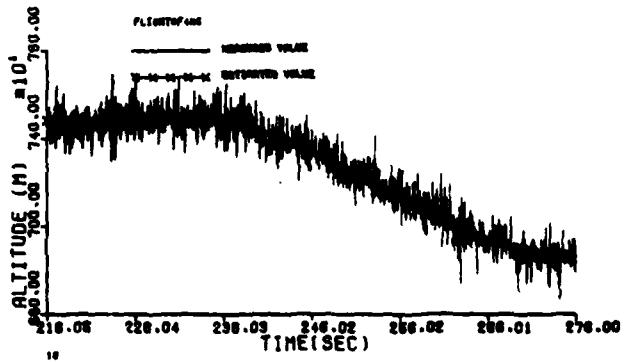
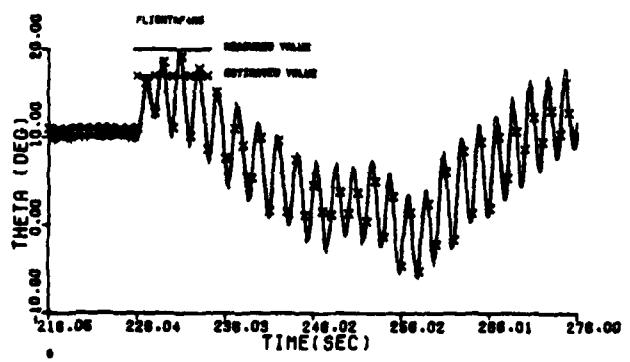
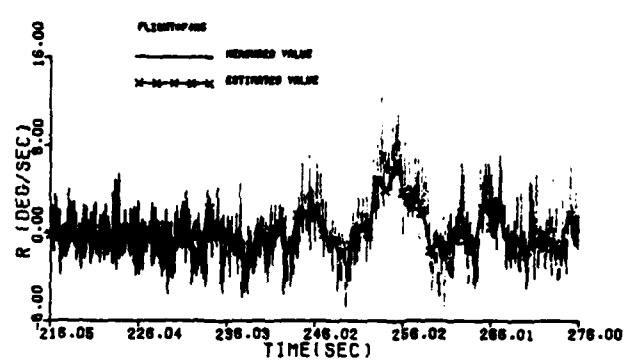
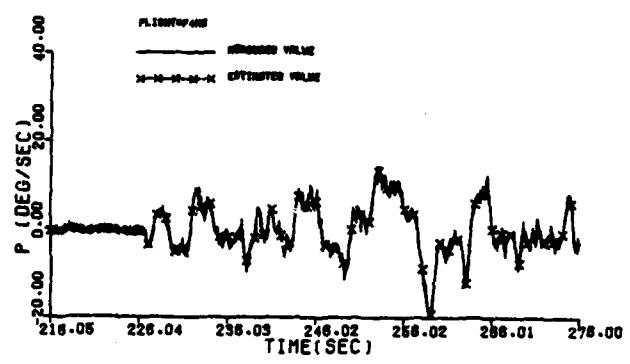
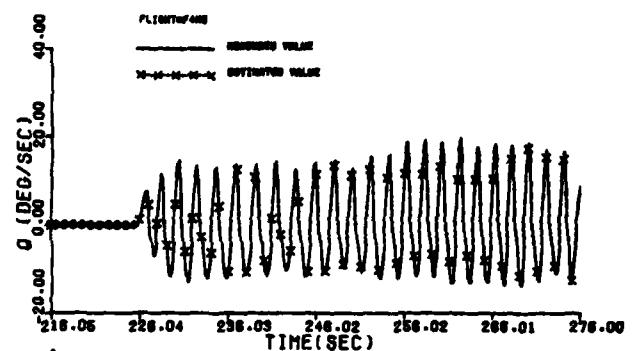
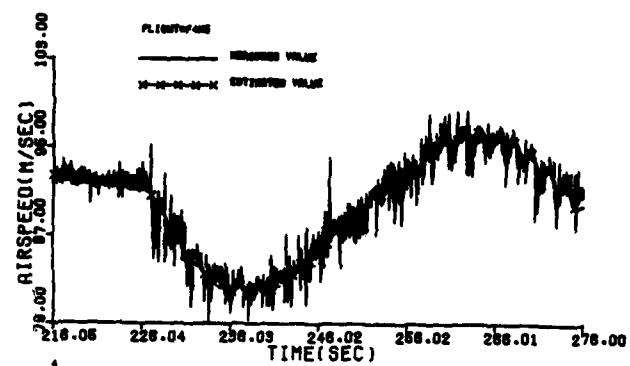


Figure B-12 (cont'd)

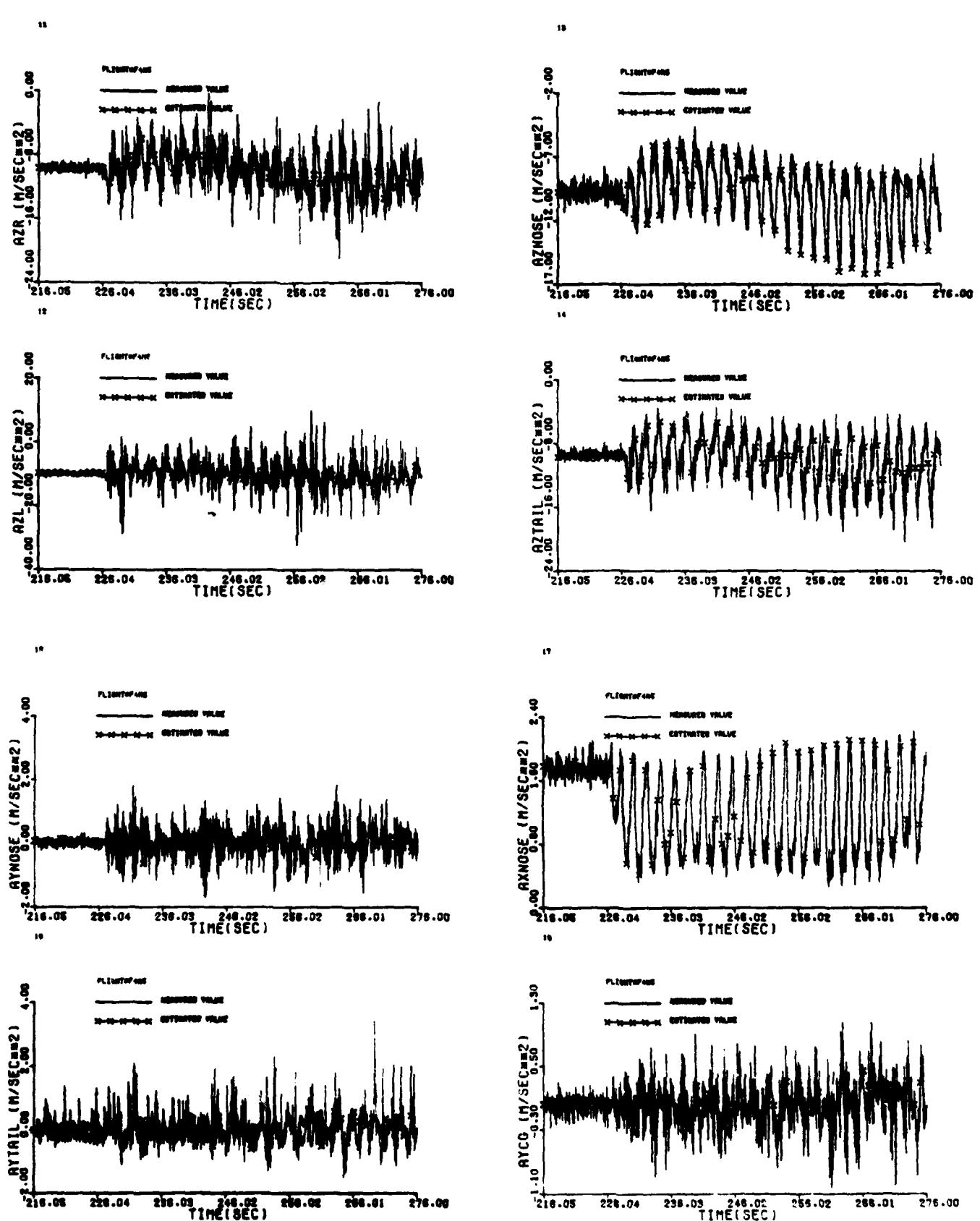


Figure B-12 (concluded)

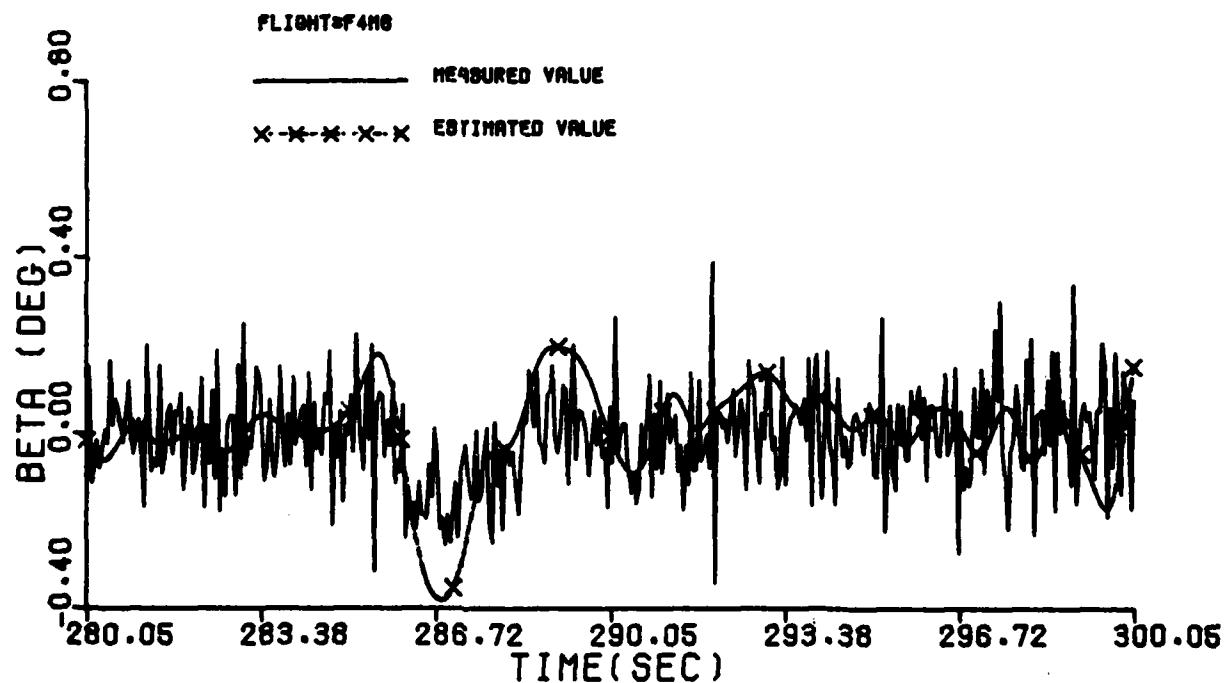
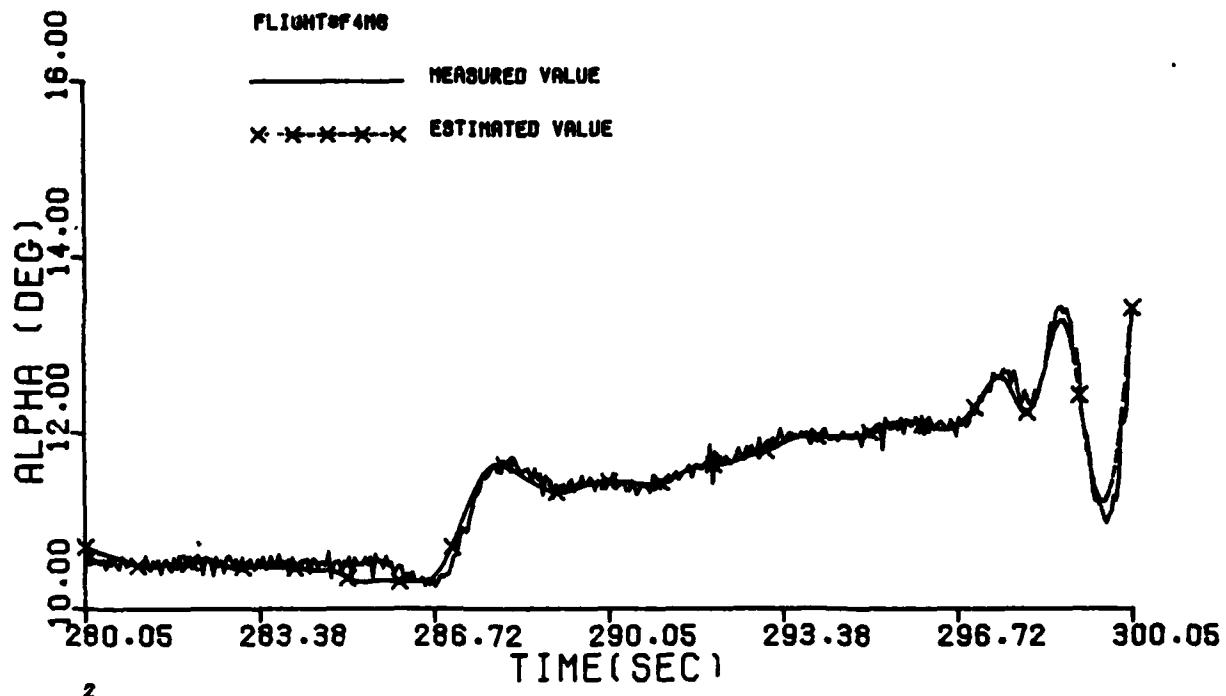


Figure B-13a Comparison Between the Measured and the Estimated Values of Maneuver 6a of Flight 4

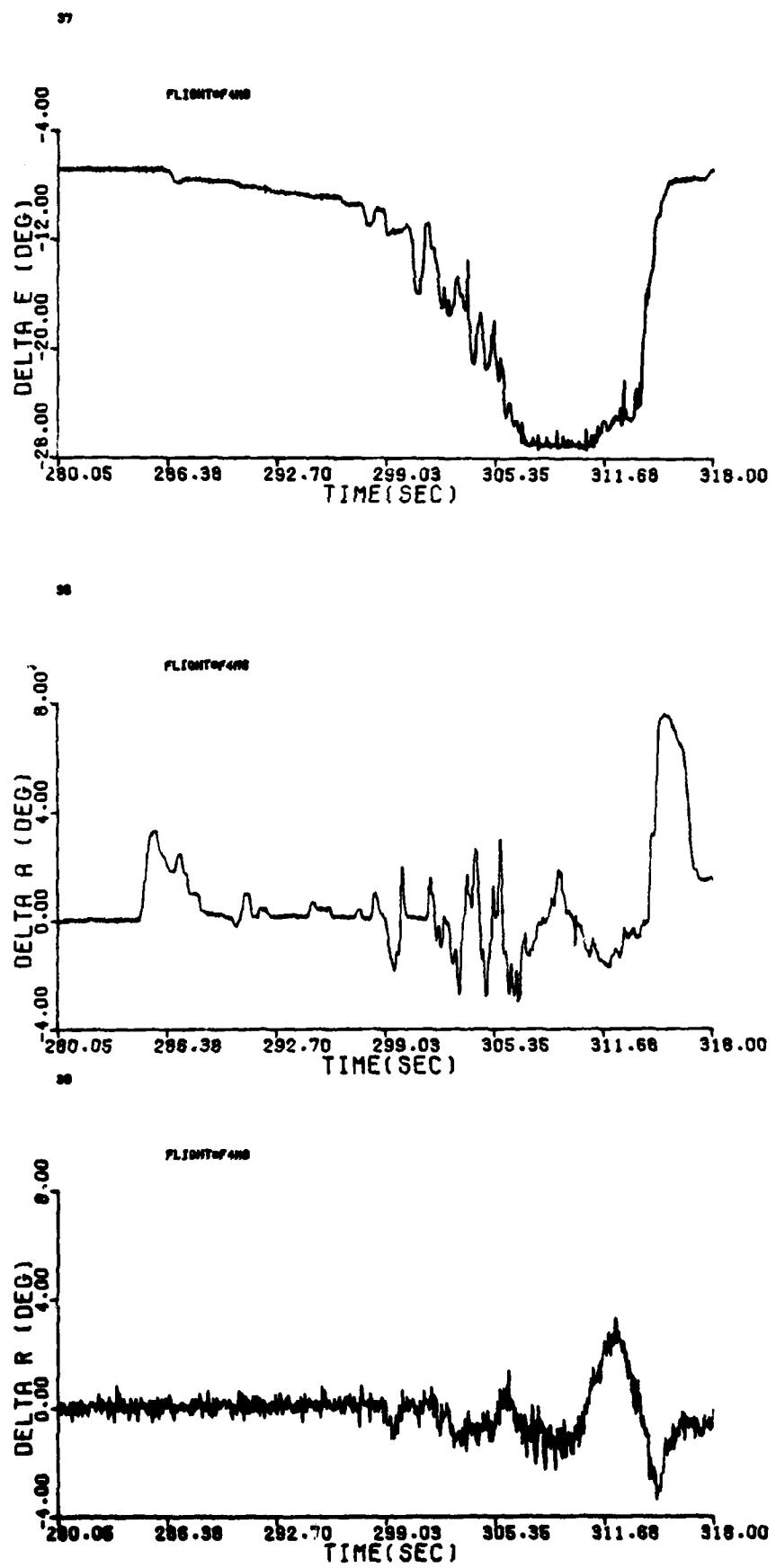


Figure B-13a (cont'd)

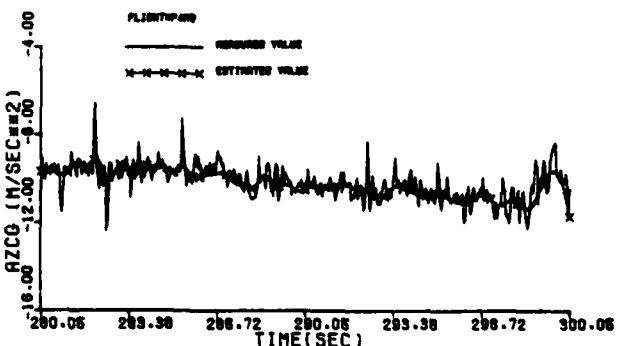
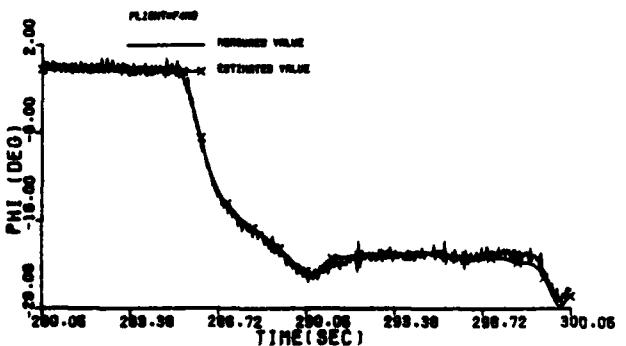
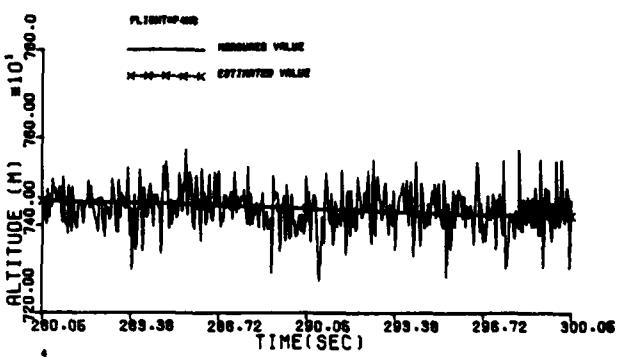
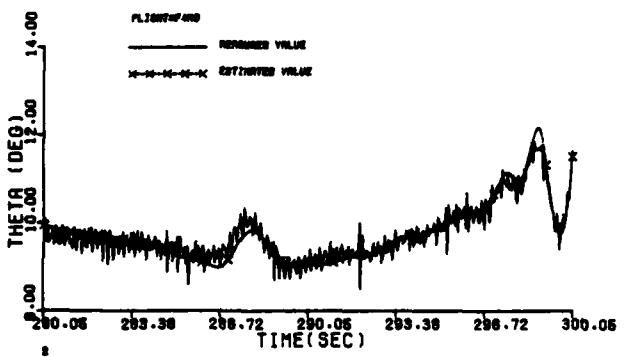
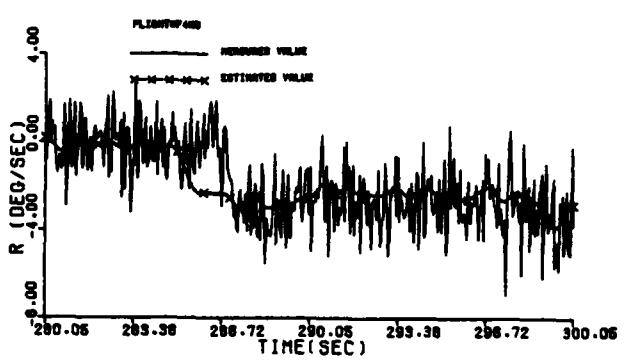
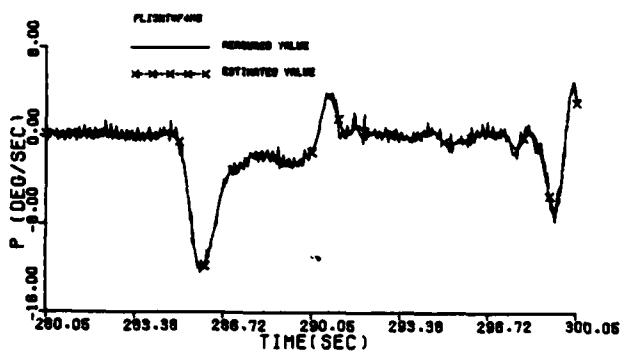
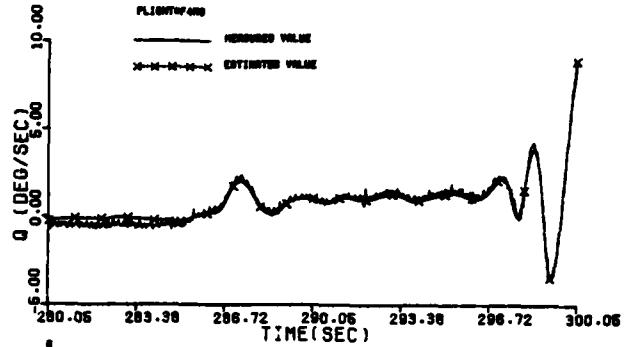
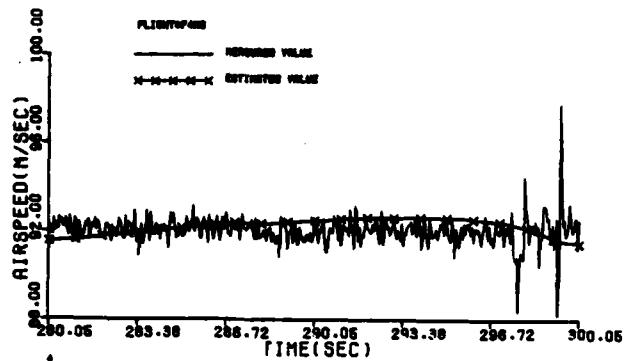


Figure B-13a (cont'd)

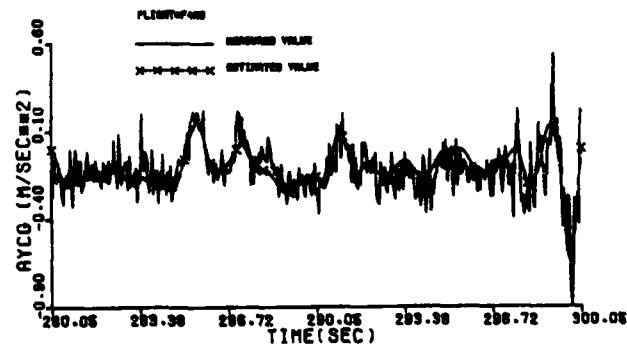
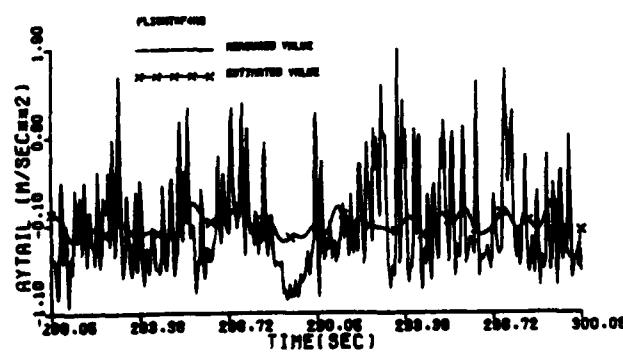
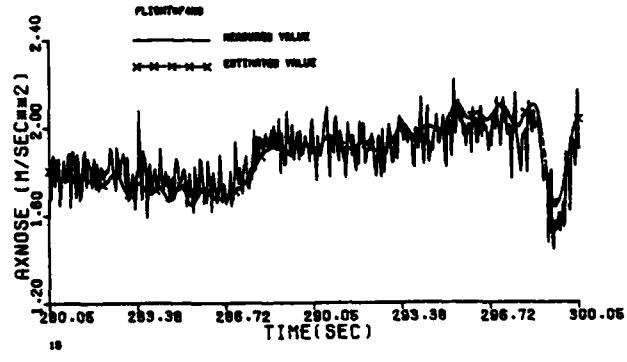
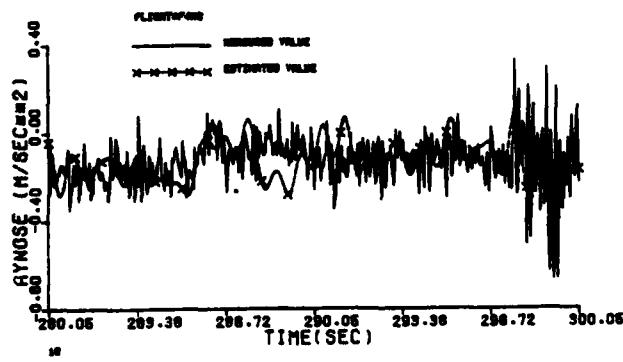
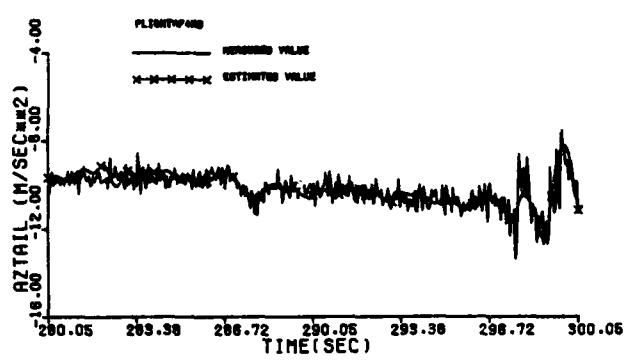
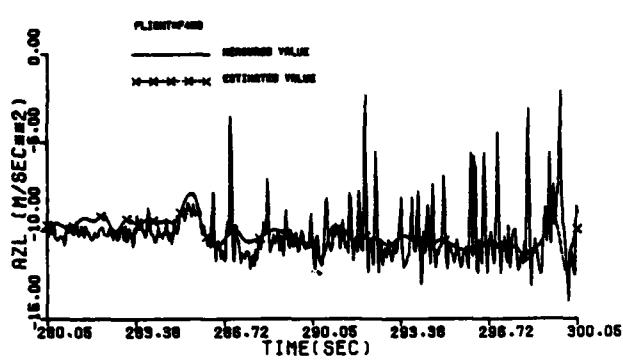
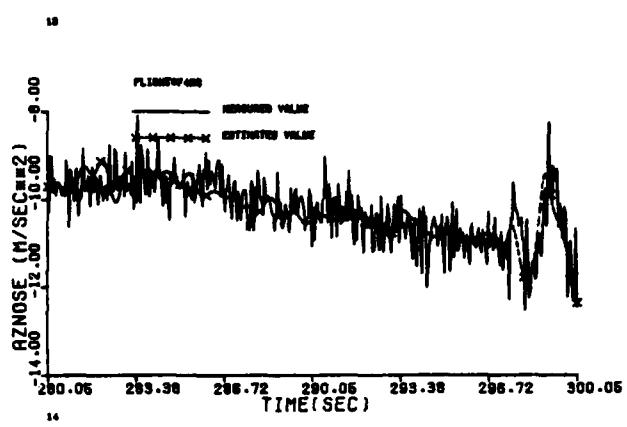
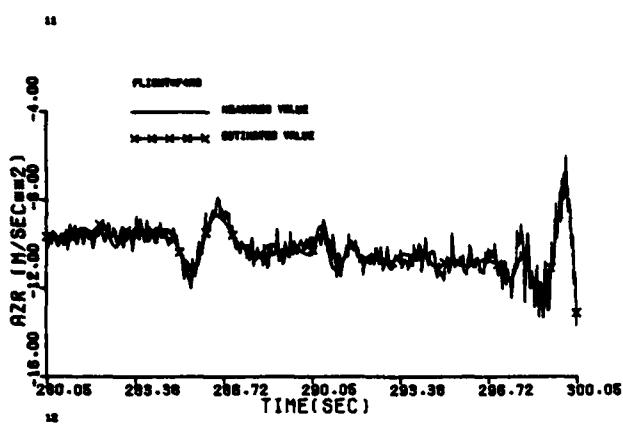


Figure B-13a (concluded)

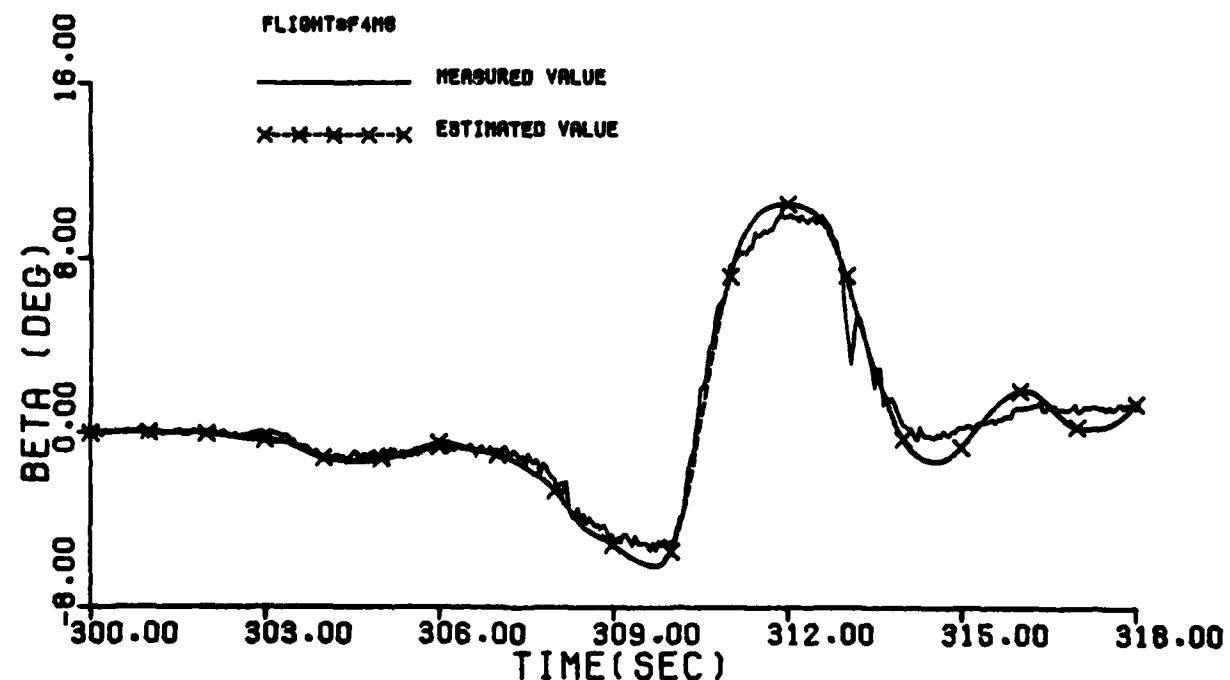
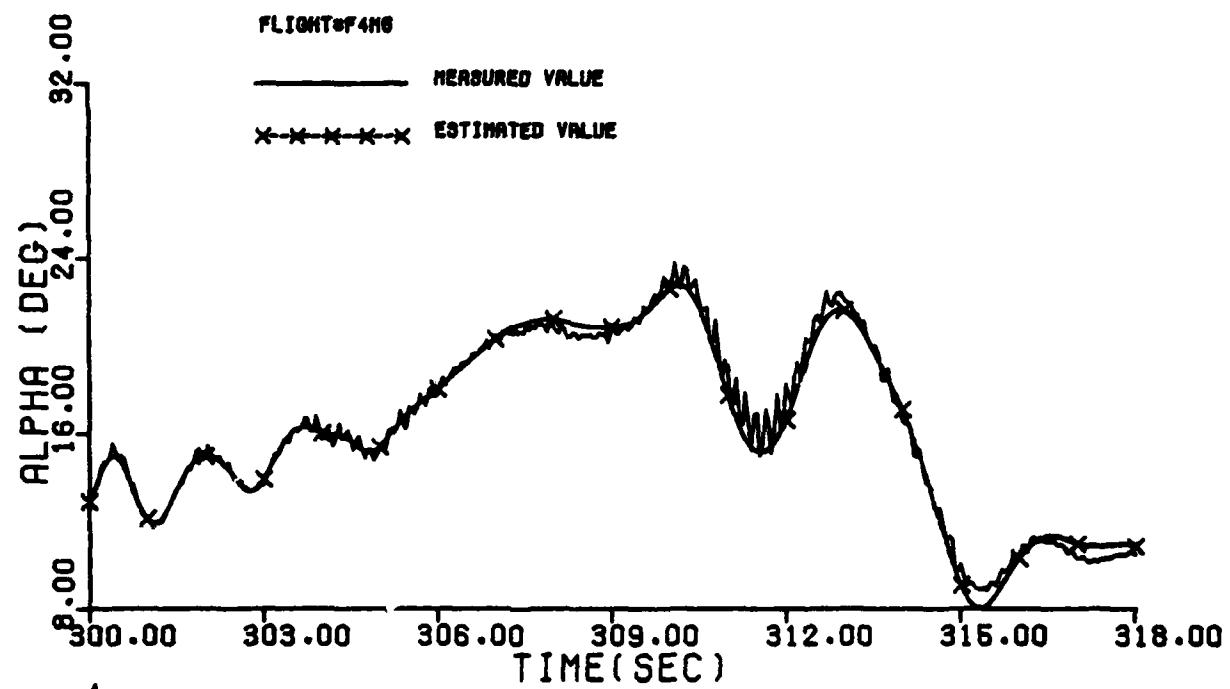
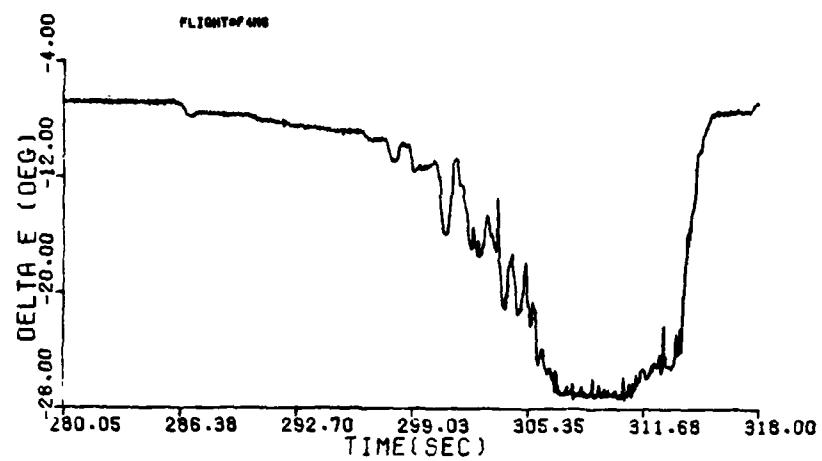
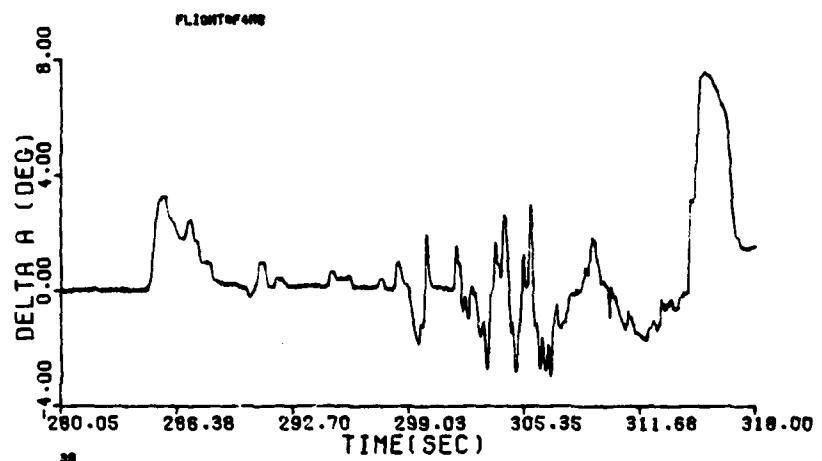


Figure B-13b Comparison Between the Measured and the Estimated Values of Maneuver 6b of Flight 4

37



38



39

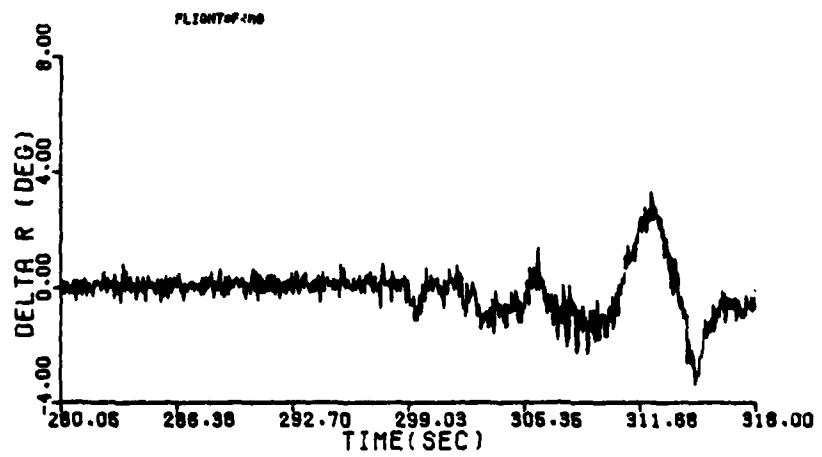


Figure B-13b (cont'd)

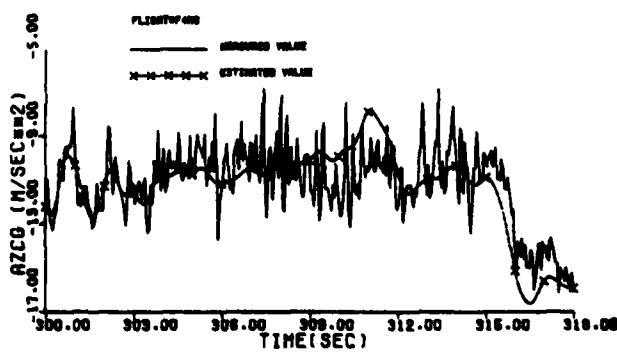
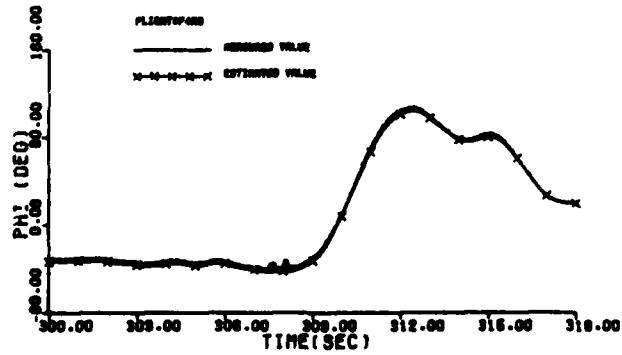
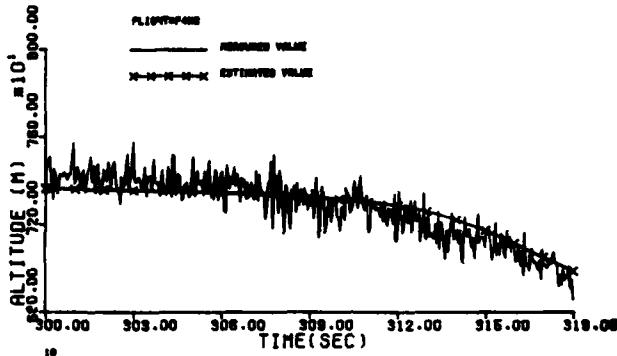
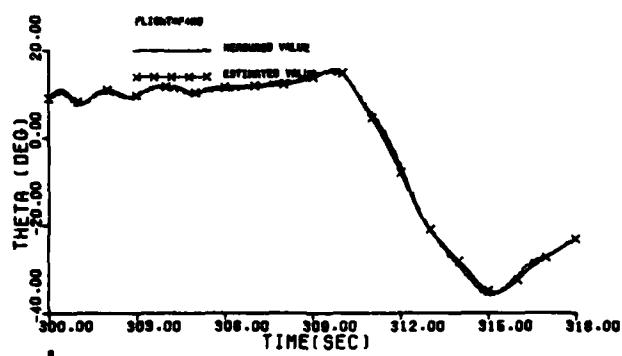
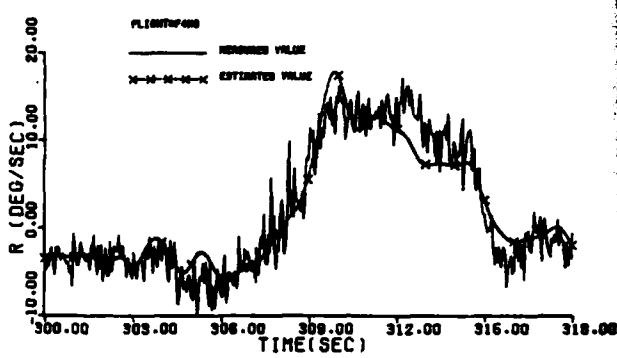
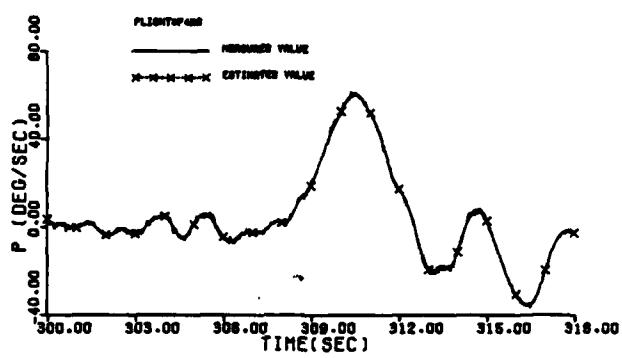
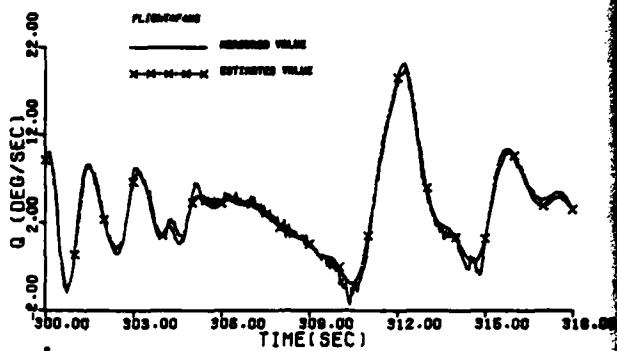
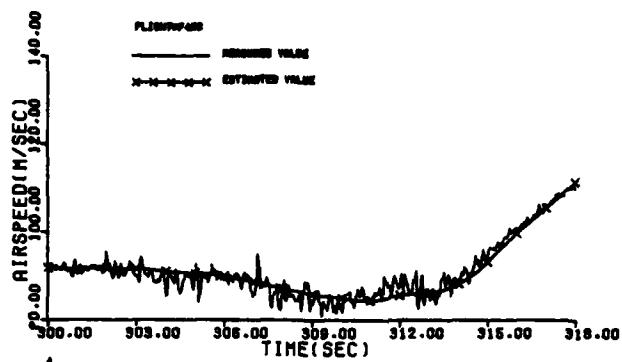


Figure B-13b (cont'd)

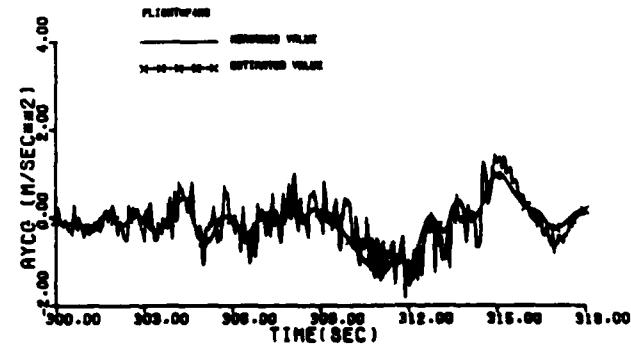
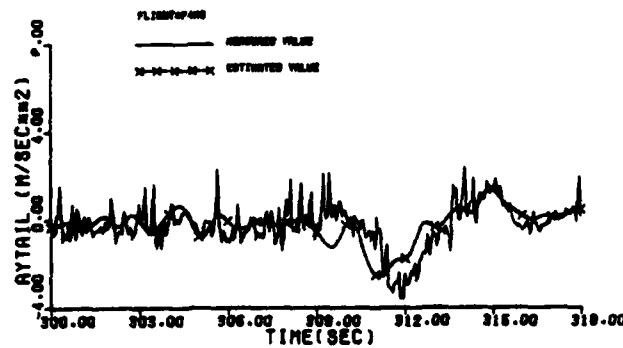
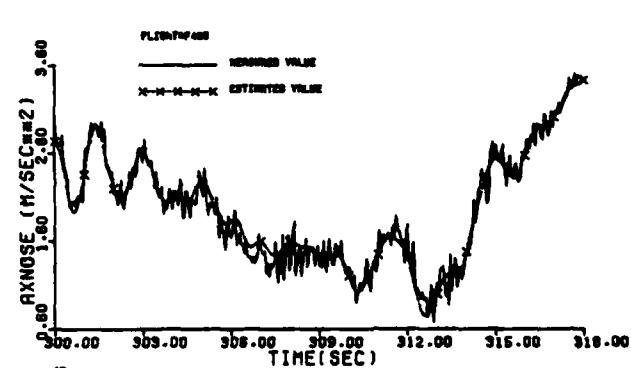
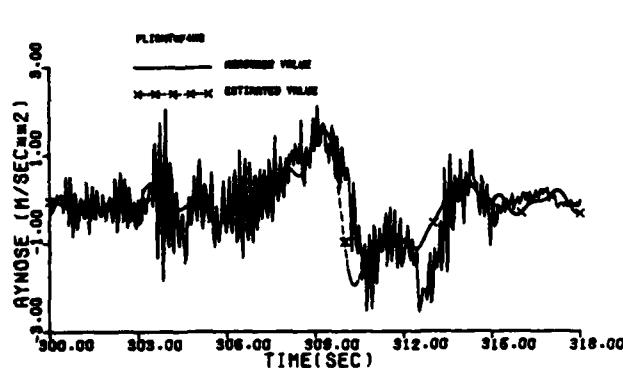
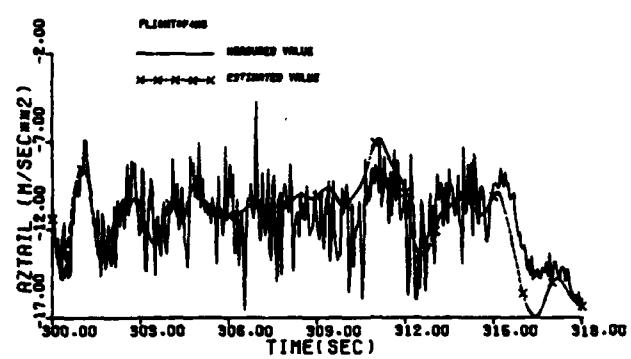
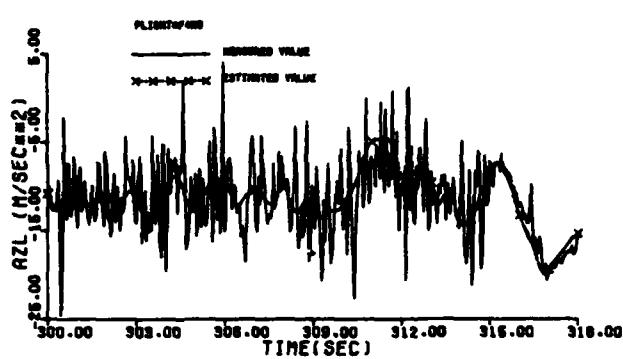
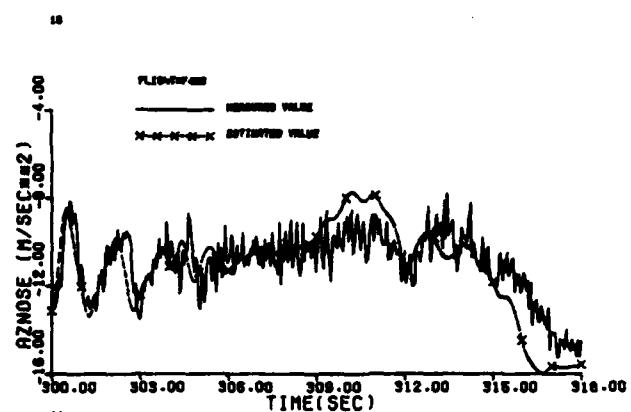
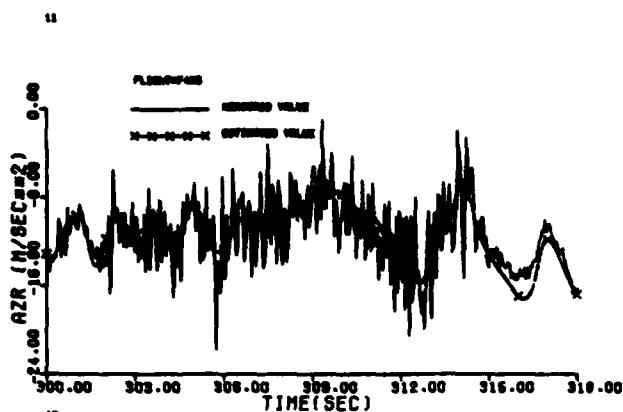


Figure B-13b (concluded)

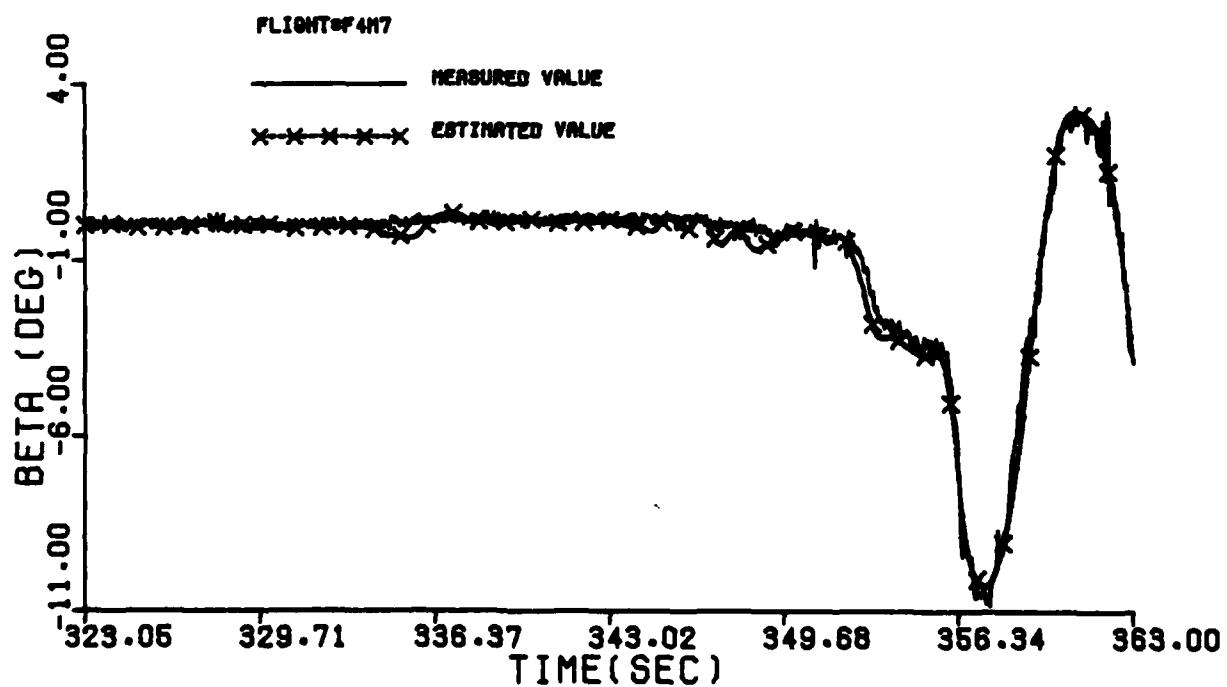
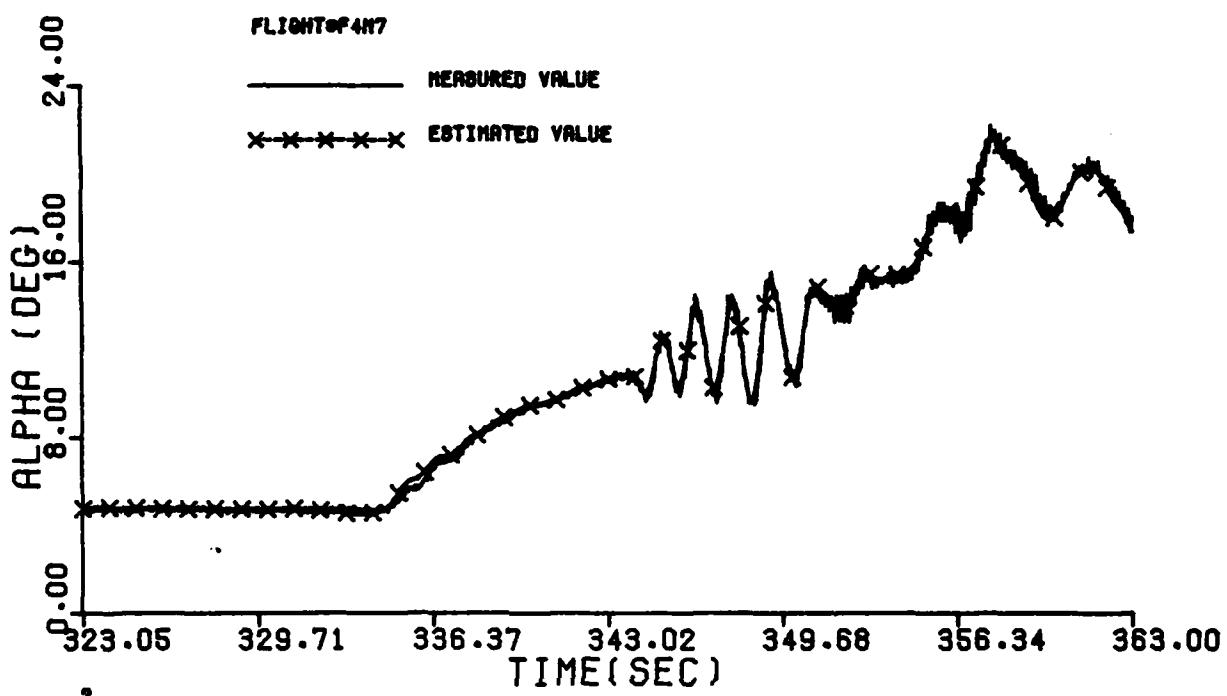


Figure B-14 Comparison Between the Measured and the Estimated Values of Maneuver 7 of Flight 4

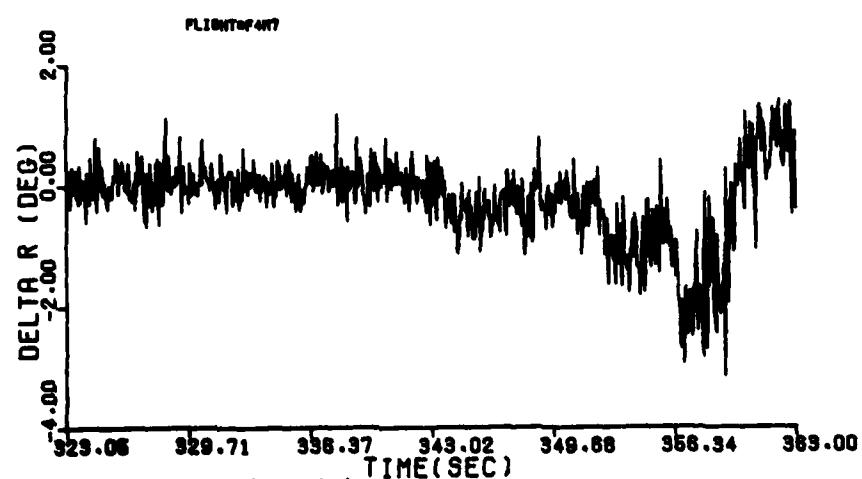
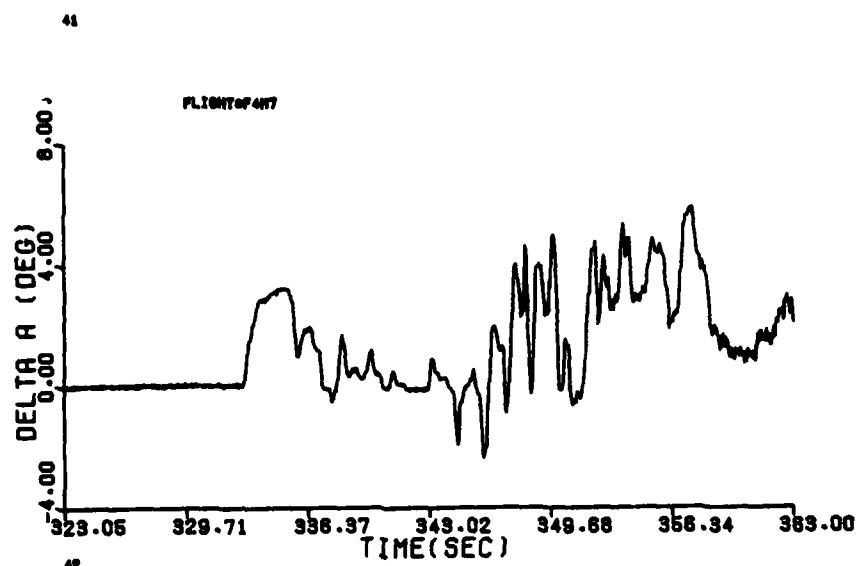
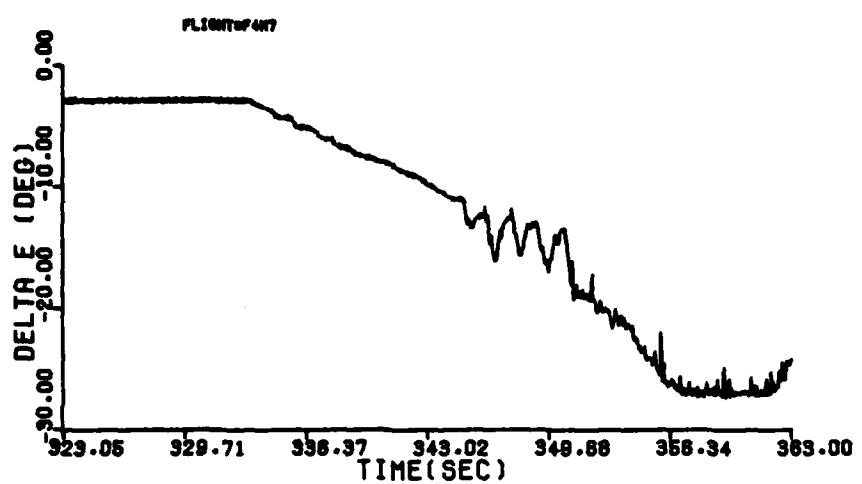


Figure B-14 (cont'd)

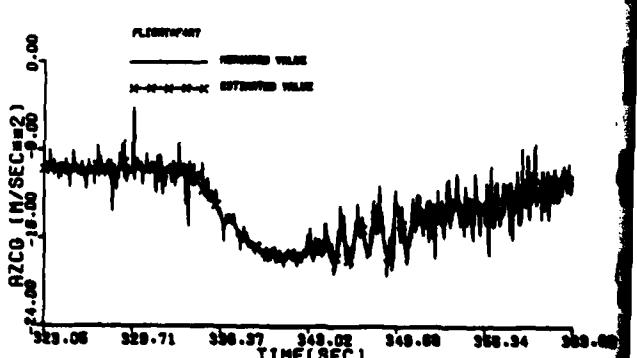
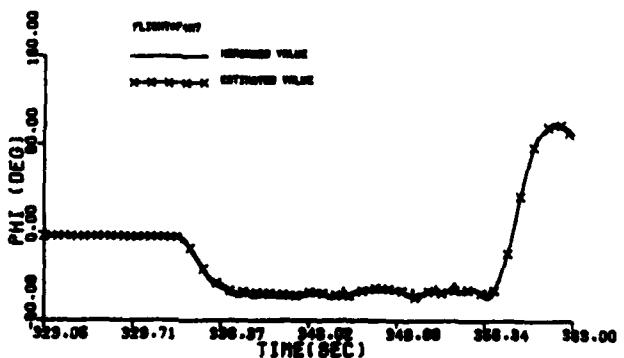
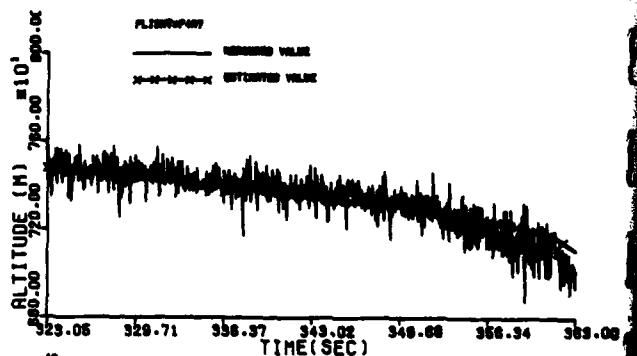
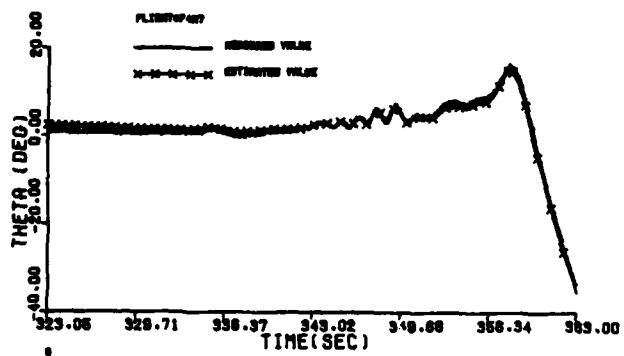
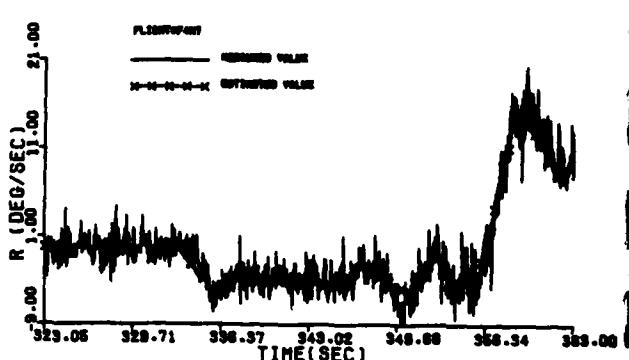
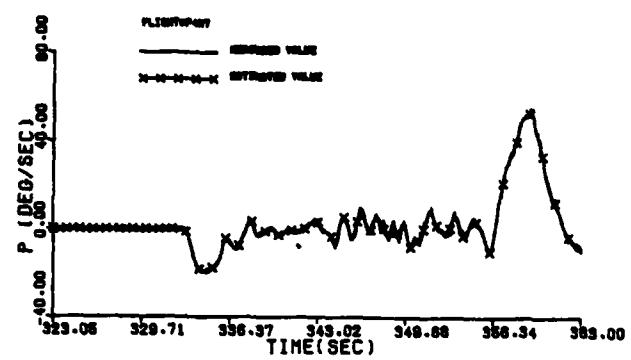
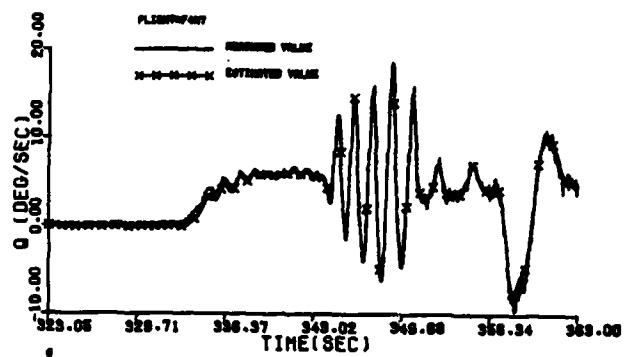
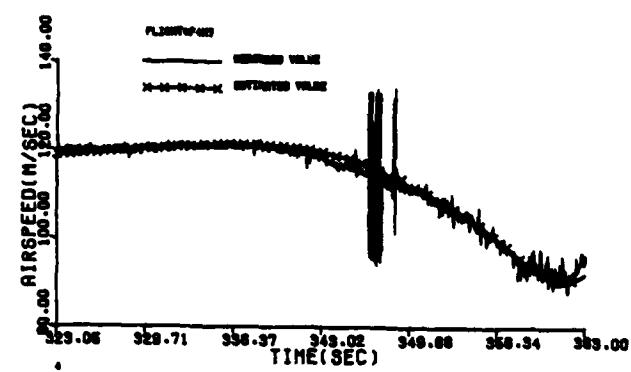


Figure B-14 (cont'd)

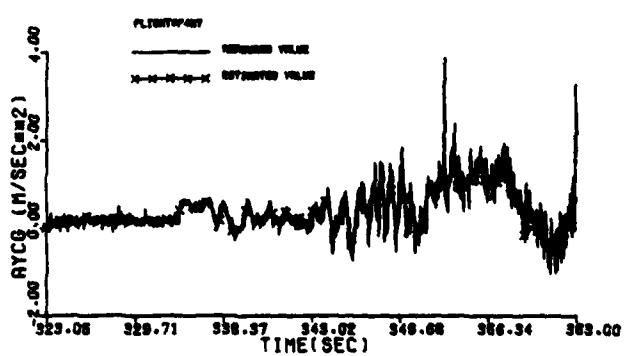
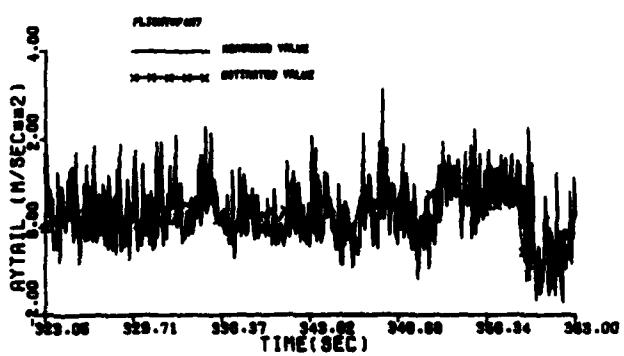
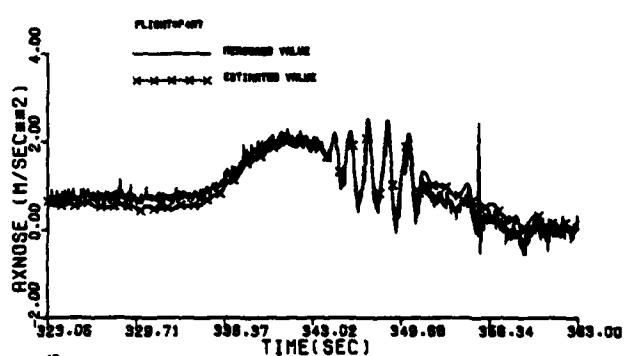
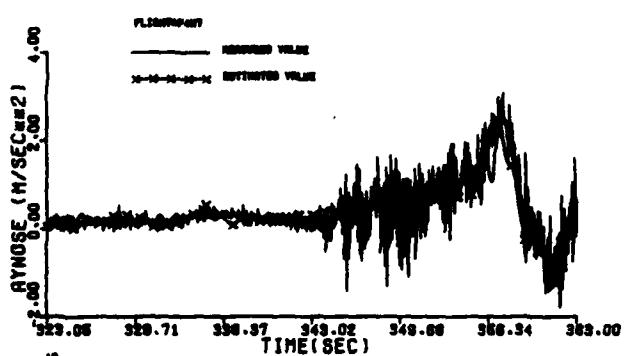
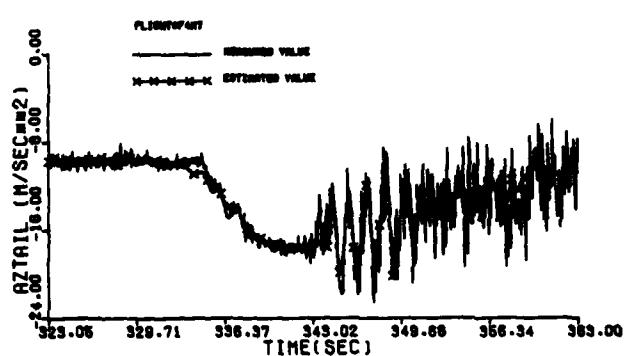
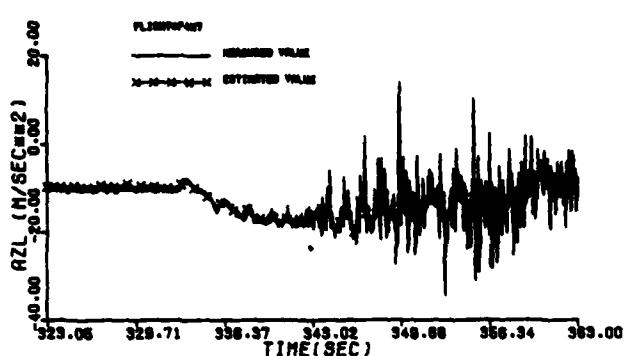
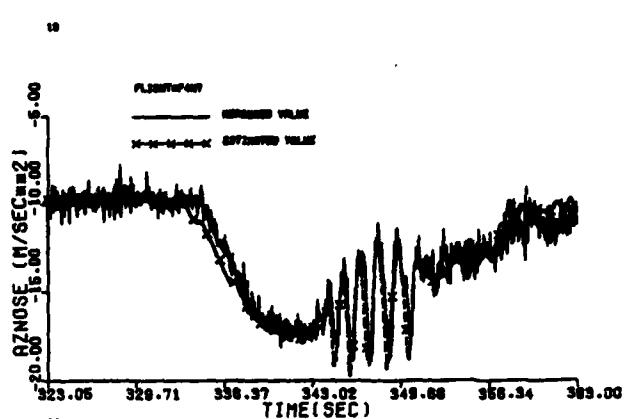
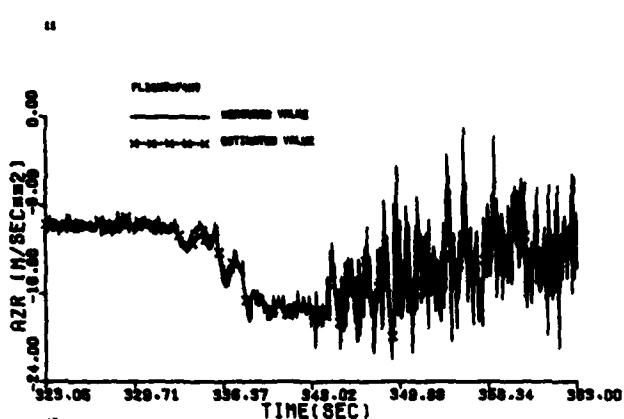


Figure B-14 (concluded)

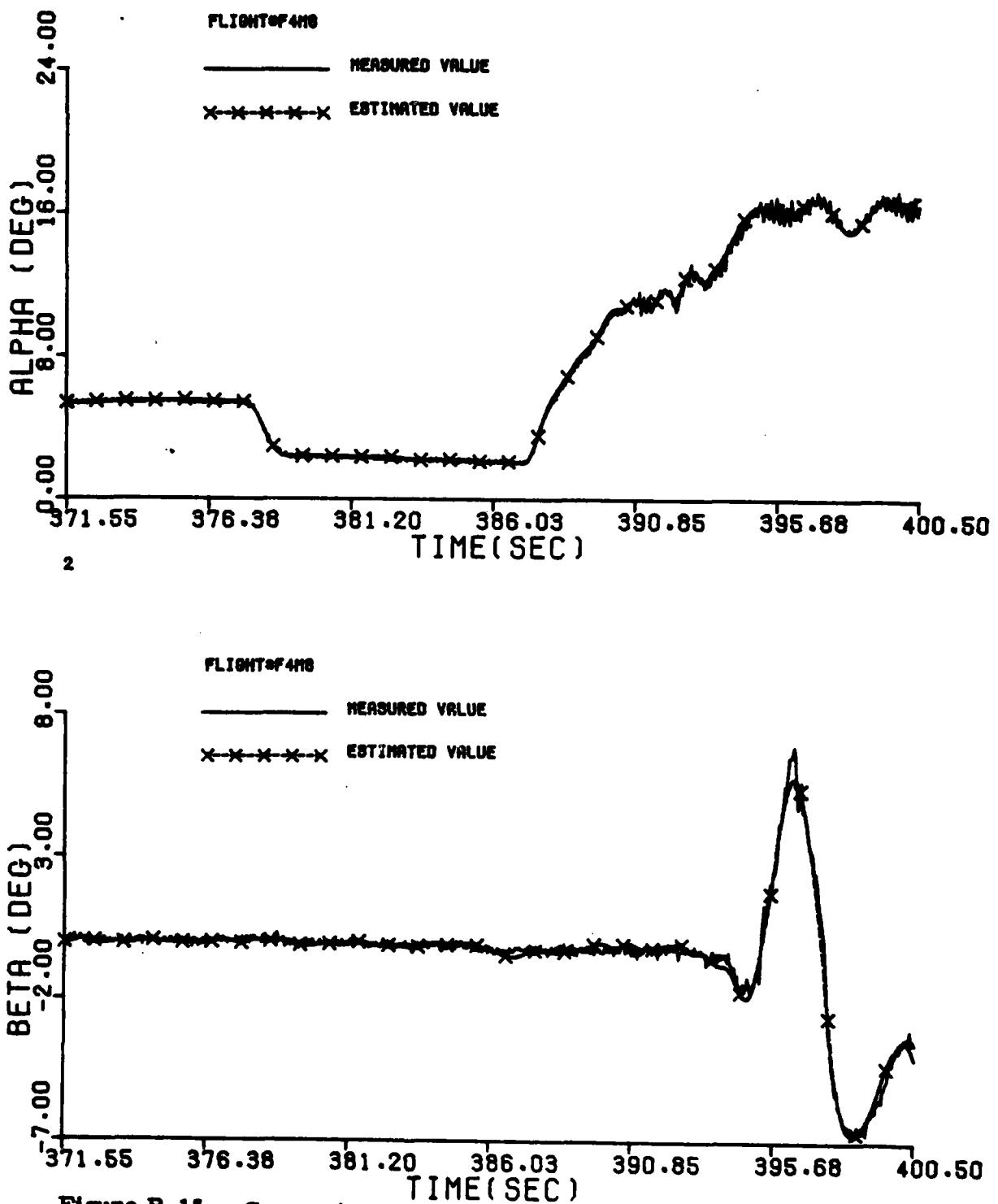


Figure B-15 Comparison Between the Measured and the Estimated Values of Maneuver 8 of Flight 4

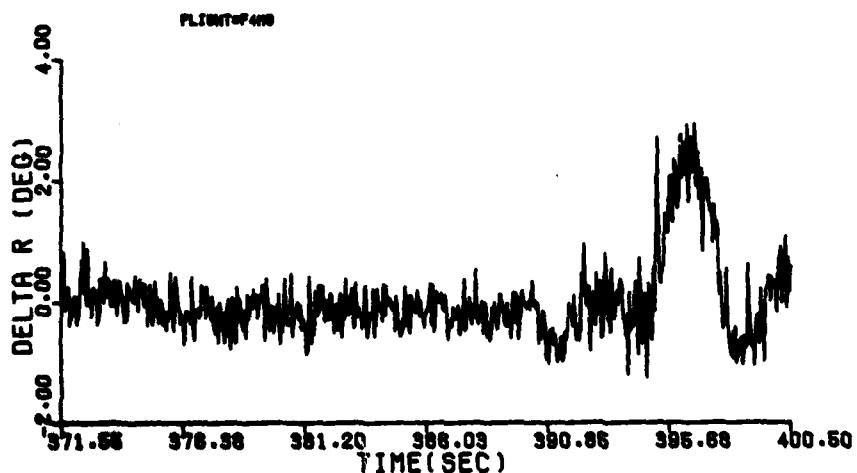
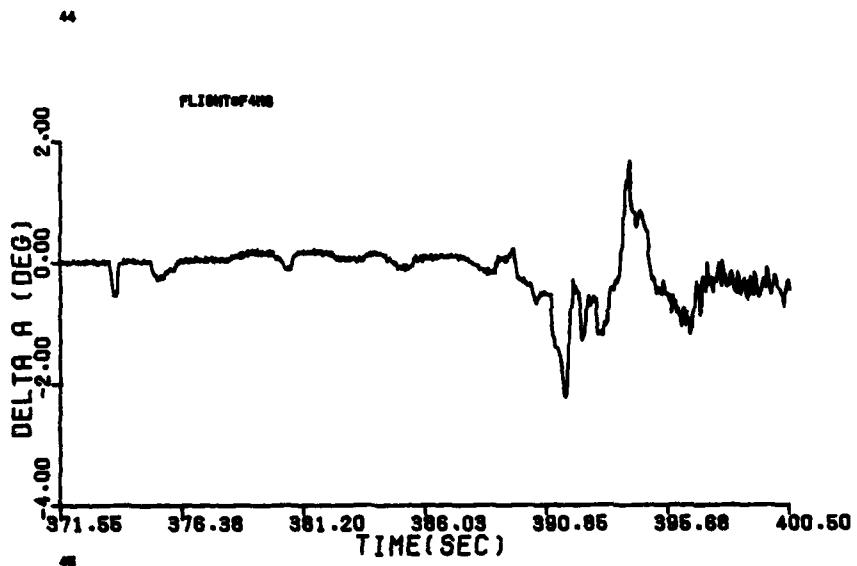
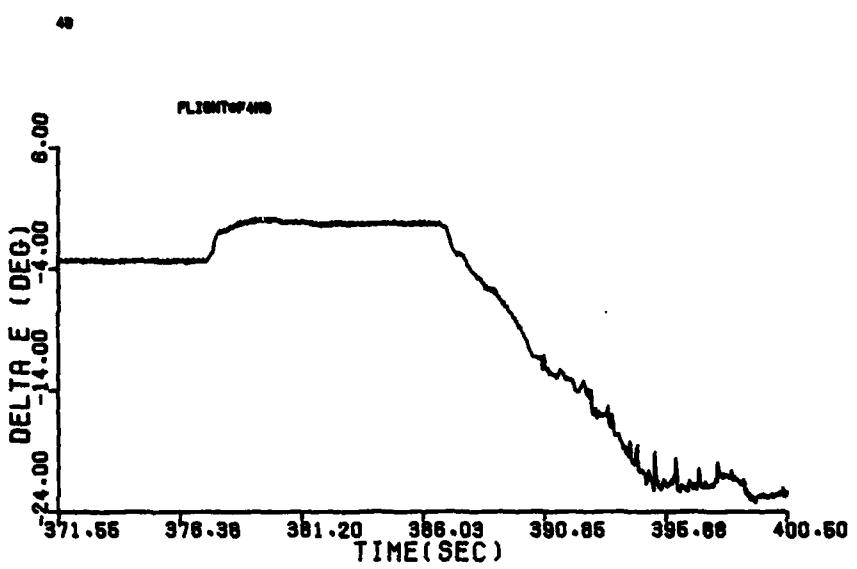


Figure B-15 (cont'd)

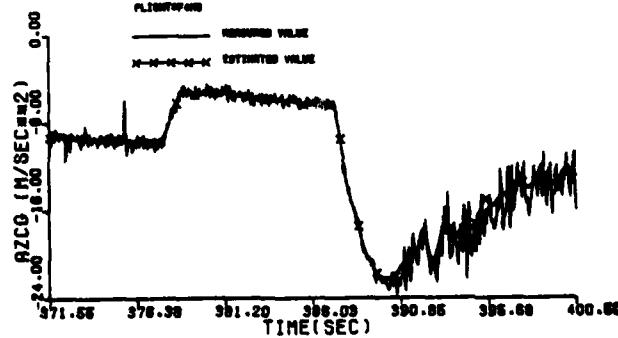
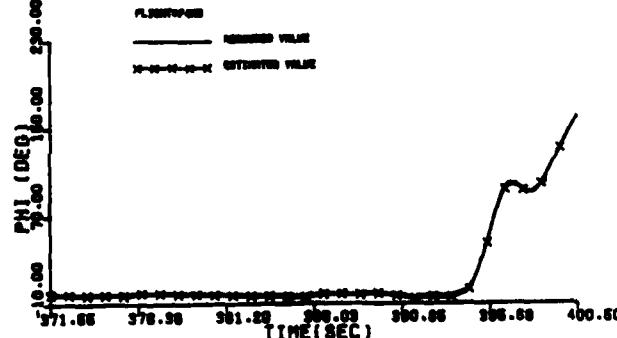
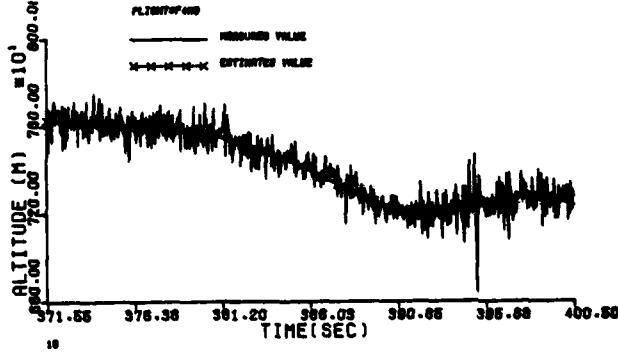
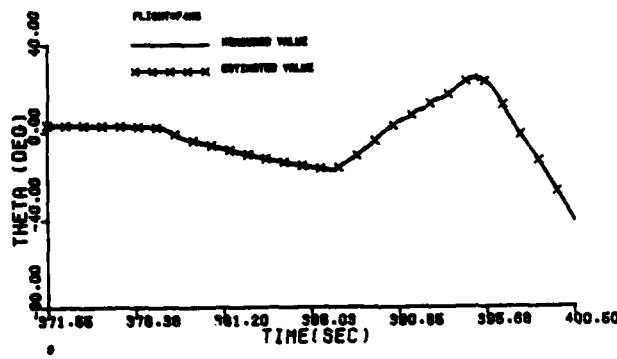
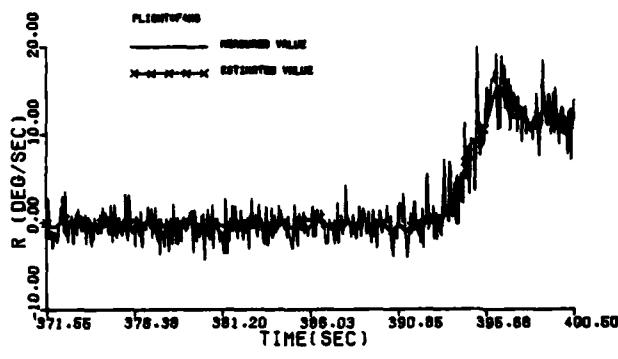
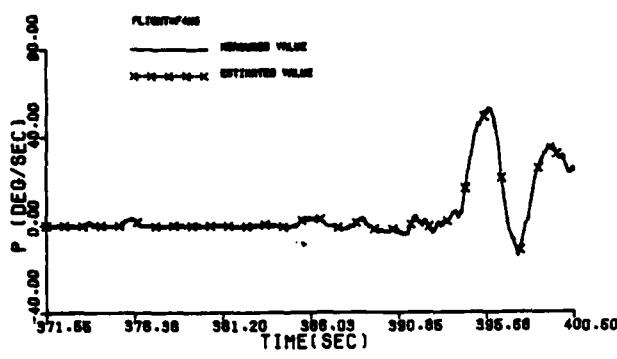
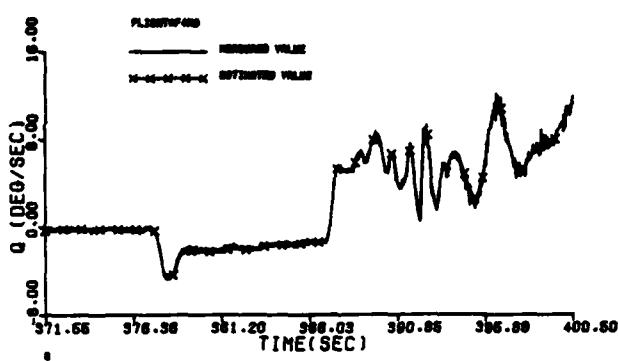
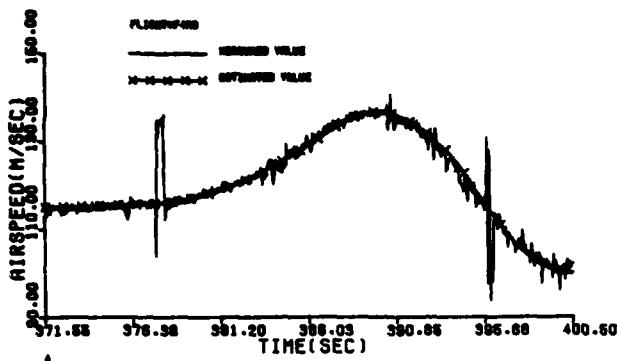


Figure B-15 (cont'd)

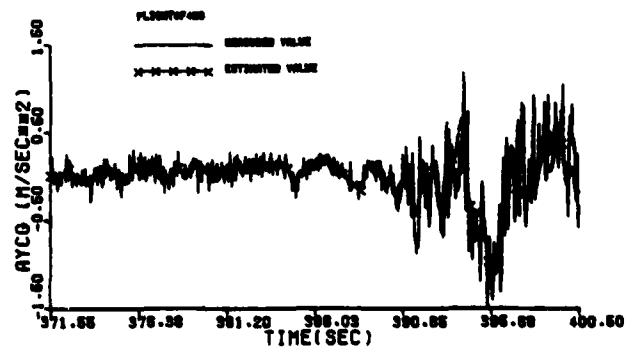
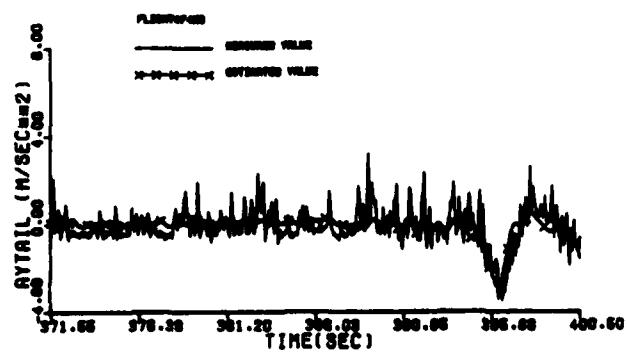
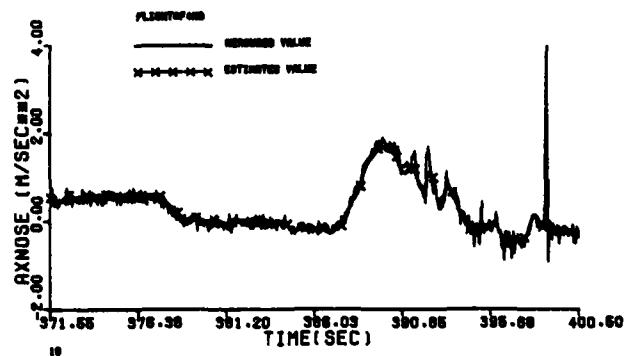
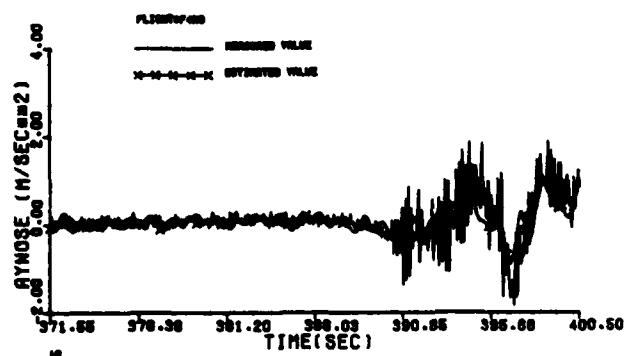
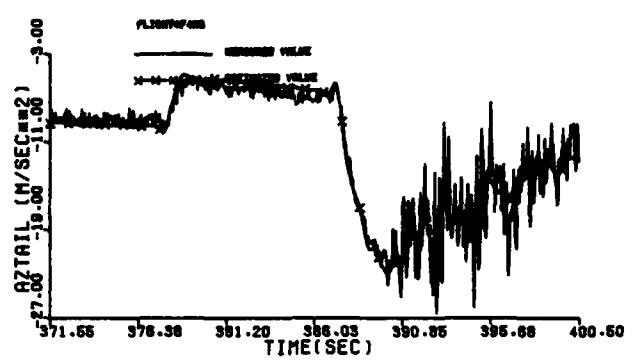
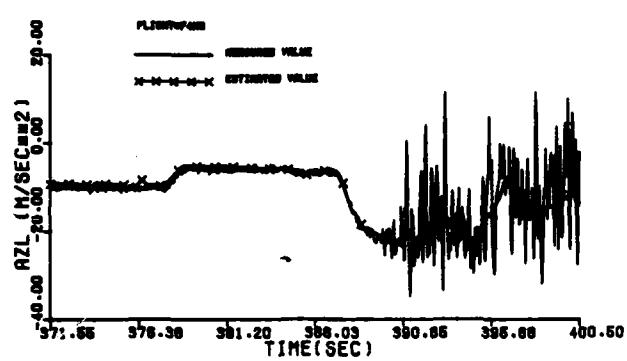
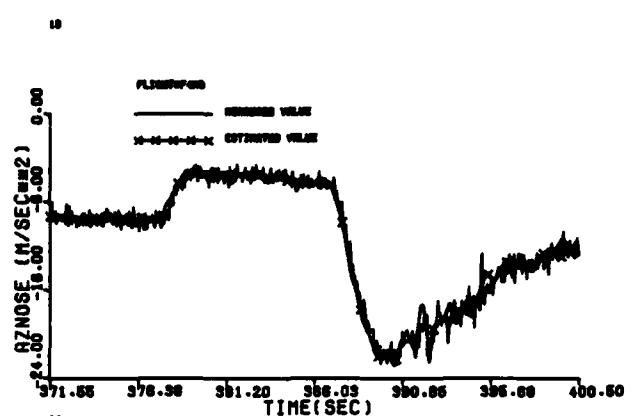
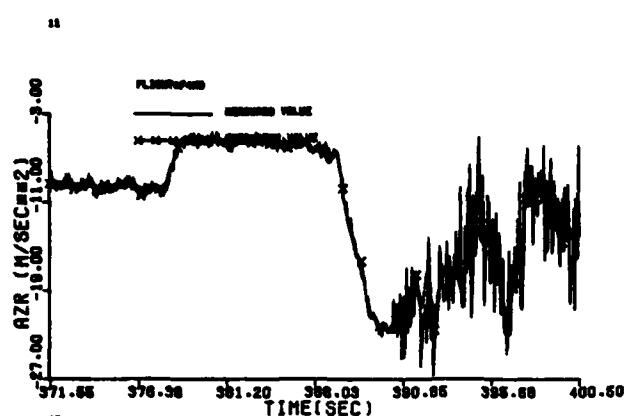


Figure B-15 (concluded)

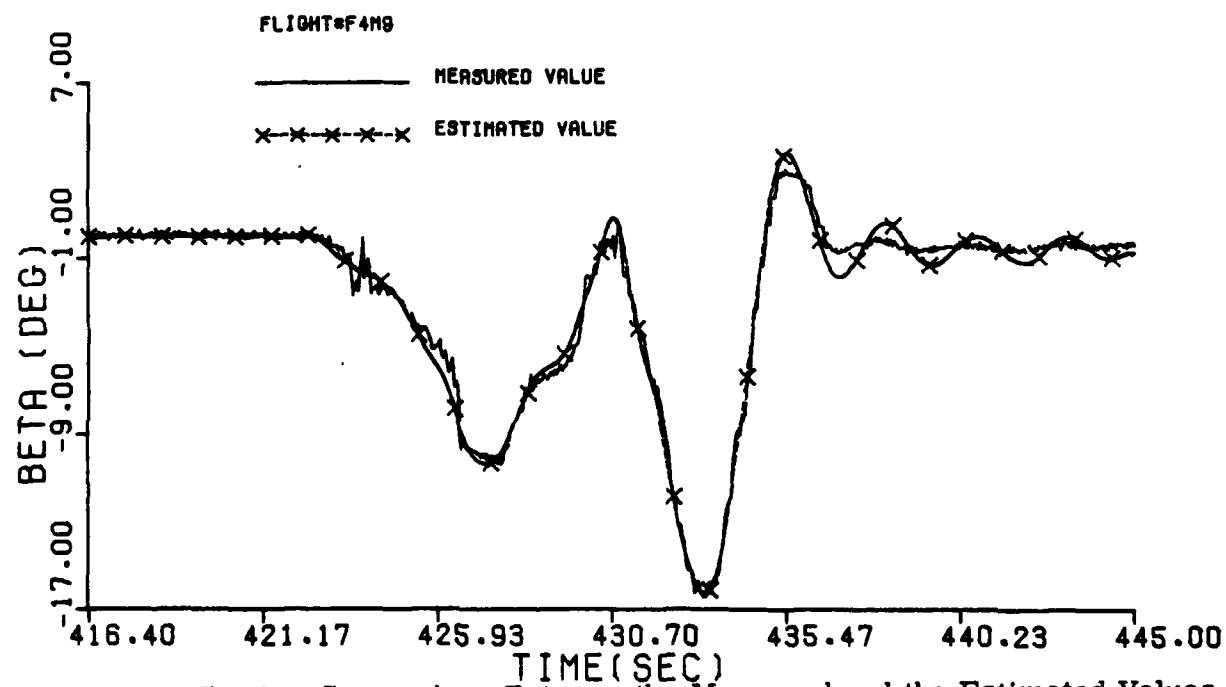
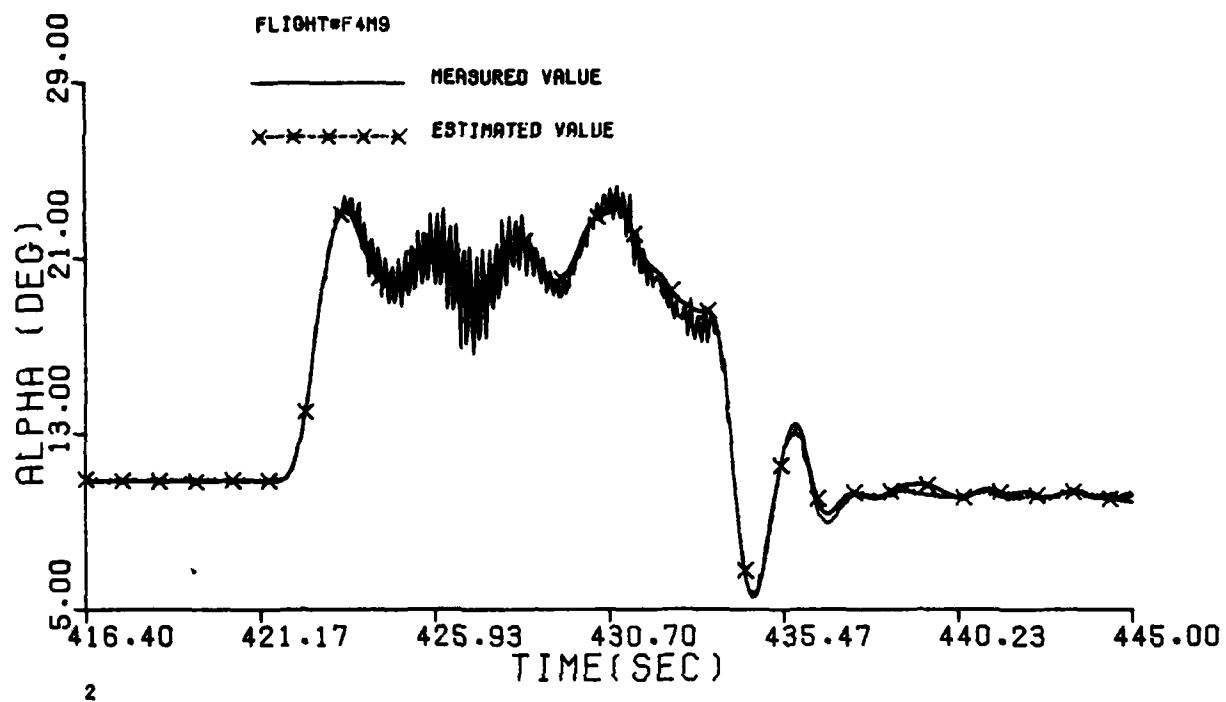


Figure B-16 Comparison Between the Measured and the Estimated Values of Maneuver 9 of Flight 4

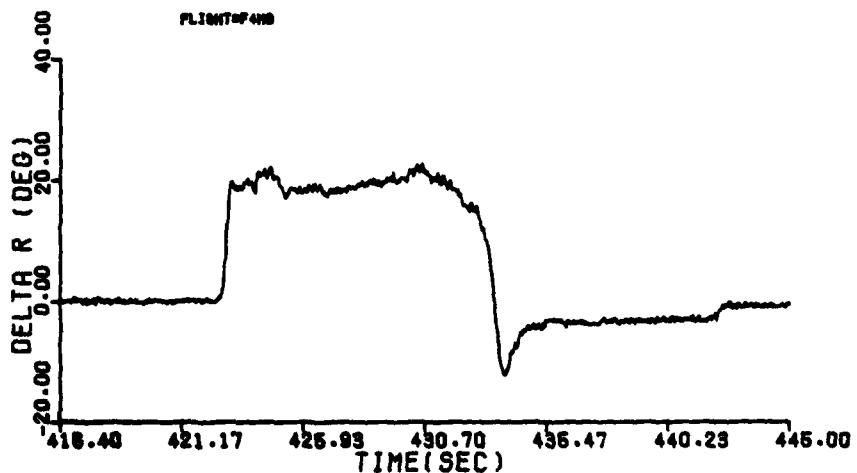
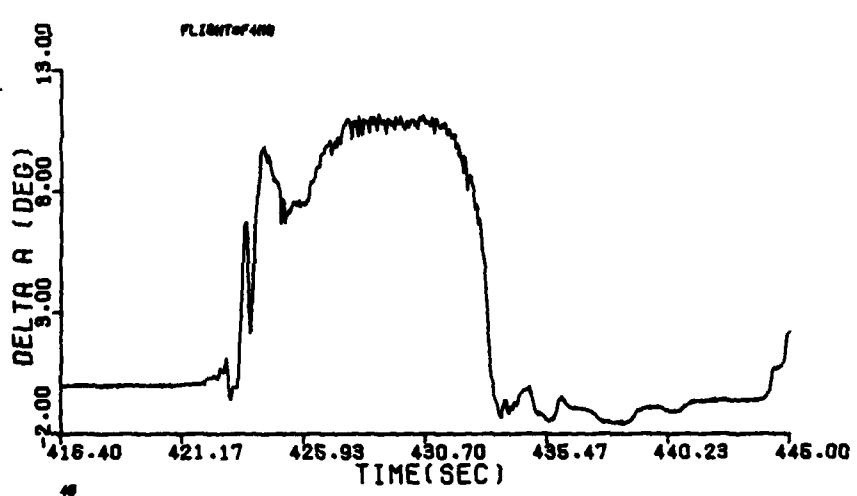
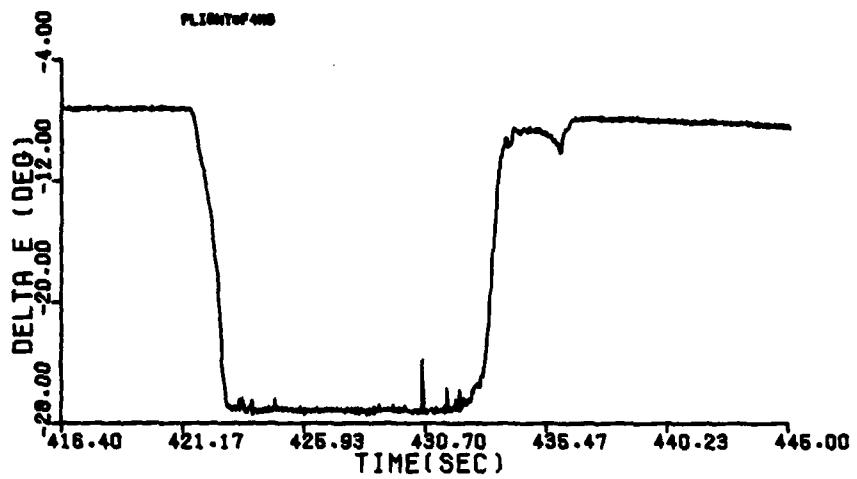


Figure B-16 (cont'd)

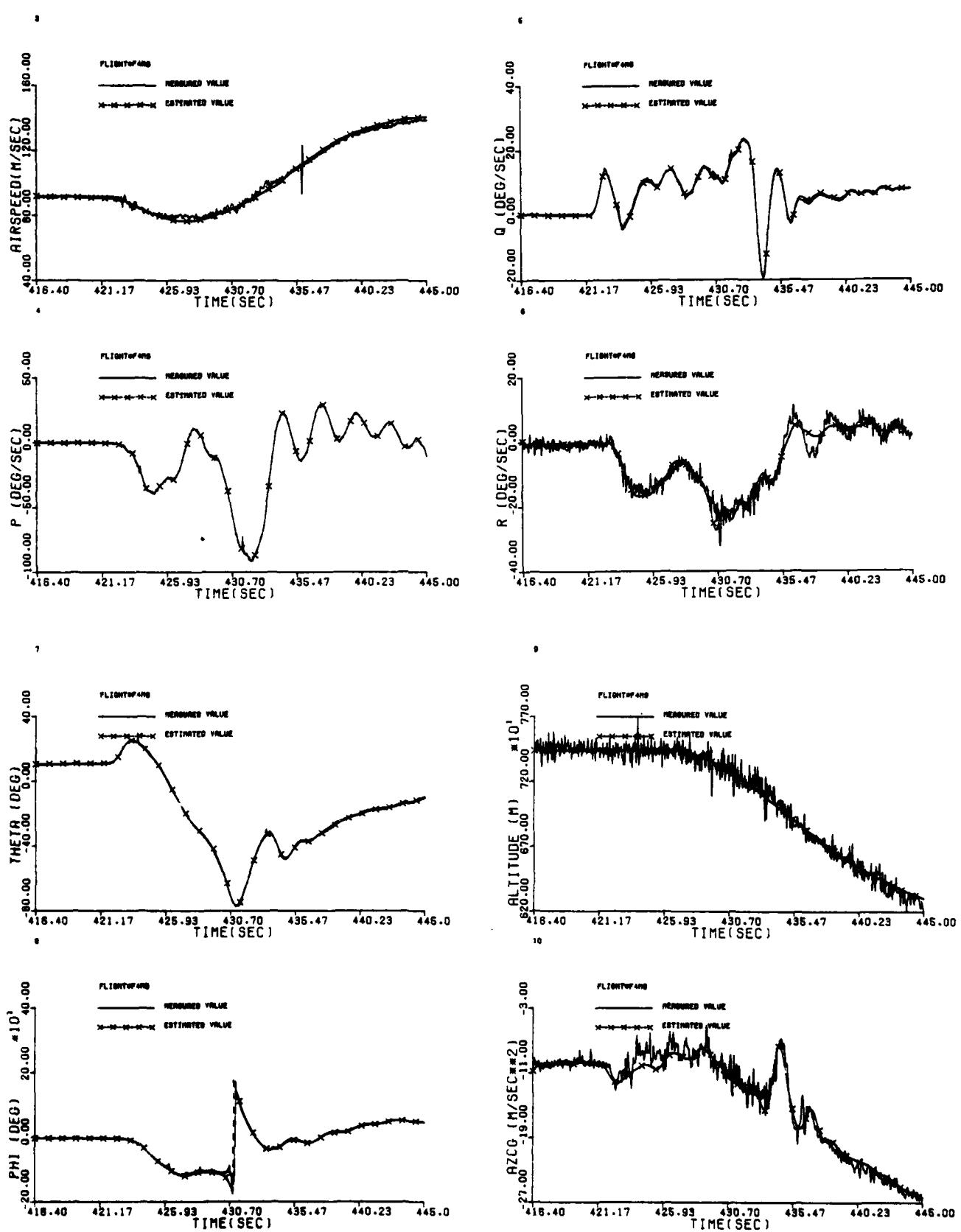
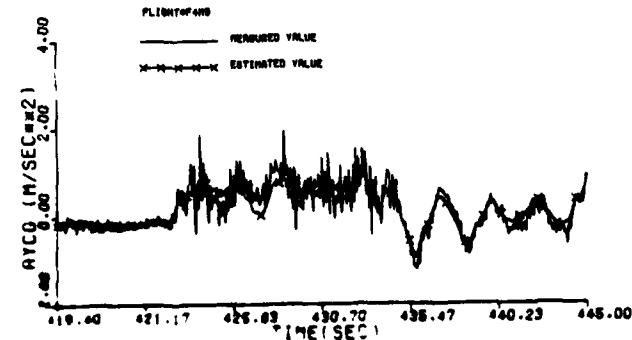
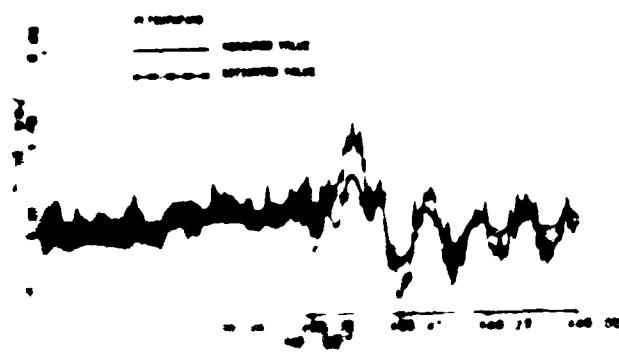
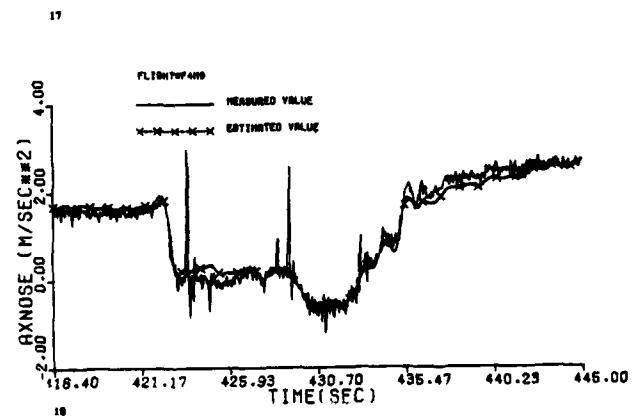
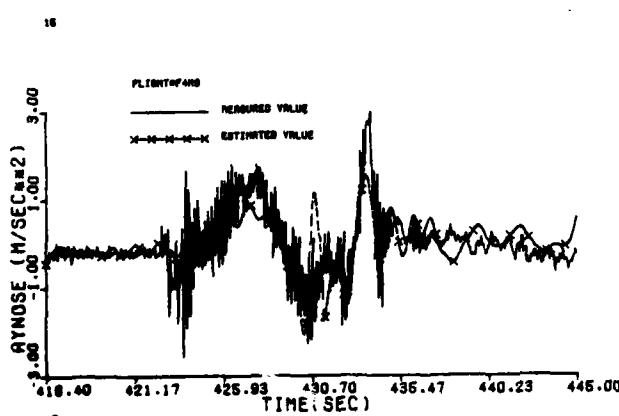
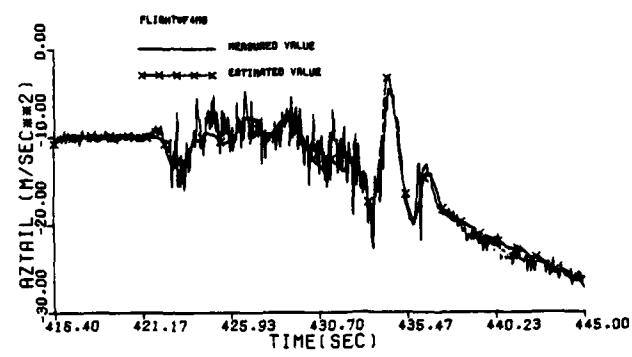
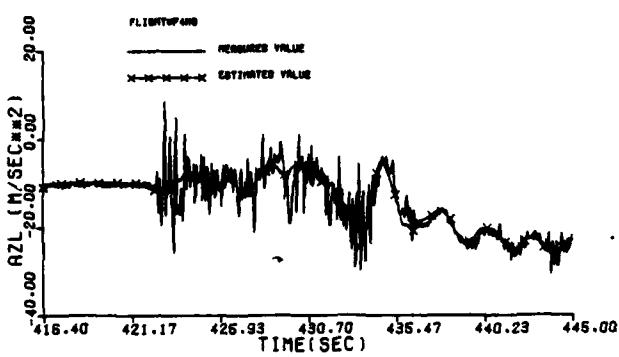
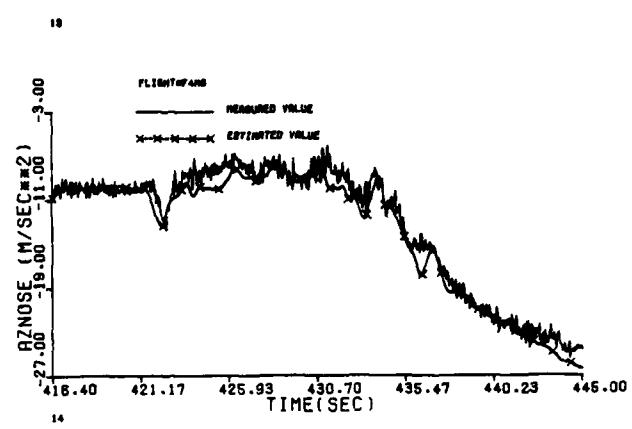
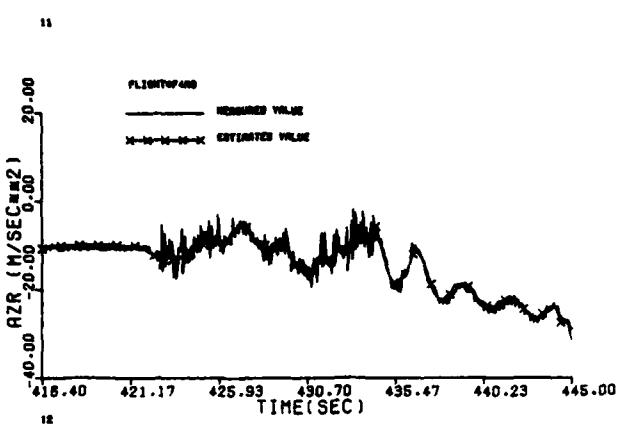


Figure B-16 (cont'd)



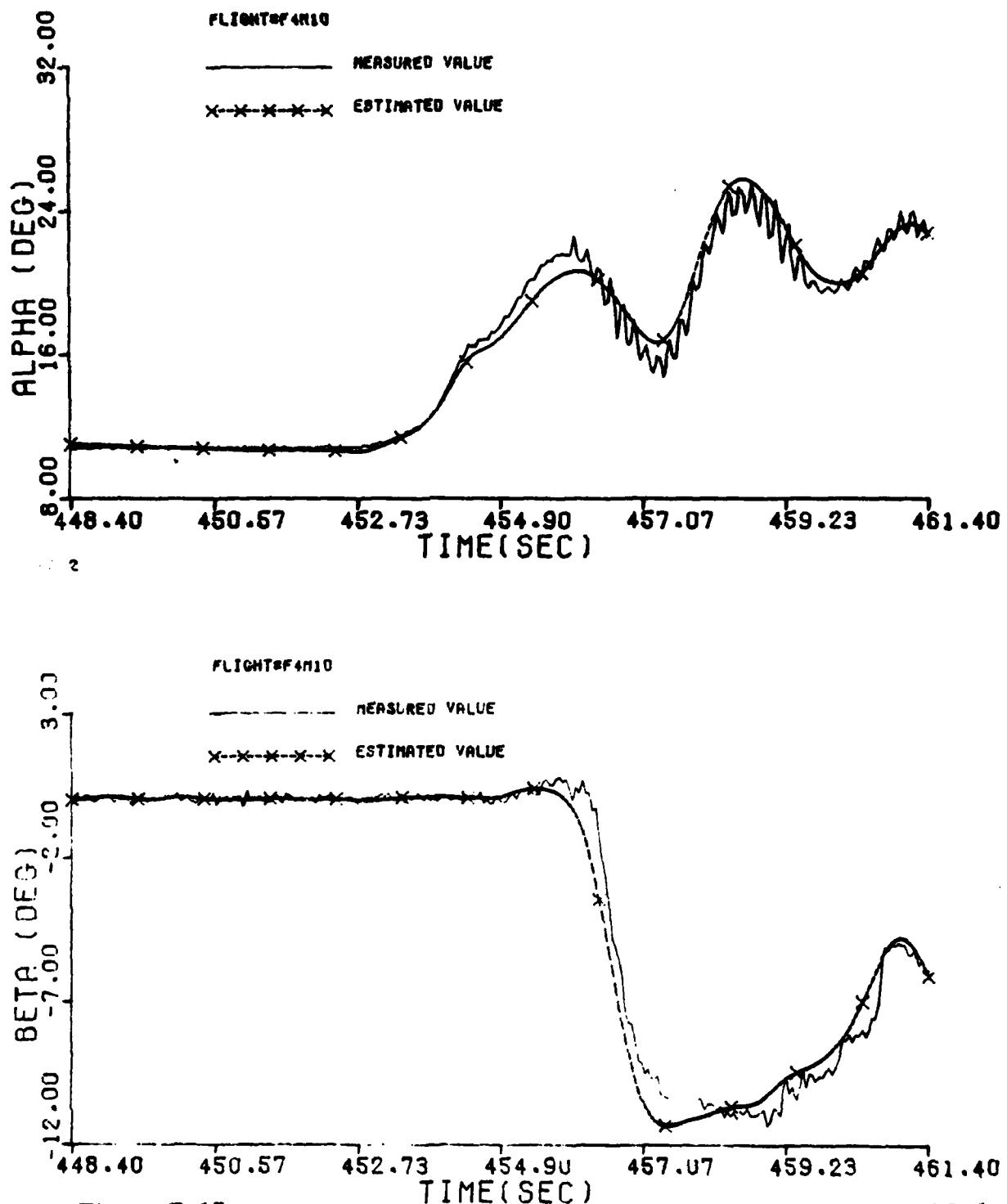


Figure B-17a Comparison Between the Measured and the Estimated Values of Maneuver 10a of Flight 4

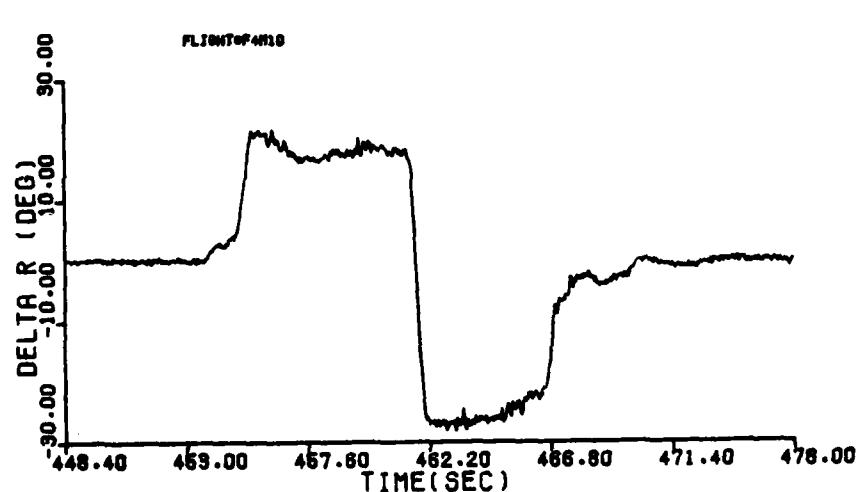
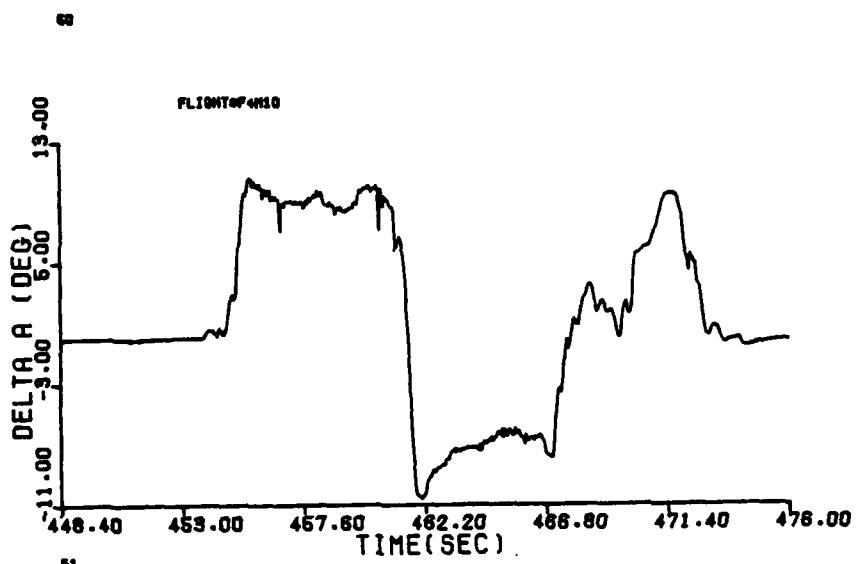
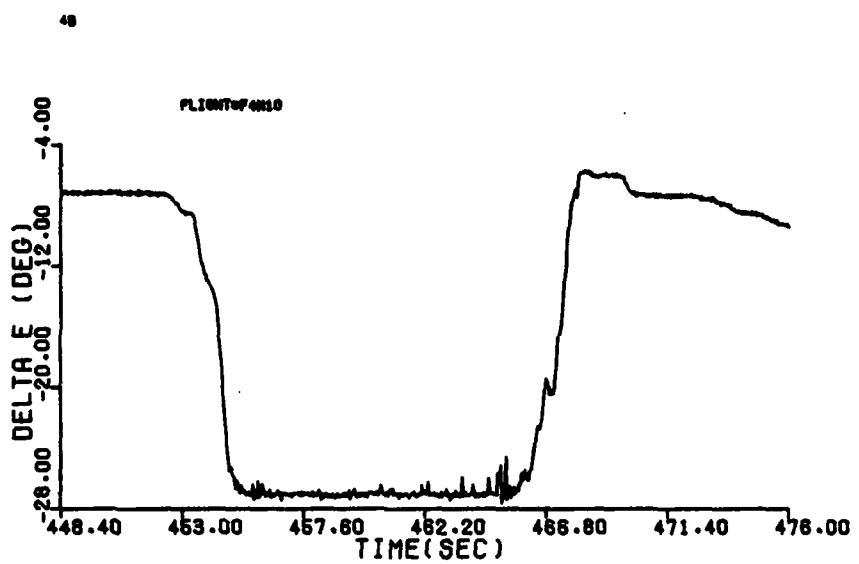


Figure B-17a (cont'd)

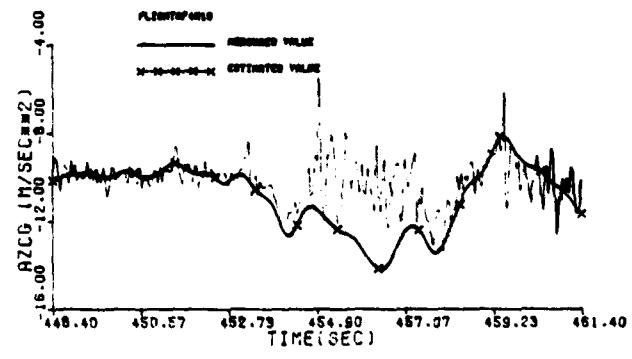
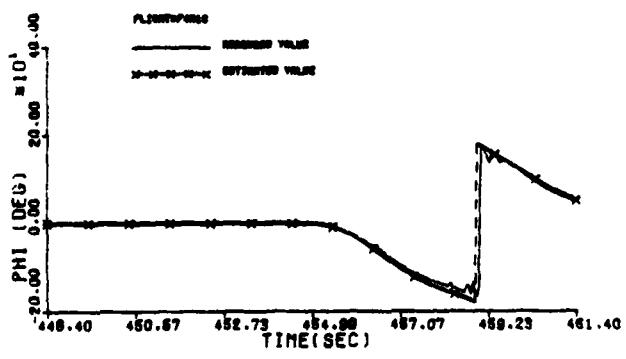
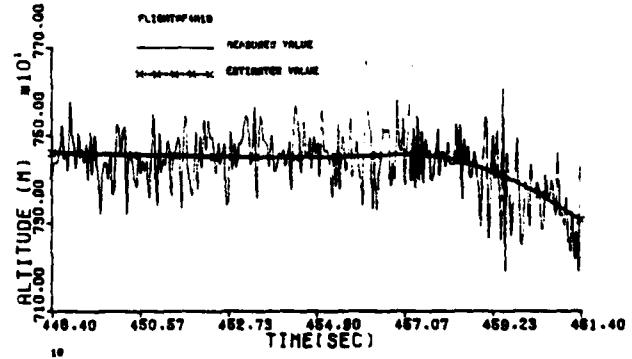
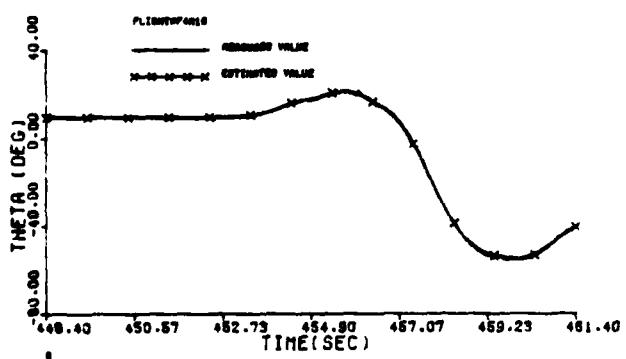
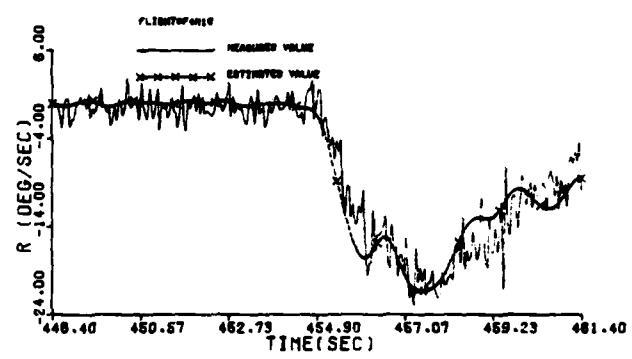
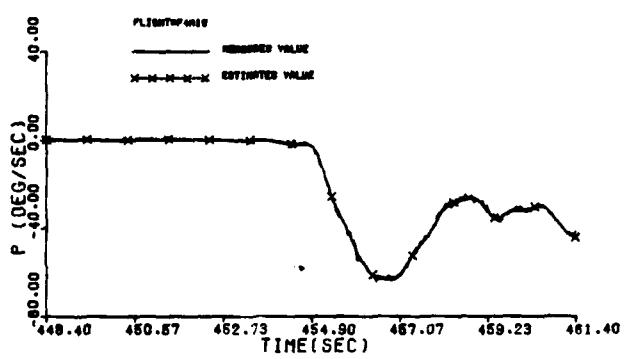
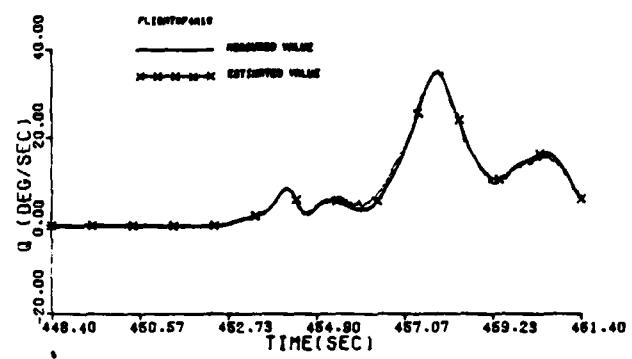
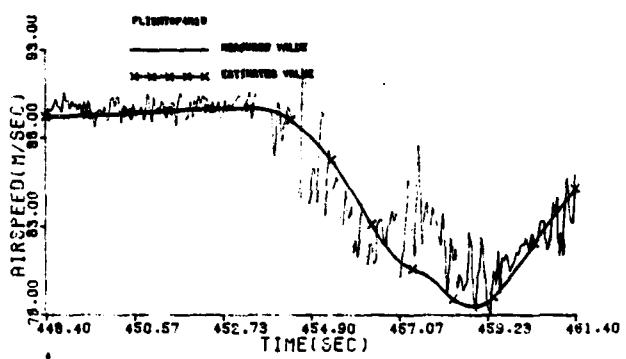


Figure B-17a (cont'd)

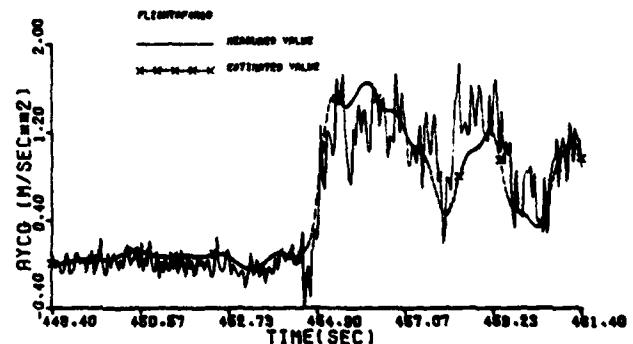
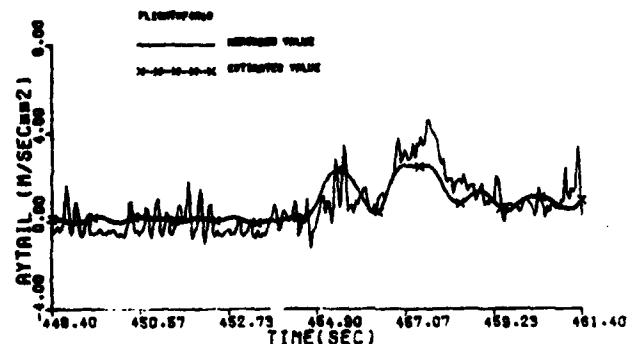
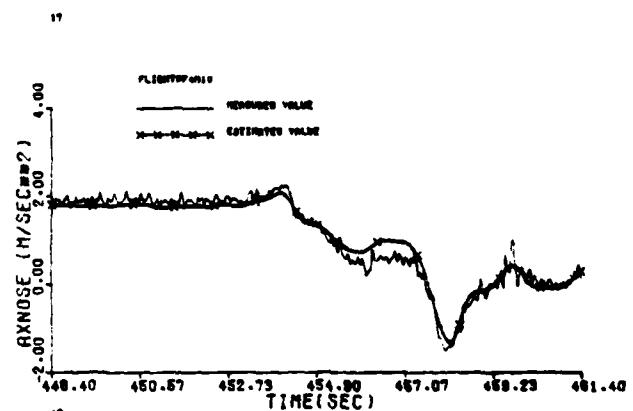
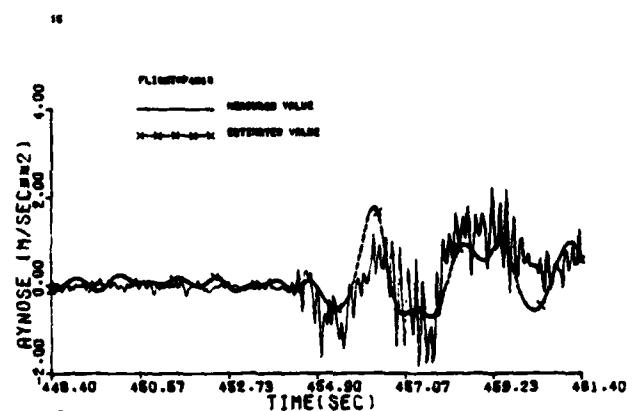
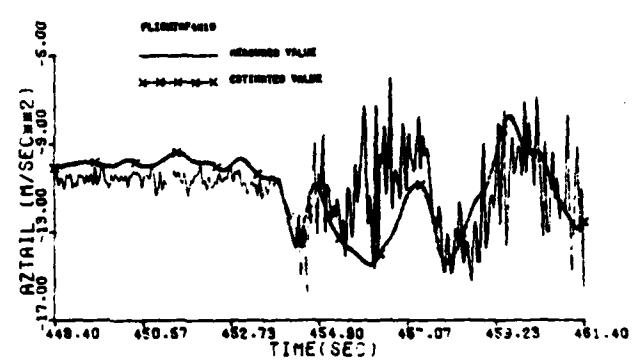
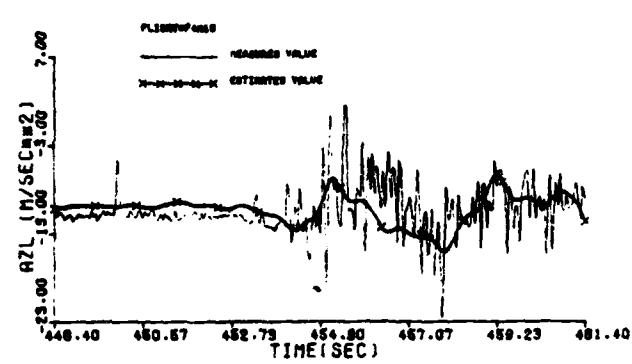
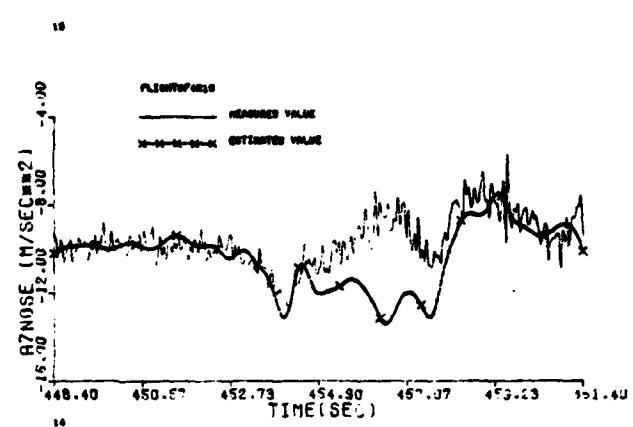
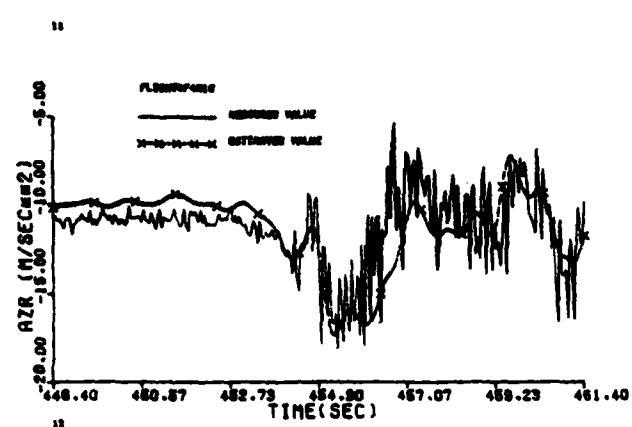


Figure B-17a (concluded)

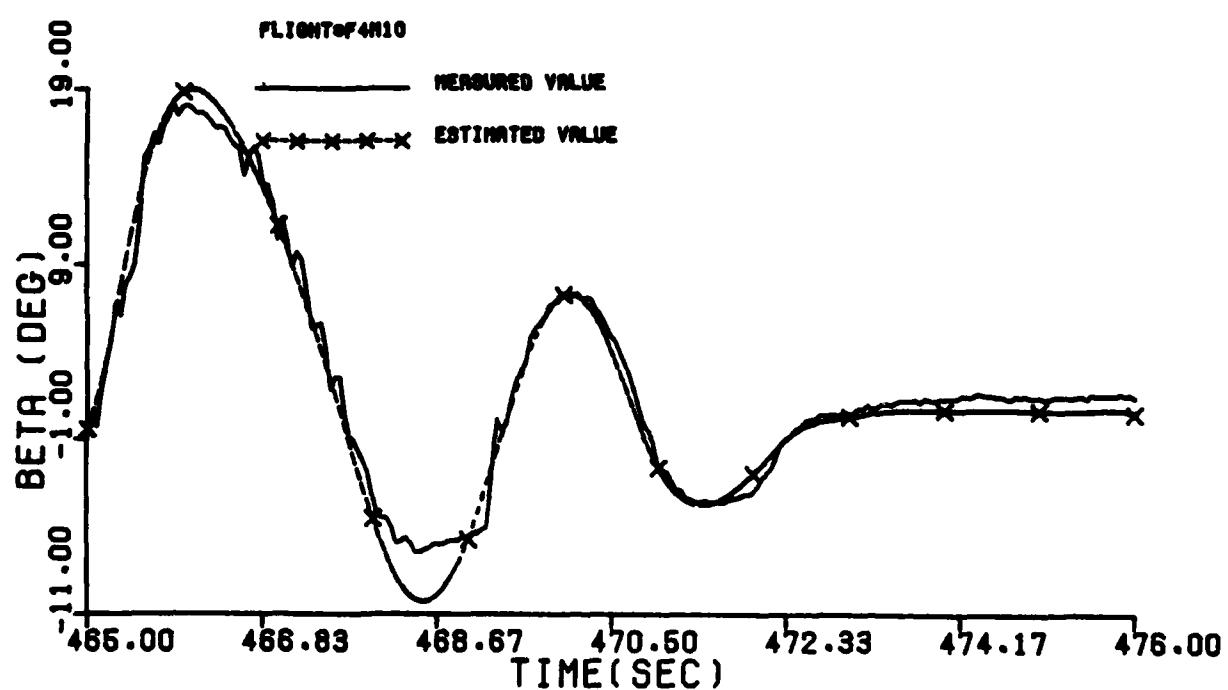
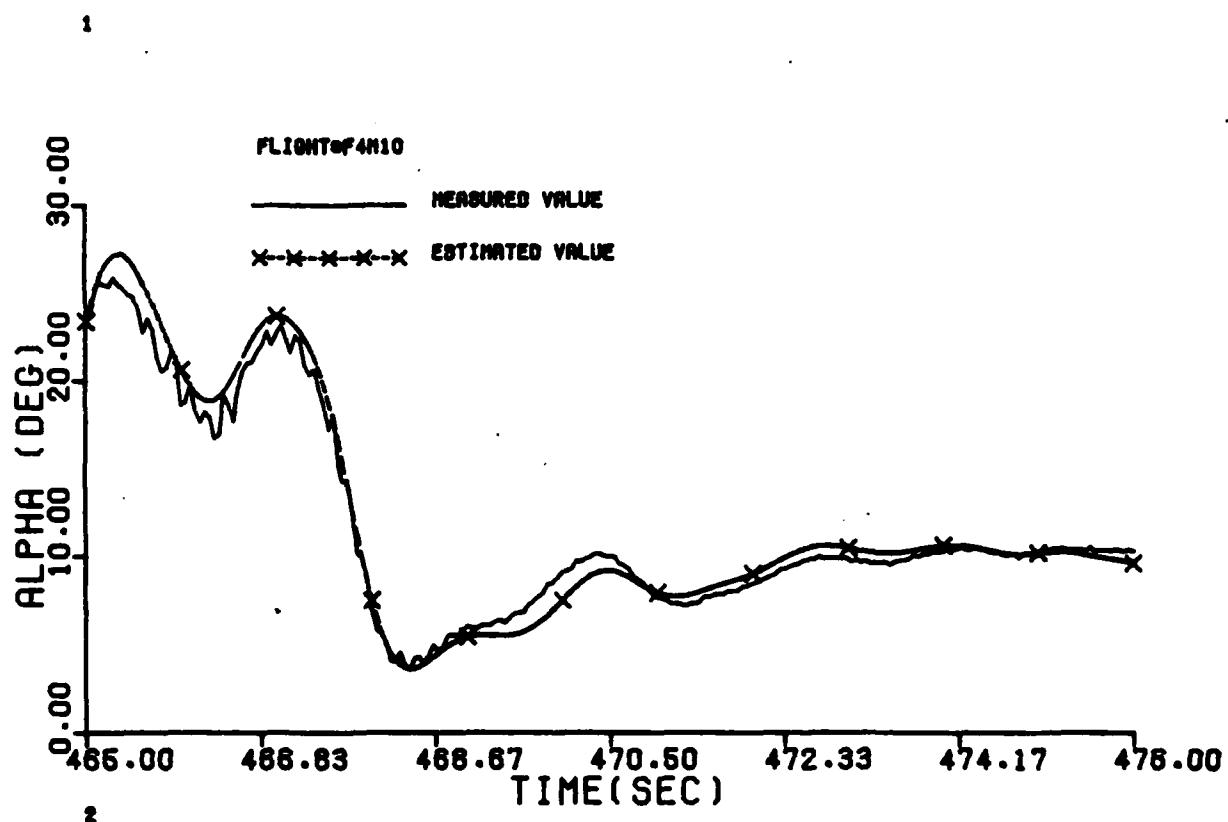


Figure B-17b Comparison Between the Measured and the Estimated Values of Maneuver 10b of Flight 4

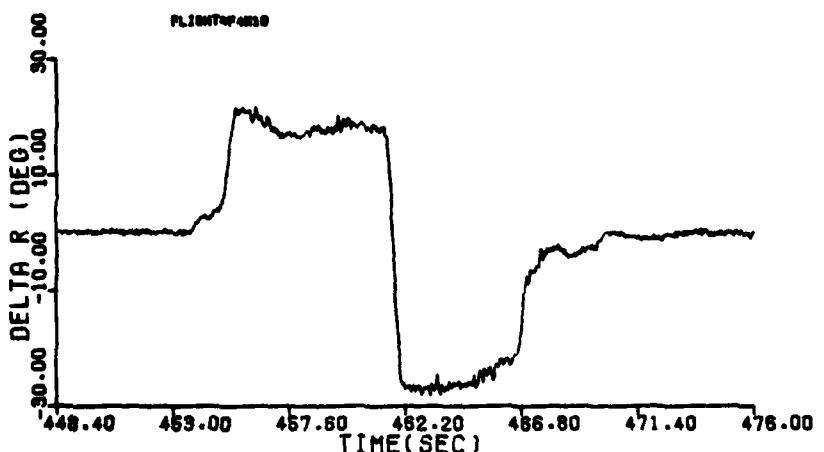
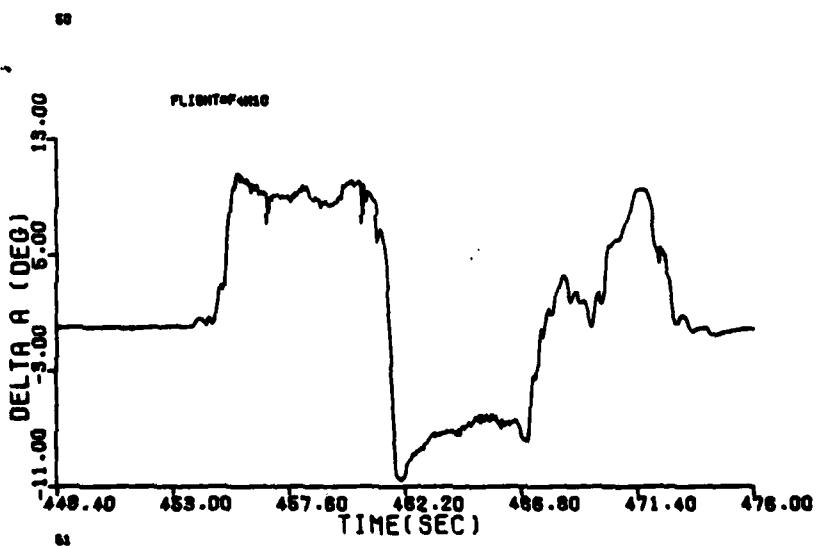
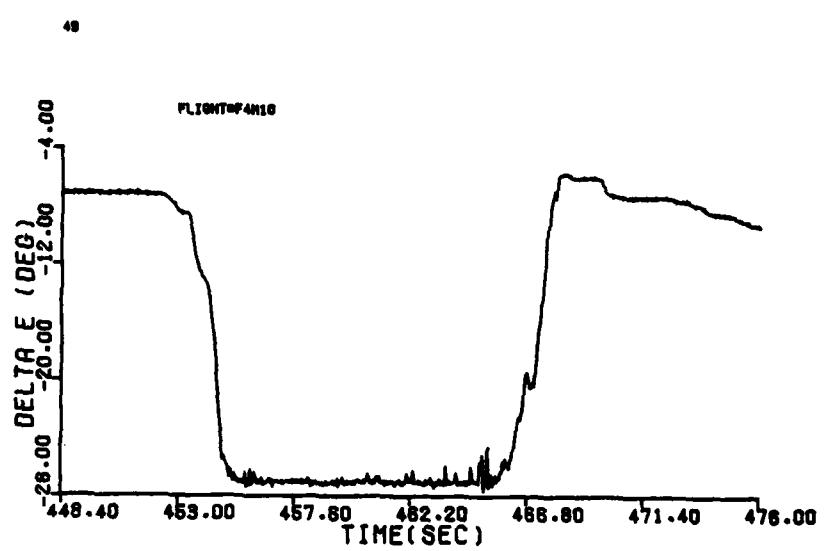


Figure B-17b (cont'd)

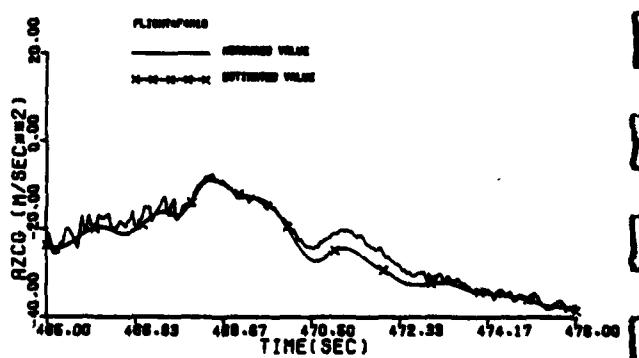
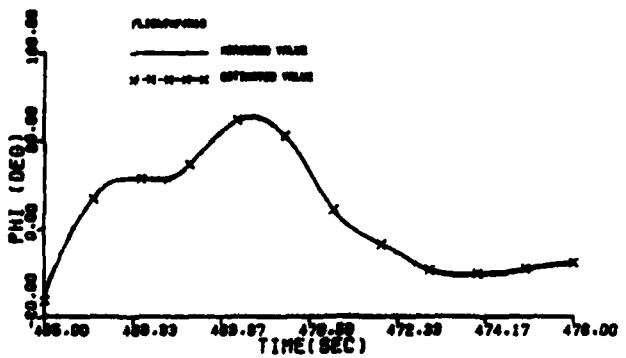
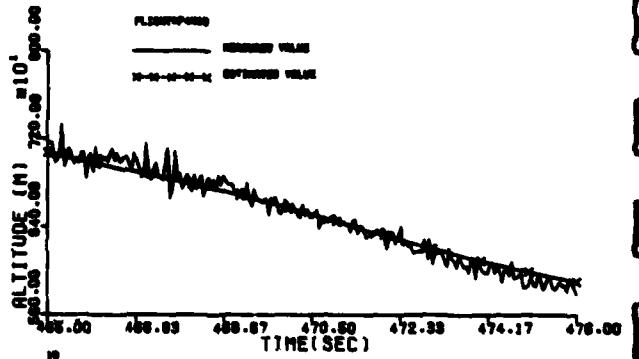
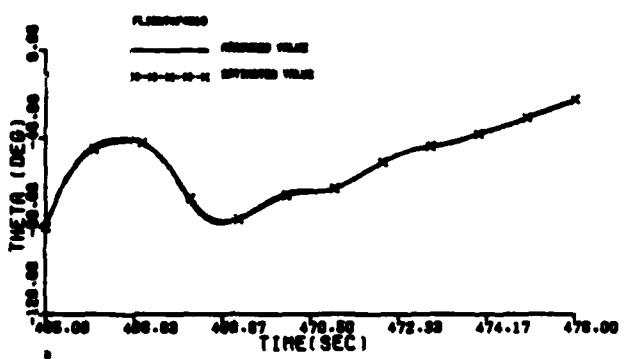
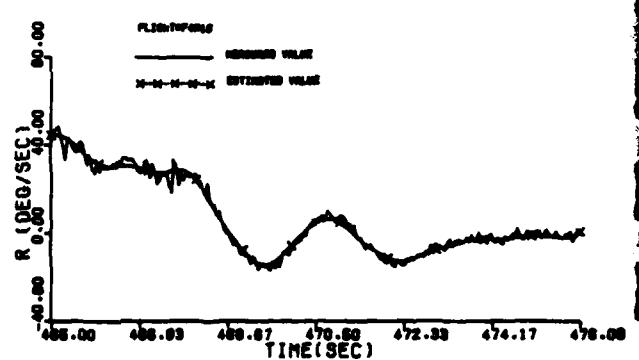
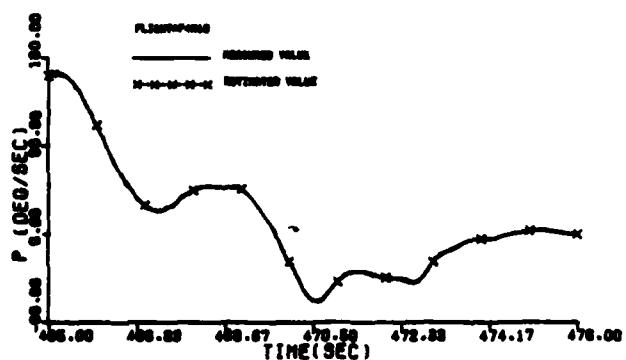
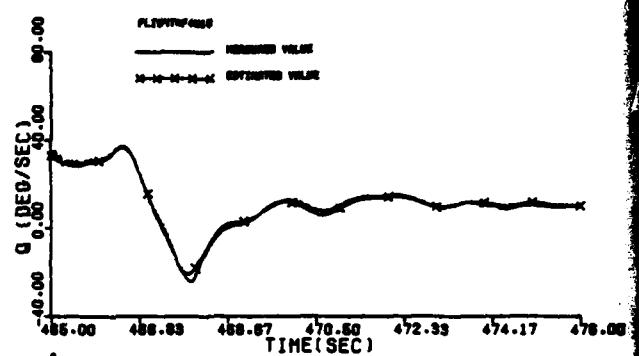
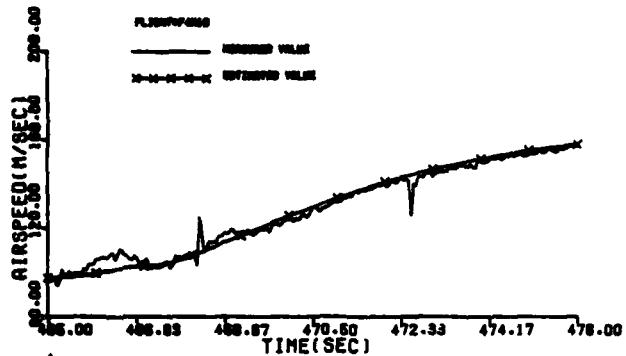


Figure B-17b (cont'd)

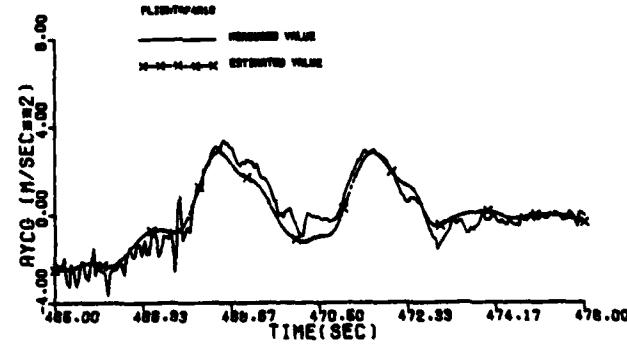
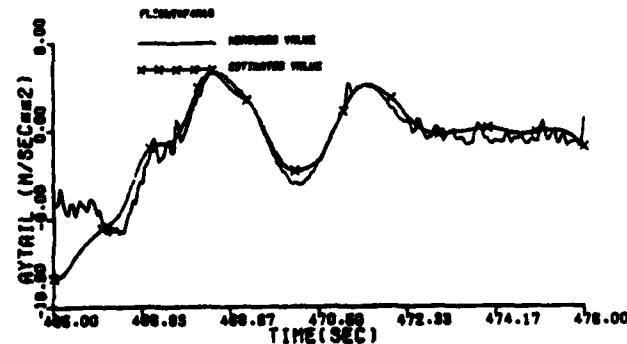
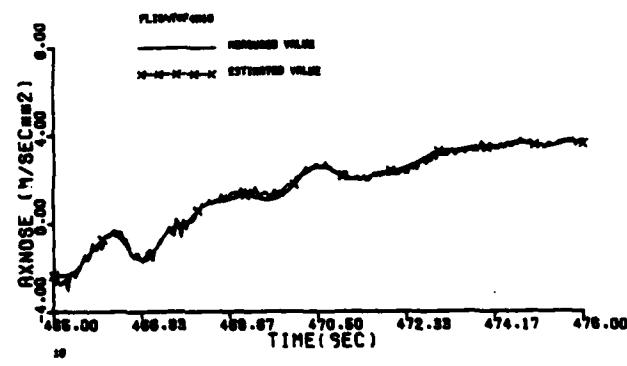
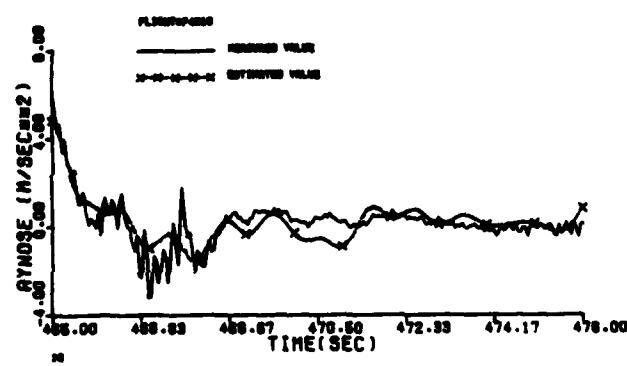
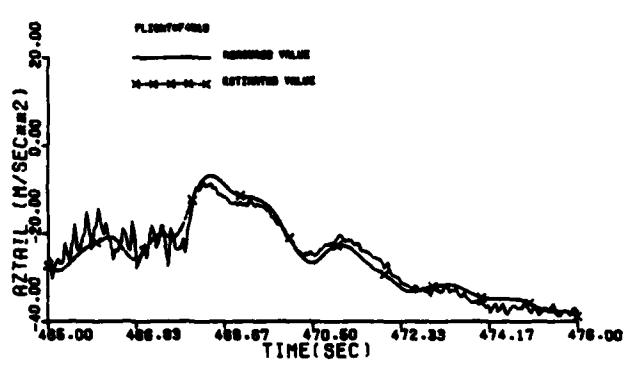
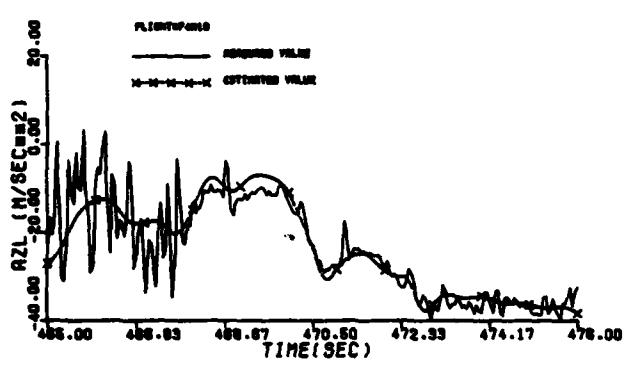
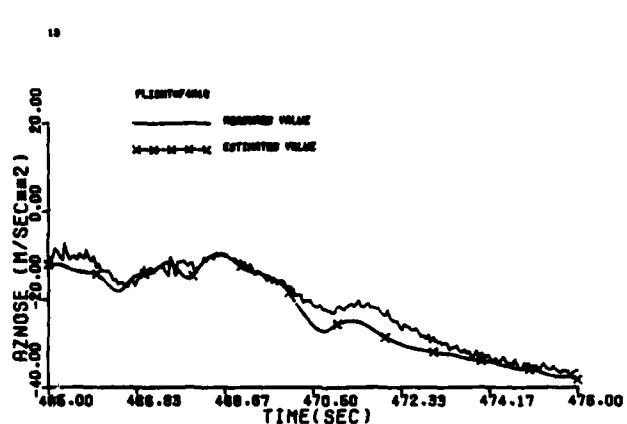
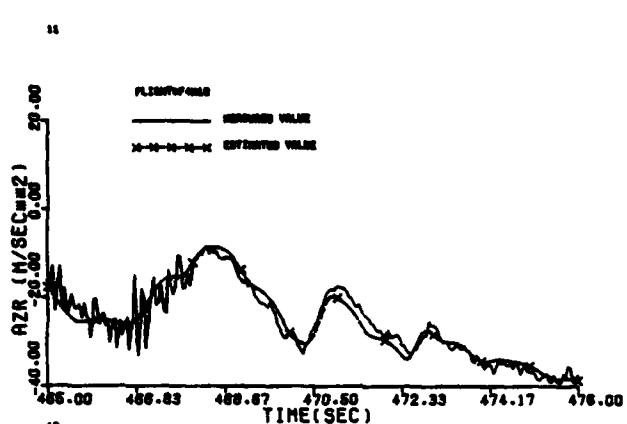


Figure B-17b (concluded)

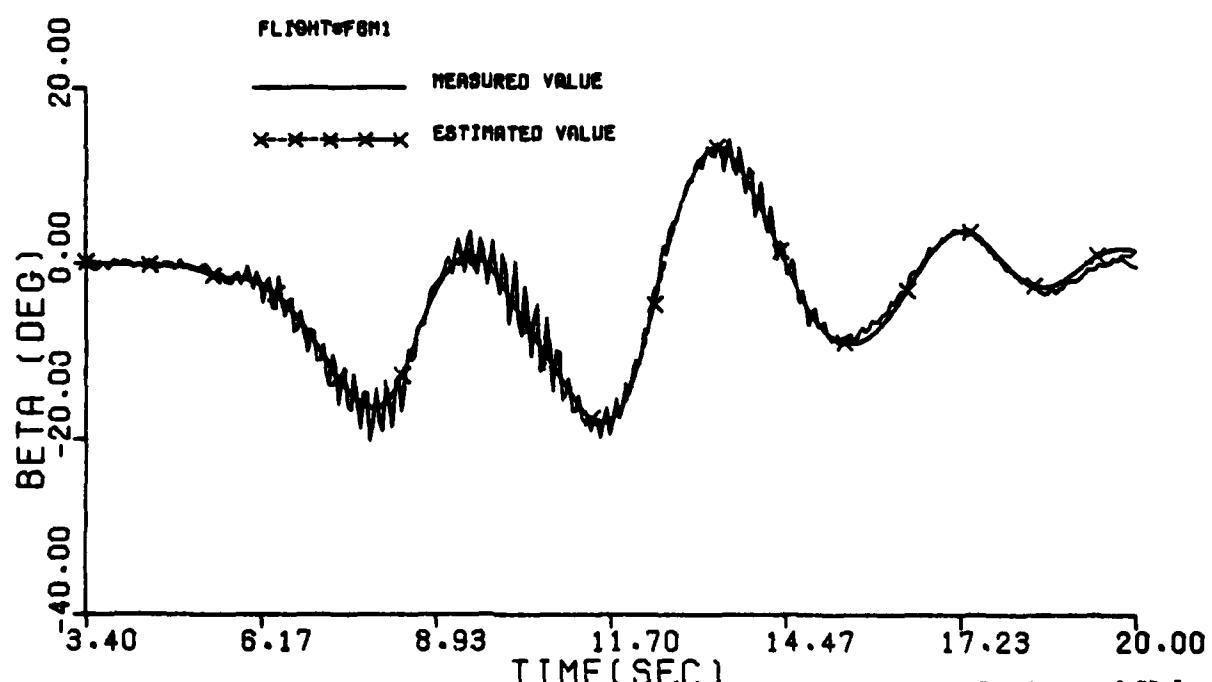
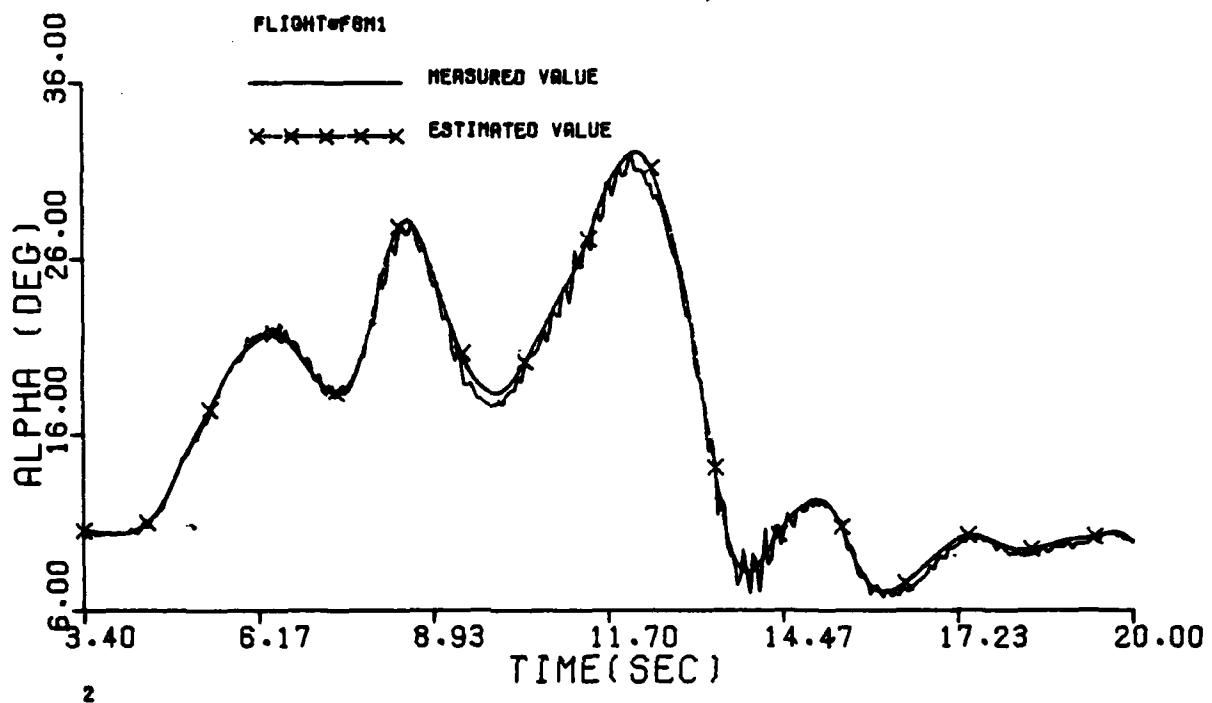


Figure B-18 Comparison Between the Measured and the Estimated Values of Maneuver 1 of Flight 6

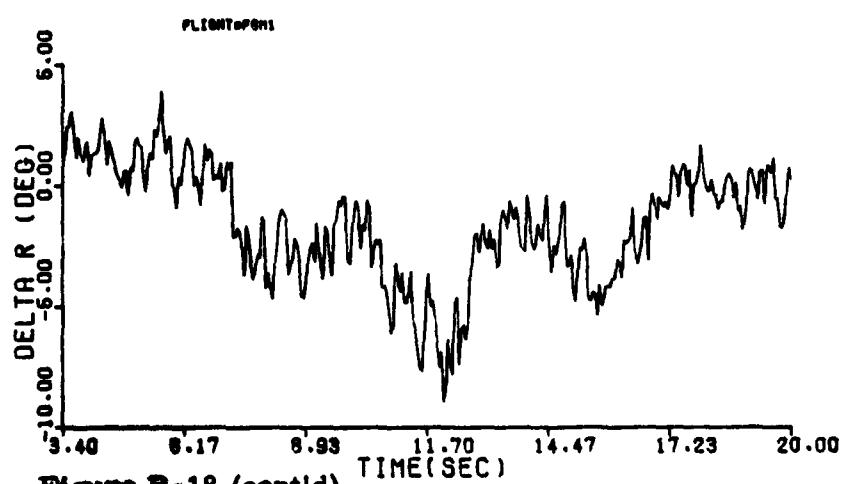
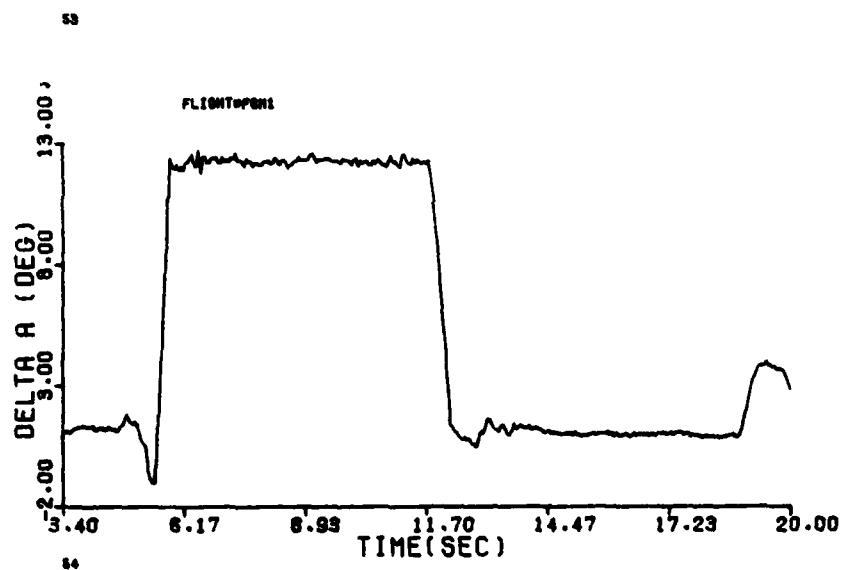
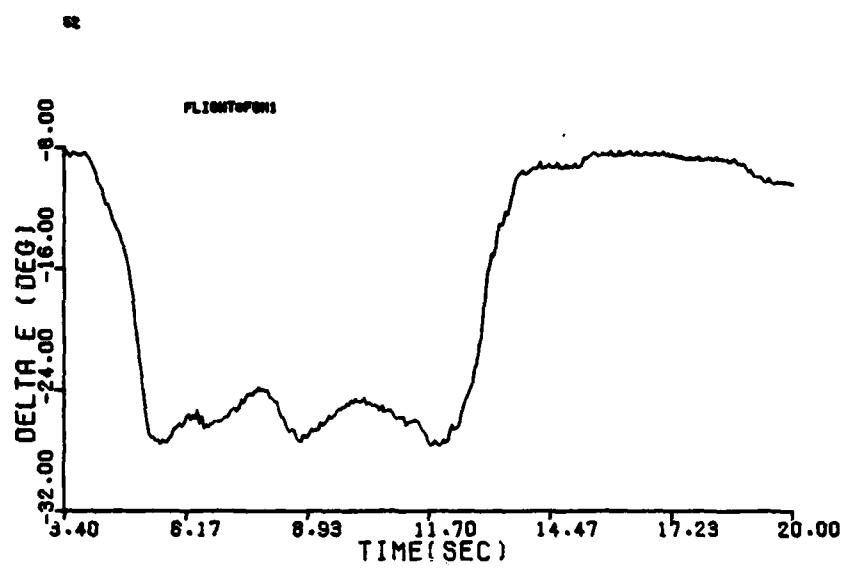


Figure B-18 (cont'd)

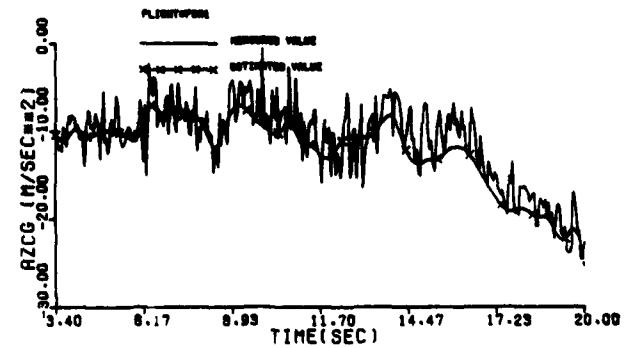
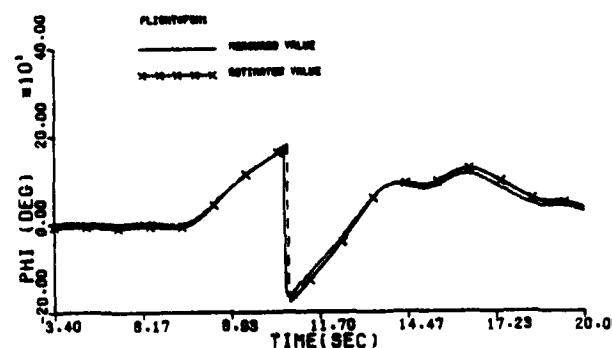
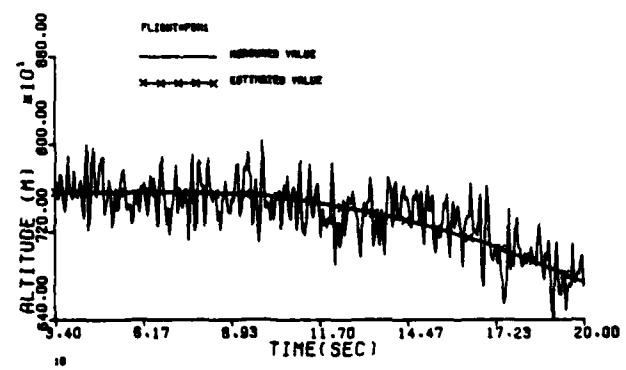
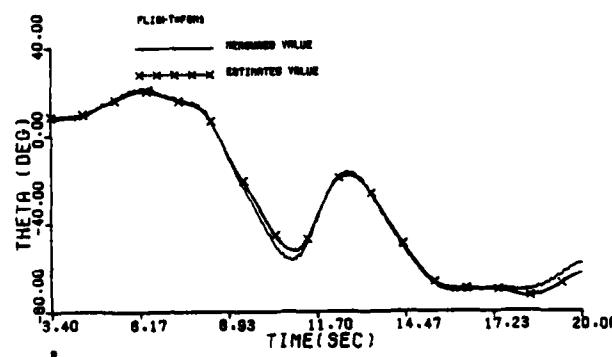
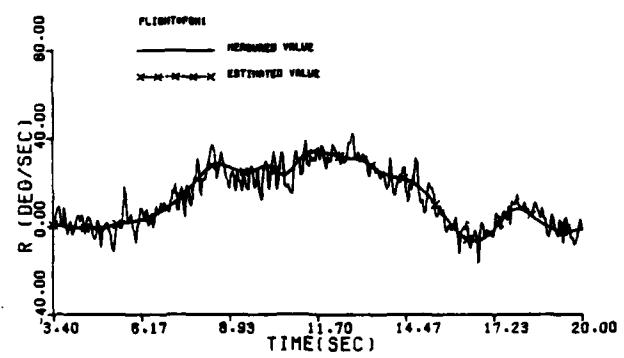
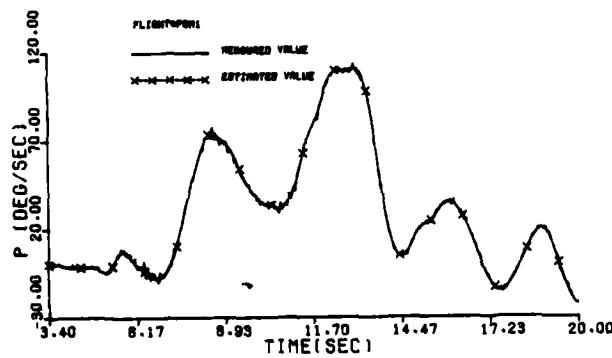
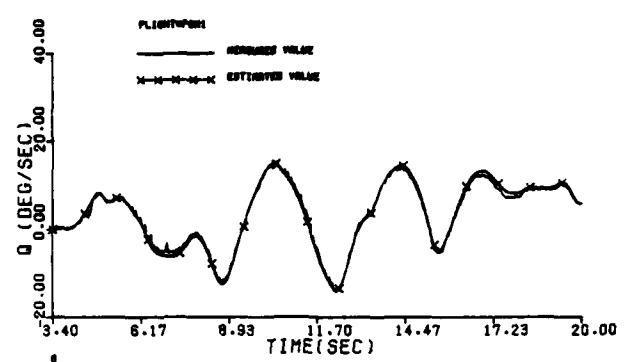
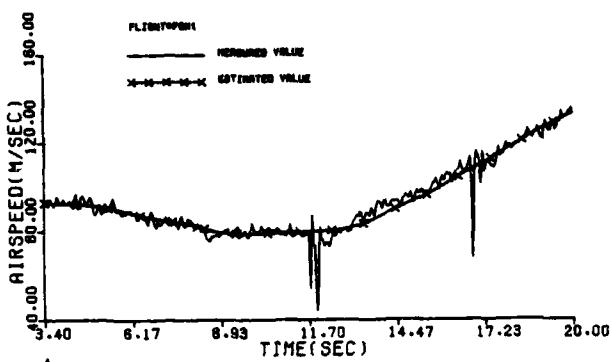


Figure B-18 (cont'd)

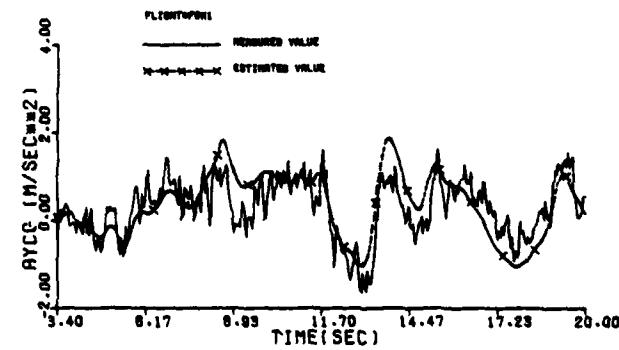
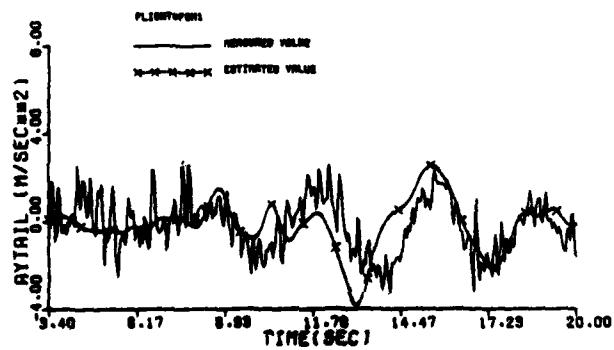
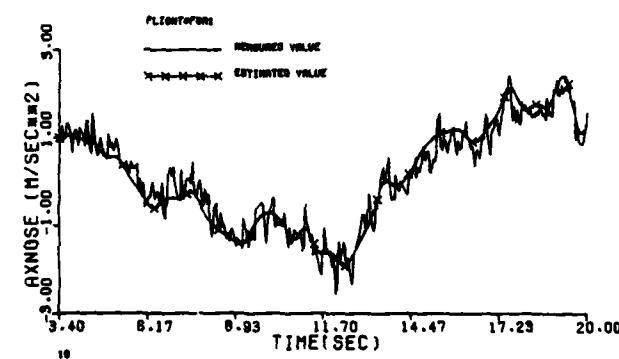
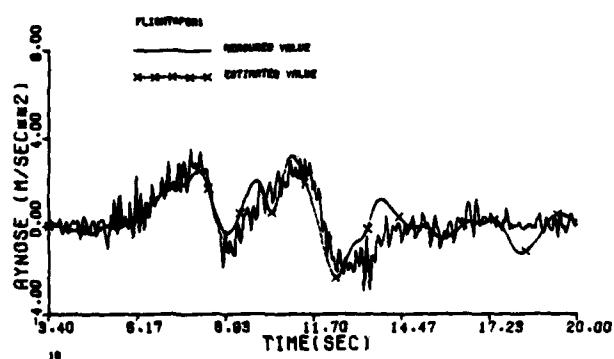
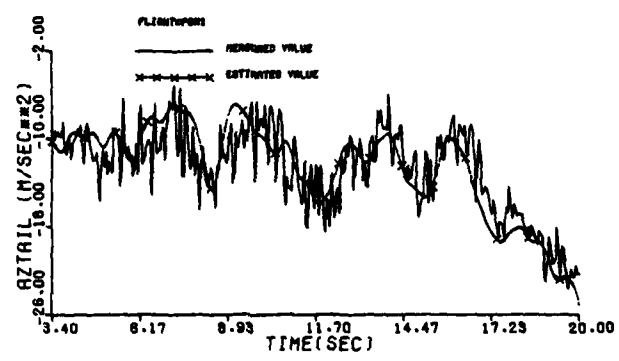
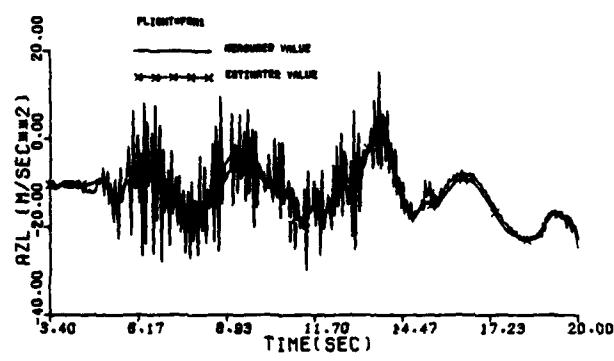
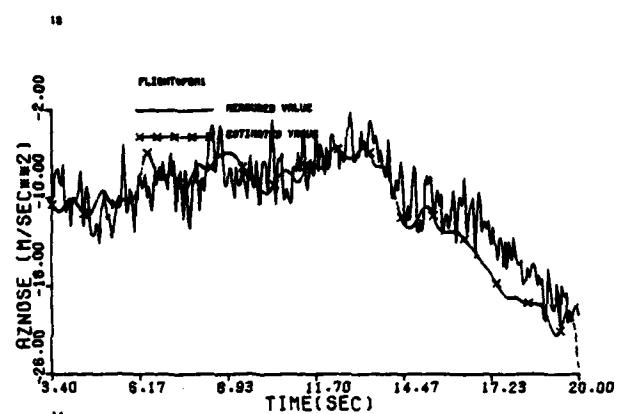
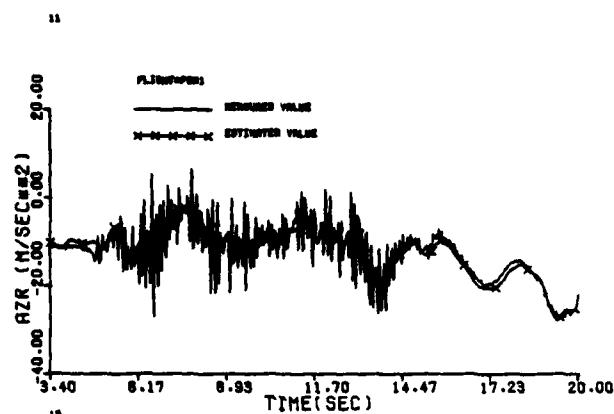


Figure B-18 (concluded)

APPENDIX C

MODELING RESULTS: C_y MODEL IN EQUATION FORM

This appendix contains the parametric model of the side force coefficient C_y , identified using the EBM system identification method. The equation model identified for C_y is:

$$C_y = C_{y_{\delta_r}}(\alpha) \cdot \delta_r + C_{y_{\beta_0}}(\alpha) \cdot \beta + \sum_{i=1}^2 C_{y_{\beta_i^3}}(\alpha) \cdot f(\beta, \beta_i, \beta_{i+1})$$

where β_i and β_{i+1} are knots on the $|\beta|$ axis satisfying $0 \leq \beta_1 < \beta_2 < \beta_3$ and where $f(\beta, \beta_i, \beta_{i+1})$ is a cubic spline function defined as

$$f(\beta, \beta_i, \beta_{i+1}) = \begin{cases} 0 & 0 \leq \beta < \beta_i \\ \frac{1}{3} (\beta - \beta_i)^3 & \beta_i \leq \beta \leq \beta_{i+1} \\ (\beta_{i+1} - \beta_i)^2 (\beta - \frac{1}{3} \beta_i - \frac{2}{3} \beta_{i+1}) & \beta_{i+1} < \beta \end{cases}$$

$$f(-\beta, \beta_i, \beta_{i+1}) = -f(\beta, \beta_i, \beta_{i+1}) \quad \beta > 0$$

The identified parameters $C_{y_{\delta_r}}$, $C_{y_{\beta_0}}$, $C_{y_{\beta_1^3}}$, and $C_{y_{\beta_2^3}}$

are given in Table C-1 as functions of the angle of attack α . The tabulated values of the parameters hold at the midpoints of the α intervals listed in the first column of the table. Interpolation is to be used in between midpoints. The last column in the table lists the knot values of the cubic spline function. For example, at the midpoint $\alpha = 19.5^\circ$, the knots are $\beta_1 = 0^\circ$, $\beta_2 = 5^\circ$ and $\beta_3 = 18^\circ$. In order to use the above equation the function

$f(\beta, \beta_i, \beta_{i+1})$ must be divided by the cube of 57.29 whenever β , β_i and β_{i+1} are in degrees.

In the first column of the table the L.H. denotes the left hand endpoint and R.H. the right hand endpoint.

Table C-1
Identified parameters of C_y

a Interval (Deg)		$C_{y_{\beta_r}}$ (per rad)	$C_{y_{\beta_o}}$ (per rad)	Cubic Spline Function Parameters			knots on $ \beta $ axis (Deg)
				$C_{y_{\beta_1}}^3$ (per rad ³)	$C_{y_{\beta_2}}^3$ (per rad ³)		
L.H.	R.H.						
-4	5	.118	-.661	-2.01	-	-	0, 10
5	6	.118	-.85	-2.40	-	-	0, 10
6	7	.118	-.788	-2.17	-	-	0, 12
7	8	.113	-.908	1.31	-	-	0, 13
8	9	.126	-.919	1.54	-	-	0, 13
9	10	.065	-.84	-1.33	-	-	0, 14
10	11	.052	-.731	-6.98	-	-	0, 14
11	12	.064	-.753	-7.80	-	-	0, 14
12	13	.082	-.705	-6.58	-	-	0, 16
13	14	.099	-.707	-9.2	-	-	0, 16
14	15	.051	-.624	-5.8	-	-	0, 15
15	16	.033	-.644	1.13	-	-	0, 15
16	17	.045	-.781	6.92	-	-	0, 15
17	18	.055	-.621	-5.15	-	-	0, 18
18	19	.076	-.67	-4.56	14.76	0, 5, 18	
19	20	.069	-.76	5.49	9.17	0, 5, 18	
20	21	.068	-1.08	76.56	-1.76	0, 5, 18	
21	22	.066	-1.03	40.55	5.78	0, 5, 20	
22	23	.064	-.88	18.54	1.15	0, 5, 20	
23	24	.063	-.86	-8.58	4.72	0, 5, 23	
24	25	.061	-.922	17.11	-4.27	0, 5, 24	
25	30	.059	-.922	17.11	-4.27	0, 5, 25	
30	35	.057	-.922	17.11	-4.27	0, 5, 28	
35	40	.056	-.922	17.11	-4.27	0, 5, 28	

APPENDIX D

MODELING RESULTS: C_L MODEL IN EQUATION FORM

This appendix contains the parametric model of the rolling moment coefficient C_L , identified using the EBM system identification method. The equation model identified for C_L is:

$$C_L = C_{L_{\delta_a}}(\alpha) \cdot \delta_a + C_{L_{\delta_r}}(\alpha) \cdot \delta_r + C_{L_{\beta_0}}(\alpha) \cdot \beta + \sum_{i=1}^3 C_{L_{\beta_i}}(\alpha) \cdot f(\beta, \beta_i, \beta_{i+1}) \beta_i^3 + C_{L_p}(\alpha) \cdot \frac{pb}{2V} + C_{L_r}(\alpha) \cdot \frac{rb}{2V}$$

where β_i and β_{i+1} are knots on the $|\beta|$ axis satisfying $0 \leq \beta_1 < \beta_2 < \beta_3 < \beta_4$ and where $f(\beta, \beta_i, \beta_{i+1})$ is a cubic spline function defined as

$$f(\beta, \beta_i, \beta_{i+1}) = \begin{cases} 0 & 0 \leq \beta \leq \beta_i \\ \frac{1}{3} (\beta - \beta_i)^3 & \beta_i \leq \beta \leq \beta_{i+1} \\ (\beta_{i+1} - \beta_i)^2 (\beta - \frac{1}{3} \beta_i - \frac{2}{3} \beta_{i+1}) & \beta_{i+1} < \beta \end{cases}$$

$$f(-\beta, \beta_i, \beta_{i+1}) = -f(\beta, \beta_i, \beta_{i+1}) \quad \beta > 0$$

The identified parameters $C_{L_{\delta_a}}, C_{L_{\delta_r}}, C_{L_{\beta_0}}, C_{L_{\beta_i}}, i = 1, 2, 3$, C_{L_p} and C_{L_r} are given as functions of the angle of attack in Tables D-1 and D-2. The tabulated values of the parameters hold at the midpoints of the α intervals listed in the first columns of these two tables. The knots of the cubic spline function are given in the last column of Table D-1. The function $f(\beta, \beta_i, \beta_{i+1})$ must be divided by the cube of 57.29 whenever β, β_i and β_{i+1} are in degrees.

In the first column of Tables D-1 and D-2 the L.H. denotes the left hand endpoint of the α interval and R.H. denotes the right hand endpoint.

Table D-1

Identified parameters of C_{ℓ}

a Interval (Deg)	C _ℓ _{δ_a} (per rad)	C _ℓ _{δ_r} (per rad)	C _ℓ _{β₀} (per rad)	Cubic Spline Function Parameters			Knots on β axis (Deg)
				C _ℓ _{β₁} β ₁ ³ (per rad ³)	C _ℓ _{β₂} β ₂ ³ (per rad ³)	C _ℓ _{β₃} β ₃ ³ (per rad ³)	
L.H. R.H.							
-4 5	-.187	.011	-.168	-.484	-	-	0, 10
5 6	-.176	.0076	-.168	-.484	-	-	0, 10
6 7	-.174	.0041	-.154	1.33	-	-	0, 12
7 8	-.154	.0113	-.151	1.05	-	-	0, 13
8 9	-.176	.0097	-.159	1.17	-	-	0, 13
9 10	-.174	.0065	-.147	.78	-	-	0, 14
10 11	-.193	.0072	-.143	.43	-	-	0, 14
11 12	-.181	.0066	-.132	.21	-	-	0, 14
12 13	-.165	.0061	-.096	-1.141	1.70	-3.44	0, 5, 10, 16
13 14	-.160	.0135	-.086	-3.05	4.36	-4.79	0, 5, 10, 16
14 15	-.148	.0127	-.037	14.23	-11.21	102.2	0, 2, 10, 15
15 16	-.118	.012	-.036	20.41	-17.68	97.17	0, 2, 10, 15
16 17	-.071	.0145	-.034	-9.44	156.5	-	0, 10, 15
17 18	-.082	.0190	-.057	-2.01	.43	-	0, 10, 18
18 19	-.059	-.0093	-.069	-.66	-12.56	-	0, 10, 18
19 20	-.087	.0123	-.053	-10.83	4.94	-	0, 5, 18
20 21	-.046	-.0144	-.084	2.64	-3.34	-	0, 5, 18
21 22	-.055	-.0012	-.076	-1.13	1.04	-	0, 5, 20
22 23	-.066	-.0009	-.028	-10.95	1.33	-	0, 5, 20
23 24	-.059	.0068	-.066	-3.52	.39	-	0, 5, 23
24 25	-.059	.0068	-.079	-6.94	-1.43	-	0, 5, 24
25 30	-.059	.0068	-.081	-1.29	-1.38	-	0, 5, 25
30 35	-.059	.0068	-.095	-1.45	-1.58	-	0, 5, 28
35 40	-.059	.0068	-.106	-1.65	-1.74	-	0, 5, 28

Table D-2
Identified dynamic derivatives of C_{ℓ}

α Interval (Deg)		C_{ℓ_p}	C_{ℓ_r}
L.H.	R.H.	(per rad)	(per rad)
-4	0	-.6100	.1102
0	1	-.6100	.1467
1	2	-.5957	.1613
2	3	-.5861	.1759
3	4	-.5766	.1904
4	5	-.5670	.205
5	6	-.5460	.2196
6	7	-.5440	.2342
7	8	-.5010	.2488
8	9	-.4940	.2634
9	10	-.4400	.278
10	11	-.4680	.290
11	12	-.4070	.288
12	13	-.4150	.312
13	14	-.2900	.326
14	15	-.2250	.310
15	16	-.0890	.357
16	17	-.0200	.183
17	18	.0330	.218
18	19	-.042	.232
19	20	.0350	.162
20	21	-.069	.116
21	22	-.069	.129
22	23	-.072	.1261
23	24	-.079	.1232
24	25	-.090	.1202
25	30	-.1338	.1115
30	35	-.2083	.0969
35	40	-.2828	.0823

APPENDIX E

MODELING RESULTS: C_n MODEL IN EQUATION FORM

This appendix contains the parametric model of the yawing moment coefficient C_n , identified using the EBM system identification method. The equation model identified for C_n is:

$$C_n = C_{n_{\delta_r}}(\alpha) \cdot \delta_r + C_{n_{\beta_o}}(\alpha) \cdot \beta + \sum_{i=1}^3 C_{n_{\beta_i}}(\alpha) \cdot f(\beta, \beta_i, \beta_{i+1}) \beta_i^3 + C_{n_p}(\alpha) \cdot \frac{pb}{2V} + C_{n_r}(\alpha) \cdot \frac{rb}{2V}$$

where β_i and β_{i+1} are knots on the $|\beta|$ axis satisfying $0 \leq \beta_1 < \beta_2 < \beta_3 < \beta_4$ and where $f(\beta, \beta_i, \beta_{i+1})$ is a cubic spline function defined as

$$f(\beta, \beta_i, \beta_{i+1}) = \begin{cases} 0 & 0 \leq \beta \leq \beta_i \\ \frac{1}{3} (\beta - \beta_i)^3 & \beta_i \leq \beta \leq \beta_{i+1} \\ (\beta_{i+1} - \beta_i)^2 (\beta - \frac{1}{3} \beta_i - \frac{2}{3} \beta_{i+1}) & \beta_{i+1} < \beta \end{cases}$$

$$f(-\beta, \beta_i, \beta_{i+1}) = -f(\beta, \beta_i, \beta_{i+1}) \quad \beta > 0$$

The identified parameters $C_{n_{\delta_r}}$, $C_{n_{\beta_o}}$, $C_{n_{\beta_i}}$, $i = 1, 2, 3$, C_{n_p} and C_{n_r} are given as functions of the angle of attack in Tables E-1 and E-2. The tabulated values of the parameters hold at the midpoints of the α intervals listed in the first columns of these two tables. The knots of the cubic spline function are presented in the last column of Table E-1. The function $f(\beta, \beta_i, \beta_{i+1})$ must be divided by the cube of

57.29 whenever β , β_i and β_{i+1} are in degrees.

In the first column of Tables E-1 and E-2 the L.H. denotes the left hand endpoint of the α interval and R.H. the right hand endpoint.

Table E-1
Identified parameters of C_n

α Interval (Deg)	$C_{n\delta_r}$ (per rad)	$C_{n\beta_0}$ (per rad)	$C_{n\beta_1^3}$ (per rad ³)	$C_{n\beta_2^3}$ (per rad ³)	$C_{n\beta_3^3}$ (per rad ³)	Knots on $ \beta $ axis (Deg)
L.H. R.H.						
-4 2	-.044	.076	.53	-	-	0, 10
2 3	-.044	.065	1.03	-	-	0, 10
3 4	-.044	.051	1.63	-	-	0, 10
4 5	-.044	.051	1.63	-	-	0, 10
5 6	-.044	.064	1.63	-	-	0, 10
6 7	-.044	.073	.55	-	-	0, 12
7 8	-.044	.096	-.473	-	-	0, 13
8 9	-.041	.089	-.397	-	-	0, 13
9 10	-.038	.081	.02	-	-	0, 14
10 11	-.040	.091	-1.03	-	-	0, 14
11 12	-.031	.082	-.42	-	-	0, 14
12 13	-.027	.058	4.93	-17.33	38.52	0, 16
13 14	-.032	.052	4.18	-15.93	32.19	0, 5, 10, 16
14 15	-.030	-.013	89.74	-6.91	-1.55	0, 5, 10, 16
15 16	-.022	.032	-5.35	.54	-20.38	0, 2, 10, 15
16 17	-.017	.011	.76	-15.4	-	0, 2, 10, 15
17 18	-.025	.015	-1.86	9.45	-	0, 10, 15
18 19	-.020	-.023	3.15	-6.32	-	0, 10, 18
19 20	-.014	-.016	.43	1.73	-	0, 5, 18
20 21	-.011	-.011	.79	-.29	-	0, 5, 18
21 22	-.014	.005	-5.58	2.46	-	0, 5, 20
22 23	-.015	-.013	-4.32	1.84	-	0, 5, 20
23 24	-.014	-.015	.29	.29	-	0, 5, 23
24 25	-.016	.006	-.01	-.01	-	0, 5, 24
25 30	-.017	-.011	.46	.46	-	0, 5, 25
30 35	-.019	-.020	.55	.55	-	0, 5, 28
35 40	-.021	.034	.80	.80	-	0, 5, 28

Table E-2
Identified Dynamic Derivatives of C_n

α Interval (Deg)		C_{n_p} (per rad)	C_{n_5} (per rad)
L.H.	R.H.		
-4	-1	.104	-.2031
-1	0	.095	-.2021
0	1	.0765	-.2016
1	2	.0582	-.2011
2	3	.04	-.2007
3	4	.0215	-.2002
4	5	.0032	-.1997
5	6	-.0261	-.1932
6	7	-.0315	-.2066
7	8	-.0188	-.2189
8	9	-.0121	-.1910
9	10	-.0546	-.170
10	11	-.0696	-.1522
11	12	-.0652	-.1611
12	13	-.0566	-.1702
13	14	-.0293	-.1804
14	15	-.0034	-.1619
15	16	.1092	-.1299
16	17	.1128	-.1279
17	18	.0362	-.0239
18	19	.0439	.008
19	20	-.0321	-.0291
20	21	-.0755	-.0693
21	22	.0483	-.0542
22	23	.048	-.0343
23	24	-.0506	.0003
24	25	-.0768	-.0363
25	30	-.0749	-.0512
30	35	-.0717	-.1098
35	40	-.0685	-.1647

APPENDIX F
MODELING RESULTS: C_m CURVES

A comparison between the wind tunnel values of C_m and the values of C_m extracted from the actual T-2C flight test data is contained in Figures F-1 through F-14. In these figures the aerodynamic coefficient C_m is shown as a function of the angle of attack for fixed one degree intervals of the elevator control. The range of the elevator control δ_e covered is from -28° to 0° .

Figures F-1 through F-14 were generated as follows: a particularly small range of the elevator control was selected from δ_e to $\delta_e + 1^\circ$ where δ_e is an integer between -28° and -1° . All $C_m(t)$ estimates (i.e., an output of the first step of the EBM method) were collected together from all maneuvers. From this collection those $C_m(t)$ estimates having a corresponding elevator control $\delta_e(t)$ within the selected range δ_e to $\delta_e + 1^\circ$ were ordered according to the angle of attack variable and then plotted as one of the "real data values" curves in Figure F-1 through F-14. The "wind tunnel values" curves were obtained by evaluating the wind tunnel model using the estimated states and the elevator control $\delta_e(t)$. This gave a collection of wind tunnel coefficient values $WTC_m(t)$ from all maneuvers. From this collection those $WTC_m(t)$ values having a corresponding elevator control $\delta_e(t)$ within the selected range δ_e to $\delta_e + 1^\circ$ were ordered according to the angle of attack variable and then plotted as one of the "wind tunnel values" curves in Figure F-1 through F-14. It should be observed that the curves in these figures have a dependency on β , q and \dot{q} built into them by the nature of the maneuvers.

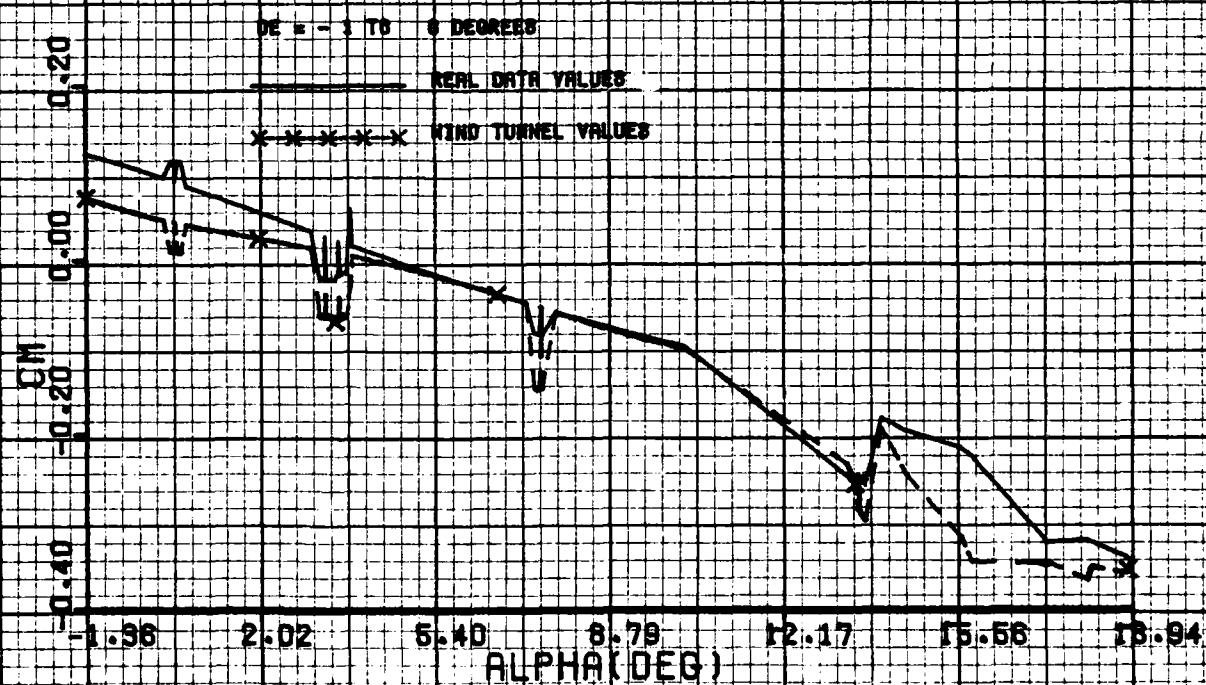
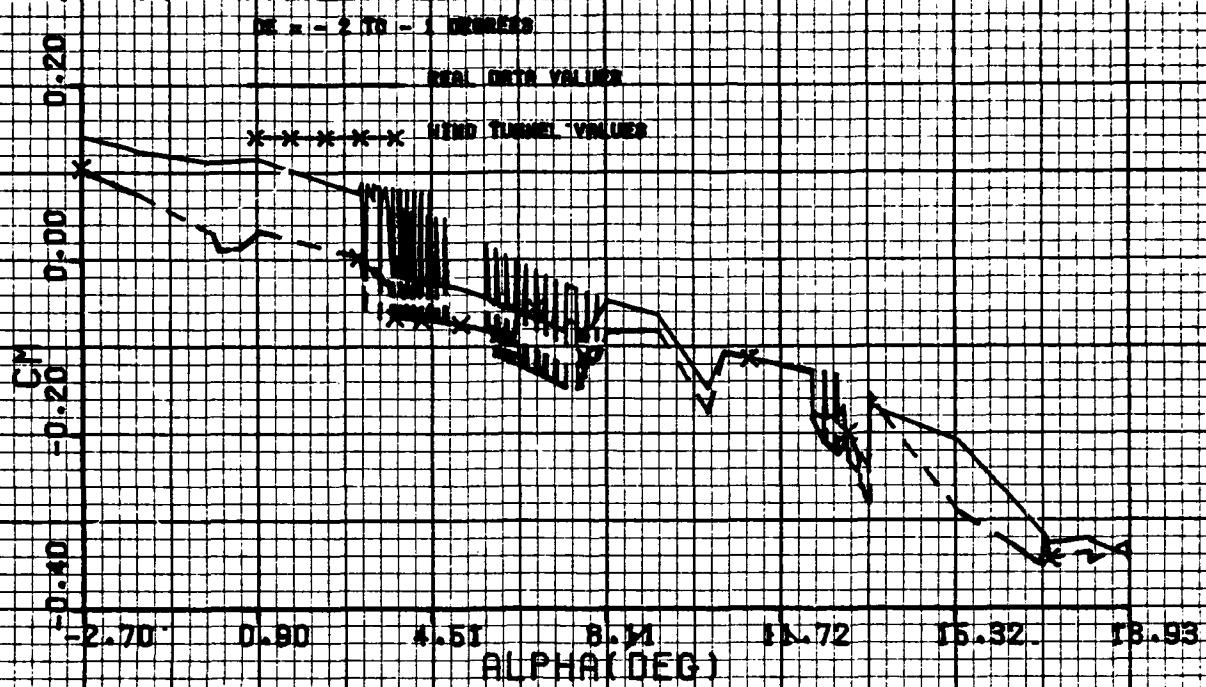


Figure F-1

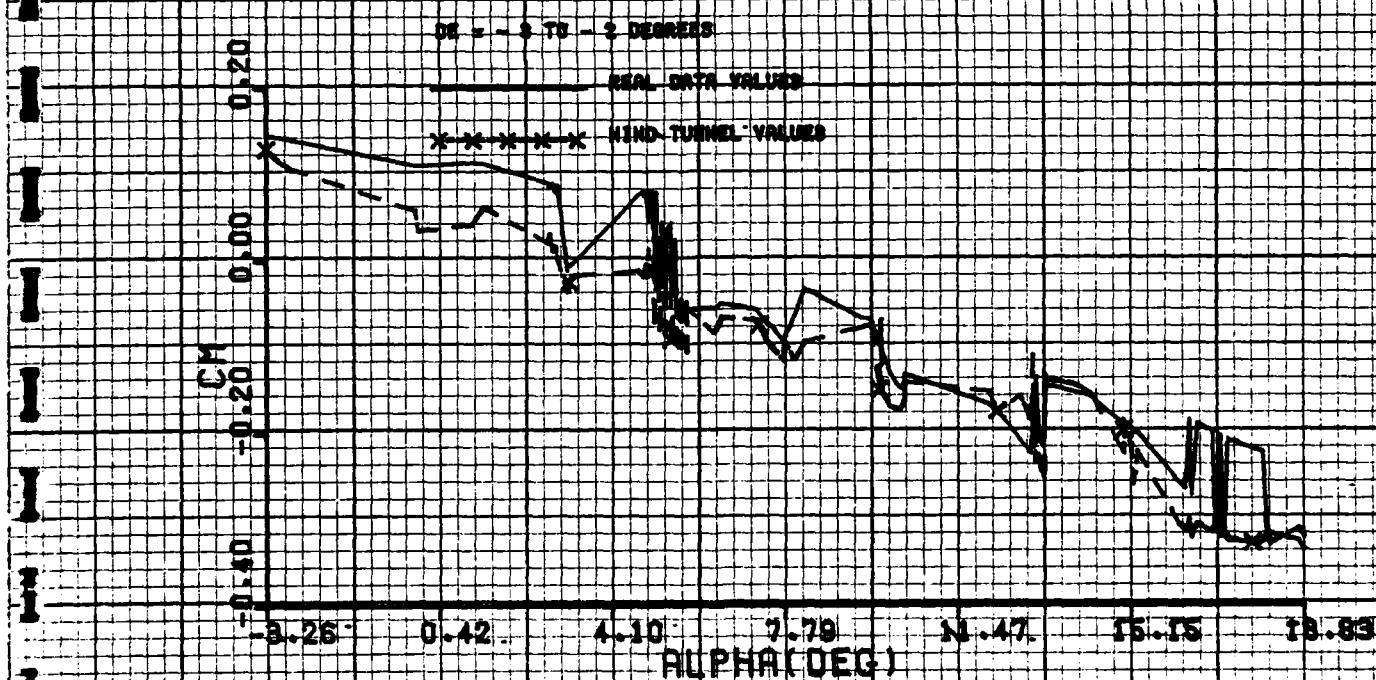
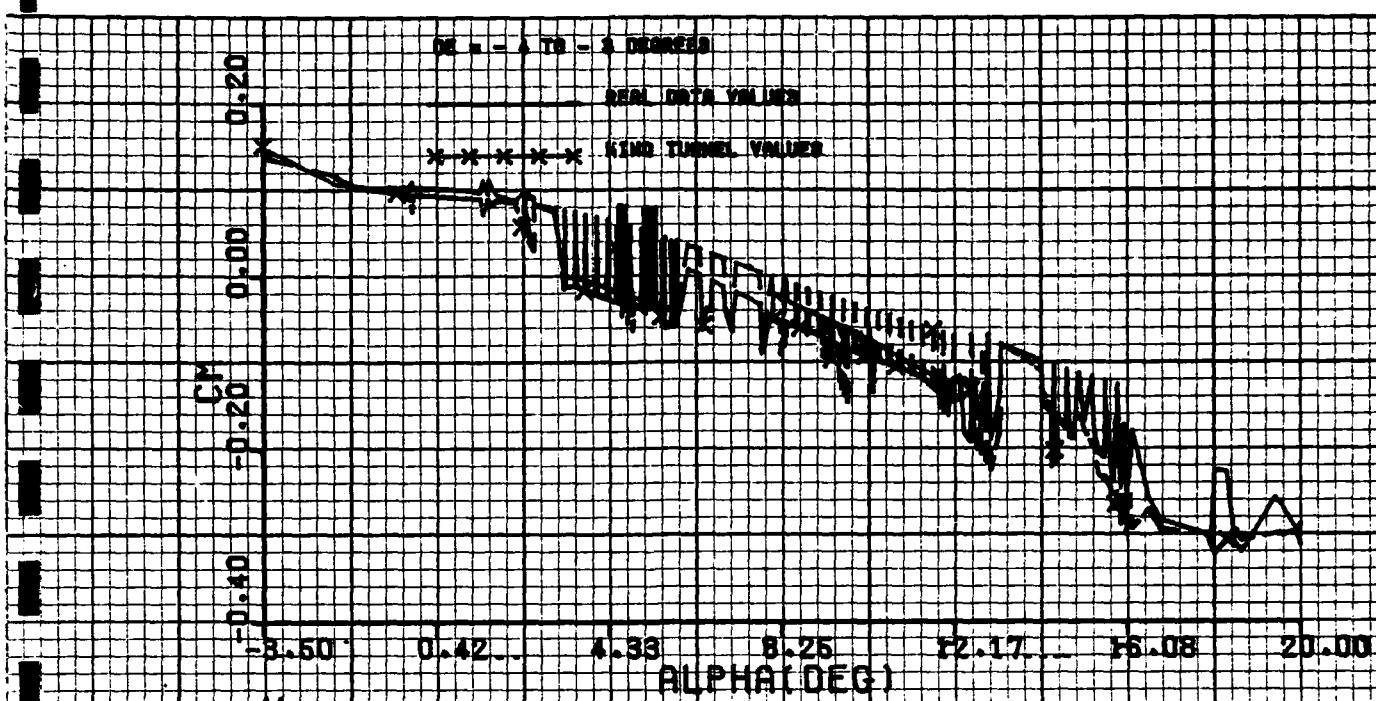


Figure F-2

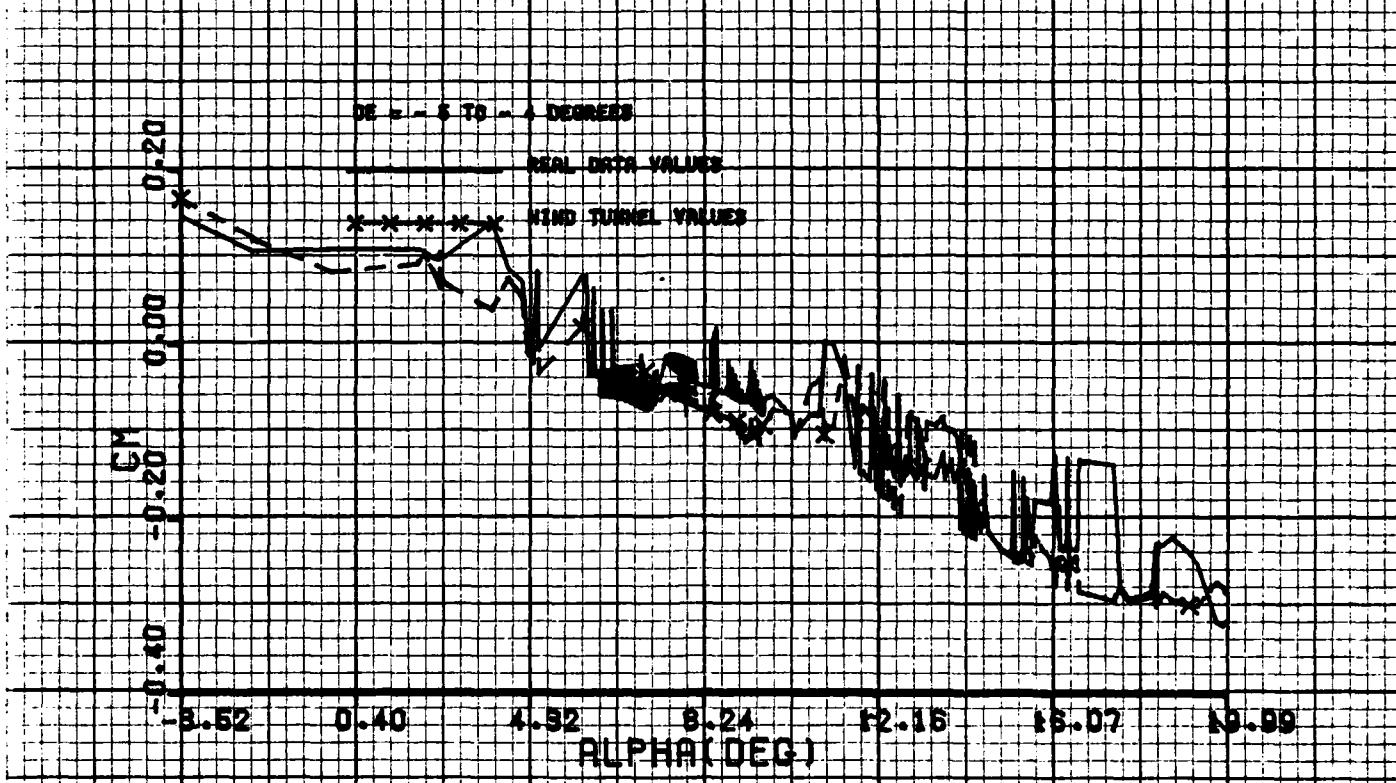
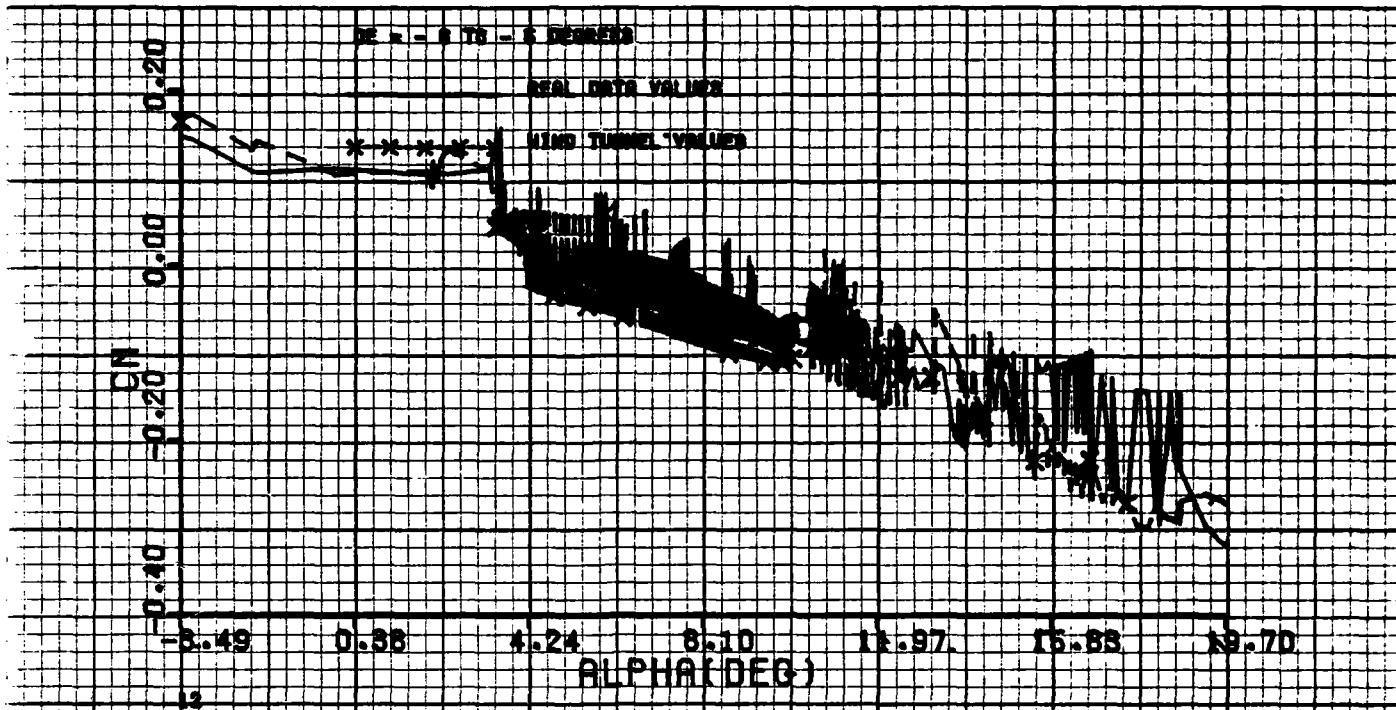


Figure F-3

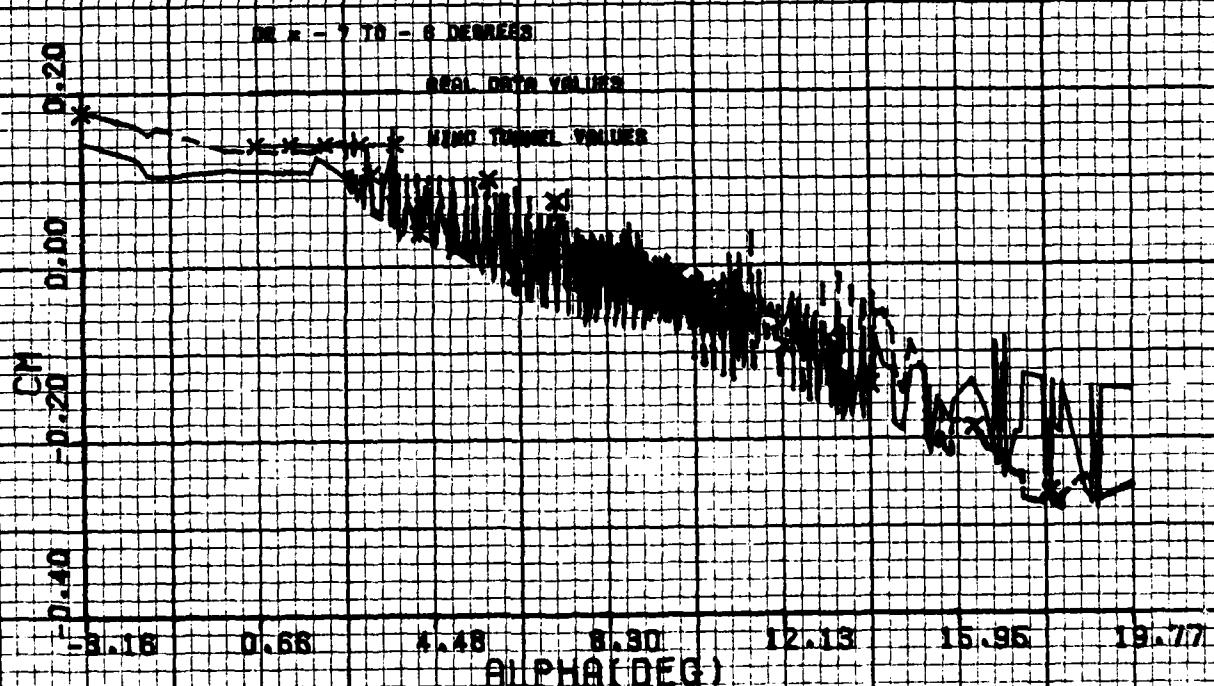
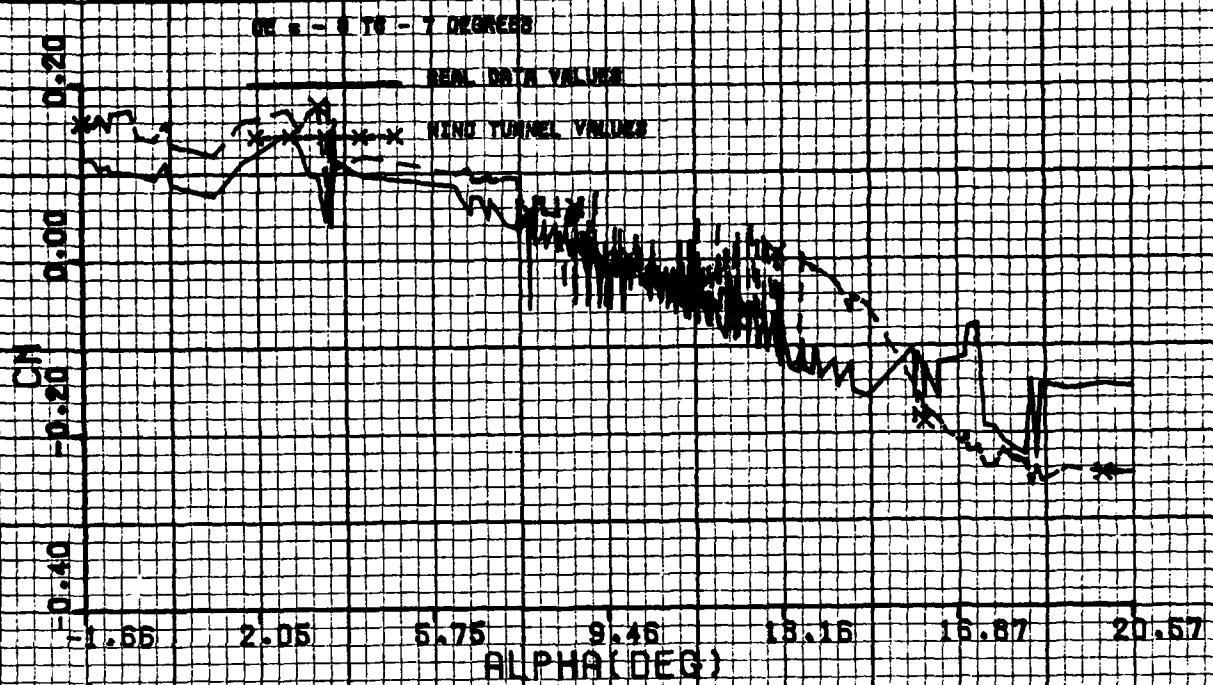


Figure F-4

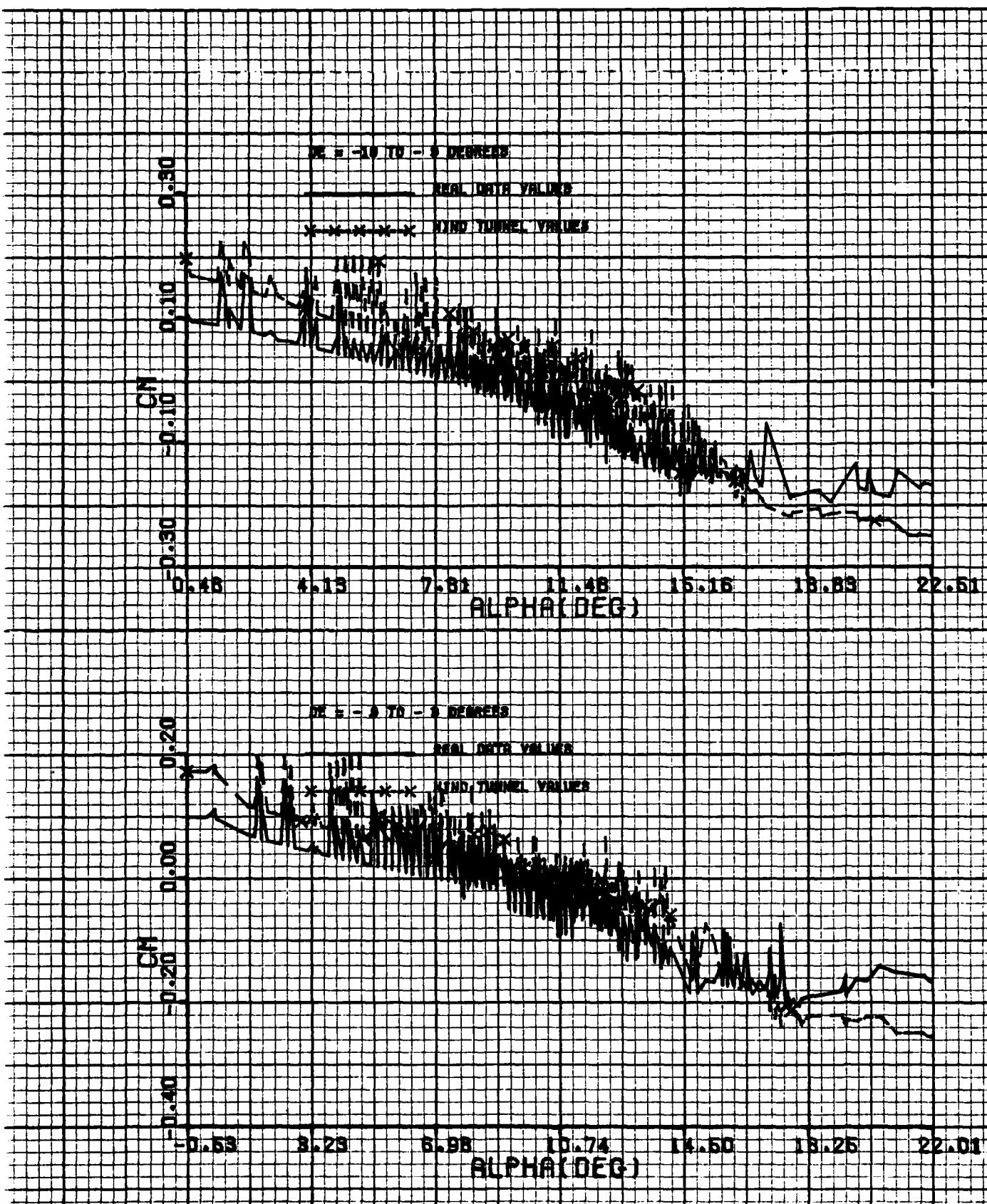


Figure F-5

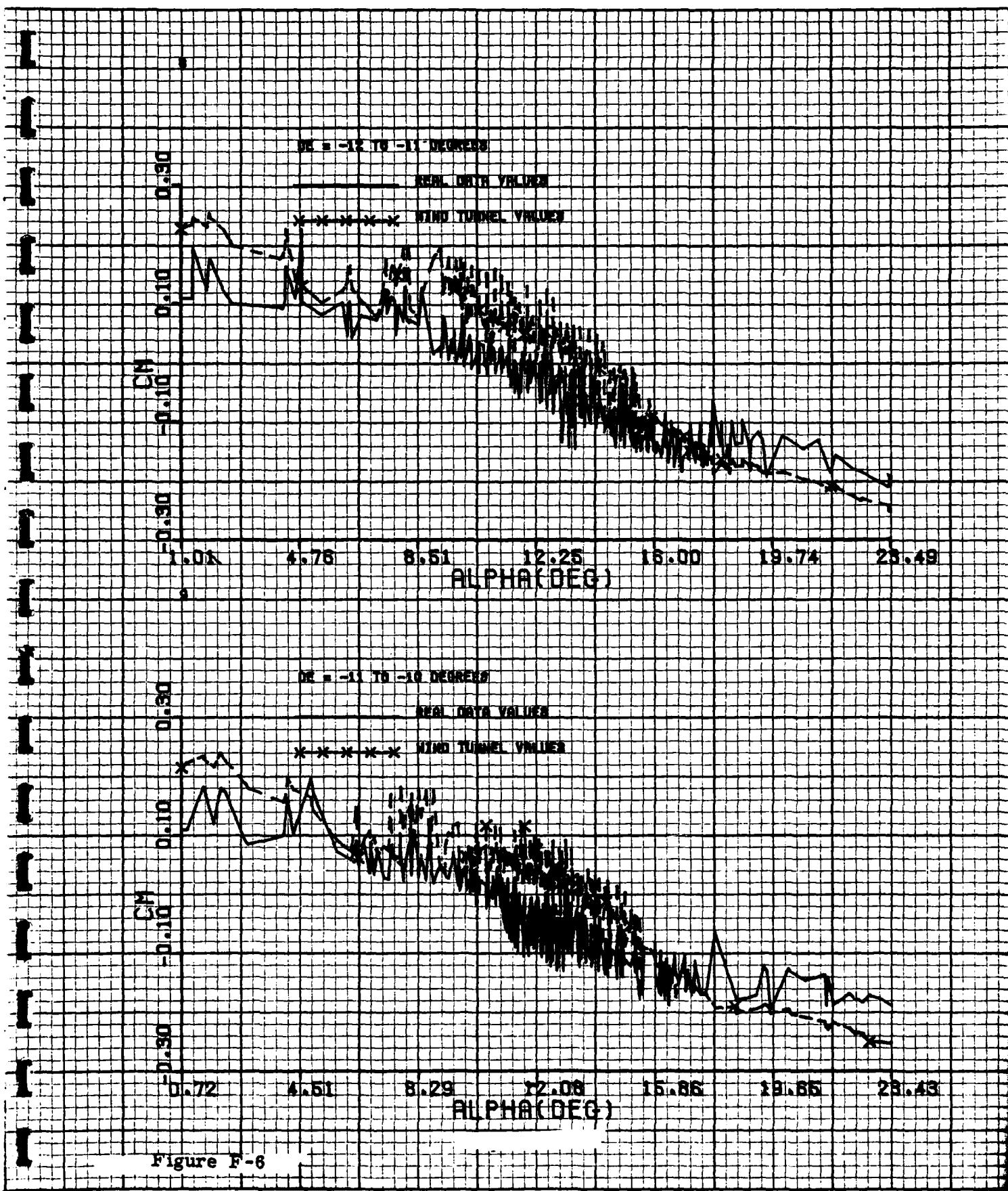
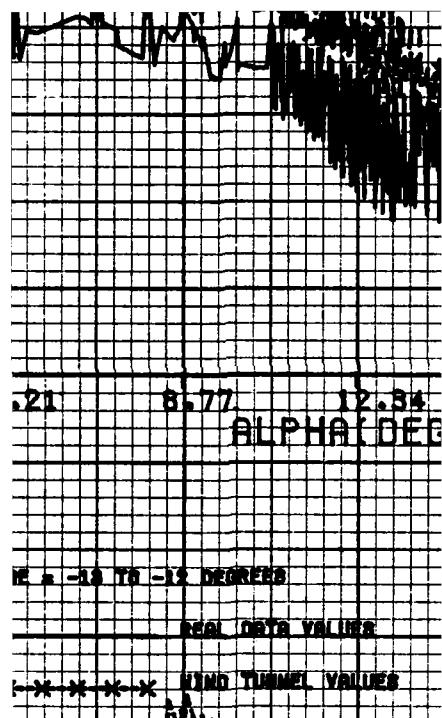


Figure F-6



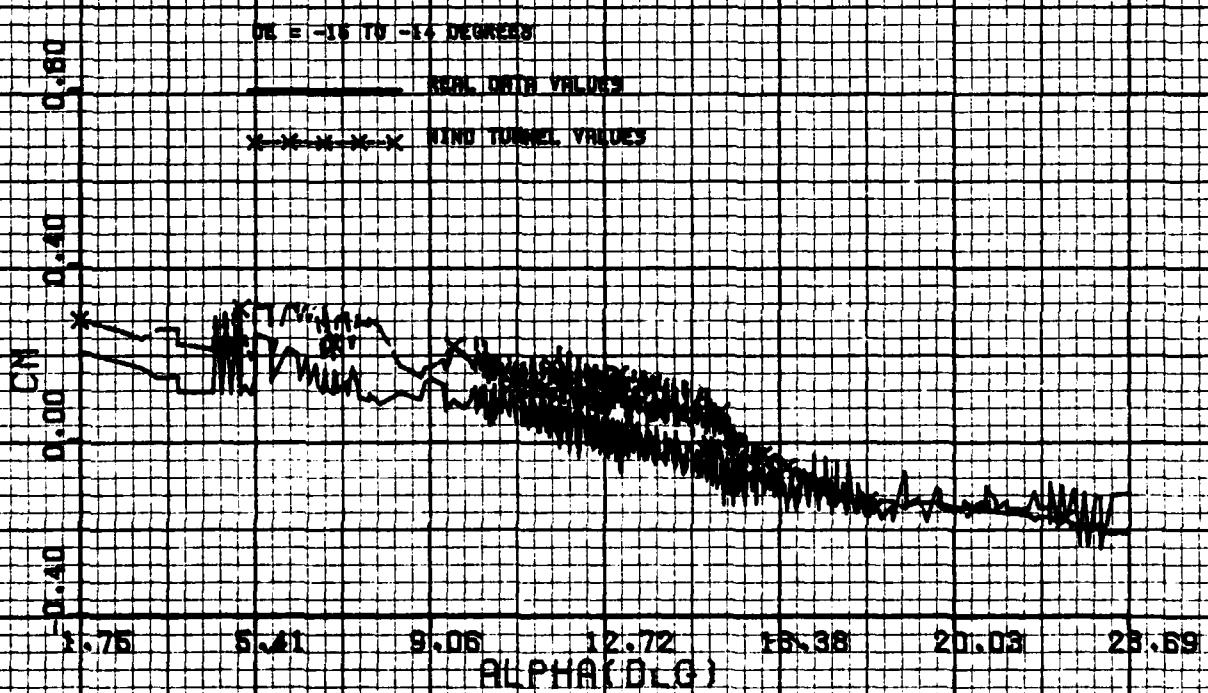
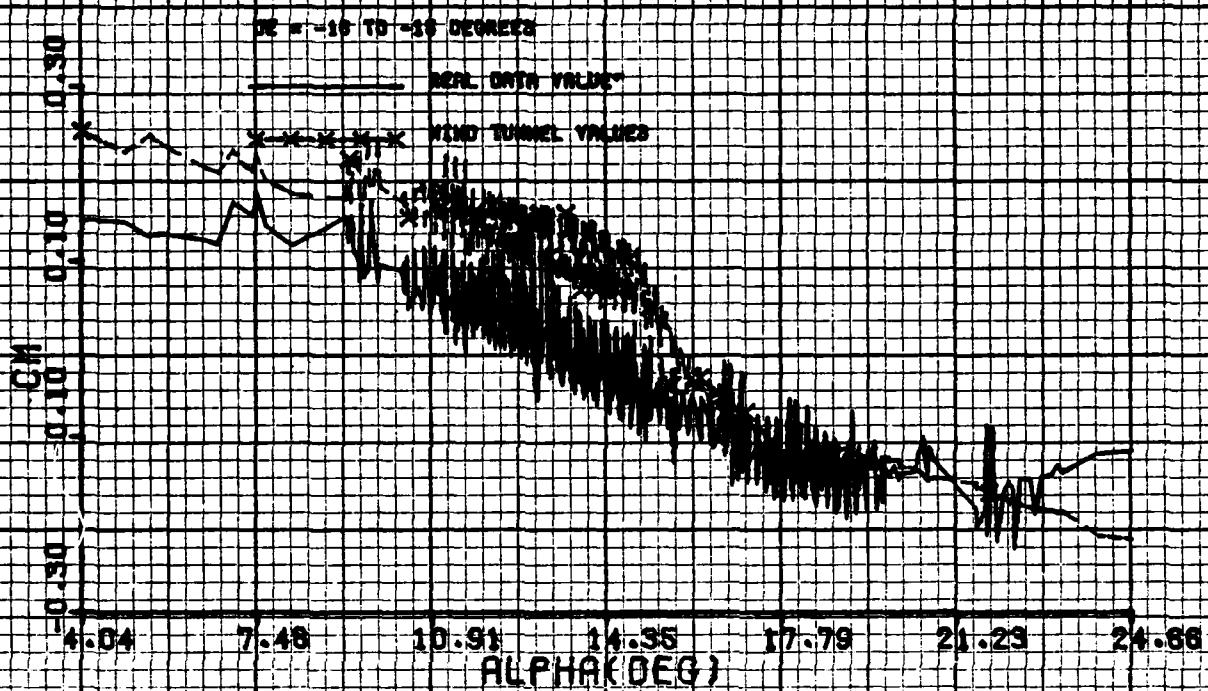


Figure F-8

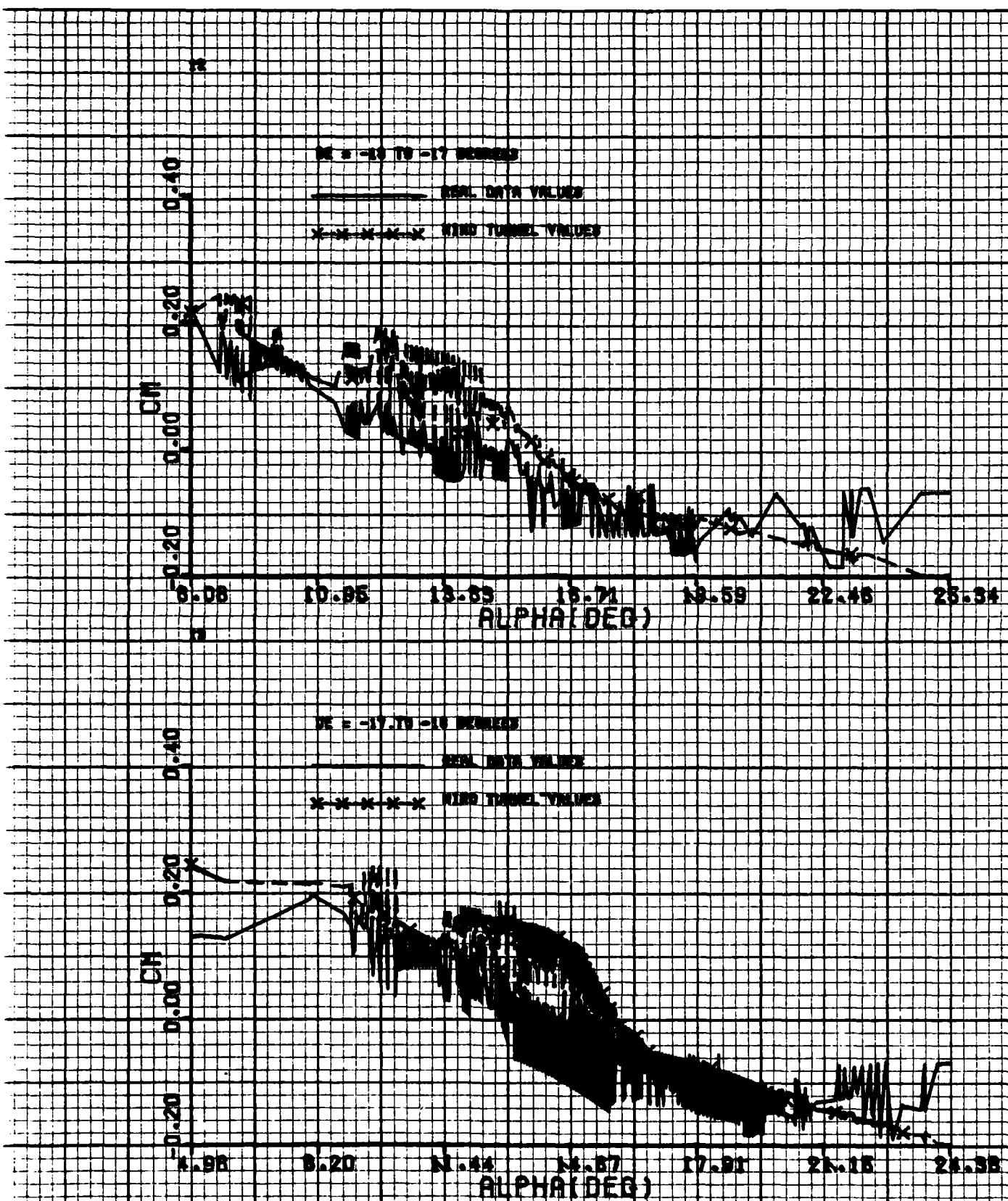


Figure F-9

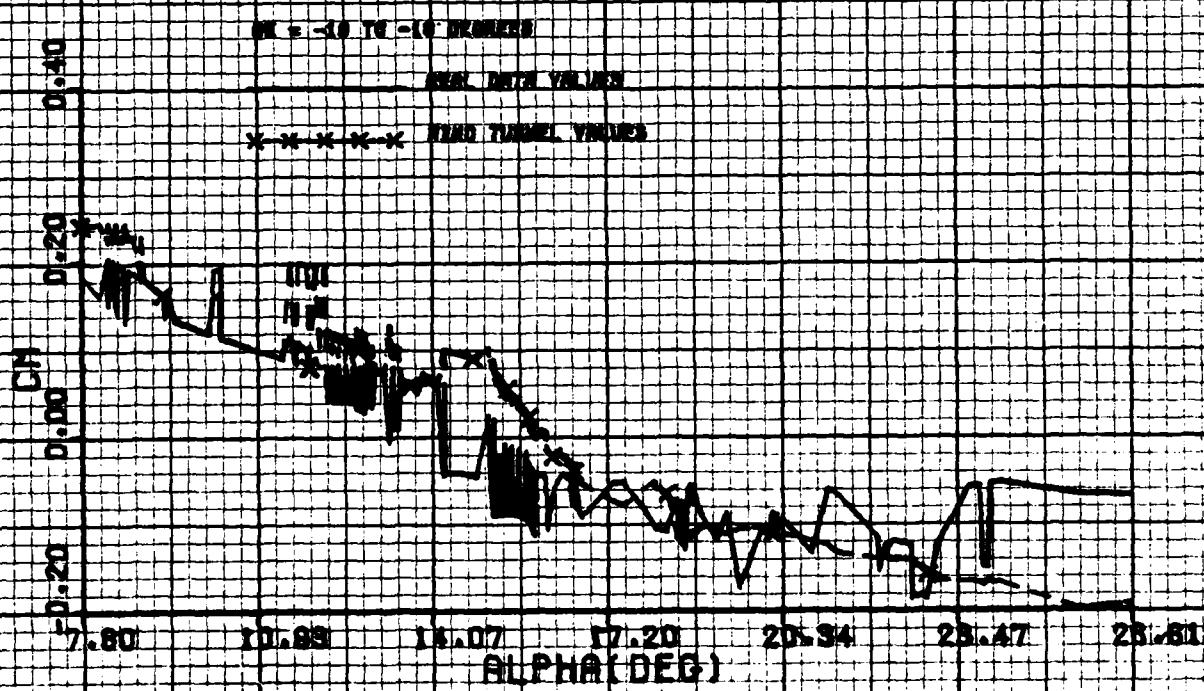
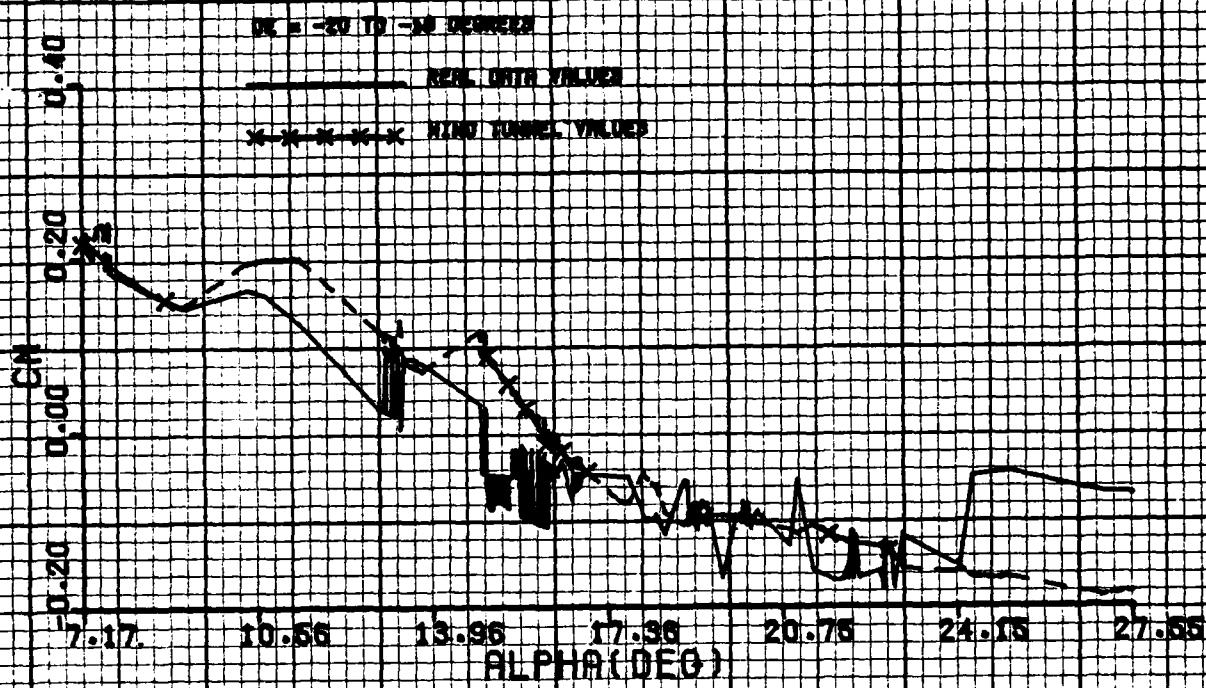


Figure F-10

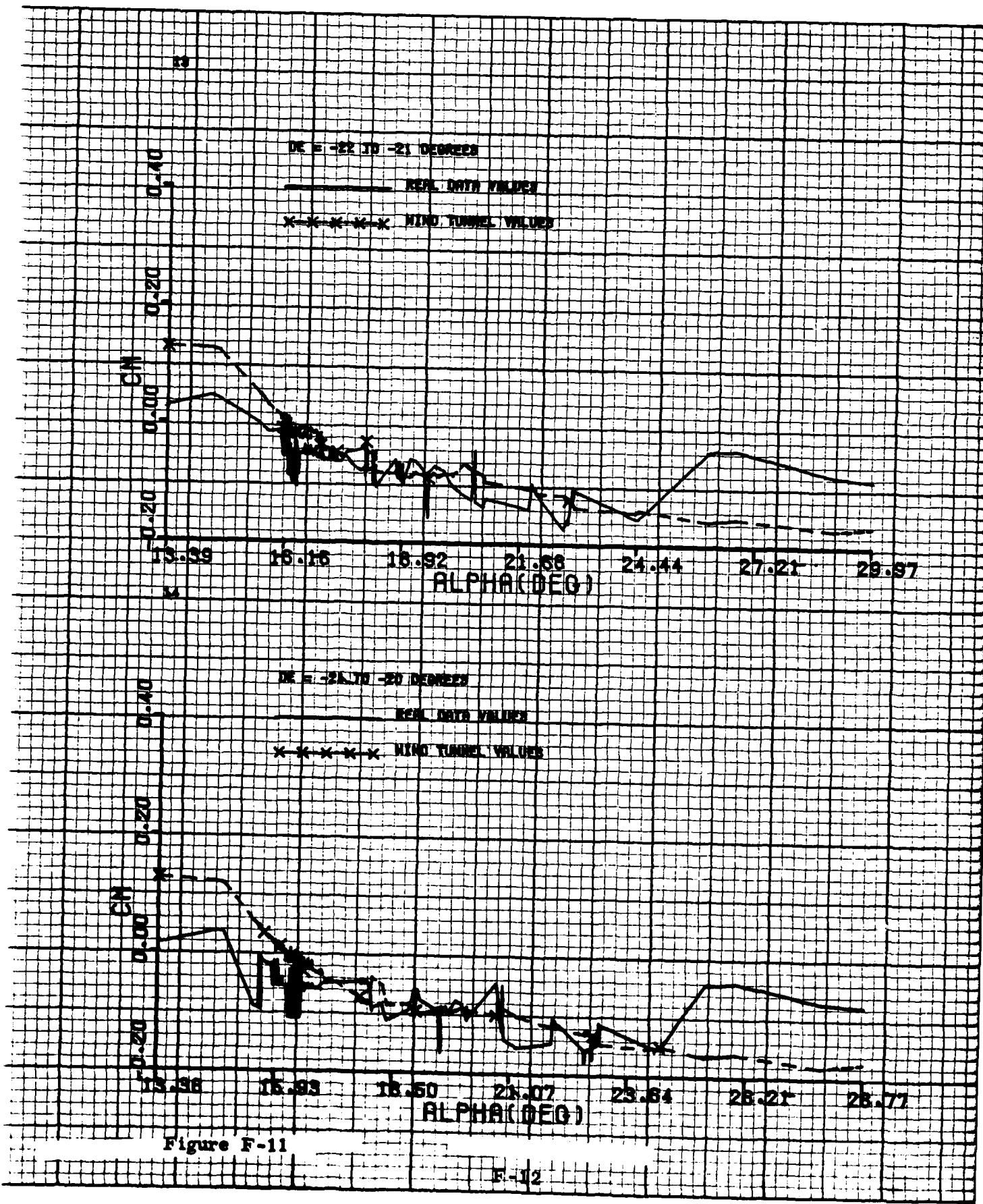


Figure F-11

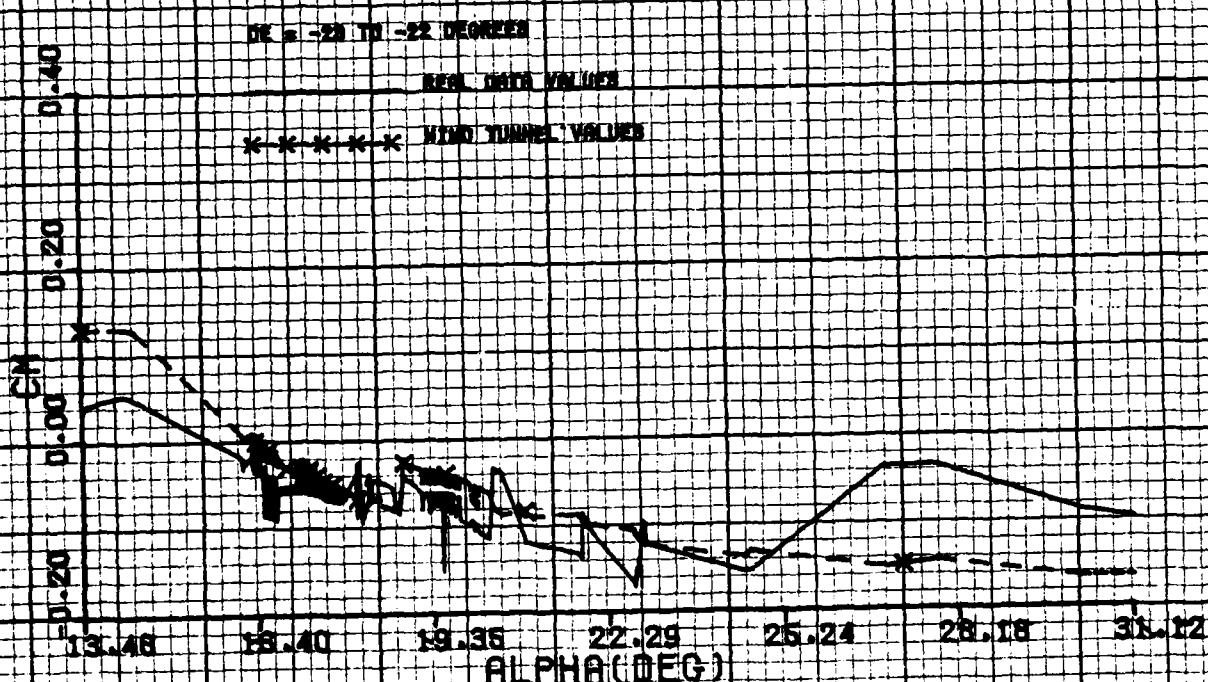
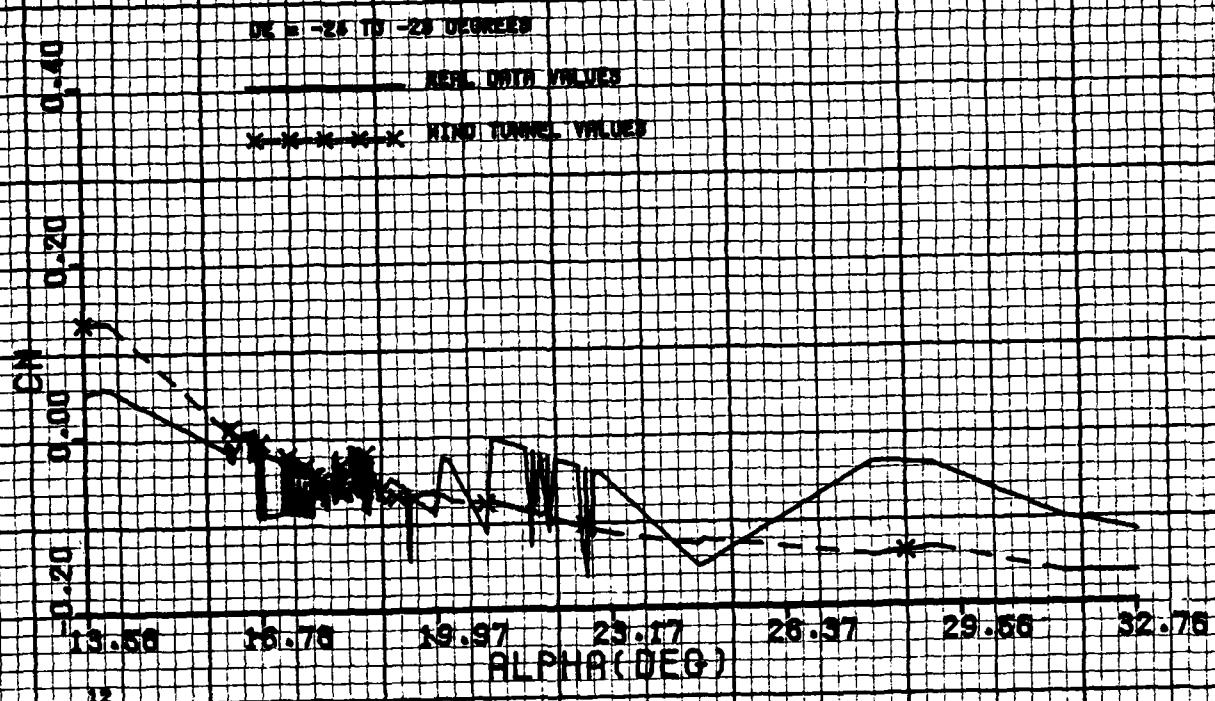


Figure F-12

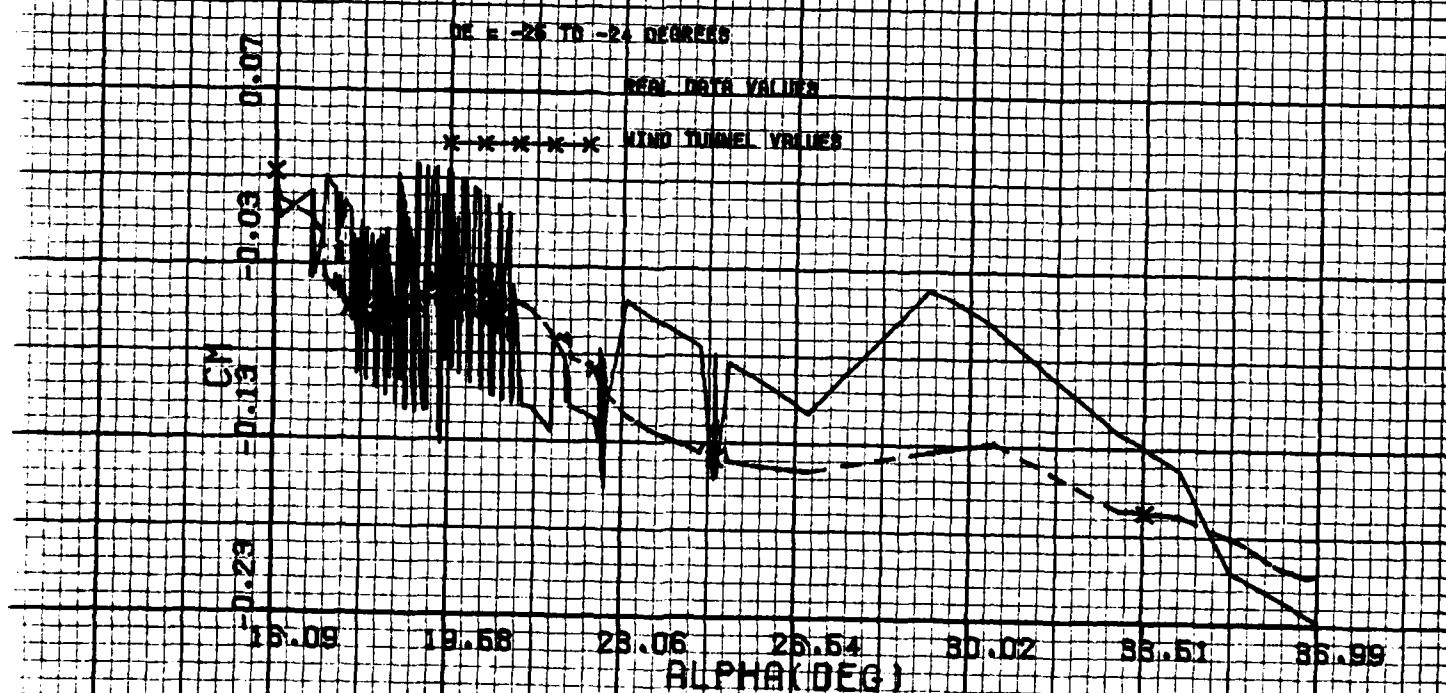
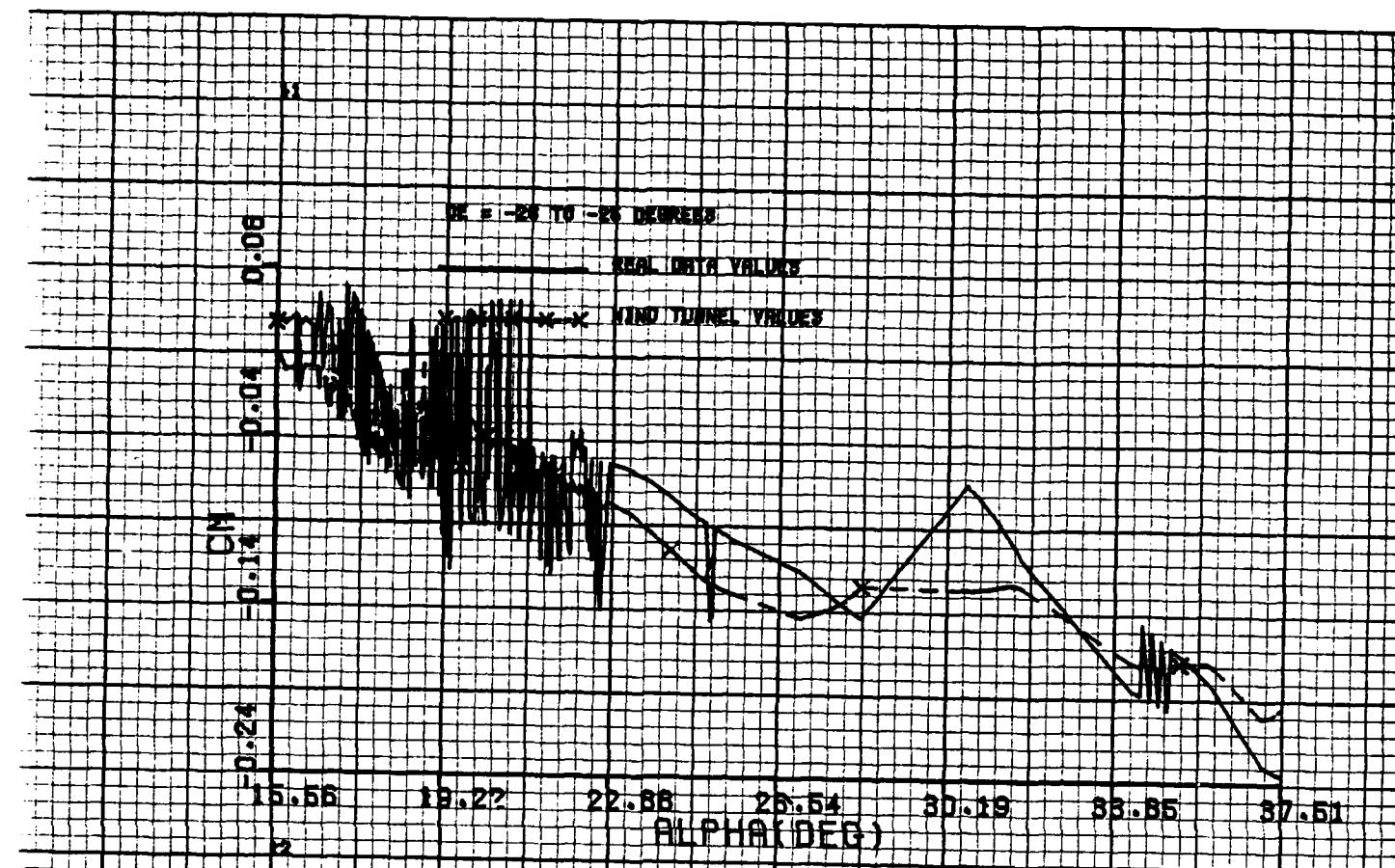


Figure F-13

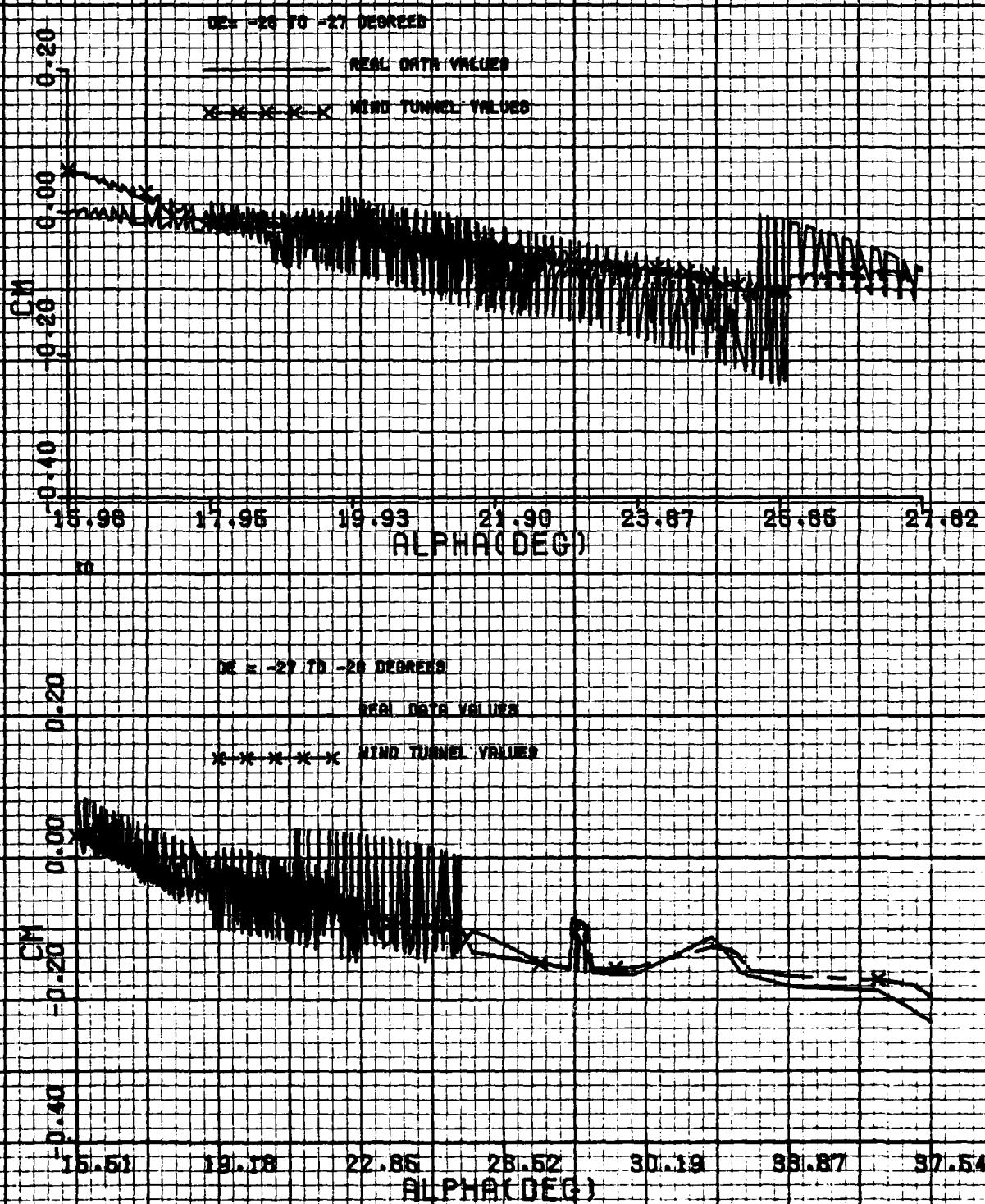


Figure F-14

APPENDIX G

MODELING RESULTS: C_z CURVES

A comparison between the wind tunnel values of C_z and the values of C_z extracted from the actual T-2C flight test data is contained in Figures G-1 through G-14. In these figures the aerodynamic coefficient C_z is shown as a function of the angle-of-attack for fixed one degree intervals of the elevator control. The range of the elevator control covered is from -28° to 0° .

Figures G-1 through G-14 were generated as follows: a particularly small range of the elevator control was selected from δ_e to $\delta_e + 1^\circ$ where δ_e is an integer between -28 and -1. All $C_z(t)$ estimates (i.e., an output of the first step of the EBM method) from all maneuvers having a corresponding elevator control $\delta_e(t)$ within the selected range δ_e to $\delta_e + 1^\circ$ were ordered according to the angle-of-attack variable and then plotted as one of the "real data values" curves in Figures G-1 through G-14. The "wind tunnel values" curves were obtained by evaluating the wind tunnel model using the estimated states which have an associated elevator control $\delta_e(t)$ in the selected range δ_e to $\delta_e + 1^\circ$, by storing the resulting wind tunnel coefficient values $WTC_z(t)$, by ordering them with respect to the angle-of-attack variable, and by plotting the ordered wind tunnel values. It should be observed that the curves in Figures G-1 through G-14 have a dependency on β , q and $\dot{\alpha}$ built into them by the nature of the maneuvers.

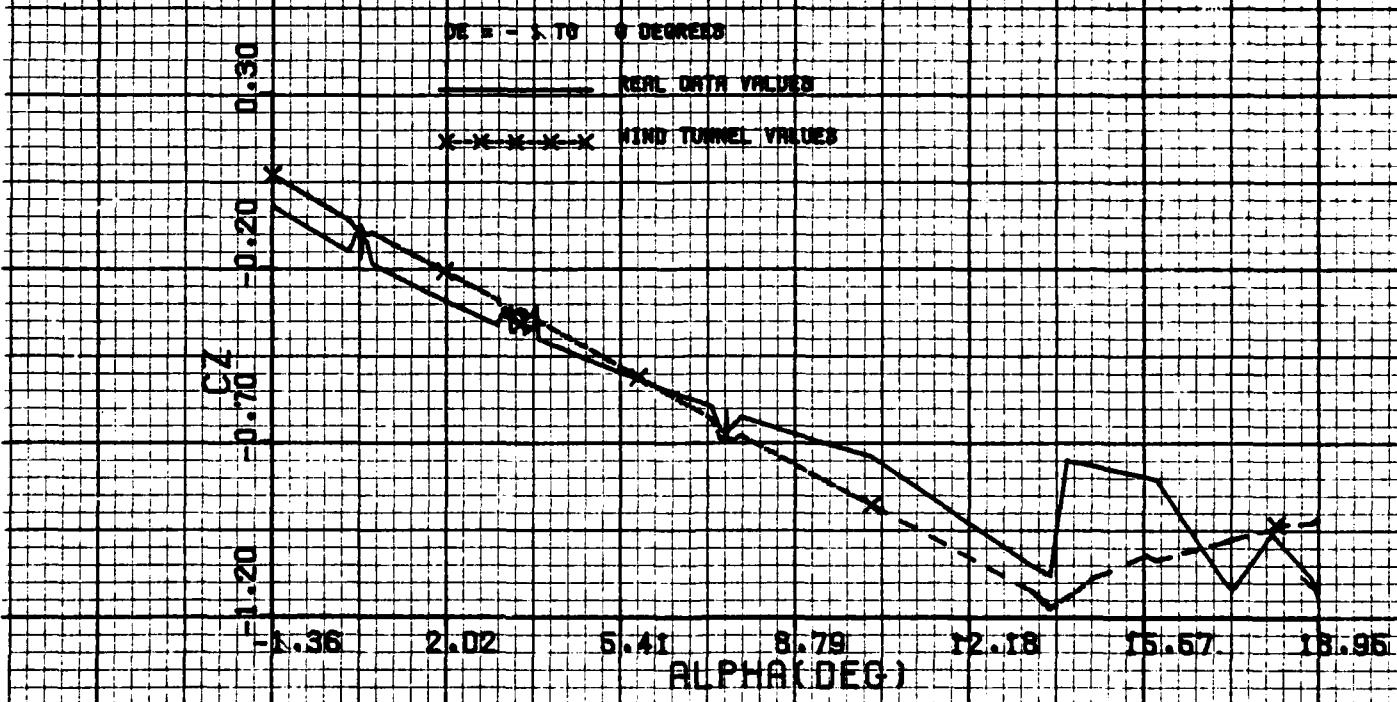
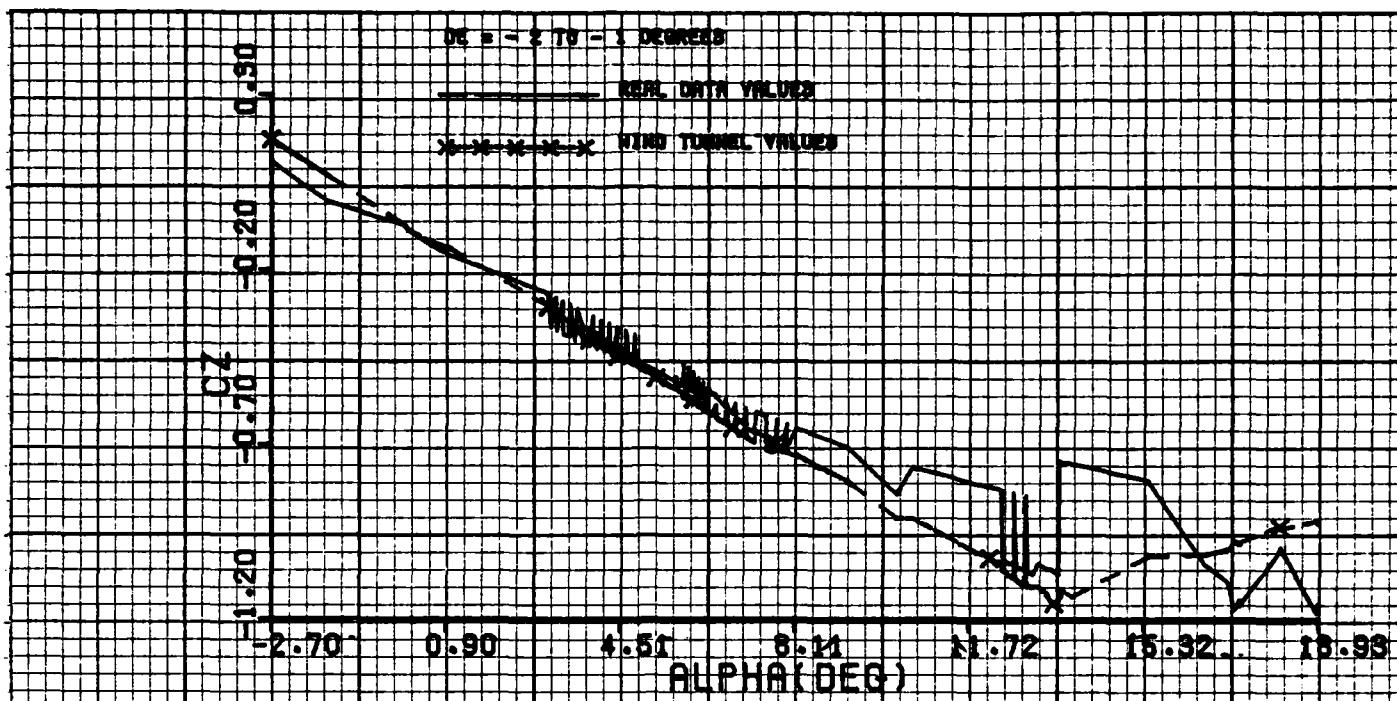


Figure G-1

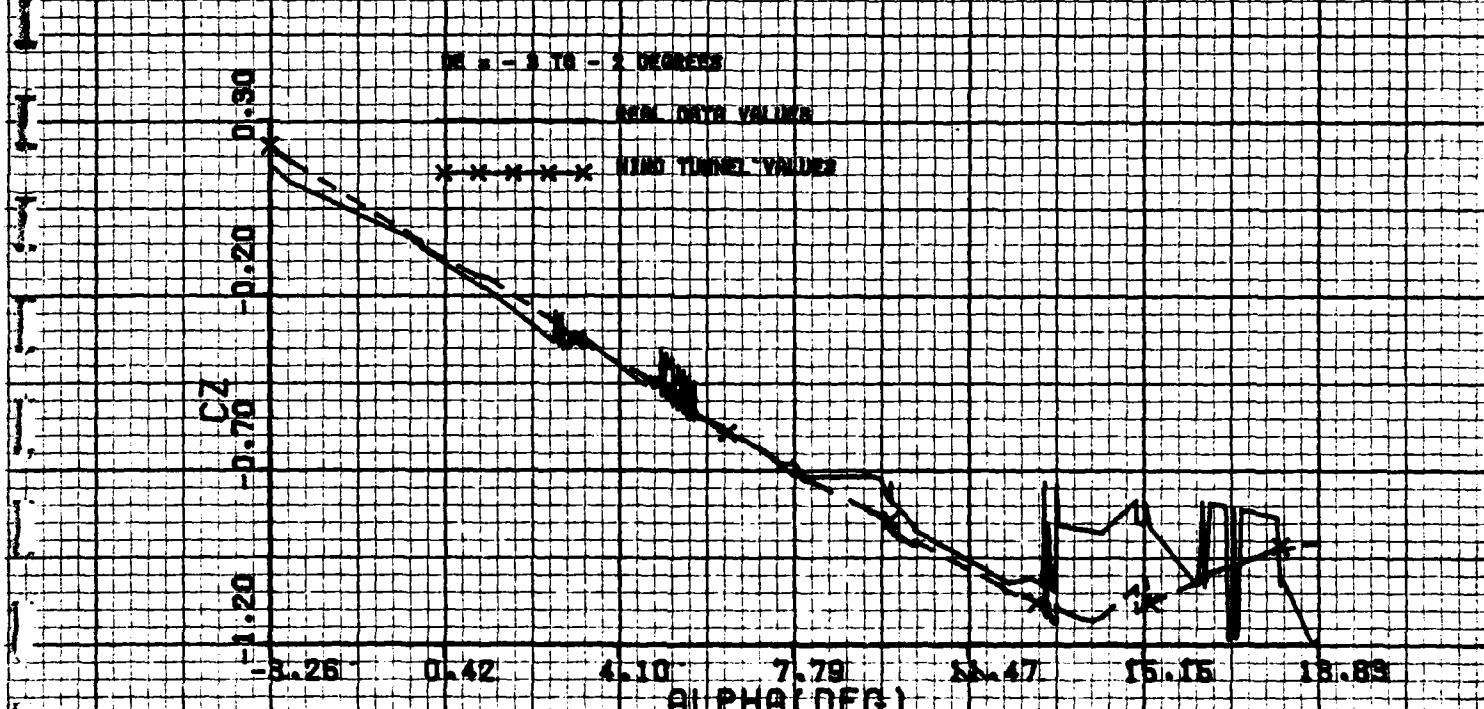
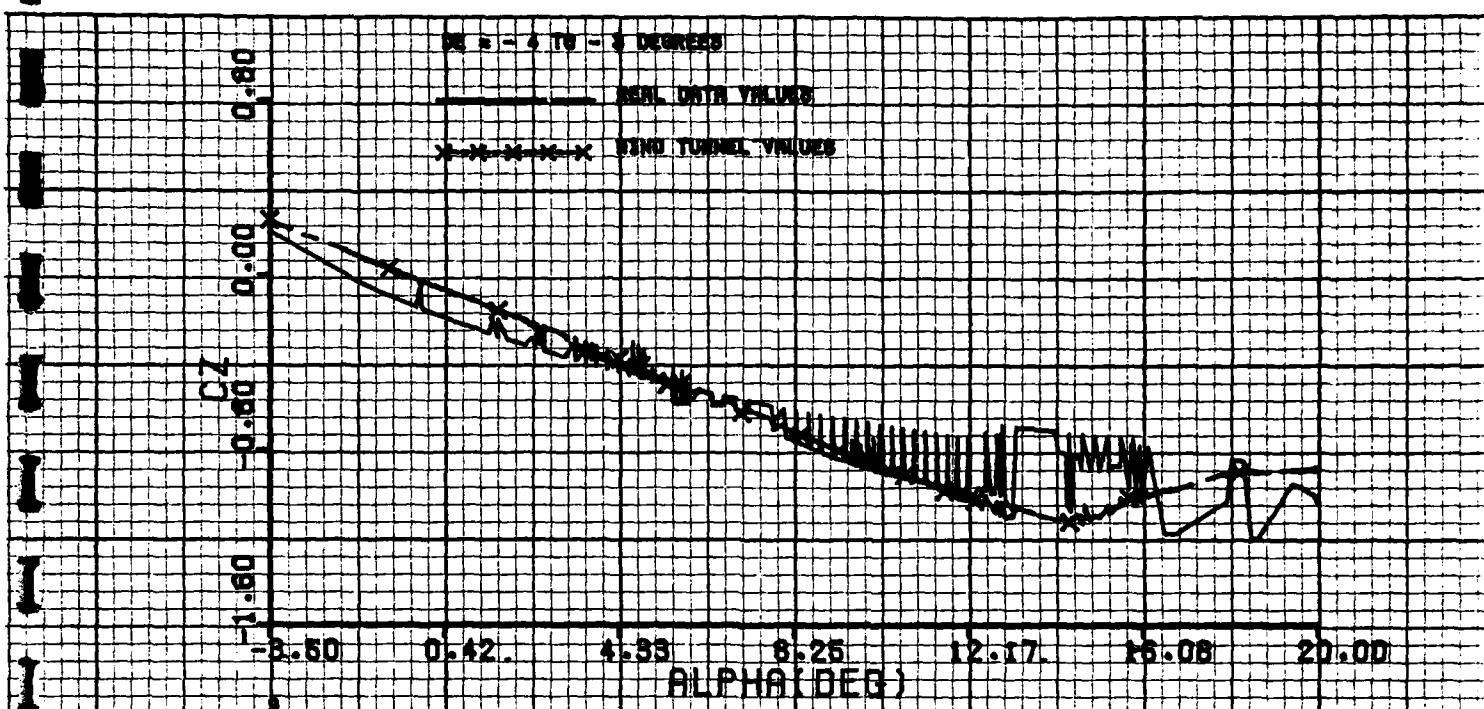


Figure G-2

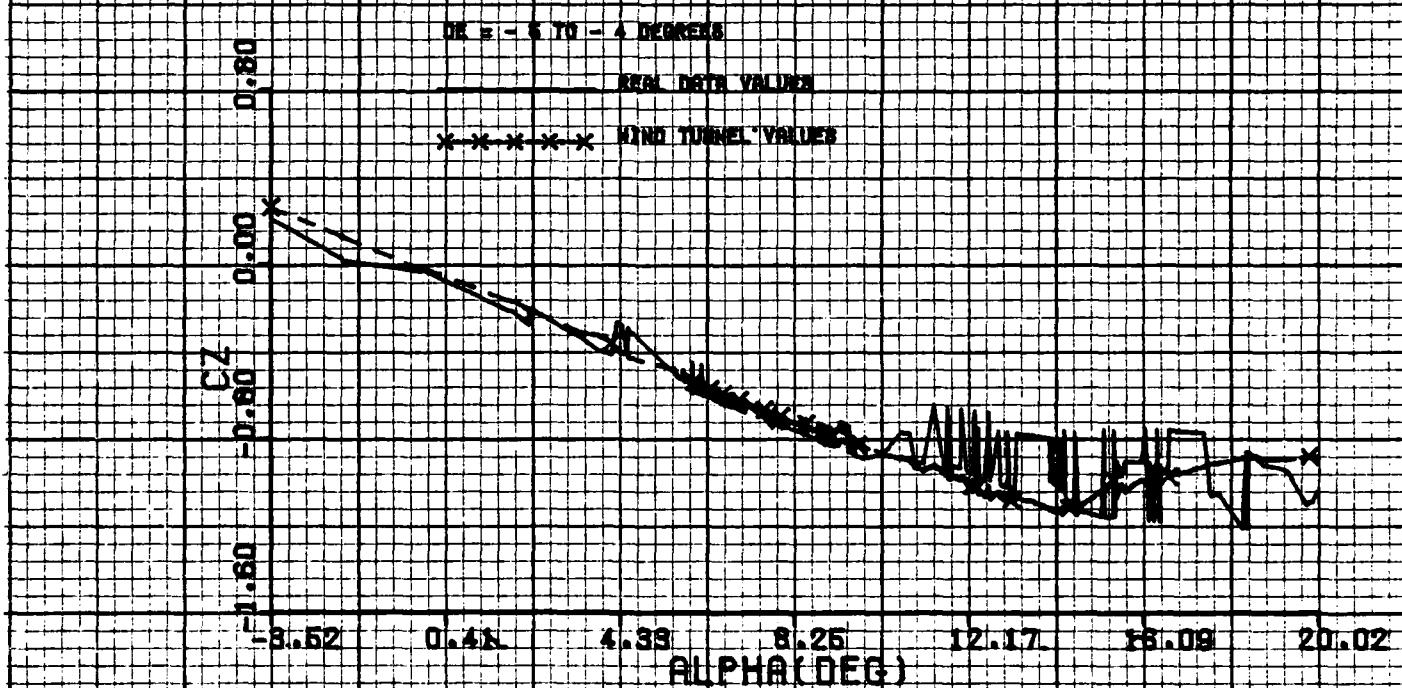
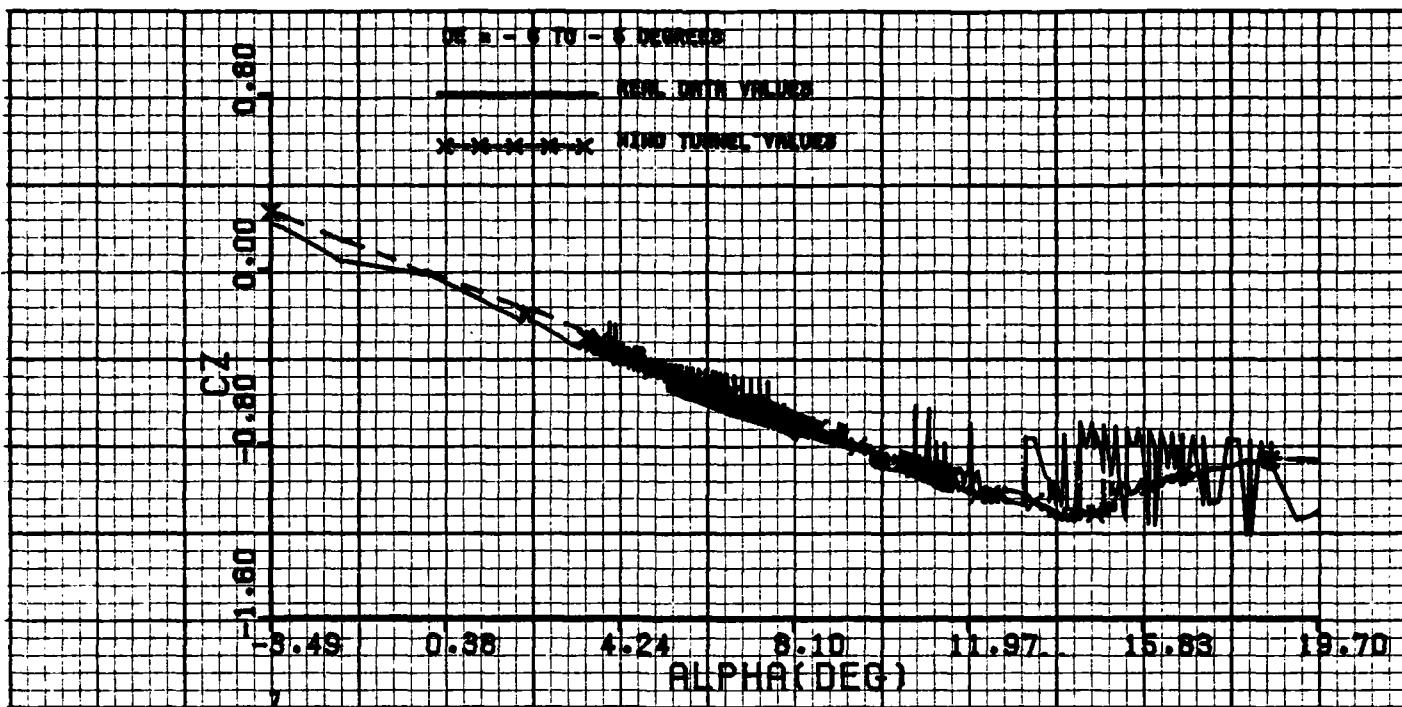


Figure G-3

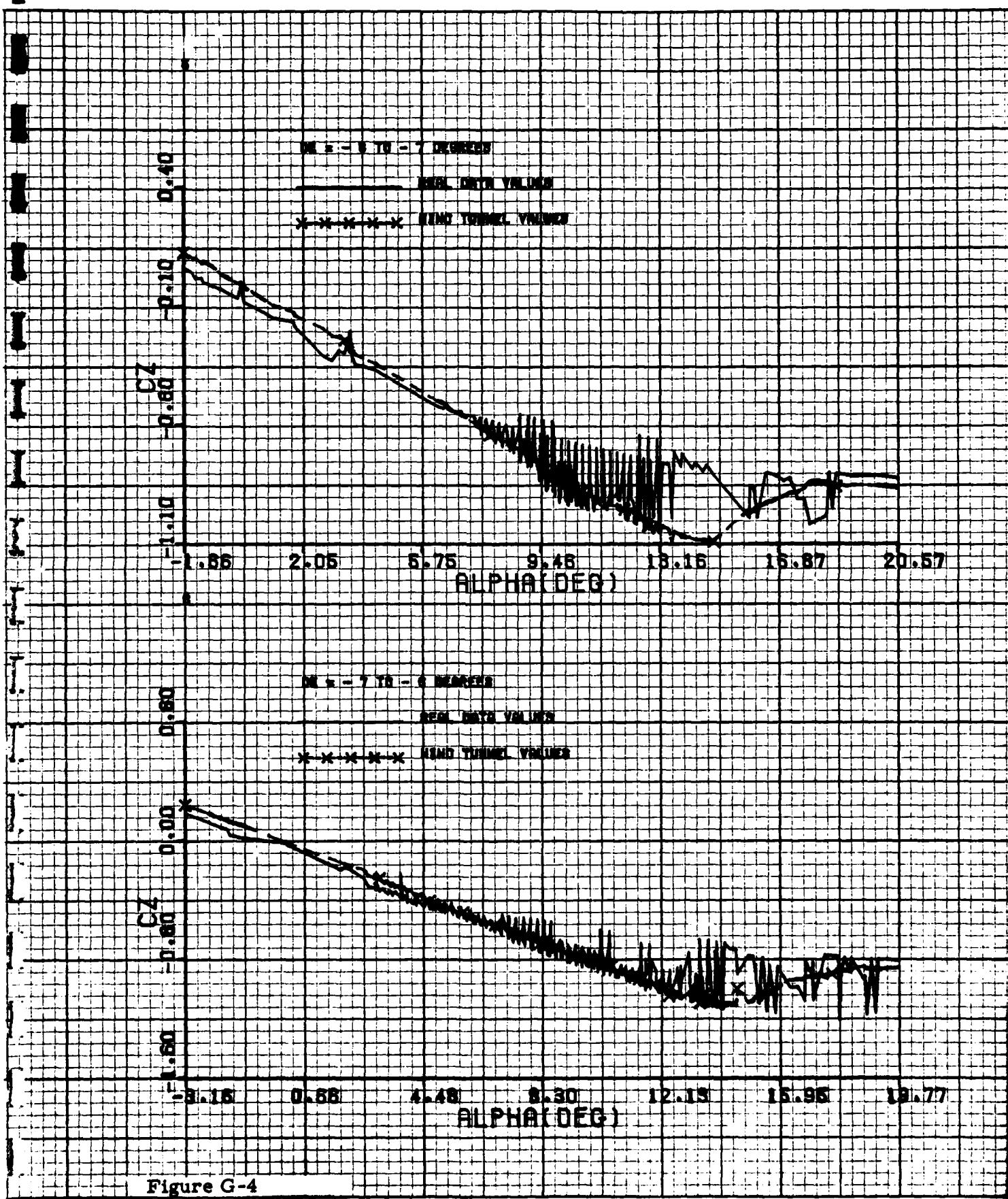


Figure G-4

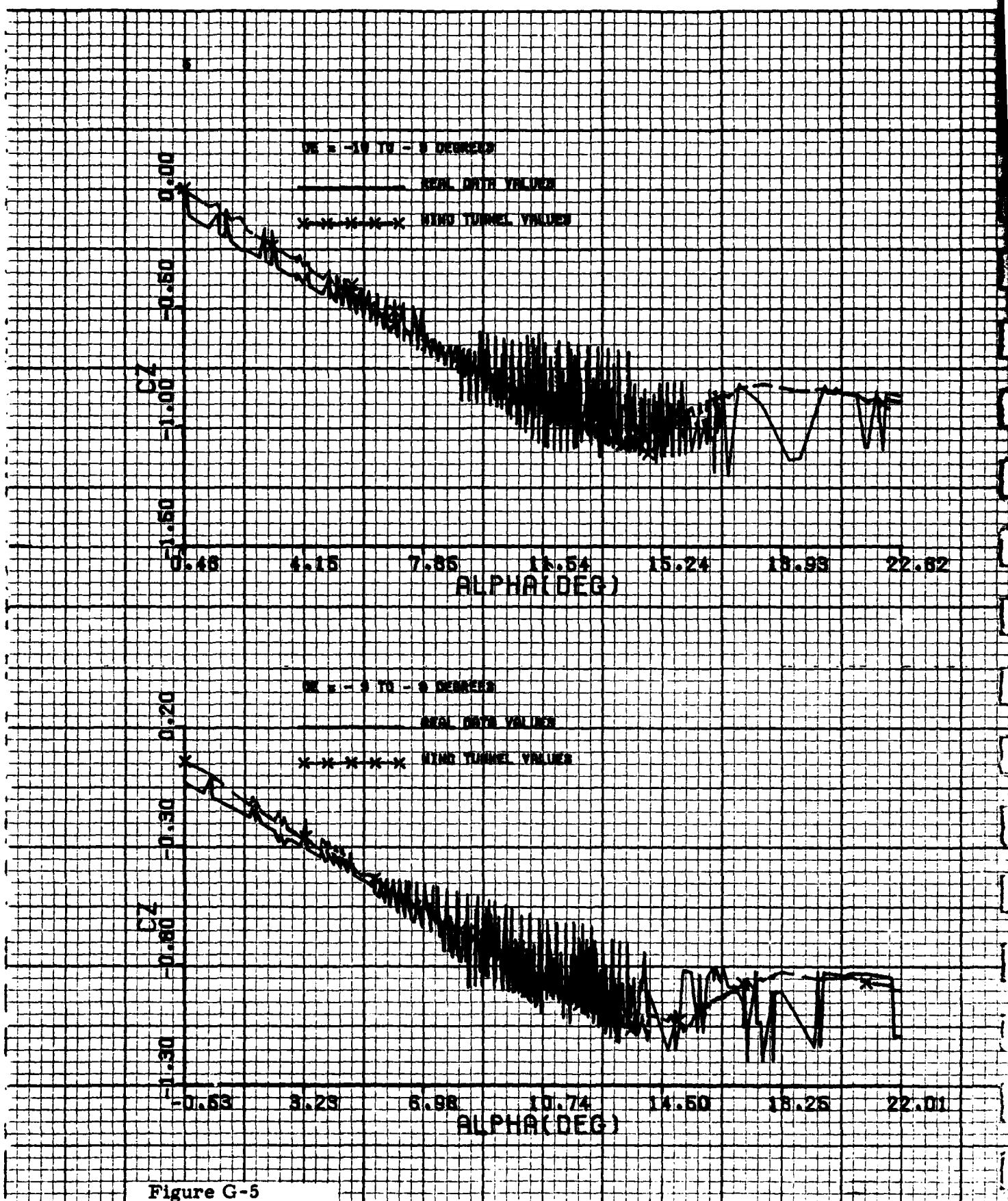


Figure G-5

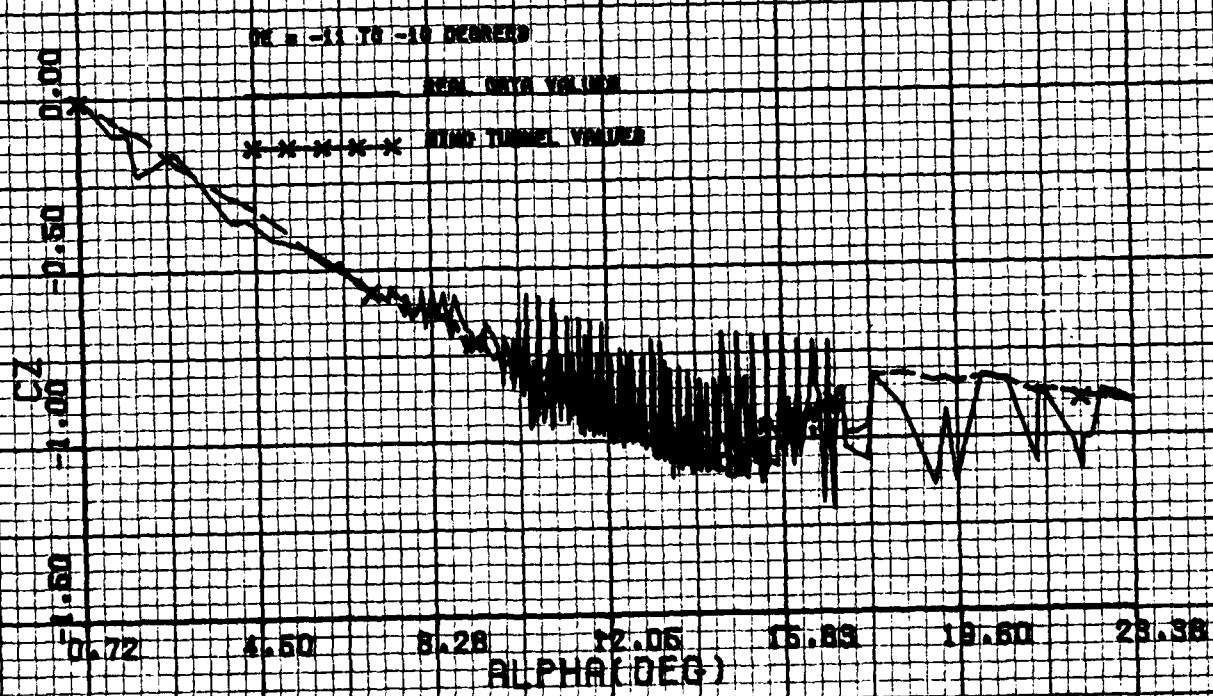
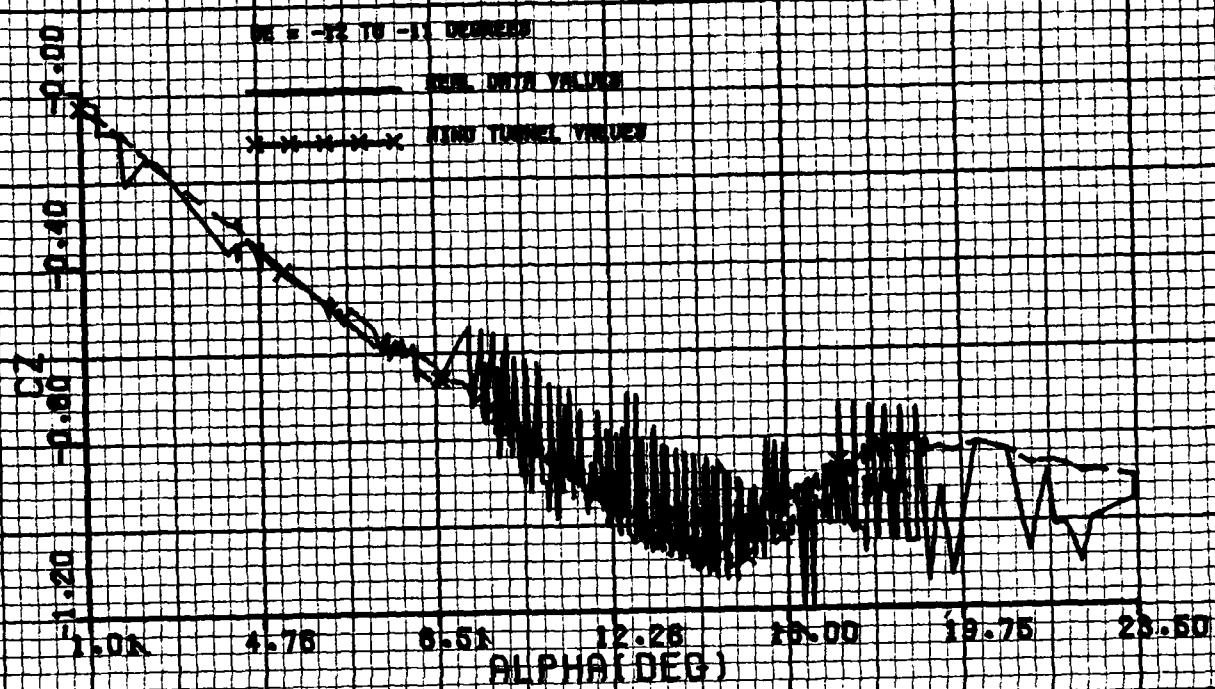


Figure G-6

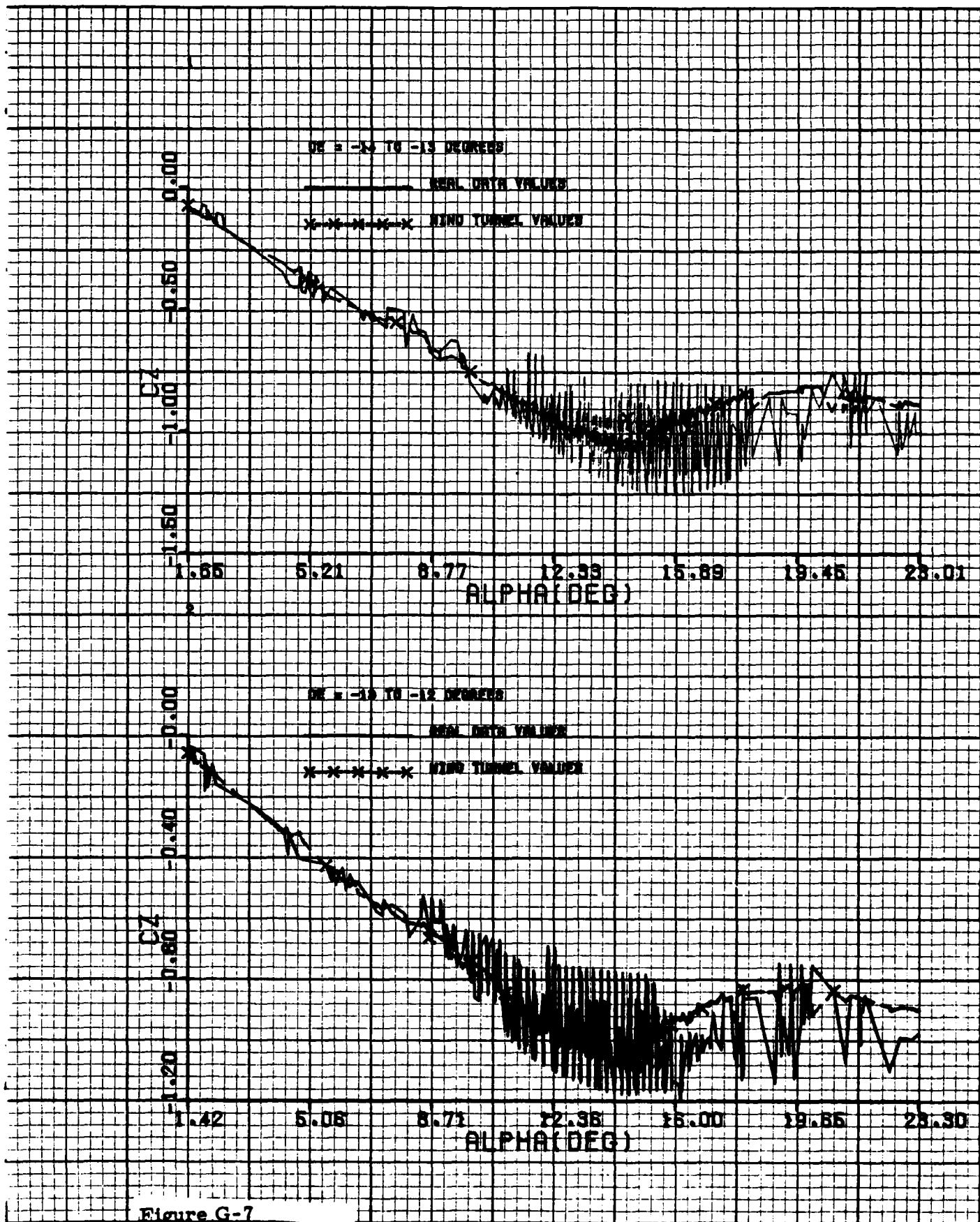


Figure G-7

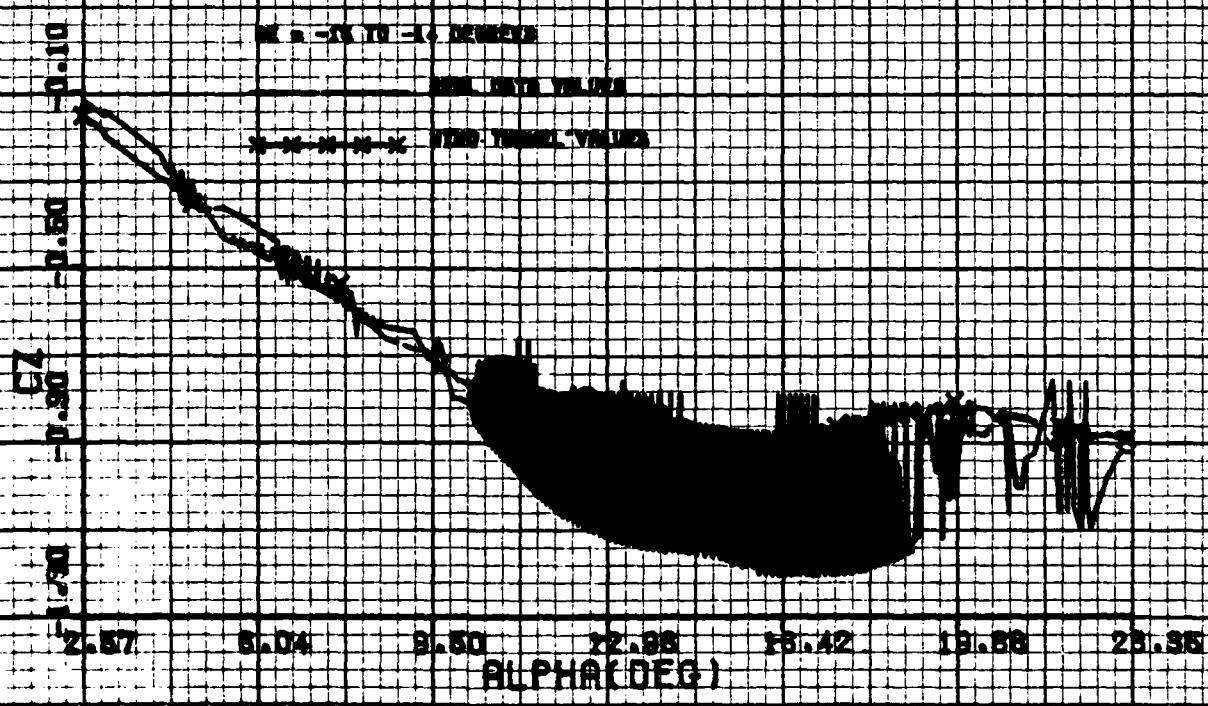
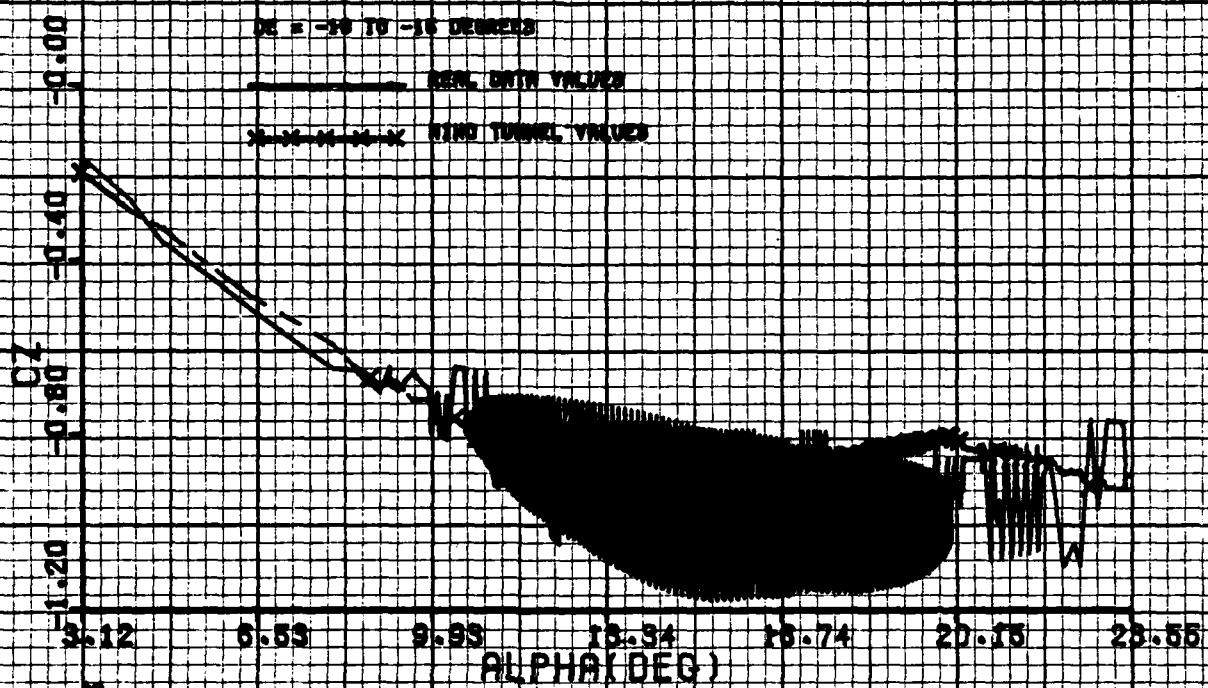
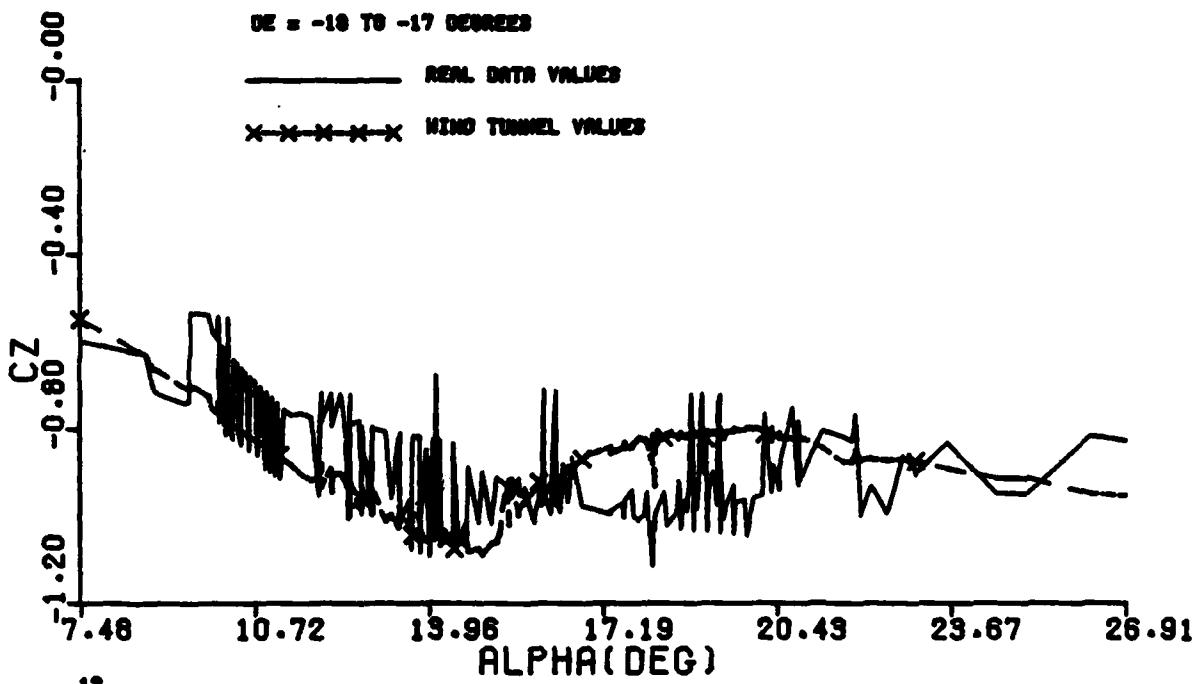


Figure G-8

11



12

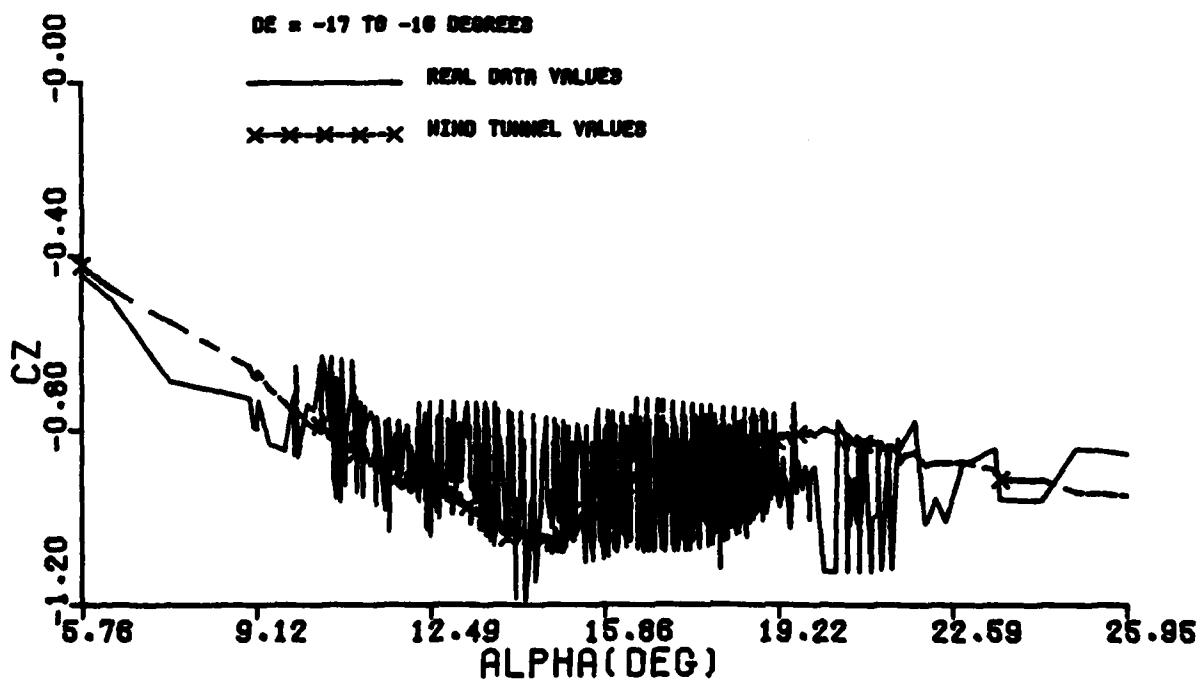


Figure G-9

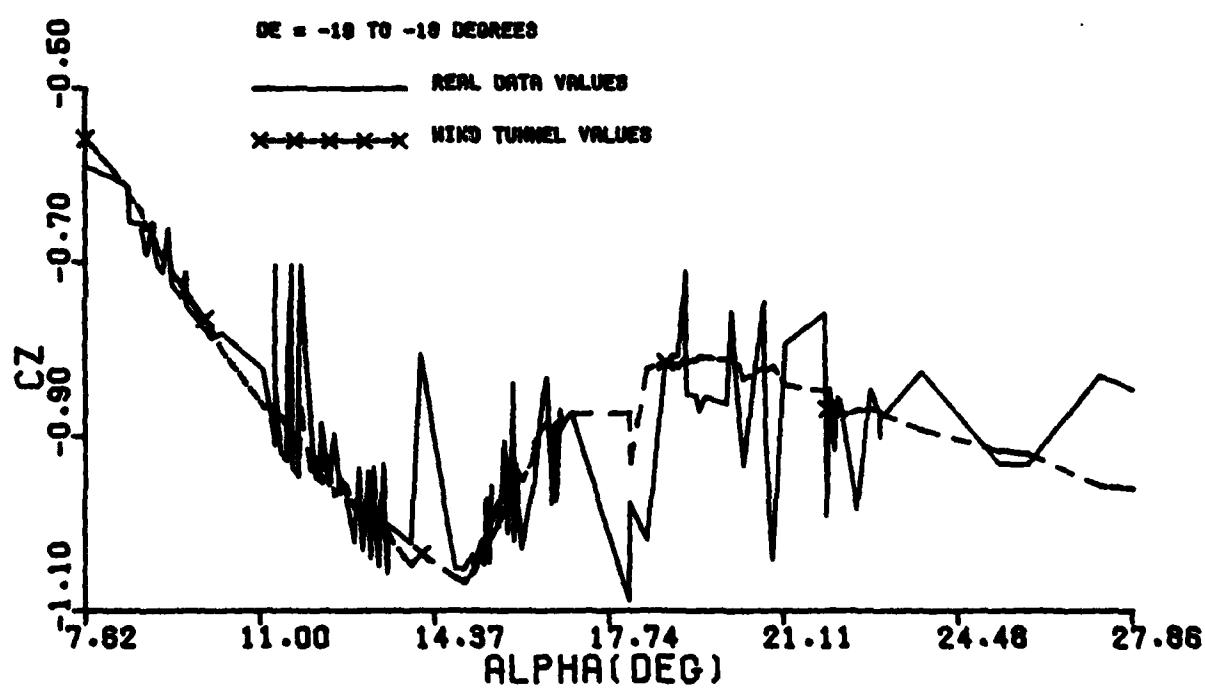
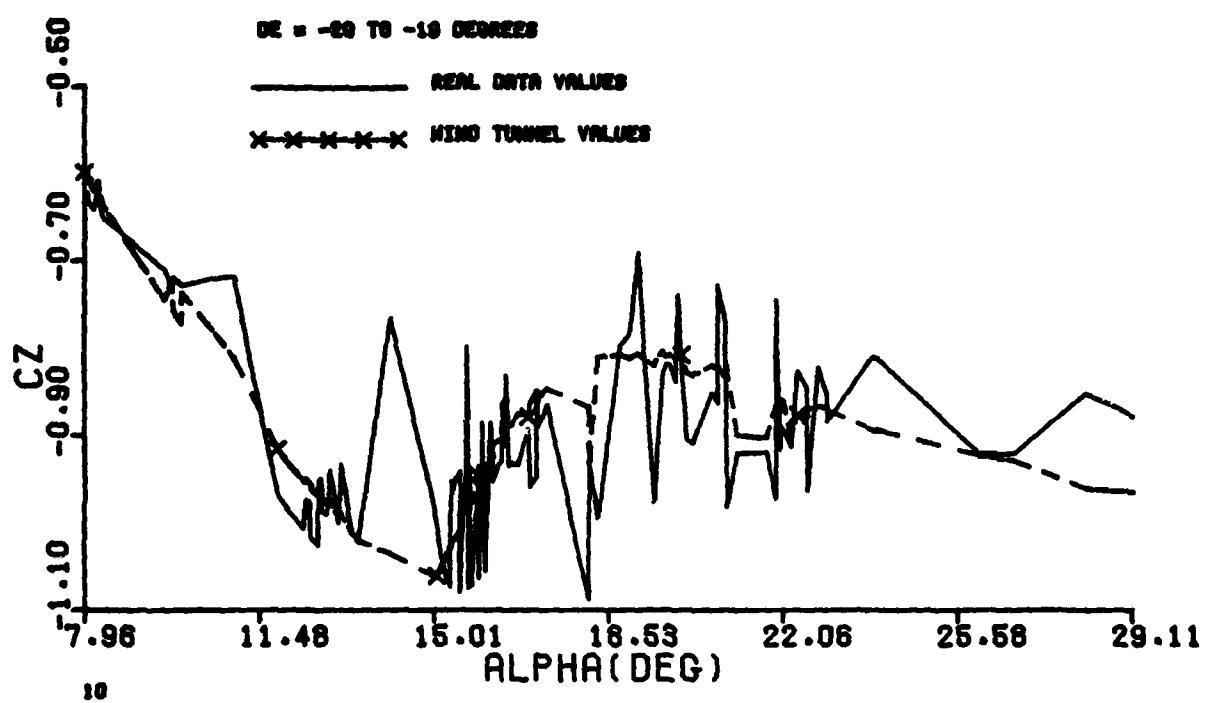


Figure G-10

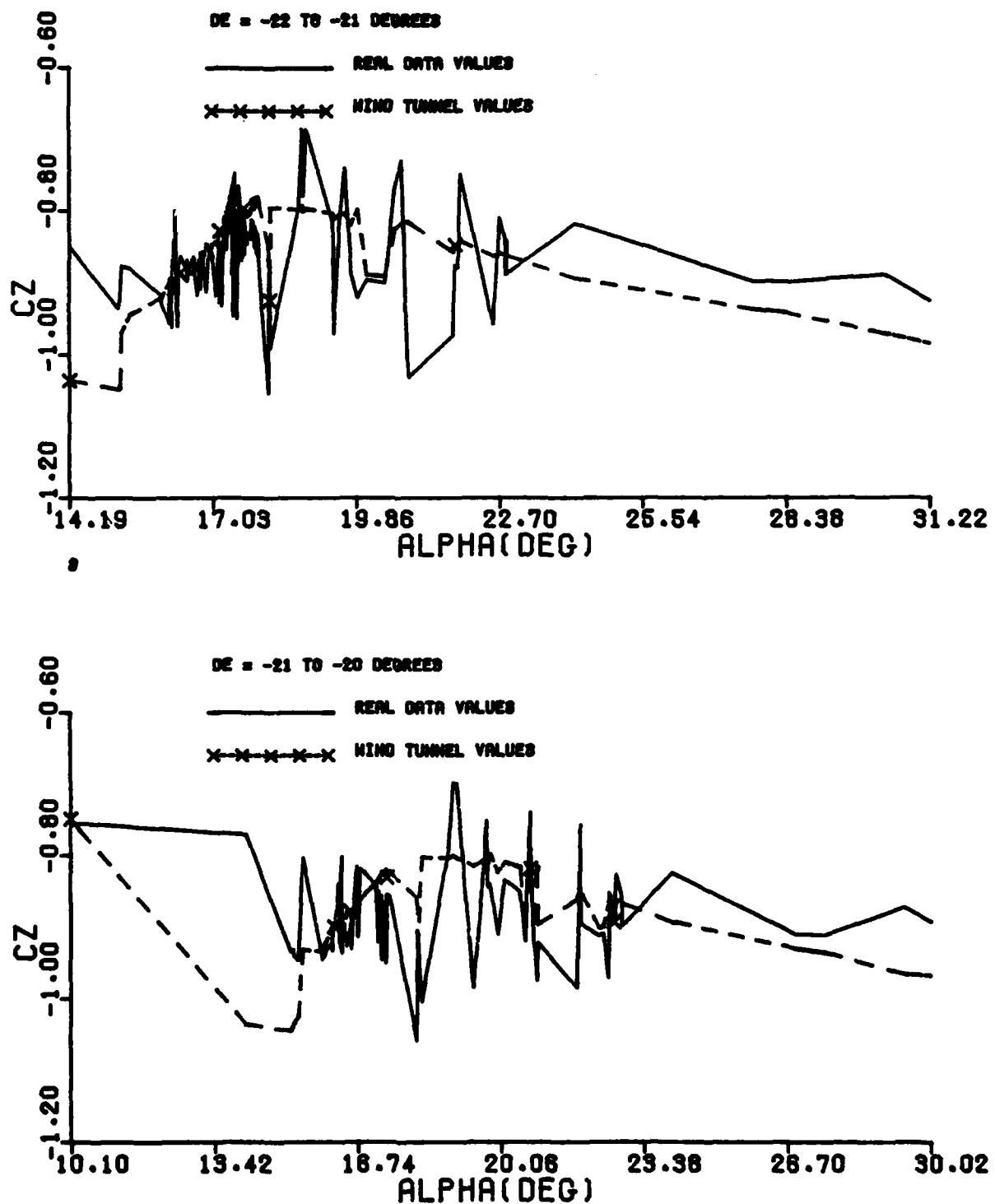


Figure G-11

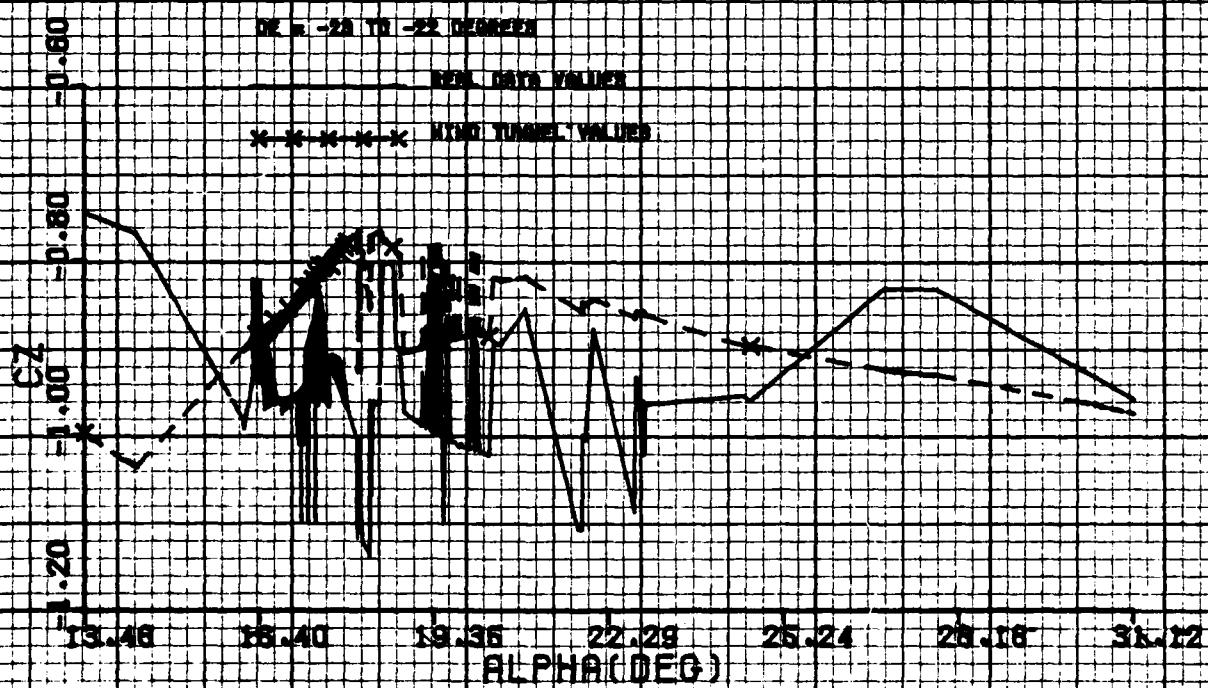
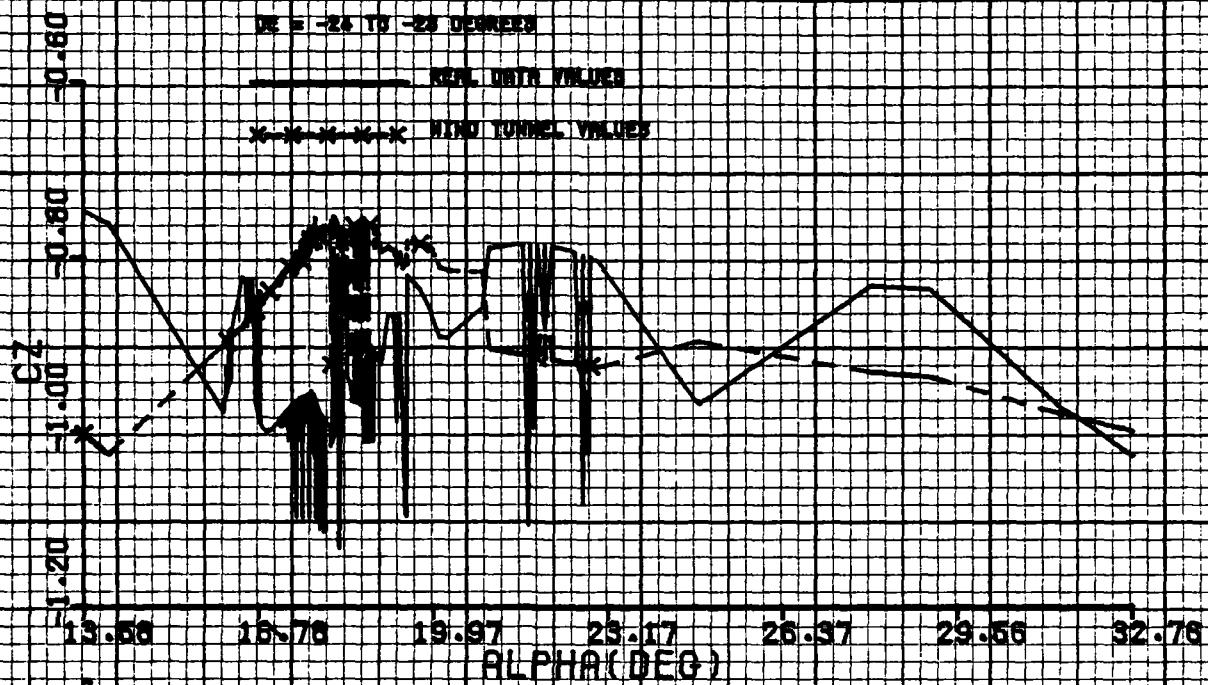


Figure G-12

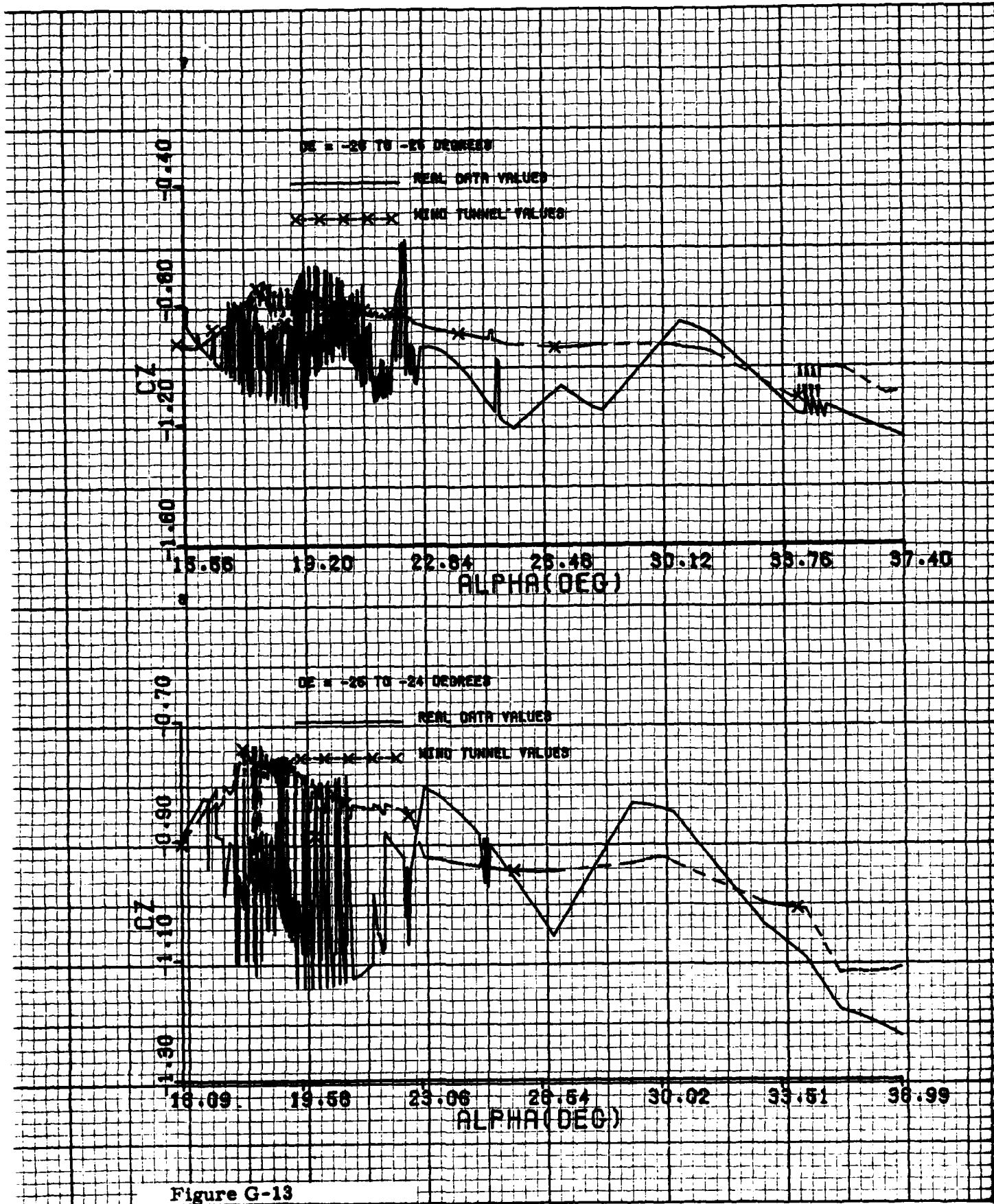


Figure G-13

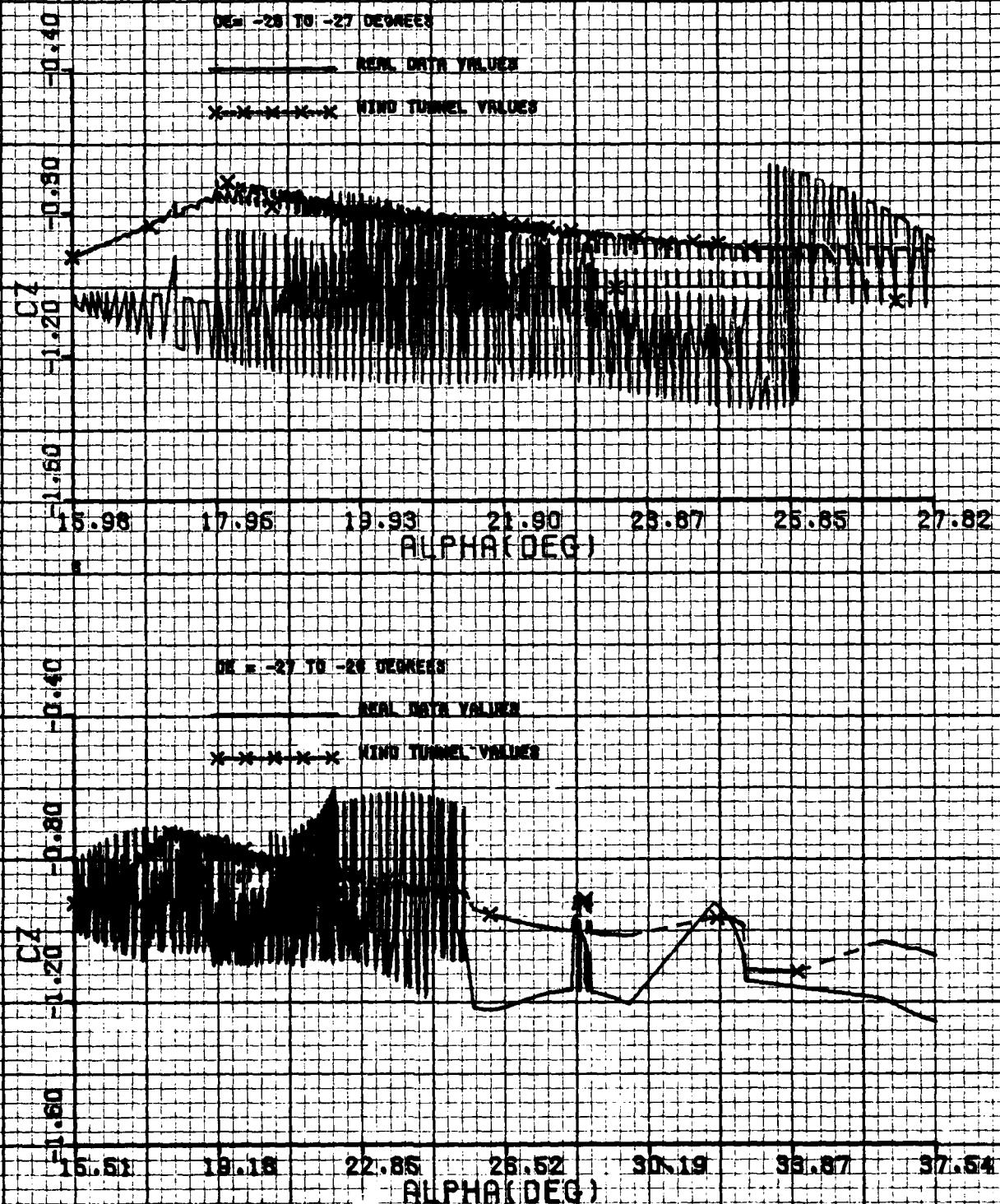


Figure G-14

APPENDIX H

MODELING RESULTS: C_x CURVES

A comparison between the wind tunnel values of C_x and the values of C_x extracted from the actual T-2C flight test data is contained in Figures H-1 through H-14. The coefficient C_x is given as a function of the angle-of-attack for fixed one degree intervals of the elevator control. The range of the elevator control covered is from -28° to 0° .

The Figures H-1 through H-14 were obtained in a way similar to those contained in Appendix G. A discussion is given therein.

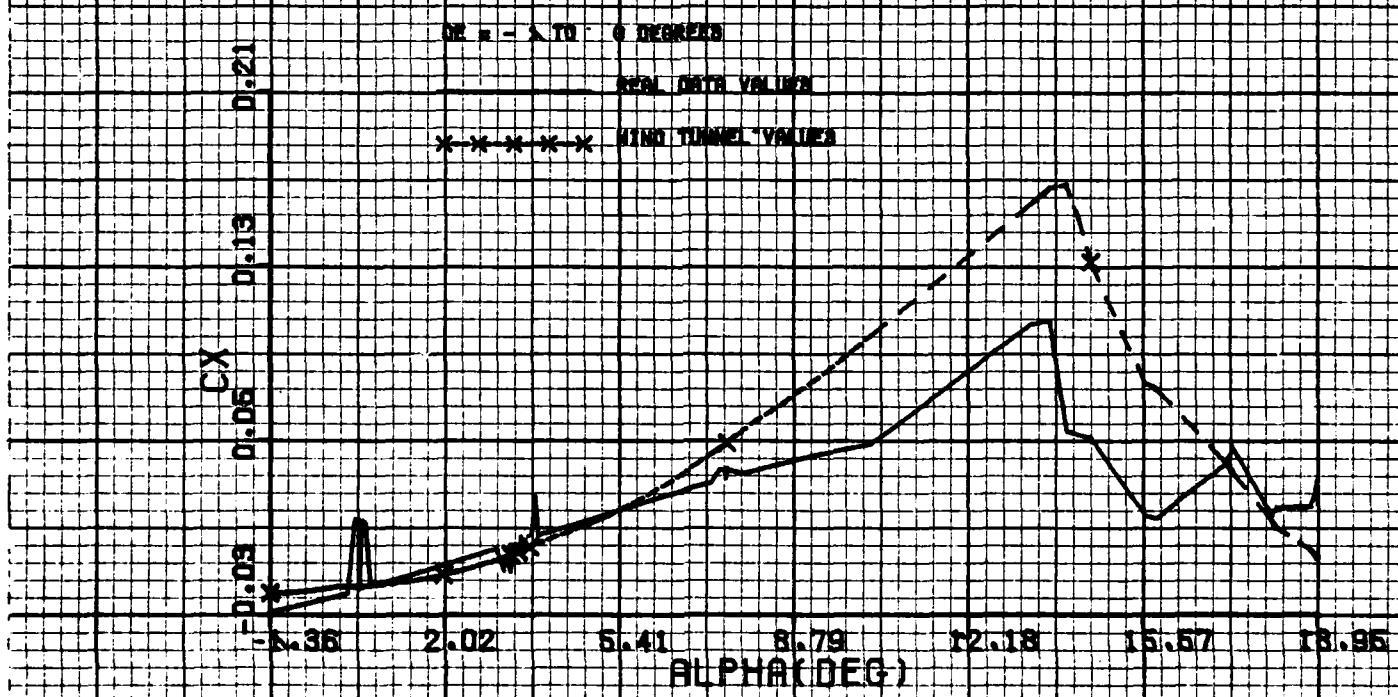
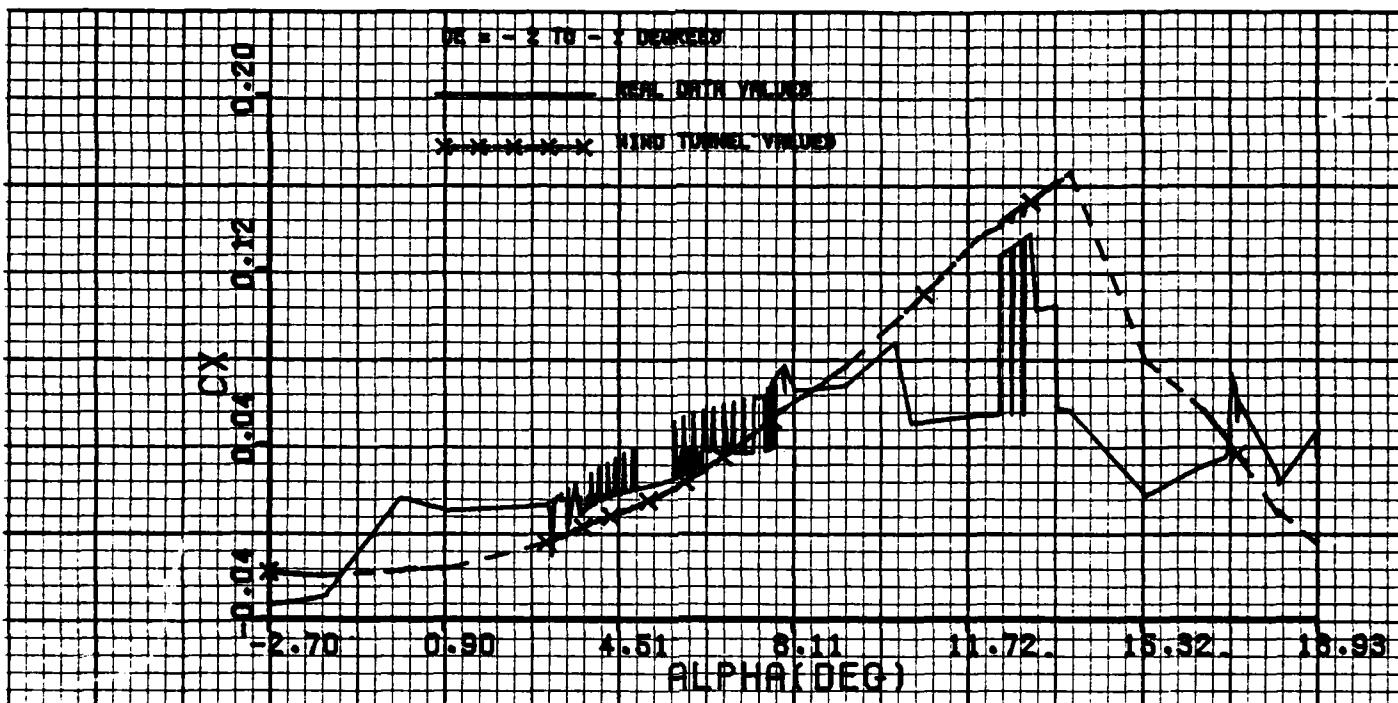


Figure H-1

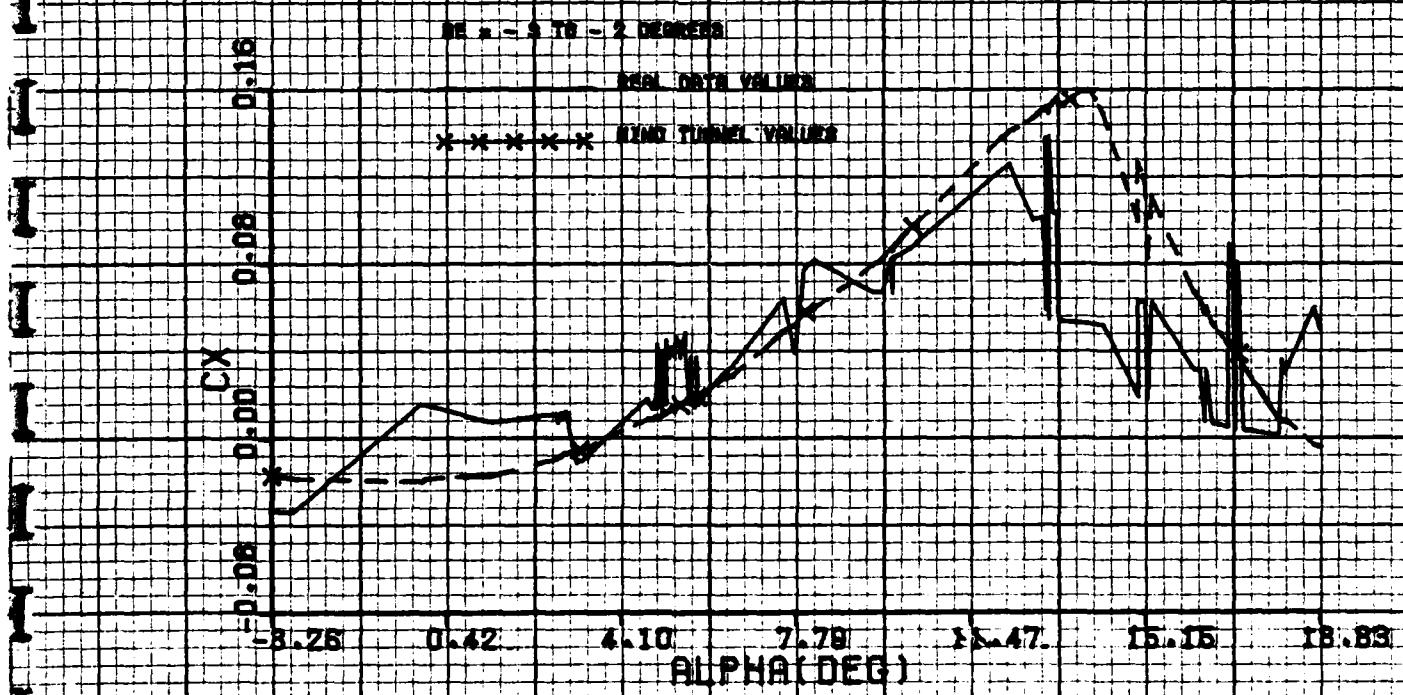
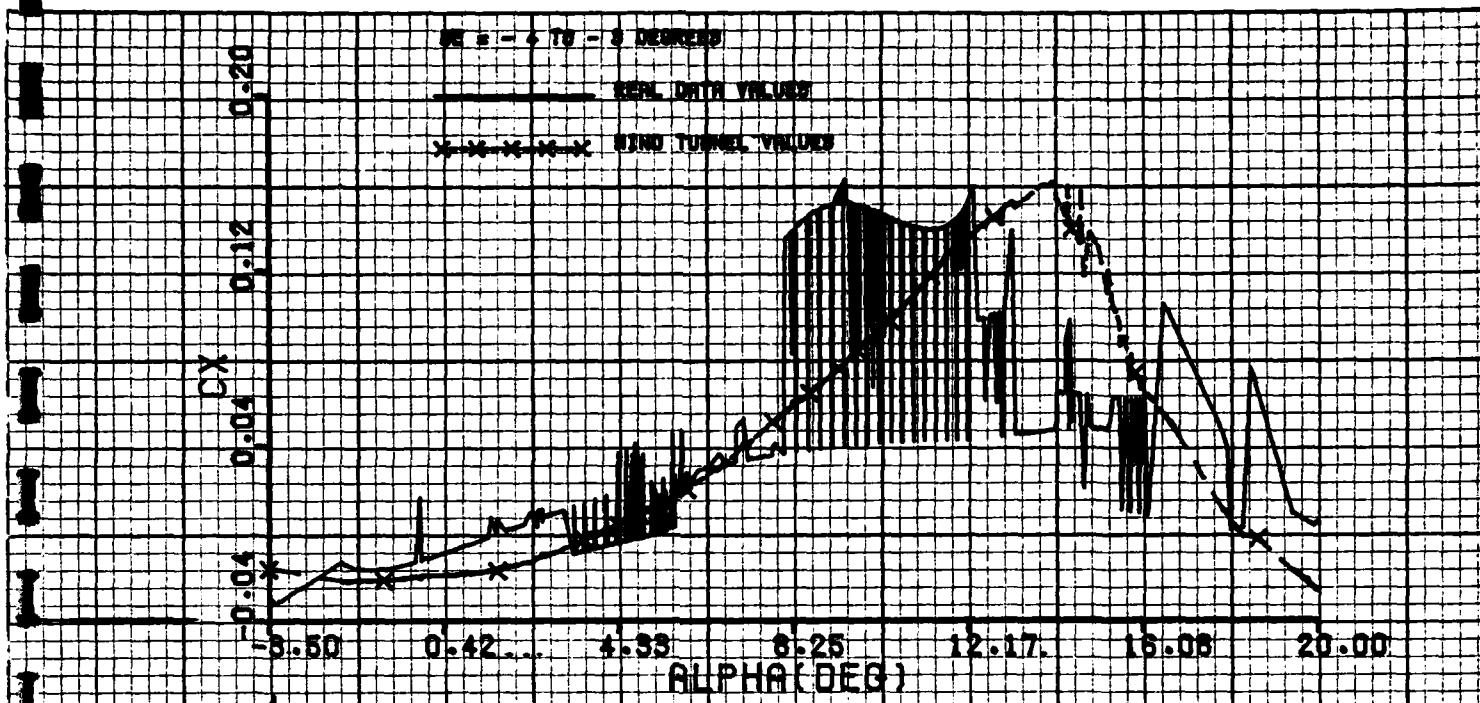


Figure H-2

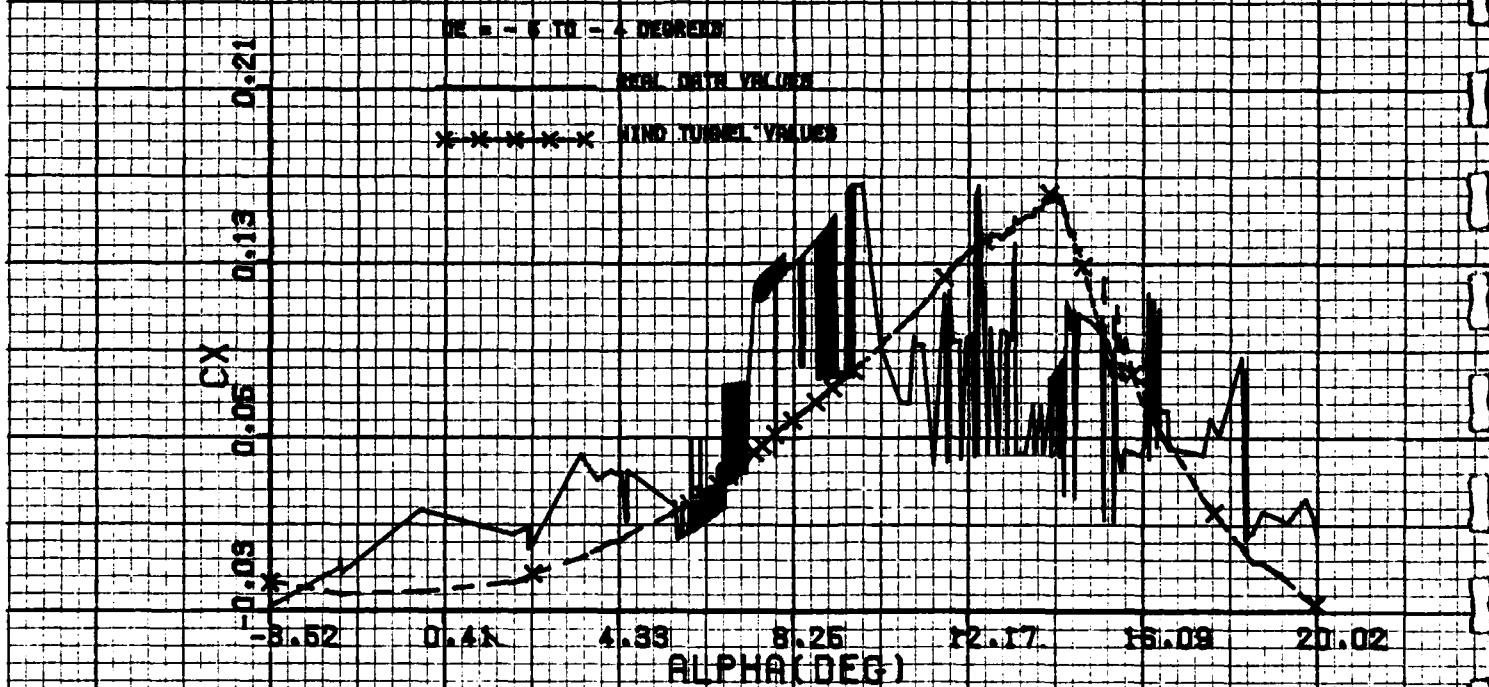
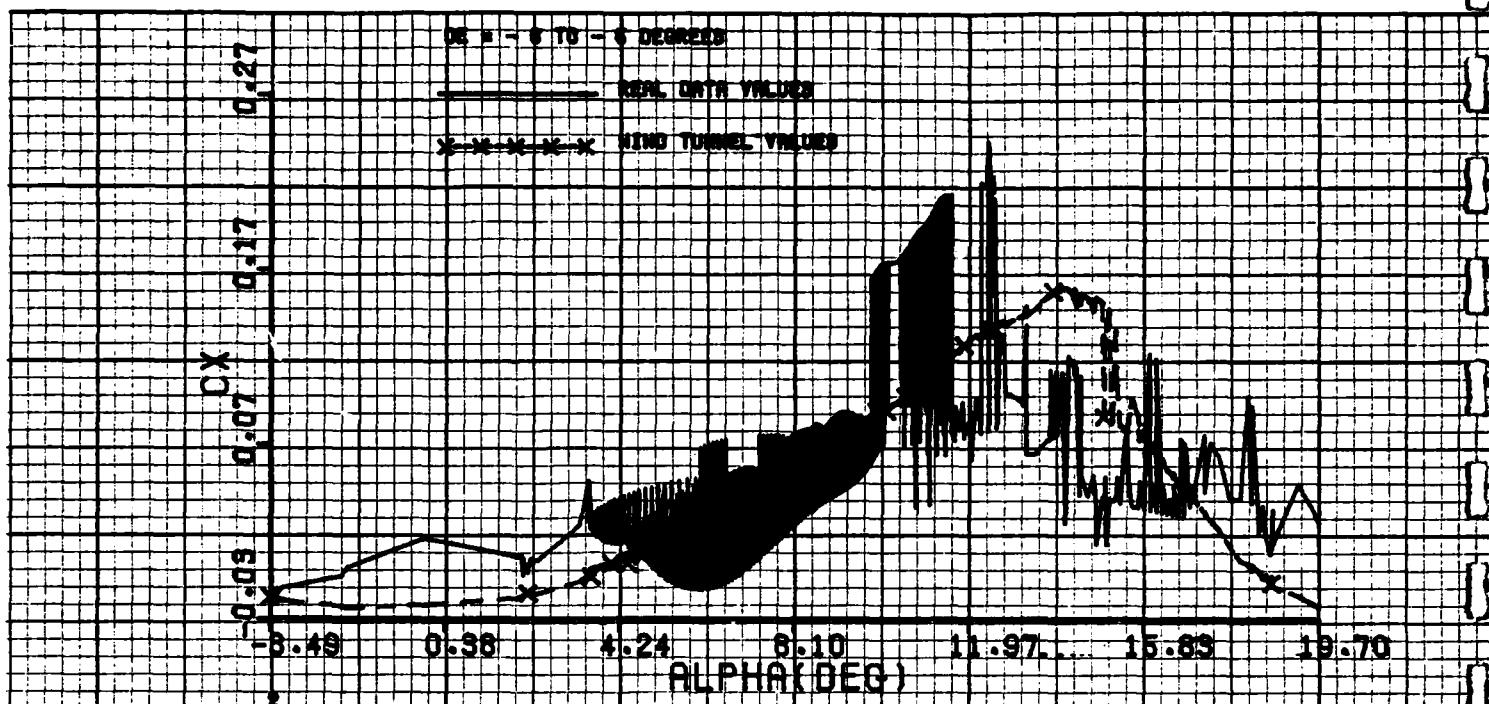


Figure H-3

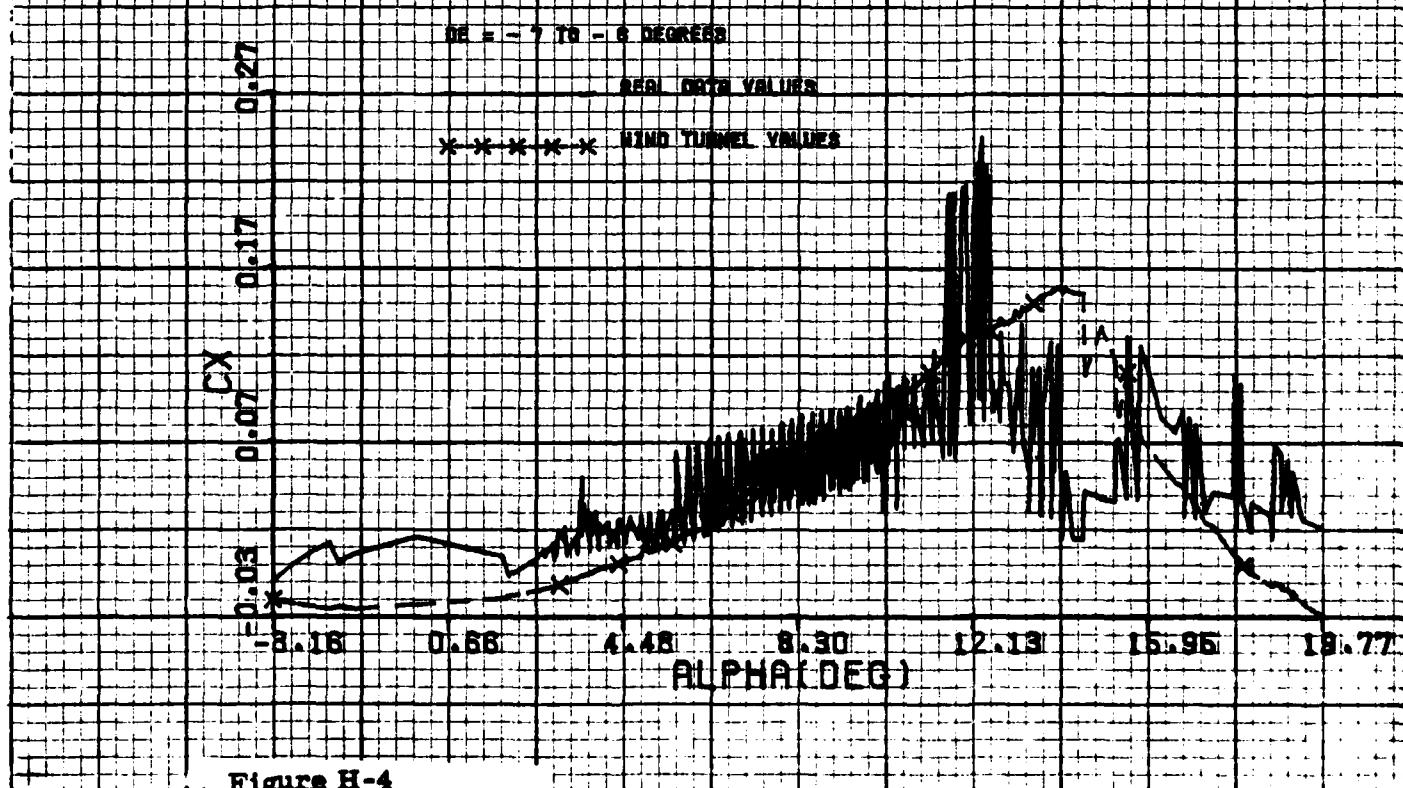
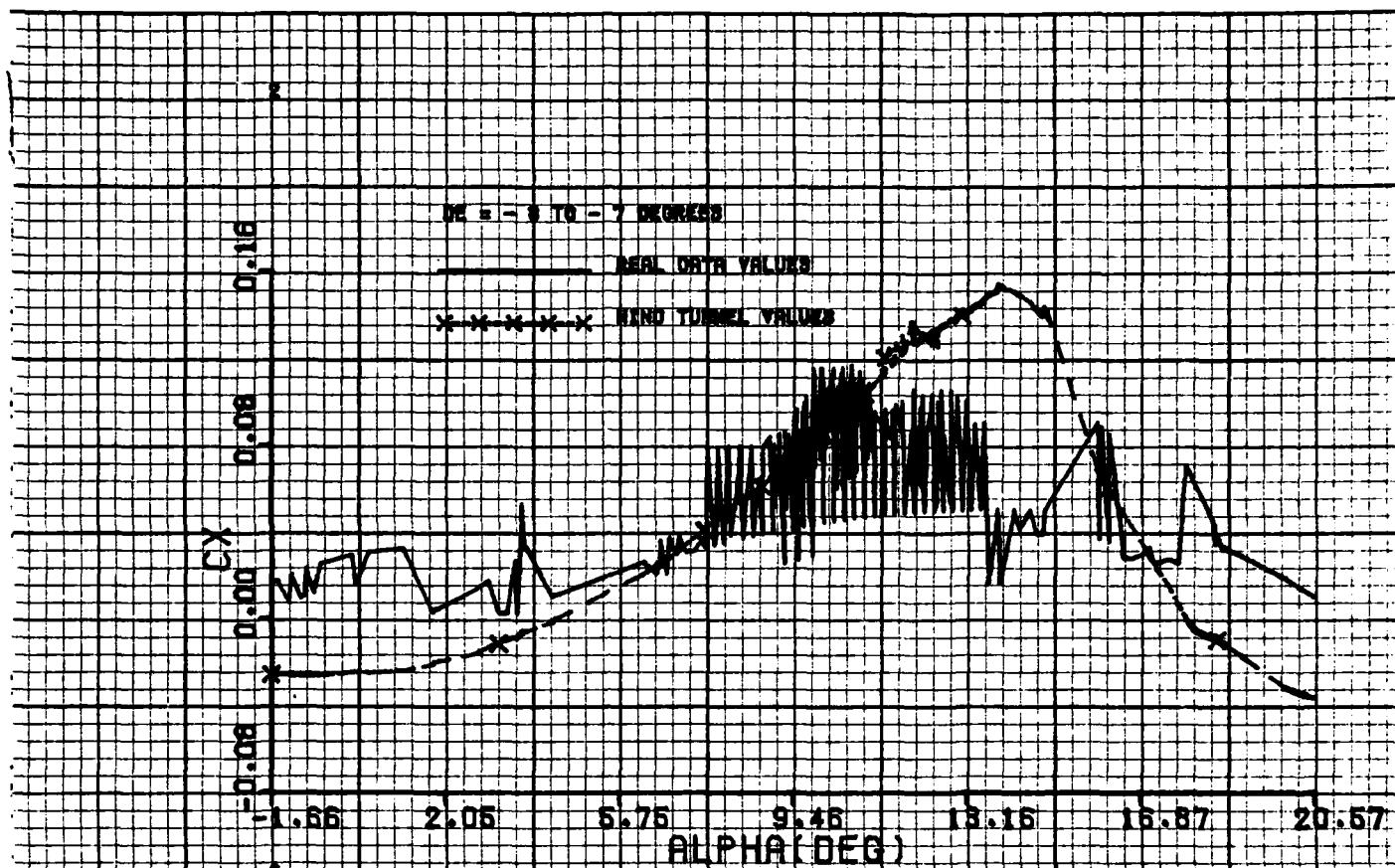


Figure H-4

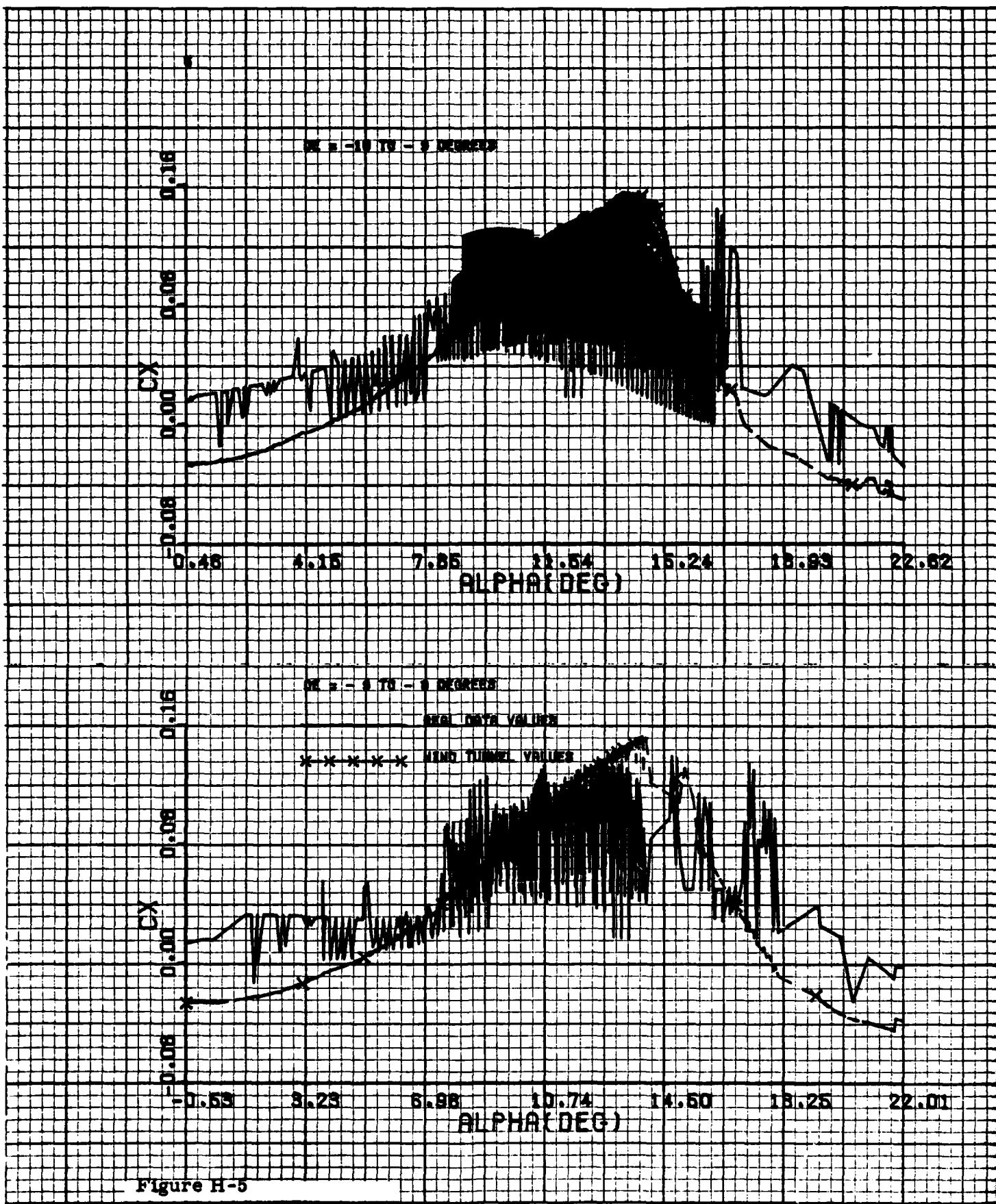


Figure H-5

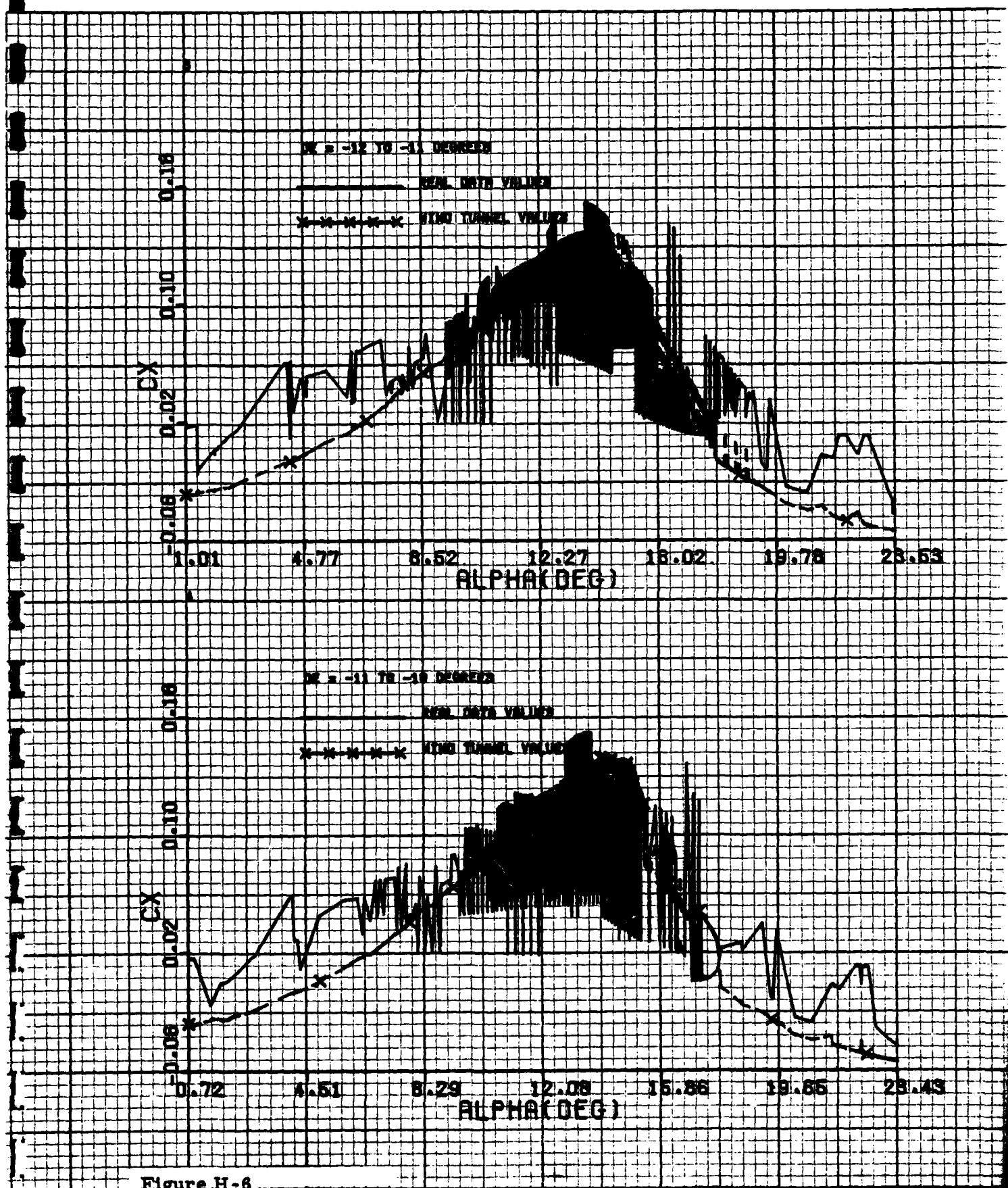


Figure H-6

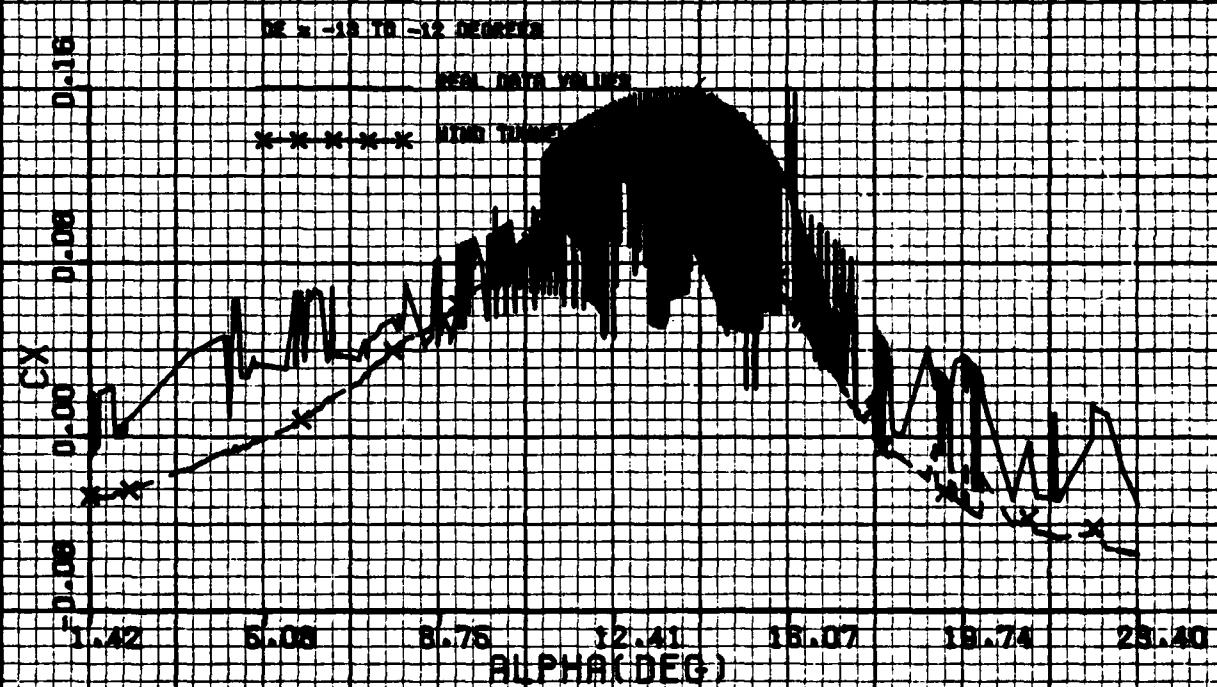
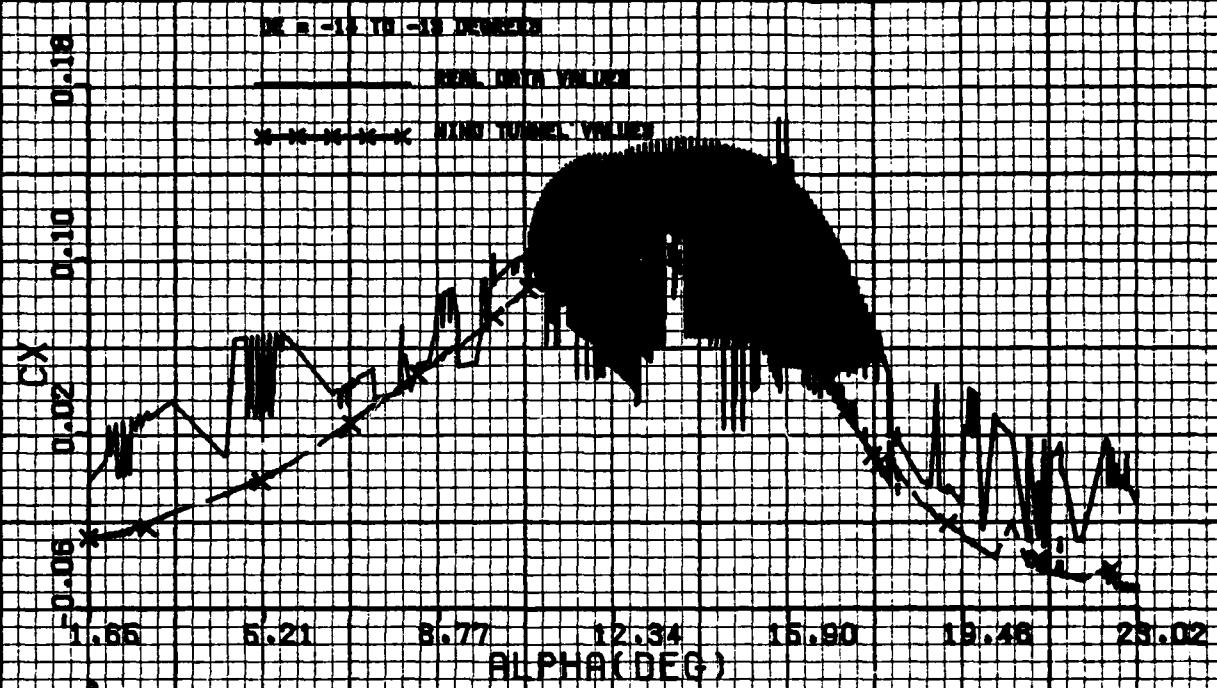


Figure H-7

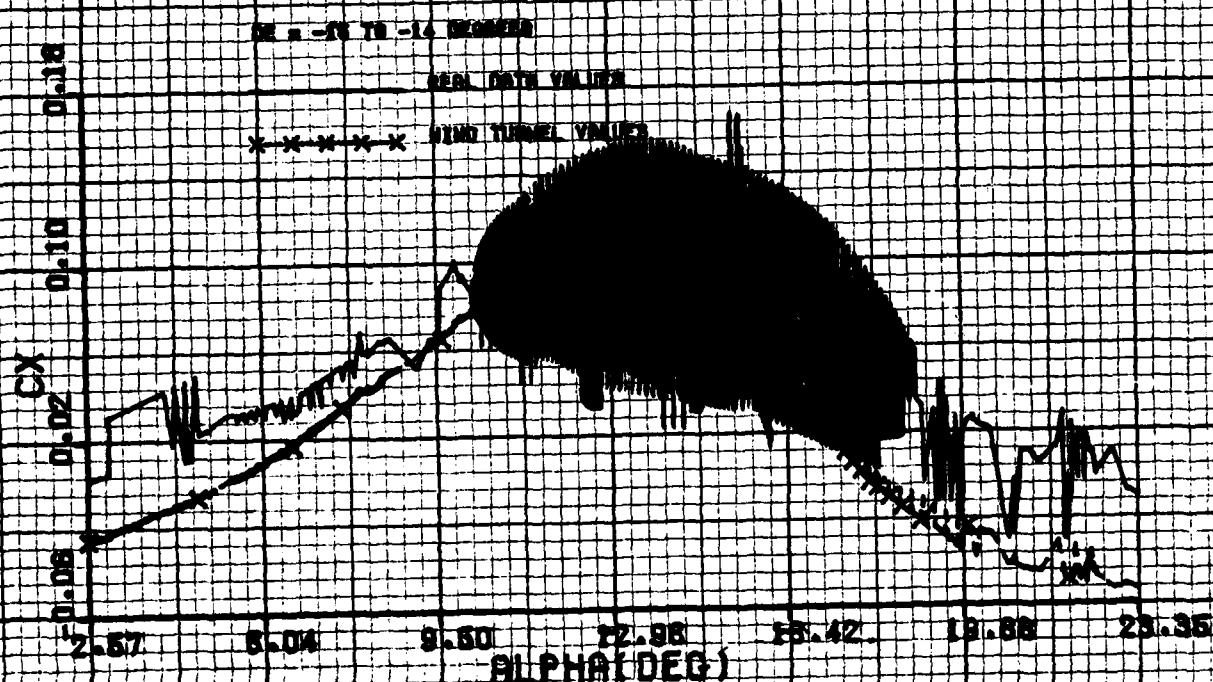
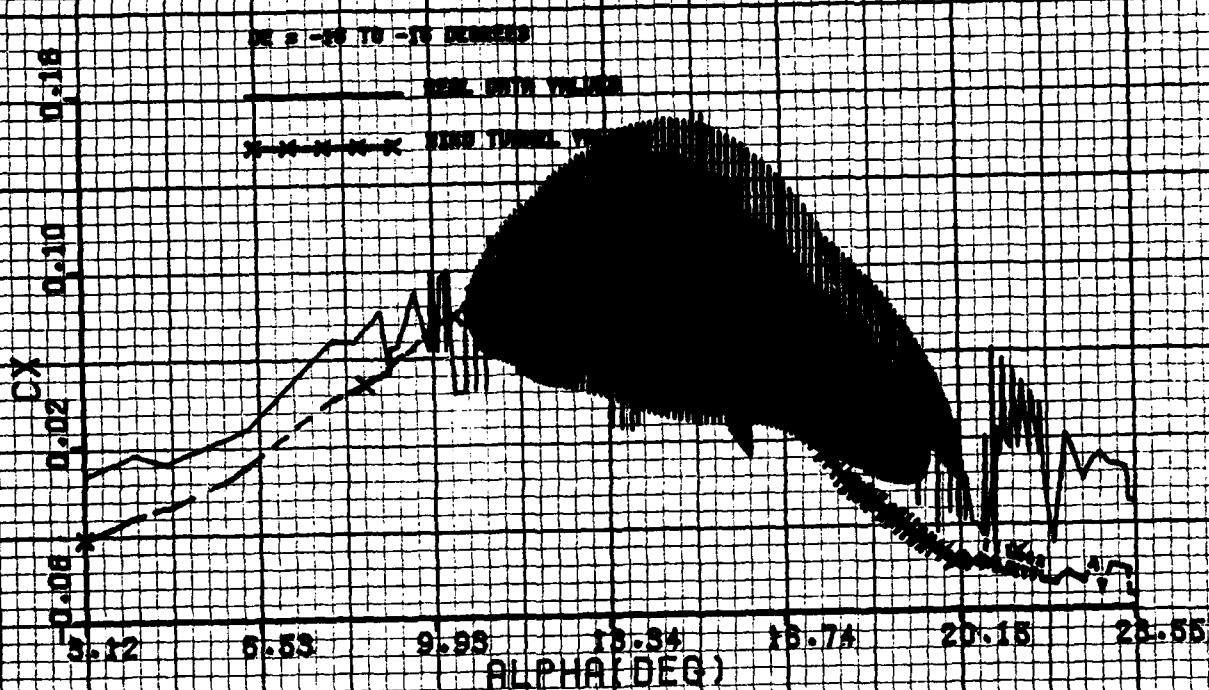


Figure H-8

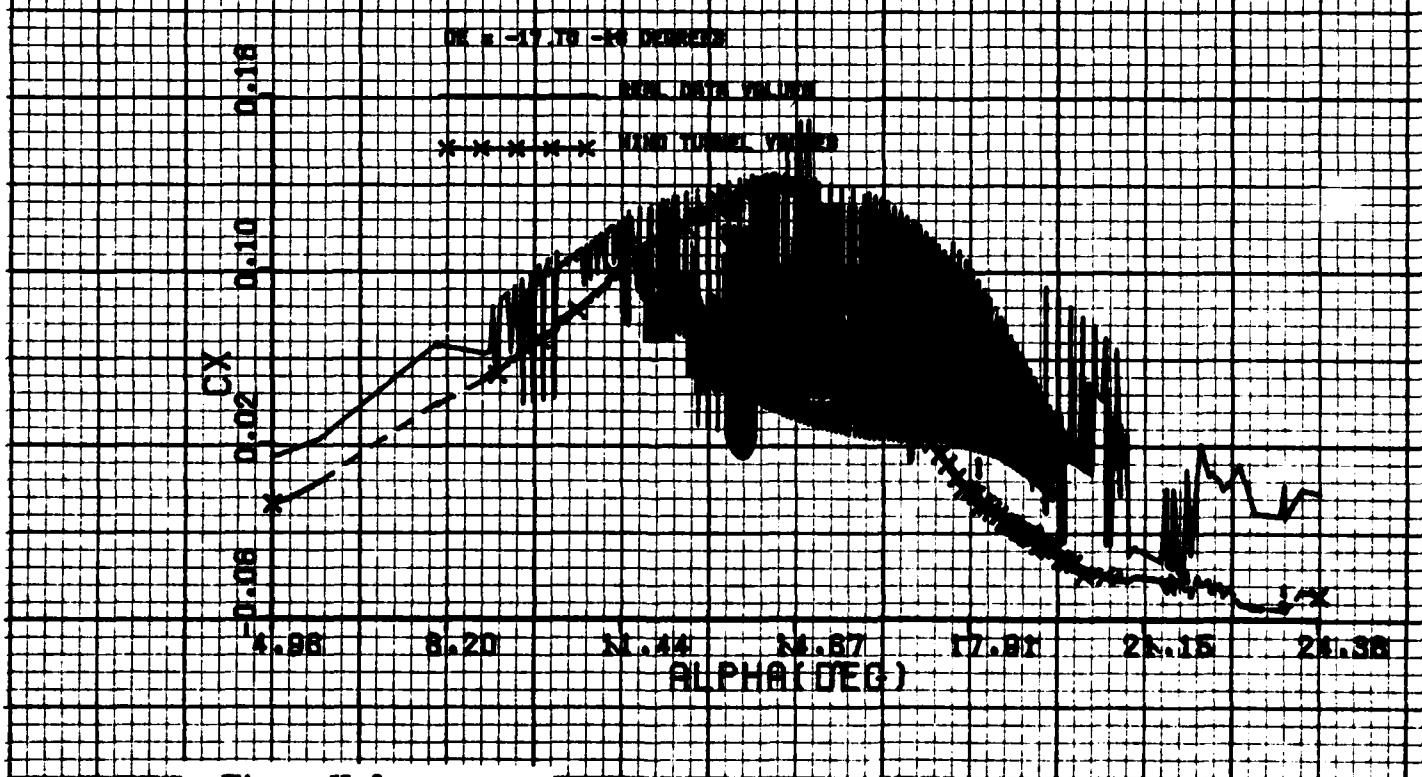
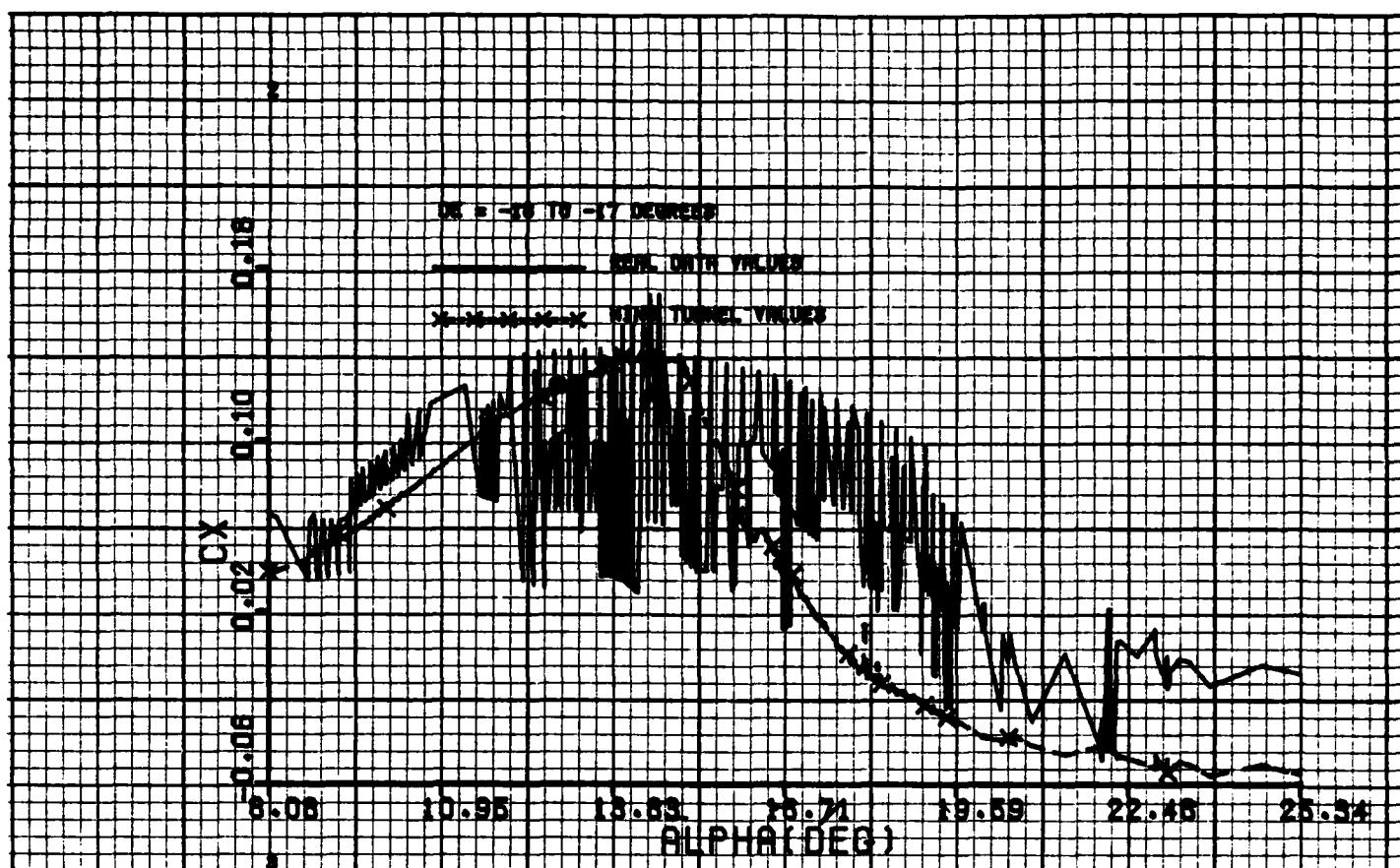


Figure H-9

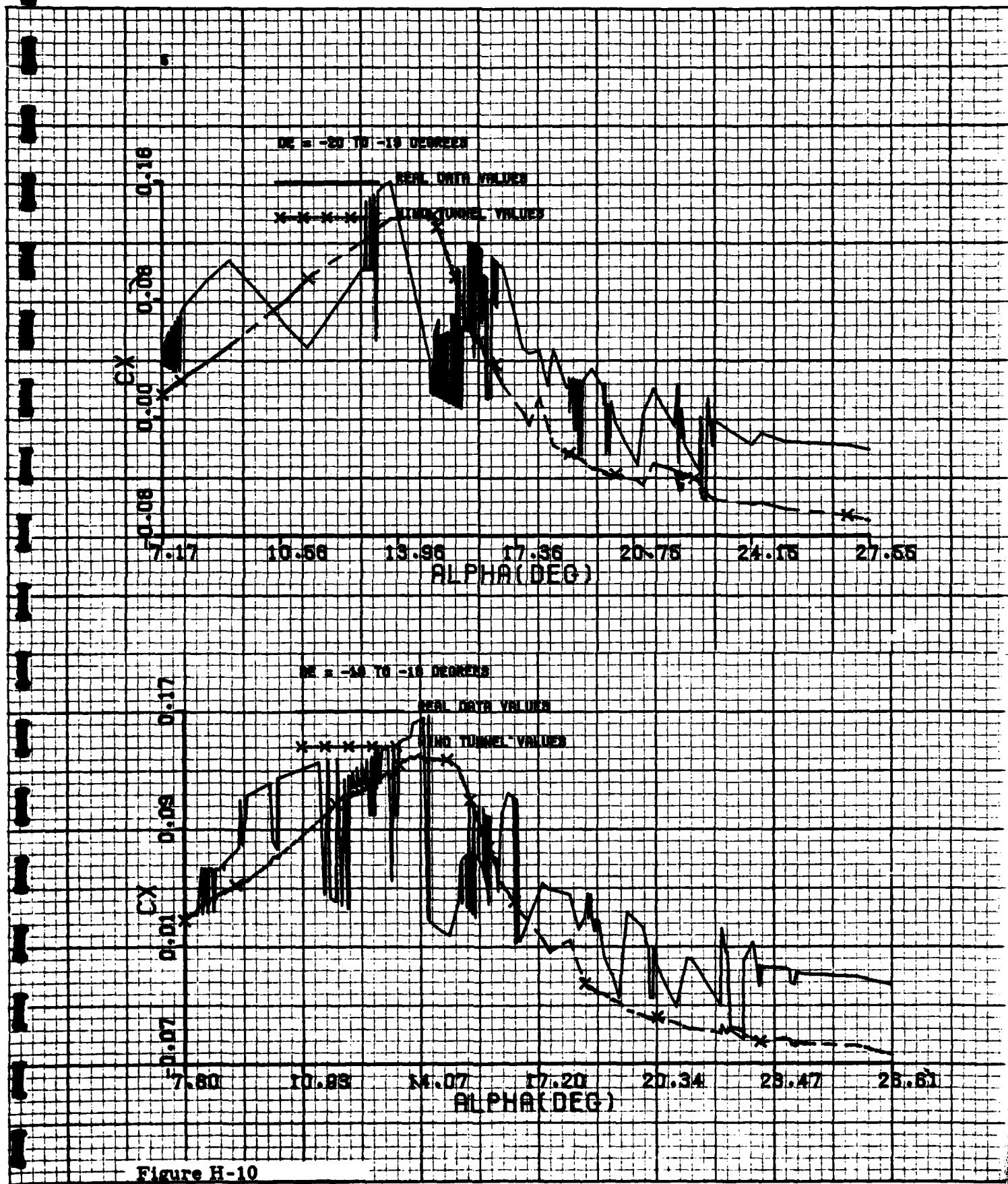


Figure H-10

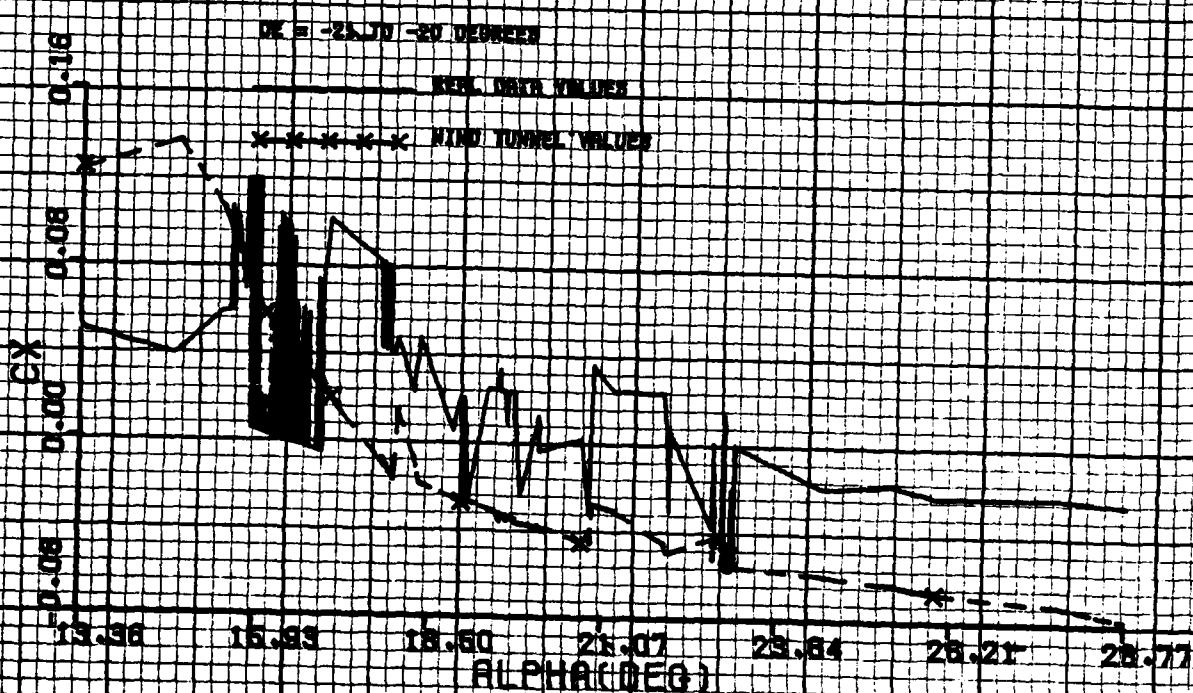
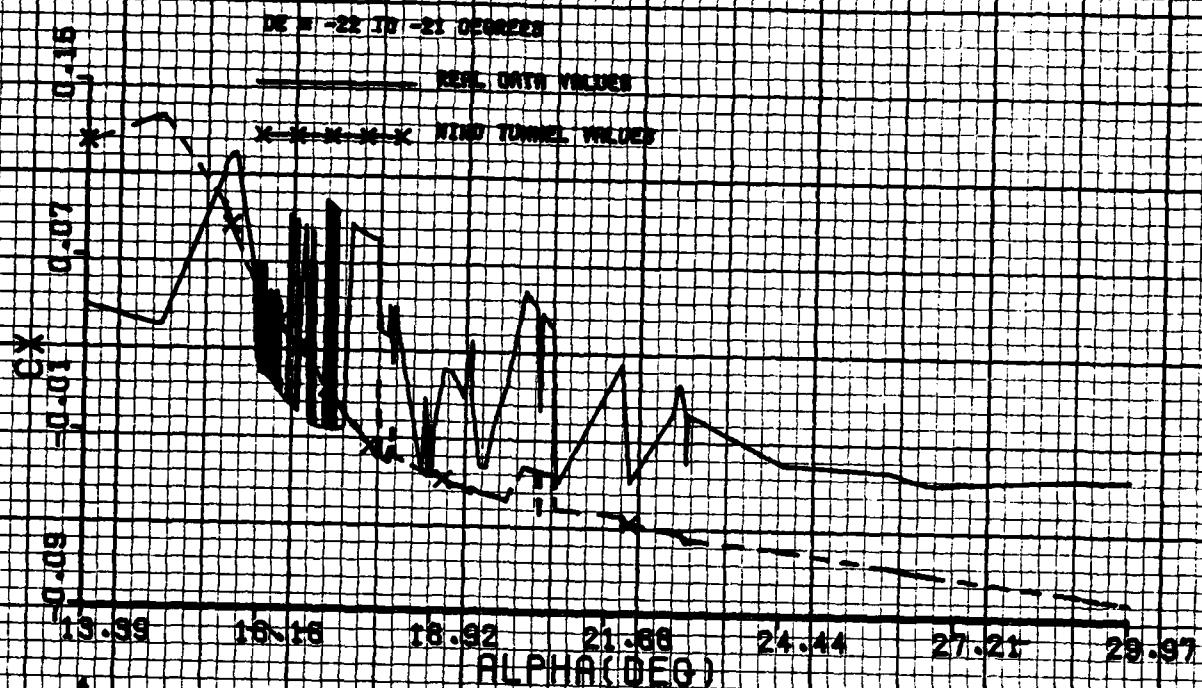


Figure H-11

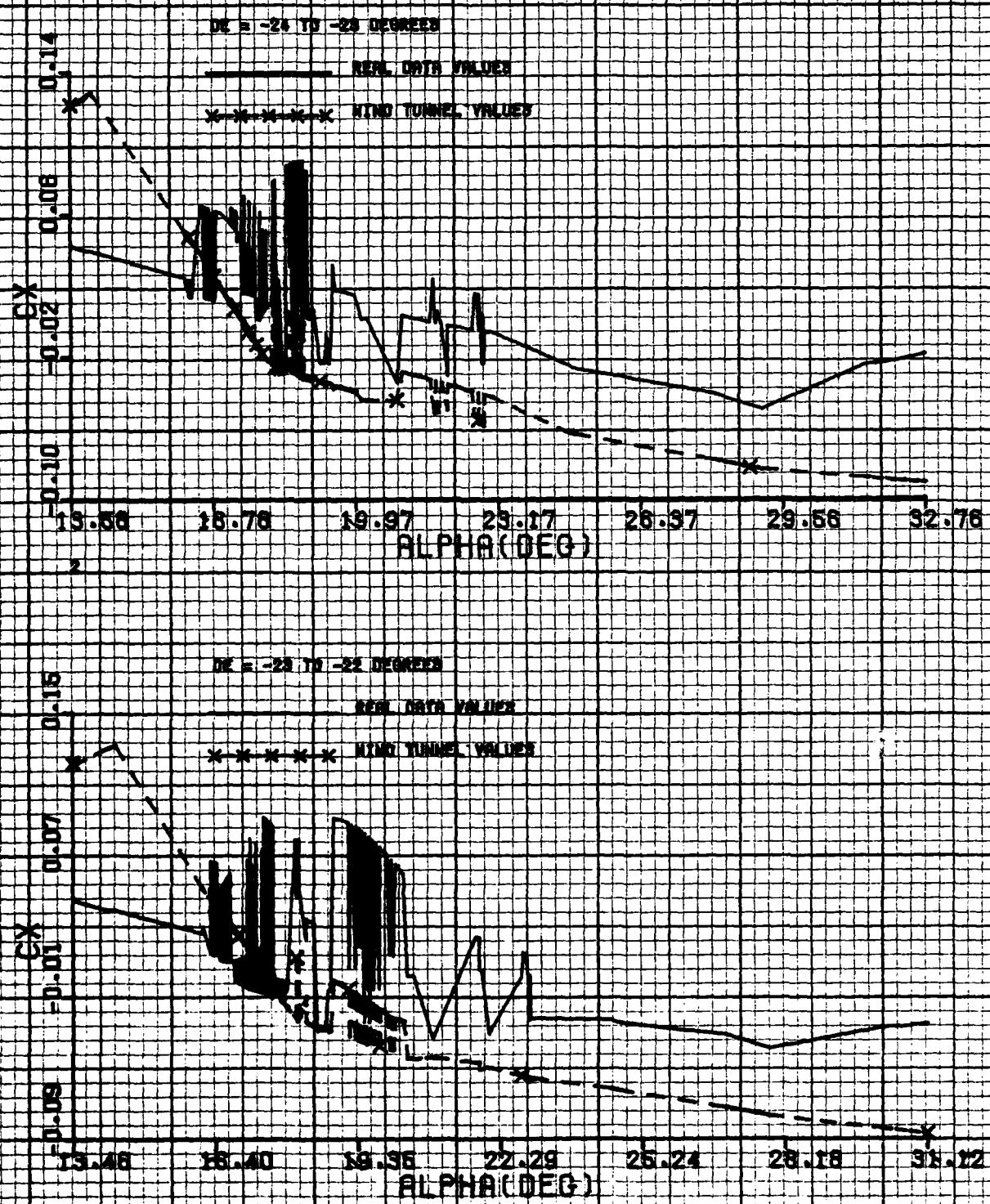


Figure H-12

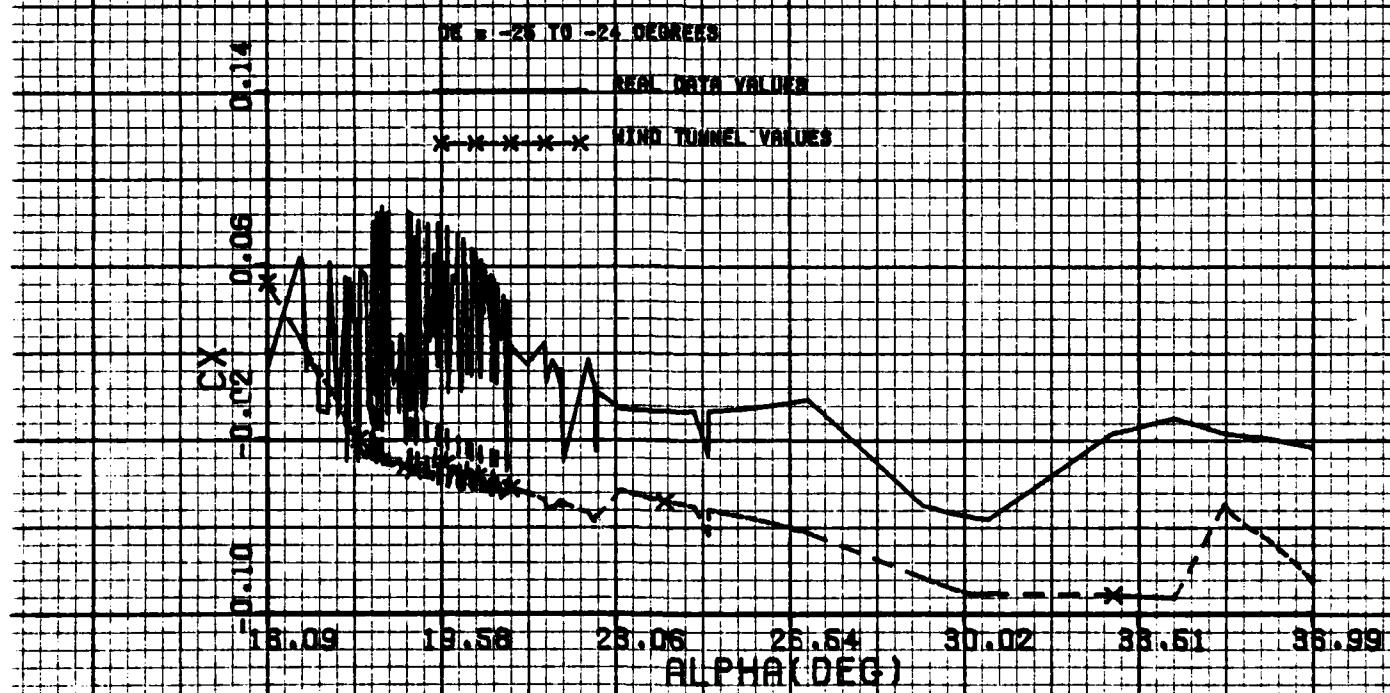
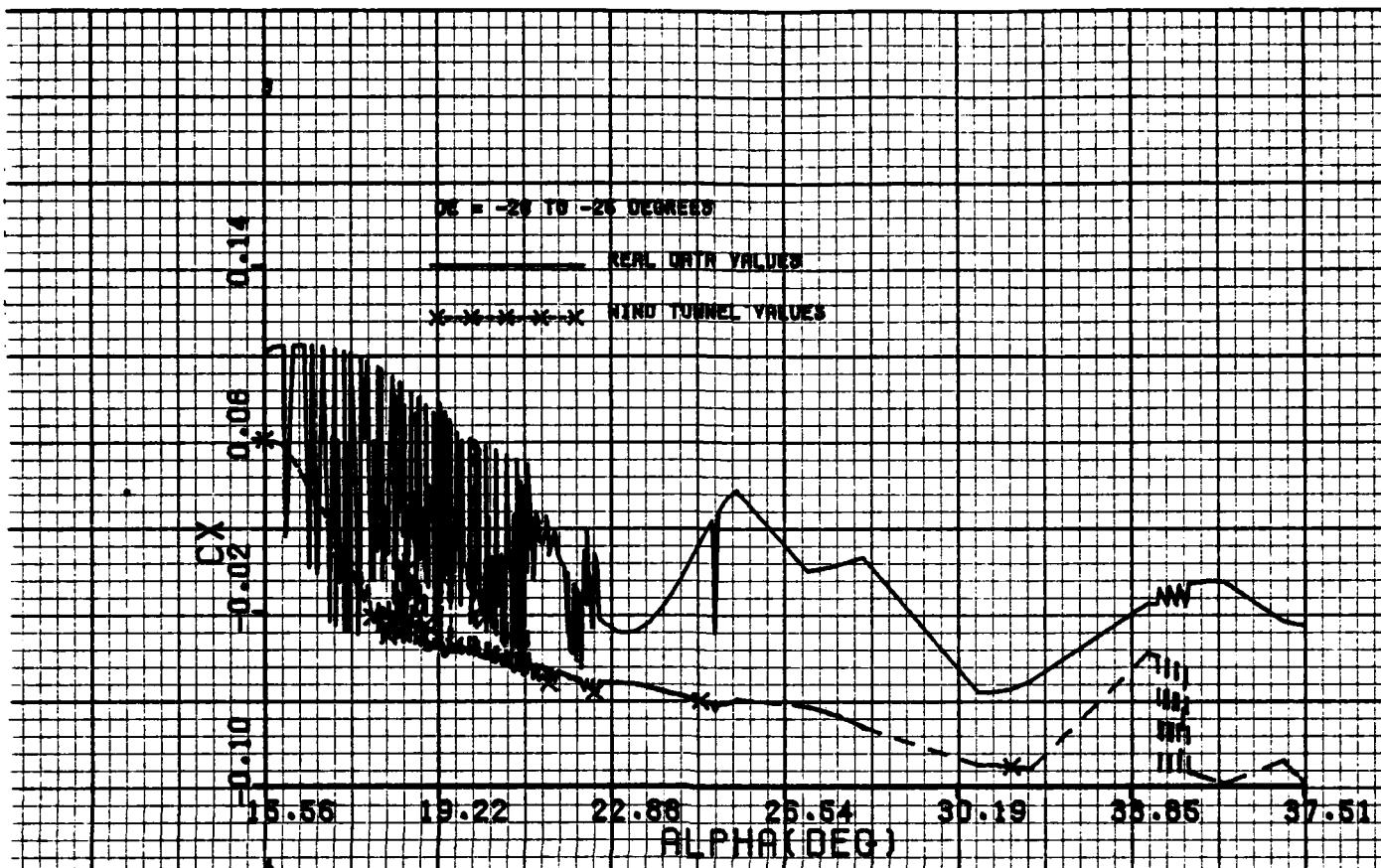


Figure H-13

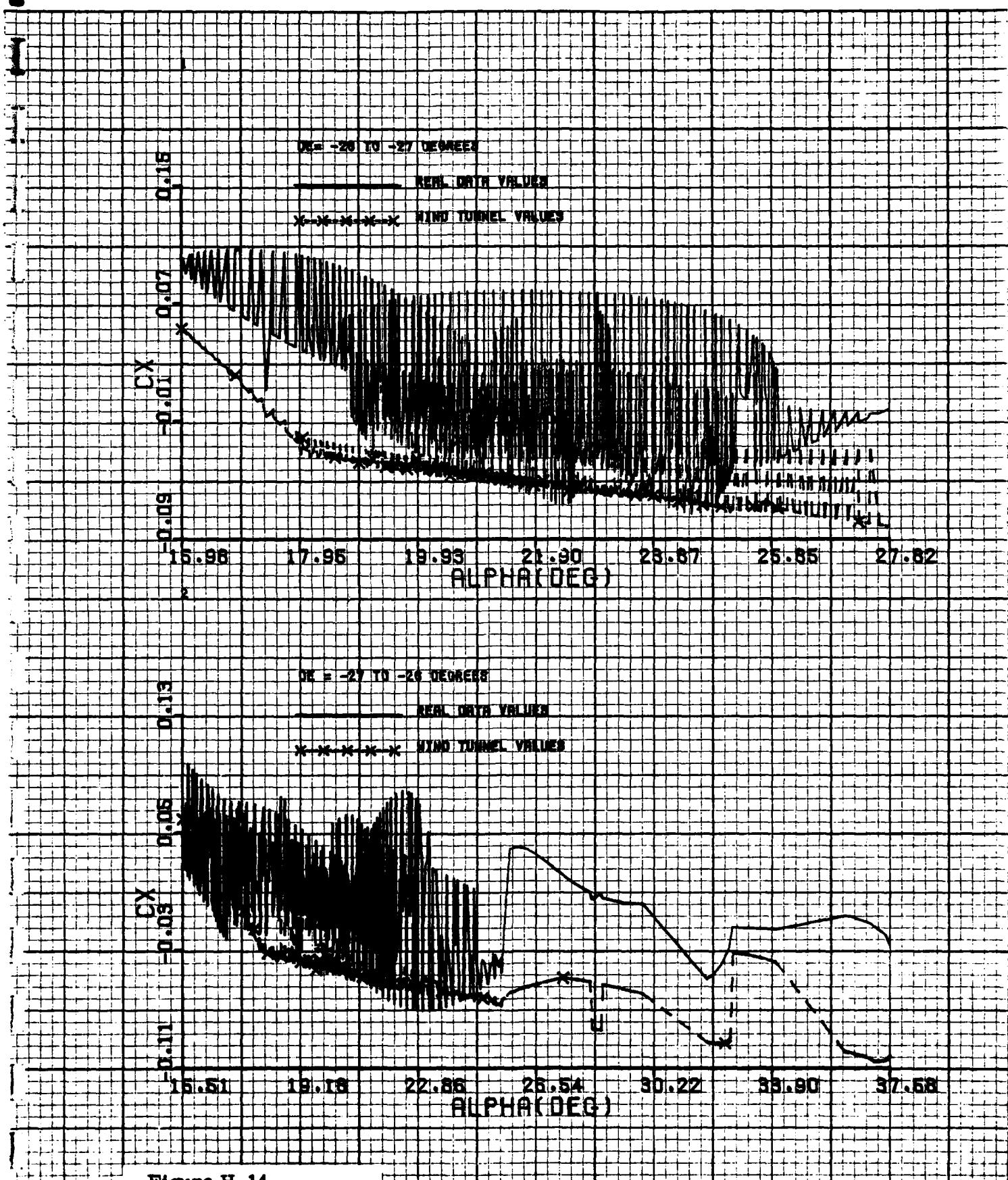


Figure H-14

APPENDIX I

MODELING RESULTS: C_m MODEL IN EQUATION FORM

This appendix contains the parametric model of the pitching moment coefficient C_m , identified using the EBM system identification method. The equation model identified for C_m is:

$$C_m = C_{m_0}(\delta_e) + C_{m_{\alpha_0}}(\delta_e) \cdot (\alpha - \alpha_1) + \sum_{i=1}^6 C_{m_{\alpha_i}}(\delta_e) \cdot g(\alpha, \alpha_i, \alpha_{i+1}) \\ + C_{m_q}(\alpha) \cdot q + C_{m_{\beta}}(\alpha) \cdot \dot{\alpha} + \sum_{j=1}^3 C_{m_{\beta_j}}(\alpha) \cdot h(\beta, \beta_j, \beta_{j+1})$$

where $\alpha_1, \dots, \alpha_7$ are the knots on the α -axis satisfying $-4 \leq \alpha_1 < \alpha_2 < \dots < \alpha_7$, where $\beta_1, \beta_2, \beta_3, \beta_4$ are the knots on the $|\beta|$ -axis satisfying $0 \leq \beta_1 < \beta_2 < \beta_3 < \beta_4$, where $g(\alpha, \alpha_i, \alpha_{i+1})$ is a quadratic spline function defined as

$$g(\alpha, \alpha_i, \alpha_{i+1}) = \begin{cases} 0 & \alpha < \alpha_i \\ \frac{1}{2}(\alpha - \alpha_i)^2 & \alpha_i \leq \alpha \leq \alpha_{i+1} \\ (\alpha_{i+1} - \alpha_i)(\alpha - \frac{1}{2}\alpha_i - \frac{1}{2}\alpha_{i+1}) & \alpha_{i+1} < \alpha \end{cases}$$

and where $h(\beta, \beta_j, \beta_{j+1})$ is a quadratic spline function defined as

$$h(\beta, \beta_j, \beta_{j+1}) = \begin{cases} 0 & |\beta| < \beta_j \\ \frac{1}{2}(|\beta| - \beta_j)^2 & \beta_j \leq |\beta| \leq \beta_{j+1} \\ (\beta_{j+1} - \beta_j)(|\beta| - \frac{1}{2}\beta_j - \frac{1}{2}\beta_{j+1}) & \beta_{j+1} < |\beta| \end{cases}$$

The identified parameters $C_{m_0}, C_{m_{\alpha_0}}, C_{m_{\alpha_0 \alpha_2}}, i = 1, 2, \dots, 6$,

are given in Table I-1 as functions of the elevator control δ_e . The tabulated values of these parameters hold at the midpoints of the δ_e intervals listed in the first column of the table. Interpolation is to be used in between midpoints. The knots $\alpha_1, \alpha_2, \dots, \alpha_7$ are presented in the table for each δ_e interval. For example, at $\delta_e = -14.5^\circ$, the knots are $\alpha_1 = 1^\circ, \alpha_2 = 14^\circ, \alpha_3 = 15^\circ, \alpha_4 = 18^\circ, \alpha_5 = 20^\circ$ and $\alpha_6 = 24^\circ$. The function $g(\alpha, \alpha_i, \alpha_{i+1})$ must be divided by the square of 57.29 whenever $\alpha, \alpha_i, \alpha_{i+1}$ are in degrees.

The identified parameters $C_{m_i}, i = 1, 2, 3, C_{m_q}, C_{m_{\dot{\alpha}}}$ are given in Tables I-2 and I-3 as functions of the angle of attack α . The tabulated values of these parameters hold at the midpoints of the α interval listed in the first column of the table. Interpolation is to be used in between midpoints. The knots $\beta_1, \beta_2, \beta_3, \beta_4$ are given in Table I-2 for each α interval. For example, at $\alpha = 14.5^\circ$, the knots are $\beta_1 = 0^\circ, \beta_2 = 5^\circ, \beta_3 = 10^\circ, \beta_4 = 15^\circ$. The function $h(\beta, \beta_i, \beta_{i+1})$ must be divided by the square of 57.29 whenever $\beta, \beta_i, \beta_{i+1}$ are in degrees.

Table I-1
Identified α -parameters of C_m Model

δ_e Interval (Deg) L. H. R. H.	C_{m_0}	$C_{m_{\alpha_0}}$ (per rad)	α Range (Deg)		Quadratic Spline Function Parameters	
			Low	High	Knots on α axis (Deg)	
-28 -27	.0993	-4.51	15.98	34.82	15, 18, 25, 30, 35	
-27 -26	.1152	-4.78	15.51	37.54	15, 18, 25, 30, 39	
-26 -25	.084	-4.71	15.56	37.51	15, 18, 25, 30, 39	
-25 -24	.066	-3.59	16.09	36.99	15, 18, 25, 30, 39	
-24 -23	.067	-1.90	14.00	32.76	14, 15, 18, 20, 25, 35	
-23 -22	.060	-2.13	14.00	31.12	14, 15, 18, 20, 25, 33	
-22 -21	.007	-.51	14.00	29.97	14, 15, 18, 20, 25, 32	
-21 -20	.117	-5.13	14.00	28.77	14, 15, 18, 20, 25, 31	
-20 -19	.256	-1.54	7.17	27.55	7, 14, 15, 18, 20, 25, 29	
-19 -18	.219	-1.03	7.80	26.61	7, 14, 15, 18, 20, 25, 28	
-18 -17	.204	-1.18	8.08	25.34	7, 14, 15, 18, 20, 25, 27	
-17 -16	.145	.66	5.00	25.38	5, 14, 15, 18, 20, 25, 26	
-16 -15	.168	.04	4.04	24.66	4, 14, 15, 18, 20, 25	
-15 -14	.164	.68	1.75	23.69	1, 14, 15, 18, 20, 24	
-14 -13	.157	.33	1.65	23.02	1, 14, 15, 18, 20, 24	
-13 -12	.158	.183	1.42	23.40	1, 14, 15, 18, 20, 25	
-12 -11	.156	-.117	1.01	23.49	1, 14, 15, 18, 20, 25	
-11 -10	.144	.008	1.00	23.43	1, 14, 15, 18, 20, 25	
-10 -9	.112	.026	1.00	22.51	1, 14, 15, 18, 20, 24	
-9 -8	.107	-.115	1.00	22.01	1, 14, 15, 18, 20, 23	
-8 -7	.133	-.415	-1.66	20.57	-2, 14, 15, 18, 20, 22	
-7 -6	.150	-.501	-3.00	20.27	-3, 14, 15, 18, 20, 21	
-6 -5	.109	-.21	-3.00	19.70	-3, 14, 15, 18, 20	
-5 -4	.143	-.83	-3.00	19.99	-3, 14, 15, 18, 20	
-4 -3	.143	-.98	-3.00	20.00	-3, 14, 15, 18, 20	
-3 -2	.125	-.795	-3.00	18.83	-3, 14, 15, 18, 19	
-2 1 -1	.111	-.92	-2.00	18.93	-2, 14, 15, 18, 19	
-1 0	.072	-1.03	-1.00	18.94	-1, 14, 15, 18, 19	
0 1	-.031	.0	3.55	17.97	3, 14, 15, 18	

Table I-1 (cont'd)

δ_e Interval (Deg) L.H. R.H.	Quadratic Spline Function Parameters (per rad ²)					
	$C_m \alpha_1^2$	$C_m \alpha_2^2$	$C_m \alpha_3^2$	$C_m \alpha_4^2$	$C_m \alpha_5^2$	$C_m \alpha_6^2$
-28 -27	85.76	-7.34	11.21	-3.09	-	-
-27 -26	85.76	-7.34	11.21	-3.09	-	-
-26 -25	85.76	-7.34	11.21	-3.09	-	-
-25 -24	60.55	-7.68	14.72	-3.12	-	-
-24 -23	0.0	13.90	9.63	15.87	-19.15	-
-23 -22	0.0	28.85	-32.18	29.14	-21.8	-
-22 -21	0.0	-17.37	3.23	21.44	-21.32	-
-21 -20	69.02	0.0	-27.3	28.14	11.57	-17.58
-20 -19	-8.45	103.88	-13.05	17.48	12.49	-21.17
-19 -18	-12.66	82.4	1.96	12.21	6.37	-18.92
-18 -17	-9.09	77.8	-11.54	36.96	-2.63	17.72
-17 -16	-20.87	89.72	-14.22	58.31	-16.66	26.54
-16 -15	-12.37	23.17	9.69	29.43	-11.48	-
-15 -14	-13.6	54.2	1.30	63.41	-55.5	-
-14 -13	-10.83	-8.55	38.94	27.3	-68.6	-
-13 -12	-10.60	30.2	27.84	22.4	-50.8	-
-12 -11	-8.11	-13.65	55.05	-40.84	-6.91	-
-11 -10	-9.56	73.9	-5.70	48.6	-29.8	-
-10 -9	-8.48	21.83	21.84	10.37	-27.75	-
-9 -8	-7.28	-45.99	60.42	-45.77	34.4	-
-8 -7	-2.95	-17.85	2.94	56.71	-13.75	-
-7 -6	-2.61	-20.18	9.83	43.06	-	-
-6 -5	-4.28	9.96	11.87	-70.1	-	-
-5 -4	-.69	-152.6	89.53	-204.1	-	-
-4 -3	-.11	-44.1	-16.75	148.0	-	-
-3 -2	-1.62	-41.6	23.57	176.	-	-
-2 -1	-1.24	-75.0	28.9	182.	-	-
-1 0	-.95	-42.5	32.0	32.0	-	-
0 1	-6.50	-126.15	27.58	-	-	-

Table I-2
Identified β -parameters of C_m Model

α Interval (Deg) L.H. R.H.	$C_m \beta_0$ (per rad)	Quadratic Spline Function Parameter (per rad ²)				Knots on $ \beta $ axis (Deg)
		$C_m \beta_1^2$	$C_m \beta_2^2$	$C_m \beta_3^2$		
-4 6	-.183	-.413	-	-	-	0, 10
6 7	-.183	-.413	-	-	-	0, 12
7 8	.137	-3.09	-	-	-	0, 13
8 9	.132	-3.14	-	-	-	0, 13
9 10	.118	-2.68	-	-	-	0, 14
10 11	-.02	-1.06	-	-	-	0, 14
11 12	-.075	-.366	-	-	-	0, 14
12 13	.37	-10.01	13.51	-19.6	-	0, 15, 10, 16
13 14	.53	-10.90	6.2	1.54	-	0, 5, 10, 16
14 15	.66	-12.91	7.98	-17.34	-	0, 5, 10, 15
15 16	.35	-6.66	2.23	-8.09	-	0, 5, 10, 15
16 17	-.000	2.08	-7.87	11.47	-	0, 5, 10, 15
17 18	.19	-.561	.26	-	-	0, 10, 18
18 19	-.15	2.80	-4.4	-	-	0, 10, 18
19 20	-.148	1.36	-.32	-	-	0, 10, 18
20 21	-.11	1.56	-3.97	-	-	0, 10, 18
21 22	.002	-.23	3.57	-	-	0, 10, 20
22 23	-.32	3.44	-3.89	-	-	0, 10, 20
23 24	-.52	3.18	2.75	-	-	0, 10, 23
24 40	-.52	3.18	2.75	-	-	0, 10, 24

Table I-3
Identified dynamic derivatives of C_m model

α Interval (Deg) L.H. R.H.	C_{m_q} (per rad)	$C_{m_{\dot{\alpha}}}$ (per rad)
-4 -1	-8.03	-.232
-1 0	-8.03	-.232
0 1	-8.37	-.232
1 2	-9.16	-.232
2 3	-9.715	-.232
3 4	-10.49	-.232
4 5	-11.41	-.232
5 6	-10.64	-.232
6 7	-8.85	-.232
7 8	-7.15	-.232
8 9	-5.64	-.232
9 10	-3.92	-.232
10 11	-.51	-.232
11 12	3.16	-.232
12 13	5.44	-.232
13 14	5.61	-.232
14 15	3.97	-.76
15 16	1.11	-1.45
16 17	-2.78	-2.26
17 18	-6.47	-2.58
18 19	-7.70	-1.68
19 20	-7.26	-1.08
20 21	-6.74	-.85
21 22	-6.24	-.89
22 23	-6.31	-.93
23 24	-6.38	-.97
24 25	-6.45	-1.01
25 30	-6.66	-1.14
30 35	-7.00	-1.39
35 40	-7.35	-1.68